N-63-4-3

ASTIA Document No. 05361 1-T

THE UNIVERSITY OF MICHIGAN

CATALOGED BY DDC
AS AD No. 410028

NOISE TRANSPORT IN CROSSED-FIELD DEVICES

TECHNICAL REPORT NO. 55

ELECTRON PHYSICS LABORATORY

Department of Electrical Engineering

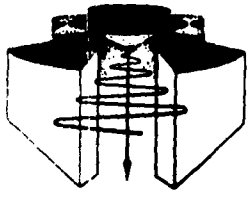

By: Jaminder P. Wadhwa

Approved By: J. E. Rowe

December, 1962

CONTRACT WITH:

THE SIGNAL CORPS, THE U. S. ARMY ELECTRONICS RESEARCH AND DEVELOPMENT LABORATORY, FORT MONMOUTH, NEW JERSEY. DEPARTMENT OF THE ARMY PROJECT NO. 3A99-13-001, CONTRACT NO. DA-36-039 AMC-00027(E).

OFFICE OF RESEARCH ADMINISTRATION · ANN ARBOR

Qualified requesters may obtain copies of this report from ASTIA.

ERRATA

for

NOISE TRANSPORT IN CROSSED-FIELD DEVICES

by

Rajindar P. Wadhwa

Electron Physics Laboratory Technical Report No. 55,
Contract DA-36-039 AMC-00027(E)

Page 122 Equation 4.61 should read:

$$\dot{y}_o = \left[2\eta V + \bar{\dot{y}}_i^2 - \omega_c^2(y+y_m)^2 - 2\omega_c(y+y_m)\,\bar{\dot{z}}_i\right]^{1/2}$$

Page 134 The right-hand side of Eq. 5.5 should read:

$$= 2\pi\, e^{-(-2\eta V_m + \omega_c^2 y_m^2)\frac{mA_1^2}{kT}} .$$

Page 136 The ordinate is f.

Page 162 The small "162" should be deleted.

Page 214 Equation 6.44 should read:

$$\vec{\tilde{V}}_i(t_i) = -\frac{m}{|e|}\left[\vec{i}\,\lambda_2\,\tilde{\dot{z}}_i(t_i) + \vec{j}\,\mu_2\,\tilde{\dot{y}}_i(t_i)\right][u_{o_i}]$$

Page 218 A bracket is missing from Eq. 6.55a. It should read:

$$R_{\tilde{V},\tilde{I}}(\mu,i) = -\left[\frac{u_{o_i}A_i}{\eta}\right]\frac{1}{N-\mu}\sum_{\nu=1}^{N-\mu}\left[\lambda_1\lambda_2\,\tilde{\dot{z}}(\nu,i)\cdot\tilde{J}_z(\nu+\mu,i) + \mu_1\mu_2\tilde{\dot{y}}(\nu,i)\,\tilde{J}_y(\nu+\mu,i)\right]$$

Page 229 Delete "159" from Table 7.1.

Pages 255 and 256 In Figs. 7.9 and 7.10 the scale for μ should be 0, 20, 40, 60, 80 and 100.

Page 272 The abscissa should be labeled "frequency".

Page 273 Equation 7.16 should read:

$$F = 10 \log_{10}\left[1 + \frac{S-N}{S_o} \frac{T_c}{T}\right]$$

THE UNIVERSITY OF MICHIGAN
ANN ARBOR, MICHIGAN

NOISE TRANSPORT IN CROSSED-FIELD DEVICES

TECHNICAL REPORT NO. 55

Electron Physics Laboratory
Department of Electrical Engineering

By

Rajindar P. Wadhwa

Approved by: J. E. Rowe

J. E. Rowe, Director
Electron Physics Laboratory

Project 05361

CONTRACT NO. DA-36-039 AMC-00027(E)
SIGNAL CORPS, DEPARTMENT OF THE ARMY
DEPARTMENT OF THE ARMY PROJECT NO. 3A99-13-001
PLACED BY THE U.S. ARMY ELECTRONICS RESEARCH AND DEVELOPMENT LABORATORY
FORT MONMOUTH, NEW JERSEY

December, 1962

This report has also been submitted as a dissertation in partial fulfillment of the requirements for the degree of Doctor of Science in The University of Michigan, 1962.

ABSTRACT

The general purpose of this study is to investigate noise transport in crossed-field devices. The present study refers to injected-beam crossed-field devices, but the results could easily be applied to the investigation of analogous phenomena in magnetrons and other types of crossed-field devices utilizing non-Cartesian geometry.

Most of the material in this report relates to noise transport in the electron gun region, but some results based upon the Llewellyn-Peterson equations and experimental studies refer to noise transport in the interaction region also. The results obtained for the gun region could easily be applied to cycloiding beams in the interaction region.

Appropriate Llewellyn-Peterson equations are derived by taking into account both current density components, and the final noise transport equations are written in a general form so that these coefficients could be evaluated for any physical model for which the velocity components and their time derivatives are specified. These coefficients are evaluated in the gun region for different physical models and for several particular cases. For the interaction region these coefficients are evaluated for ideal conditions as well as for arbitrary input conditions which will usually lead to cycloiding beams in the interaction region. The velocity fluctuations are decreased while the current fluctuations are increased providing the perturbation frequency is increased. The perturbations are found to increase as ω_p/ω_c is increased.

On the basis of a Maxwellian velocity distribution, expressions are derived for the space-charge density and voltage distribution in the potential minimum region and the gun region. From the boundary conditions the unknown parameters y_m and V_m are evaluated for a special case and several d-c parameters are evaluated for two values of the cyclotron frequency. Introducing a small-signal perturbation in the d-c parameters and using the equations of motion for an electron along with Maxwell's equations permits the determinantal equation to be derived. This determinantal equation is solved for several cases in order to determine the propagation of a perturbation originating at the potential minimum. The synchronous wave and the two space-charge waves are attenuated during the earlier part of the cycloid. During the latter part of the first half cycloid the synchronous wave is increasingly attenuated while the two space-charge waves are amplified. These results are compared for several values of ω and ω_c.

In the Monte Carlo technique, the equations of motion for an electron are numerically integrated to determine the position and velocity coordinates. Electrons are generated in a random manner and the two velocity components and the emission time associated with these electrons are also generated in a random manner. In the first phase of the program some initial conditions are specified in order to fill the diode. In the second phase the electrons drift according to the space-charge fields determined by the distribution of the electrons. The three-dimensional

space-charge potential is derived using Green's function and is self-consistent. In the third phase the instantaneous velocity components and the electron distribution are determined for a larger number of unit time intervals. Fluctuations in the current and velocity components are determined in order to evaluate the spectral power densities and consequently the noise figure of the various portions of the beam.

It is found that the current fluctuations are greatly reduced because of the presence of the potential minimum although the velocity fluctuations are not reduced but increased as the beam is accelerated. These velocity fluctuations are decreased as the beam is decelerated. However, in traversing a complete cycloid there is an overall growth in the velocity fluctuations which are larger at the inner edge of the beam. The slow and fast space-charge waves experience similar changes although the overall growth for the slow wave is larger than that for the fast wave in traversing a complete cycloid. Similarly there is an overall increase in the value of the noise figure in traversing a complete cycloid and this value is found to decrease as the frequency is increased.

The dependence of the frequency and the strength of the r-f signal as a result of internal oscillations on the various d-c parameters are measured experimentally. It is noticed that these oscillations can be controlled by adjusting the d-c parameters. The effect of one beam on the other as a result of bending of the first beam in a crossed-field geometry is discussed. The emission from one part of the cathode is considerably affected due to bending of the beam from the other part and thus causing a space-charge depression in front of the first part. The electron equivalent temperature is evaluated from volt-ampere characteristics. The dependence of the propagation of an r-f signal injected near the cathode on the various d-c parameters is measured. Variation of the r-f signal along the beam in the interaction region is also measured. The propagation of a signal along the beam can be controlled by adjusting the various d-c parameters. This study has been limited up to 250 mc since for higher frequencies the direct r-f transmission is found to be very high and any change due to the presence of the beam cannot be detected.

ACKNOWLEDGMENTS

The author wishes to express his gratitude to Professor Joseph E. Rowe, the chairman of his doctoral committee, for his guidance and helpful suggestions during the course of this work. The contributions of E. Fronczak and A. Collins in programming the computer are acknowledged. The various parts of the noise analyzer were machined by H. Sanford and O. Wagner. The device was assembled by D. Williams and J. Murphy. R. Burris made several helpful suggestions regarding the design of the noise analyzer and K. McCrath contributed in making the instrumentation panel. Special thanks are due to those who assisted in preparing this text.

TABLE OF CONTENTS

	Page
ABSTRACT	iii
ACKNOWLEDGMENTS	v
LIST OF ILLUSTRATIONS	ix
LIST OF TABLES	xvii
CHAPTER I. INTRODUCTION	1
1.1 Noise in Crossed-Field Devices	1
1.2 Previous Studies of Noise in Crossed-Field Devices	5
1.3 Outline of the Present Analysis	9
CHAPTER II. DEVELOPMENT OF LLEWELLYN-PETERSON EQUATIONS	12
2.1 Introduction	12
2.2 Assumptions Made in This Analysis	15
2.3 Trajectory Equations	15
2.4 Perturbation Techniques for the Derivation of the Final Noise Transport Equations	26
2.5 Derivation of Coefficients in Terms of y-Component D-c Velocity	32
2.6 Some Checks on the Primed and Unprimed Coefficients	36
2.6.1 No Magnetic Field	36
2.6.2 Correspondence Between the Primed and Unprimed Coefficients	37
2.6.3 Comparison with Van Duzer's Coefficients	38
2.7 Propagation of Perturbations in the Interaction Region	38
CHAPTER III. RESULTS OF LLEWELLYN-PETERSON ANALYSIS	43
3.1 Introductory Remarks	43
3.2 Cyclotron Frequency Perturbation	44
3.3 Numerical Evaluation of the Coefficients	45
3.4 Arbitrary Input Conditions in the Interaction Region	69
3.5 Evaluation of the A-c Fluctuations in Terms of a Single Variable	85
3.6 Conclusions	100
CHAPTER IV. DEVELOPMENT OF DENSITY FUNCTION ANALYSIS	102
4.1 Introduction	102
4.2 Assumption Made in This Analysis	103

Page

4.3 Derivation of Steady-State Space-Charge Density (Boundary Value Problem) 105
4.4 Derivation of the Initial Normal Critical Velocity and the Two Velocity Components 112
4.5 Potential Variation Along the Beam (Boundary Value Problem) 117
4.6 Derivation of Expressions for the Space-Charge Density and Other Related Functions (Initial Value Problem) 119
4.7 Propagation of a Perturbation Along the Beam 125

CHAPTER V. RESULTS OF DENSITY FUNCTION ANALYSIS 132

5.1 Evaluation of the Parameters V_m and y_m 132
5.2 Normalized Current Transmitted Across the Potential Minimum 140
5.3 Evaluation of Space-Charge Density and Other Related Functions 143
5.4 Numerical Results for the D-c Parameters 150
5.5 Evaluation of Noise Transport in the Gun Region 159
5.6 Application of the Results to Various Cases 174
5.7 Conclusions 186

CHAPTER VI. DERIVATION OF MONTE CARLO EQUATIONS 188

6.1 Introduction 188
6.2 Assumptions Made in This Analysis 191
6.3 Random Electron Emission Number 192
6.4 Random Electron Emission Velocity 193
6.5 Random Electron Emission Time 195
6.6 Trajectory Equations for Electrons 197
6.7 Derivation of the Three-Dimensional Space-Charge Potential and Fields 200
6.8 Space-Charge Weighting Constants 205
6.9 A-c Electric Fields, Velocities and Current Densities 207
6.10 Correlation Functions and Spectra of Diode Noise 213

CHAPTER VII. RESULTS OF MONTE CARLO ANALYSIS 226

7.1 Introduction 226
7.2 Choice of Parameters 226
7.2.1 Spatial Division of the Diode 226
7.2.2 Choice of Unit Time Interval 230
7.2.3 Number of Electrons Emitted Per Unit Time Interval 231
7.3 Initial Conditions and Execution of the Program 236
7.4 Results 241
7.5 Correlation Functions 253
7.6 Noise Parameters 254
7.7 Conclusions 276

		Page
CHAPTER VIII.	EXPERIMENTAL INVESTIGATION OF NOISE IN INJECTED-BEAM CROSSED-FIELD DEVICES	279
8.1	Introduction	279
8.2	The Electron Gun	281
8.3	The Sole and the Sole Segments	292
8.4	The Slotted Anode	295
8.5	The Collector	295
8.6	R-f Injection and Detection	295
8.7	Push-Pull Seal and Driving Mechanism	297
CHAPTER IX.	EXPERIMENTAL RESULTS	307
9.1	Introductory Remarks	307
9.2	Evaluation of Electron Equivalent Temperature	319
9.3	R-f Studies of the Beam	327
9.4	Variation of R-f Signal Along the Beam	330
9.5	R-f Injection	336
CHAPTER X.	SUMMARY, CONCLUSIONS AND SUGGESTIONS FOR FURTHER STUDY	345
10.1	Summary and Conclusions	345
10.2	Suggestions for Further Study	349
APPENDIX A.	DERIVATION OF THE TIME PERTURBATION δ_z	353
APPENDIX B.	DERIVATION OF INITIAL CONDITIONS	356
APPENDIX C.	DERIVATION OF THE MATRIX COEFFICIENTS FOR NOISE TRANSPORT EVALUATIONS	358
APPENDIX D.	REDUCTION OF NOISE TRANSPORT COEFFICIENTS TO VAN DUZER'S COEFFICIENTS	363
APPENDIX E.	DERIVATION OF EXPRESSIONS FOR E_{z_1} AND E_{y_1}	367
APPENDIX F.	DERIVATION OF THE THREE-DIMENSIONAL SPACE-CHARGE POTENTIAL	373
APPENDIX G.	AVERAGING METHODS FOR VELOCITY AND CURRENT-DENSITY COMPONENTS	379
APPENDIX H.	DERIVATION FOR THE FINAL POWER SPECTRUM FOR FINITE DISCRETE DATA	386
BIBLIOGRAPHY		389
LIST OF SYMBOLS		392

LIST OF ILLUSTRATIONS

Figure		Page
2.1	Schematic of an Ideal Steady-State Electron Beam in a Crossed-Field Device.	14
2.2	Comparison of the Normalized z-Component as a Function of $\omega_c T$ with that of Leblond. $(0 \leq \omega_c T \leq \pi)$	24
2.3	Comparison of the Normalized y-component as a Function of $\omega_c T$ with that of Leblond. $(0 \leq \omega_c T \leq \pi)$	25
2.4	Ideal Beam in the Interaction Region.	40
3.1	$\lvert a_{22} + a_{23} \rvert$ vs. $\omega_c T/\pi$. Interaction Region, Temperature-Limited Case, Kino Gun.	51
3.2	$\lvert a_{24} + a_{25} \rvert/\omega_c^2$ vs. $\omega_c T/\pi$. Interaction Region, Temperature-Limited Case, Kino Gun.	52
3.3	$\lvert a_{32} + a_{33} \rvert$ vs. $\omega_c T/\pi$.	53
3.4	$\lvert a_{34} + a_{35} \rvert/\omega_c^2$ vs. $\omega_c T/\pi$.	54
3.5	$\lvert a_{42} + a_{43} \rvert$ ω_c^2 vs. $\omega_c T/\pi$.	55
3.6	$\lvert a_{44} + a_{45} \rvert$ vs. $\omega_c T/\pi$.	56
3.7	$\lvert a_{52} + a_{53} \rvert$ ω_c^2 vs. $\omega_c T/\pi$.	57
3.8	$\lvert a_{54} + a_{55} \rvert$ vs. $\omega_c T/\pi$.	58
3.9	$\lvert a_{22} + a_{23} \rvert$ vs. $\omega_c T/\pi$.	60
3.10	$\lvert a_{24} + a_{25} \rvert/\omega_c^2$ vs. $\omega_c T/\pi$.	61
3.11	$\lvert a_{32} + a_{33} \rvert$ vs. $\omega_c T/\pi$.	62
3.12	$\lvert a_{34} + a_{35} \rvert/\omega_c^2$ vs. $\omega_c T/\pi$.	63
3.13	$\lvert a_{42} + a_{43} \rvert$ ω_c^2 vs. $\omega_c T/\pi$.	64
3.14	$\lvert a_{44} + a_{45} \rvert$ vs. $\omega_c T/\pi$.	65
3.15	$\lvert a_{52} + a_{53} \rvert$ ω_c^2 vs. $\omega_c T/\pi$.	66
3.16	$\lvert a_{54} + a_{55} \rvert$ vs. $\omega_c T/\pi$.	67

Figure		Page
3.17	The First Cycles of the Trajectories of a Cycloiding Beam.	71
3.18	Electron Trajectories for Arbitrary Input Conditions in the Crossed-Field Interaction Region.	75
3.19	$\lvert a_{32} + a_{33} \rvert$ vs. $\omega_c T/\pi$ for Interaction Region.	77
3.20	$\lvert a_{34} + a_{35} \rvert / \omega_c^2$ vs. $\omega_c T/\pi$ for Interaction Region.	78
3.21	$\lvert a_{42} + a_{43} \rvert \ \omega_c^2$ vs. $\omega_c T/\pi$ for Interaction Region.	79
3.22	$\lvert a_{44} + a_{45} \rvert$ vs. $\omega_c T/\pi$ for Interaction Region.	80
3.23	$\lvert a_{52} + a_{53} \rvert \ \omega_c^2$ vs. $\omega_c T/\pi$ for Interaction Region.	81
3.24	$\lvert a_{54} + a_{55} \rvert$ vs. $\omega_c T/\pi$ for Interaction Region.	82
3.25	A_{11} vs. $\omega_c T/\pi$. $(\omega_p/\omega_c = 0.8)$	88
3.26	A_{11} vs. $\omega_c T/\pi$. $(\omega_p/\omega_c = 1.0)$	89
3.27	A_{11} vs. $\omega_c T/\pi$. $(\omega_p/\omega_c = 1.2)$	90
3.28	A_{12} vs. $\omega_c T/\pi$. $(\omega_p/\omega_c = 0.8)$	91
3.29	A_{12} vs. $\omega_c T/\pi$. $(\omega_p/\omega_c = 1.0)$	92
3.30	A_{12} vs. $\omega_c T/\pi$. $(\omega_p/\omega_c = 1.2)$	93
3.31	A_{13} vs. $\omega_c T/\pi$. $(\omega_p/\omega_c = 0.8)$	94
3.32	A_{13} vs. $\omega_c T/\pi$. $(\omega_p/\omega_c = 1.0)$	95
3.33	A_{13} vs. $\omega_c T/\pi$. $(\omega_p/\omega_c = 1.2)$	96
3.34	A_{14} vs. $\omega_c T/\pi$. $(\omega_p/\omega_c = 0.8)$	97
3.35	A_{14} vs. $\omega_c T/\pi$. $(\omega_p/\omega_c = 1.0)$	98
3.36	A_{14} vs. $\omega_c T/\pi$. $(\omega_p/\omega_c = 1.2)$	99
4.1	A Filamentary Beam in the Gun Region (Position of Potential Minimum Exaggerated).	104
4.2	Potential Distribution Assumed to Derive an Expression for the Initial Normal Critical Velocity.	114

Figure		Page
5.1	f vs. s_1'. ($\omega_c = \omega_{cc}$)	136
5.2	The Variation of the Normalized V_m and y_m as a Function of ω_c. ($I_s = 0.5 \times 10^4$ Amps/m^2, T = 1000° K, $\omega_{cc} = 2.66 \times 10^9$ Rad/Sec)	138
5.3	The Normalized Voltage Variation with Normalized Distance in the Potential Minimum Region.	139
5.4	I/I_o vs. B/B_c. All Curves are Normalized with Respect to I_o, the Current at the Cutoff Value of the Magnetic Field.	142
5.5	G_{min} vs. v.	147
5.6	Voltage Distribution Along the y-Axis.	151
5.7	Voltage Distribution Along the y-Axis.	152
5.8	Space-Charge Density vs. y.	154
5.9	Velocity Components vs. $\omega_c T$.	155
5.10	Trajectories vs. $\omega_c T$.	156
5.11	Current Density Components vs. y.	158
5.12	α_1 and $-\alpha_2$ vs. y.	161
5.13	β_1 and β_2 vs. y.	162
5.14	α_1 and β_1 vs. y. ($\omega_c = 5 \times 10^9$ Rad/Sec, R = 0.2)	164
5.15	α_1 and β_1 vs. y. ($\omega_c = 5 \times 10^9$ Rad/Sec, R = 0.6)	165
5.16	α_1 and β_1 vs. y. ($\omega_c = 5 \times 10^9$ Rad/Sec, R = 1.0)	166
5.17	α_1 and β_1 vs. y. ($\omega_c = 5 \times 10^9$ Rad/Sec, R = 2.6)	167
5.18	α_1, $-\alpha_2$, β_1, and β_2 vs. y. ($\omega_c = 1 \times 10^9$ Rad/Sec)	171
5.19	α_1 and β_1 vs. y. ($\omega_c = 1 \times 10^9$ Rad/Sec, R = 1.0)	172
5.20	α_1 and β_1 vs. y. ($\omega_c = 1 \times 10^9$ Rad/Sec, R = 5.0 α_3 is Found Equal to 0)	173
5.21	α_1 and $-\alpha_2$ vs. y. ($\omega = 5 \times 10^9$ Rad/Sec)	175

Figure		Page
5.22	A Crossed-Field Diode with a Screen-Grid.	178
5.23	Anode Current Spectrum vs. f/F_o. (Pollack)	181
5.24	Anode Velocity Spectrum vs. f/F_o. (Pollack)	182
5.25	R^2 vs. B/B_c. (Pollack)	183
5.26	Cycloiding Beam in the Interaction Region.	185
6.1	A Schematic of Trajectory of a Single Electron in a Crossed-Field Diode.	190
6.2	A Uniform Electron Distribution Assumed to Evaluate the Space-Charge Weighting Constant.	206
6.3	Spectral Window vs. Normalized Frequency.	223
7.1	F(s) vs. s. (n_a = 7.0)	237
7.2	Flow Diagram for Monte Carlo Analysis.	238
7.3	Beam Profile in y-z Plane Under Steady-State Conditions. (V_o = 500 Volts, $\omega_c = 4.75 \times 10^9$ Rad/Sec, $d = 5 \times 10^{-3}$ m)	239
7.4	Total Number of Electrons vs. $T/\Delta t$.	242
7.5	Trajectories vs. $\omega_c T$.	243
7.6	Velocity Components vs. $\omega_c T$.	244
7.7	Potential Variation Along the Beam. (V_o = 500 Volts, $\omega_c = 4.75 \times 10^9$ Rad/Sec, $d = 5 \times 10^{-3}$ m)	246
7.8	Potential Variation Along the Beam. (V_o = 500 Volts, $\omega_c = 4.75 \times 10^9$ Rad/Sec, $d = 5 \times 10^{-3}$ m)	248
7.9	Normalized Auto-Correlation Function for the A-c Kinetic Voltage vs. μ.	255
7.10	Normalized Auto-Correlation Function for the Current Fluctuations vs. μ.	256
7.11	Π/S vs. f.	257
7.12	Π/S vs. f.	258

Figure		Page
7.13	S/S_o vs. f.	261
7.14	S/S_o vs. f.	262
7.15	$(S-\Pi)/S_o$ vs. f.	263
7.16	$(S-\Pi)/S_o$ vs. f.	264
7.17	$(S+\Pi)/S_o$ vs. f.	265
7.18	$(S+\Pi)/S_o$ vs. f.	266
7.19	ψ/ψ_o vs. f.	268
7.20	ψ/ψ_o vs. f.	269
7.21	Φ vs. f.	271
7.22	Φ vs. f.	272
7.23	F vs. f.	274
7.24	F vs. f.	275
8.1	An Overall Assembly of the Crossed-Field Device.	280
8.2	An Ideal Trajectory of an Electron Emitted from the Center of the Cathode.	284
8.3	Electron Trajectories from the Three Cathodes. (Zero Space Charge)	286
8.4	Electron Trajectories from the Three Cathodes. (Zero Space Charge)	287
8.5	Electron Trajectories from the Three Cathodes. (Zero Space Charge)	289
8.6	Electron Trajectories from the Three Cathodes. (Zero Space Charge)	290
8.7	Electron Trajectories from the Three Cathodes. (Zero Space Charge)	291
8.8	Cathode Block with Slots for Three Cathodes and Holes for R-f Probes Mounted on the Cathode Block Mount.	293
8.9	Sole Structure with Glazed Molybdenum Blocks.	294
8.10	Assembly of Gun Anode, Anode, Sole and Base Plate.	296

Figure		Page
8.11	Probes and Cathodes Configuration.	298
8.12	Assembly Drawing of Push-Pull Seal.	300
8.13	Assembly of the Crossed-Field Noise Analyzer (Tube and Push-Pull Seal).	301
8.14	Assembly of the Crossed-Field Noise Analyzer (Wheel and Gear-Screw Mechanism).	302
8.15	The Overall Assembly of the Noise Analyzer Mounted on the Vacuum Station.	303
8.16	The Right-Hand Side of the Noise Analyzer Showing the Collector, Sole, Anode, Base-Plate and Supporting Rods.	304
8.17	R-f Input Probes and the Movable Probes.	305
9.1	Normalized Cathode Current vs. Magnetic Field.	309
9.2	I_3/I_{o3} vs. I_1/I_{o1}.	311
9.3	I_3/I_{o3} vs. I_2/I_{o2}.	312
9.4	I_2/I_{o2} vs. I_1/I_{o1}.	313
9.5	I_{o1}/I_{o3} and I_{o2}/I_{o3} vs. B.	315
9.6	Dimensions of the Inner and Outer Conductors for the Glass-Vacuum Seal.	316
9.7	VSWR Characteristics of Glass Vacuum Seal with Two Types of Connectors.	317
9.8	Probe Current vs. Probe Voltage. B = 120 Gauss, I_{o2} = 3.4 ma, V_{acc} = 420 Volts, V_{an} = 360 Volts.	320
9.9	Probe Current vs. Probe Voltage. B = 140 Gauss, I_{o3} = 2.8 ma, V_{acc} = 420 Volts, V_{an} = 360 Volts.	321
9.10	Variation of Electron Equivalent Temperature vs. B. Cathode No. 1. V_{acc} = 420 Volts, V_{an} = 360 Volts, V_{Sole} = 0 Volt.	322
9.11	Variation of Electron Equivalent Temperature vs. B. Cathode No. 2. V_{acc} = 420 Volts, V_{an} = 360 Volts, V_{Sole} = 0 Volt.	323

Figure		Page
9.12	Variation of Electron Equivalent Temperature vs. B. Cathode No. 3. V_{acc} = 420 Volts, V_{an} = 360 Volts, V_{Sole} = 0 Volt.	324
9.13	Volt-Ampere Characteristics for Probe No. a for Different Values of z. B = 120 Gauss, $I_{Cathode}$ = 3 ma, V_{acc} = 420 Volts, V_{an} = 360 Volts, V_{Sole} = 0 Volt.	326
9.14	R-f Signal Level, Cathode Current and Change in Signal Frequency as a Function of Cathode Bias. B = 150 Gauss, V_{acc} = 356 Volts, V_{an} = 260 Volts.	328
9.15	R-f Signal Level and Change in Signal Frequency as a Function of Magnetic Field. (Probe No. a) I_k = 1.75 ma, V_{acc} = 356 Volts, V_{an} = 246.5 Volts.	329
9.16	R-f Signal Level as a Function of Anode Voltage. (Probe No. a) B = 150 Gauss, I_k = 1.75 ma, V_{acc} = 260 Volts.	331
9.17	Variation of R-f Signal Level on Probe No. a vs. Distance. B = 150 Gauss, I_k = 0.9 ma, V_{acc} = 356 Volts, V_{an} = 260 Volts, $V_{Probe\ No.\ c}$ = 190 Volts, $V_{Probe\ No.\ a}$ = 220 Volts.	332
9.18	Variation of R-f Signal Level on Probe No. c vs. Distance. B = 150 Gauss, I_k = 0.9 ma, V_{acc} = 356 Volts, V_{an} = 260 Volts, $V_{Probe\ No.\ a}$ = 190 Volts, $V_{Probe\ No.\ c}$ = 220 Volts.	333
9.19	Probe Current vs. z. (Probe No. a) B = 150 Gauss, I_k = 0.9 ma, V_{acc} = 356 Volts, V_{an} = 260 Volts, V_{p_1} = 220 Volts.	335
9.20	R-f Signal Level and Cathode Current vs. Cathode Bias. (Probe No. a) B = 164 Gauss, V_{acc} = 292 Volts, V_{an} = 425 Volts, f = 95 mc, P_h = 22.3 Watts.	338
9.21	R-f Signal Level vs. Magnetic Field. (Probe No. a) V_{acc} = 290 Volts, V_{an} = 411 Volts, f = 95 mc, P_h = 22.3 Watts.	339
9.22	R-f Signal Level and Cathode Current vs. Gun Anode Voltage. (Probe No. a) B = 160 Gauss, V_{an} = 425 Volts, f = 95 mc, P_h = 22.3 Watts.	340

Figure		Page
9.23	R-f Signal Level vs. Anode Voltage. (Probe No. a) B = 160 Gauss, I_k = 0.54 ma, V_{acc} = 290 Volts, f = 95 mc, P_h = 22.3 Watts.	341
9.24	R-f Signal Level and Cathode Current vs. Heater Power. (Probe No. a) B = 160 Gauss, V_{acc} = 412 Volts, V_{an} = 403 Volts, f = 140 mc, Cathode Bias = 0 Volt.	342
9.25	R-f Signal Level vs. z. (Probe No. a) B = 164 Gauss, V_{acc} = 292 Volts, V_{an} = 425 Volts, f = 170 mc, P_h = 22.3 Watts.	343
F.1	Space-Charge Distribution in an Elementary Box of Volume h dy_o dz_o.	374

LIST OF TABLES

Table		Page
7.1	Division of the Diode and Beam Configuration	229
7.2a	Average Values of the Number and Velocity Components of Electrons in Rectangle 1	249
7.2b	Average Values of the Number and Velocity Components of Electrons in Rectangle 11	250
7.2c	Average Values of the Number and Velocity Components of Electrons in Rectangle 14	251
7.3	Average Values of the Number of Electrons, Velocity and Current Density Components (Averaged Over 1000 Unit Time Intervals)	252
8.1	G as a Function of d for Idealized Flow	283
8.2	Maximum Deviation in Trajectories as a Function of Angle θ	292
9.1	Individual Cathode Currents as a Function of the Magnetic Field	314
9.2	Variation of Beam Transmission with Beam Current	318

CHAPTER I. INTRODUCTION

1.1 Noise in Crossed-Field Devices

Noise phenomena in conventional magnetrons and injected beam crossed-field devices have drawn considerable attention ever since their initial development. The maximum available output of these devices is always limited by the presence of this noise.

It has been found experimentally that the large amplitude noise in crossed-field devices appears under space-charge-limited operation and this noise disappears (or at least is significantly reduced) as soon as the operation of the cathode is changed from space-charge-limited to temperature-limited.

Basically crossed-field devices* employ electron beams which travel at right angles to mutually perpendicular d-c electric and magnetic fields. Different versions of these devices all involve an interaction between the electron beam and an electromagnetic wave traveling on a slow-wave structure. These devices are characterized by high efficiency, electronic tunability and reasonable bandwidth but, because of a relatively high noise output, their full potential has not been reached. It has also been found that an electron beam traveling in a drift region of the crossed-field device with no slow-wave structure gives rise to an amplification of the signal and this phenomenon is usually referred to as diocotron gain. Because of the development of

---

* In crossed-field devices (also known as M-type devices) the energy transfer from the electrons to the wave is accompanied by a fall in the potential energy of the electrons. In O-type devices there are no static transverse fields and the energy transfer from the electrons to the wave is accompanied by a loss of the kinetic energy of the electrons.

new crossed-field devices such as the M-carcinotron, the amplitron and the magnetron amplifier, a great interest has developed in the study of noise in crossed-field devices and a determination of the best possible noise performance.

The study of noise in electron devices is almost as old as the devices themselves. The first studies of noise were quite theoretical; for example, in the field of instrumentation it was felt that noise would eventually limit the sensitivity of the measuring instrument, but, since the limit was far from attainment, the problem of noise was not considered serious. Similarly radio communication in the broadcast and high frequency bands had little need for supersensitive receivers, since the limiting noise was generated outside the receiver in the atmosphere. The need for increased receiver sensitivity led to the requirement for low noise electron devices and in the past decade considerable attention has been given to the study of noise generation and propagation.

Noise in a practical system is due to the various components such as resistors, capacitors, measuring instruments, oscillators, amplifiers, etc., and may be present due to several reasons such as thermal noise, shot noise, partition noise, flicker noise, etc. The main source of noise in electron devices is considered to be the shot noise which occurs essentially due to the discrete nature of emission of the electrons from the cathode. The mean square value of the Fourier coefficients i_s of the fluctuation in the emission current I_o in a bandwidth Δf is given by

$$\overline{i_s^2} = 2eI_o\Delta f \quad , \tag{1.1}$$

where e is the electronic charge. This formula for shot noise current for a diode is valid when the transit angle from the cathode to the anode is much less than one radian.

Whether the output noise in a practical device will be less or more than the shot noise depends upon the effect of the potential minimum and the manner in which noise is propagated along the beam. Some instabilities in the beam due to space-charge or edge effects may also modify the noise content.

In O-type devices, such as the klystron and traveling-wave amplifier, the potential minimum plays a sorting role and the fluctuations in the current crossing the potential minimum are not as large as the fluctuations in the emission current from the cathode. The potential minimum in O-type devices has been extensively studied by Siegman[*1], Watkins[2], Bloom[3] and Whinnery[4] and their studies have led to an equivalent resonant circuit for the potential minimum. The resonant frequency of this equivalent circuit is equal to the plasma frequency corresponding to the space-charge density at the potential minimum. From this study the effect of the potential minimum as a sorting means has been calculated particularly at high frequencies. The potential minimum in crossed-field devices may also be approximated by an equivalent resonant circuit although this does not help very much in giving an understanding of the noise behavior in crossed-field devices.

The study of the potential minimum and the transmission-line analogy[5] for electron beams in O-type devices has led to a better understanding of the noise phenomenon and has been useful in obtaining a considerable reduction of noise figure of these devices, namely, from

---

* Superscript numbers refer to references listed in the bibliography.

about 12 db originally given by Pierce[6] to about 3-4 db in the present day technology. With the growing desire of low-noise devices, new devices such as the parametric amplifier, maser amplifier and laser amplifier have also been developed.

The study of noise in crossed-field devices is in a stage of infancy and, in order to achieve the maximum potential of these devices in terms of high efficiency, large power output, electronic tunability and larger bandwidth, a great deal of theoretical as well as experimental study of noise in these devices is required. The most recent studies on magnetrons and injected-beam crossed-field devices seem to indicate that the presence of noise is independent of the geometry and is an inherent property of the crossed electric and magnetic field configuration which exists in the gun region. The phenomenon and origin of this noise, though not yet completely understood, are important in the operation of magnetrons and injected-beam-type crossed-field devices.

It was suggested by Professor J. E. Rowe that the origin of the noise in crossed-field devices is very likely due to the presence of the potential minimum and/or due to a nonlaminar flow expected to be maximum in the gun region because of the right-angle bend in the beam. Again this nonlaminar flow seems to be reduced considerably in temperature-limited operation of the tube because of the absence of noise. A study of noise propagation in the gun region is equally important. Evidentally the effect of space-charge-limited operation of the crossed-field devices is contradictory to that of space-charge-limited operation of O-type devices as far as the noise behavior is concerned. It is for these reasons that the study of noise transport in the gun region of the crossed-field devices is important. A multivelocity analysis in a

space-charge-limited device is also desirable. Because of the ease of solving problems in a cartesian coordinate system and because of the difficulties involved in handling beam re-entrant problems in magnetrons, the present study pertains to planar crossed-field devices.

1.2 Previous Studies of Noise in Crossed-Field Devices

As mentioned in Section 1.1, the noise problem in crossed-field devices has drawn considerable attention ever since their first use. This noise was found earlier in magnetrons and was mentioned by Sproul[7], Mayper[8] and others. The maximum available output power from a magnetron is always limited because of the presence of this noise which is also associated with the presence of a finite current in the anode even beyond cutoff conditions[9]. In the last few years a great deal of analytical, as well as experimental, work concerning noise has been carried out on injected beam crossed-field devices (also known as planar crossed-field devices). Epsztein[10], Van Duzer[11] and Little-Rupel-Smith[12] have mentioned the presence of noise in injected beam crossed-field devices only under space-charge-limited conditions. The noise power is very large and in Epsztein's experimental study this noise was so intense that it could easily be detected by means of an ordinary radio broadcast receiver located a few meters away from the tube. The most recent studies on magnetrons and injected beam crossed-field devices indicate that the presence of noise in these devices is independent of the geometry and is accompanied by a large fraction of the electron beam collected on the sole, even though it may be many volts negative with respect to the cathode from which the beam originated. This phenomenon was extensively studied by Miller[13] on a segmented sole noise analyzer.

A recent experiment by Anderson[14] on an M-type backward-wave amplifier using an electron gun design based on an analysis by Kino[15] also indicates the presence of noise accompanied by a comparatively small value of sole current. The possibility of obtaining a more laminar flow and the presence of low noise with a Kino gun design seems to indicate that the noise in crossed-field devices may be due to nonlaminar flow as suggested above and may be reduced considerably by a proper design of a crossed-field gun.

Small-signal and large-signal analyses of crossed-field devices have been carried out by many authors, but their analyses have been restricted to the interaction region and very little effort has been made to apply them to the gun region, primarily because of the increased number of dependent variables such as the y- and z-component velocities, space-charge density, etc. Any perturbation or noise in the region of the potential minimum will propagate along the beam in a crossed-field device in quite a different manner compared to that in O-type devices. This perturbation at the cathode in crossed-field devices will also grow, due to the diocotron effect which arises due to the velocity slipping nature of the crossed-field beams. An expression for diocotron gain in the interaction region has been derived by Gould[16] assuming that the y-component of the d-c electron velocity is zero. This assumption is not valid in the cathode region and the dimensions of the beam do not remain constant as the beam progresses from the cathode to the interaction region. The study of the propagation of some perturbation at the potential minimum along the beam under space-charge-limited operation with multi-valued initial velocity is of prime importance in understanding the noise behavior of injected beam crossed-field devices.

However a great deal can also be learned by considering the propagation of some perturbation which assumes a single velocity flow with mean square fluctuations at the potential minimum and a finite value of the d-c current density.

Van Duzer[11] has carried out an analysis for the noise transport in crossed-field devices for a Kino gun design and the method is based upon that of Llewellyn[17] in obtaining the Llewellyn-Peterson equations[18] for a one-dimensional O-type diode. Van Duzer's analysis involves the y-component of the d-c velocity in most of the denominators of the noise transport coefficients and thus his analysis is limited in use because the y-component d-c velocity is zero both at the cathode and the entrance to the interaction region when initial velocities are neglected. This causes a singularity at the two planes and the small-signal analysis assumption is completely violated. Rando[19] has modified Van Duzer's analysis and the noise transport coefficients obtained by Rando involve the total electron velocity in the denominator, which results in justification of the small-signal analysis assumption. However, neither Van Duzer's analysis nor Rando's modification takes into account the z-component current density fluctuations. The use of these analyses as such is limited to the Kino gun model and as shown in Appendix D of this report it seems that the two analyses are valid for low frequencies only.

Twiss[20] has described a density method for determining the d-c parameters such as current density, velocity components, etc., but this analysis does not take into account the initial tangential velocity for determining the normal critical velocity. Only those electrons for which the initial normal velocity is greater than the normal critical velocity will be able to cross the potential minimum barrier and the

other electrons will be reflected back toward the cathode. It has been found in the present analysis that the contribution of the initial tangential velocity in the potential minimum region is quite important. According to the author's information no effort has been made as yet to solve the characteristic equation in order to determine the propagation constants in the gun region. Needless to say these propagation constants are to be solved for different points in the gun region because the d-c parameters vary continuously in the gun region.

During the last few years a great interest has developed in the Monte Carlo technique for studying noise phenomenon in electron devices. Because of the close simulation of an actual device by this technique and because the assumption of a small-signal analysis is not necessary in this method, it is considered to be much superior to the density method. This technique was first applied to a one-dimensional O-type device by Tien and Moshman[21], assuming that the diode is short circuited, so that the a-c fields due to the variations in the current are neglected. Dayem and Lambert[22] have used this technique for an open-circuited diode and have taken into account the effects due to the discrete and noninfinite nature of the data available from the computer. C. Wen* has also used the Monte Carlo method in a two-dimensional O-type device noise study. The various limitations in evaluating the noise characteristics from a statistical analysis particularly for a discrete and noninfinite data have been discussed by Blackman and Tukey[23]. Because of the greater accuracy of the Monte Carlo method as compared to other methods such as the density method where a small-signal analysis

---

* Electron Physics Laboratory, The University of Michigan, forthcoming report.

assumption is made, it has become desirable to apply this method to study noise in a crossed-field diode.

A great deal of experimental work concerning noise in crossed-field devices has been done at the CSF Laboratories in France. By biasing some electrodes near the cathode it has been made possible to reduce the noise content considerably, but there has not been a clear understanding of this noise reduction technique. It has been noticed that the ratio B/B_c, where B is the actual magnetic field intensity and B_c is the cutoff magnetic field intensity, plays an important part in the amount of noise output in an actual crossed-field device. By introducing a screen grid electrode between the cathode and the gun anode, the noise content has been considerably reduced. In spite of these noise reduction methods, the noise output is still larger than shot noise and the generation and propagation of noise in the gun region are not yet understood.

1.3 Outline of the Present Analysis

In Chapter II, the derivation of the Llewellyn-Peterson equations is discussed. The noise transport coefficients which relate the fluctuations at the b-plane to those at the a-plane are derived separately in terms of the two velocity components. These equations can be applied in evaluating the noise transport coefficients for any physical model in which the two velocity components and their two time derivatives are specified and provided the small-signal assumption is not violated. Several checks for these coefficients are made.

In Chapter III, the noise transport coefficients derived in terms of the tangential velocity are evaluated for a few physical models in the gun region. These coefficients are also evaluated for different

input conditions in the interaction region. The noise transport equations derived in Chapter II are modified for the interaction region only so that the fluctuations at the b-plane may be defined in terms of a single variable, and these coefficients are evaluated for different values of ω_c/ω_p.

In Chapter IV, the evaluation of the parameters V_m and y_m is discussed as a boundary value problem. The evaluation of the steady-state parameters such as V, ρ, $\dot{y}$, $\dot{z}$, z and T as a function of y is discussed as an initial value problem. The characteristic equation for solving propagation constants is derived.

In Chapter V, the cathode current is evaluated in terms of the parameters V_m and y_m. The steady-state parameters are evaluated at various planes in the gun region and the characteristic equation is solved to evaluate the propagation constants at these planes.

In Chapter VI, the Monte Carlo technique for the noise transport in the crossed-field diode is discussed. The evaluation of the space-charge potential, the trajectory equations and the initial conditions are also discussed. The expressions for the auto-correlation and cross-correlation functions for the kinetic voltage and the current fluctuations are derived. The expressions for the self-power and cross-power spectrum density are derived and the formula for the noise figure is given in terms of these parameters. The modification of the various functions due to noninfinite and discrete nature of the data is also considered.

Chapter VII deals with the application of the equations derived in Chapter VI to evaluate noise figure at various locations of the beam. The choice of the various parameters, such as division of the

crossed-field diode into various rectangles, unit of time and the scaling parameter, is discussed on the basis of practical limitations. The advantage of using initial conditions is also discussed.

Chapter VIII deals with the design of the experimental noise analyzer. The designs of the various parts such as the gun, sole, anode, collector, and push-pull seal are discussed. Chapter IX deals with the experimental results of electron equivalent temperature, r-f oscillations and injection of r-f signal at the input probes.

Chapter X gives the summary of the preceding chapters and a few suggestions for an extension of this work.

CHAPTER II. DEVELOPMENT OF LLEWELLYN-PETERSON EQUATIONS

2.1 Introduction

It was mentioned in Chapter I that Van Duzer[11] has carried out an analysis of noise transport in the gun region of a crossed-field diode. This analysis is based upon a method originally developed by Llewellyn[17] and assumes a Kino gun model[15]. In Van Duzer's analysis it is assumed that the y-component of the current density remains constant throughout the cathode region. The equations thus obtained by Van Duzer for the noise transport involve $\dot{y}$ in the denominator and lead to a singularity when $\dot{y}$ approaches zero at the entrance to the interaction region. Moreover these equations cannot be used for evaluating noise transport in the interaction region even for conditions not far from ideal. The reason for this limitation is that $\dot{y}$ under such circumstances is either zero or very small and, because of the fact that $\dot{y}$ is in the denominator of these equations, the small-signal assumption used in the derivation of the equations is completely violated. Van Duzer's analysis does not seem to predict the high noise power usually observed in the crossed-field tubes for space-charge-limited operation.

In recent work by Rando[19], Van Duzer's equations have been modified in terms of the total velocity instead of the y-component of the d-c velocity. The final noise transport equations obtained by Van Duzer and Rando for an open-circuited diode show proportional or inversely proportional dependence on the signal frequency (except for a phase difference term) in some of the coefficients. Moreover these analyses do not include the z-component of the a-c current density fluctuations. These equations written as such are applicable only to the Kino gun

model. The physical model used in the present derivation for the Llewellyn-Peterson equations is that of a quasi space-charge-limited diode. Expressions for the y-component and the z-component of d-c current densities are derived for this model. It should be mentioned here that this choice of the physical model is mainly for the convenience of deriving the final equations. When these final equations are written in an appropriate form, they are then of a general form and any physical model may be used for evaluating the noise transport from an arbitrary a-plane to another arbitrary b-plane, provided it is assumed that the diode is open-circuited and that the total a-c current density in the diode is equal to zero. For the physical model considered to derive the final equations, the restriction of an open-circuited diode is not necessary. This point will become clear in the following sections of this chapter. Needless to say, the b-plane follows the a-plane along the path of the beam and the coordinate configuration is shown in Fig. 2.1.

In this chapter two sets of equations are derived for evaluating the noise transport; one set involves $\dot{z}$ in the denominator and the other involves $\dot{y}$ in the denominator. The use of the former set of equations makes it convenient to evaluate noise transport in the gun region as well as in the interaction region for small-signal conditions. The choice of the a-plane is important to avoid small-signal violations. However, the restrictions on the selection of the a-plane are of small importance when initial velocities are considered.

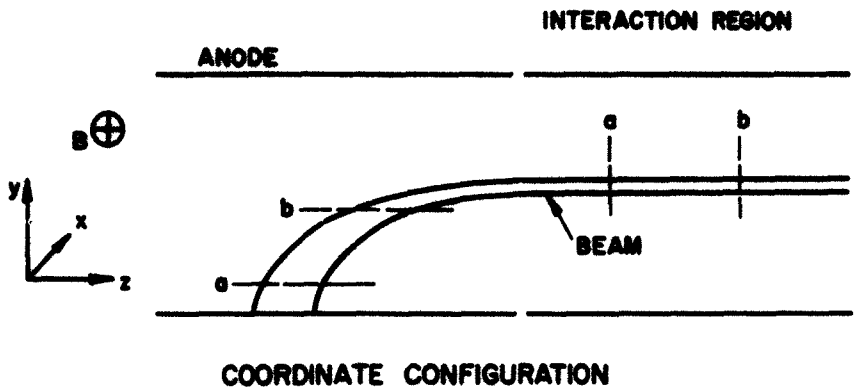

FIG. 2.1 SCHEMATIC OF AN IDEAL STEADY-STATE ELECTRON BEAM IN A CROSSED-FIELD DEVICE.

2.2 Assumptions Made in This Analysis

The following assumptions are made in this analysis.

1. Nonrelativistic mechanics.
2. The force due to r-f magnetic field on an electron is neglected.
3. The magnetic field has a uniform x-component only.
4. The electrons are confined in a filamentary beam of noninfinite current density.
5. The velocities and other associated functions are single valued functions of space; in other words, a laminar flow and no crossing of electrons is assumed.
6. The a-c fluctuations vary as exp $j\omega t$ and the magnitude of these fluctuations is taken as the mean square fluctuation.
7. A small-signal analysis is assumed.

2.3 Trajectory Equations

The equations of motion for an electron in a crossed-field tube in a coordinate system shown in Fig. 2.1 are given by

$$\ddot{y} = -\eta[E_y + B\dot{z}] \tag{2.1a}$$

and

$$\ddot{z} = -\eta[E_z - B\dot{y}] \quad , \tag{2.1b}$$

where it is assumed that the magnetic field B is uniform and has only an x-component and that $E_x = 0$; in other words, the motion of the electron is confined in the y-z plane only. Differentiate Eqs. 2.1a and 2.1b with respect to t and assume that these two equations correspond to two independent one-dimensional problems with a coupling due to the magnetic field. Then the following equations are obtained in a manner similar to that of Llewellyn:

$$\dot{y} = \tilde{I}_{y_o} - \omega_c \dot{z} \tag{2.2a}$$

and

$$\dot{z} = \tilde{I}_{z_o} + \omega_c \dot{y} \quad , \tag{2.2b}$$

where

$$\tilde{I}_{y_o} = \frac{e}{m\epsilon_o} I_{y_o} \quad , \tag{2.3a}$$

$$\tilde{I}_{z_o} = \frac{e}{m\epsilon_o} I_{z_o} \quad , \tag{2.3b}$$

and η is taken as the absolute value of the ratio of the electron charge to its mass, ϵ_o is the free-space dielectric constant, ω_c is the cyclotron frequency given by

$$\omega_c = \eta B \tag{2.4}$$

and I_{y_o} and I_{z_o} are the y- and z-components of the current density respectively. Suffix "o" is used to indicate d-c parameters.

It may be mentioned here that, in deriving Eq. 2.2a, variations in the z-direction are neglected and, in deriving Eq. 2.2b, variations in the y-direction are neglected. This is one of the assumptions made in the derivation of the equations and in this manner the two current density components may be considered separately. However, as mentioned in Section 2.1, when the final equations are written in an appropriate form (see Section 2.4) for an open-circuited diode, the analysis is not restricted to such an assumption. Any physical model may be considered

and the steady-state results may be used in the final equations for evaluating the noise transport in such a physical model.

The total convection current density $\vec{I}_{T_o}$ is given by

$$\vec{I}_{T_o} = \rho_o \vec{v}_o \quad , \tag{2.5}$$

where ρ_o is the space-charge density and $\vec{v}_o$ is the total velocity vector. Similarly the expressions for the two convection current density components are written as

$$I_{y_o} = \rho_o \dot{y}_o \tag{2.6a}$$

and

$$I_{z_o} = \rho_o \dot{z}_o \quad . \tag{2.6b}$$

For a free space-charge motion of an electron in the gun region, it can be shown that the expressions for I_{y_o} and I_{z_o} are given by

$$\left|\frac{I_{z_o}}{I_{T_o}}\right| \simeq \left\{\frac{1 - \cos[\omega_c(t-t_o) - \Phi]}{2}\right\}^{1/2}$$

$$= \sin\left[\frac{\omega_c}{2}(t-t_o) - \frac{\Phi}{2}\right] \tag{2.7a}$$

and

$$\left|\frac{I_{y_o}}{I_{T_o}}\right| \simeq \cos\left[\frac{\omega_c}{2}(t-t_o) - \frac{\Phi}{2}\right] \quad , \tag{2.7b}$$

where $E_{z_o} < E_{y_o}$ and small initial velocities are assumed. The parameter t_o is taken as the emission time of the electron and Φ is given by

$$\tan \Phi = \frac{\frac{E_{z_o}}{B} - \dot{y}_i}{-\frac{E_{y_o}}{B} - \dot{z}_i} , \tag{2.8}$$

where $\dot{y}_i$ and $\dot{z}_i$ are the initial y- and z-components of the velocity respectively.

It is assumed that a small perturbation in $\tilde{I}_D$ is given by

$$\tilde{I}_T = \tilde{I}_D + \tilde{I}_1 e^{j\omega t} , \tag{2.9}$$

where

$$\tilde{I}_T = \frac{e}{m\epsilon_o} I_T \tag{2.10}$$

and I_D is the total d-c current density. By combining Eqs. 2.2, 2.3, 2.7 and 2.9, the following is obtained:

$$\ddot{y} = \tilde{I}_D \cos\left[\frac{\omega_c}{2}(t-t_o) - \frac{\Phi}{2}\right] + \tilde{I}_1 e^{j\omega t} \cos\left[\frac{\omega_c}{2}(t-t_o) - \frac{\Phi}{2}\right] - \omega_c \dot{z} \tag{2.11a}$$

and

$$\ddot{z} = \tilde{I}_D \sin\left[\frac{\omega_c}{2}(t-t_o) - \frac{\Phi}{2}\right] + \tilde{I}_1 e^{j\omega t} \sin\left[\frac{\omega_c}{2}(t-t_o) - \frac{\Phi}{2}\right] + \omega_c \dot{y} . \tag{2.11b}$$

In the following suff xes a and b correspond to the two planes, the a-plane and the b-plane respectively. For a special case when the

a-plane coincides with the cathode (or the potential minimum for a space-charge-limited diode) $t_a = t_o$. As mentioned in Section 2.1, such a substitution will be restricted by the small-signal assumption made in this analysis. In the final form of the noise transport coefficients given by Eqs. 2.25 the expressions for the d-c terms involving the current density in Eqs. 2.11 are written in terms of the total time derivatives of $\dot{y}$ and $\dot{z}$. It is because of this reason that the final noise transport coefficients could be used in any physical model for the case of an open-circuited diode, i.e., when $I_1 = 0$.

Integrate Eq. 2.11a with respect to t and substitute for $\dot{y}$ in Eq. 2.11b to give

$$\ddot{z} = 3\tilde{I}_D \sin\left[\frac{\omega_c}{2}(t-t_o) - \frac{\Phi}{2}\right] + \tilde{I}_1 e^{j\omega t} \sin\left[\frac{\omega_c}{2}(t-t_o) - \frac{\Phi}{2}\right]$$

$$+ \frac{\omega_c}{2}\tilde{I}_1 \left[\frac{e^{j\left(\omega + \frac{\omega_c}{2}\right)t - j\left(\frac{\omega_c}{2}t_o + \frac{\Phi}{2}\right)}}{j\left(\omega + \frac{\omega_c}{2}\right)} + \frac{e^{j\left(\omega - \frac{\omega_c}{2}\right)t + j\left(\frac{\omega_c}{2}t_o + \frac{\Phi}{2}\right)}}{j\left(\omega - \frac{\omega_c}{2}\right)}\right]$$

$$- \omega_c^2 \dot{z} - 2\tilde{I}_D \sin\left[\frac{\omega_c}{2}(t_a-t_o) - \frac{\Phi}{2}\right]$$

$$- \frac{\omega_c}{2}\tilde{I}_1 \left[\frac{e^{j\left(\omega + \frac{\omega_c}{2}\right)t_a - j\left(\frac{\omega_c}{2}t_o + \frac{\Phi}{2}\right)}}{j\left(\omega + \frac{\omega_c}{2}\right)} + \frac{e^{j\left(\omega - \frac{\omega_c}{2}\right)t_a + j\left(\frac{\omega_c}{2}t_o + \frac{\Phi}{2}\right)}}{j\left(\omega - \frac{\omega_c}{2}\right)}\right]$$

$$+ \omega_c^2\left(\dot{z}_a + \dot{z}_{a1} e^{j\omega t_a}\right) + \omega_c\left(y_a + y_{a1} e^{j\omega t_a}\right) . \quad (2.12)$$

Similarly by integrating Eq. 2.11b with respect to t and substituting for $\ddot{z}$ in Eq. 2.11a, the following is obtained:

$$\ddot{y} = 3\tilde{I}_D \cos\left[\frac{\omega_c}{2}(t-t_o) - \frac{\Phi}{2}\right] + \tilde{I}_1 e^{j\omega t} \cos\left[\frac{\omega_c}{2}(t-t_o) - \frac{\Phi}{2}\right]$$

$$- \frac{\omega_c \tilde{I}_1}{2j}\left[\frac{e^{j\left(\omega + \frac{\omega_c}{2}\right)t - j\left(\frac{\omega_c}{2}t_o + \frac{\Phi}{2}\right)}}{j\left(\omega + \frac{\omega_c}{2}\right)} - \frac{e^{j\left(\omega - \frac{\omega_c}{2}\right)t + j\left(\frac{\omega_c}{2}t_o + \frac{\Phi}{2}\right)}}{j\left(\omega - \frac{\omega_c}{2}\right)}\right]$$

$$- \omega_c^2 \dot{y} - 2\tilde{I}_D \cos\left[\frac{\omega_c}{2}(t_a-t_o) - \frac{\Phi}{2}\right]$$

$$+ \frac{\omega_c \tilde{I}_1}{2j}\left[\frac{e^{j\left(\omega + \frac{\omega_c}{2}\right)t_a - j\left(\frac{\omega_c}{2}t_o + \frac{\Phi}{2}\right)}}{j\left(\omega + \frac{\omega_c}{2}\right)} - \frac{e^{j\left(\omega - \frac{\omega_c}{2}\right)t_a + j\left(\frac{\omega_c}{2}t_o + \frac{\Phi}{2}\right)}}{j\left(\omega - \frac{\omega_c}{2}\right)}\right]$$

$$+ \omega_c^2\left(\dot{y}_a + \dot{y}_{a1} e^{j\omega t_a}\right) - \omega_c\left(\ddot{z}_a + \ddot{z}_{a1} e^{j\omega t_a}\right) , \tag{2.13}$$

where the fluctuations referred to by the suffix 1 in $\dot{y}$, $\ddot{y}$, $\dot{z}$, $\ddot{z}$ at the a-plane are assumed to be of sinusoidal variations. For arbitrary fluctuations it will be necessary to make a Fourier analysis and consider each sinusoidal fluctuation separately.

In deriving Eqs. 2.12 and 2.13, initial conditions referred to by the suffix a are used in evaluating the constants of integration involved

in the integration of Eqs. 2.11a and 2.11b with respect to t. The suffix 1 is included here to indicate the a-c variations in the corresponding parameters. Small-signal conditions are assumed and a variation of the type exp $j\omega t$ in the a-c parameters is also assumed. For a d-c solution of Eqs. 2.12 and 2.13, the a-c parameters are substituted equal to zero and these equations then reduce to

$$\ddot{z} + \omega_c^2 \dot{z} = 3\tilde{I}_D \sin\left[\frac{\omega_c}{2}(t-t_a) + \bar{\alpha}\right] - 2\tilde{I}_D \sin\bar{\alpha} + \omega_c^2 \dot{z}_a + \omega_c \dot{y}_a \tag{2.14a}$$

and

$$\ddot{y} + \omega_c^2 \dot{y} = 3\tilde{I}_D \cos\left[\frac{\omega_c}{2}(t-t_a) + \bar{\alpha}\right] - 2\tilde{I}_D \cos\bar{\alpha} + \omega_c^2 \dot{y}_a - \omega_c \dot{z}_a \quad , \tag{2.14b}$$

where

$$\bar{\alpha} = \frac{\omega_c}{2}(t_a - t_o) - \frac{\Phi}{2} \quad . \tag{2.15}$$

Equations 2.14a and 2.14b can be solved to give

$$z = \frac{\tilde{I}_D}{\omega_c^3}\left[6 - 8\cos\left(\frac{\omega_c}{2}T + \bar{\alpha}\right) + 2\cos(\omega_c T + \bar{\alpha})\right] + \frac{\dot{z}_a}{\omega_c^2}(1 - \cos\omega_c T) + \dot{z}_a T + \frac{\dot{y}_a}{\omega_c^2}(\omega_c T - \sin\omega_c T) \tag{2.16a}$$

and

$$y = \frac{\tilde{I}_D}{\omega_c^3}\left[-2\omega_c T + 8\sin\left(\frac{\omega_c}{2}T + \bar{\alpha}\right) - 2\sin(\omega_c T + \bar{\alpha})\right] + \dot{y}_a T - \frac{\dot{z}_a}{\omega_c^2}(\omega_c T - \sin\omega_c T) + \frac{\dot{y}_a}{\omega_c^2}(1 - \cos\omega_c T) \quad , \tag{2.16b}$$

where $T = t - t_a$ and represents the transit time of the electron from time t_a corresponding to the a-plane to the time t. Equations 2.16a and 2.16b describe the trajectory equations of electrons confined in a filamentary beam with the initial values at $t = t_a$ given by the average ensemble values. Further, these equations reduce to the corresponding Llewellyn equations for space-charge-limited operation and temperature-limited operation under the condition $\omega_c = 0$. The reduction of Eqs. 2.16a and 2.16b for both space-charge-limited operation and temperature-limited operation are given in the following two cases.

Case A. Space-Charge-limited Operation

For space-charge-limited operation, if

$$\ddot{z}_a = \dot{z}_a = \ddot{y}_a = \dot{y}_a = 0$$

is substituted, the following equations are obtained:

$$z = \frac{\tilde{I}_D}{\omega_c^3}\left[6 - 8\cos\frac{\omega_c}{2}T + 2\cos\omega_c T\right] \tag{2.17a}$$

and

$$y = \frac{\tilde{I}_D}{\omega_c^3}\left[-2\omega_c T + 8\sin\frac{\omega_c}{2}T - 2\sin\omega_c T\right] . \tag{2.17b}$$

In deriving Eqs. 2.17 $\Phi = 0$ and $t_a = t_o$ are also assumed. A similar set of equations for y and z were derived by Brillouin and Leblond[24] considering that $E_z = 0$ and the y-directed current density is equal to a constant. These equations are given by

$$z = \frac{\tilde{I}_d}{\omega_c^3}\left(\frac{\omega_c^2 T^2}{2} + \cos\omega_c T - 1\right) \tag{2.18a}$$

and

$$y = \frac{\tilde{I}_D}{\omega_c^3}\left(\omega_c T - \sin \omega_c T\right) \tag{2.18b}$$

for $0 \leq \omega_c T \leq 2\pi$.

Equations 2.18a and 2.18b have also been used in the design of the Kino gun[15] for crossed-field devices. The physical model discussed here is quite different from that of Leblond[24], but Figs. 2.2 and 2.3 have been drawn to compare the two results in the common region of validity. In Leblond's model only the y-component of the current density is taken and this is perhaps the reason why Leblond's model gives larger values of y and smaller values of z than those given in the present analysis.

Case B. Temperature-Limited Operation

For temperature-limited operation, substitute $\tilde{I}_D \to 0$ to obtain from Eqs. 2.16a and 2.16b

$$z = \frac{\ddot{z}_a}{\omega_c^2}(1 - \cos \omega_c T) + \dot{z}_a T + \frac{\ddot{y}_a}{\omega_c^2}(\omega_c T - \sin \omega_c T) \tag{2.19a}$$

and

$$y = \frac{\ddot{y}_a}{\omega_c^2}(1 - \cos \omega_c T) - \frac{\ddot{z}_a}{\omega_c^2}(\omega_c T - \sin \omega_c T) + \dot{y}_a T \quad . \tag{2.19b}$$

These equations are the same as those derived directly from the equations of motion, assuming that the field components E_y and E_z remain constant. The values of $\ddot{y}_a$ and $\ddot{z}_a$ are determined from the equations of motion given by Eqs. 2.1.

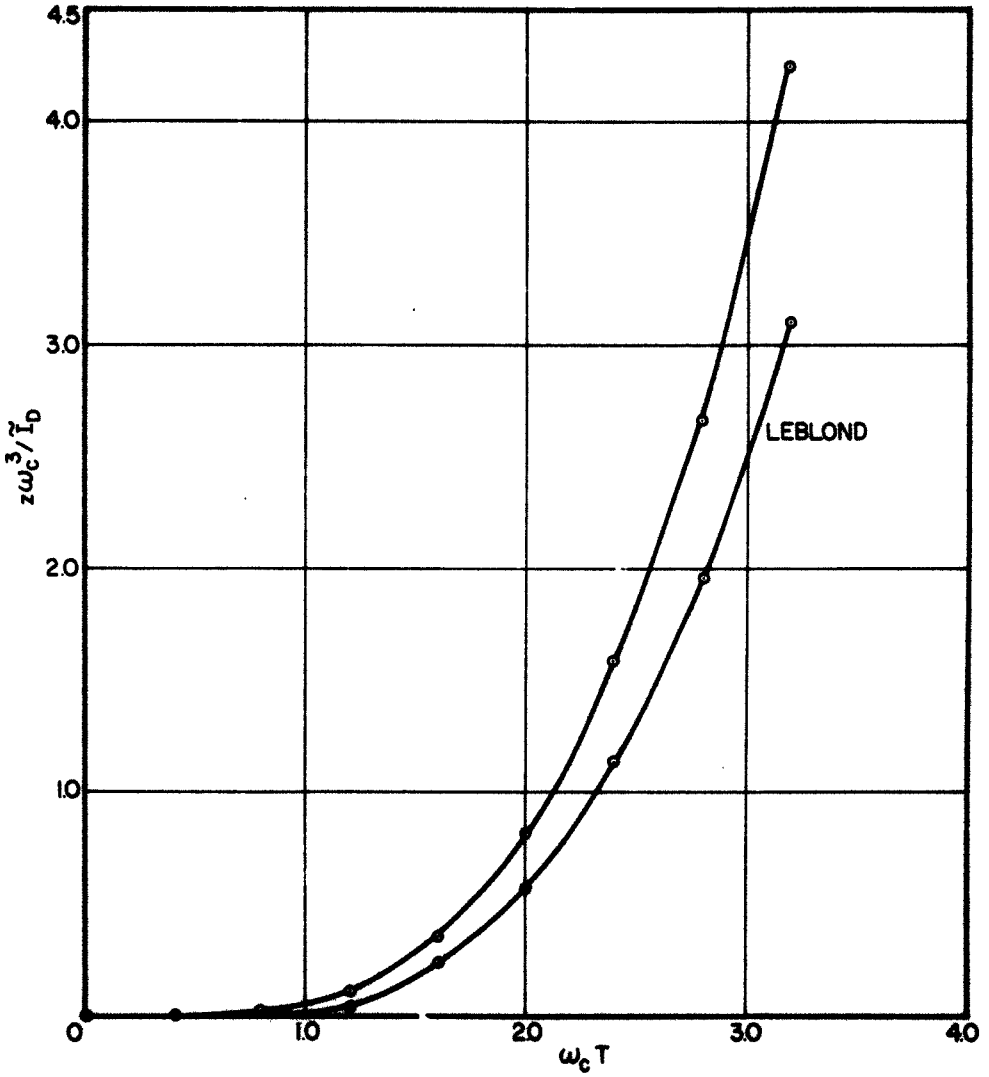

FIG. 2.2 COMPARISON OF THE NORMALIZED z-COMPONENT AS A FUNCTION OF $\omega_c T$ WITH THAT OF LEBLOND. $(0 \leq \omega_c T \leq \pi)$

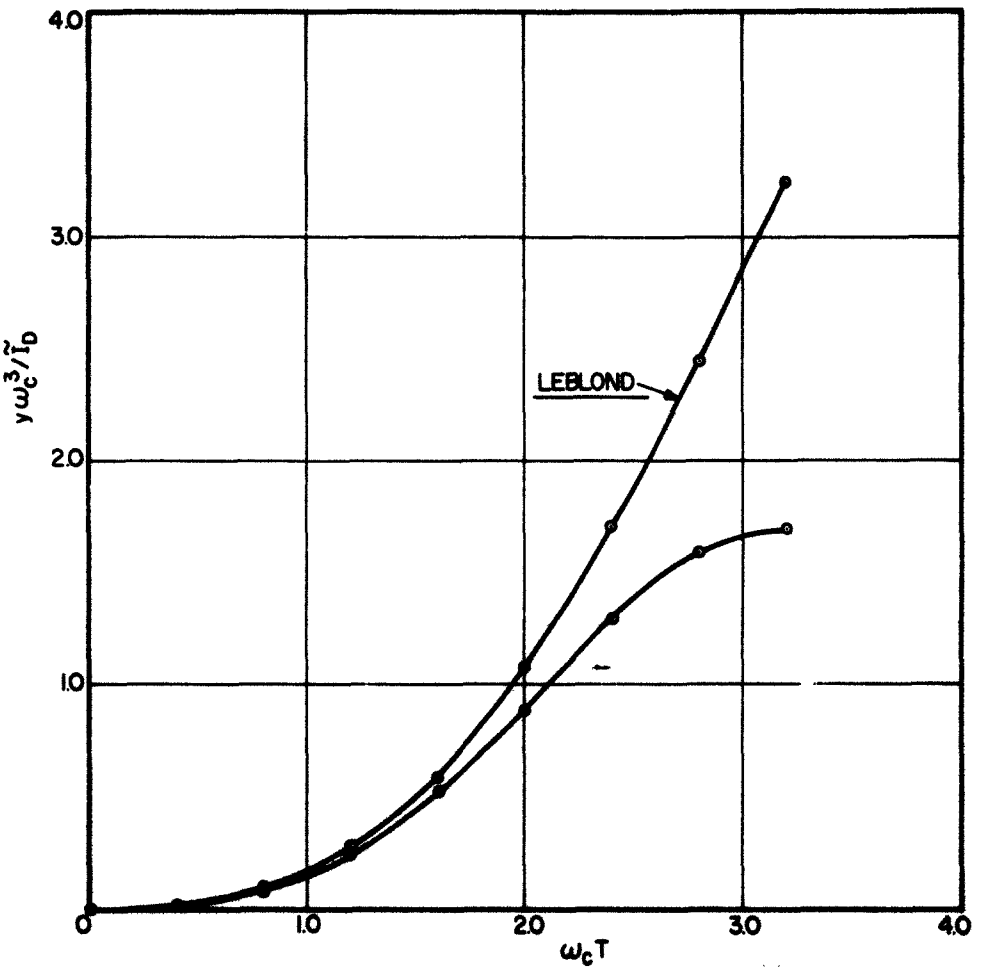

FIG. 2.3 COMPARISON OF THE NORMALIZED y-COMPONENT AS A FUNCTION OF $\omega_c T$ WITH THAT OF LEBLOND. $(0 \leq \omega_c T \leq \pi)$

2.4 Perturbation Techniques for the Derivation of the Final Noise Transport Equations

Equations 2.12 and 2.13 derived in the last section include the a-c variations in the various parameters such as $\tilde{I}_D$, $\ddot{z}_a$, $\dot{z}_a$, $\ddot{y}_a$ and $\dot{y}_a$ and form the two basic equations used to derive the final noise transport equations. By integrating Eq. 2.12 term by term three times with respect to t, applying the initial conditions at $t = t_a$ corresponding to the a-plane and introducing a perturbation, δ_z in time T given by

$$t - t_a = T + \delta_z \quad , \tag{2.20}$$

the following is obtained as derived in Appendix A:

$$- \dot{z}_{d-c}\delta_z \, e^{-j\omega t} = \tilde{I}_1 \, \delta_{z_1} + \tilde{q}_{z_{a1}} \, \delta_{z_2} + \tilde{q}_{y_{a1}} \, \delta_{z_3} + \dot{z}_{a1} \, \delta_{z_4} + \dot{y}_{a1} \, \delta_{z_5} \quad , \tag{2.21}$$

where the functions δ_{z_1}, δ_{z_2}, δ_{z_3}, δ_{z_4} and δ_{z_5} are defined by Eqs. A.2 through A.6. The terms $\tilde{q}_{z_{a1}}$ and $\tilde{q}_{y_{a1}}$ in Eq. 2.21 are the two a-c components of the current density respectively multiplied by a common factor $e/m\epsilon_o$. The initial conditions given by

$$\ddot{y}_{a1} = \frac{\tilde{I} \cos \bar{\alpha} - \tilde{q}_{y_{a1}} - jR\omega_c^2 \, \dot{z}_{a1}}{jR\omega_c} \tag{2.22a}$$

and

$$\ddot{z}_{a1} = \frac{\tilde{I} \sin \bar{\alpha} - \tilde{q}_{z_{a1}} + jR \, \omega_c^2 \, \dot{y}_{a1}}{jR\omega_c} \tag{2.22b}$$

are derived in Appendix B and are used in the derivation of Eq. 2.21. The parameter R is defined as

$$R \triangleq \frac{\omega}{\omega_c} \quad . \tag{2.23}$$

After having defined the function δ_z in terms of the functions δ_{z_1}, δ_{z_2}, δ_{z_3}, δ_{z_4} and δ_{z_5} as in Eq. 2.21, it is possible to write down the expressions for the matrix coefficients which designate the transformation of the fluctuations at the a-plane to those at the b-plane. A brief summary of the procedure for deriving these coefficients is given in Appendix C. The relations between the fluctuations at the a-plane designated by the suffix a and the fluctuations at the b-plane designated by the suffix b are given by the matrix equations

$$\begin{bmatrix} V \\ q_{z_b} \\ q_{y_b} \\ \dot{z}_b \\ \dot{y}_b \end{bmatrix} = \begin{bmatrix} a_{11} & a_{12} & a_{13} & a_{14} & a_{15} \\ a_{21} & a_{22} & a_{23} & a_{24} & a_{25} \\ a_{31} & a_{32} & a_{33} & a_{34} & a_{35} \\ a_{41} & a_{42} & a_{43} & a_{44} & a_{45} \\ a_{51} & a_{52} & a_{53} & a_{54} & a_{55} \end{bmatrix} \begin{bmatrix} I \\ q_{z_a} \\ q_{y_a} \\ \dot{z}_a \\ \dot{y}_a \end{bmatrix} , \qquad (2.24)$$

where V refers to the a-c voltage at the b-plane with respect to the a-c voltage at the a-plane and is induced as a result of other fluctuations. The coefficients a_{ij} in Eq. 2.24 are referred to as the noise transport coefficients in the latter part of the text.

The parameters in the two column matrices are essentially a-c quantities and suffix 1 has been omitted. The coefficients of I in Eqs. 2.24 correspond to the case of the physical model considered here and the other coefficients correspond to a general case. Thus the coefficients of I are given in Appendix C while the other coefficients are given in this section. The a-c voltage V is due to the two field components E_y and E_z and, because of rather more involved expressions for

$\dot{z}_{d-c}$ and $\dot{y}_{d-c}$ as a function of the transit time from the a-plane to the b-plane, the expression for the a-c voltage V is not derived for a general case. However, the sixteen coefficients a_{ij} $(i \geq 2,\ j \geq 2)$ in the above matrix are given in a general form by the following equations:

$$a_{22} = \frac{\dddot{z} - \omega_c \ddot{y}}{\omega_c^2 \dot{z}} jW_1 + jW_2 + e^{-jR\,\omega_c T} , \tag{2.25a}$$

$$a_{23} = -\frac{\ddot{z} - \omega_c \dot{y}}{\omega_c^2 \dot{z}} \frac{F_2}{2} + \frac{F_4}{2} - jW_3 , \tag{2.25b}$$

$$a_{24} = \left[-j \frac{\ddot{z} - \omega_c \dot{y}}{\omega_c^2 \dot{z}} W_4 + j\left(\frac{F_4}{2} - jW_3\right)\right] \frac{m\epsilon_o}{e} R\,\omega_c^2 , \tag{2.25c}$$

$$a_{25} = \left[\frac{\ddot{z} - \omega_c \dot{y}}{\omega_c^2 \dot{z}} W_1 + W_2 \right] \frac{m\epsilon_o}{e} R\,\omega_c^2 , \tag{2.25d}$$

$$a_{32} = \frac{\ddot{y} + \omega_c \dot{z}}{\omega_c^2 \dot{z}} jW_1 - \left(\frac{F_4}{2} - jW_3\right) , \tag{2.25e}$$

$$a_{33} = -\frac{\ddot{y} + \omega_c \ddot{z}}{\omega_c^2 \dot{z}} \frac{F_2}{2} + jW_2 + e^{-jR\,\omega_c T} , \tag{2.25f}$$

$$a_{34} = \left[-j \frac{\dddot{y} + \omega_c \ddot{z}}{\omega_c^2 \dot{z}} W_4 - W_2 \right] \frac{m\epsilon_o}{e} R\,\omega_c^2 , \tag{2.25g}$$

$$a_{35} = \left[\frac{\dddot{y} + \omega_c \ddot{z}}{\omega_c^2 \dot{z}} W_1 + j\left(\frac{F_4}{2} - jW_3\right)\right] \frac{m\epsilon_o}{e} R\,\omega_c^2 , \tag{2.25h}$$

$$a_{42} = -\frac{e}{m\epsilon_o}\left[\frac{\ddot{z}}{\omega_c^2 \ell} W_1 + W_3\right]\frac{1}{R\omega_c^2} , \tag{2.25i}$$

$$a_{43} = \frac{je}{m\epsilon_o}\left[-\frac{\ddot{z}}{\omega_c^2 \ell}\frac{F_2}{2} + \frac{F_6}{2}\right]\frac{1}{R\omega_c^2} , \tag{2.25j}$$

$$a_{44} = \frac{\ddot{z}}{\omega_c^2 \ell} W_4 - \frac{F_6}{2} + e^{-jR\omega_c T} , \tag{2.25k}$$

$$a_{45} = j\left(\frac{\ddot{z}}{\omega_c^2 \ell} W_1 + W_3\right) , \tag{2.25l}$$

$$a_{52} = \frac{e}{m\epsilon_o}\left\{-\frac{\ddot{y}}{\omega_c^2 \ell} W_1 - j\frac{F_6}{2}\right\}\frac{1}{R\omega_c^2} , \tag{2.25m}$$

$$a_{53} = \frac{e}{m\epsilon_o}\left\{-j\frac{\ddot{y}}{\omega_c^2 \ell} F_2 - W_3\right\}\frac{1}{R\omega_c^2} , \tag{2.25n}$$

$$a_{54} = \frac{\ddot{y}}{\omega_c^2 \ell} W_4 - jW_3 \tag{2.25o}$$

and

$$a_{55} = j\frac{\ddot{y}}{\omega_c^2 \ell} W_1 - \frac{F_6}{2} + e^{-jR\omega_c T} , \tag{2.25p}$$

where the functions F_1, F_2, F_3, F_4, F_5 and F_6 are defined in Appendix A and

$$W_1 = -\left[\frac{F_1}{2} + \frac{\omega_c^2 T^2}{2j} e^{-jR\omega_c T} \right] , \tag{2.26a}$$

$$W_2 = \frac{F_3}{2} - j \frac{F_6}{2} , \tag{2.26b}$$

$$W_3 = \frac{F_5}{2} + \frac{\omega_c T}{j} e^{-jR\omega_c T} \tag{2.26c}$$

and

$$W_4 = \frac{F_2}{2} - \omega_c T \, e^{-jR\omega_c T} . \tag{2.26d}$$

In Eqs. 2.25, the terms $\dot{y}$, $\ddot{y}$, $\dot{z}$, $\ddot{z}$ and $\dddot{z}$ without any suffix refer to the d-c quantities and, in view of the manner in which these equations have been written, any physical model may be considered in evaluating the coefficients. For example, for the physical model described in Section 2.1, the following can be written:

$$\dot{y} = \frac{\tilde{I}_D}{\omega_c^2} \left[4 \cos \left(\frac{\omega_c}{2} T + \bar{\alpha} \right) - 2 \cos \bar{\alpha} - 2 \cos (\omega_c T + \bar{\alpha}) \right] + \dot{y}_a$$

$$- \frac{\ddot{z}_a}{\omega_c} (1 - \cos \omega_c T) + \frac{\ddot{y}_a}{\omega_c} \sin \omega_c T , \tag{2.27a}$$

$$\dot{z} = \frac{\tilde{I}_D}{\omega_c^2} \left[4 \sin \left(\frac{\omega_c}{2} T + \bar{\alpha} \right) - 2 \sin (\omega_c T + \bar{\alpha}) \right] + \frac{\ddot{z}_a}{\omega_c} \sin \omega_c T$$

$$+ \dot{z}_a + \frac{\ddot{y}_a}{\omega_c} (1 - \cos \omega_c T) \tag{2.27b}$$

and

$$\ddot{y} + \omega_c \dot{z} = \tilde{I}_D \cos\left(\frac{\omega_c T}{2} + \bar{\alpha}\right) , \tag{2.28a}$$

$$\ddot{z} - \omega_c \dot{y} = \tilde{I}_D \sin\left(\frac{\omega_c T}{2} + \bar{\alpha}\right) . \tag{2.28b}$$

While for the Kino gun model the corresponding equations are

$$\dot{y} = \frac{\tilde{I}_D}{\omega_c^2}(1 - \cos \omega_c T) + \frac{\dot{y}_a}{\omega_c} \sin \omega_c T + \dot{y}_a \cos \omega_c T , \tag{2.29a}$$

$$\dot{z} = \frac{\tilde{I}_D}{\omega_c^2}(\omega_c T - \sin \omega_c T) + \frac{\dot{y}_a}{\omega_c}(1 - \cos \omega_c T) + \dot{y}_a \sin \omega_c T + \dot{z}_a \tag{2.29b}$$

and

$$\ddot{y} + \omega_c \dot{z} = \tilde{I}_D , \tag{2.30a}$$

$$\ddot{z} - \omega_c \dot{y} = 0 . \tag{2.30b}$$

In general, if the conditions in the interaction region are not far from ideal, the function $\dot{z}$ is never zero and $\dot{y}$ is either zero or of very small magnitude. Thus the coefficients given by Eqs. 2.25 have an advantage in that they may also be used for evaluating the noise transport in the interaction region without any modification of the equations. In this manner the singularity discussed by Van Duzer[11] can easily be avoided. In case the diode consists of two parallel plates, $\dot{z}$ approaches zero only when the electrons, during their cycloidal motion, approach the electrode with the lower d-c potential; for the purposes of computing noise transport, these regions should be avoided, otherwise the small-signal assumption is violated. By assuming that there is no

change in the fluctuations in the low velocity regions, it is possible to extend the time range for computing the noise transport to several times the transit time for each cycloid by taking the product of the transformation matrices for each cycloid. It may be pointed out here that the functions $\dot{y}$, $\ddot{y}$, $\dddot{y}$, $\dot{z}$, $\ddot{z}$ and $\ddot{z}'$ to be used in evaluating the coefficients are different when the electron is traveling toward the anode and when it is traveling away from the anode.

As mentioned in Section 2.1 the equations derived by Van Duzer involve $\dot{y}$ in the denominator. For the sake of comparison and completeness of this analysis, equations for computing noise transport involving $\dot{y}$ in the denominator are also derived. These equations are helpful when the electrons move in the diode such that $\dot{y}$ is quite appreciable. In practice this occurs for a small fraction of time during the cycloidal path and the derivation of these equations is thus primarily for academic interest and for some checks to be made to establish the correctness of the coefficients given by Eqs. 2.25. This derivation is discussed in the following section, and the reduction of these coefficients to the corresponding Van Duzer's coefficients for the Kino gun model and $\omega \to 0$ is discussed in Appendix D for an open-circuited diode. This shows that the set of Van Duzer's coefficients is a special case of the present analysis.

2.5 Derivation of Coefficients in Terms of y-Component D-c Velocity

The coefficients given by Eqs. 2.25 for computing the noise transport were derived by integrating Eq. 2.12 three times step by step with respect to t and introducing the initial conditions corresponding to the a-plane in order to solve for the constants of integrations involved in the three integrations. Then a perturbation δ_z given by Eq. 2.20 is

introduced. The procedure for this derivation is given in Appendix C. In order to derive similar coefficients in terms of $\dot{y}$, Eq. 2.13 is integrated three times step by step with respect to t and the constant of integration in each integration is determined from the initial conditions at $t = t_a$ corresponding to the a-plane. The procedure in this derivation is very similar to that used in deriving the coefficients given in Eqs. 2.25 and hence the details are not given. In the expression for y, a perturbation δ_y given by

$$t - t_a = T + \delta_y \tag{2.31}$$

is introduced. Then the expression for δ_y is given by

$$- \dot{y}\delta_y e^{-j\omega t} = \tilde{I}_1 \delta_{y_1} + \tilde{q}_{z_{a1}} \delta_{y_2} + \tilde{q}_{y_{a1}} \delta_{y_3} + \dot{z}_{a1} \delta_{y_4} + \dot{y}_{a1} \delta_{y_5} \quad , \tag{2.32}$$

where

$$\delta_{y_1} = - \frac{j(H_2 - H_4)}{\omega_c^3} + \frac{T^2}{2jR\omega_c} e^{-jR\omega_c T} \cos \bar{\alpha} \quad , \tag{2.33a}$$

$$\delta_{y_2} = - \delta_{z_3} \quad , \tag{2.33b}$$

$$\delta_{y_3} = \delta_{z_2} \quad , \tag{2.33c}$$

$$\delta_{y_4} = - \delta_{z_5} \tag{2.33d}$$

and

$$\delta_{y_5} = \delta_{z_4} \quad , \tag{2.33e}$$

where the functions δ_{z_2}, δ_{z_3}, δ_{z_4} and δ_{z_5} are defined in Appendix A, the functions H_2 and H_4 are defined in Appendix C, and R is given by Eq. 2.23. The relationships between the various δ_y's and δ_z's given by Eqs. 2.33b through 2.33e can easily be interpreted physically; the plus or minus sign in these equations is due to the terms involving vector products in the equations of motion of an electron given by Eqs. 2.1. For the case of an open-circuited diode, $I_1 = 0$ and the coefficients of $\tilde{I}_1$ in various equations are not considered. However, these coefficients are given in Appendix C. In a manner similar to the derivation of the coefficients given by Eqs. 2.25, the coefficients involving $\dot{y}$ can be derived. These coefficients are indicated by primes and are given by the following equations:

$$a'_{22} = \frac{\ddot{z}-\omega_c\ddot{y}}{\omega_c^2\dot{y}}\,\frac{F_2}{2} + jW_2 + e^{-jR\omega_c T} \quad , \tag{2.34a}$$

$$a'_{23} = j\,\frac{\ddot{z}-\omega_c\ddot{y}}{\omega_c^2\dot{y}}\,W_1 + \frac{F_4}{2} - jW_3 \quad , \tag{2.34b}$$

$$a'_{24} = \left\{ -\frac{\dddot{z}-\omega_c\dddot{y}}{\omega_c^2\dot{y}}\,W_1 + j\left(\frac{F_4}{2} - jW_3\right)\right\}\frac{m\epsilon_o}{e}\,R\omega_c^2 \quad , \tag{2.34c}$$

$$a'_{25} = \left\{ -j\,\frac{\ddot{z}-\omega_c\ddot{y}}{\omega_c^2\dot{y}}\,W_4 + W_2\right\}\frac{m\epsilon_o}{e}\,R\omega_c^2 \quad , \tag{2.34d}$$

$$a'_{32} = \frac{\dddot{y}+\omega_c\dddot{z}}{\omega_c^2\dot{y}}\,\frac{F_2}{2} - \left(\frac{F_4}{2} - jW_3\right) \quad , \tag{2.34e}$$

$$a'_{33} = j\,\frac{\mathcal{Y}+\omega_c\mathcal{Z}}{\omega_c^2\mathcal{Y}}\,W_1 + jW_2 + e^{-jR\omega_c T}\ , \tag{2.34f}$$

$$a'_{34} = \left\{-\frac{\mathcal{Y}+\omega_c\mathcal{Z}}{\omega_c^2\mathcal{Y}}\,W_1 - W_2\right\}\frac{m\epsilon_o}{e}\,R\omega_c^2\ , \tag{2.34g}$$

$$a'_{35} = \left\{-j\,\frac{\mathcal{Y}+\omega_c\mathcal{Z}}{\omega_c^2\mathcal{Y}}\,W_4 + j\left(\frac{F_4}{2} - jW_3\right)\right\}\frac{m\epsilon_o}{e}\,R\omega_c^2\ , \tag{2.34h}$$

$$a'_{42} = \left\{j\,\frac{\mathcal{Z}}{\omega_c\mathcal{Y}}\,\frac{F_2}{2} - W_3\right\}\frac{1}{R\omega_c^2}\,\frac{e}{m\epsilon_o}\ , \tag{2.34i}$$

$$a'_{43} = \left\{-\frac{\mathcal{Z}}{\omega_c\mathcal{Y}}\,W_1 + j\,\frac{F_6}{2}\right\}\frac{1}{R\omega_c^2}\,\frac{e}{m\epsilon_o}\ , \tag{2.34j}$$

$$a'_{44} = -j\,\frac{\mathcal{Z}}{\omega_c\mathcal{Y}}\,W_1 - \frac{F_6}{2} + e^{-jR\omega_c T}\ , \tag{2.34k}$$

$$a'_{45} = \frac{\mathcal{Z}}{\omega_c\mathcal{Y}}\,W_4 + jW_3\ , \tag{2.34l}$$

$$a'_{52} = \left\{\frac{\mathcal{Y}}{\omega_c\mathcal{Y}}\,\frac{F_2}{2} - \frac{F_6}{2}\right\}\frac{1}{R\omega_c^2}\,\frac{je}{m\epsilon_o}\ , \tag{2.34m}$$

$$a'_{53} = -\left\{\frac{\mathcal{Y}}{\omega_c\mathcal{Y}}\,W_1 + W_3\right\}\frac{1}{R\omega_c^2}\,\frac{e}{m\epsilon_o}\ , \tag{2.34n}$$

$$a'_{54} = -j\left(\frac{\mathcal{V}}{\omega_c \mathcal{J}} W_1 + W_3\right) \tag{2.34o}$$

and

$$a'_{55} = \frac{\mathcal{V}}{\omega_c \mathcal{J}} W_4 - \frac{F_e}{2} + e^{-jR\omega_c T} \quad , \tag{2.34p}$$

where the various functions in these equations have been described earlier in connection with the coefficients given by Eqs. 2.25.

2.6 Some Checks on the Primed and Unprimed Coefficients

As mentioned in Section 2.4, one of the purposes of deriving the coefficients given by Eqs. 2.34 is to make some checks on the coefficients given by Eqs. 2.25. These checks are discussed below.

2.6.1 No Magnetic Field. For the case of no magnetic field, i.e., $\omega_c = 0$, these coefficients should reduce to the Llewellyn coefficients in the general form before the introduction of the space-charge parameter ξ. In such a case all the current flows along the y-axis except for the effect due to some finite initial values of the z-component velocity. For such a case it will be more appropriate to consider the primed coefficients; by substituting $\omega_c = 0$ in those coefficients, it is found that they do reduce to the Llewellyn coefficients. For this purpose, the coefficients of I in Eqs. 2.24, which are given in Appendix C, also reduce to the corresponding Llewellyn coefficients for $\omega_c = 0$. For the unprimed coefficients, the reduction to the Llewellyn coefficients is not directly evident. However, after $\omega_c = 0$ is substituted, the use of the transformation

$$\frac{P_{z_a}}{\dot{z}} a_{ij} \longleftrightarrow \frac{P_{y_a}}{\dot{y}} a_{ij} \tag{2.35}$$

does reduce the unprimed coefficients to the Llewellyn coefficients. In Eq. 2.35 P refers to the perturbation of the current density or the velocity. For $\omega_c = 0$, the fluctuations P_{z_b} are independent of the fluctuations P_{y_a} and similarly the fluctuations P_{y_b} are independent of the fluctuations P_{z_a}. In other words there is no coupling between the two component parameters. The nature of the equations given by Eqs. 2.25 is such that after a substitution of $\omega_c = 0$, it is found that the fluctuations P_{z_b} depend upon the fluctuations P_{y_a} and the fluctuations P_{y_b} depend upon the fluctuations P_{z_a}. This requires the use of the transformation given by Eq. 2.35. For a general case when $I_1 \neq 0$, the coefficients in the two cases also reduce to the corresponding Llewellyn coefficients except for a_{51} which does not reduce to the Llewellyn coefficient G^*. This is because the two components of I_1 have not been considered separately and the transformation given by Eq. 2.35 cannot be used. Since this reduction is made just for the purpose of checking the coefficients, the fact that a_{51} does not reduce to G^* for $\omega_c = 0$ is not of importance, particularly when an open-circuited diode is being considered.

2.6.2 Correspondence Between the Primed and Unprimed Coefficients. From Eqs. 2.25 and 2.34, designating the unprimed and the primed coefficients respectively, a good deal of similarity may be seen. In fact the two sets of coefficients reduce to a common set when

$$\dot{y} \ , \ \dot{\mathcal{Y}} \rightarrow 0 \tag{2.36a}$$

and

$$\ddot{z} \ , \ \ddot{z}' \rightarrow 0 \ . \tag{2.36b}$$

The parameter I_D, the current density, does not appear explicitly in Eqs. 2.36, but appears in expressions for the four quantities mentioned in Eq. 2.36. The conditions given by Eq. 2.36 are satisfied when electrons are injected continuously in the interaction region with only the z-component of velocity to form an ideal flow of electrons and when the electrons are drifting at a constant velocity $\dot{z}$. Equations 2.36 are also satisfied for a Brillouin flow when the velocity $\dot{z}$ of the electrons varies across the thickness of the beam.

Additional correspondence in terms of the equivalence between the primed and the unprimed coefficients may also be seen when use of the transformation given by Eq. 2.35 is used. This correspondence is limited to only those coefficients for which the two suffixes on either side of Eq. 2.35 are the same. For other coefficients this transformation cannot be used.

2.6.3 Comparison with Van Duzer's Coefficients. In Appendix D it is shown that the magnitudes of Van Duzer's coefficients are the same as those of the corresponding coefficients from Eqs. 2.34 for the case of an open-circuited diode when $\omega \rightarrow 0$ and $\dot{z}' = \omega_c \dot{y}$ (a result of the Kino gun model) are substituted in Eqs. 2.34, indicating thereby that the coefficients given by Eqs. 2.25 and 2.34 correspond to a general case.

2.7 Propagation of Perturbations in the Interaction Region

For the evaluation of noise transport in the interaction region of crossed-field devices the coefficients given by Eqs. 2.25 will be used. The use of coefficients given by Eqs. 2.34 is very much limited

to some special applications of academic interest only. The use of the coefficients given by Eqs. 2.25 for evaluating noise transport for some specialized cases depends upon the selection of the functions $\dot{y}$, $\ddot{y}$, $\dddot{y}$, $\dot{z}$, $\ddot{z}$ and $\dddot{z}$ for the corresponding case. For a special case when $\dot{z}$ = constant in the interaction region (implying thereby that $\dot{y} = \ddot{y} = \dddot{y} = \ddot{z} = \dddot{z} = 0$) with some mean square fluctuations in $\dot{z}$ and other functions at the input plane, it is much easier to evaluate these coefficients. For this case the conditions given by Eq. 2.36 are satisfied and the unprimed and the primed coefficients are equal. The corresponding geometry for this case is shown in Fig. 2.4. For the case when $\dot{z}$ = constant, it may be assumed that the a-c voltage V given by Eq. 2.24 is due to the E_z component only. The contribution due to the E_y component is negligible because $\dot{y} \simeq 0$. Then the a-c voltage V_b at the b-plane and the a-c voltage V_a at the a-plane are given by

$$V = V_b - V_a = - \int_0^T E_{z_1} \dot{z} \, dT \quad , \tag{2.37}$$

where T = 0 is referred to at the a-plane. By taking $\dot{z}$ = constant as assumed in this case, the final result is given by

$$V = a_{12} q_{z_a} + a_{13} q_{y_a} + a_{14} \dot{z}_a + a_{15} \dot{y}_a \quad . \tag{2.38}$$

The expression for E_{z_1} is given in Appendix E. In writing Eq. 2.38, I = 0 is assumed and the various coefficients are given by

$$a_{12} = \frac{\dot{z}}{\epsilon_o} \left(\frac{M_1}{2} + \frac{e^{-jR\omega_c T} - 1}{R} + \frac{M_4}{2j} \right) \frac{1}{R\omega_c^2} \quad , \tag{2.39a}$$

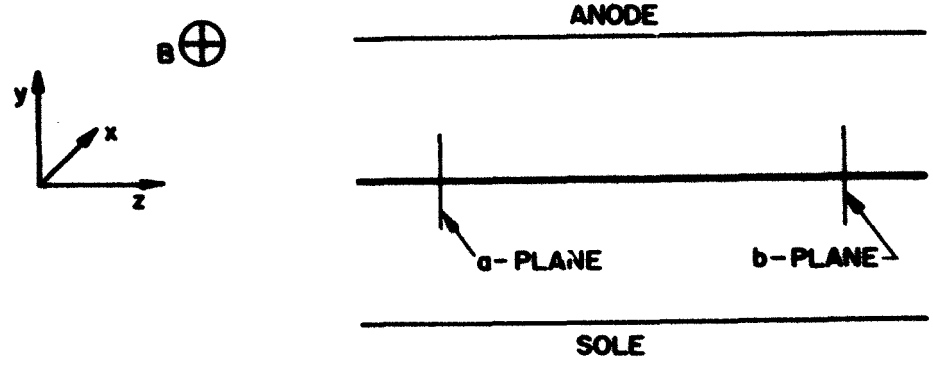

FIG. 2.4 IDEAL BEAM IN THE INTERACTION REGION.

$$a_{13} = \frac{\dot{z}}{\epsilon_o}\left(\frac{M_2}{2j} - \frac{M_3}{2} - \frac{\omega_c T\, e^{-jR\omega_c T}}{R} - \frac{e^{-jR\omega_c T} - 1}{jR^2}\right)\frac{1}{R\omega_c^2} , \quad (2.39b)$$

$$a_{14} = -\frac{\dot{z}}{\eta}\left(\frac{M_2}{2} + \frac{M_3}{2j} + \frac{\omega_c T\, e^{-jR\omega_c T}}{jR} - \frac{e^{-jR\omega_c T} - 1}{R^2}\right) \quad (2.39c)$$

and

$$a_{15} = -\frac{\dot{z}}{\eta}\left(\frac{M_1}{2j} - \frac{M_4}{2}\right) , \quad (2.39d)$$

where

$$M_{1,2} = \frac{1}{j(R+1)}\left(\frac{e^{j\omega_c T} - 1}{j} + \frac{e^{-jR\omega_c T} - 1}{jR}\right)$$

$$\mp \frac{1}{j(R-1)}\left(-\frac{e^{-j\omega_c T} - 1}{j} + \frac{e^{-jR\omega_c T} - 1}{jR}\right)$$

(2.40a)

and

$$M_{1,3} = \frac{1}{[j(R+1)]^2}\left[\frac{e^{j\omega_c T} - 1}{j} + \frac{e^{-jR\omega_c T} - 1}{jR} + \frac{(R+1)\omega_c T\, e^{-jR\omega_c T}}{R} - \frac{j(R+1)}{R^2}\left(e^{-jR\omega_c T} - 1\right)\right]$$

$$\mp \frac{1}{[j(R-1)]^2}\left[-\frac{e^{-j\omega_c T} - 1}{j} + \frac{e^{-jR\omega_c T} - 1}{j} + \frac{(R-1)\omega_c T}{R} e^{-jR\omega_c T} - \frac{j(R-1)}{R^2}\left(e^{-jR\omega_c T} - 1\right)\right] , \quad (2.40b)$$

and the first and second suffixes with M's correspond to the upper and lower signs respectively on the right-hand side of Eqs. 2.40.

CHAPTER III. RESULTS OF LLEWELLYN-PETERSON ANALYSIS

3.1 Introductory Remarks

In the last chapter expressions for the noise transport coefficients were derived. These coefficients are related to the independent variables, namely I_1, q_{z_1}, q_{y_1}, $\dot{z}_1$ and $\dot{y}_1$ at the "a" and "b" planes by the matrix relation given in Eq. 2.24. For the case of an open-circuited diode when $I_1 = 0$, the noise transport coefficients given by Eqs. 2.25 and 2.34 in terms of $\dot{z}$ and $\dot{y}$ respectively become general in nature and, as mentioned in Section 2.3, any physical model may be used for the evaluation of these coefficients provided the small-signal assumption is not violated. It can be seen from Eqs. 2.25 and 2.34 that the values of these coefficients depend upon I_D, V_o, d, ω, ω_c, T and the initial velocities. Whether these coefficients are to be evaluated for a space-charge-limited case or for a temperature-limited case depends upon the selection of the values of the d-c parameters $\dot{z}$, $\dot{y}$, $\ddot{z}$, $\ddot{y}$, $\dddot{z}$ and $\dddot{y}$ as a function of the transit time in these coefficients. These d-c parameters are single valued functions.

In evaluating the noise transport coefficients, if the initial values of the velocity components are assumed to be equal to zero for convenience, the selection of the a-plane is restricted because $\dot{z}$ in the unprimed coefficients (or $\dot{y}$ in the primed coefficients) is equal to zero at T = 0 for both space-charge-limited and temperature-limited operation. This causes a singularity in the noise transport coefficients and for the analysis to be valid it becomes necessary to select the a-plane appropriately. In the expressions most commonly used for a physical model, $\dot{y} = \dot{z} = 0$ for T = 0 when initial velocities are neglected and

$\dot{y} = 0$ again (or of a small value) at the entrance to the interaction region for conditions not far from ideal. Thus the selection of the unprimed coefficients will not cause any singularity except at $T = 0$ and hence the small-signal assumption is not violated.

For nonideal conditions, when the electron beam or a fraction of the electron beam either touches or grazes the sole electrode during the cycloidal movement of the beam, $\dot{z}$ or $\dot{y}$ are of small magnitude. Under these conditions the small-signal assumption is violated and the coefficients derived by Rando[19] in terms of the total velocity do not seem to show any advantage. In order to evaluate the unprimed noise transport coefficients under these conditions it is necessary to by-pass the regions of small values of $\dot{z}$ and assume that the values of these coefficients are not changed in the regions of low velocities. This point has been discussed in Section 2.4.

In the following paragraphs the evaluation of the noise transport coefficients will be referred to as the evaluation of the unprimed coefficients given by Eqs. 2.25 unless otherwise specified.

3.2 Cyclotron Frequency Perturbation

In evaluating the noise transport coefficients given by Eqs. 2.25 it can be seen that for the case $\omega = \omega_c$, i.e., $R = 1$, each of the F functions defined by Eqs. A.7 through A.9 in Appendix A causes an apparent singularity. By applying L'Hospital's rule this singularity can be removed and these F functions are then given by

$$F_{1,2} = -\frac{1}{8}\left[2 \sin \omega_c T - 2\omega_c T\, e^{-j\omega_c T} - 2j\omega_c^2 T^2 e^{-j\omega_c T} \pm \frac{8}{6}\,\omega_c^3 T^3\, e^{-j\omega_c T}\right], \tag{3.1}$$

$$F_{3,4} = \sin \omega_c T \mp \omega_c T \, e^{-j\omega_c T} \tag{3.2}$$

and

$$F_{5,6} = \frac{1}{2}\left[j\omega_c T \, e^{-j\omega_c T} - j \sin \omega_c T \mp \omega_c^2 T^2 \, e^{-j\omega_c T} \right] . \tag{3.3}$$

The W functions which are also involved in the noise transport coefficients are related to the F functions by Eqs. 2.26 and can easily be evaluated for the case R = 1 when the F functions have been evaluated from Eqs. 3.1 through 3.3. As before, the upper and lower signs in Eqs. 3.1 through 3.3 correspond to the first and second suffixes respectively.

3.3 Numerical Evaluation of the Coefficients

From the matrix relation given by Eq. 2.24 for the noise transport from the a-plane to the b-plane, it can be seen that for the case of an open-circuited diode it is necessary to evaluate sixteen noise transport coefficients for different values of R for each different physical model. In order to reduce the magnitude of the computations it is assumed that the two a-c components of the current density are in the same phase and of the same magnitude at the input plane. The same thing is assumed for the two a-c velocity components but the dependence of the numerical results on this assumption has not been investigated. In a simplified case for the interaction region when $\dddot{z} = \dddot{y} = \dot{y} = \ddot{y} = \dddot{z} = 0$ and $\dot{z}$ = constant, the following relations are true for the various coefficients:

$$a_{22} = a_{33} \ , \quad a_{23} = -a_{32} \ ,$$

$$a_{24} = a_{35} \ , \quad a_{25} = -a_{34} \ ,$$

$$a_{42} = a_{53} \ , \quad a_{43} = -a_{52} \ ,$$

$$a_{44} = a_{55} \ , \quad a_{45} = -a_{54} \ . \tag{3.4}$$

The plus or minus signs involved in the above relations are due to the vector cross products involved in the equations of motion and are analogous to the plus or minus signs involved in Eqs. 2.33. From the matrix equation given by Eqs. 2.24 and 3.4, it is evident that in spite of the fact that the two a-c components of the same variable (current density or velocity) are assumed to be in phase and of equal magnitude at the a-plane these a-c components are in different phases and of different magnitudes at the b-plane. This is true because of the different functions in the corresponding coefficients and because of the relations given by Eqs. 3.4.

In this section four cases are considered which correspond to the selection of different expressions for the d-c terms in Eqs. 2.25.

Case A. Kino Gun Model.

The d-c parameters are given by Eqs. 2.29 and 2.30 for the case of Kino[15] gun model and the following equations are true:

$$\frac{\ddot{z} - \omega_c \dot{y}}{\omega_c^2 z} = 0 \ , \tag{3.5a}$$

$$\frac{\dddot{y}+\omega_c\ddot{z}}{\omega_c^2\dot{z}} = \frac{1}{R_1} , \tag{3.5b}$$

$$\frac{\ddot{z}}{\omega_c\dot{z}} = \left[(1 - \cos\theta) + \frac{\omega_c^2}{\tilde{I}_D}(\dot{y}_a \cos\theta - \dot{z}_a \sin\theta)\right]\frac{1}{R_1} \tag{3.5c}$$

and

$$\frac{\ddot{y}}{\omega_c\dot{z}} = \left[\sin\theta - \frac{\omega_c^2}{\tilde{I}_D}(\dot{y}_a \sin\theta + \dot{z}_a \cos\theta)\right]\frac{1}{R_1} , \tag{3.5d}$$

where

$$R_1 = \theta - \sin\theta + \frac{\omega_c^2}{\tilde{I}_D}(\dot{z}_a \cos\theta + \dot{y}_a \sin\theta) , \tag{3.6a}$$

$$\tilde{I}_D = I_D \frac{\epsilon}{m\epsilon_o} , \tag{3.6b}$$

$$\theta = \omega_c T \tag{3.6c}$$

and $\dot{y}_a$ and $\dot{z}_a$ refer to the d-c velocities at the a-plane.

Case B. Temperature-Limited Case.

For a temperature-limited case, free space-charge trajectories are assumed and then the following equations are true:

$$\ddot{z} - \omega_c\dot{y} = 0 , \tag{3.7a}$$

$$\ddot{y} + \omega_c \dot{z} = 0 \quad , \tag{3.7b}$$

$$\frac{\dot{z}}{\omega_c \dot{z}} = \frac{\sin\theta + \frac{\omega_c}{\ddot{y}_a}\dot{y}_a \cos\theta}{R_2} \tag{3.7c}$$

and

$$\frac{\ddot{y}}{\omega_c \dot{z}} = \frac{\cos\theta - \frac{\omega_c}{\ddot{y}_a}\dot{y}_a \sin\theta}{R_2} \quad , \tag{3.7d}$$

where

$$R_2 = (1 - \cos\theta) + \frac{\omega_c}{\ddot{y}_a}(\dot{z}_a + \dot{y}_a \sin\theta) \tag{3.8a}$$

and

$$\ddot{y}_a = -\eta E_{y_a} - \omega_c \dot{z}_a \quad . \tag{3.8b}$$

<u>Case C. Quasi Space-Charge-Limited Case.</u>

For this case, the physical model discussed in Section 2.3 is considered and the following equations are derived from Eqs. 2.27 and 2.28:

$$\frac{\ddot{z} - \omega_c \dot{y}}{\omega_c^2 \dot{z}} = \frac{\sin\left(\frac{\theta}{2} + \bar{\alpha}\right)}{R_3} \quad , \tag{3.9a}$$

$$\frac{\ddot{y} + \omega_c \dot{z}}{\omega_c^2 \dot{z}} = \frac{\cos\left(\frac{\theta}{2} + \bar{\alpha}\right)}{R_3} \quad , \tag{3.9b}$$

$$\frac{\ddot{z}}{\omega_c^2} = \left[2\cos\left(\frac{\theta}{2}+\bar{\alpha}\right) - 2\cos(\theta+\bar{\alpha}) + \frac{\omega_c^2}{\tilde{I}_D}(\dot{y}_a\cos\theta - \dot{z}_a\sin\theta)\right]\frac{1}{R_3} \tag{3.9c}$$

and

$$\frac{\ddot{y}}{\omega_c^2} = \left[-2\sin\left(\frac{\theta}{2}+\bar{\alpha}\right) + 2\sin(\theta+\bar{\alpha}) - \frac{\omega_c^2}{\tilde{I}_D}(\dot{z}_a\cos\theta + \dot{y}_a\sin\theta)\right]\frac{1}{R_3}\ , \tag{3.9d}$$

where

$$R_3 = 4\sin\left(\frac{\theta}{2}+\bar{\alpha}\right) - 2\sin(\theta+\bar{\alpha}) + \frac{\omega_c^2}{\tilde{I}_D}(\dot{y}_a\sin\theta + \dot{z}_a\cos\theta) \tag{3.10}$$

and $\bar{\alpha}$ is defined by Eq. 2.15. When the initial velocities $\dot{y}_a$ and $\dot{z}_a$ are negligible and $E_{zo} \ll E_{yo}$ giving $\tan\Phi \simeq 0$, then $\bar{\alpha} = 0$ for $t_a = t_o$. When $E_{zo} \ll E_{yo}$, but the two initial velocity components are of equal magnitude and are not negligible, $\Phi = \pi/4$ and $\bar{\alpha} = -\pi/8$ for $t_a = t_o$. When $E_{zo} = B\dot{y}_a$, $\Phi = 0$ again and $\bar{\alpha} = 0$ for $t_a = t_o$.

Case D. Interaction Region (Ideal Conditions).

It has been mentioned in Section 2.4 that the unprimed coefficients given by Eqs. 2.25 can be used for evaluating noise transport in the interaction region. In this section ideal conditions are considered and in Section 3.4 the evaluation of these coefficients for arbitrary input conditions (i.e., nonideal conditions) is also considered. For the case of a laminar beam in the interaction region the following equations are true:

$$\dot{z} = \ddot{z} = \dot{y} = \ddot{y} = \dddot{y} = 0 \tag{3.11a}$$

and

$$\dot{z} = \text{constant} \quad . \tag{3.11b}$$

Figures 3.1 through 3.8 show the plots of the combination of the various coefficients (as indicated on each graph) versus $\omega_c T/\pi$ for different values of R. In these computations the initial velocities are neglected and the plots are made for the two cases, namely Case A (Kino gun model) and Case B (temperature-limited model) over the common range, $0 < \theta \leq \pi$.

In addition Figs. 3.1 and 3.2 represent the plots for Case D (interaction region). Figures 3.3 and 3.4 for Case B also correspond to Case D, but these plots are shown again in Figs. 3.19 and 3.20 to compare these results with those for the values of m = -0.1 and 0.1 for arbitrary input conditions in the interaction region discussed in the next section.

In Section 3.1 it was shown that in evaluating the noise transport coefficients the selection of the a-plane is important. This is due to the fact that when the initial velocities are neglected $\dot{z}$ for small values of T is very small. If the a-plane is not selected properly, the small-signal assumption made in this analysis is violated and the results cannot be interpreted appropriately. In this respect some of the points corresponding to small values of θ only in Figs. 3.1 through 3.8 are of negligible importance. This corresponds to the results for the Kino gun model in Figs. 3.3, 3.4, 3.7 and the results for the temperature-limited case in Figs. 3.7 and 3.8. Comparing these

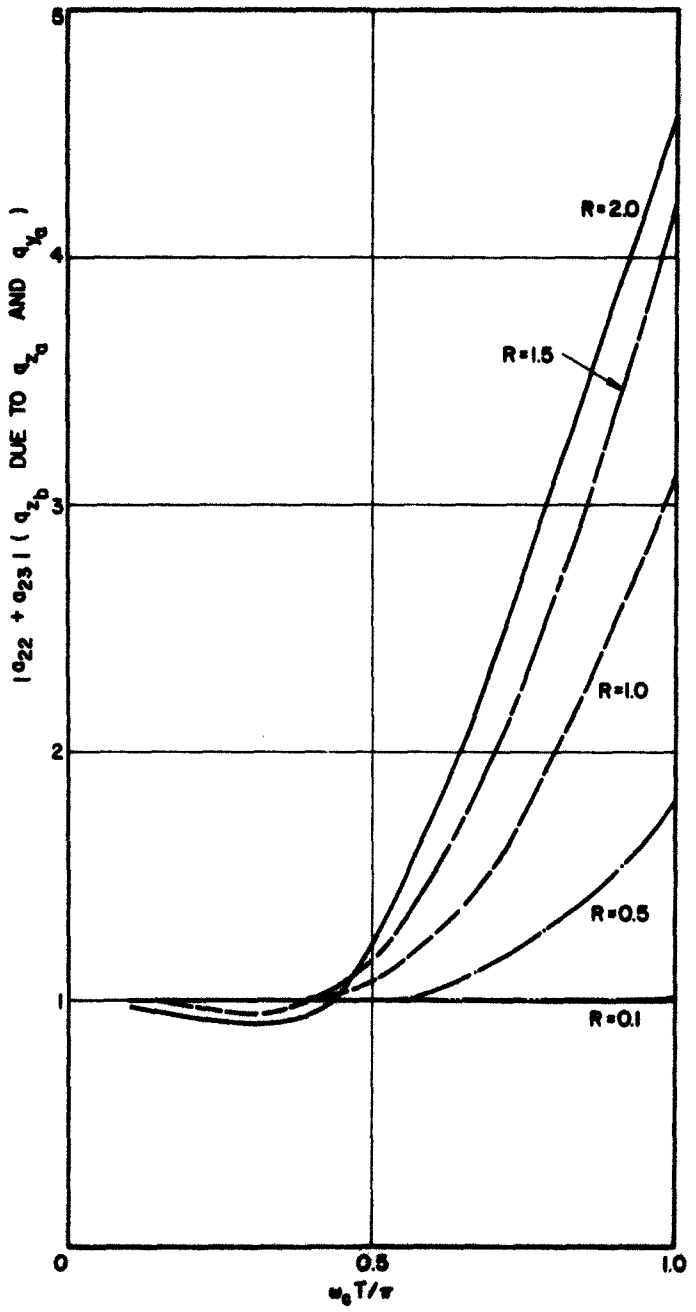

FIG. 3.1 $|a_{22} + a_{23}|$ VS. $\omega_c T/\pi$. INTERACTION REGION, TEMPERATURE-LIMITED CASE, KINO GUN.

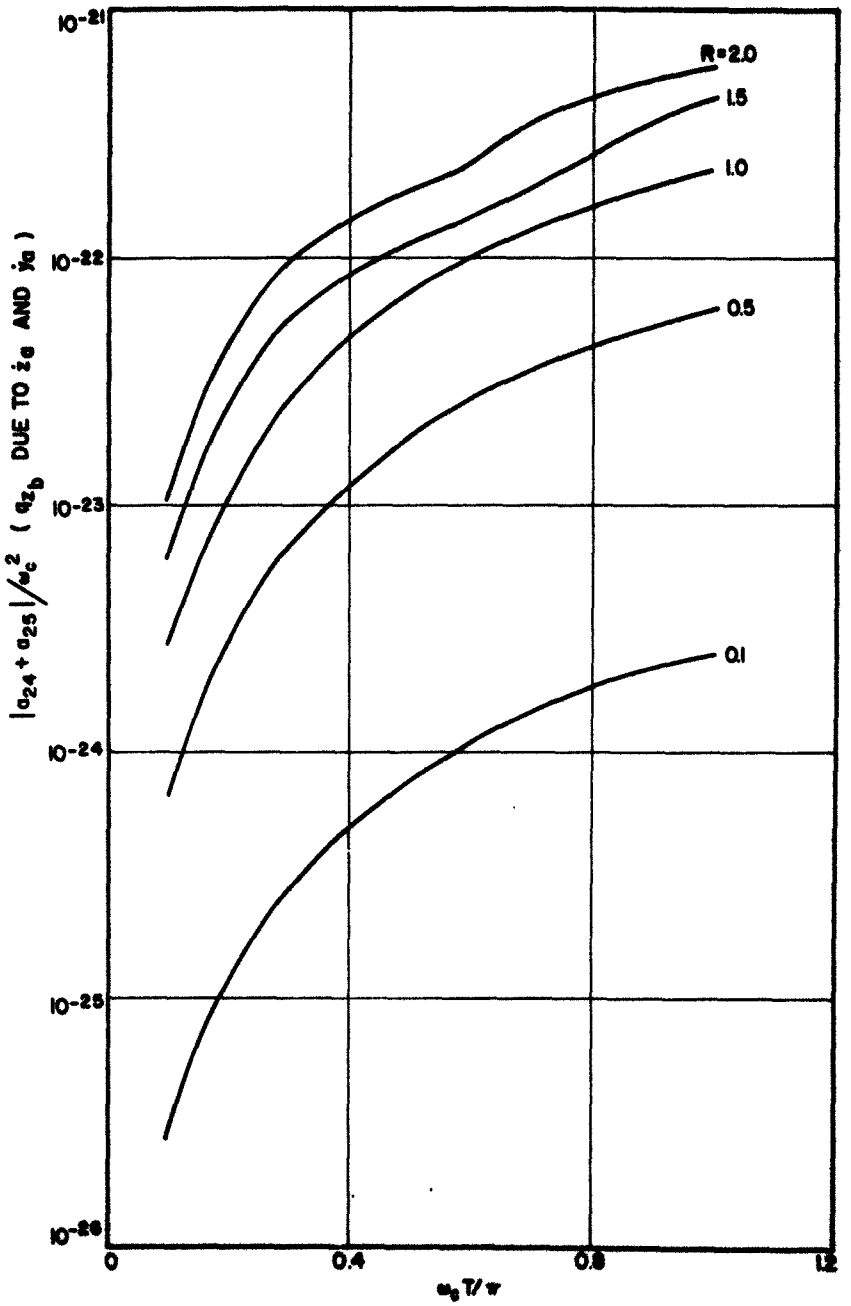

FIG. 3.2 $|a_{24} + a_{25}|/\omega_c^2$ VS. $\omega_c T/\pi$. INTERACTION REGION, TEMPERATURE-LIMITED CASE, KINO GUN.

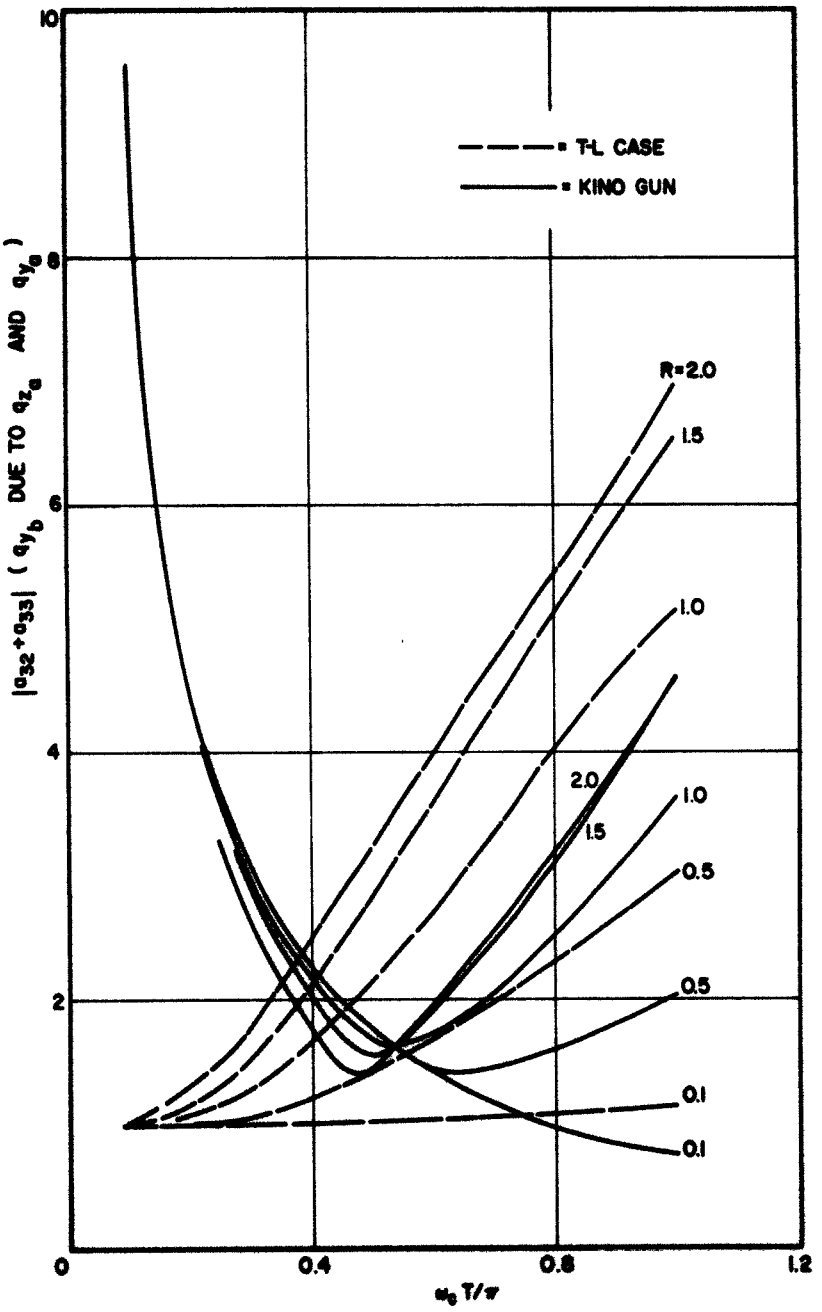

FIG. 3.3 $|a_{32} + a_{33}|$ VS. $\omega_c T/\pi$.

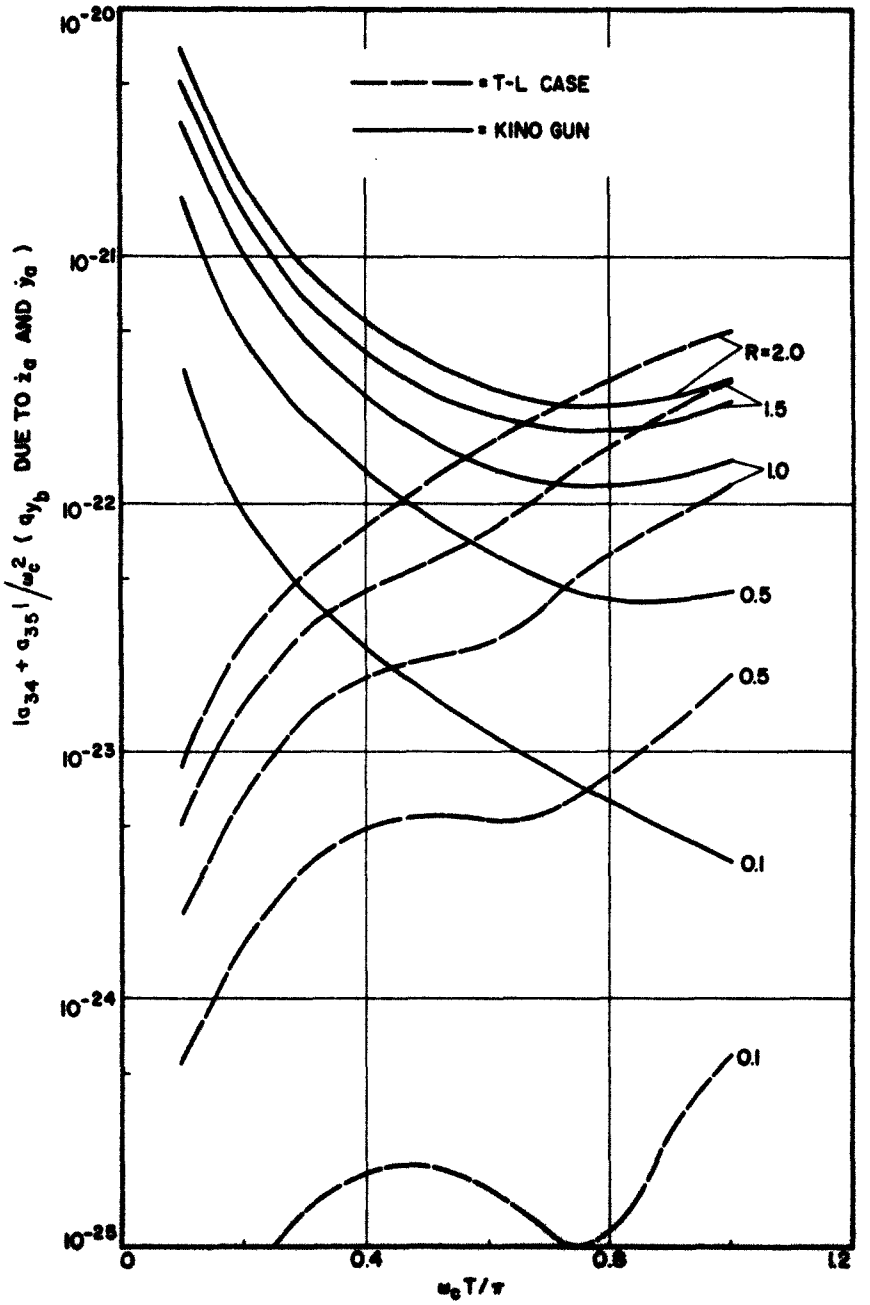

FIG. 3.4 $|a_{34} + a_{35}|/\omega_c^2$ VS. $\omega_c T/\pi$.

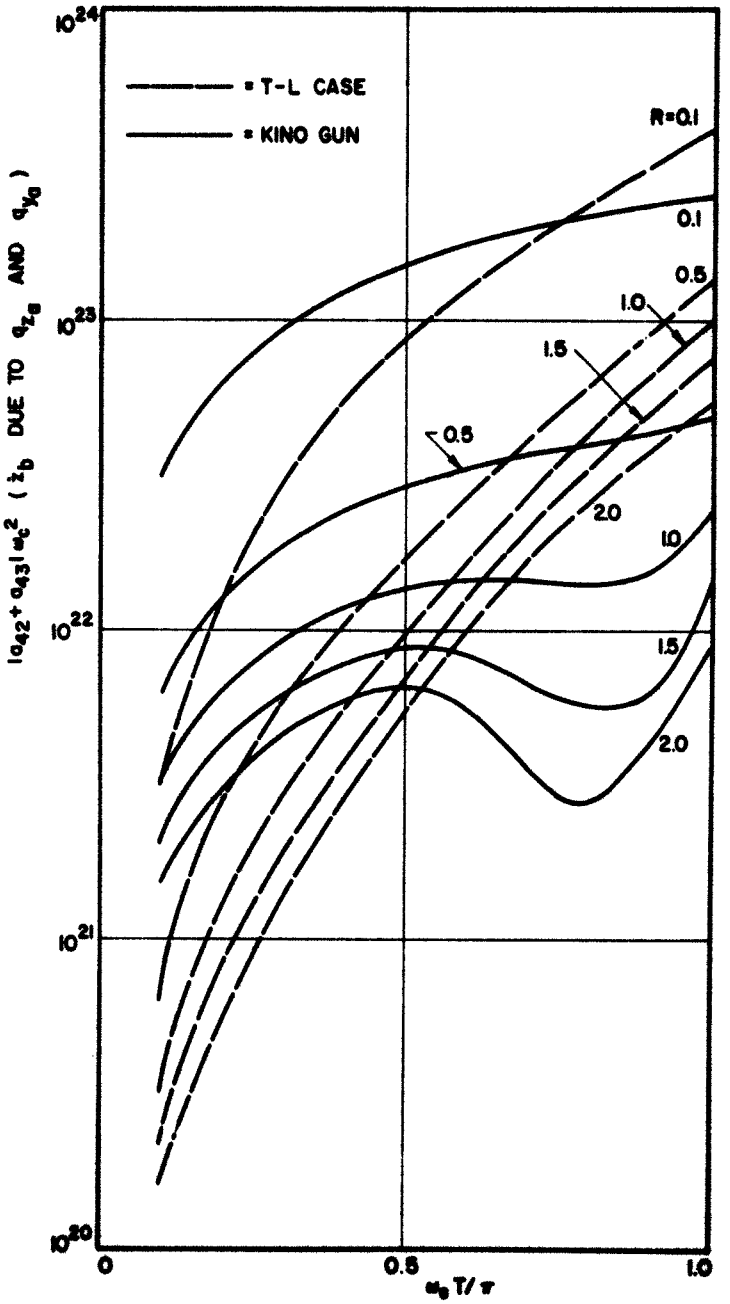

FIG. 3.5 $|a_{42} + a_{43}|\ \omega_c^2$ VS. $\omega_c T/\pi$.

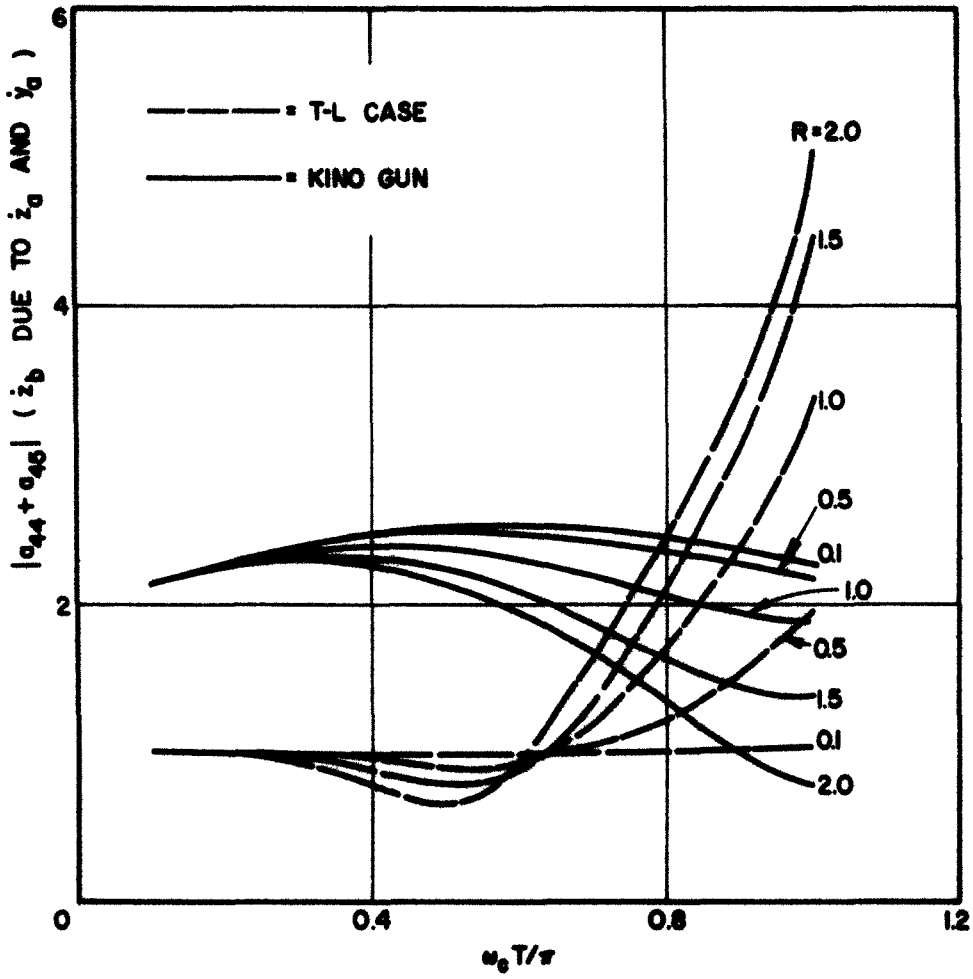

FIG. 3.6 $|a_{44} + a_{45}|$ VS. $\omega_c T/\pi$.

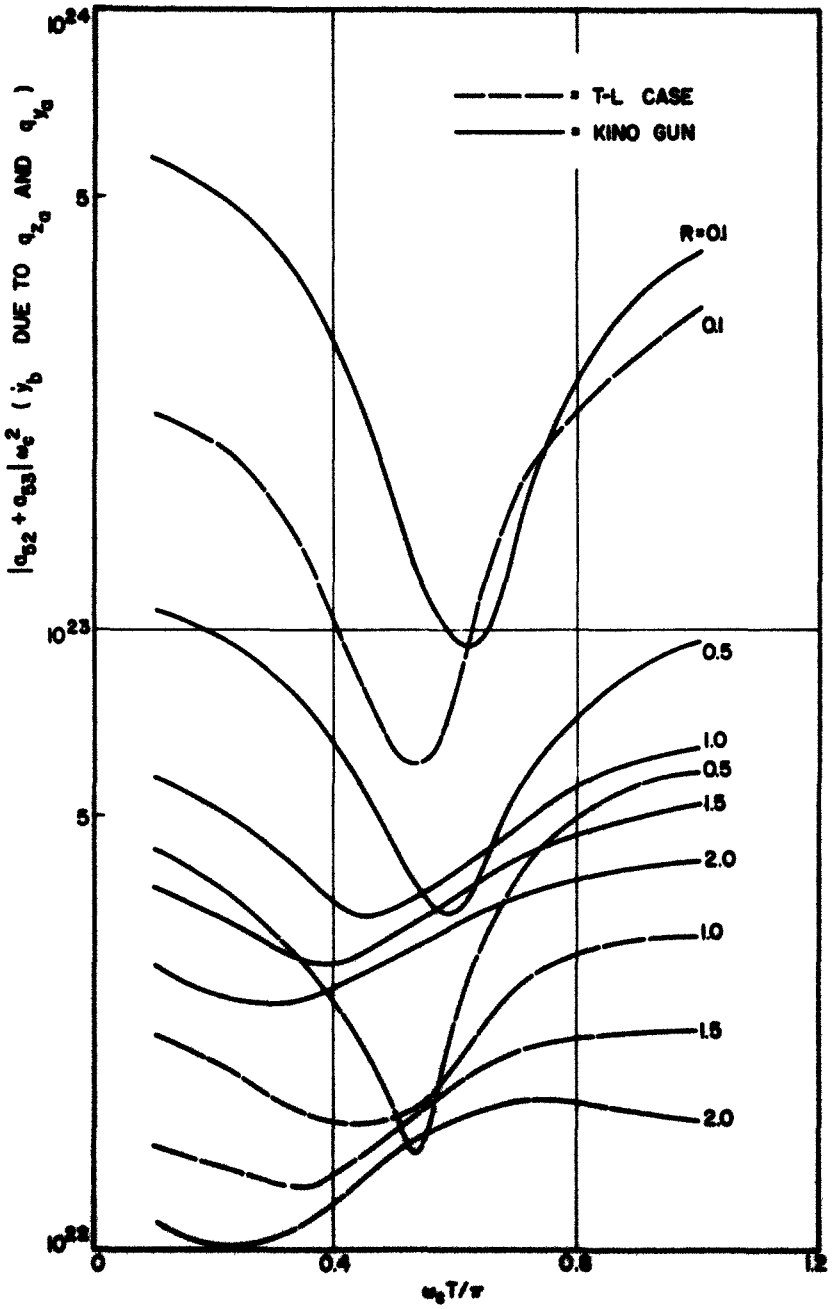

FIG. 3.7 $|a_{52} + a_{53}| \omega_c^2$ VS. $\omega_c T/\pi$.

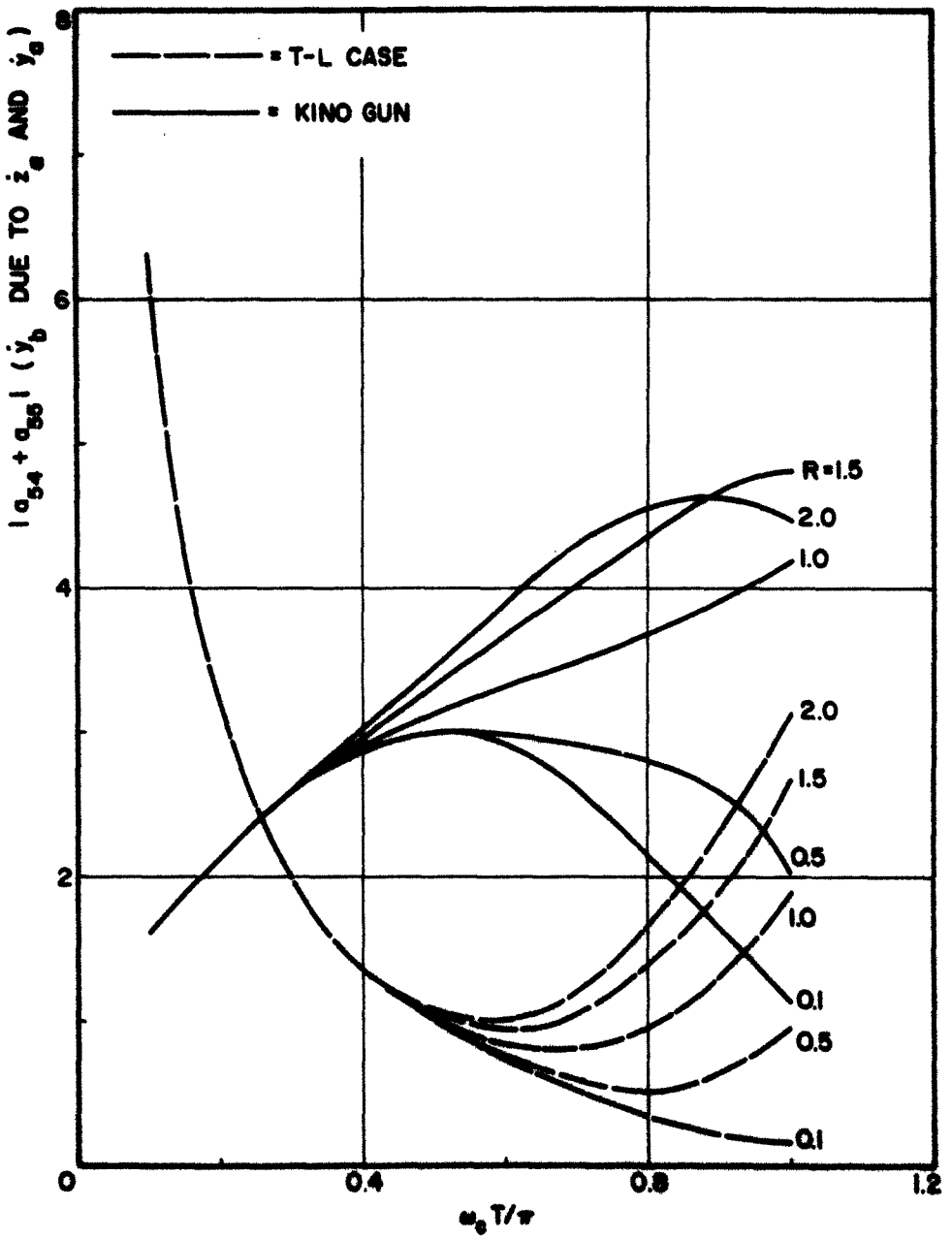

FIG. 3.8 $|a_{54} + a_{55}|$ VS. $\omega_c T/\pi$.

plots with the corresponding plots for Case D (when $\dot{z}$ = constant) shown in Figs. 3.19 through 3.24, the validity of the other points in the various plots shown in Figs. 3.1 through 3.8 is justified. It is for this reason that some of the minima in Figs. 3.3, 3.4, 3.7 and 3.8 cannot be interpreted appropriately.

For the case of finite initial velocities, the plots in Figs. 3.3 and 3.4 (for the case of the Kino gun) and Figs. 3.7 and 3.8 will not show large values at small values of θ. Instead, the values of the coefficients plotted in these figures will be very close to those in the corresponding plots in Figs. 3.19 through 3.24. The effect of the initial velocities vanishes at the following values of θ:

$$\theta_o = \tan^{-1} \frac{-\dot{z}_a}{\dot{y}_a} \quad \text{for Case A and Case C} \tag{3.12a}$$

and

$$\theta_o = \sin^{-1} \frac{-\dot{z}_a}{\dot{y}_a} \quad \text{for Case B} \quad . \tag{3.12b}$$

For values of $\theta > \theta_o$, the effect of the initial velocities is small and the plots for the various coefficients would not be very much different from those plotted in Figs. 3.1 through 3.16.

By considering the variation of the values of the plots given in Figs. 3.1 through 3.8, as a function of R (for diff rent values of ω and for fixed values of ω_c), it can be seen in Figs. 3.1 through 3.4, 3.6 (Case B only for Fig. 3.6) and 3.8 that the coefficients plotted in these figures are monotonically increasing functions of R. In order to show the exact variation of noise with R for a fixed value of ω_c, it will be necessary to consider some numerical values of the various a-c

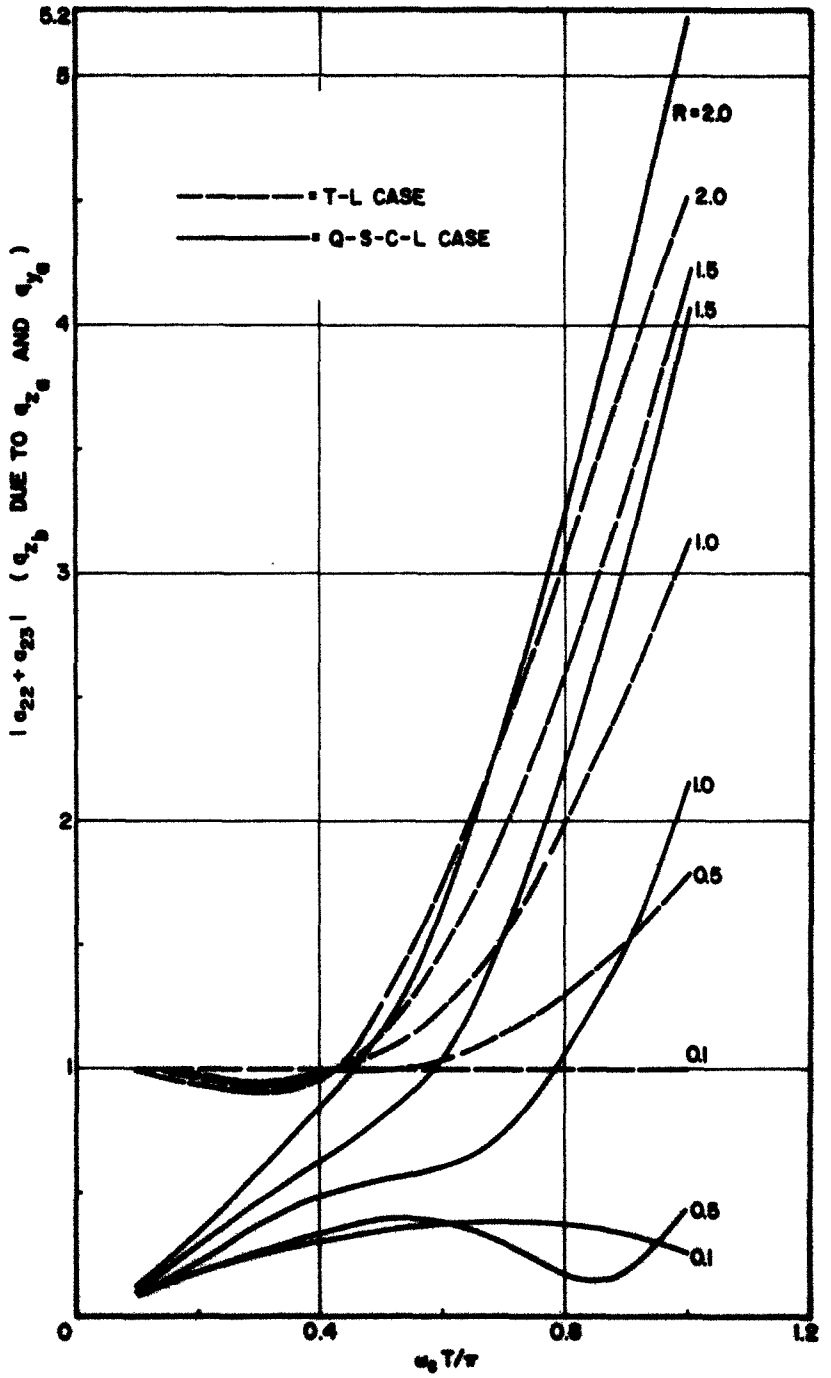

FIG. 3.9 $|a_{22} + a_{23}|$ VS. $\omega_c T/\pi$.

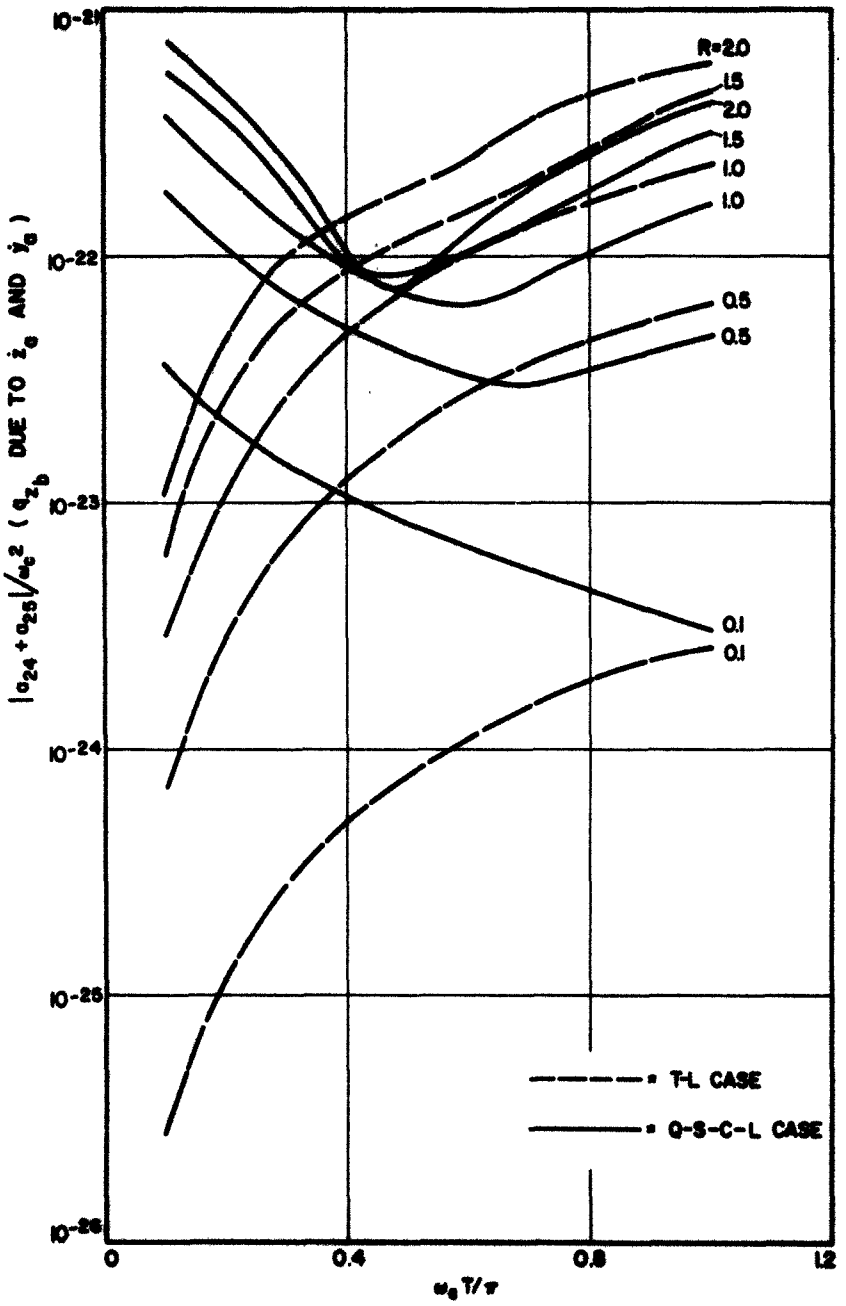

FIG. 3.10 $|a_{24} + a_{25}|/\omega_c^2$ VS. $\omega_c T/\pi$.

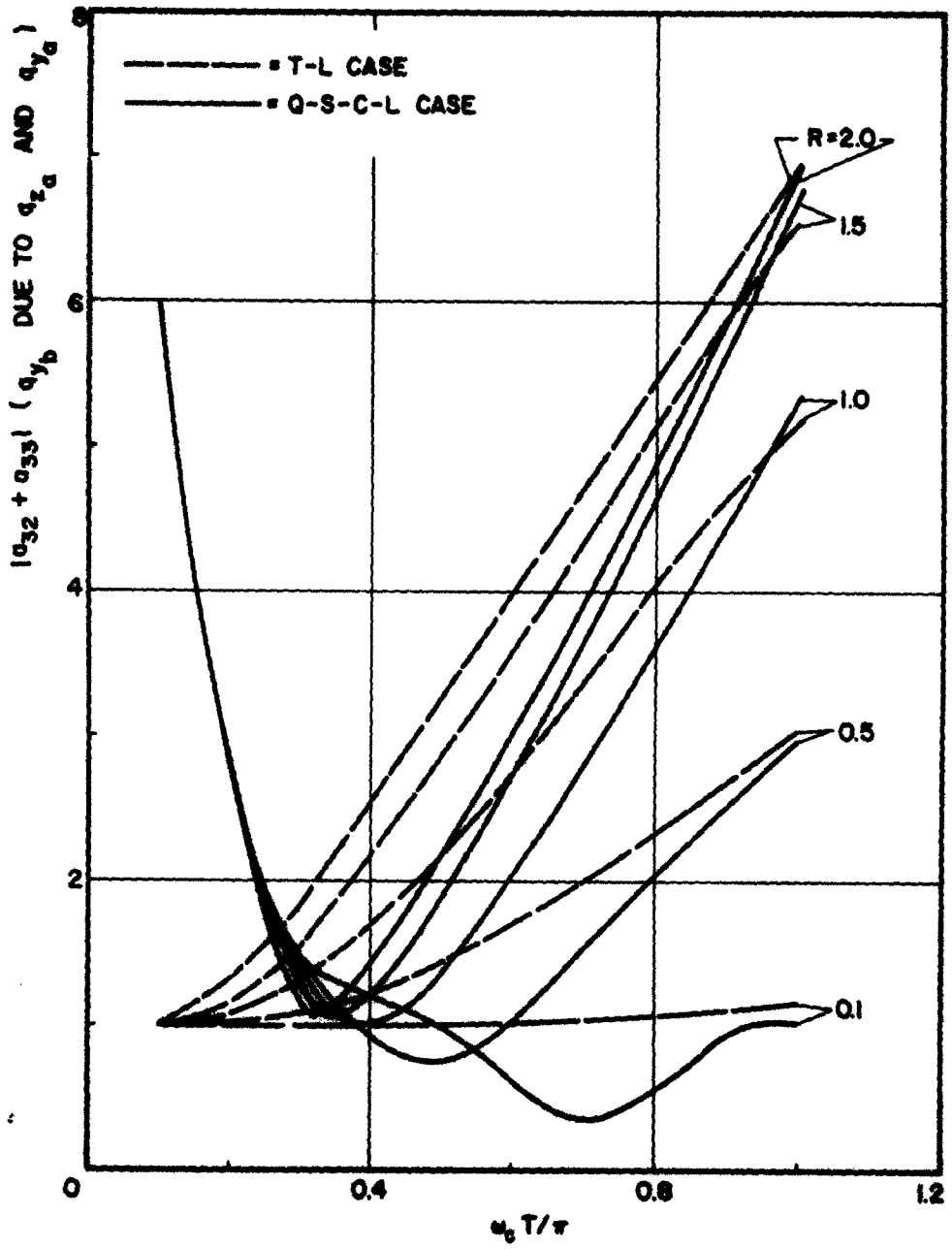

FIG. 3.11 $|a_{32} + a_{33}|$ VS. $\omega_c T/\pi$.

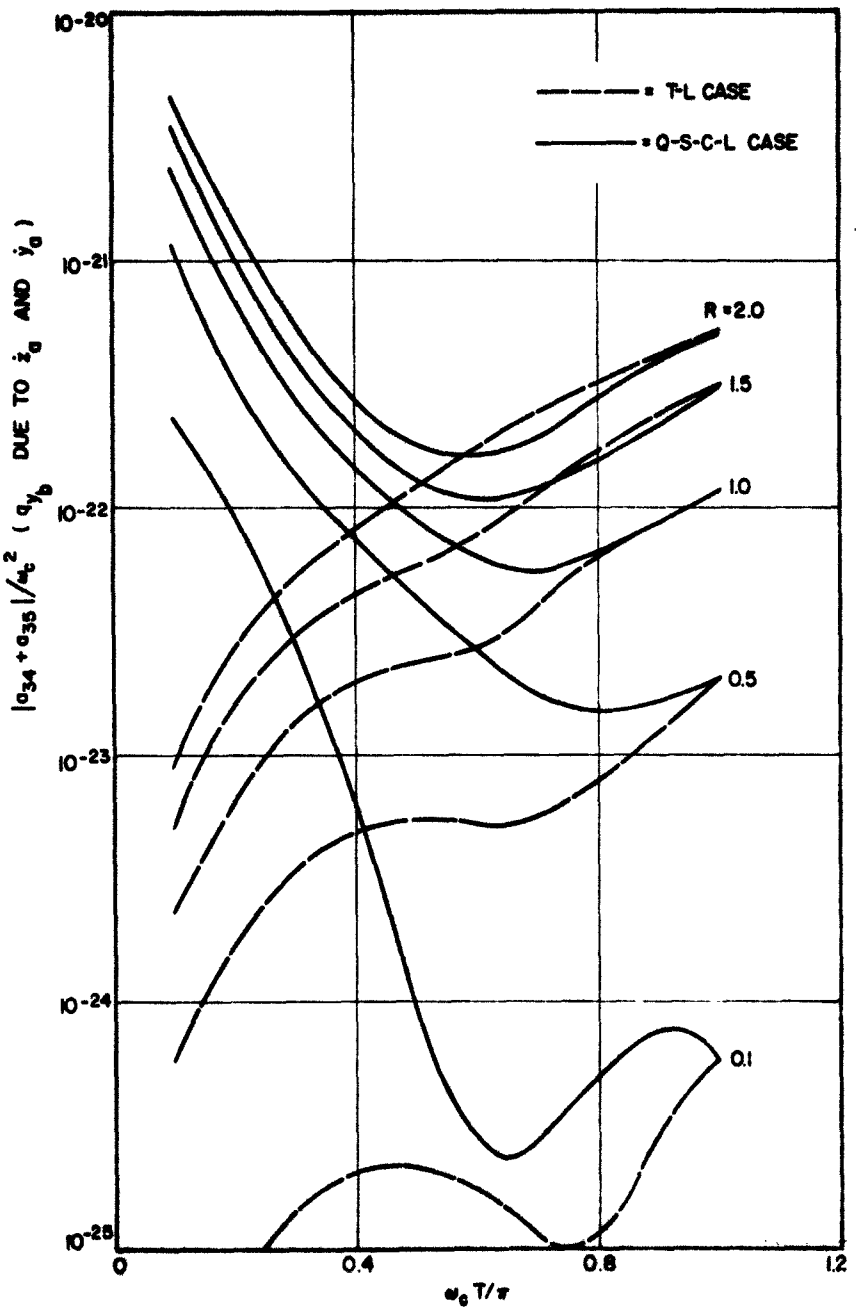

FIG. 3.12 $|a_{34} + a_{35}|/\omega_c^2$ VS. $\omega_c T/\pi$.

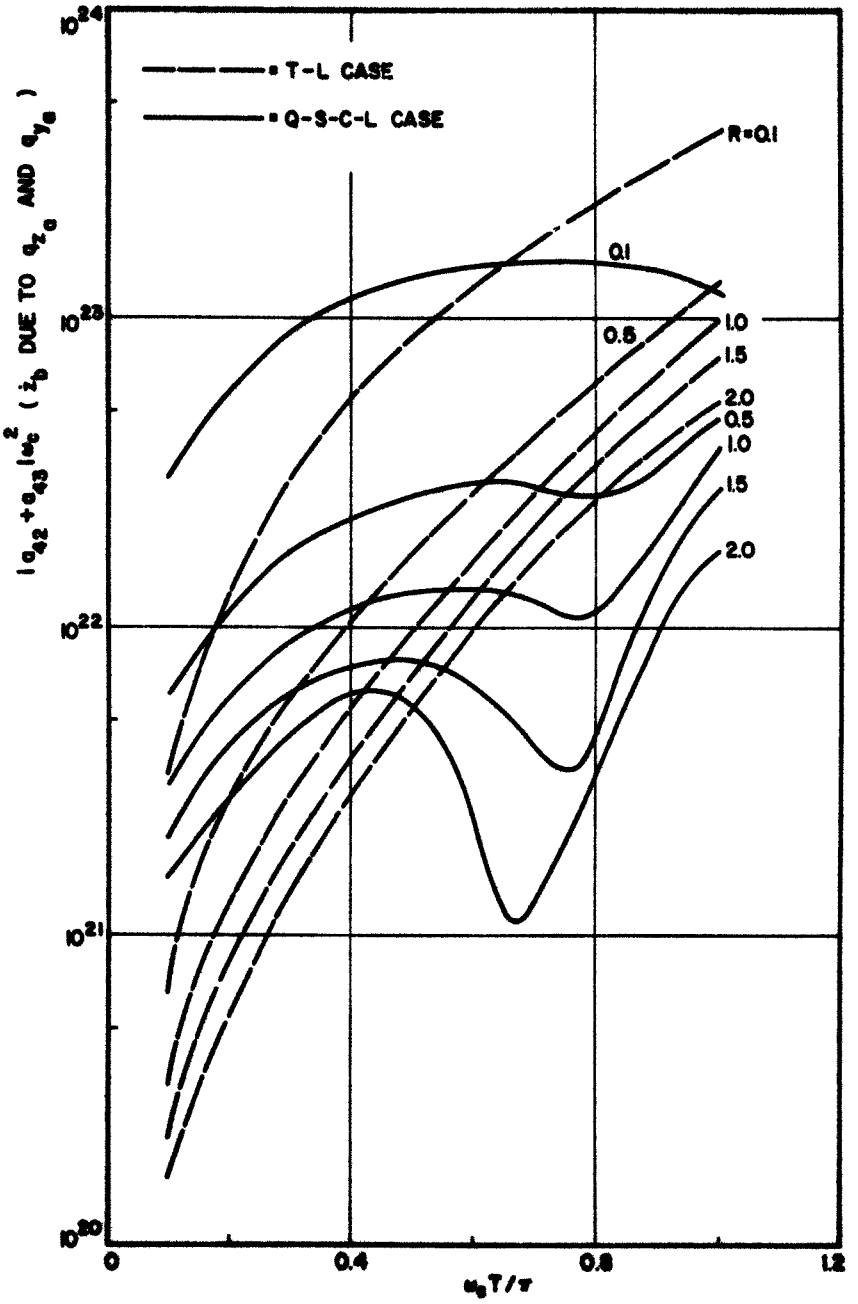

FIG. 3.13 $|a_{42} + a_{43}|\ \omega_c^2$ VS. $\omega_c T/\pi$.

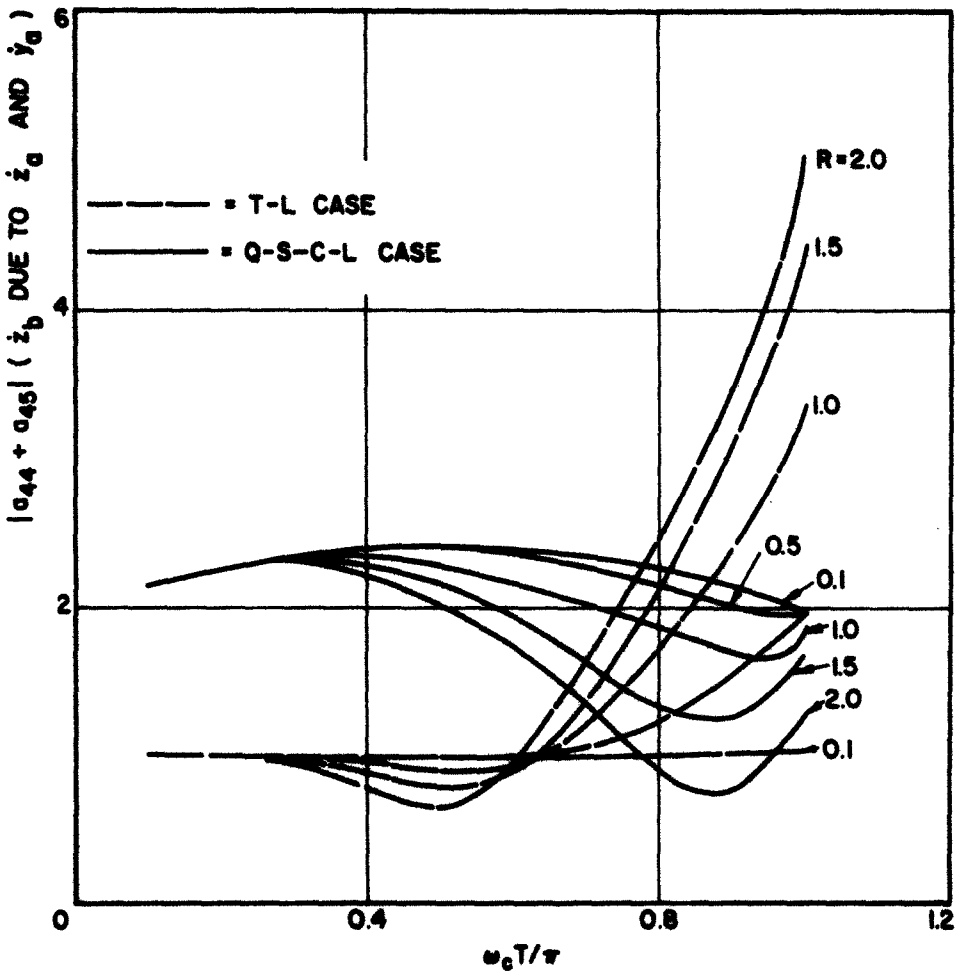

FIG. 3.14 $|a_{44} + a_{45}|$ VS. $\omega_c T/\pi$.

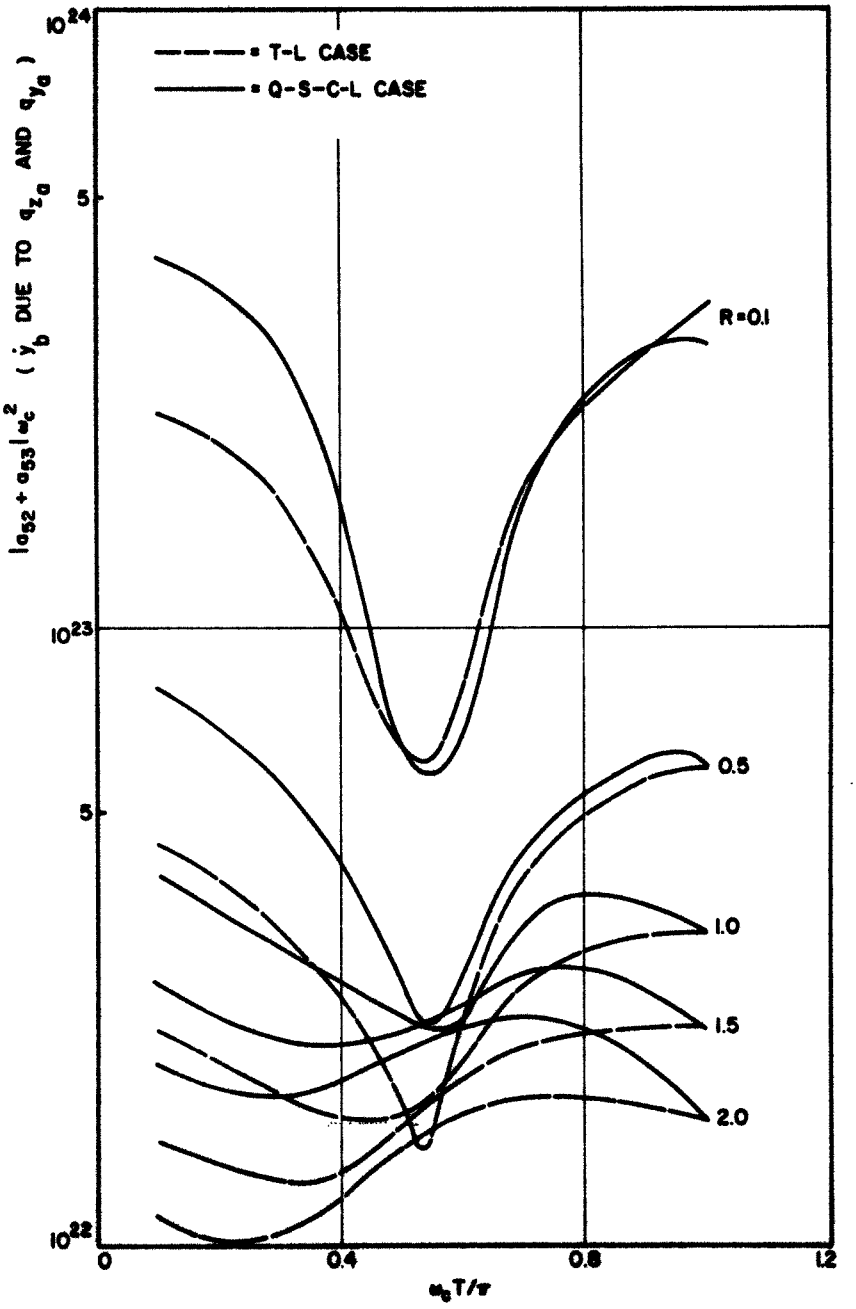

FIG. 3.15 $|a_{52} + a_{53}| \omega_c^2$ VS. $\omega_c T/\pi$.

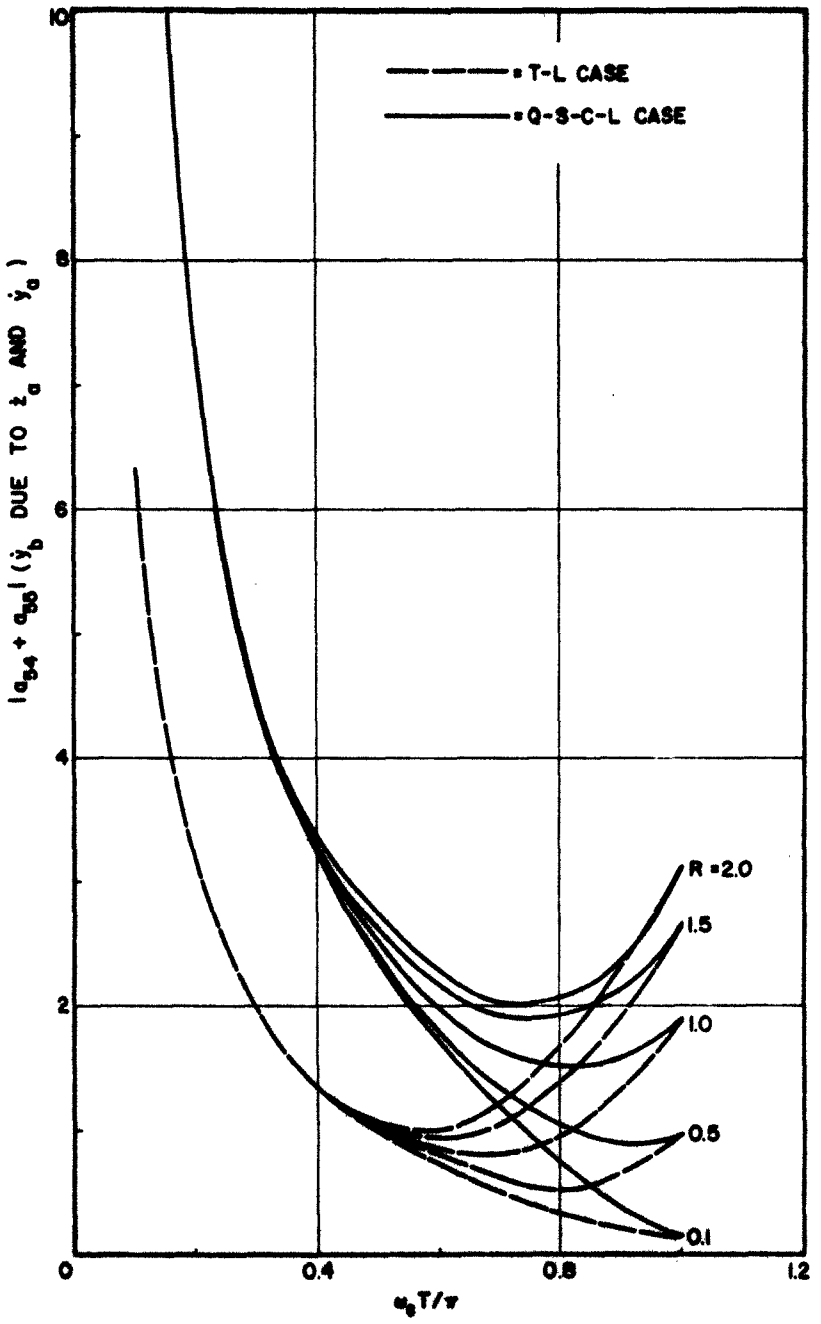

FIG. 3.16 $|a_{54} + a_{55}|$ VS. $\omega_c T/\pi$.

variables at the a-plane. However, a qualitative estimate for the noise as a function of R can be made by comparing the variation of the values of the coefficients with R in Figs. 3.1 through 3.4, 3.6 and 3.8 with those in Figs. 3.5 and 3.7. From this comparison it can be seen qualitatively that the noise output is a monotonically increasing function of R, i.e., the higher the value of the ratio ω/ω_c, the larger the total noise output.

In a practical device the noise output depends upon the type of coupling from the electron beam to the output. For example if the output is coupled to the current density fluctuations it can be seen from Figs. 3.1 through 3.6 that the output is definitely a monotonic increasing function of R. However, if the output is coupled to the velocity fluctuations also, the noise will be a monotonic increasing or decreasing function of R, depending upon the actual magnitudes of the velocity and current density fluctuations at the a-plane.

In order to analyze the variation of the values of the noise transport coefficients with ω_c for a fixed value of ω, it can be seen directly in Figs. 3.1, 3.3, 3.6 (Case B for Fig. 3.6) and 3.8 that the coefficients plotted in these figures are monotonically decreasing functions of ω_c. From Fig. 3.2 it may be seen that the magnitude of $|a_{24} + a_{25}|$ remains almost constant as ω_c is varied. This is because the plots in Fig. 3.2 have to be multiplied by ω_c^2 and the variation of R with ω_c also has to be taken into account. The same is true for the coefficient $|a_{34} + a_{35}|$ plotted in Fig. 3.4. Similarly it can be seen that the coefficients $|a_{42} + a_{43}|$ and $|a_{52} + a_{53}|$, of Figs. 3.5 and 3.7, respectively, are monotonic decreasing functions of ω_c. Thus in general the noise output should decrease as ω_c increases.

Figures 3.9 through 3.16 show the plots of the same coefficients as plotted in Figs. 3.1 through 3.8, but for a different physical model. This physical model corresponds to that of a quasi space-charge-limited diode discussed in Section 2.3. For the sake of comparison the corresponding plots of the temperature-limited case are also drawn in these figures. As mentioned before, because of the singularity in these coefficients for small values of θ, the comparison between the two plots in Figs. 3.9 through 3.16 for small values of θ is not of great importance. In general for large values of θ, the difference in the two plots is not significant and this is primarily because the quasi space-charge-limited model was based upon the trajectories for a temperature-limited model. In order to show the larger noise output for a space-charge-limited case in actual devices, one may think that the a-c fluctuations at the potential minimum are larger in magnitude for the case of a space-charge-limited device than those for a temperature-limited device. This is definitely contradictory to what happens in the case of the O-type devices where the variations in the potential minimum result in space-charge smoothing of the noise content in the beam. This may also indicate the necessity for an appropriate model of the space-charge-limited case in order to explain large noise output in space-charge-limited operation.

3.4 Arbitrary Input Conditions in the Interaction Region

In the last section the coefficients for the interaction region with ideal conditions given by Eqs. 3.11 are described. In this section it is assumed that the conditions given by Eqs. 3.11 are not true. This may happen because of some deviations in the space and velocity coordinates or the actual configuration from those for the ideal conditions

at the input to the interaction region. For this purpose two cases are considered, namely the space-charge-limited and temperature-limited operation of the diode. In both cases the trajectory equations given by Leblond[24] have been modified to correspond to small deviations at the input to the interaction region.

Case A. Space-Charge-Limited Operation.

For the configuration shown in Fig. 3.17, the trajectory equations (as given by Leblond) are given by

$$y = \frac{D}{2\pi}(\theta - \sin\theta) \tag{3.13}$$

and

$$z = \frac{D}{2\pi}\left(\frac{\theta^2}{2} + \cos\theta - 1\right) \tag{3.14}$$

for $0 \leq \theta \leq 2\pi$ and the initial velocities are neglected. For the second half cycle ($2\pi \leq \theta < 4\pi$), the trajectory equations are given by

$$y = 2D - \frac{D}{2\pi}(\theta - \sin\theta) \tag{3.15}$$

and

$$z = 2D(\theta-\pi) - \frac{D}{2\pi}\left(\frac{\theta^2}{2} + \cos\theta - 1\right) , \tag{3.16}$$

where

$$D = 2\pi \frac{\tilde{I}_D}{\omega_c^3} . \tag{3.17}$$

For a Kino gun, Eqs. 3.13 and 3.14 are used. The space coordinates and velocity components of the beam at the entrance of the interaction

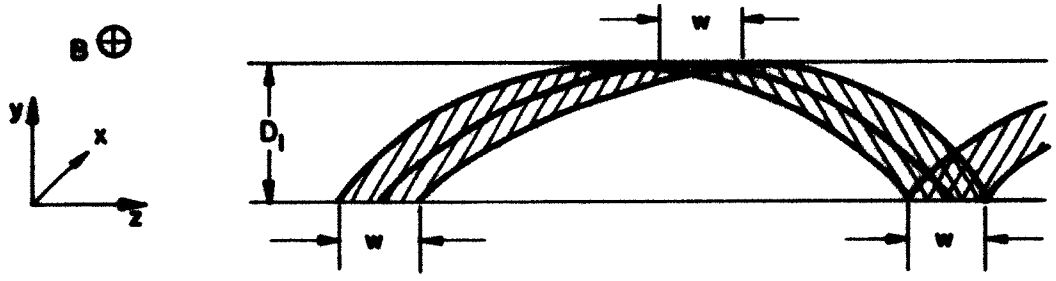

FIG. 3.17 THE FIRST CYCLES OF THE TRAJECTORIES OF A CYCLOIDING BEAM.

region, denoted by suffix o, are obtained by substituting $\theta = 2\pi$ in Eqs. 3.13 and 3.14 and are given by

$$y_o = D_o \ , \quad z_o = \pi D_o$$

and

$$\dot{y}_o = 0 \quad \text{and} \quad \dot{z}_o = \omega_c D_o \ . \tag{3.18}$$

For an ideal condition in the interaction region, the design of the transition region between the gun region and the interaction region is important and the magnitude of the E_y field in the interaction region is given by

$$|E_y| = \frac{\dot{z}_o \omega_c}{\eta} = \frac{\omega_c^2 D_o}{\eta} \tag{3.19}$$

so that the electrons confined in a filamentary beam (space-charge forces neglected) travel at a constant velocity $\dot{z}_o$ in the interaction region and the conditions given by Eqs. 3.11 are true. In case the input conditions do not correspond to the conditions given by Eqs. 3.18, the beam will traverse a cycloidal path in the interaction region with an average velocity $\dot{z}$ and the trajectory equations will be modified. It is for this purpose that the trajectory equations given by Eqs. 3.15 and 3.16 are modified to correspond to a small deviation from the ideal conditions. The cycloid period is assumed to be equal to $4\pi/\omega_c$.

For an ideal case the trajectory equations in the interaction region are given by

$$y = D_o$$

and

$$z = D_o(\theta + \pi) \ , \tag{3.20}$$

where the time origin is shifted so that $\theta = 0$ corresponds to the a-plane located at the input to the interaction region. It is assumed that the transition region between the gun region and the interaction region corresponds to that for ideal conditions. The input conditions will deviate from the ideal conditions when the parameter $D \neq D_o$. This may correspond to different values of I_D and/or ω_c. For reasons of simplicity it is assumed that $\dot{y} = 0$ at the input to the interaction region even if $D \neq D_o$. Now if $D < D_o$, the trajectory equations in the interaction region will be governed by a modification of Eqs. 3.13 and 3.14 and if $D > D_o$, the trajectory equations are determined by a modification of Eqs. 3.15 and 3.16. However if the input conditions at the interaction region are accounted for properly, it is not necessary to consider two different sets of trajectory equations for the two conditions, namely $D < D_o$ and $D > D_o$. This is done by writing the following expressions for the trajectory equations:

$$y = D - \frac{D_1}{\pi}(\theta - \sin\theta) \quad , \tag{3.21}$$

$$\begin{aligned} \dot{z} &= \omega_c y \\ &= \omega_c D - \frac{\omega_c D_1}{\pi}(\theta - \sin\theta) \quad , \end{aligned} \tag{3.22}$$

therefore,

$$z = D(\theta + \pi) - \frac{D_1}{\pi}\left(\frac{\theta^2}{2} + \cos\theta - 1\right) \tag{3.23}$$

for $0 \leq \theta < 2\pi$.

Equations 3.21 through 3.23 are written in such a manner that the initial condition, i.e., $\theta = 0$, corresponds to the condition $\theta = 2\pi$ substituted in Eqs. 3.13 and 3.14. The parameter D_1 is given by

$$D_1 = D - D_o \quad . \tag{3.24}$$

Thus for the condition $D_1 > 0$ the electron beam tends to move away from the anode as θ is increased and if $D_1 < 0$ the electron beam tends to move toward the anode. This is shown in Fig. 3.18. In both cases the beam traverses a cycloidal trajectory around the mean value of $y = D_o$. Since a time period $T = 4\pi/\omega_c$ is assumed, $y = D-2D_1$ and $z = 3\pi D - 2\pi D_1$ for $\theta = 2\pi$. For the next half period, namely $2\pi \leq \theta \leq 4\pi$, a modification of Eqs. 3.21 through 3.23 will be necessary to satisfy the initial conditions at $\theta = 2\pi$. Under the conditions given by Eqs. 3.21 through 3.23, the d-c parameters in the noise transport coefficients given by Eqs. 2.25 are given by

$$\frac{\ddot{z}-\omega_c\ddot{y}}{\omega_c^2 z} = 0 \quad , \tag{3.25}$$

$$\frac{\ddot{y}+\omega_c\ddot{z}}{\omega_c^2 z} = -\frac{m}{\pi - m(\theta-\sin\theta)} \quad , \tag{3.26}$$

$$\frac{\ddot{z}}{\omega_c^2 z} = -\frac{m(1-\cos\theta)}{\pi - m(\theta-\sin\theta)} \tag{3.27}$$

and

$$\frac{\ddot{y}}{\omega_c^2 z} = -\frac{m\sin\theta}{\pi - m(\theta-\sin\theta)} \quad , \tag{3.28}$$

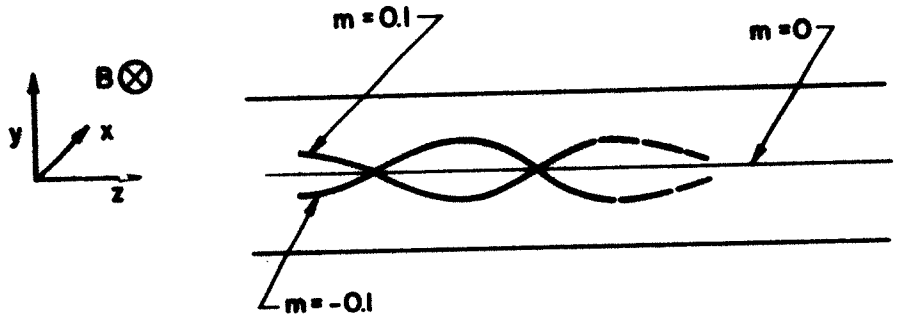

FIG. 3.18 ELECTRON TRAJECTORIES FOR ARBITRARY INPUT CONDITIONS IN THE CROSSED-FIELD INTERACTION REGION.

where

$$m = \frac{D_1}{D} \quad . \tag{3.29}$$

By assuming $D_1/D \ll 1$, $D_1/D \simeq D_1/D_o$ and then m represents the fractional deviation of D from D_o.

Figures 3.19 through 3.24 show the plots of the terms, $|a_{32} + a_{33}|$, $|a_{34} + a_{35}|(1/\omega_c^2)$, $|a_{42} + a_{43}|\ \omega_c^2$, $|a_{44} + a_{45}|$, $|a_{52} + a_{53}|\ \omega_c^2$ and $|a_{54} + a_{55}|$ versus $\omega_c T/\pi$ for different values of R. Three different values of m, namely m = -0.1, 0, and 0.1, are considered in this set of curves. The case m = 0 corresponds to the case of ideal conditions discussed under Case D in Section 3.3. The terms $|a_{22} + a_{23}|$ and $|a_{24} + a_{25}|(1/\omega_c^2)$ are not plotted because for any finite value of m for the physical model considered in this section, the term $\ddot{z}-\omega_c\dot{y} = 0$ and the values of these two terms are the same as those for the corresponding plots when the Kino gun model or the temperature-limited case are considered in the gun region. These terms are plotted in Figs. 3.1 and 3.2 respectively. It can be seen that all the plots in Figs. 3.19 through 3.24 show a larger growth rate for m > 0 and less growth rate for m < 0. However the difference in the numerical values of the coefficients plotted in these figures for m = -0.1, 0.0 and m = 0.1 is not much and one would expect the same results since these equations are derived for a small-signal analysis.

The variation of the growth rate of the a-c fluctuations with the parameter m can be explained physically as follows. A negative value of m indicates $D < D_o$ and this may be due to a smaller value of I_D and/or a larger value of ω_c. Gould[16] has shown that the effect of the space charge is to increase the rate of gain in the forward direction for the

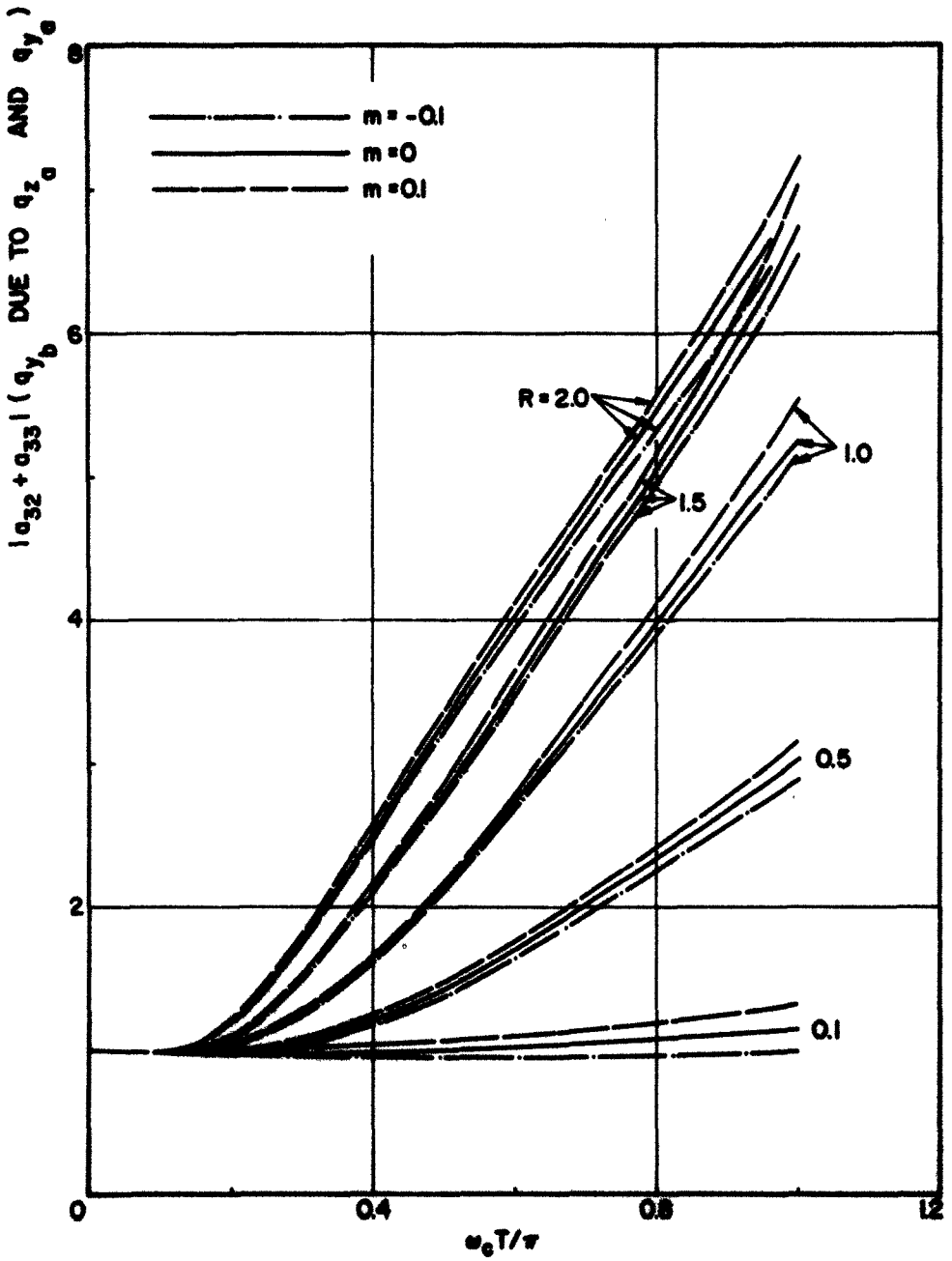

FIG. 3.19 $|a_{32} + a_{33}|$ VS. $\omega_c T/\pi$ FOR INTERACTION REGION.

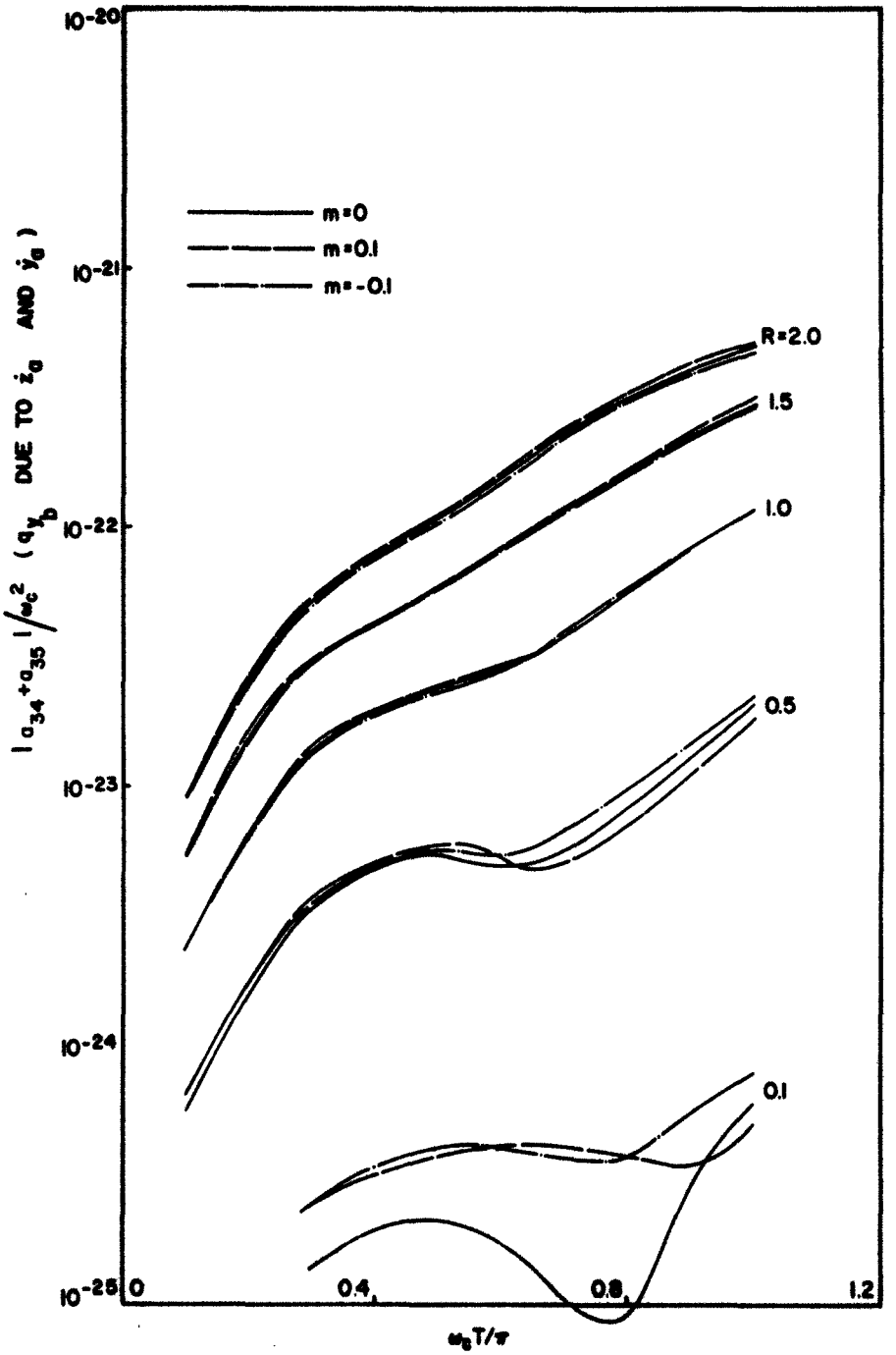

FIG. 3.20 $|a_{34} + a_{35}|/\omega_c^2$ VS. $\omega_c T/\pi$ FOR INTERACTION REGION.

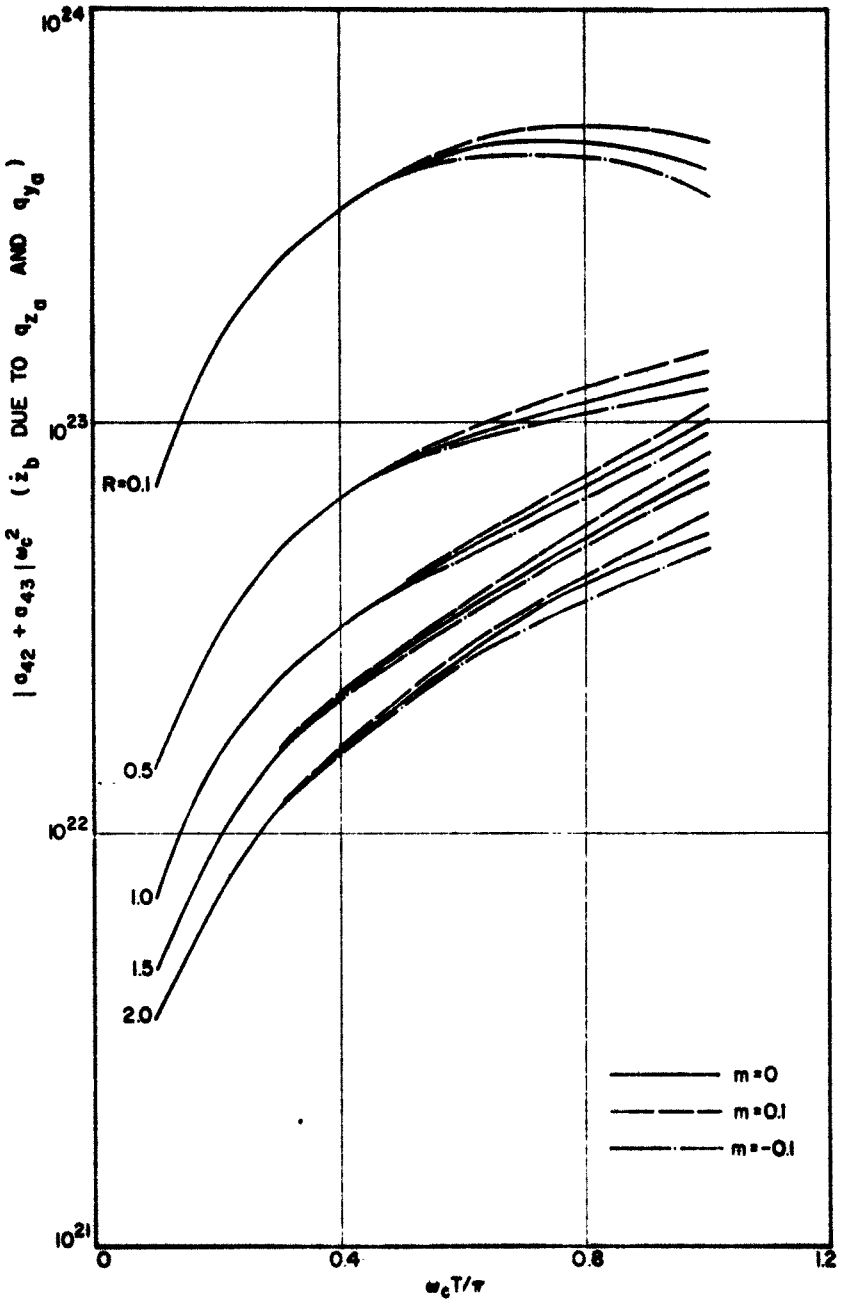

FIG. 3.21 $|a_{42} + a_{43}|\,\omega_c^2$ VS. $\omega_c T/\pi$ FOR INTERACTION REGION.

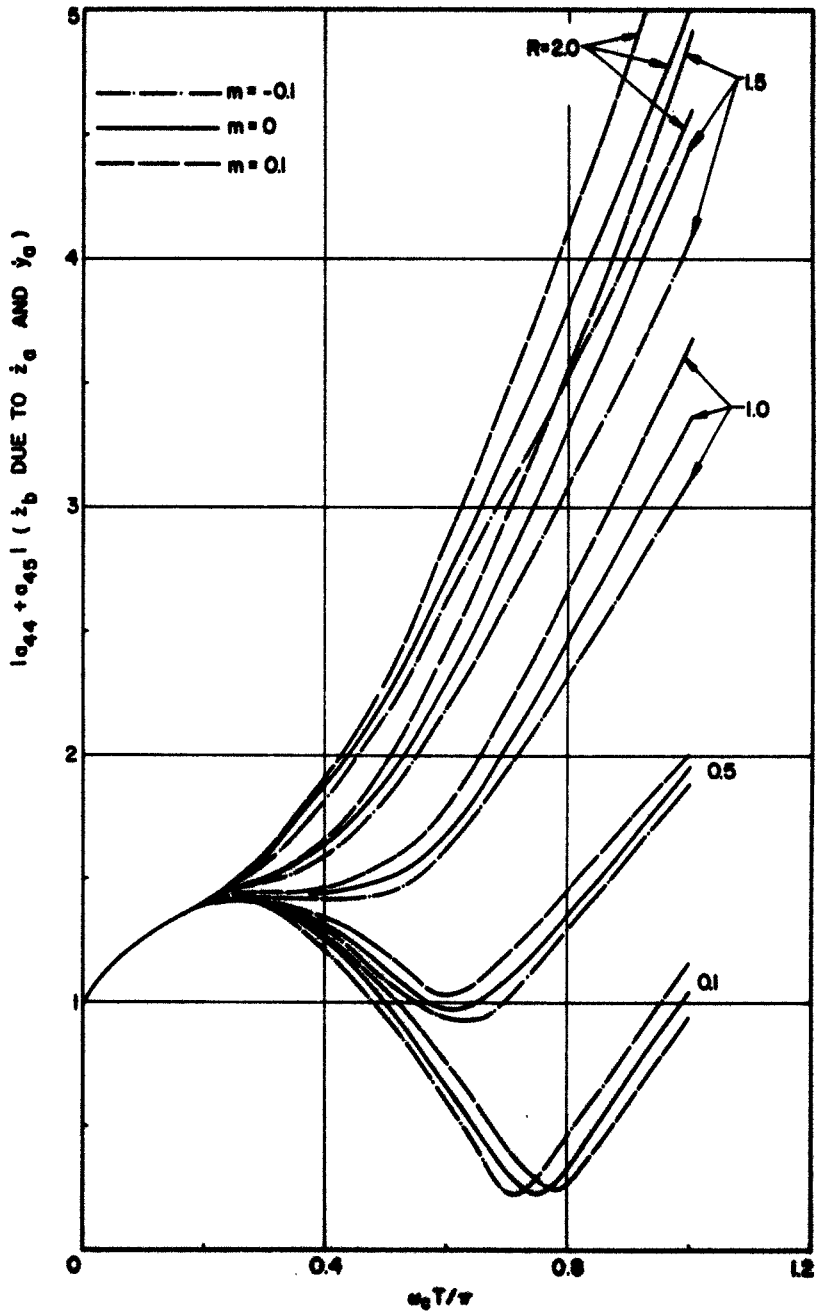

FIG. 3.22 $|a_{44} + a_{45}|$ VS. $\omega_c T/\pi$ FOR INTERACTION REGION.

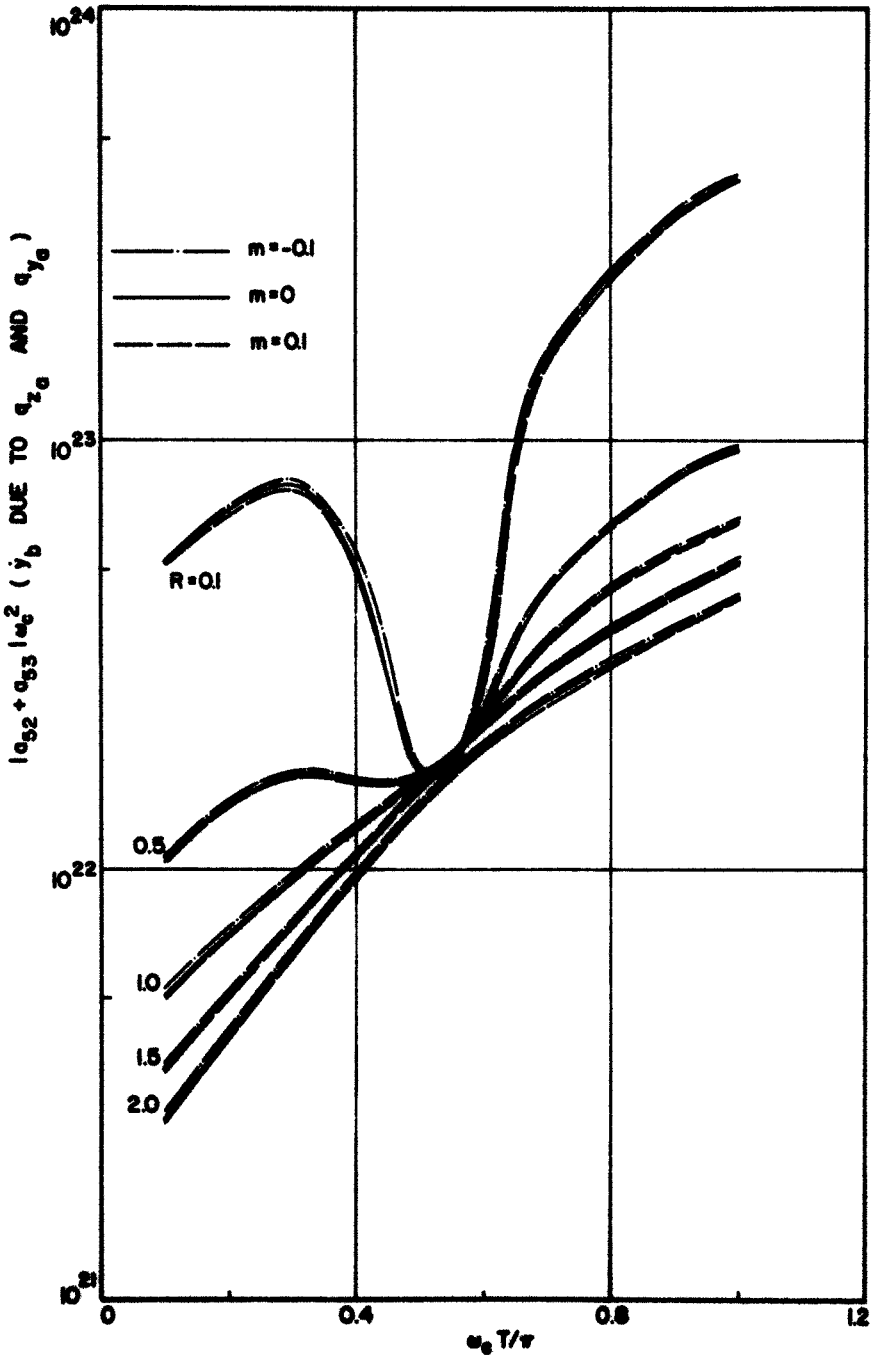

FIG. 3.23 $|a_{52} + a_{53}| \omega_c^2$ VS. $\omega_c T/\pi$ FOR INTERACTION REGION.

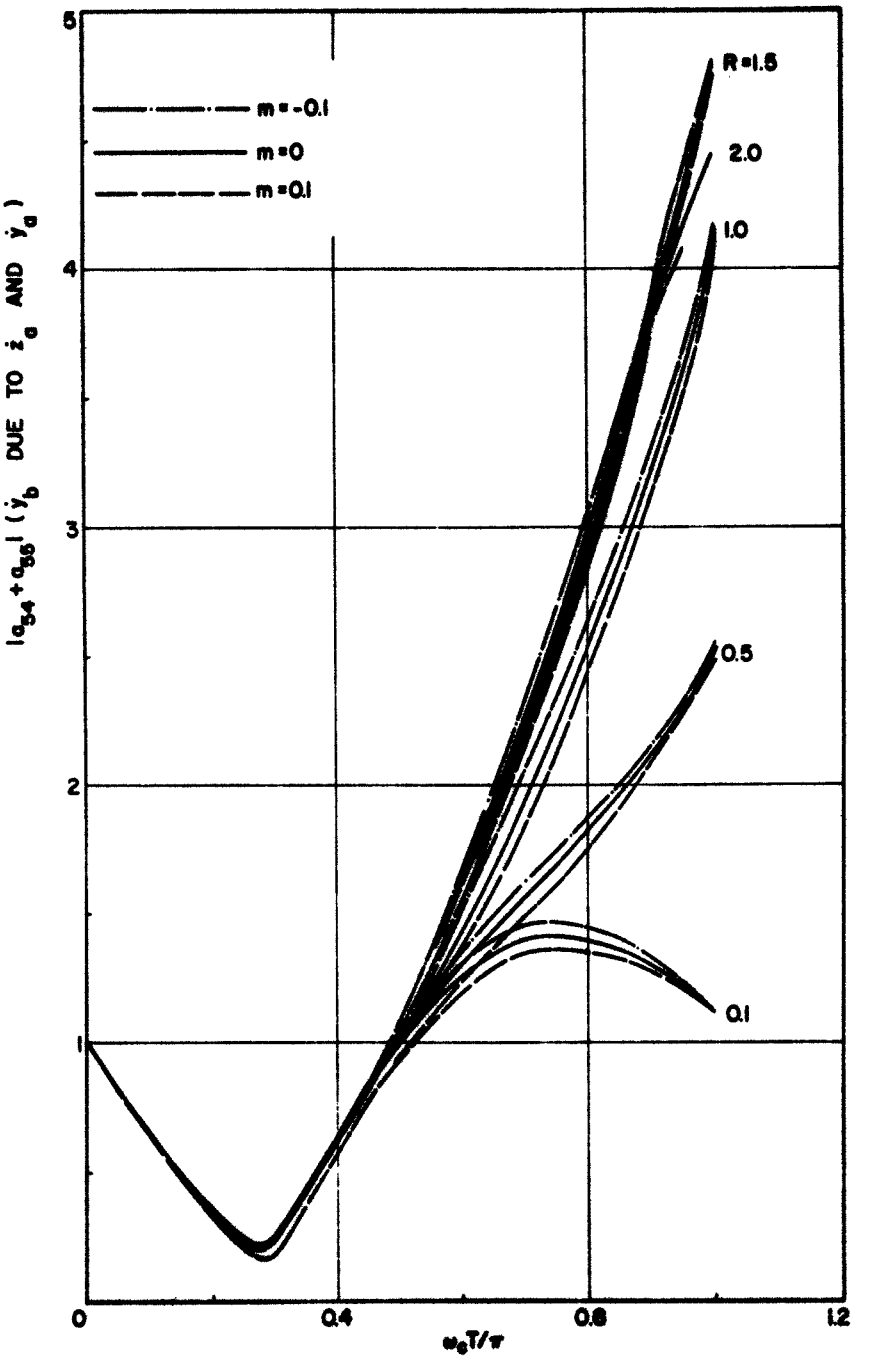

FIG. 3.24 $|a_{54} + a_{55}|$ VS. $\omega_c T/\pi$ FOR INTERACTION REGION.

crossed-field device. A smaller value of I_D means a lower value of the space-charge parameter S and hence a smaller growth rate should be expected. It has been noted in Section 3.3 that the rate of growth of the a-c fluctuations is reduced if ω_c is increased. Thus the reduced growth rate for $m < 0$, i.e., $D < D_o$, is in agreement with the physical argument*. Similarly the increase in the growth rate for $m > 0$, i.e., $D > D_o$, may be explained as a result of an increase in the value of I_D and/or a decrease in the value of ω_c.

It is interesting to note the minima in some of the plots shown in Figs. 3.19 through 3.24 and in Fig. 3.1. The physical significance of these minima is not yet clear theoretically but from a practical viewpoint the significance is very important. The minima in Figs. 3.1 and 3.24 occur at approximately the same value of $\omega_c T$, namely, $\omega_c T \simeq 0.3\pi$ while the other minima occur at different values of $\omega_c T$. It is interesting to note that minima in Figs. 3.20 and 3.22 shift to the left as the value of R is increased and the value is also increased. In addition it is possible to have some minima for larger values of $\omega_c T$ but those minima are not of much importance for noise reduction purposes.

Case B. Temperature-Limited Operation

For the case of a temperature-limited diode, the trajectory equations in the gun region are given by

$$y = \frac{D_T}{2}(1 - \cos\theta) \tag{3.30}$$

---

* This observation is also in agreement with some of the experimental results concerning noise in crossed-field devices. The noise content is increased if the total current is increased and is reduced if ω_c is increased.

and

$$z = \frac{D_T}{2}(\theta - \sin\theta) \quad , \tag{3.31}$$

and $0 \leq \theta \leq \pi$ and the initial velocities are neglected. The space coordinates and the velocity components at the entrance of the interaction region are given by substituting $\theta = \pi$ in Eqs. 3.30 and 3.31 and are given by

$$y_o = D_T \tag{3.32}$$

and

$$z_o = \frac{\pi D_T}{2} \quad , \tag{3.33}$$

where

$$D_T = \frac{2\eta E_o}{\omega_c^2} \quad , \tag{3.34}$$

E_o being the y-component of the d-c field and considered constant. As in Case A for the space-charge-limited case, the trajectory equations for the interaction region, when ideal conditions are not met, are given by

$$y = D - D_1(1 - \cos\theta) \tag{3.35}$$

and

$$z = D\left(\theta + \frac{\pi}{2}\right) - D_1(\theta - \sin\theta) \quad , \tag{3.36}$$

where again the parameter $D_1/D \simeq D_1/D_T$ is taken as the fractional deviation in D from D_T which corresponds to that for the ideal conditions. However, the symbols D and D_1 in Case A and Case B represent the analogous quantities of different expressions. From Eqs. 3.35 and 3.36 the following may be written:

$$\dot{z} - \omega_c y = 0 \quad , \tag{3.37}$$

$$\ddot{y} + \omega_c \dot{z} = 0 \quad , \tag{3.38}$$

$$\frac{\dot{z}}{\omega_c \dot{z}} = - \frac{m \sin \theta}{1 - m(1-\cos \theta)} \tag{3.39}$$

and

$$\frac{\dot{y}}{\omega_c \dot{z}} = - \frac{m \cos \theta}{1 - m(1-\cos \theta)} \quad , \tag{3.40}$$

where

$$m = \frac{D_1}{D} \simeq \frac{D_1}{D_T} \quad . \tag{3.41}$$

Equations 3.37 through 3.40 may be used in evaluating the noise transport coefficients. These expressions are very similar to those given by Eqs. 3.25 through 3.28 and it is expected that this model will not show any remarkable difference from that used in Case B of Section 3.3. For this purpose the coefficients for Case B are not computed.

3.5 Evaluation of the A-c Fluctuations in Terms of a Single Variable

From the matrix relation given by Eq. 2.24 it can be seen that in order to evaluate any a-c fluctuation such as q_{y_b}, q_{z_b}, $\dot{z}_b$ and $\dot{y}_b$ it is necessary to substitute some numerical values for the a-c fluctuations at the a-plane. In this section it is shown that the a-c fluctuations at the output may be represented by a single arbitrary independent variable. The selection of the independent variable is quite arbitrary. This treatment is confined only to the interaction region for the reasons mentioned in the following paragraphs.

From the transmission-line analogy of the crossed-field beams[25] it is shown that

$$\dot{y}_1 = - \frac{\omega_c}{(j\omega - \Gamma \dot{z}_o) + \dfrac{\omega_p^2}{j\omega\left(1 + \dfrac{c^2}{\omega^2}\Gamma^2\right)}} \dot{z}_1 \quad , \tag{3.42}$$

$$q_y = \rho_o \dot{y}_1 \tag{3.43}$$

and

$$q_z = \frac{j\omega\rho_o \dot{z}_1}{j\omega - \Gamma \dot{z}_o} \quad , \tag{3.44}$$

where it is assumed that $\dot{z}_o$ and ρ_o are constant and the y-component of the d-c velocity is equal to zero; c is the velocity of light, Γ is j times the propagation constant and ω_p is the plasma frequency.

In evaluating the noise transport coefficients by the Llewellyn-Peterson equations only transit time effects are considered. For this reason it is justified to substitute $\Gamma = 0$ in Eqs. 3.42 and 3.44. Now using Eqs. 2.24, and 3.42 through 3.44, the various fluctuations at the b-plane may be written in terms of a single variable, namely $\dot{z}_a$, the z-component of the velocity fluctuations at the a-plane, as given by the following equations:

$$q_{z_b} = A_{11} \omega_c^2 \dot{z}_a \quad , \tag{3.45}$$

$$q_{y_b} = A_{12} \omega_c^2 \dot{z}_a \quad , \tag{3.46}$$

$$\dot{z}_b = A_{13} \dot{z}_a \tag{3.47}$$

and

$$\dot{y}_b = A_{14} \dot{z}_a \quad , \tag{3.48}$$

where

$$A_{11} = - a_{22} \frac{\epsilon_o}{\eta} \frac{\omega_p^2}{\omega_c^2} - \left(- a_{23} \frac{\epsilon_o}{\eta} \frac{\omega_p^2}{\omega_c^2} + \frac{a_{25}}{\omega_c^2} \right) \frac{jR}{\frac{\omega_p^2}{\omega_c^2} - R^2} + \frac{a_{24}}{\omega_c^2} , \quad (3.49)$$

$$A_{12} = - a_{32} \frac{\epsilon_o}{\eta} \frac{\omega_p^2}{\omega_c^2} - \left(- a_{33} \frac{\epsilon_o}{\eta} \frac{\omega_p^2}{\omega_c^2} + \frac{a_{35}}{\omega_c^2} \right) \frac{jR}{\frac{\omega_p^2}{\omega_c^2} - R^2} + \frac{a_{34}}{\omega_c^2} , \quad (3.50)$$

$$A_{13} = - \omega_c^2 a_{42} \frac{\epsilon_o}{\eta} \frac{\omega_p^2}{\omega_c^2} - \left(- \omega_c^2 a_{43} \frac{\epsilon_o}{\eta} \frac{\omega_p^2}{\omega_c^2} + a_{45} \right) \frac{jR}{\frac{\omega_p^2}{\omega_c^2} - R^2} + a_{44} \quad (3.51)$$

and

$$A_{14} = - \omega_c^2 a_{52} \frac{\epsilon_o}{\eta} \frac{\omega_p^2}{\omega_c^2} - \left(- \omega_c^2 a_{53} \frac{\epsilon_o}{\eta} \frac{\omega_p^2}{\omega_c^2} + a_{55} \right) \frac{jR}{\frac{\omega_p^2}{\omega_c^2} - R^2} + a_{54} . \quad (3.52)$$

The coefficients a_{ij} (i,j = 2, 3, 4 and 5) have been defined by Eqs. 2.25.

The coefficients in Eqs. 3.45 through 3.48 are evaluated for various combinations of the values of R and ω_p/ω_c. However, the coefficients in the above equations will give rise to a singularity for the case $\omega = \omega_p$. Thus this case, i.e., $\omega = \omega_p$, must be avoided in evaluating these coefficients.

Figures 3.25 through 3.36 show the plots of the coefficients in Eqs. 3.49 through 3.52 versus $\omega_c T/\pi$ for various values of R and ω_p/ω_c. It is interesting to note that the current density fluctuations are increased while the velocity fluctuations are decreased as the value of R is increased. It may be noticed that the plots of the coefficients A_{12} do

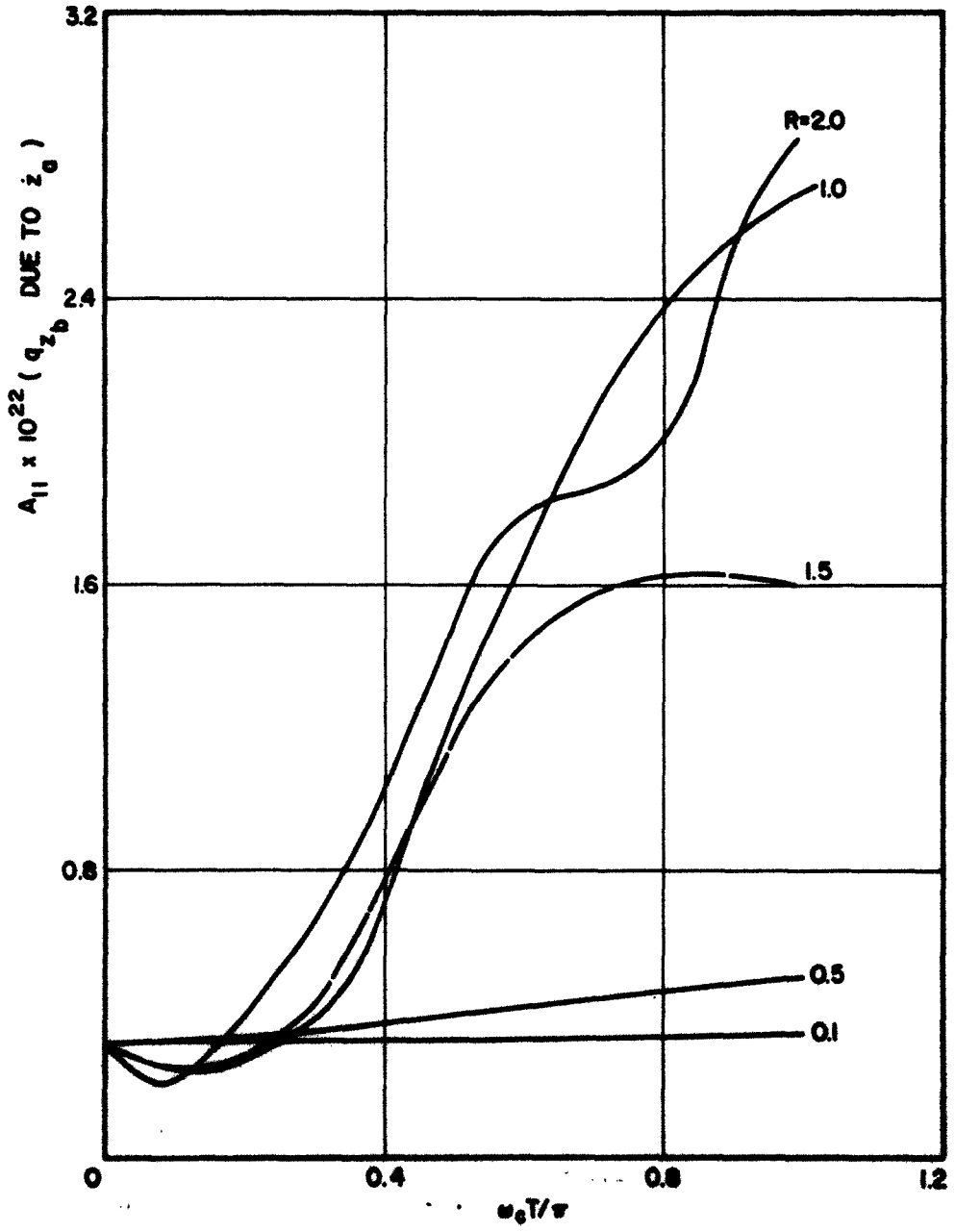

FIG. 3.25 A_{11} VS. $\omega_c T/\pi$. ($\omega_p/\omega_c = 0.8$)

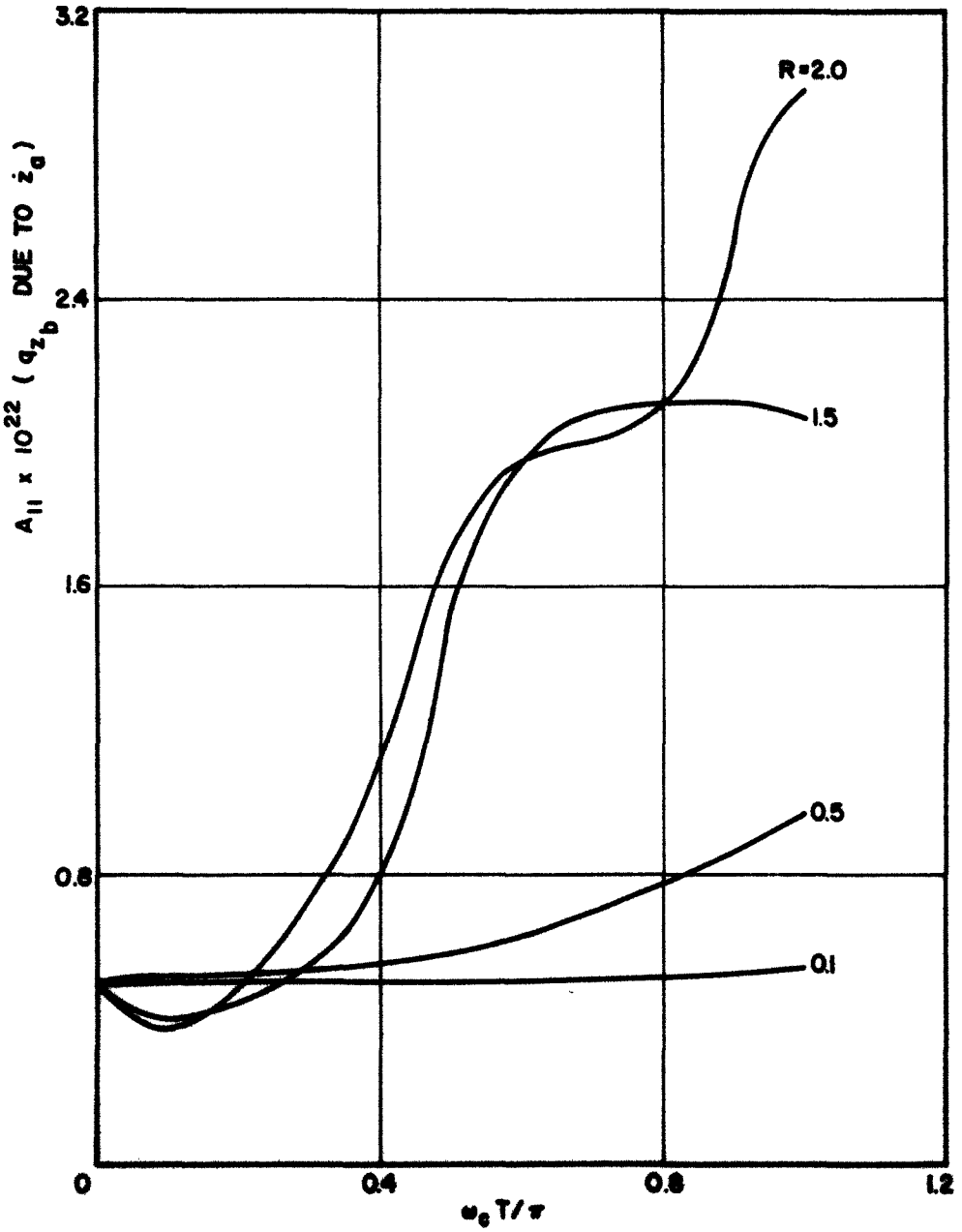

FIG. 3.26 A_{11} VS. $\omega_c T/\pi$. ($\omega_p/\omega_c = 1.0$)

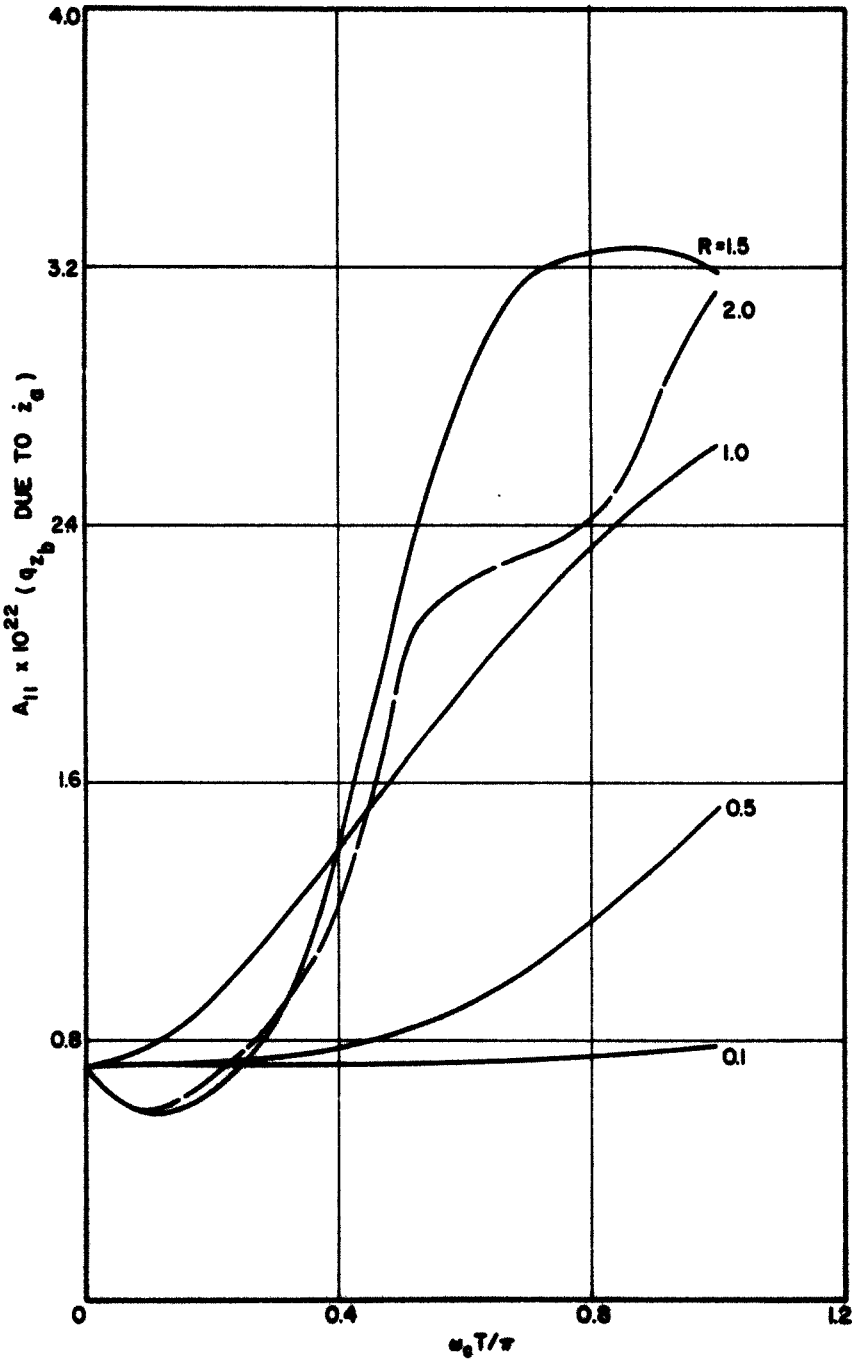

FIG. 3.27 A_{11} VS. $\omega_c T/\pi$. $(\omega_p/\omega_c = 1.2)$

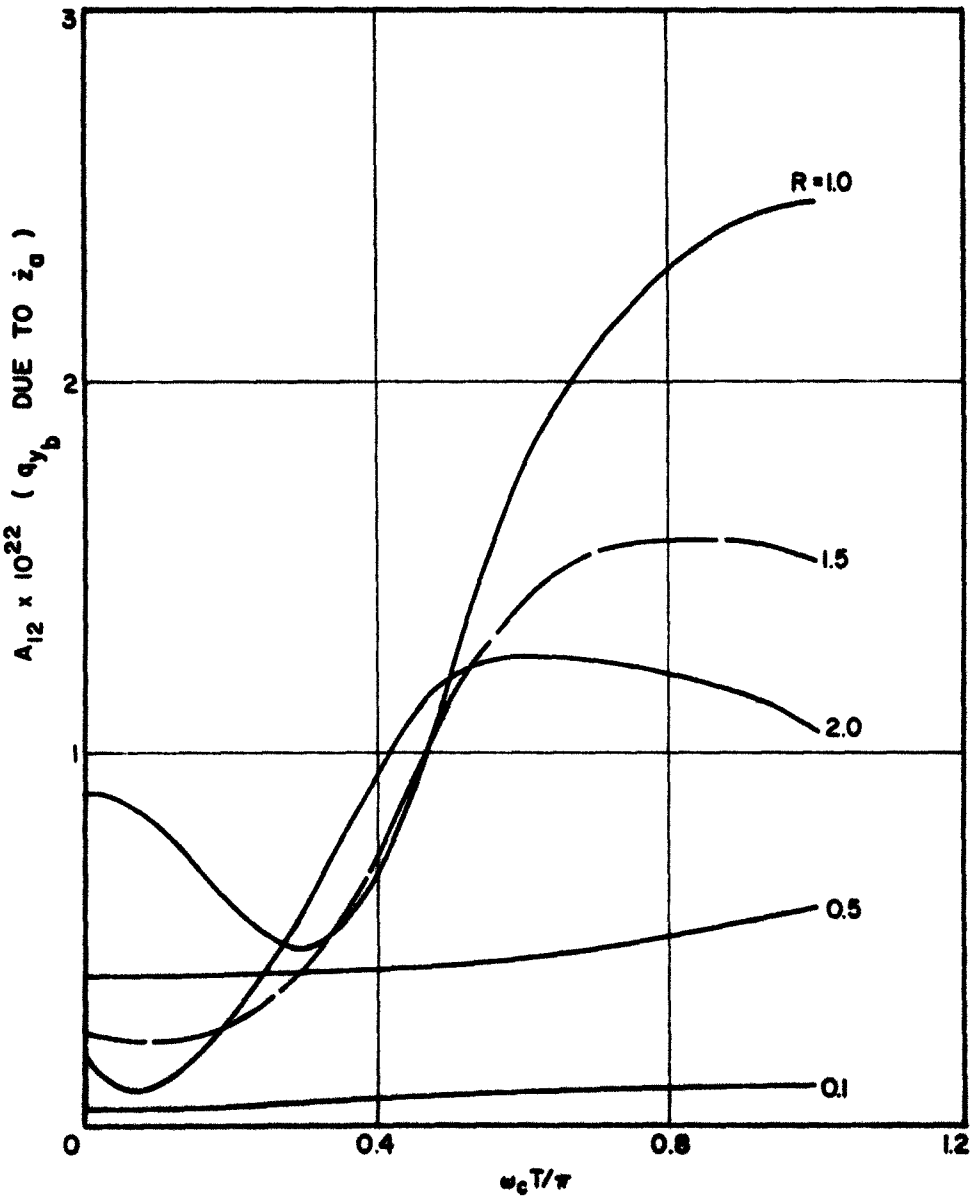

FIG. 3.28 A_{12} VS. $\omega_c T/\pi$. $(\omega_p/\omega_c = 0.8)$

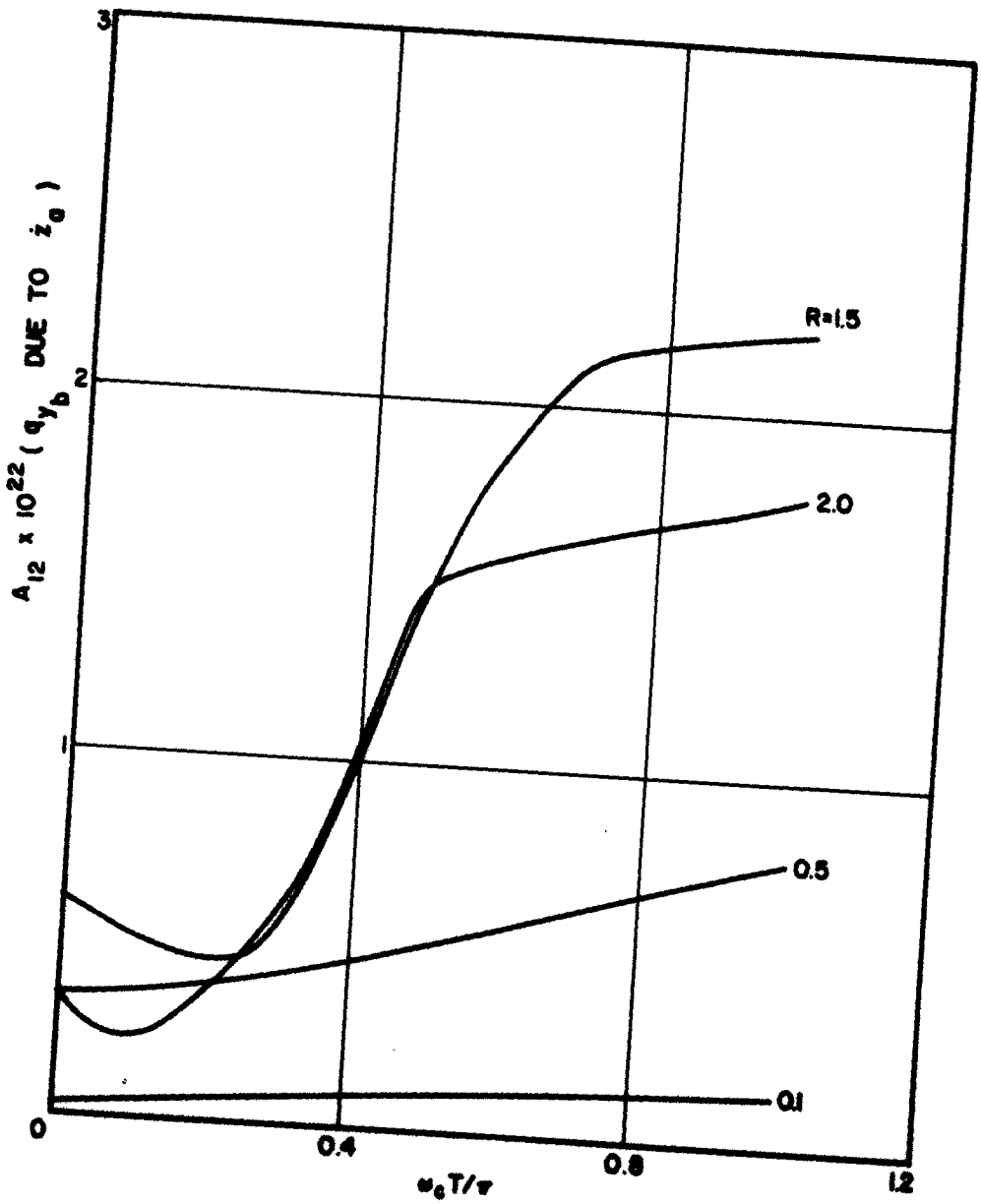

FIG. 3.29 A_{12} VS. $\omega_c T/\pi$. $(\omega_p/\omega_c = 1.0)$

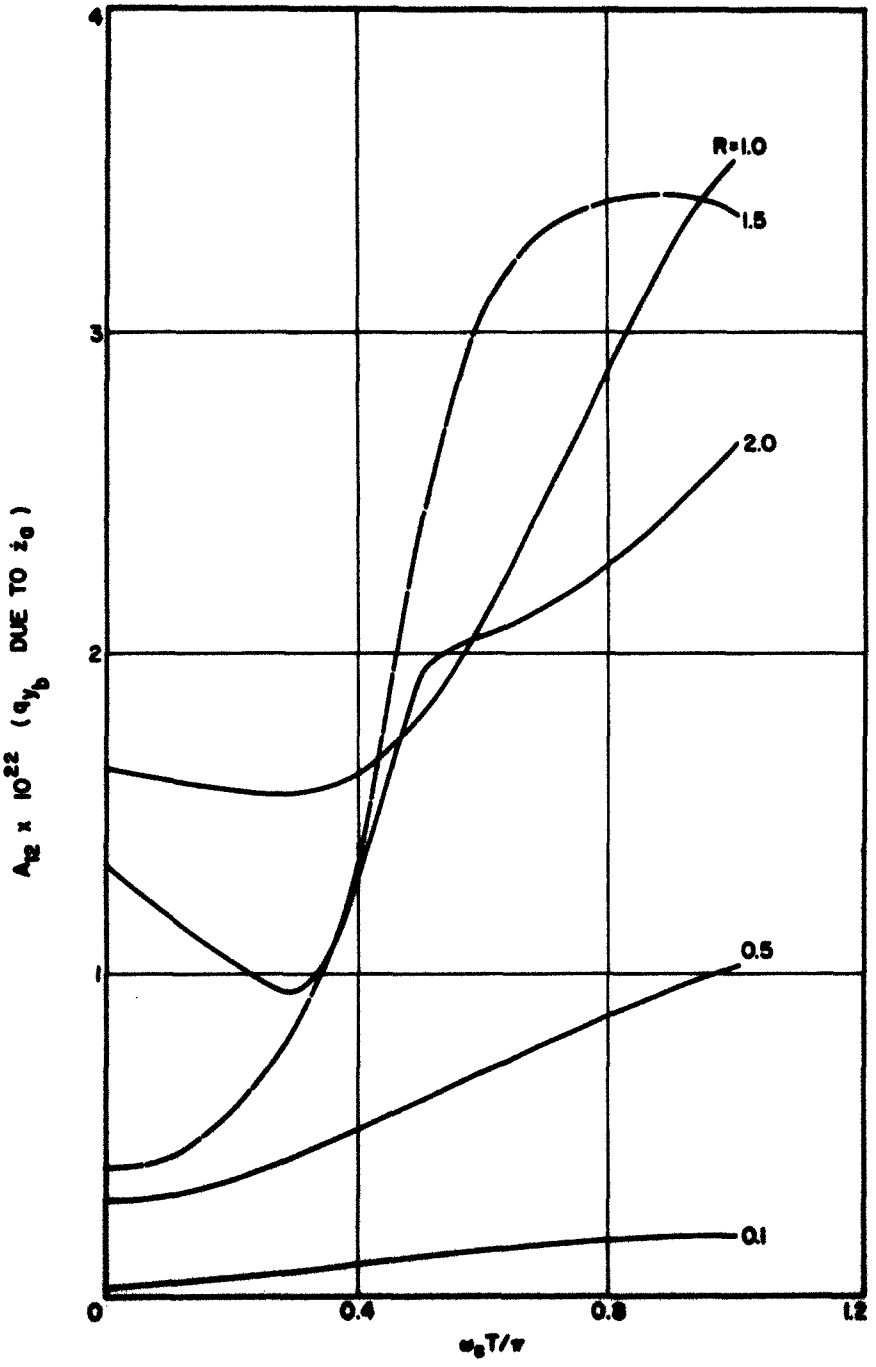

FIG. 3.30 A_{12} VS. $\omega_c T/\pi$. $(\omega_p/\omega_c = 1.2)$

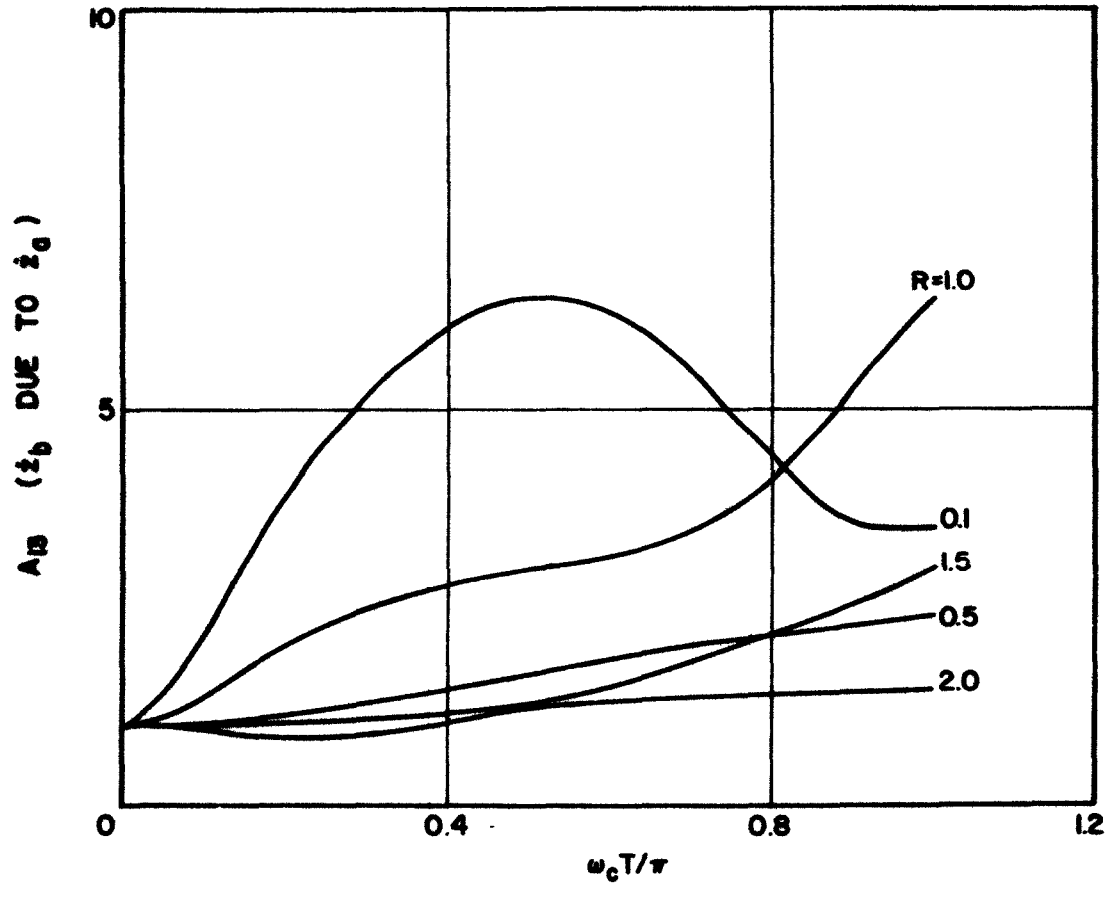

FIG. 3.31 A_{13} VS. $\omega_c T/\pi$. $(\omega_p/\omega_c = 0.8)$

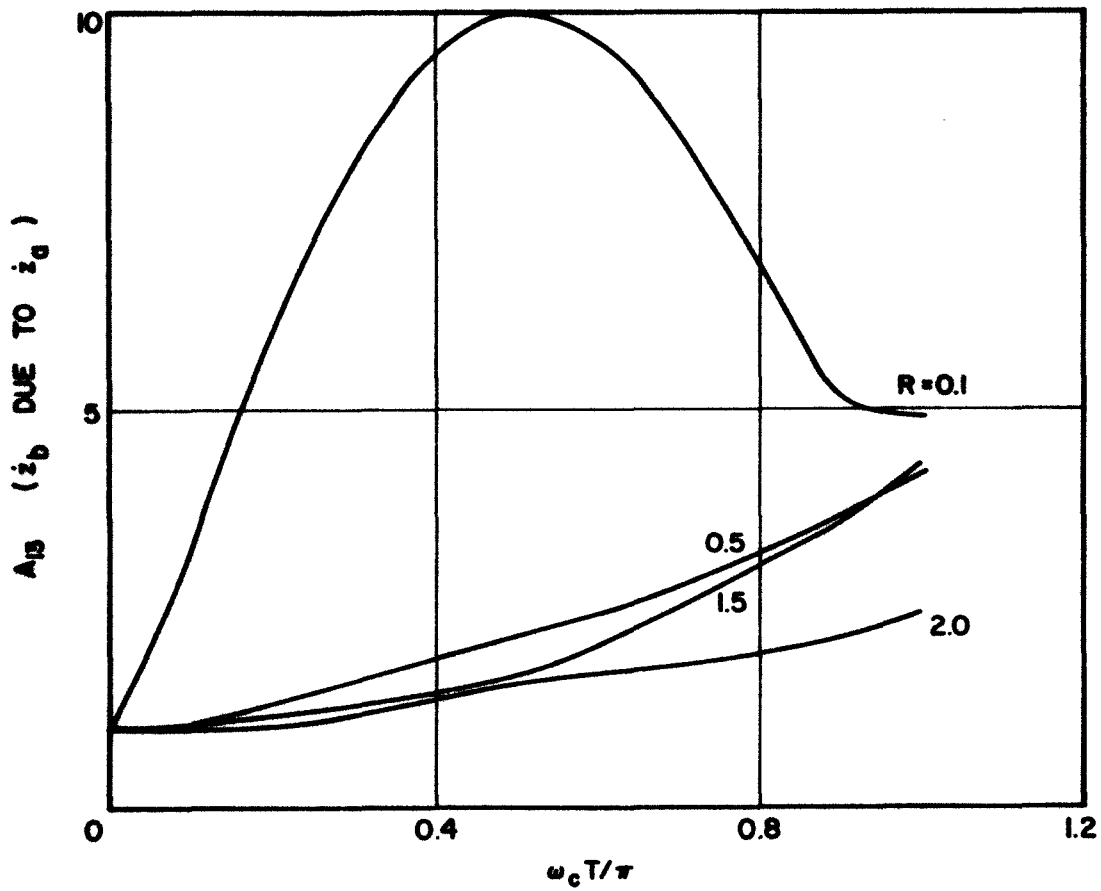

FIG. 3.32 A_{13} VS. $\omega_c T/\pi$. $(\omega_p/\omega_c = 1.0)$

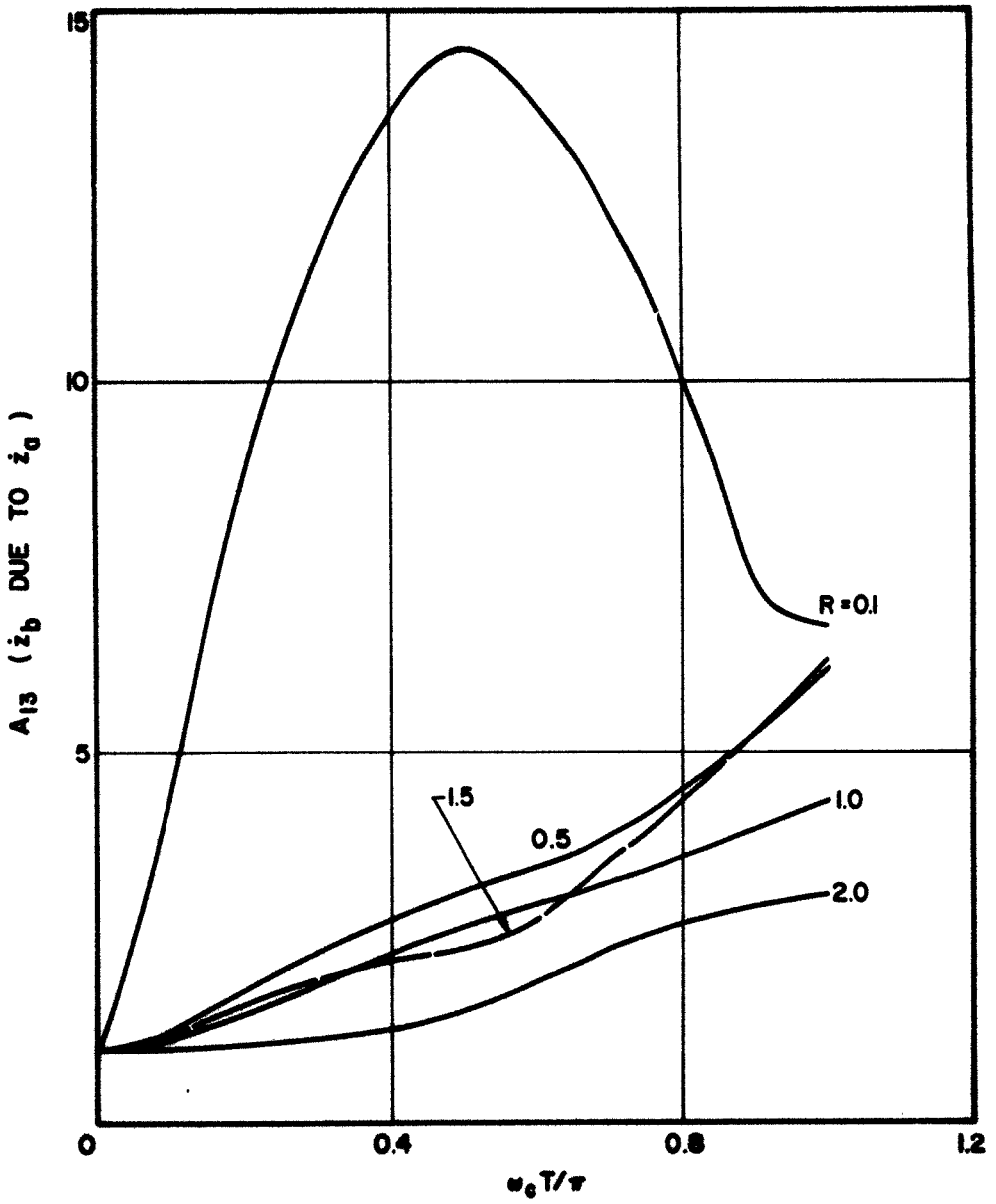

FIG. 3.33 A_{13} VS. $\omega_c T/\pi$. $(\omega_p/\omega_c = 1.2)$

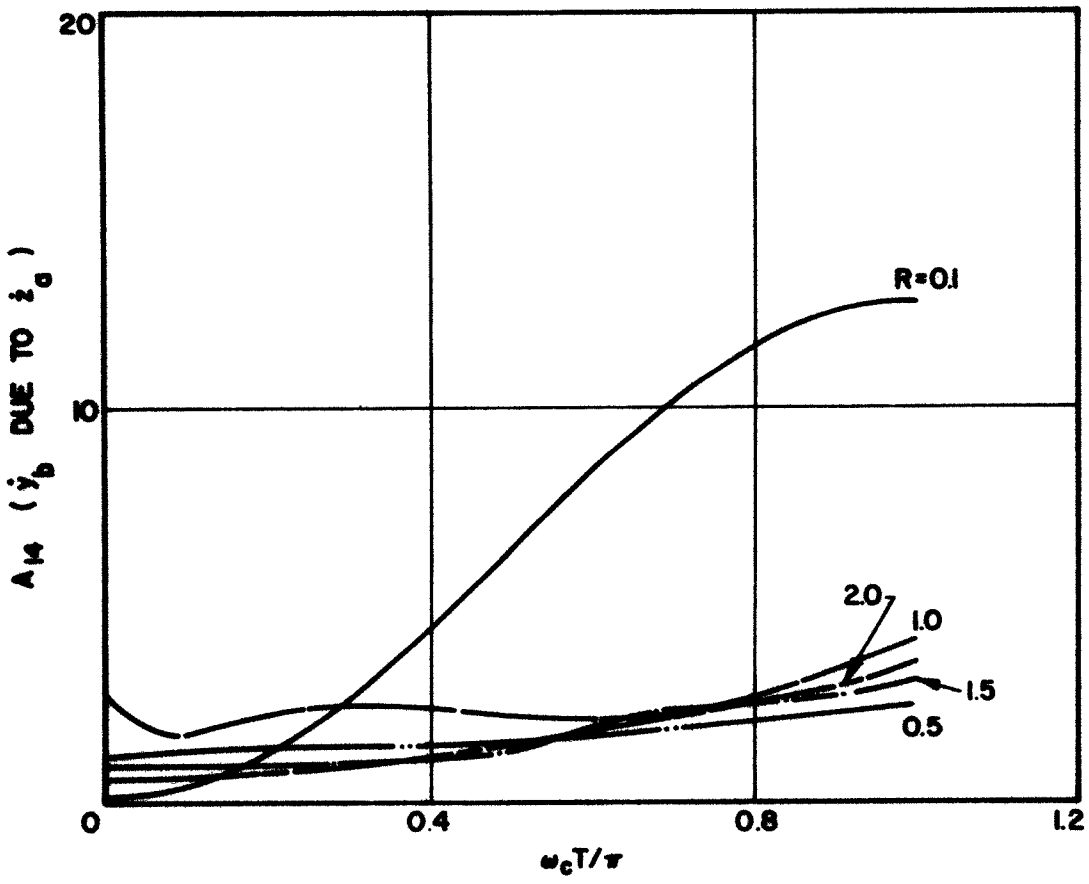

FIG. 3.34 A_{14} VS. $\omega_c T/\pi$. $(\omega_p/\omega_c = 0.8)$

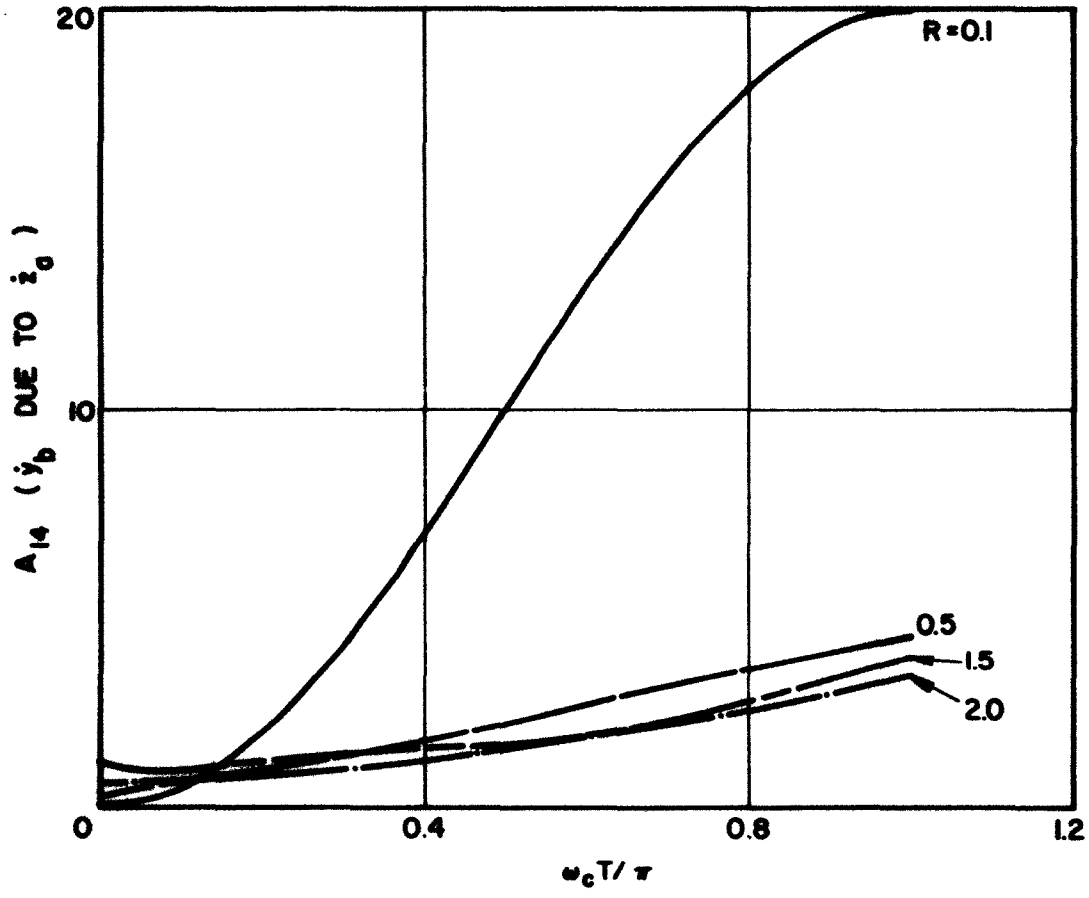

FIG. 3.35 A_{14} VS. $\omega_c T/\pi$. $(\omega_p/\omega_c = 1.0)$

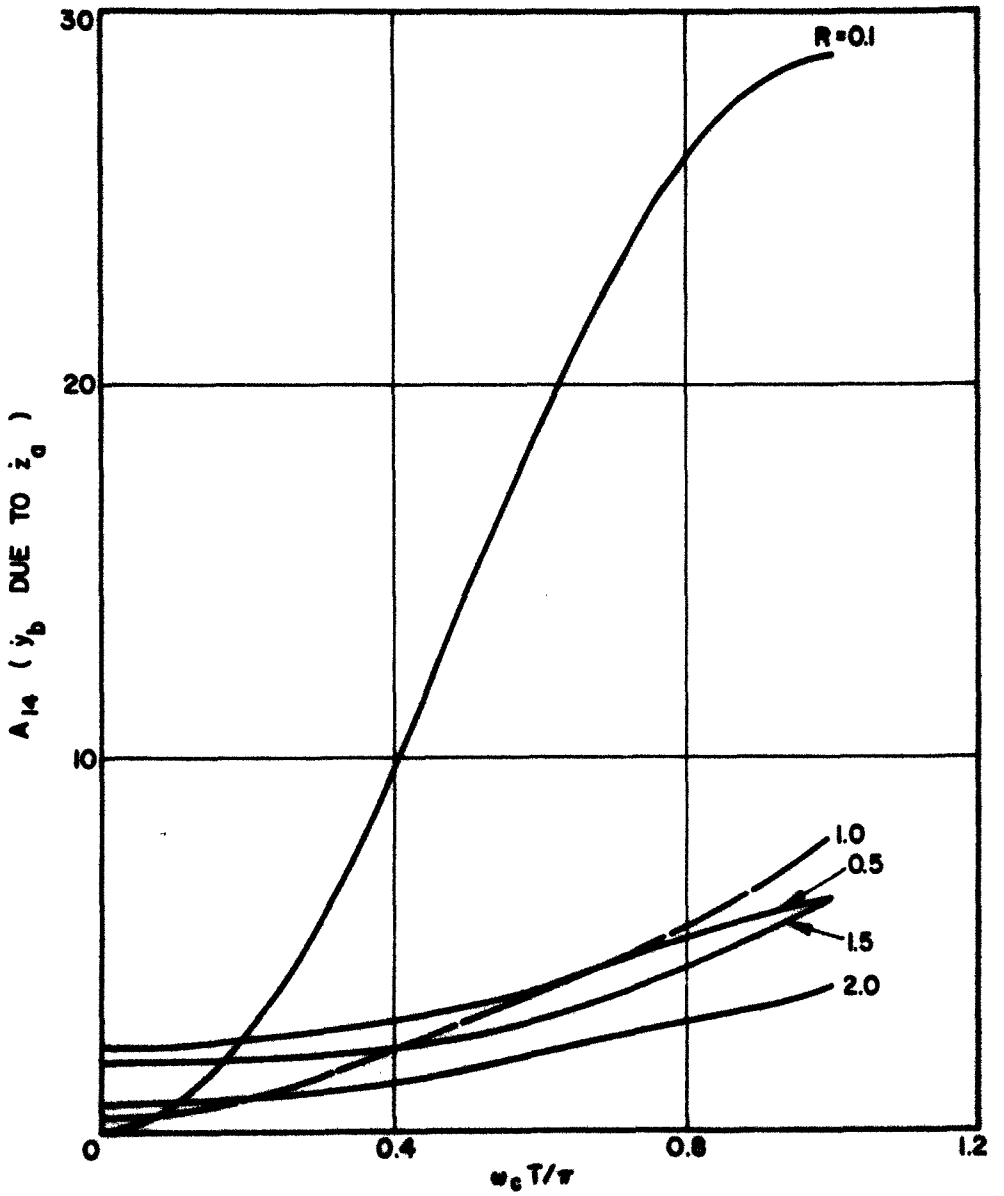

FIG. 3.36 A_{14} VS. $\omega_c T/\pi$. $(\omega_p/\omega_c = 1.2)$

not have the same values for different values of R at $\omega_c T/\pi = 0$. This is because of the fact that the various fluctuations are functions of R as shown by Eqs. 3.42 through 3.44. The plots in Figs. 3.28 through 3.30 may be normalized so that A_{12} equals the same for all values of R for $\omega_c T/\pi = 0$ and in that case the variation of these plots as a function of R would become more evident, i.e., the fluctuations in the current density components increase as R is increased.

A similar normalization for the plots of A_{14} in Figs. 3.34 through 3.36 would also make it more evident that the velocity fluctuations are decreased as R is increased. Whether the total noise would increase or decrease as R is varied would involve substitution for the numerical values of the variation perturbations.

Unfortunately the case $\omega = \omega_p$ would lead to a singularity in the coefficients given by Eqs. 3.49 through 3.52. This corresponds to $\omega_p/\omega_c = 1$ for R = 1 and this situation is not considered in evaluating these plots. In Figs. 3.25 through 3.36 it can be seen that the values of all the coefficients given by Eqs. 3.49 through 3.52 increase with increasing ω_p/ω_c. This indicates that higher values of the plasma frequency or the space-charge parameter S as defined by Gould[16] would lead to larger noise content which is in agreement with results given by Gould[16].

3.6 Conclusions

The noise transport coefficients defined by Eqs. 2.25 have been evaluated for one case, namely, when the two a-c components of the current density (also velocity) are in the same phase and of the same magnitude at the input plane. Because of this assumption it will be difficult to generalize the results shown in the various figures in this

chapter. However it can be seen in some of e plots that for a Kino gun model the coefficients plotted in the respec ive figures show minima in the neighborhood of $\omega_c T = \pi$. From these cur es it is anticipated that the values of these coefficients will incres e for $\omega_c T > \pi$. The same thing is true for a temperature-limited ope ation in the neighborhood of $\omega_c T = \pi/2$. These results correspond to the case that, when $d\dot{y}_o/dy < 0$, the perturbations grow along the beam. Th same conclusion has been obtained from the results of the density thod given in Chapter V.

The values of $\omega_c T$ for which the mi ma mentioned above occur seem to be greatly dependent upon the value o R. Also in some plots these minima occur around $\omega_c T = \pi/2$ for the Ki gun model. For the quasi space-charge-limited case some minima oc r around $\omega_c T = \pi$ and others occur around $\omega_c T = \pi/2$. For more under anding of these variations it will be necessary to assume finite valu s of the initial velocities and compute the coefficients for each physi al model under different combinations of the velocity (and current ensity) components perturbations at the input plane.

From the plots of the coefficie ts A_{11}, A_{12}, A_{13} and A_{14} in Figs. 3.25 through 3.36 it can be seen that the perturbation grows faster if ω_p/ω_c is increased. This is in quali tive agreement with the results of Gould[16]. It can also be seen from these figures that the current density perturbation at the output pl ne is minimum for the lowest value of R, while the velocity perturbation at the output plane is minimum for the maximum value of R. This is ver helpful in reducing the noise content at the output plane because an ppropriate type of coupling can be incorporated depending upon the ran of frequencies in the noise content.

CHAPTER IV. DEVELOPMENT OF DENSITY FUNCTION ANALYSIS

4.1 Introduction

The output noise of crossed-field devices is usually quite significant under space-charge-limited operation of the device and this noise disappears (or at least is significantly reduced) as soon as the operation of the cathode is changed to temperature-limited conditions. This is contrary to the behavior of O-type devices under the same conditions of operation. Under space-charge-limited conditions the potential minimum in O-type devices plays a sorting role in which the variations in current flowing across the minimum are not as large as the fluctuations in emission from the cathode, thereby reducing the noise output. The potential minimum behavior in O-type configurations has been extensively studied by Siegman[1], Watkins[2], Bloom[3], and Whinnery[4] on a one-dimensional basis and their studies have led to an equivalent resonant circuit for this region. The resonant frequency of the equivalent circuit is equal to the plasma frequency corresponding to the space-charge density at the potential minimum. As a result of these studies, the noise reduction factor due to the sorting action of the potential minimum has also been calculated.

The above O-type analyses are based upon the density function method assuming small-signal conditions and considering both single and multiple velocity distributions. Even though the potential minimum region includes electrons at zero velocities and small-signal conditions are violated, the results obtained from the density function methods are quite reasonable and are reasonably close to the experimental results. Thus the density function method may be considered as a reasonably

accurate method. The electron beam is considered as a continuous stream of fluid and the particle nature of the electrons is ignored. So far most of the studies involving small-signal analyses of crossed-field devices have been restricted to the interaction region where a one-dimensional flow of electrons may be assumed with reasonable accuracy. For the above reasons it becomes of great interest to study the noise transport in the gun region. The study outlined in this chapter is based upon the density function method. Due to the continuous variation of the two velocity components in the gun region, the equations become quite complicated. In order to reduce the complexity of the problem, a number of assumptions are made. As a result of this analysis the potential distribution, the space-charge distribution, the two velocity components, the cathode current and the propagation of an arbitrary signal along the beam are evaluated with the help of the IBM 709 computer. The coordinate configuration is shown in Fig. 4.1.

4.2 Assumptions Made in This Analysis

In this analysis, the following assumptions are made.

1. Nonrelativistic mechanics.
2. The force due to r-f magnetic field on an electron is neglected.
3. The z-component of d-c electric field is zero and the potential distribution under steady-state conditions is a function of y for all values of ω_c.
4. There are no variations of any quantity in the direction of the magnetic field.
5. All perturbations in the steady-state analysis are of the form

$$f(y,z,t) = F_1(y,z)\, e^{j\omega t}$$

and small-signal conditions are considered.

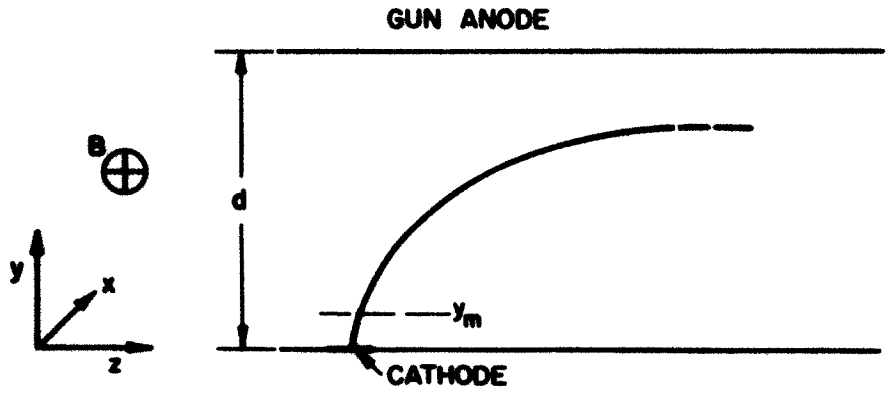

FIG. 4.1 A FILAMENTARY BEAM IN THE GUN REGION.(POSITION OF POTENTIAL MINIMUM EXAGGERATED)

6. The effect of collisions is neglected.

7. A half-Maxwellian distribution for the y-component velocity and a full-Maxwellian distribution for the z-component velocity are assumed. The electrons returning to the cathode due to the presence of the potential minimum do not change this velocity distribution.

8. A filamentary beam of finite charge density is considered.

4.3 Derivation of Steady-State Space-Charge Density (Boundary Value Problem)

The emitted electrons are considered to have a Maxwellian velocity distribution and electrons with negative values of initial y-component velocity are not considered. The expression for ρ_o is derived in a manner similar to that of Twiss[20] and the dependence of the initial normal critical velocity on the initial tangential velocity is also considered. For the initial velocity components the normal critical velocity for a given value of tangential velocity and cyclotron frequency is the y-component velocity which will be just enough for the electron to escape the potential minimum barrier for a particular potential distribution in that region. The expression for this velocity is derived in Section 4.4. In determining the space-charge density it is necessary to include all electrons with all possible electron velocities. Let n(v) dv represent the number of electrons per unit volume in the vicinity of the cathode with initial velocity components given by

$$\dot{y}_i < \dot{y} < \dot{y}_i + d\dot{y}_i$$

and

$$\dot{z}_i < \dot{z} < \dot{z}_i + d\dot{z}_i \, . \qquad (4.1)$$

Then, according to the Maxwellian velocity distribution law,

$$n(v)\, dv = A\, e^{-m\frac{\dot{y}_i^2+\dot{z}_i^2}{2kT}}\, d\dot{y}_i\, d\dot{z}_i \quad , \tag{4.2}$$

where

$$A = \frac{-I_s m^2}{|e|\, kT\sqrt{2\pi mkT}}$$

and $0 < \dot{y}_i < \infty$, $-\infty < \dot{z}_i < \infty$ and I_s = saturation current density. The y-component of the current density dI_o due to electrons with their initial velocity components given by Eq. 4.1 is

$$dI_o = -A|e|\, e^{-m\frac{\dot{y}_i^2+\dot{z}_i^2}{2kT}}\, \dot{y}_i\, d\dot{y}_i\, d\dot{z}_i \quad . \tag{4.3}$$

Substitution of A in Eq. 4.3 yields

$$dI_o = \frac{I_s m^2}{kT\sqrt{2\pi mkT}}\, e^{-m\frac{\dot{y}_i^2+\dot{z}_i^2}{2kT}}\, \dot{y}_i\, d\dot{y}_i\, d\dot{z}_i \quad . \tag{4.4}$$

From the conservation of charge, it follows that

$$dI_o = -\dot{y}\, d\rho_o \quad , \tag{4.5}$$

where $\dot{y}$ is the y-component of velocity and $d\rho_o$ is the space-charge density contribution due to electrons with their initial velocities given by Eq. 4.1. From Eqs. 4.4 and 4.5, the following is obtained:

$$d\rho_o = -\frac{I_s\, e^{-m\frac{\dot{y}_i^2+\dot{z}_i^2}{2kT}}\, m^2\, \dot{y}_i\, d\dot{y}_i\, d\dot{z}_i}{kT\sqrt{2\pi mkT}\,[2\eta V(y) + \dot{y}_i^2 - \omega_c^2 y^2 - 2\omega_c y\, \dot{z}_i]^{1/2}} \quad , \tag{4.6}$$

where $\dot{y}$ has been substituted from Eq. 4.39. Because of the assumption that $V(y)$ is a function of y, $\dot{y}$ is also a function of y and this makes $d\rho_o$ a function of y only. The following variables are introduced:

$$V_{y_i} = \frac{m\dot{y}_i^2}{2kT} \tag{4.7}$$

and

$$\psi(y) = \frac{|e|V(y)}{kT} - \frac{m\omega_c^2 y^2}{2kT} , \tag{4.8}$$

where V_{y_i} represents the normalized value of $\dot{y}_i^2$ and $\psi(y)$ corresponds to the normalized normal velocity neglecting the initial velocities. Equation 4.6 is then given by

$$d\rho_o = - \frac{I_s \, e^{-m\frac{\dot{y}_i^2+\dot{z}_i^2}{2kT}} \, m \, dV_{y_i} \, d\dot{z}_i}{\sqrt{2\pi mkT}\left\{\frac{2kT}{m}\left[\psi(y) + V_{y_i} - \frac{m\omega_c y\dot{z}_i}{kT}\right]\right\}^{1/2}} . \tag{4.9}$$

The total space-charge density $\rho_o(y)$ for temperature-limited operation is given by integrating Eq. 4.9 with respect to $\dot{y}_i$ and $\dot{z}_i$ within appropriate limits. For space-charge-limited operation the crossed-field diode is divided into two regions, namely:

1. Potential minimum region, i.e., the region between the cathode and the potential minimum; this is the decelerating region and all electrons emitted with their initial normal velocities $\leq \dot{y}_{i_c}$ are turned back to the cathode.
2. Gun region, i.e., the region between the potential minimum and the anode; this is the accelerating region and all the electrons with their initial normal velocities $> \dot{y}_{i_c}$ can cross the potential minimum barrier and are then accelerated toward the anode.

The electrons reflected from the minimum may hit the cathode and change the value of the saturation current density I_s instantaneously. It is assumed that I_s remains constant and its value is not affected by the reflected electrons which may tend to oscillate back and forth in this region, imparting under favorable conditions a part of their energy to a small perturbation at the potential minimum. For simplicity this energy exchange phenomenon will be neglected. For the evaluation of the space-charge density from Eq. 4.9 for Region 1, it is also necessary to take into account the reflected electrons. Then the expressions for ρ_{o1} and ρ_{o2} representing the steady-state space-charge densities in the two regions are given by

$$\rho_{o1,2} = -\frac{mI_s}{\sqrt{2\pi mkT}} \int_{-\infty}^{\infty} d\dot{z}_i \int_0^{\infty} \frac{e^{-V_{y_i} - \frac{m\dot{z}_i^2}{2kT}}}{\left\{ \frac{2kT}{m} \left[\psi(y) + V_{y_i} - \frac{m\omega_c y \dot{z}_i}{kT} \right] \right\}^{1/2}} dV_{y_i}$$

$$\mp \frac{mI_s}{\sqrt{2\pi mkT}} \int_{-\infty}^{\infty} d\dot{z}_i \int_0^{V_{y_c}} \frac{e^{-V_{y_i} - \frac{m\dot{z}_i^2}{2kT}}}{\left\{ \frac{2kT}{m} \left[\psi(y) + V_{y_i} - \frac{m\omega_c y \dot{z}_i}{kT} \right] \right\}^{1/2}} dV_{y_i} \quad , \qquad (4.10)$$

where

$$V_{y_c} = \frac{m\dot{y}_{i_c}^2}{2kT} = \frac{mA_1^2}{2kT}\left(-2\eta V_m + \omega_c^2 y_m^2 + 2\omega_c y_m \dot{z}_i \right) \qquad (4.11)$$

represents the normalized value of $\dot{y}_{i_c}^2$. The first and second suffixes in Eq. 4.10 correspond to the upper and lower signs respectively. The significance of the parameter A_1 is discussed in Section 4.4. Now substitute

$$\psi(y) + V_{y_i} - \frac{m\omega_c y\dot{z}_i}{kT} = U^2 \tag{4.12}$$

into Eq. 4.10. After simplification, the following equation is obtained:

$$\rho_{o1,2} = -\frac{mI_s}{2kT} e^{\psi(y)} \left\{ \int_{-\infty}^{\infty} e^{-\frac{m\omega_c y\dot{z}_i}{kT} - \frac{m\dot{z}_i^2}{2kT}} \left[1 - \mathrm{erf}\,(\alpha_1)\right] d\dot{z}_i \right.$$

$$\left. \pm \int_{-\infty}^{\infty} e^{-\frac{m\omega_c y\dot{z}_i}{kT} - \frac{m\dot{z}_i^2}{2kT}} \left[\mathrm{erf}\,(\alpha_2) - \mathrm{erf}\,(\alpha_1)\right] d\dot{z}_i \right\} , \tag{4.13}$$

where

$$\alpha_1 = \sqrt{\psi(y) - \frac{m\omega_c y\dot{z}_i}{kT}} , \tag{4.14}$$

$$\alpha_2 = \sqrt{\psi(y) + V_{y_c} - \frac{m\omega_c y\dot{z}_i}{kT}} \tag{4.15}$$

and erf(t) is defined by

$$\int_0^t e^{-u^2} du = \frac{\sqrt{\pi}}{2} - \int_t^{\infty} e^{-u^2} du = \frac{\sqrt{\pi}}{2} \mathrm{erf}(t) . \tag{4.16}$$

In order to determine the potential distribution in the two regions, Poisson's equation in the form

$$\frac{d^2V}{dy^2} = -\frac{\rho_o}{\epsilon_o} \tag{4.17}$$

is utilized and this form is valid in the case of a one-dimensional potential distribution. It is evident from Eqs. 4.13 and 4.17 that a solution for V(y) involves three integrations and it becomes necessary

to make a few approximations in Eq. 4.13 so that a solution for V(y) may be obtained conveniently and within a reasonable accuracy. For this purpose the following two cases for the arguments α_1 and α_2 involved in the error functions are considered.

Case A

Argument t of erf(t) as defined in Eq. 4.16 is large, so that

$$\frac{\sqrt{\pi}}{2}\,\mathrm{erf}(t) = \int_0^t e^{-u^2}\,du = \frac{\sqrt{\pi}}{2} - \frac{e^{-t^2}}{2t}\left(1 - \frac{1}{2t^2} + \frac{1.3}{(2t^2)^2} - \cdots\right), \tag{4.18a}$$

$$\simeq \frac{\sqrt{\pi}}{2} - \frac{e^{-t^2}}{2t}, \tag{4.18b}$$

where the higher order terms in Eq. 4.18a have been neglected.

Case B

Argument t of erf(t) as defined in Eq. 4.16 is small, so that

$$\frac{\sqrt{\pi}}{2}\,\mathrm{erf}(t) = \int_0^t e^{-u^2}\,du = t - \frac{t^3}{3} + \frac{t^5}{5.2!} - \cdots, \tag{4.19a}$$

$$\simeq t, \tag{4.19b}$$

where again, as in Eq. 4.18b, higher order terms in Eq. 4.19a have been neglected.

First consider Case A. This assumption leads to the following expressions for ρ_{o1} and ρ_{o2}.

$$\rho_{o1} = -\frac{mI_s}{kT\sqrt{\pi}}\left\{\int_{-\infty}^{\infty}\frac{e^{-\frac{m\dot{z}_i^2}{2kT}}}{\left[\psi(y) - \frac{m\omega_c y\dot{z}_i}{kT}\right]^{1/2}}d\dot{z}_i\right.$$

$$\left. - \int_{-\infty}^{\infty}\frac{e^{-\frac{m\dot{z}_i^2}{2kT} - V_{y_c}}}{2\left[\psi(y) + V_{y_c} - \frac{m\omega_c y\dot{z}_i}{kT}\right]^{1/2}}d\dot{z}_i\right\} \qquad (4.20)$$

and

$$\rho_{o2} = -\frac{mI_s}{kT\sqrt{\pi}}\int_{-\infty}^{\infty}\frac{e^{-\frac{m\dot{z}_i^2}{2kT} - V_{y_c}}}{2\left[\psi(y) + V_{y_c} - \frac{m\omega_c y\dot{z}_i}{kT}\right]^{1/2}}d\dot{z}_i \quad . \qquad (4.21)$$

By substituting for V_{y_c} from Eq. 4.13 (actually derived in Section 4.4) in Eqs. 4.20 and 4.21 and simplifying further, the following equations are obtained:

$$\rho_{o1} = -\frac{I_s}{4\sqrt{\pi}}\Gamma(1/4)\left(\frac{2m}{\omega_c^2 kT}\right)^{1/4}$$

$$\left[2y^{-1/2} - \left(y_m A_1^2 - y\right)^{-1/2} e^{-\frac{mA_1^2}{2kT}(-2\eta V_m + \omega_c^2 y_m^2)}\right] \qquad (4.22)$$

and

$$\rho_{o2} = -\frac{I_s}{4\sqrt{\pi}}\Gamma(1/4)\left(\frac{2m}{\omega_c^2 kT}\right)^{1/4}\left(y - y_m A_1^2\right)^{-1/2} e^{-\frac{mA_1^2}{2kT}(-2\eta V_m + \omega_c^2 y_m^2)} \quad . \qquad (4.23)$$

Equations 4.22 and 4.23 are valid for values of y other than those given by

$$y = y_m A_1^2$$

and

$$y = 0 \quad , \tag{4.24}$$

and $\Gamma(1/4)$ represents the gamma function of argument 1/4. For negative values of $\dot{z}_1$ the justification for considering Case A to simplify Eqs. 4.13 through 4.15 is evident for the arguments α_1 and α_2 given by Eqs. 4.14 and 4.15 respectively. For positive values of $\dot{z}_1$, the value of V_{y_c} given by Eq. 4.11 is increased and this corresponds to a very small number of electrons in the Maxwellian velocity distribution curve. Thus the approximation made in considering Case A would yield a very small error in the final results. Consideration of Case B will be discussed in Section 5.1. It should be pointed out here that these approximations are made in solving for the values of V_m and y_m for a given set of parameters. Once these values are determined, the various d-c quantities and the propagation of a perturbation along the beam in the gun region can be determined with the potential minimum taken as the origin. This is discussed in detail in Sections 4.6 and 4.7.

4.4 Derivation of the Initial Normal Critical Velocity and the Two Velocity Components

In Section 4.3, the initial normal critical velocity given by Eq. 4.11 was used to develop expressions for the steady-state space-charge densities for the two regions. As mentioned in Section 4.3, all the electrons having their initial normal velocity $> \dot{y}_{1_c}$ cross the potential minimum barrier and the electrons for which $\dot{y}_1 \leq \dot{y}_{1_c}$ are reflected back toward the cathode. In developing an expression for $\dot{y}_{1_c}$, a parabolic

potential distribution in the potential minimum region is assumed. In practice the potential distribution determined by using Eq. 4.22 in conjunction with Poisson's equation may be used to determine a new value of $\dot{y}_{i_c}$ and the iteration process is repeated until convergence is obtained. The potential distribution assumed is shown in Fig. 4.2 and is given by

$$V - V_m = -\frac{V_m}{y_m^2}(y - y_m)^2 \quad \text{for} \quad y \leq y_m \ , \tag{4.25}$$

so that, at $y = y_m$,

$$V = V_m \tag{4.26}$$

and

$$\frac{dV}{dy} = 0 \ ,$$

where V_m and y_m correspond to the potential and the position of the potential minimum respectively. By using the steady-state equations of motion for an electron given by

$$\ddot{z} = \omega_c \dot{y} \tag{4.27a}$$

and

$$\ddot{y} = -\eta E_y - \omega_c \dot{z} \ , \tag{4.27b}$$

the following may be obtained for Region 1:

$$y = \frac{\dot{y}_i}{\Omega}\sin \Omega t + \frac{2\eta \frac{V_m}{y_m} - \omega_c \dot{z}_i}{\Omega^2}(1 - \cos \Omega t) \ , \tag{4.28a}$$

$$\dot{y} = \dot{y}_i \cos \Omega t + \frac{2\eta \frac{V_m}{y_m} - \omega_c \dot{z}_i}{\Omega}\sin \Omega t \tag{4.28b}$$

and

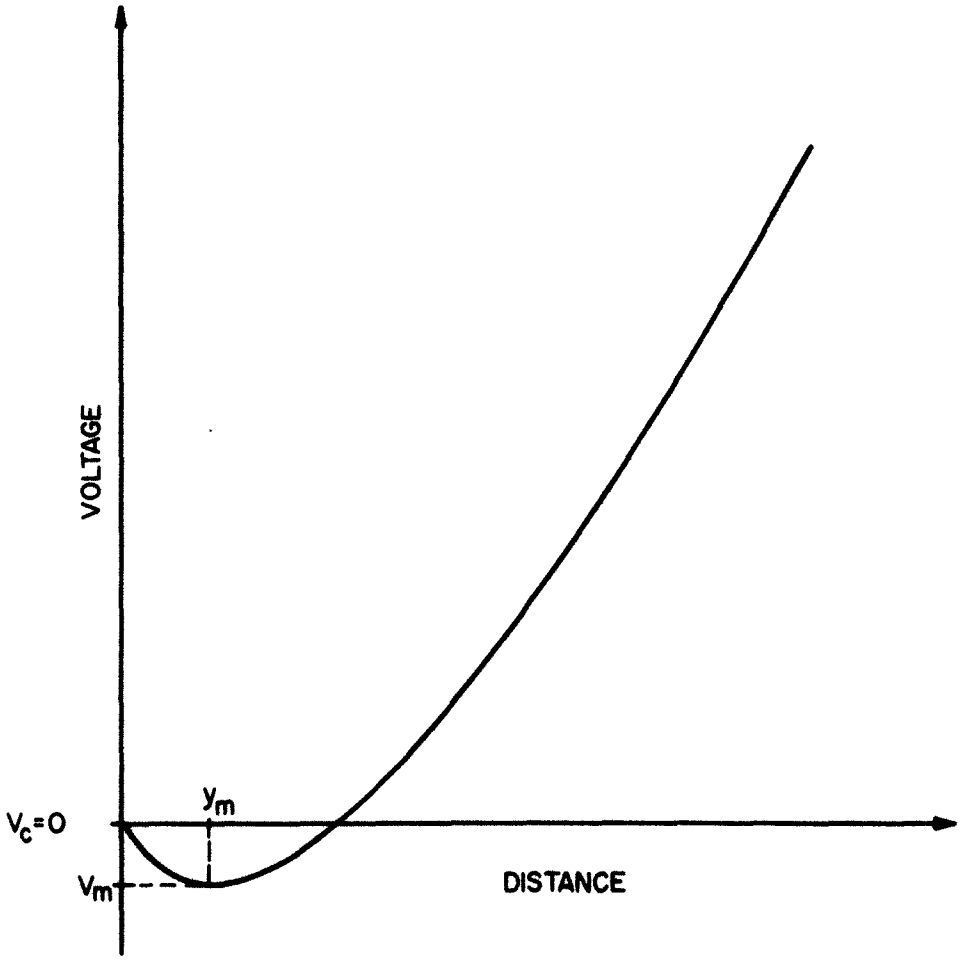

FIG. 4.2 POTENTIAL DISTRIBUTION ASSUMED TO DERIVE AN EXPRESSION FOR THE INITIAL NORMAL CRITICAL VELOCITY.

$$\dot{y} = -\Omega\,\dot{y}_i \sin \Omega t + \left(2\eta \frac{V_m}{y_m} - \omega_c \dot{z}_i\right) \cos \Omega t \quad , \tag{4.28c}$$

where

$$\Omega^2 = 2\eta \frac{V_m}{y_m^2} + \omega_c^2 \quad . \tag{4.29}$$

The coordinate system used for the development of the above equations is shown in Fig. 4.1 and $E_z = 0$ is assumed. For the development of an expression for $\dot{y}_{i_c}$

$$\dot{y}_i = \dot{y}_{i_c} \tag{4.30}$$

if

$$\dot{y} = 0 \quad \text{at} \quad y = y_m \quad .$$

Under these conditions

$$\dot{y}_{i_c} = \left(-2\eta V_m + \omega_c^2 y_m^2 + 2\omega_c y_m \dot{z}_i\right)^{1/2} \tag{4.31}$$

and

$$\ddot{y}\Big|_{y=y_m} = -\left(\omega_c^2 y_m + \omega_c \dot{z}_i\right) \quad . \tag{4.32}$$

Even though for $\dot{y}_i = \dot{y}_{i_c}$, $\dot{y} = 0$ at $y = y_m$ and the electrons may experience a decelerating force depending upon the sign and the magnitude of $\dot{z}_i$. To be sure that all electrons with $\dot{y}_i > \dot{y}_{i_c}$ move into Region 2, a constant A_1 is introduced to give

$$\dot{y}_{i_c} = A_1 \left(-2\eta V_m + \omega_c^2 y_m^2 + 2\omega_c y_m \dot{z}_i\right)^{1/2} \quad , \tag{4.33}$$

where

$$A_1 > 1 \quad . \tag{4.34}$$

A special case of academic interest is the one in which

$$\Omega^2 = 2\eta \frac{V_m}{y_m^2} + \omega_c^2 = 0 \tag{4.35a}$$

and

$$\dot{z}_i = -\omega_c y_m \quad . \tag{4.35b}$$

Under these conditions, Eqs. 4.28 become

$$y = \dot{y}_i t \quad , \tag{4.36a}$$

$$\dot{y} = \dot{y}_i \quad , \tag{4.36b}$$

$$\ddot{y} = 0 \quad . \tag{4.36c}$$

In other words, for the conditions given by Eqs. 4.35, the effects of the potential minimum and the initial tangential velocity compensate for each other. The electron moves with a constant initial normal velocity $\dot{y}_i$ and is accelerated in Region 2 only. In such a case all the emitted electrons are able to cross the potential minimum.

From Eq. 4.27a the z-component velocity is given by

$$\dot{z}_o = \omega_c y + \dot{z}_i \quad , \tag{4.37}$$

where $\dot{z}_i$ is the initial tangential velocity. The conservation of energy gives the following:

$$\dot{y}_o^2 + \dot{z}_o^2 = 2\eta V + \dot{y}_i^2 + \dot{z}_i^2 \quad , \tag{4.38}$$

where $\dot{y}_o$ and $\dot{z}_o$ correspond to the two velocity components at a point (y,z) corresponding to the voltage V and $\dot{y}_i$ is the initial normal velocity. By using Eqs. 4.37 and 4.38 the expression for $\dot{y}_o$ is obtained as

$$\dot{y}_o = \left[2\eta V + \dot{y}_i^2 - \omega_c^2 y^2 - 2\omega_c y \dot{z}_i\right]^{1/2} \quad . \tag{4.39}$$

4.5 Potential Variation Along the Beam (Boundary Value Problem)

The potential distribution for the two regions is determined by using Poisson's equation and the expression for the space-charge density for the two respective regions given by Eqs. 4.22 and 4.23.

Region 1.

$$\frac{d^2V}{dy^2} = -\frac{\rho_{o1}}{\epsilon_o}$$

$$= \frac{I_s}{4\sqrt{\pi}\,\epsilon_o}\,\Gamma(1/4)\left(\frac{2m}{\omega_c^2 kT}\right)^{1/4}\Bigg[2y^{-1/2}$$

$$-\left(y_m A_1^2 - y\right)^{-1/2} e^{-\frac{mA_1^2}{2kT}(-2\eta V_m + \omega_c^2 y_m^2)}\Bigg] \quad . \quad (4.40)$$

The boundary conditions are

$$\frac{dV}{dy} = 0 \quad \text{at} \quad y = y_m \qquad (4.41a)$$

and

$$V = 0 \quad \text{at} \quad y = 0 \ . \qquad (4.41b)$$

Equation 4.40 can be integrated to give

$$V_{o1} = \frac{I_s}{4\sqrt{\pi}\,\epsilon_o}\,\Gamma(1/4)\left(\frac{2m}{\omega_c^2 kT}\right)^{-1/4}\Bigg\{4\,y_m^{3/2}\left[\frac{2}{3}\left(\frac{y}{y_m}\right)^{3/2} - \frac{y}{y_m}\right]$$

$$+\frac{4}{3}\,y_m^{3/2}\,A_1^3\left[1-\left(1-\frac{y}{y_m A_1^2}\right)^{3/2}\right] e^{-\frac{mA_1^2}{2kT}(-2\eta V_m + \omega_c^2 y_m^2)}\Bigg\} \quad . \qquad (4.42)$$

Region 2.

$$\frac{d^2V}{dy^2} = -\frac{\rho_{o2}}{\epsilon_o}$$

$$= \frac{I_s}{4\sqrt{\pi}\,\epsilon_o}\,\Gamma(1/4)\left(\frac{2m}{\omega_c^2 kT}\right)^{1/4}\left(y - y_m A_1^2\right)^{-1/2} e^{-\frac{mA_1^2}{2kT}(-2\eta V_m + \omega_c^2 y_m^2)} . \tag{4.43}$$

Then the boundary condition is

$$\frac{dV}{dy} = 0 \quad \text{at} \quad y = y_m \ . \tag{4.44}$$

Equation 4.43 can be integrated to give

$$V_{o2} = \frac{I_s}{3\sqrt{\pi}\,\epsilon_o}\,\Gamma(1/4)\left(\frac{2m}{\omega_c^2 kT}\right)^{1/4}\left(y - y_m\right)^{3/2} e^{-\frac{mA_1^2}{2kT}(-2\eta V_m + \omega_c^2 y_m^2)} + K_1 \ . \tag{4.45}$$

The boundary condition given by

$$V_{o2} = V_m \quad \text{at} \quad y = y_m \tag{4.46}$$

does not lead to any useful information and thus the constant of integration K_1 in Eq. 4.45 is evaluated from the following boundary condition.

$$V = V_o \ , \quad \omega_c = \omega_{cc} \quad \text{at} \quad y = d \ , \tag{4.47}$$

where V_o is the d-c potential applied to the anode at a distance d from the cathode and ω_{cc} corresponds to the cutoff cyclotron frequency for the crossed-field diode under investigation. Equation 4.47 is also valid for $\omega_c < \omega_{cc}$ since in that case all the electrons are collected at the anode. Our interest is, however, when $\omega_c \geq \omega_{cc}$ and the constant K_1 is thus evaluated by using Eq. 4.47 to give

$$V_{o2} = V_o - \frac{I_s}{3\sqrt{\pi}\,\epsilon_o}\Gamma(1/4)\left(\frac{2m}{kT}\right)^{1/4}\left[\frac{(d-y_m)^{3/2}}{\sqrt{\omega_{cc}}}e^{-\frac{mA_1^2}{2kT}(-2\eta V_m' + \omega_{cc}^2 y_m'^2)}\right.$$

$$\left. - \frac{(y-y_m)^{3/2}}{\sqrt{\omega_c}}e^{-\frac{mA_1^2}{2kT}(-2\eta V_m + \omega_c^2 y_m^2)}\right], \quad (4.48)$$

where V_m' and y_m' correspond to the values of V_m and y_m respectively for $\omega_c = \omega_{cc}$. As mentioned in Section 4.3 the expressions for the voltage along the beam given by Eqs. 4.42 and 4.48 are developed in order to determine the values of y_m and V_m for a given set of parameters. A more rigorous derivation for the space-charge density and the potential distribution in the gun region as an initial value problem is given in Section 4.6 and the values of y_m and V_m determined in Section 5.1 are utilized in this derivation.

4.6 Derivation of Expressions for the Space-Charge Density and Other Related Functions (Initial Value Problem)

In Sections 4.3 and 4.5 expressions for the space-charge distribution and the potential distribution for the two regions were developed. In the boundary value problem these expressions are used at $y = y_m$ to evaluate the values of V_m and y_m for a given set of parameters. This is discussed in Section 5.1. In the gun region the z-component of the current density cannot be neglected and thus the total velocity vector and the total current density vector are considered in this section for the derivation of the various functions.

In treating this as a boundary value problem it becomes necessary to predetermine the dependent variables such as V and ρ_o at the entrance to the interaction region. The procedure involved in the solution

concerns a trial and error method and is generally time consuming. The problem treated as an initial value problem requires the values of the dependent variables at the input plane. Integration is carried out along the beam trajectory to determine ρ_o, V, $\dot{y}_o$, $\dot{z}_o$ and the propagation of a perturbation along the beam. By considering again a Maxwellian velocity distribution for the electrons crossing the potential minimum, the current density dI_o due to electrons with their velocities given by Eq. 4.1 is determined in a manner similar to that used in deriving the y-component current density given by Eq. 4.4.

$$dI_o = \frac{2I_s}{\left(\frac{\pi kT}{m}\right)^{3/2}\sqrt{2}} e^{-m\frac{\dot{y}_i^2 + \dot{z}_i^2}{2kT}} \left(\dot{y}_i^2 + \dot{z}_i^2\right)^{1/2} d\dot{y}_i \, d\dot{z}_i \quad . \tag{4.49}$$

From the conservation of energy, it is seen that

$$\vec{\dot{r}} = \vec{v} = \left(\dot{z}^2 + \dot{y}^2\right)^{1/2} \vec{a} = \left(\dot{z}_i^2 + \dot{y}_i^2 + 2\eta V\right)^{1/2} \vec{a} \quad , \tag{4.50}$$

where $\vec{a}$ is a unit vector in the direction of the total velocity. By making use of the following three equations,

$$dI_o = -\dot{r}\, d\rho \quad , \tag{4.51}$$

$$\sqrt{\frac{m}{2kT}}\, \dot{y}_i = u \tag{4.52}$$

and

$$\sqrt{\frac{m}{2kT}}\, \dot{z}_i = v \quad , \tag{4.53}$$

and Eqs. 4.49 and 4.50, the space-charge density ρ_o in the gun region may be expressed as

$$\rho_o = -2I_s\left(\frac{2m}{\pi^3 kT}\right)^{1/2}\int_{-\infty}^{\infty} dv \int_{u_c}^{\infty} \frac{e^{-(u^2+v^2)}(u^2+v^2)^{1/2}}{\left(u^2+v^2+\frac{|e|V}{kT}\right)^{1/2}}\,du \;, \quad (4.54)$$

where, as was the case in deriving Eq. 4.10 from Eq. 4.9, integration over all possible values of u and v is made to obtain Eq. 4.54 from Eq. 4.51. The parameters u and v are the normalized dimensionless variables and u_c is given by

$$u_c = \sqrt{\frac{m}{2kT}}\,\dot{y}_{i_c} \;, \quad (4.55)$$

where $\dot{y}_{i_c}$ given by Eq. 4.33 is rewritten after making use of Eq. 4.53.

$$\dot{y}_{i_c} = A_1\left(-2\eta V_m + \omega_c^2 y_m^2 + 2\omega_c y_m\sqrt{\frac{2kT}{m}}\;v\right)^{1/2} \;. \quad (4.56)$$

For some negative values of v it is possible that $\dot{y}_{i_c}^2$ can become negative so that all the electrons with these negative values of v can cross the potential minimum. For these electrons $\dot{y}_{i_c}$ (or u_c) is taken to be equal to zero.

By using the one-dimensional Poisson's equations, substituting for ρ_o from Eq. 4.54, multiplying this result by 2(dV/dy), and integrating with respect to y, the following equation is obtained:

$$\frac{dV}{dy} = \left[\frac{8I_s}{\epsilon_o \pi}\frac{kT}{|e|}\left(\frac{2m}{\pi kT}\right)^{1/2}\right]^{1/2}\left\{\int_{-\infty}^{\infty} dv \int_{u_c}^{\infty} e^{-(u^2+v^2)}(u^2+v^2)^{1/2}\left(u^2+v^2 + \frac{|e|V}{kT}\right)^{1/2} du - D_m\right\}^{1/2} , \qquad (4.57)$$

where D_m is given by

$$D_m = \int_{-\infty}^{\infty} dv \int_{u_c}^{\infty} e^{-(u^2+v^2)}(u^2+v^2)^{1/2}\left(u^2+v^2+\frac{|e|V_m}{kT}\right)^{1/2} du \qquad (4.58)$$

and where it has been assumed that

$$\frac{dV}{dy} = 0 \quad \text{at} \quad y = 0 , \qquad (4.59)$$

($y = 0$ refers to the input plane which now corresponds to the position of the potential minimum). The expressions for the two velocity components given by Eqs. 4.37 and 4.39 are rewritten as

$$\dot{z}_o = \omega_c(y + y_m) + \bar{\dot{z}}_i \qquad (4.60)$$

and

$$\dot{y}_o = \left[2\eta V + \bar{\dot{y}}_i^2 - \omega_c(y+y_m)^2 - 2\omega_c(y+y_m)\bar{\dot{z}}_i\right]^{1/2} \qquad (4.61)$$

in the new coordinate system, where $\bar{\dot{y}}_i$ and $\bar{\dot{z}}_i$ correspond to the ensemble averages of the initial velocity components and these are given respectively by

$$\bar{\dot{y}}_i = \frac{1}{I_n}\sqrt{\frac{2kT}{m}}\int_{-\infty}^{\infty} dv \int_{u_c}^{\infty} u\, e^{-(u^2+v^2)}\, du$$

$$= \frac{1}{I_n}\sqrt{\frac{\pi kT}{2m}}\, e^{-\frac{mA_1^2}{2kT}\left[-2\eta V_m - (A_1^2 - 1)\,\omega_c^2 y_m^2\right]} \tag{4.62}$$

and

$$\bar{\dot{z}}_i = \frac{1}{I_n}\sqrt{\frac{2kT}{m}}\int_{-\infty}^{\infty} dv \int_{u_c}^{\infty} v\, e^{-(u^2+v^2)}\, du \quad , \tag{4.63}$$

where I_n corresponds to the normalization constant given by

$$I_n = \int_{-\infty}^{\infty} dv \int_{u_c}^{\infty} e^{-(u^2+v^2)}\, du \quad . \tag{4.64}$$

The solution for V from Eq. 4.57 in the potential minimum region is discussed in Section 5.1. For V in the gun region, two divisions are made.

1. For $y_m < y \leq y_1$, the solution is given by numerical methods and is discussed in Section 5.3.
2. For $y \geq y_1$, when

$$\frac{|e|V(y_1)}{kT} \gg (u_o^2 + v_o^2) \quad , \tag{4.65}$$

Eq. 4.57 may be simplified as

$$\frac{dV}{dy} = \left[\frac{8I_s}{\epsilon_o \pi}\left(\frac{2m}{\pi|e|}\right)^{1/2}\right]^{1/2} V^{1/4}\left\{\int_{-\infty}^{\infty} dv \int_{u_c}^{\infty} e^{-(u^2+v^2)}(u^2+v^2)^{1/2}\, du\right\}^{1/2} , \tag{4.66}$$

where D_m in Eq. 4.57 is also neglected because of the condition given by Eq. 4.65.

Because the integrand in Eq. 4.57 includes an exponentially decreasing term, it is not necessary to carry on the integration over the infinite range. Since the integration was done numerically with the aid of an IBM 709 computer, the limiting values u_o and v_o for the two variables u and v are included in Eq. 4.65. The determination of the values for u_o and v_o is discussed in Section 5.1. The condition given by Eq. 4.65 reduces the computer time significantly. Equation 4.66 may be integrated with respect to y to give

$$(V)^{3/4} = k_1(y-y_1) + (V_1)^{3/4} \quad \text{for} \quad y \geq y_1 \ , \tag{4.67}$$

where the voltage V_1 corresponds to the position $y = y_1$ and K_1 is given by

$$K_1 = \frac{3}{4}\left[\frac{8I_s}{\epsilon_o\pi}\left(\frac{2m}{\pi|e|}\right)^{1/2}\right]^{1/2}\left[\int_{-\infty}^{\infty} dv \int_{u_c}^{\infty} e^{-(u^2+v^2)}(u^2+v^2)^{1/2}\, du\right]^{1/2}. \tag{4.68}$$

Under the conditions give by Eq. 4.65, ρ_o can be rewritten from Eq. 4.54 as

$$\rho_o = -2I_s\left(\frac{2m}{\pi^3|e|}\right)^{1/2} V^{-1/2} \int_{-\infty}^{\infty} dv \int_{u_c}^{\infty} e^{-(u^2+v^2)}(u^2+v^2)^{1/2}\, du \ . \tag{4.69}$$

Once the potential distribution along the y-axis is determined, $\dot{z}_o$ and $\dot{y}_o$ can be determined as given by Eqs. 4.60 and 4.61 respectively. The trajectories are determined by a numerical method given in Section 5.3 and the current density components are evaluated from the following equations:

$$I_y = \rho_o \dot{y}_o \tag{4.70}$$

and

$$I_z = \rho_o \dot{z}_o \quad . \tag{4.71}$$

4.7 Propagation of a Perturbation Along the Beam

In this section Maxwell's equations and the equations of motion are used to develop five working equations for evaluating the propagation of any perturbation originating at the potential minimum. These equations may be solved for small-signal conditions. It is also possible to develop five similar working equations for the large-signal analysis. From Maxwell's equations the following equations may be derived:

$$\frac{\partial^2 E_z}{\partial y^2} - \frac{\partial^2 E_y}{\partial z \partial y} = \epsilon_o \mu_o \frac{\partial^2 E_z}{\partial t^2} + \mu_o \frac{\partial}{\partial t}(\rho \dot{z}) \tag{4.72a}$$

and

$$\frac{\partial^2 E_y}{\partial z^2} - \frac{\partial^2 E_z}{\partial z \partial y} = \epsilon_o \mu_o \frac{\partial^2 E_y}{\partial t^2} + \mu_o \frac{\partial}{\partial t}(\rho \dot{y}) \quad , \tag{4.72b}$$

where

$$B_y = B_z = E_x = 0 \tag{4.73}$$

is assumed. Now assuming that all the dependent variables may be written as

$$f(y,z,t) = f_o(y) + f_1(y,z)\, e^{j\omega t} \tag{4.74}$$

and that

$$E_{z_o} = 0 \quad , \tag{4.75}$$

where suffix o refers to the d-c quantity and suffix 1 refers to the a-c quantity, Eqs. 4.72 reduce to the following for small-signal conditions:

$$\frac{\partial^2 E_{z_1}}{\partial y^2} - \frac{\partial^2 E_{y_1}}{\partial z \partial y} = -\epsilon_o \mu_o \omega^2 E_{z_1} + j\omega \mu_o (\dot{z}_o \rho_1 + \rho_o \dot{z}_1) \tag{4.76a}$$

and

$$\frac{\partial^2 E_{y_1}}{\partial z^2} - \frac{\partial^2 E_{z_1}}{\partial z \partial y} = -\epsilon_o \mu_o \omega^2 E_{y_1} + j\omega \mu_o (\dot{y}_o \rho_1 + \rho_o \dot{y}_1) \quad . \tag{4.76b}$$

The equations of motion for an electron in a crossed-field geometry shown in Fig. 4.1 are given by

$$\ddot{z} = \frac{\partial \dot{z}}{\partial t} + \frac{\partial \dot{z}}{\partial y}\dot{y} + \frac{\partial \dot{z}}{\partial z}\dot{z} = -\eta E_z + \omega_c \dot{y} \tag{4.77a}$$

and

$$\ddot{y} = \frac{\partial \dot{y}}{\partial t} + \frac{\partial \dot{y}}{\partial y}\dot{y} + \frac{\partial \dot{y}}{\partial z}\dot{z} = -\eta E_y - \omega_c \dot{z} \quad . \tag{4.77b}$$

For steady-state conditions Eqs. 4.77 lead to

$$\ddot{z}_o = \omega_c \dot{y}_o \tag{4.78a}$$

and

$$\ddot{y}_o = -\eta E_{y_o} - \omega_c \dot{z}_o \quad . \tag{4.78b}$$

The a-c parts of Eqs. 4.77 are written as

$$j\omega \dot{z}_1 + \frac{\partial \dot{z}_1}{\partial y}\dot{y}_o + \frac{\partial \dot{z}_1}{\partial z}\dot{z}_o = -\eta E_{z_1} \tag{4.79a}$$

and

$$j\omega \dot{y}_1 + \frac{\partial \dot{y}_o}{\partial y}\dot{y}_1 + \frac{\partial \dot{y}_1}{\partial y}\dot{y}_o + \frac{\partial \dot{y}_1}{\partial z}\dot{z}_o = -\eta E_{y_1} - \omega_c \dot{z}_1 \quad , \tag{4.79b}$$

where the second-order terms are neglected. The other equation used to evaluate the propagation of any perturbation is given by

$$\frac{\partial E_{z_1}}{\partial z} + \frac{\partial E_{y_1}}{\partial y} = \frac{\rho_1}{\epsilon_o} \quad . \tag{4.80}$$

Equations 4.76a, 4.76b, 4.79a, 4.79b and 4.80 are the five working equations used to evaluate the propagation of a perturbation. Now if it is assumed that these perturbations are functions of y only, the equations reduce to

$$\frac{d^2E_{z_1}}{dy^2} = -\epsilon_o\mu_o\,\omega^2E_{z_1} + j\omega\,\mu_o(\dot{z}_o\rho_1 + \rho_o\dot{z}_1) \quad , \tag{4.81a}$$

$$0 = -\epsilon_o\mu_o\,\omega^2E_{y_1} + j\omega\,\mu_o(\dot{y}_o\rho_1 + \rho_o\dot{y}_1) \quad , \tag{4.81b}$$

$$j\omega\,\dot{z}_1 + \frac{d\dot{z}_1}{dy}\,\dot{y}_o = -\eta E_{z_1} \quad , \tag{4.81c}$$

$$j\omega\,\dot{y}_1 + \frac{d\dot{y}_o}{dy}\,\dot{y}_1 + \frac{d\dot{y}_1}{dy}\,\dot{y}_o = -\eta E_{y_1} - \omega_c\dot{z}_1 \tag{4.81d}$$

and

$$\frac{dE_{y_1}}{dy} = \frac{\rho_1}{\epsilon_o} \quad . \tag{4.81e}$$

From these equations it is possible to determine the five unknown a-c variables, namely E_{z_1}, E_{y_1}, $\dot{z}_1$, $\dot{y}_1$ and ρ_1, as a function of y. By assuming that these a-c quantities vary as exp γy, the following fifth degree determinantal equation may be obtained.

$$\gamma^5 \dot{y}_o^3 + \gamma^4 \dot{y}_o^2 \left(3j\omega + \frac{d\dot{y}_o}{dy}\right) + \gamma^3 \dot{y}_o \left[-3\omega^2\left(1 - \frac{\dot{y}_o^2}{3c^2}\right) + 2j\omega \frac{d\dot{y}_o}{dy} + \omega_p^2\right]$$

$$+ \gamma^2 j\omega \left[-\omega^2\left(1 - 3\frac{\dot{y}_o^2}{c^2}\right) + \left(j\omega \frac{d\dot{y}_o}{dy} + \omega_p^2\right)\left(1 - \frac{\dot{y}_o^2}{c^2}\right)\right]$$

$$+ \gamma \left[-3\frac{\omega^4}{c^2}\dot{y}_o\left(1 - \frac{\omega_p^2}{\omega^2}\right) + j\omega^3 \frac{\dot{y}_o}{c^2}\frac{d\dot{y}}{dy}\left(2 - \frac{\omega_p^2}{\omega^2}\right) - \frac{j\omega}{c^2}\omega_p^2 \omega_c \dot{z}_o\right]$$

$$- j\frac{\omega^5}{c^2}\left(1 - 2\frac{\omega_p^2}{\omega^2}\right) - \frac{\omega^4}{c^2}\left(1 - \frac{\omega_p^2}{\omega^2}\right)\frac{d\dot{y}_o}{dy} - \frac{j\omega}{c^2}\omega_p^4 = 0 \quad , \qquad (4.82)$$

where

$$\omega_p^2 = -\eta \frac{\rho_o}{\epsilon_o} \quad , \qquad (4.83)$$

ω_p is the plasma frequency and c is the velocity of light. The various functions such as ω_p, $\dot{y}_o$, $d\dot{y}_o/dy$, and $\dot{z}_o$ are functions of y. These functions are not known analytically (except for $\dot{z}_o$ which is given by $\dot{z}_o = \omega_c y + \bar{\dot{z}}_1$) and are evaluated at some values of y only. Thus it is necessary to solve Eq. 4.82 for the five roots of γ for each value of y and the positive real roots will correspond to the growth of the perturbation for that value of y. (This is how the nonlinear problem has been reduced to a linear problem.)

An approximation of an open-circuited diode leads to a simplified expression. For an open-circuited diode the total a-c current density components are zero and the left-hand side of Eqs. 4.72a, 4.76a and 4.81a reduce to zero. Under this condition E_{z_1} and E_{y_1} are given by Eqs. 4.81a and 4.81b respectively as

$$E_{z_1} = \frac{j}{\omega\epsilon_o}\left(\dot{z}_o\rho_1 + \rho_o\dot{z}_1\right) \tag{4.84a}$$

and

$$E_{y_1} = \frac{j}{\omega\epsilon_o}\left(\dot{y}_o\rho_1 + \rho_o\dot{y}_1\right) \quad . \tag{4.84b}$$

By substituting E_{z_1} and E_{y_1} from Eqs. 4.84 in Eqs. 4.81c, 4.81d, 4.81e, the following equations are obtained:

$$j\omega\left(1 - \frac{\omega_p^2}{\omega^2}\right)\dot{z}_1 + \dot{y}\frac{d\dot{z}_1}{dy} - \frac{\eta}{j\omega\epsilon_o}\dot{z}_o\rho_1 = 0 \quad , \tag{4.85a}$$

$$j\omega\left(1 - \frac{\omega_p^2}{\omega^2}\right)\dot{y}_1 + \dot{y}\frac{d\dot{y}_1}{dy} + \dot{y}_1\frac{d\dot{y}_o}{dy} + \omega_c\dot{z}_1 - \frac{\eta}{j\omega\epsilon_o}\dot{y}_o\rho_1 = 0 \tag{4.85b}$$

and

$$\rho_o\frac{d\dot{y}_1}{dy} + \dot{y}_1\frac{d\rho_o}{dy} + \dot{y}_o\frac{d\rho_1}{dy} + \rho_1\frac{d\dot{y}_o}{dy} + j\omega\rho_1 = 0 \quad . \tag{4.85c}$$

From Eqs. 4.85 the expressions for $d\dot{z}_1/dy$, $d\dot{y}_1/dy$ and $d\rho_1/dy$ are written as

$$\frac{d\dot{z}_1}{dy} = -\frac{j\omega}{\dot{y}_o+\dot{y}_1}\left[\left(1 - \frac{\omega_p^2}{\omega^2}\right)\dot{z}_1 + \frac{\eta\rho_1}{\omega^2\epsilon_o}\dot{z}_o\right] \quad , \tag{4.86a}$$

$$\frac{d\dot{y}_1}{dy} = -\frac{1}{\dot{y}_o+\dot{y}_1}\left\{\left[\left(1 - \frac{\omega_p^2}{\omega^2}\right)\dot{y}_1 + \frac{\eta\rho_1}{\omega^2\epsilon_o}\dot{y}_o\right]j\omega + \dot{y}_1\frac{d\dot{y}_o}{dy} + \omega_c\dot{z}_1\right\} \tag{4.86b}$$

and

$$\frac{d\rho_1}{dy} = -\frac{1}{\dot{y}_o}\left\{\rho_1\frac{d\dot{y}_o}{dy} + j\omega\rho_1 + \dot{y}_1\frac{d\rho_o}{dy} + \rho_o\frac{d\dot{y}_1}{dy}\right\} \quad . \tag{4.86c}$$

Assuming again that the a-c quantities vary as exp γy, Eqs. 4.85 can be reduced to algebraic equations and a determinantal equation of the third degree in γ can be found. The roots of γ will determine the growth or decay of the perturbation.

Equations 4.86 can be used in order to determine the propagation of a perturbation originating at the potential minimum for an open-circuited diode treated as an initial value problem. A similar set of equations may be obtained when the assumption of an open-circuited diode is not made. This initial value problem requires numerical values of the various fluctuations at the input plane (the potential minimum) and the selection of such values becomes quite important when some of the d-c parameters are extremely small. Another disadvantage of the initial value problem treatment is that the significance of the various waves (space-charge waves, cyclotron waves, synchronous wave, etc.) is completely lost. Thus the problem of determining the propagation of an arbitrary perturbation in the gun region is solved as an eigenvalue problem, i.e., by solving for the roots of Eq. 4.82. This is discussed in detail in Section 5.5.

In deriving Eqs. 4.82, the variations along the z-axis are neglected. This is necessary because, if these variations are also taken into account, the problem of determining the propagation of any arbitrary perturbation in the gun region becomes nonseparable. In other words when the variations along the z- and y-axes are considered simultaneously, it becomes difficult to separate the two variations in the two corresponding functional forms and in order to solve for propagation of a perturbation along the beam it is necessary to solve for γ from Eq. 4.82 for several values of γ' (defined in developing Eq. 4.87). The corresponding

determinantal equation when the variations along the z-axis only are considered is given by

$$\gamma'^5 \dot{z}_o^3 + \gamma'^4 \dot{z}_o^2 \left(\frac{d\dot{y}_o}{dy} + 3j\omega \right) + \gamma'^3 \left[\dot{z}_o \omega^2 \left(-3 + \frac{\dot{z}_o^2}{c^2} \right) + \omega_p^2 \dot{z}_o + j\omega \dot{z}_o \frac{d\dot{y}_o}{dy} \right]$$

$$+ \gamma'^2 \left[j\omega^3 \left(3 \frac{\dot{z}_o^2}{c^2} - 1 \right) + \left(\omega_p^2 - \omega^2 + \omega^2 \frac{\dot{z}_o^2}{c^2} \right) \frac{d\dot{y}_o}{dy} - \omega_p^2 \, j\omega \frac{\dot{z}_o^2}{c^2} \right]$$

$$+ \gamma' \left[3 \frac{\omega^2}{c^2} \dot{z}_o \left(\omega_p^2 - \omega^2 \right) + 2j\omega \frac{\omega^2}{c^2} \dot{z}_o \frac{d\dot{y}_o}{dy} \right]$$

$$- \frac{j\omega^5}{c^2} + \frac{\omega^2}{c^2} \frac{d\dot{y}_o}{dy} \left(\omega_p^2 - \omega^2 \right) + \left(2\omega^2 - \omega_p^2 \right) \frac{j\omega}{c^2} \omega_p^2 \quad . \quad (4.87)$$

The d-c parameters are functions of one coordinate only. This is why the terms like the variation of the d-c y-component velocity with respect to y are written as such in Eq. 4.87. The propagation constant γ is written with a prime sign so as to distinguish γ in Eq. 4.82. It may be seen that Eq. 4.87 is very similar to Eq. 4.82 and thus the nature of the roots obtained from the two equations will not be very much different. The results obtained from solving Eq. 4.82 are discussed in Section 5.5.

CHAPTER V. RESULTS OF DENSITY FUNCTION ANALYSIS

5.1 Evaluation of the Parameters V_m and y_m

Expressions for the space-charge density and the potential distribution in the potential minimum region and the gun region were developed in Sections 4.3 and 4.5 and are given by Eqs. 4.22, 4.23, 4.42 and 4.48. These expressions may be used to evaluate V_m and y_m as a boundary value problem. The two parameters are equated at $y = y_m$ as shown by the following equations:

$$V_{o2}\left(d,T,I_s,\omega_c,V_o\right) = V_{o1}\left(T,I_s,\omega_c\right) \quad \text{at} \quad y = y_m \tag{5.1a}$$

and

$$\rho_{o2}\left(T,I_s,\omega_c\right) = \rho_{o1}\left(T,I_s,\omega_c\right) \quad \text{at} \quad y = y_m \ , \tag{5.1b}$$

where V_{o2} and V_{o1} are the voltages and ρ_{o2} and ρ_{o1} are the space-charge densities in the two regions. Because of the simplification involved in developing the expressions for the space-charge density and the potential distribution, V_{o1}, ρ_{o1} and ρ_{o2} are functions of T,I_s and ω_c only while V_{o2} is a function of d,T,I_s,ω_c and V_o. In Section 4.4 a parameter A_1 in the expression for $\dot{y}_{1_c}$, the initial normal critical velocity, was introduced. The value of this parameter is to be taken such that the electrons with their initial velocities $\dot{y}_1 > \dot{y}_{1_c}$ do not experience a decelerating force corresponding to Eq. 4.32 and thus are not reflected back into the potential minimum region. Some simple calculations indicated that a value of A_1 slightly greater than 1 is sufficient for this purpose. Certainly a very large value of A_1 cannot be selected because this would mean that some of the electrons which

actually cross the potential minimum barrier are not taken into account in the gun region. For the present analysis a value of $A_1 = 1.01$ was selected and found quite reasonable. Thus an approximation given by

$$y_m A_1^2 \simeq y_m \tag{5.2}$$

was made in the operations given by Eqs. 5.1. To avoid a singularity caused by substitution for y_m from Eq. 5.2 in Eqs. 4.22 and 4.23 evaluated at $y = y_m$, Eq. 4.11 (for $A_1 = 1.01$) is substituted in Eq. 4.13 and by making use of Eq. 5.2 the following equations are obtained for Case A of Section 4.3 after simplification:

$$\rho_{o1}\Big|_{y=y_m} = -\frac{I_s}{2kT\sqrt{\pi}}\left[kT\left(\frac{2m}{\omega_c^2\, y_m^2\, A_1^2\, kT}\right)^{1/4}\Gamma(1/4) - \frac{e^{-\frac{mA_1^2}{2kT}(-2\eta V_m+\omega_c^2 y_m^2)}\sqrt{2\pi mkT}}{\sqrt{\psi(y_m)+\frac{mA_1^2}{2kT}(-2\eta V_m+\omega_c^2 y_m^2)}}\right] \tag{5.3}$$

and

$$\rho_{o2}\Big|_{y=y_m} = -\frac{I_s}{2kT\sqrt{\pi}}\;\frac{e^{-\frac{mA_1^2}{2kT}(-2\eta V_m+\omega_c^2 y_m^2)}\sqrt{2\pi mkT}}{\sqrt{\psi(y_m)+\frac{mA_1^2}{2kT}(-2\eta V_m+\omega_c^2 y_m^2)}}\,. \tag{5.4}$$

Using the boundary condition given by Eq. 5.1b and Eqs. 5.3 and 5.4, the following is obtained after simplification:

$$\frac{1}{y_m A_1^2}\left(\frac{2m}{\omega_c^2 kT}\right)^{1/2}\left[\Gamma(1/4)\right]^2\left\{(A^2-1)\left(\frac{\omega_c^2 y_m^2}{2}-\eta V_m\right)\right\}$$

$$= 2\pi\, e^{-(-2\eta V_m+\omega_c^2 y_m^2)\frac{mA_1^2}{2kT}} \quad . \qquad (5.5)$$

Equation 5.5 is one of the two equations used in evaluating y_m and V_m as a function of the other parameters. By using Eqs. 4.42, 4.48 and 5.1a, the other relation is obtained and is given below after simplification:

$$V_o = \frac{I_s}{3\epsilon_o\sqrt{\pi}}\,\Gamma(1/4)\left(\frac{2m}{kT}\right)^{1/4}\left(\frac{d^3}{\omega_{cc}}\right)^{1/2}\left[e^{-\frac{s_1'}{2}}-\left(\frac{y_m}{d}\right)^{3/2}\left(\frac{\omega_{cc}}{\omega_c}\right)^{1/2}\right.$$

$$\left.\cdot\left(1-e^{-\frac{s_1}{2}}\right)\right] , \qquad (5.6)$$

where

$$s_1 = \frac{mA_1^2}{kT}\left(-2\eta V_m+\omega_c^2 y_m^2\right) \qquad (5.7a)$$

and

$$s_1' = \frac{mA_1^2}{kT}\left(-2\eta V_m'+\omega_{cc}^2 y_m'^2\right) , \qquad (5.7b)$$

where s_1' corresponds to the value of s_1 for cutoff cyclotron frequency ω_{cc}.

Equation 5.5 may also be simplified to give

$$\omega_c y_m = s_1\, e^{s_1}\left[\Gamma(1/4)\right]^2\left(\frac{2kT}{m}\right)^{1/2}\frac{A_1^2-1}{4\pi A_1^4} \quad . \qquad (5.8)$$

By substituting for y_m from Eq. 5.8 in Eq. 5.6, the following is obtained:

$$K_1 \frac{V_o}{I_s}\left(\frac{\omega_{cc}}{d^3}\right)^{1/2} = \left[e^{-\frac{s_1'}{2}} - K_2\left(\frac{\omega_{cc}}{d^3\omega_c^4}\right)^{1/2} s_1^{3/2}\, e^{(3/2)s_1}\left(1 - e^{-\frac{s_1}{2}}\right)\right]$$

$$= f(s_1, V_o, d, \omega_c, T) \quad , \tag{5.9}$$

where

$$K_1 = \frac{3\epsilon_o \pi}{\Gamma(1/4)\left(\frac{2m}{kT}\right)^{1/4}} \tag{5.10}$$

and

$$K_2 = \left[\Gamma(1/4)\right]^3 \left(\frac{2kT}{m}\right)^{3/4} \left(\frac{A_1^2-1}{4\pi A_1^4}\right)^{3/2} \quad . \tag{5.11}$$

When $\omega_c = \omega_{cc}$ is substituted in Eq. 5.9, it is possible to determine the value of s_1'. Figure 5.1 shows the plots of the right-hand side of Eq. 5.9 versus s_1' for $\omega_c = \omega_{cc}$ for three different values of V_o. For a given value of V_o the left-hand side of Eq. 5.9 is evaluated and this determines the value of s_1' from the plots shown in Fig. 5.1. As the value of V_o is changed the value of s_1' may increase or decrease depending upon the values of the operating parameters. For large values of V_o, it can be seen from the plots shown in Fig. 5.1 that the value of s_1' is decreased. This corresponds to a decrease in the values of $|V_m|$ and y_m which is in qualitative agreement considering the fact that as the anode voltage is increased, the operation of a diode becomes less and less space-charge-limited. By making use of Eqs. 5.6 and 5.8 the values of V_m and y_m for different values of ω_c can be determined for a given set of values of V_o, d, I_s and T. The cutoff frequency ω_{cc} is given by

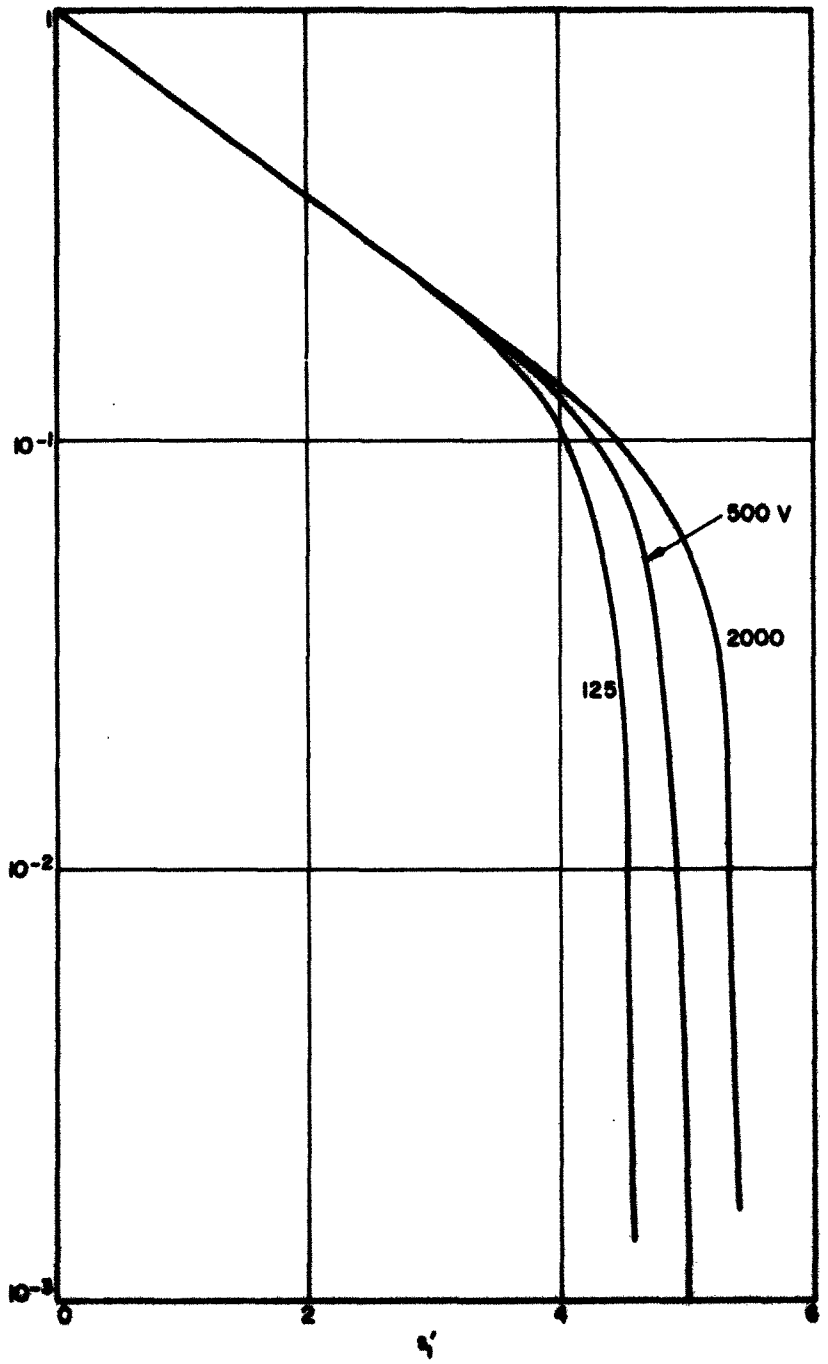

FIG. 5.1 f VS. s_1'. $(\omega_c = \omega_{cc})$

$$\omega_{cc} = \frac{\sqrt{2\eta V_o}}{d} \tag{5.12}$$

for small initial velocities.

A graph showing the variation of the normalized V_m and y_m as a function of ω_c is shown in Fig. 5.2. There are some limitations in the range of ω_c for which satisfactory values of y_m and V_m can be determined. This occurs because of the several assumptions made in simplifying the integral equations. One limitation is evident from Eq. 5.9 in which the value of the function of $f(s_1, V_o, d, \omega_c, T)$ must be positive and less than 1 because s_1 is always positive. This puts a limit on the values of V_o, I_s and d which can be selected in this problem. For values of $\omega_c > \omega_{cc}$ the value of V_m calculated as outlined above was found to be positive and those results had to be discarded because for a space-charge-limited operation V_m cannot be positive. In order to fill in the data for $\omega_c > \omega_{cc}$, a similar analysis was carried out for Case B described in Section 4.3 and efforts were made to calculate values of V_m and y_m in the same manner so that values obtained from the two cases at different values of ω_c may be matched also. However, for the given data, no value of ω_c was found for Case B for which V_m will be negative. Thus, the curves for V_m and y_m for values of $\omega_c > \omega_{cc}$ have been extended to follow the same curvature and this has been indicated by dotted lines. Also a straight-line approximation to these two curves for $\omega_c > \omega_{cc}$ has been used and this is also shown in Fig. 5.2. After having determined the values of V_m and y_m it is possible to plot V/V_m, i.e., normalized voltage given by Eq. 4.43 versus y/y_m in the potential minimum region. In Fig. 5.3 the variation of the normalized potential according to the equation

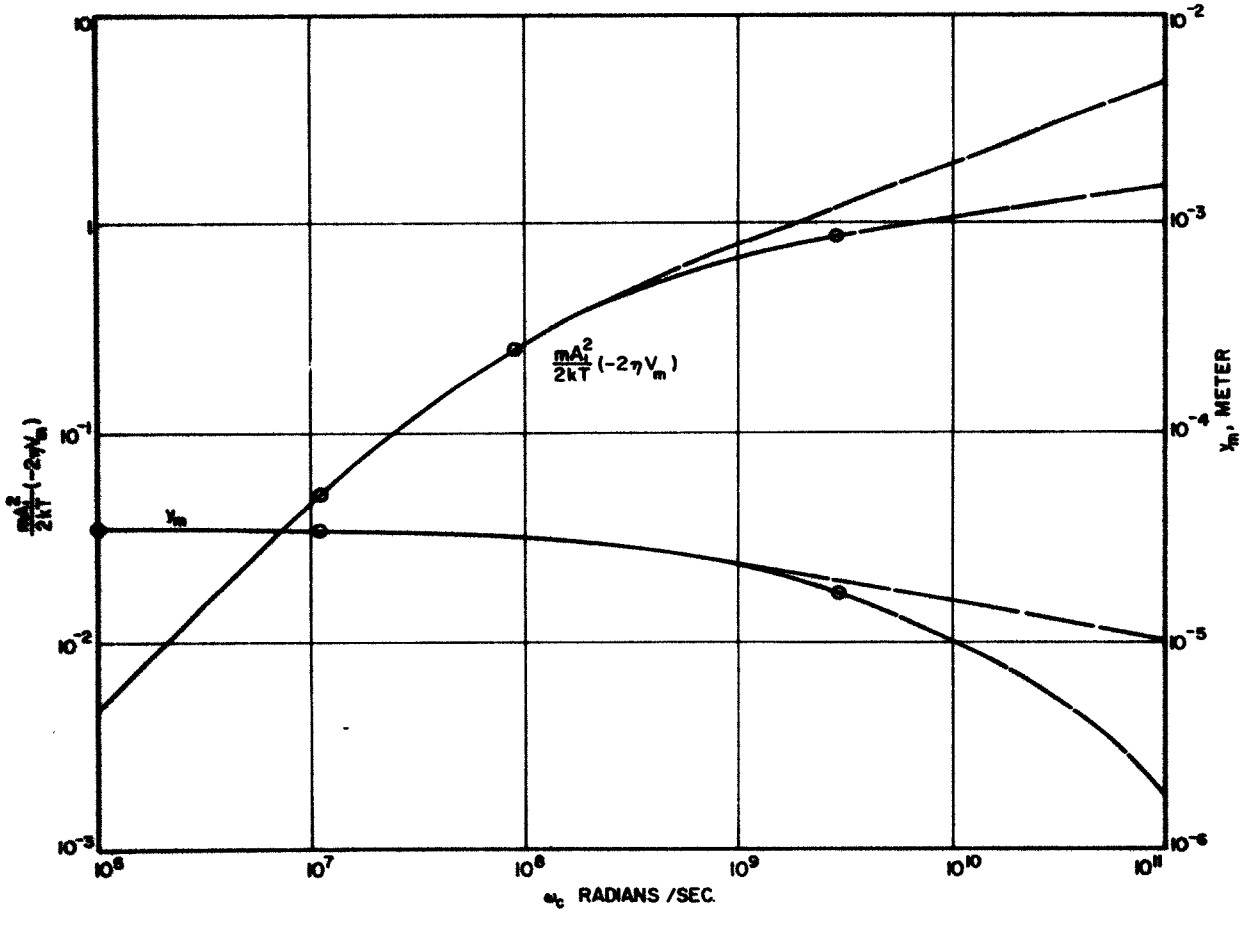

FIG. 5.2 THE VARIATION OF THE NORMALIZED V_m AND y_m AS A FUNCTION OF ω_c.

($I_s = 0.5 \times 10^4$ AMPS/m^2, T = 1000°K, $\omega_{cc} = 2.66 \times 10^9$ RAD/SEC)

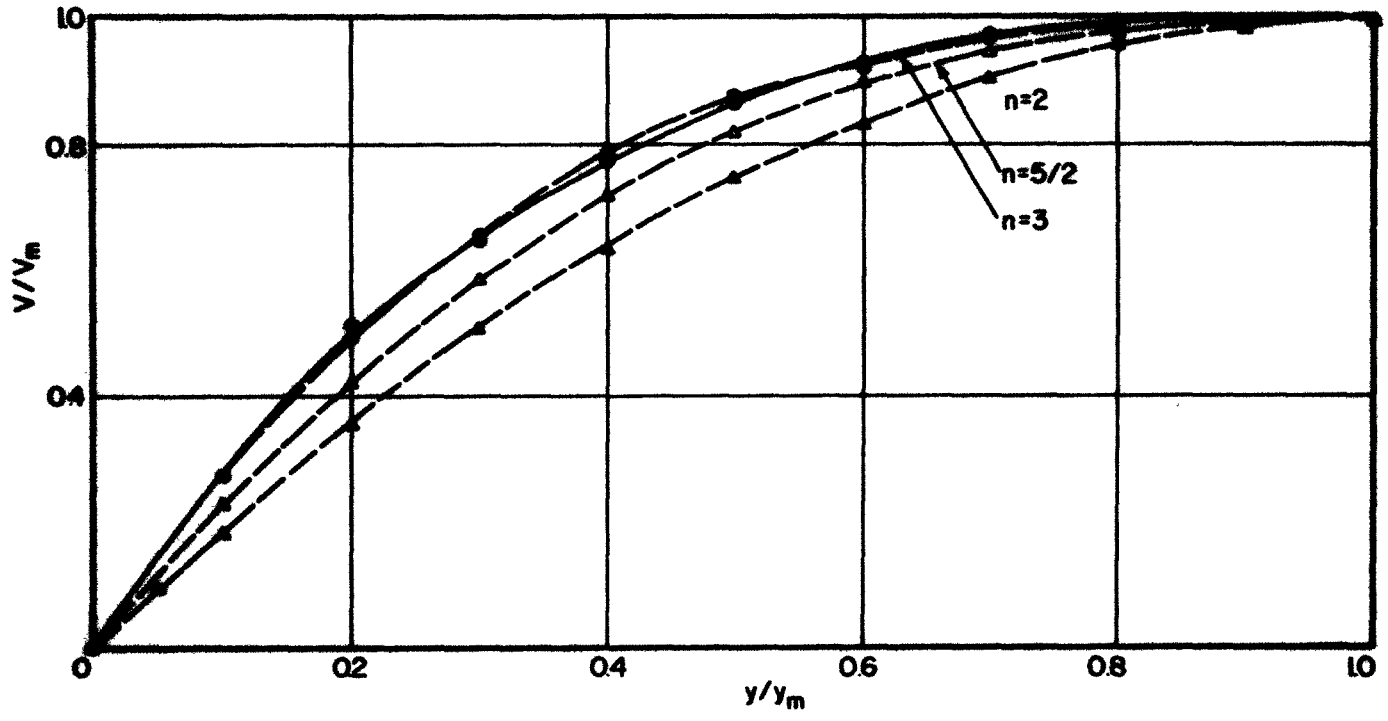

FIG. 5.3 THE NORMALIZED VOLTAGE VARIATION WITH NORMALIZED DISTANCE IN THE POTENTIAL MINIMUM REGION.

$$\frac{V}{V_m} = 1 - \left(1 - \frac{y}{y_m}\right)^n \tag{5.13}$$

for three values of n is also shown for the sake of comparison. The actual curve seems to follow variations corresponding to $n = 3$.

The variation of V_m and y_m as a function of ω_c can be explained qualitatively as follows. When the cyclotron frequency is increased, the curvature of the trajectory of a particular electron is increased. This follows from the fact that the radius of the cycloidal path of a single electron is inversely proportional to the square of the magnetic field. Thus, an electron for a given set of two velocity components travels through a shorter distance along the y-axis as the magnetic field is increased and will return to the cathode if it did not cross the potential minimum barrier. This means that as the magnetic field is increased a greater number of electrons will return to the cathode which results in more depression of the potential in the potential minimum region, thereby increasing the value of the magnitude of the potential minimum.

5.2 Normalized Current Transmitted Across the Potential Minimum

The current density is given by Eqs. 4.49, 4.52 and 4.53 for $0 \leq u < \infty$ and $-\infty < u < \infty$:

$$dI_o = \frac{4I_s}{\pi^{3/2}} e^{-(u^2+v^2)} (u^2+v^2)^{1/2} \, du \, dv \quad . \tag{5.14}$$

The total current density I transmitted across the potential minimum is given by

$$\frac{I}{I_s} \frac{\pi^{3/2}}{4} = \sum_{v=-\infty}^{\infty} \sum_{u=u_c}^{\infty} e^{-(u^2+v^2)} (u^2+v^2) \, du_i \, dv_i \quad . \tag{5.15}$$

If it is assumed that the effective cross-sectional area of the beam remains constant for a range of values of ω_c under consideration, the variation of the total current transmitted across the potential minimum (usually referred to as the cathode current) can be computed from Eq. 5.15 and these results are compared with experimental results given by Miller and Dow[27] and by Epsztein[10]. This is shown in Fig. 5.4 where I/I_o is plotted versus B/B_c for various cases mentioned below. These curves have been normalized with respect to I_o, which corresponds to the current at the cutoff value of the magnetic field. In one approximation the dependence of v upon u_c given by Eq. 4.55 was neglected and the right-hand side of Eq. 5.15 was converted into a single integral, namely

$$\frac{I}{I_s}\,\frac{\pi^{3/2}}{4} = \pi \int_{x=x_c=u_c}^{\infty} x^2\, e^{-x^2}\, dx = \frac{\pi}{2}\, x_c\, e^{-x_c^2} + \frac{\pi^{3/2}}{4}\left[1 - \mathrm{erf}(x_c)\right] . \tag{5.16}$$

This variation is shown in Fig. 5.4 by Curve A. The different values of x_c for different values of ω_c were obtained from Fig. 5.2 by using the IBM 704 computer for the same variations of V_m and y_m as used for Curve A. Curve B corresponds to the variation of V_m and y_m with ω_c obtained from the straight-line approximation shown in Fig. 5.2. It may be pointed out here that in evaluating the right-hand side of Eq. 5.15 the limits for the variables u and $|v|$ were kept at 5 to give a reasonable accuracy.

Curves D and E correspond to experimental data by Miller-Dow[27] and Epsztein[10] respectively. The difference in the two sets of experimental data seems to reflect the significance of the geometrical factors, the operating parameters such as I, V_o, and the type of cathode used.

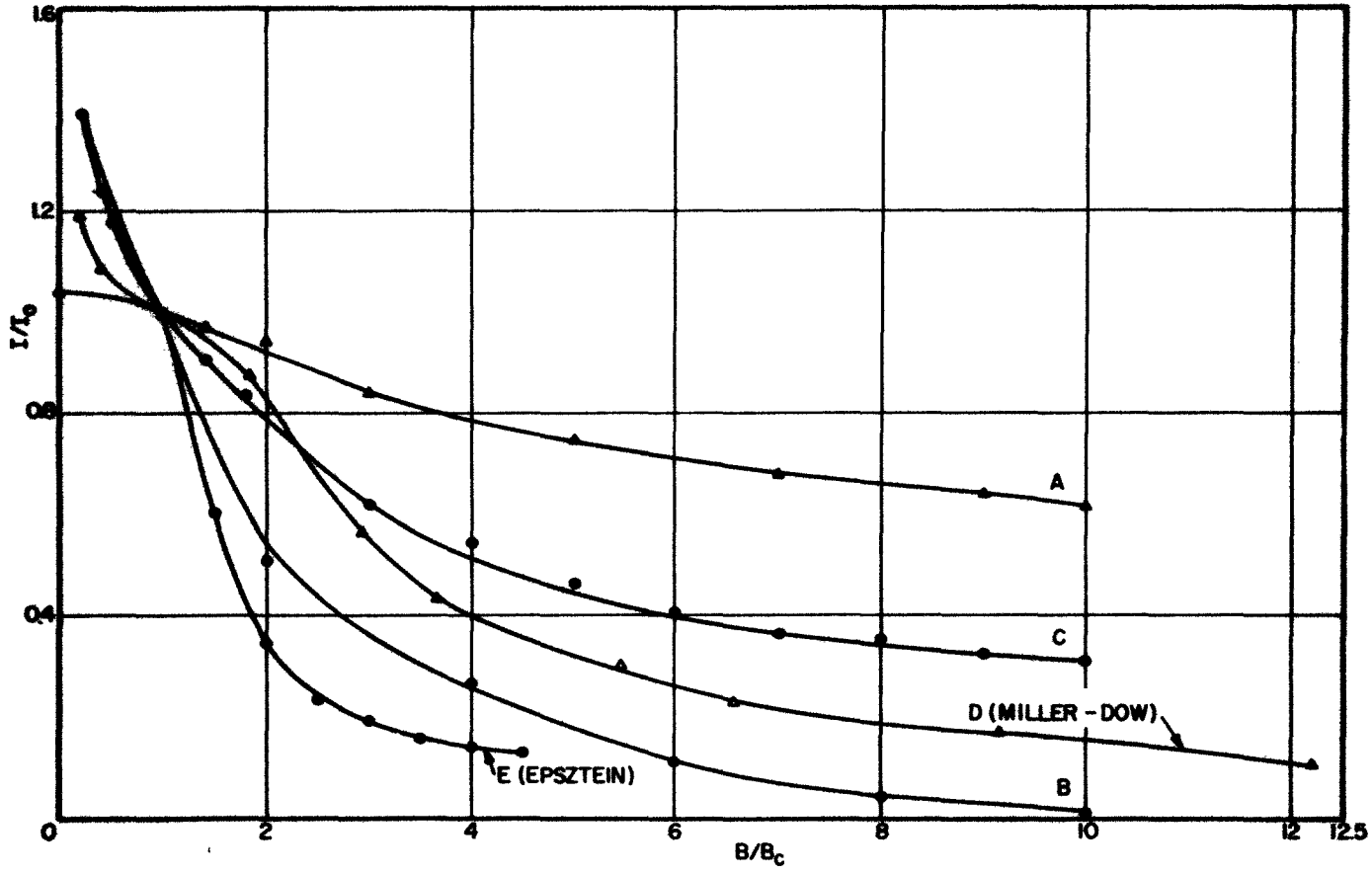

FIG. 5.4 I/I_o VS. B/B_c. (ALL CURVES ARE NORMALIZED WITH RESPECT TO I_o, THE CURRENT AT THE CUTOFF VALUE OF THE MAGNETIC FIELD)

This also indicates that if all these factors were taken into account and equations similar to Eqs. 5.6 and 5.8 were obtained without any approximation, the resulting curves for V_m and y_m would be very close to the two curves shown in Fig. 5.2. It is interesting to note that in spite of the several approximations made in developing this analysis and that the solution is also limited by the proper selection of the parameters V_o, d and I_s the results seem to give a fair agreement between the theoretical and experimental results.

5.3 Evaluation of Space-Charge Density and Other Related Functions

In the last chapter equations of ρ_o and dV/dy were developed in an integral form. These integrals are evaluated by numerical methods and for this purpose Eqs. 4.54 and 4.57 are rewritten as

$$\rho_o = -2I_s\left(\frac{2m}{\pi^3 kT}\right)^{1/2} \sum_{v=-\infty}^{\infty} \sum_{u=u_c}^{\infty} \frac{e^{-(u^2+v^2)}(u^2+v^2)^{1/2}}{\left(u^2+v^2+\frac{|e|V}{kT}\right)^{1/2}} du_i\, dv_i \qquad (5.17)$$

and

$$\frac{dV}{dy} = \left[\frac{8I_s}{\epsilon_o \pi}\,\frac{kT}{|e|}\left(\frac{2m}{\pi kT}\right)^{1/2}\right]^{1/2} \left\{ \sum_{v=-\infty}^{\infty} \sum_{u=u_c}^{\infty} e^{-(u^2+v^2)}\,(u^2+v^2)^{1/2} \cdot \left(u^2+v^2+\frac{|e|V}{kT}\right)^{1/2} du_i\, dv_i - D_m \right\}^{1/2} , \qquad (5.18)$$

where

$$D_m = \sum_{v=-\infty}^{\infty} \sum_{u=u_c}^{\infty} e^{-(u^2+v^2)}\,(u^2+v^2)^{1/2}\left(u^2+v^2+\frac{|e|V_m}{kT}\right)^{1/2} du_i\, dv_i \; . \qquad (5.19)$$

In evaluating the double summations in Eqs. 5.17 through 5.19 by the use of an IBM 709 computer it is necessary to restrict the values of the two variables u and v within a reasonable range to give a good compromise between computer time and accuracy. Fortunately in these summations there is an exponentially decreasing term and the exponent varies as the sum of the squares of the two variables. For this reason it was noticed in the evaluation of Eq. 5.15 that the range of the two variables may be limited according to

$$-5 < v < 5$$

and

$$0 < u < 5 \tag{5.20}$$

and increments in u and v by 0.05 seemed to give a reasonable compromise between the computer time and accuracy.

For evaluating ρ_o from Eq. 5.17 it is necessary to determine V first from Eq. 5.18. For this purpose the diode was divided into several rectangles distributed along the y-axis and infinitely extended along the z and x axes, and the y-coordinates of these rectangles are taken as y_o, y_1, y_2 ... y_j ... with y_o being that for the potential minimum. With a certain potential distribution assumed as a first approximation, the value of dV/dy at $y = y_1$ can be evaluated with the use of Eq. 5.18 for a given set of values of V_m, y_m and ω_c. With this value of dV/dy at y_1 a new value of V at y_1 can be computed by the relation

$$V_{j+1} - V_j = \left[\left(\frac{dV}{dy}\right)_{y_{j+1}} + \left(\frac{dV}{dy}\right)_{y_j} \right] \frac{y_{j+1} - y_j}{2} , \tag{5.21}$$

where j = 0 corresponds to the potential minimum and $(dV/dy)_{y_o} = 0$. From this new value of V_1, dV/dy at $y = y_1$ can again be computed and then a

new value of V_1 is computed as before. This method of iteration is found to be very slow and for this purpose it was decided to compute dV/dy from Eq. 5.18 for a given value of V and then determine the corresponding value of y from Eq. 5.21 rewritten as

$$y_{j+1} - y_j = \Delta y_j = \frac{2\left[V(y_{j+1}) - V(y_j)\right]}{\left(\frac{dV}{dy}\right)_{y_{j+1}} + \left(\frac{dV}{dy}\right)_{y_j}} . \qquad (5.22)$$

This procedure corresponds to selecting an arbitrary value of V and then correlating a value of y with this voltage. Therefore it is not necessary to make any first approximation for the voltage distribution and then worry about the convergence of the iteration process. This process involves less computer time and the error involved will be less if the value of ΔV measured in terms of percentage increases in the voltage from one position to the next is taken as small.

In evaluating ρ_o and dV/dy from Eqs. 5.17 and 5.18 in the manner described above it is necessary to check the minimum value of the term G involved in the expression for D_m given by Eq. 5.19. G is defined as

$$G = u^2 + v^2 + \frac{|e|V_m}{kT} \qquad u^2 \geq u_c^2 \geq 0$$

$$= v^2 + \frac{|e|V_m}{kT} \qquad u_c^2 \leq 0 . \qquad (5.23)$$

It is necessary to consider the value of G_{min} so that the evaluation of the square root of G does not lead to any computer problem, i.e., G does not become negative for the values of ω_c, y_m and V_m selected in evaluating Eqs. 5.17 and 5.18. By substituting for u_c^2 from Eq. 4.55 the minimum value of G is found to be

$$G_{min} = \frac{m}{2kT}\left[-(A_1^2-1)\,2\eta V_m + A_1^2\,\omega_c^2 y_m^2 + 2A_1\,\omega_c y_m\,\sqrt{\frac{2kT}{m}}\,v + \frac{2kT}{m}\,v^2\right]$$

$$\text{for} \quad u_c^2 \geq 0 \qquad (5.24a)$$

and

$$G_{min} = v^2 + \frac{|e|V_m}{kT} \quad \text{for} \quad u_c^2 \leq 0 \ . \qquad (5.24b)$$

The value of v for which $u_c^2 = 0$ is found to be equal to -1.47 for the parameters

$$\omega_c = 5 \times 10^9 \text{ rad/sec} \ ,$$

$$V_m = -0.104 \text{ volts} \ ,$$

$$y_m = 0.172 \times 10^{-4} \text{ m}$$

and

$$T = 1000° \text{ K} \ . \qquad (5.25)$$

Under these conditions G_{min} for $u_c^2 \leq 0$ is always positive. For values of $u_c^2 \geq 0$, the value of $G_{min} = 0.022$, which occurs at $v = -0.5$, and a plot of G_{min} versus v is shown in Fig. 5.5. In the gun region $V \geq V_m$ and it is concluded from this that there is no problem in evaluating the square roots of the functions in Eqs. 5.17 and 5.18. It also indicates a reasonable set of values of V_m and y_m selected in this problem.

After various values of V are correlated with corresponding values of y, it is possible to determine the two velocity components at these values and also determine the time taken to move from one position to the next. The values of $\dot{z}_o$ and $\dot{y}_o$ are given by Eqs. 4.60 and 4.61 respectively. The trajectories can then be determined from the following equations:

$$(\Delta t)_j = 2\,\frac{y_{j+1} - y_j}{\dot{y}_{o_{j+1}} + \dot{y}_{o_j}} \qquad (5.26)$$

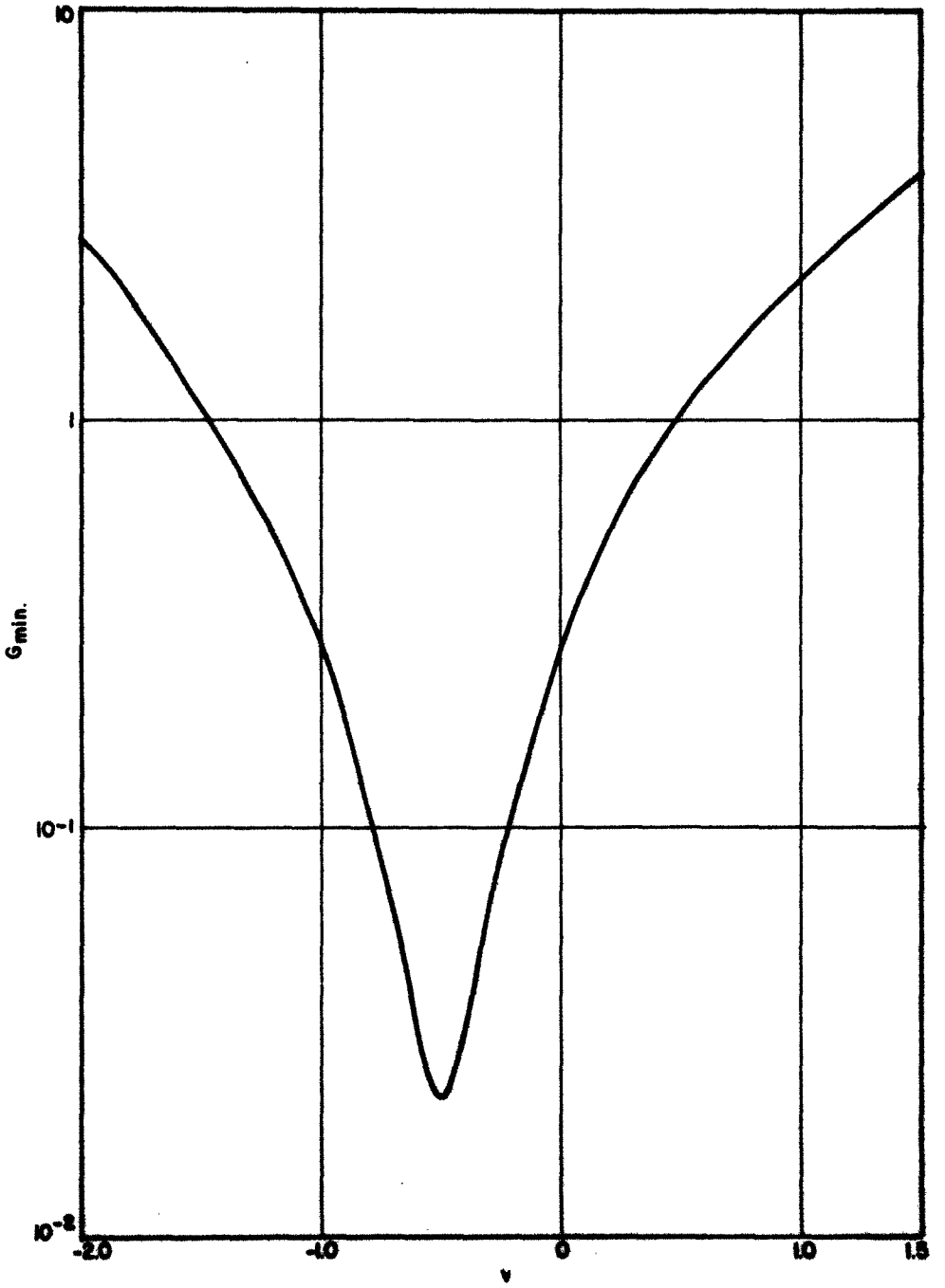

FIG. 5.5 $G_{min.}$ VS. v.

and

$$z_{j+1} - z_j = \left(\dot{z}_{o_{j+1}} + \dot{z}_{o_j}\right)\frac{(\Delta t)_j}{2} \quad , \tag{5.27}$$

where $(\Delta t)_j$ represents the time taken to move from y_j to y_{j+1} and is computed from Eq. 5.26. Once the value of $(\Delta t)_j$ is computed the corresponding change in the z-coordinate during the time interval $(\Delta t)_j$ is determined by Eq. 5.27. In this manner it is possible to plot trajectories, i.e., the y and z positions as a function of time.

The values of $\bar{\dot{y}}_i$ and $\bar{\dot{z}}_i$ are determined from Eqs. 4.62 and 4.63 respectively and are written in summation form as

$$\bar{\dot{y}}_i = \frac{1}{I_n}\sqrt{\frac{\pi kT}{2m}}\, e^{-\frac{mA_i^2}{2kT}\left[-2\eta V_m\,(A_i-1)\,\omega_c^2 y_m^2\right]} \tag{5.28}$$

and

$$\bar{\dot{z}}_i = \frac{1}{I_n}\sqrt{\frac{2kT}{m}} \sum_{v=-\infty}^{\infty} \sum_{u=u_c}^{\infty} v\, e^{-(u^2+v^2)}\, du_i\, dv_i \quad , \tag{5.29}$$

where

$$I_n = \sum_{v=-\infty}^{\infty} \sum_{u=u_c}^{\infty} e^{-(u^2+v^2)}\, du_i\, dv_i \quad . \tag{5.30}$$

The range for the variables u and v is given by Eqs. 5.20 and as mentioned above the increments in du and dv are taken as 0.05 each.

The variation of the two current densities J_y and J_z at the corresponding values of y and z are determined by the following relations:

$$J_y(y_j) = \rho_o(y_j) \cdot \dot{y}_o(y_j) \tag{5.31}$$

and

$$J_z(y_j) = \rho_o(y_j) \cdot \dot{z}_o(y_j) \quad . \tag{5.32}$$

The coordinate z_j is not included in the above two equations because once y_j is determined, z_j is automatically determined by Eq. 5.27, thus y_j (actually V, in the manner in which Eqs. 5.17 and 5.18 are evaluated) is the only independent variable.

For conditions given by Eq. 4.65, Eq. 4.66 is written as

$$\frac{dV}{dy} = \left[\frac{8I_s}{\epsilon_o \pi} \left(\frac{2m}{\pi |e|}\right)^{1/2} \right]^{1/2} V^{1/4} \left[\sum_{-\infty}^{\infty} \sum_{u_c}^{\infty} e^{-(u^2+v^2)} (u^2+v^2)^{1/2} \cdot du_i \, dv_i \right]^{1/2} \quad . \tag{5.33}$$

Equation 5.33 is integrated to give

$$(V)^{3/4} = \frac{3}{4} K_1 (y-y_1) + V_1^{3/4} \quad \text{for} \quad y \geq y_1 \quad , \tag{5.34}$$

where the voltage V_1 corresponds to the position $y = y_1$ and K_1 is given by

$$K_1 = \left[\frac{8I_s}{\epsilon_o \pi} \left(\frac{2m}{\pi |e|}\right)^{1/2} \right]^{1/2} \left[\sum_{-\infty}^{\infty} \sum_{u_c}^{\infty} e^{-(u^2+v^2)} (u^2+v^2)^{1/2} du_i \, dv_i \right]^{1/2} \quad . \tag{5.35}$$

Similarly ρ_o, the space-charge density, is given by

$$\rho_o = -2I_s \left(\frac{2m}{\pi^3 |e|}\right)^{1/2} V^{-1/2} \sum_{-\infty}^{\infty} \sum_{u_c}^{\infty} e^{-(u^2+v^2)} (u^2+v^2)^{1/2} \cdot du_i \, dv_i \quad \text{for} \quad y \geq y_1 \quad . \tag{5.36}$$

The double summation on the right-hand side of Eq. 5.36 is made once for a given set of values of ω_c, y_m and V_m, and the evaluation of the d-c parameters for $y \geq y_1$ becomes very convenient.

5.4 Numerical Results for the D-c Parameters

Once the values of ω_c, y_m and V_m are determined, it is possible to determine the potential distribution in the diode from Eqs. 5.18 and 5.33 by numerical methods. It is mentioned in Section 5.3 that dV/dy is evaluated from Eq. 5.18 for a given value of V and then Eq. 5.22 is used to evaluate the corresponding value of Δy. In the negative potential region Eq. 5.18 is evaluated for V increasing in steps of $|V_m|/2$. In the positive potential region the value of ΔV is taken as equal to 0.5 volt for small values of V and for larger values the value of ΔV is increased to as large as 30 volts.

The potential distribution thus evaluated is shown in Fig. 5.6 for small values of voltages where the potential minimum may be seen distinctively. Figure 5.7 gives the potential distribution for large values of V where the potential minimum is not as evident as in Fig. 5.6 because of a difference in scale. It is also noted that for larger values of ω_c the beam bends over rapidly. Since the potential is determined along the beam, the evaluation of the potential distribution is limited to small values of y for large values of ω_c. For this reason the potential distribution is determined in the diode for two values of ω_c, namely $\omega_{c1} = 1 \times 10^9$ rad/sec and $\omega_{c2} = 5 \times 10^9$ rad/sec.

It may be seen from Fig. 5.6 that in the common range of the values of y there is little difference in the potential distribution for the two cases outlined above except that the potential at a point y_1 for the case of the larger value of ω_c is slightly greater than that for the

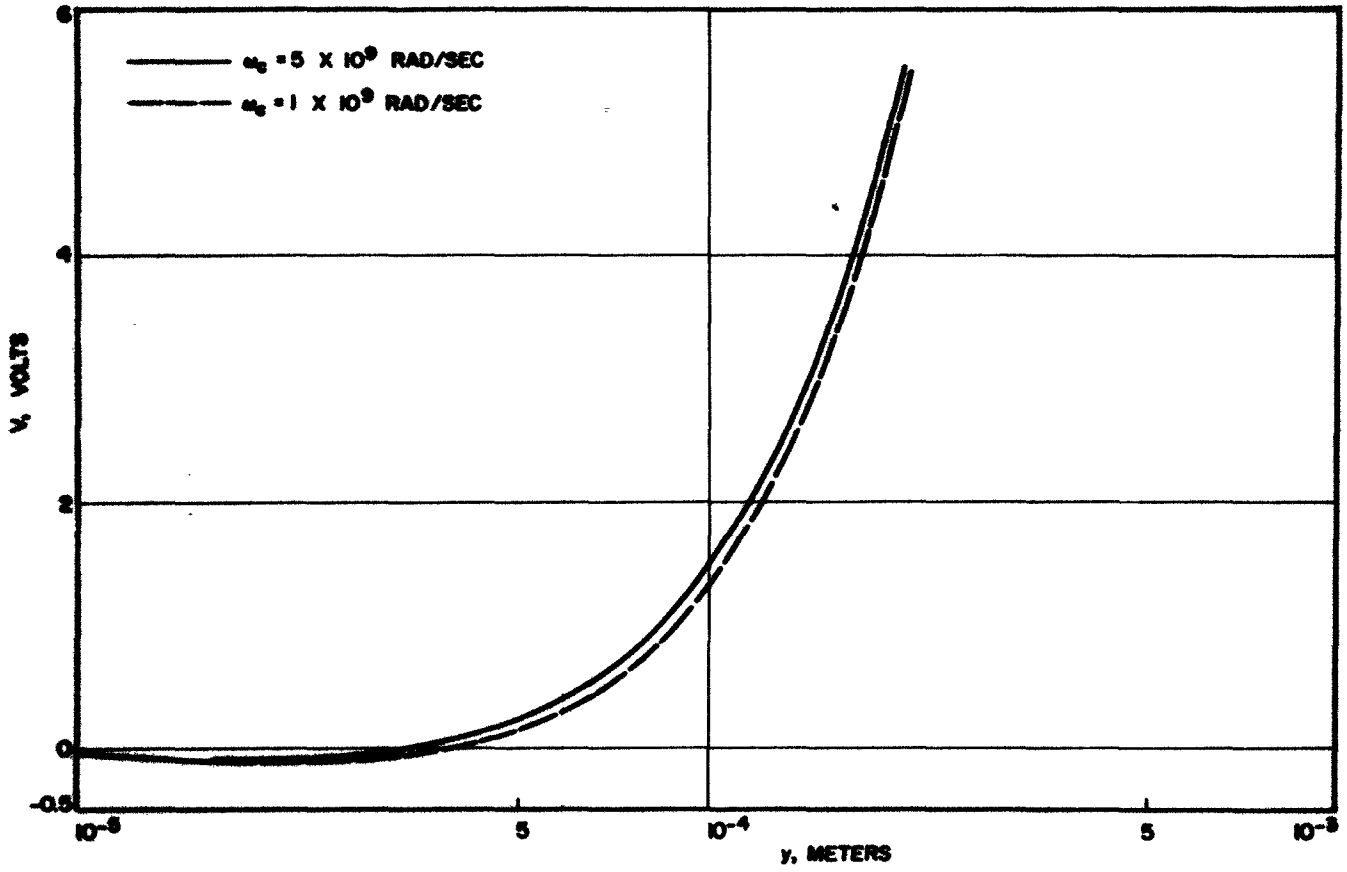

FIG. 5.6 VOLTAGE DISTRIBUTION ALONG THE y-AXIS.

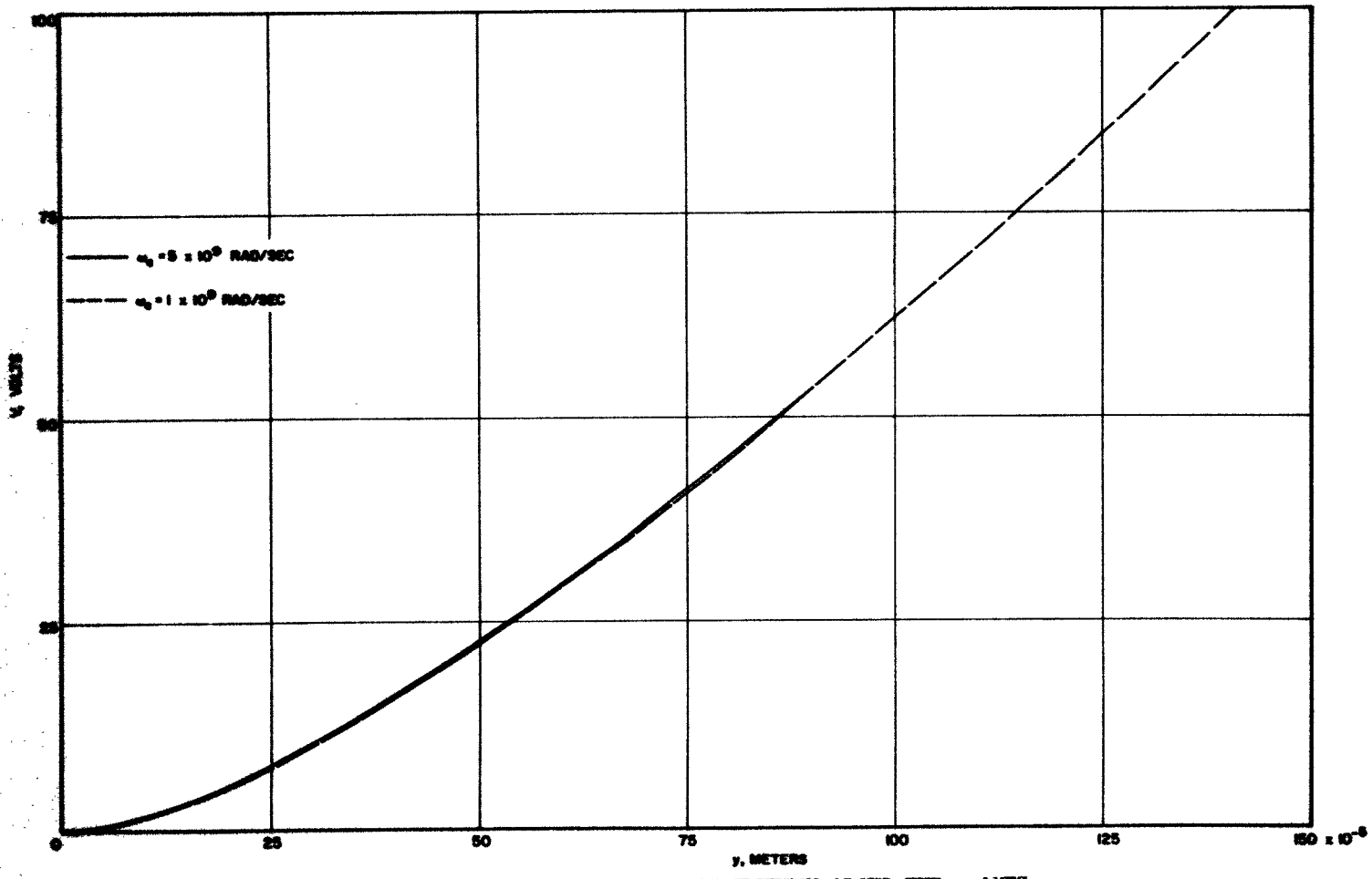

FIG. 5.7 VOLTAGE DISTRIBUTION ALONG THE y-AXIS.

case of the smaller value of ω_c. This may be qualitatively explained in terms of less space-charge depression in voltage because of the less emitted current for the case of the larger value of ω_c. Figure 5.8 shows the space-charge density evaluated from Eqs. 5.17 and 5.36 for two values of ω_c. It may be seen that because of less emitted current for the case of the larger value of ω_c, the value of the space-charge density is less than that for the case of the smaller value of ω_c.

The velocity components $\dot{z}_o$ and $\dot{y}_o$ are evaluated from Eqs. 4.37 and 4.39 which are rewritten as

$$(\dot{z}_o)_j = \omega_c y_j + \dot{z}_i \tag{5.37}$$

and

$$(\dot{y}_o)_j = \left[2\,\eta\,V_j + \bar{\dot{y}}_i^2 - \omega_c^2 y_j^2 - 2\,\omega_c y_j\,\bar{\dot{z}}_i\right]^{1/2} . \tag{5.38}$$

Thus the two velocity components may be evaluated from the above equations in terms of y_j. Figure 5.9 shows the plots of the two velocity components for the two values of ω_c as a function of $\omega_c T$. The parameter T refers to the transit time from the potential minimum to the point (y_j, z_j) along the beam in the y-z plane. This is done in order to compare the results with those obtained from the Kino gun model[15]. The variation of the velocity components, such as $1/\omega_c^2$ for a fixed large value of $\omega_c T$, may easily be seen. For small values of $\omega_c T$ the effect of the initial velocities is significant. It is interesting to note that $\dot{y}$ is a maximum at $\omega_c T \simeq 3.1$ while the corresponding value of $\omega_c T$ for the Kino gun model is equal to π when the initial velocities are neglected. According to the Kino gun model the ratio $(\dot{z}/\dot{y})_{\dot{y}=max} = \pi/2$ and the corresponding ratio in this case is equal to 1.5. Figure 5.10

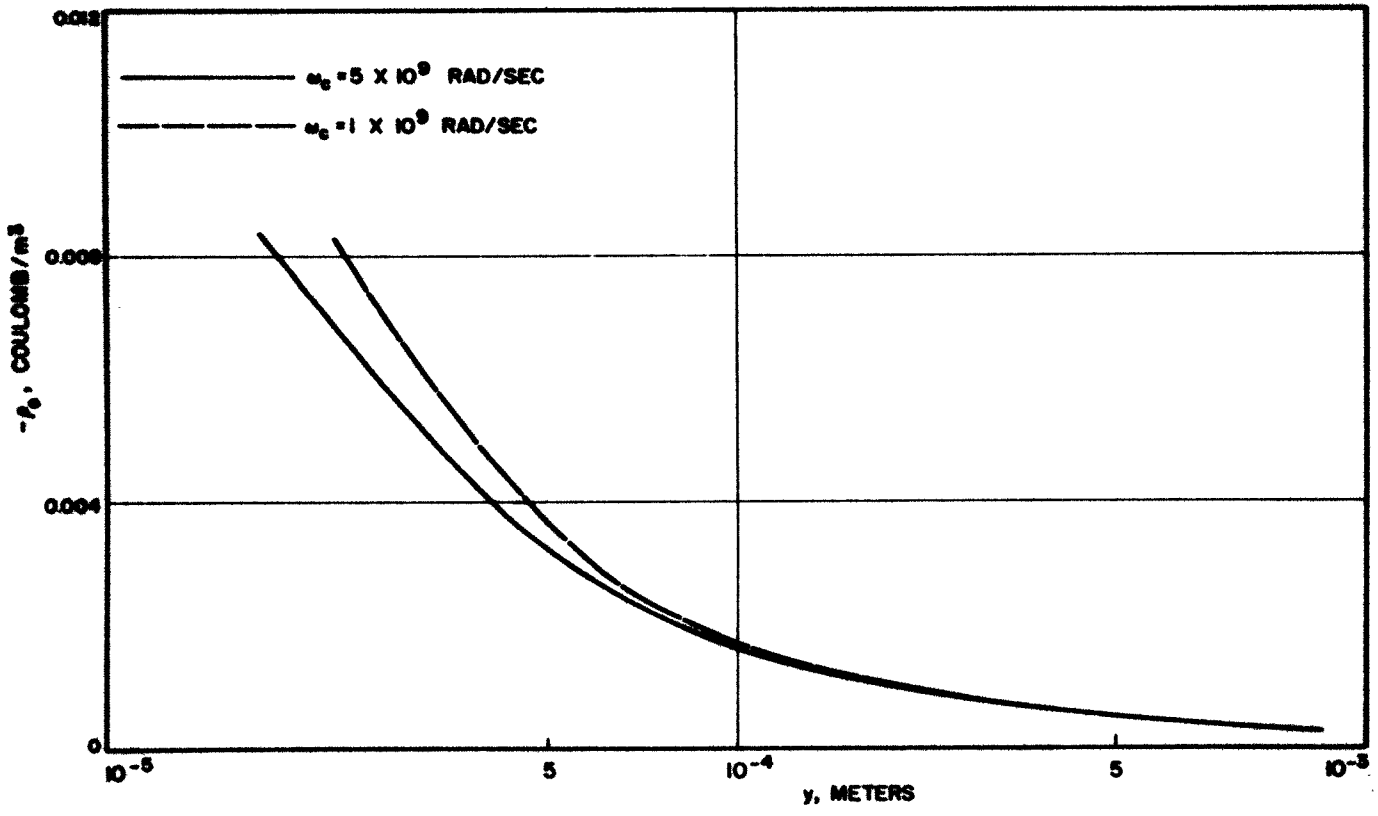

FIG. 5.8 SPACE-CHARGE DENSITY VS. y.

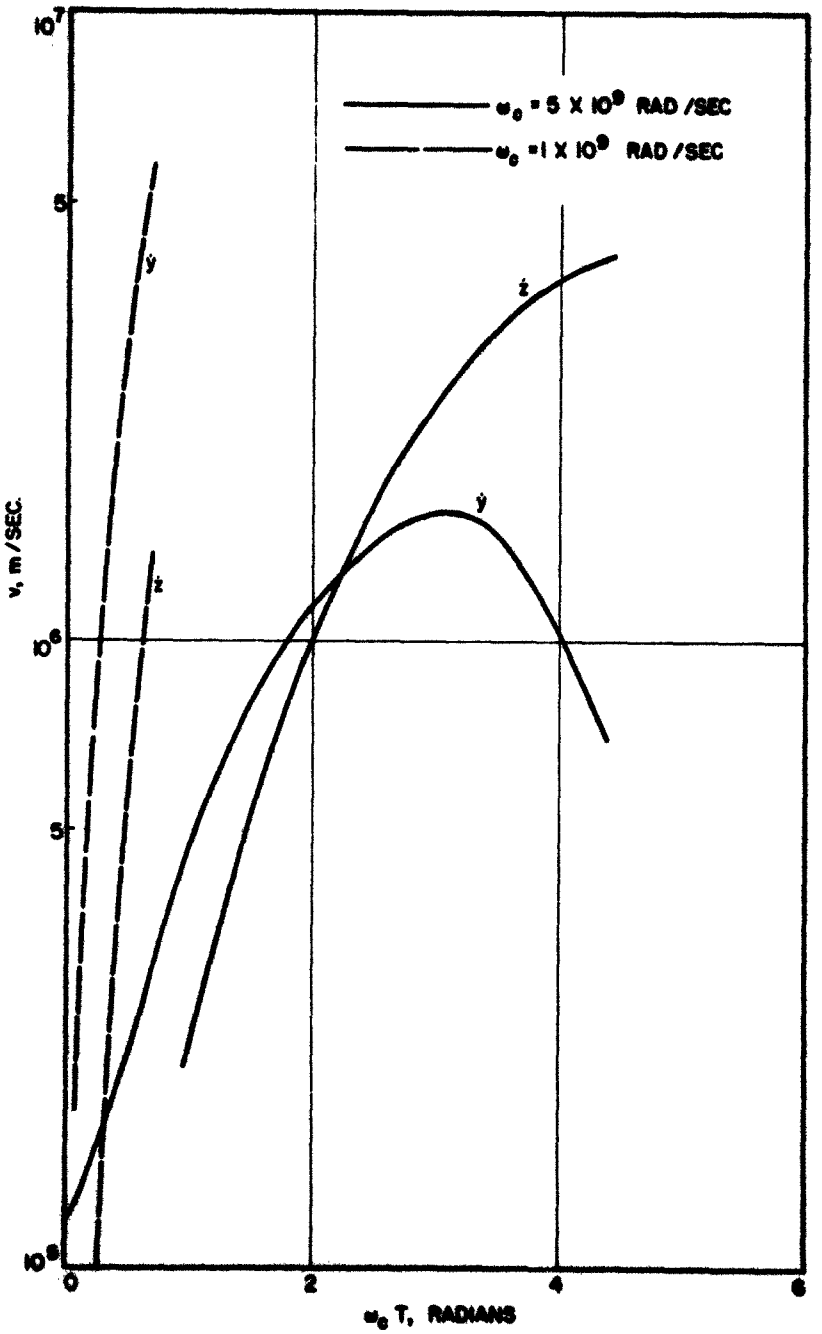

FIG. 5.9 VELOCITY COMPONENTS VS. $\omega_c T$.

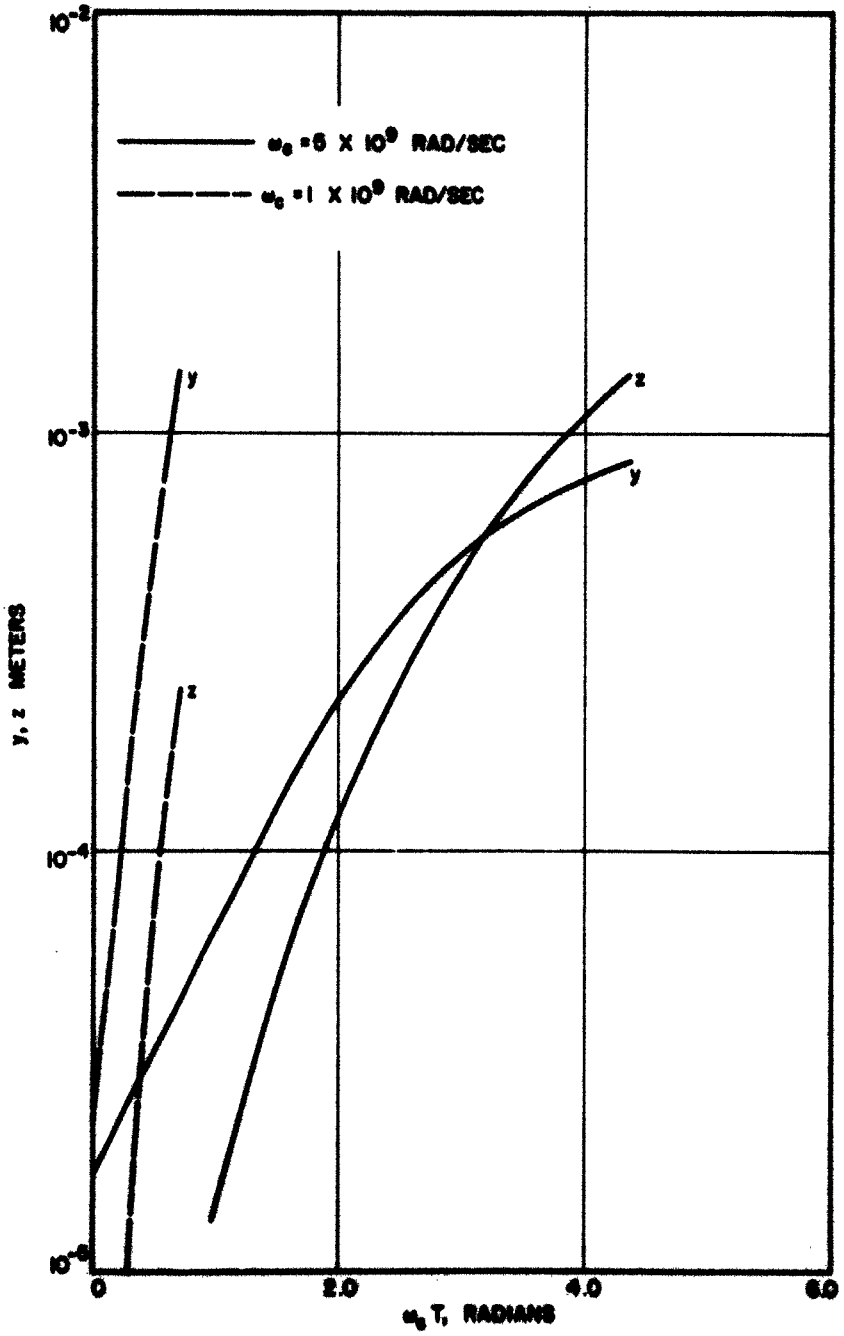

FIG. 5.10 TRAJECTORIES VS. $\omega_c T$.

presents the trajectory plots for the two values of ω_c as a function of $\omega_c T$. The variation of the trajectories y and z as $1/\omega_c^3$ for a fixed large value of $\omega_c T$ may easily be seen. These results show a very close agreement with those obtained from the Kino gun model but it should be pointed out here that these calculations give the accurate values of $\dot{y}$, $\dot{z}$, y and z in terms of the saturation current density. To obtain these results it is not necessary to assume that the y-component of the current density is constant as is assumed in the case of the Kino gun model.

Figure 5.11 shows the plots for the current density components versus y as evaluated from Eqs. 5.31 and 5.32 for two values of ω_c. It is interesting to note that the y-component of the current density does not remain constant along the beam as assumed in the Kino gun model. It can be seen that this assumption is justified for small values of ω_c only.

The various plots for the d-c parameters are referred to as two different values of the cyclotron frequency instead of in terms of the cutoff cyclotron frequency. This is due to the fact that the results are obtained as an initial value problem and this does not give the potential at the anode. However this initial value problem when solved for very small values of the cyclotron frequency would increase the range of the values of y for which the potential distribution is known. The potential distribution curve for the case of $\omega_c = 1 \times 10^9$ rad/sec was extended to a point $y = 5 \times 10^{-3}$ m and the corresponding value of V at $y = d = 5 \times 10^{-3}$ m was found to be very close to 500 volts which is approximately the same as assumed in the original calculations for determining V_m and y_m. This gives the value of the cutoff cyclotron frequency as 2.6×10^9 rad/sec. These calculations give fairly accurate values of ω_{cc} but since this is an approximate method the magnetic fields

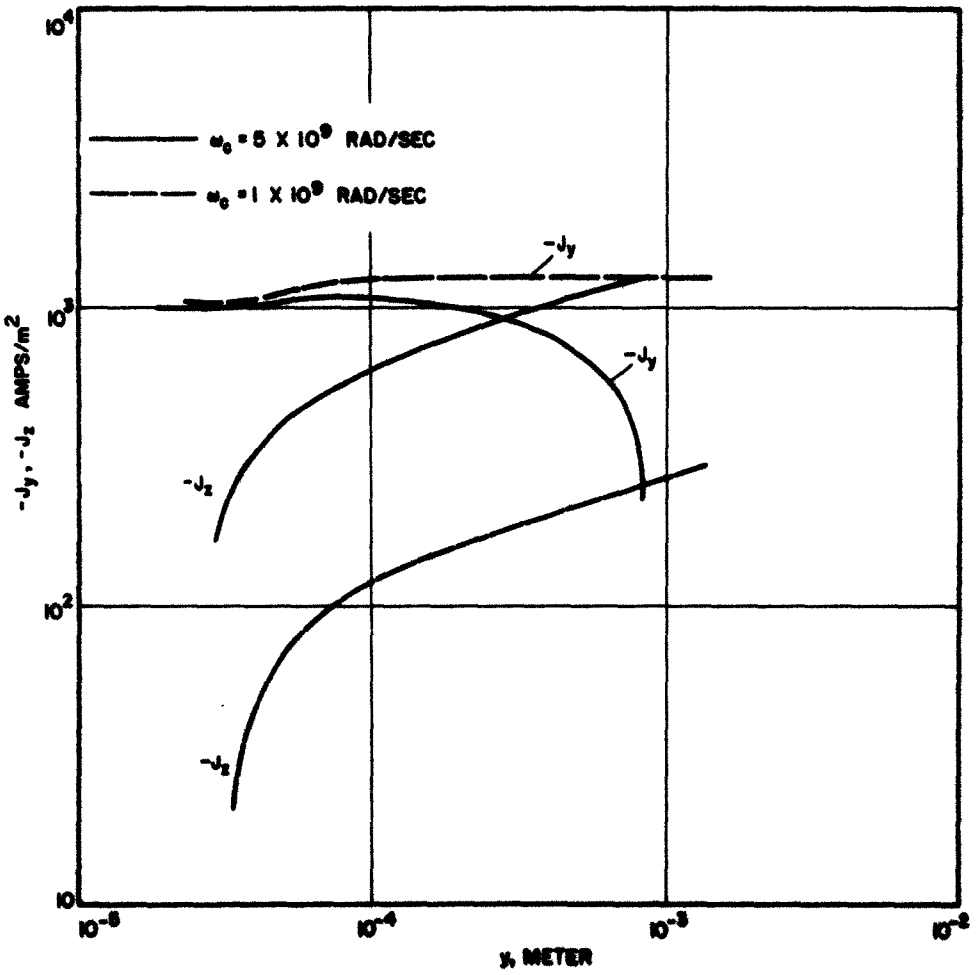

FIG. 5.11 CURRENT DENSITY COMPONENTS VS. y.

as indicated in Figs. 5.6 through 5.11 are given as absolute values rather than as relative values.

5.5 Evaluation of Noise Transport in the Gun Region

In order to evaluate the noise transport in the gun region, the problem may be treated either as an initial value problem or an eigenvalue problem. The two possibilities are discussed in Section 4.7. Because of the continuous variation of the d-c parameters in the gun region it becomes necessary to solve this problem at several points (y_j, z_j) for which the d-c parameters have been evaluated as mentioned in an earlier section. This is true whether the noise transport is evaluated as an initial value problem or an eigenvalue problem. However the solution of the eigenvalue problem is advantageous because it is not necessary to consider the exact values of the various parameters as discussed in Section 4.7. For this reason the propagation constants γ's are evaluated by evaluating the roots of Eq. 4.82 at several points (y_j, z_j) along the beam in the y-z plane. Since the d-c parameters are continuously varying along the beam, the problem of evaluating the propagation constants which are continuously varying along the beam is a nonlinear one. However the problem is linearized when the propagation constants are evaluated at several locations of the beam by considering the corresponding values of the d-c parameters.

It may be pointed out here that the imaginary parts of the propagation constants γ can lead to amplification of a signal of an angular frequency ω at some point (y_j, z_j) due to a beating-wave phenomenon. It is anticipated that the large noise output in crossed-field devices cannot be explained from this beating-wave phenomenon due to its low

gain. It can be noticed that the roots of Eq. 4.82 would correspond to five different waves. In order to show more explicitly the variations of the roots as a function of y, the roots are divided into two groups. Figure 5.12 shows the plots of α_1 and $-\alpha_2$ ($\gamma = \alpha + j\beta$) as a function of y for four values of the perturbation frequency ω. The value of $R \triangleq \omega_c/\omega = 2.6$ in Fig. 5.12 corresponds to ω = the plasma frequency at the potential minimum. The two waves correspond to one amplifying wave and the other attenuating wave. The positive values of α indicate the growth mechanism and this mechanism may be considered as an equivalent diocotron gain in the gun region. The expression for diocotron gain as evaluated by Gould[16] for the interaction region is given by

$$h = \frac{\omega_p^2}{2\,\omega_c\,u_o}\left(\frac{\omega t}{u_o}\right) , \tag{5.39}$$

where ω_p = plasma frequency, u_o = d-c z-component velocity and t = thickness of the beam along the y-axis, and is considered small. It can be seen that there is a qualitative agreement between the results for α for a given value of R as shown in Fig. 5.12 with the corresponding value of h obtained from Eq. 5.39. It may be pointed out here that the values of α as plotted in Fig. 5.12 are obtained without considering the velocity slipping stream. Figure 5.13 shows the plots of β_1 and β_2 versus y for four different values of R. It is noticed that, except for R = 2.6, the values of β_1 and β_2 are positive for small values of y and these waves correspond to backward waves, with small values of the propagation constants. These results are analogous to the results obtained from the transmission-line analogy of crossed-field beams[25] and correspond to small values of ω/ω_p. As the value of y is increased (or ω/ω_p is increased) the values of α_1 and $-\alpha_2$ decrease and the two

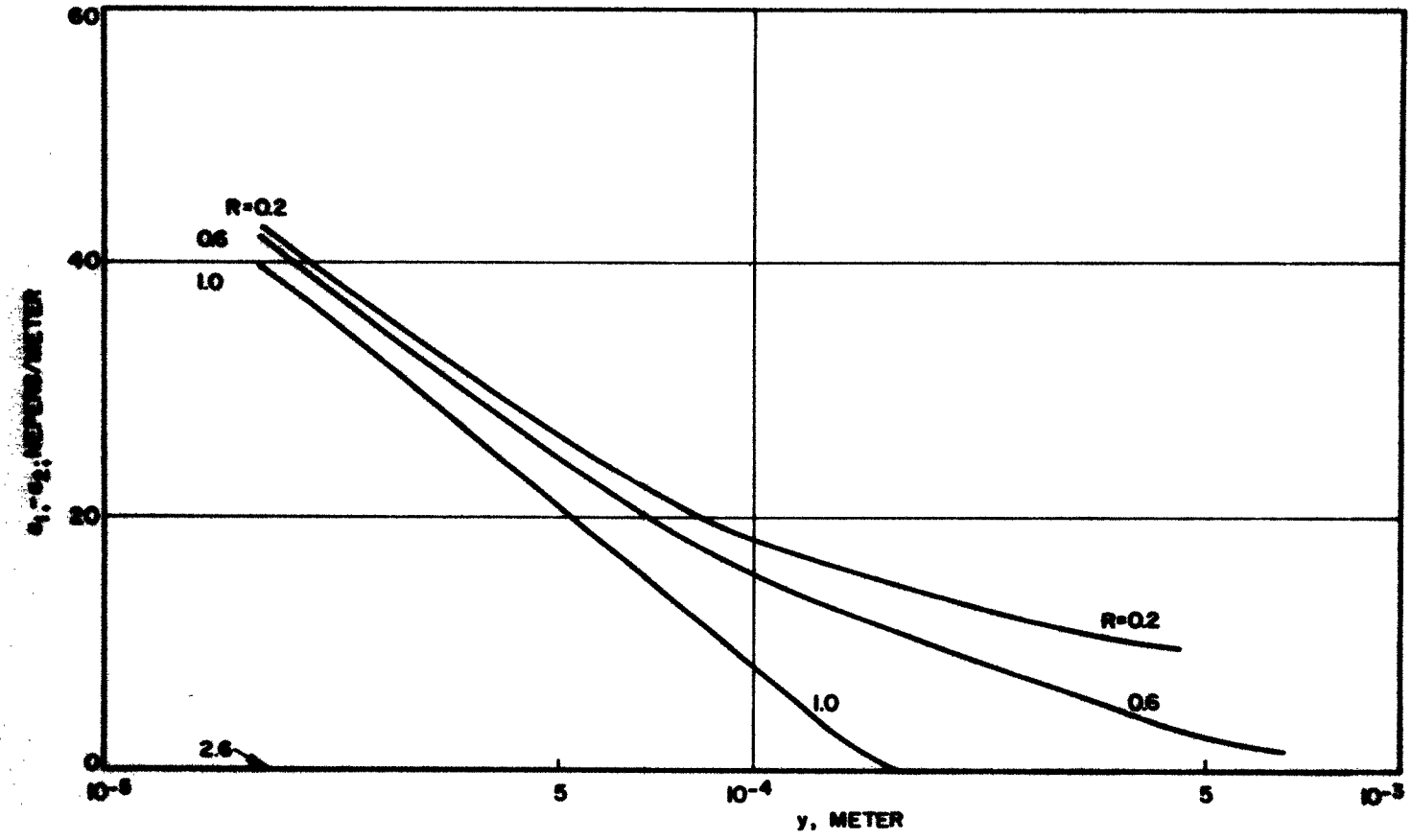

FIG. 5.12 α_1 AND $-\alpha_2$ VS. y.

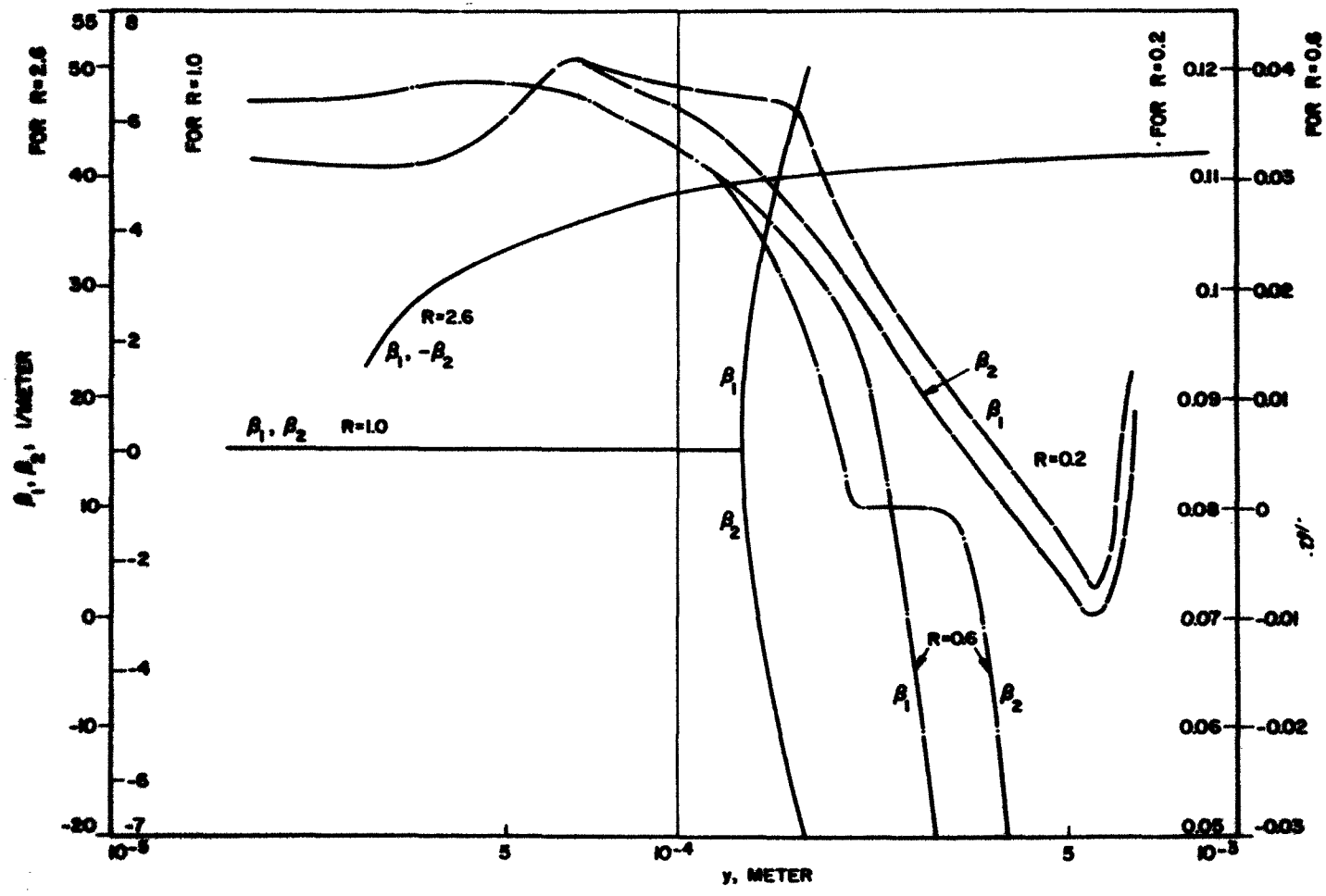

FIG. 5.13 β_1 AND β_2 VS. y.

waves tend to become a forward wave and a backward wave with increasing values of β as ω/ω_p is increased. For large values of ω/ω_p as is the case for R = 2.6, the absolute values of the two β's reach constant values. For R = 0.2, the two waves remain as backward waves at least within the range of y for which the d-c parameters have been evaluated. For larger values of ω (actually ω/ω_p) this transition from the two backward waves to a forward and a backward wave occurs at smaller values of y. For R = 2.6, which corresponds to ω = the plasma frequency at the potential minimum, the two waves correspond to forward and backward waves with unchanging amplitudes.

Figures 5.14 through 5.17 show the variations of α and β corresponding to the three waves for four values of R respectively. It can be seen that for small values of y there are two forward waves and one backward wave except for the case of R = 2.6 where all three waves are forward waves. In a crossed-field configuration the cyclotron and space-charge waves are present. Due to some finite coupling between the two sets of waves only one set of two waves may be present and it may be difficult to identify these waves separately. If it is assumed that the convergence ratio (ratio of the cross-sectional area of the beam at the cathode to that in the interaction region) is small, it is justified to assume that the space-charge density in the gun region is large. This corresponds to a pronounced effect due to space-charge waves with their propagation constants modified because of the presence of magnetic field. The fact that, as the value of y is increased, (or the value of ω_p is decreased) the backward wave tends to become a forward wave seems also to indicate that the waves corresponding to their β's as β_4 and β_5 in Figs. 5.14 through 5.17 are space-charge waves with their

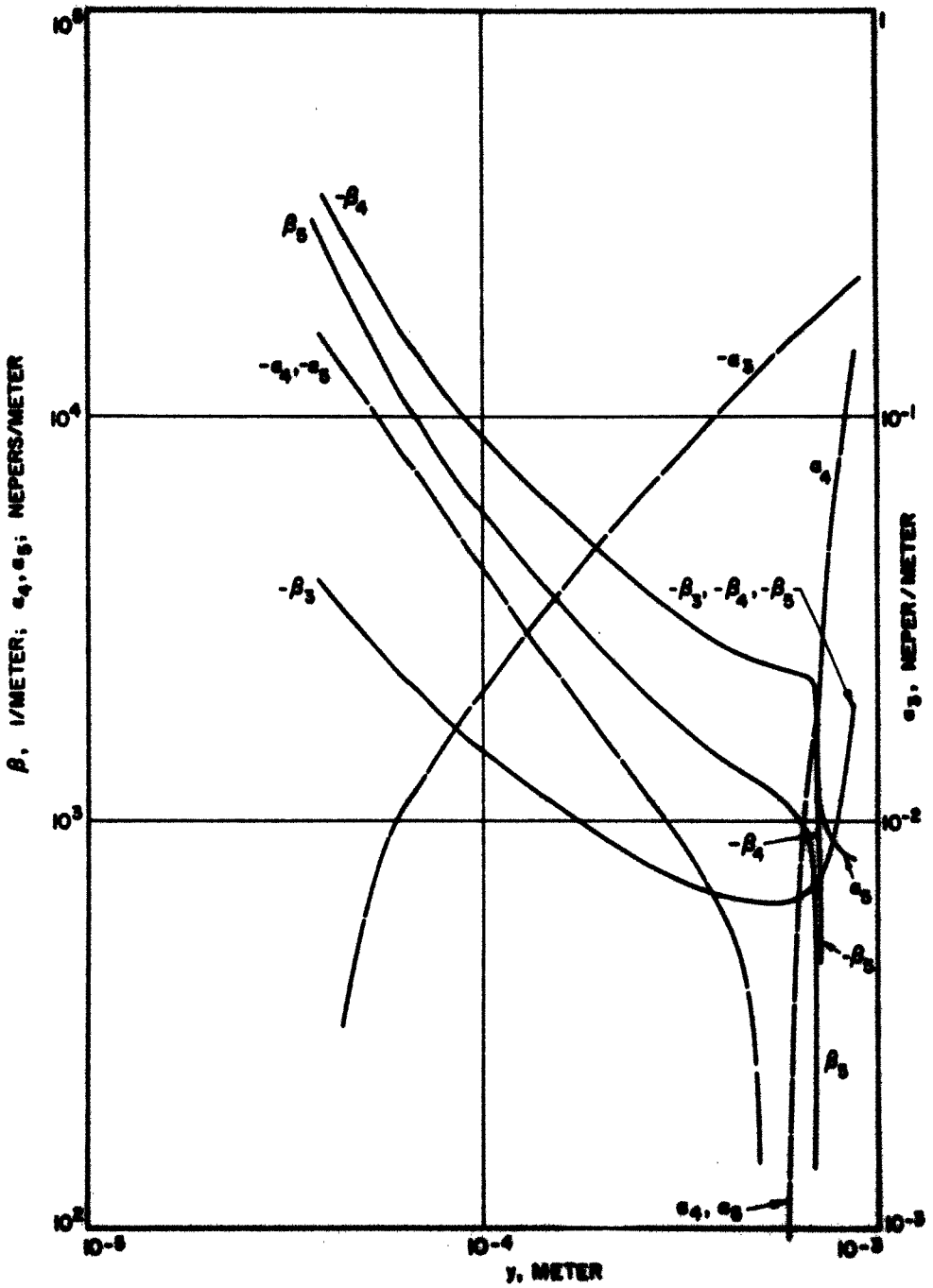

FIG. 5.14 α_1 AND β_1 VS. y. ($\omega_c = 5 \times 10^9$ RAD/SEC, R = 0.2)

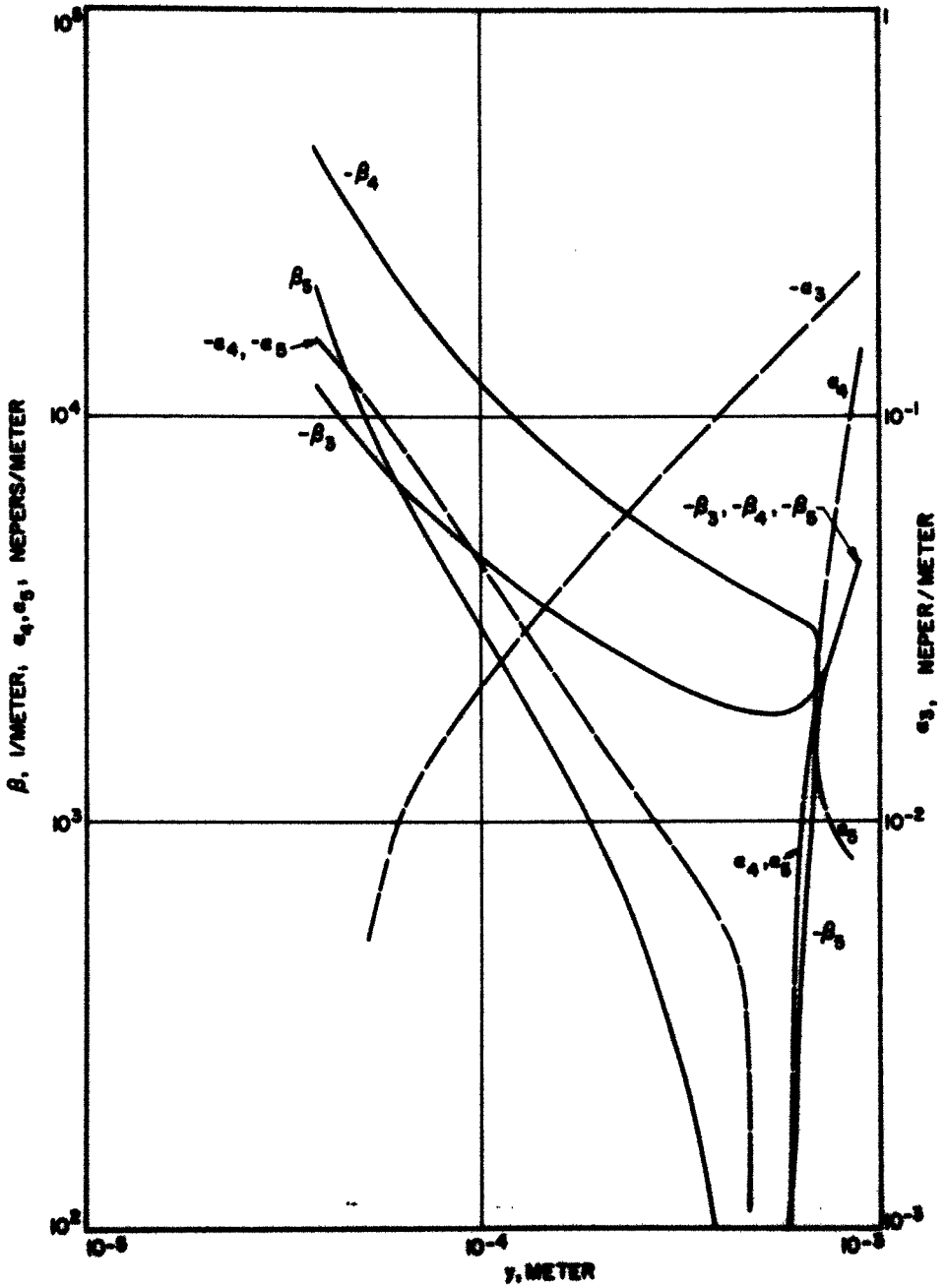

FIG. 5.15 α_i AND β_i VS. y. ($\omega_c = 5 \times 10^9$ RAD/SEC, R = 0.6)

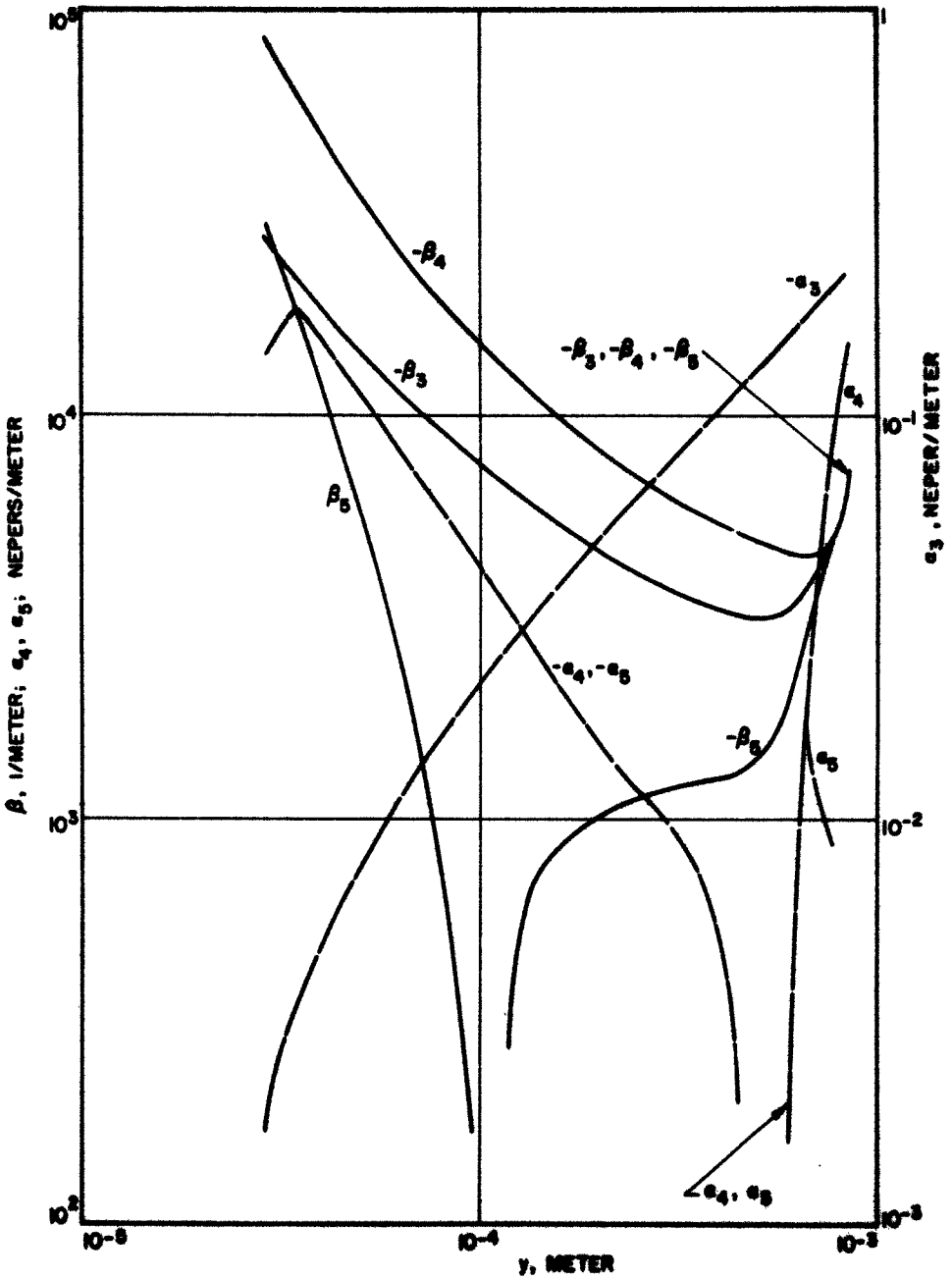

FIG. 5.16 α_1 AND β_1 VS. y. ($\omega_c = 5 \times 10^9$ RAD/SEC, R = 1.0)

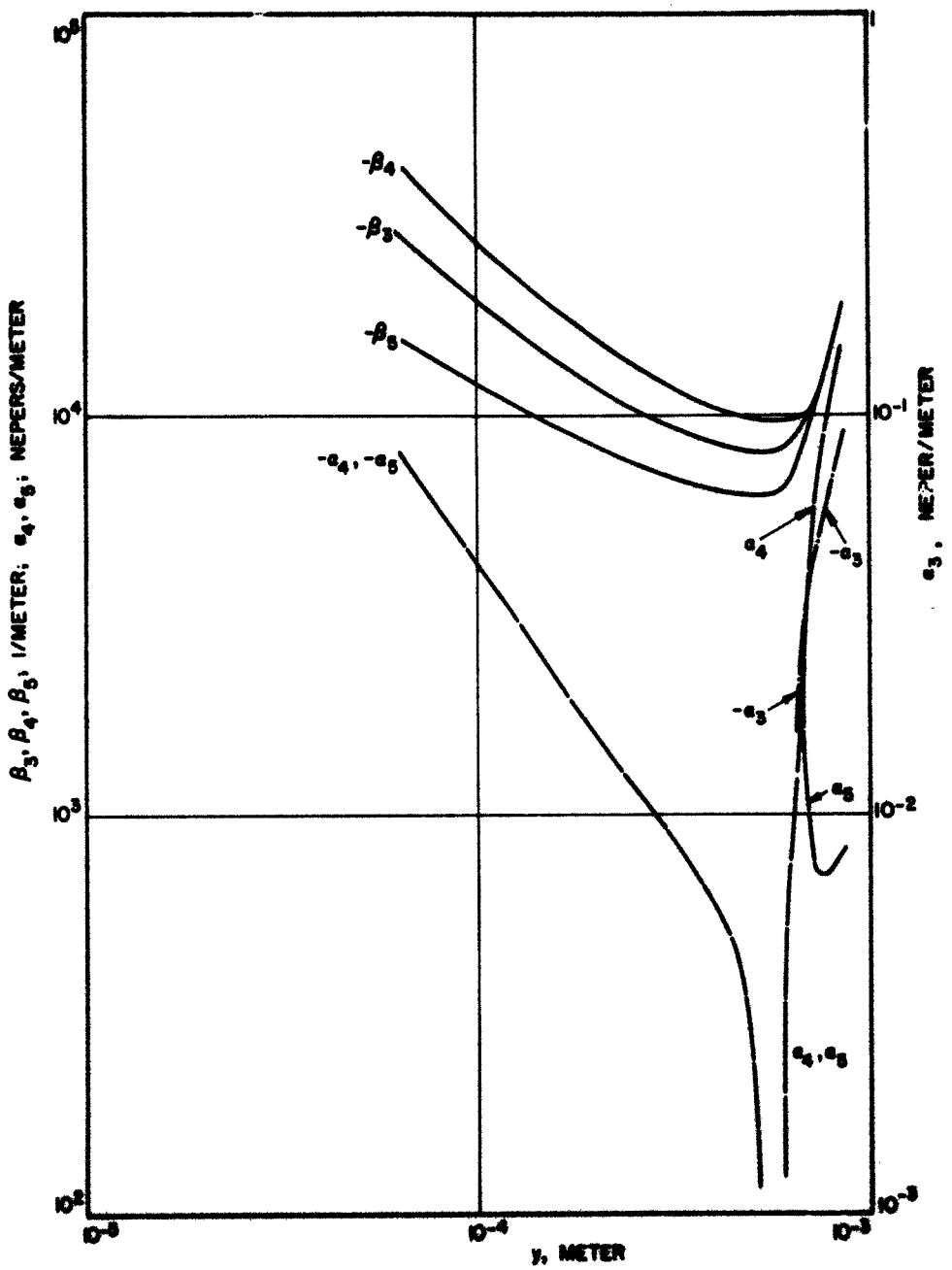

FIG. 5.17 α_i AND β_i VS. y. ($\omega_c = 5 \times 10^9$ RAD/SEC, R = 2.6)

β's modified due to the presence of the magnetic field. This is true because if these waves correspond to cyclotron waves the backward wave (for $R \leq 1$) for small values of y will never transform into a forward wave.

For this reason the three waves are referred to as the synchronous wave and the two space-charge waves. The slow space-charge wave is a forward wave referred to with suffix 4 while the conventionally known fast space-charge wave is a backward wave for small values of y (or large values of ω_p) and transforms into a forward wave as the plasma frequency is reduced. This wave is referred to with suffix 5. The synchronous wave is always a forward wave as it should be and is referred to with suffix 3. The value of $|\beta_s|$ is very nearly equal to $\omega/\dot{y}_o$ in all cases. For $y < y_{cr}$, where y_{cr} corresponds to the value of y for which $\dot{y}$ = maximum, the two space-charge waves and the synchronous wave are continuously attenuated. For $R > 1$, it is seen that the synchronous wave has an unchanging amplitude. The attenuation constant for the space-charge waves decreases as y is increased (or ω_p is decreased) whereas the attenuation constant for the synchronous wave increases continuously as y is increased. For $y > y_{cr}$, the two space-charge waves experience amplification and the growth factors are extremely large. Whether the two space-charge waves are forward waves or whether one is a forward wave and the other a backward wave in this region ($y > y_{cr}$) depends upon the value of R. The growth factor for the slow space-charge wave continues increasing while the growth factor of the fast space-charge wave decreases from its maximum value as y is increased further. The synchronous wave is attenuated continuously and its attenuation constant increases gradually as y is increased. For some value of y ($y > y_{cr}$)

the values of the propagation constants for the two space-charge waves approach that of the synchronous wave.

It is in this region ($y > y_{cr}$) that any perturbation will grow up rapidly. Though the growth rate is extremely large and does violate the small-signal assumption made in this analysis the overall gain will not be very large because of the finite range of y for which this condition is satisfied. In order to determine the absolute values of the perturbations at a given value of y, it will be necessary to solve for the excitation of the various waves as a boundary-value problem. A perturbation in this region ($y > y_{cr}$) will also cause an amplifying backward wave with a growth factor α_1 and may eventually modify the conditions in the neighborhood of the potential minimum. It can be noticed from the plots in Fig. 5.12 that low-frequency perturbations will be more effective in modifying the conditions in the neighborhood of the potential minimum. This indicates that the conditions in the gun region are more favorable for low-frequency perturbations. This also indicates why the noise output in crossed-field devices is usually dominant at low frequencies.

It can be deduced from Eq. 4.92 that

$$\sum_{i=1}^{5} \alpha_i = -\frac{1}{\dot{y}_o} \frac{d\dot{y}_o}{dy} . \tag{5.40}$$

Thus the signs of α's as evaluated from Eq. 4.92 depend upon the signs of $\dot{y}_o$ and $d\dot{y}_o/dy$. For $\omega_c T < \pi$, $\dot{y}_o$ and $d\dot{y}_o/dy$ are both positive and under these conditions $\sum_{i=1}^{5} \alpha_i < 0$. In general these conditions do not lead to large values of α. Some boundary and/or particular operating conditions may lead to large values of α with different signs. From

Fig. 5.9 it is noticed that for $\pi < \omega_c T < 2\pi$, $d\dot{y}_o/dy < 0$ and $\dot{y} > 0$. Thus in this region the signs of α's are changed and it is possible to expect large positive values of the growth rate. It can be seen that as the magnitude of $d\dot{y}_o/dy$ increases from a zero value the values of α also increase and very large values of α are obtained.

Figure 5.18 shows the plots of α's and β's for the first two waves as a function of y for two values of R for the case of $\omega_c = 1 \times 10^9$ rad/sec. These results are similar to the results shown in Figs. 5.12 and 5.13 for the case of $\omega_c = 5 \times 10^9$ rad/sec.

Figures 5.19 and 5.20 show the plots of α's and β's for the synchronous wave and the two space-charge waves as a function of y for two values of R respectively. For the range of y for which the d-c parameters have been evaluated, $d\dot{y}_o/dy > 0$ and thus the values of α's for the two space-charge waves are negative. For R = 1.0, the conventional fast space-charge wave is a backward wave and for R = 5.0 this backward wave becomes a forward wave for large values of y. The plots in Figs. 5.16 and 5.20 correspond to the same value of the perturbation frequency but different values of ω_c. It is interesting to note from these two figures that the value of y for which transformation from the backward space-charge wave to the forward space-charge wave occurs is larger for the case of $\omega_c = 5 \times 10^9$ rad/sec but only by a very small amount. The space-charge density at this value of y (for which this transformation occurs) is somewhat larger for the case of $\omega_c = 1 \times 10^9$ rad/sec. This does indicate that the propagation constants of the space-charge waves are modified by the d-c parameters which happen to be quite different for the two values of ω_c. If this were not so the value of y at which the transformation from the backward space-charge wave to the forward

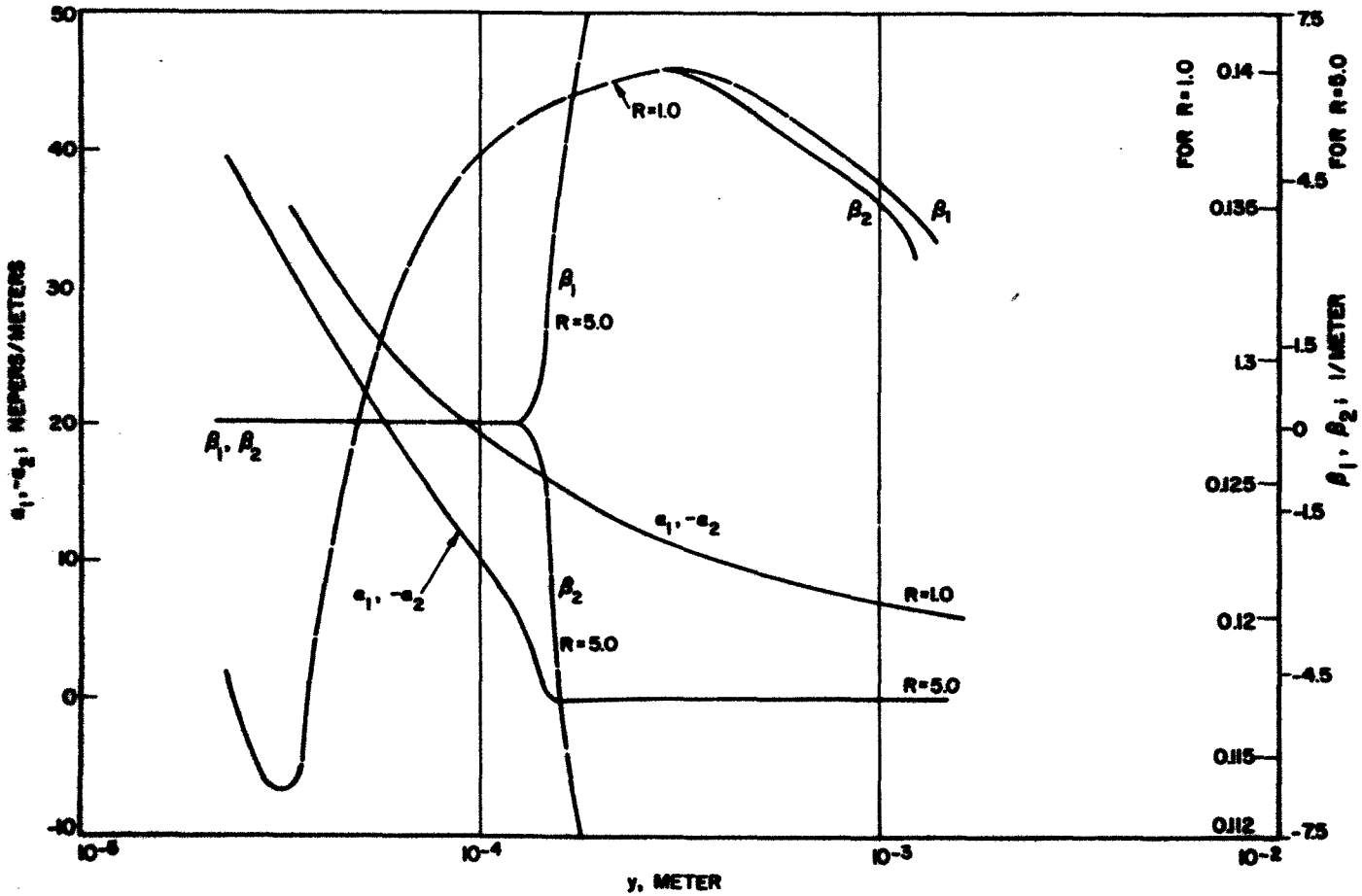

FIG. 5.18 $\alpha_1, -\alpha_2, \beta_1$ AND β_2 VS. y. ($\omega_c = 1 \times 10^9$ RAD/SEC)

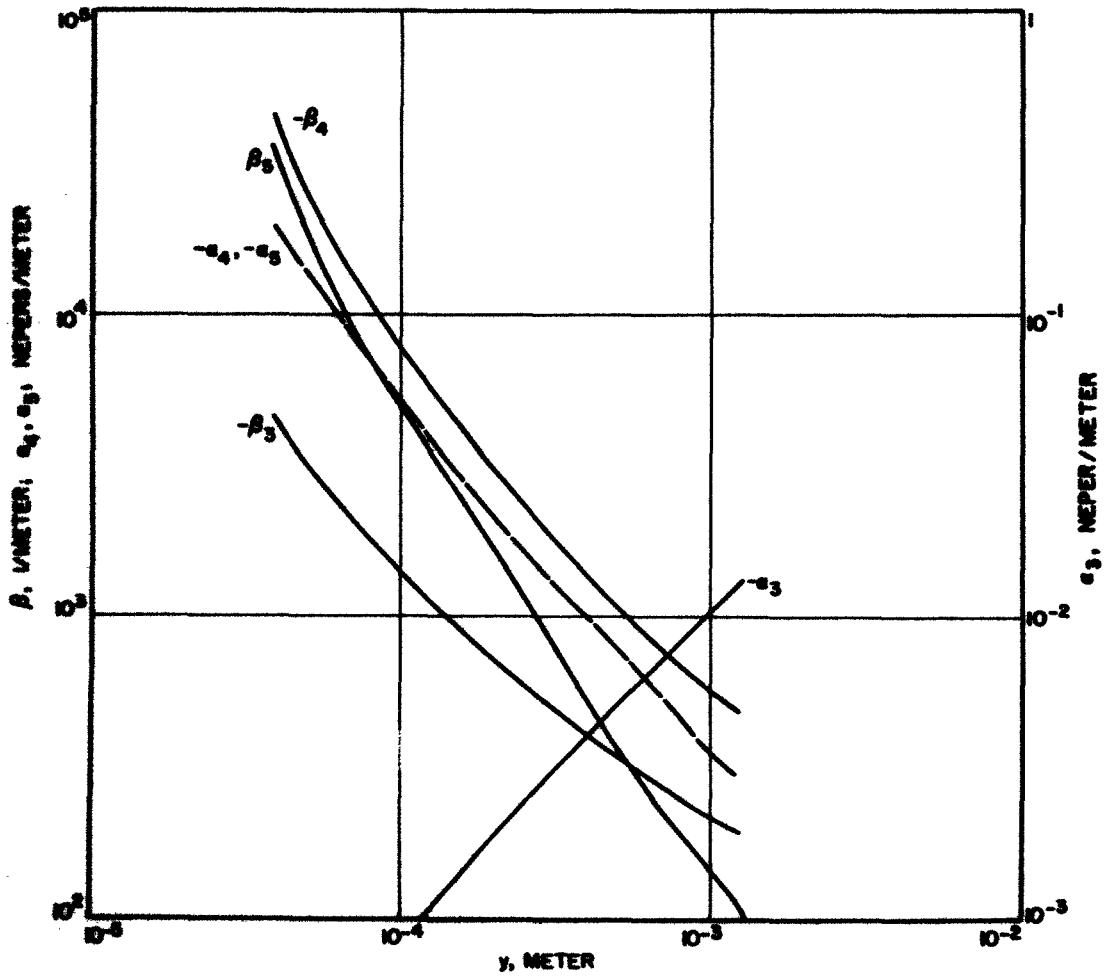

FIG. 5.19 α_i AND β_i VS. y. (ω_c = 1 x 10^9 RAD/SEC, R = 1.0)

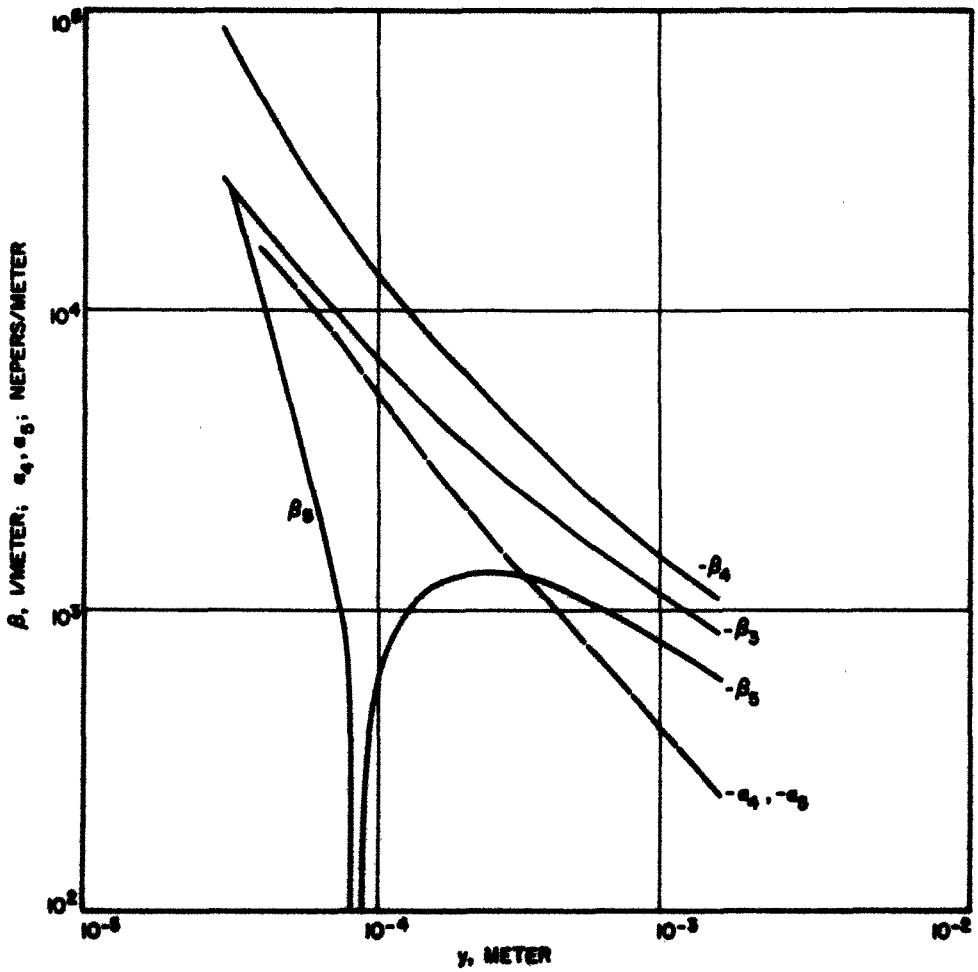

FIG. 5.20 α_1 AND β_1 VS. y. ($\omega_c = 1 \times 10^9$ RAD/SEC, R = 5.0, α_3 IS FOUND EQUAL TO 0)

space-charge wave occurs would have been larger for the case of $\omega_c = 1 \times 10^9$ rad/sec than for the case of $\omega_c = 5 \times 10^9$ rad/sec since the space-charge density evaluated for the former case is larger than that for the latter case. It may be pointed out here that the modification of the space-charge wave propagation constants, as determined by the results shown in Figs. 5.14 through 5.17, 5.19 and 5.20, is a first-order modification. It is not yet clear what d-c parameters are significant in causing this modification.

From the plots shown in Figs. 5.14 through 5.17 it can be seen that the synchronous wave is always attenuated for all values of R except for R > 1 when $\alpha_3 = 0$ in the region for which $d\dot{y}_o/dy > 0$. In general the value of $-\alpha_3$ increases with y. The plots in Fig. 5.20 for the case of $\omega_c = 1 \times 10^9$ rad/sec and R = 5.0 show that $\alpha_3 = 0$. It may be concluded, in general, that $\alpha_3 = 0$ for large values of R.

Figure 5.21 has been drawn in order to show the variation of the values of α_1 and $-\alpha_2$ with ω_c. This shows the variation of α_1 and $-\alpha_2$ as a function of y for two values of ω_c but for $\omega = 5 \times 10^9$ rad/sec. It is noticed that the growth rate (α_1), which has been referred to as the diocotron gain in the above paragraphs, is reduced as ω_c is increased. This variation might also be thought of in terms of the change in the value of the plasma frequency. For low values of ω_c, ω_p is large and consequently the growth rate is larger. This variation is in qualitative agreement with the results obtained by Gould[16].

5.6 Application of the Results to Various Cases

The physical significance of the very large values of α obtained in the previous section is not quite clear but it is possible to explain

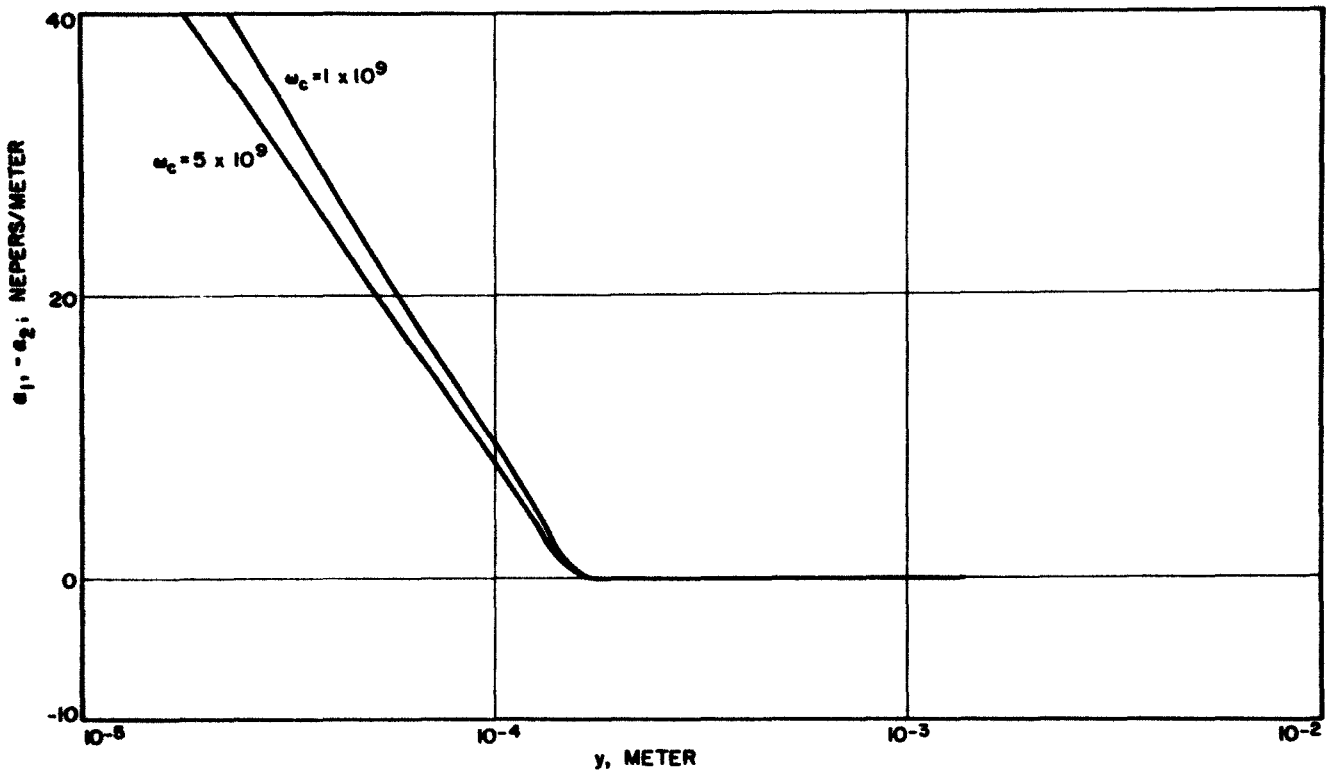

FIG. 5.21 α_1 AND $-\alpha_2$ VS. y. ($\omega = 5 \times 10^9$ RAD/SEC)

qualitatively several experimental and theoretical observations made at different laboratories from these results. These observations and the corresponding explanations are outlined below.

1. By substituting $E_{z1} = 0$ in Eqs. 4.91, it can be shown that all the perturbations such as E_{y1}, $\dot{y}_1$, $\dot{z}_1$ and ρ_1 are reduced to zero values. This is not true if any perturbation other than E_{z1} is made equal to zero. Thus the z-component of the a-c field plays an important role as far as the noise propagation along the beam is concerned. From experimental results obtained at The University of California[26] there is evidence that the inner edge of the beam is noisier than the outer edge of the beam and the E_z component is larger at the inner edge than at the outer edge.

In short focus crossed-field guns, the electrode configuration is not adjusted to make the d-c component of the E_z-field equal to zero. This component of the d-c field is smaller than the y-component of the d-c field and arises primarily due to the space-charge effects in the device. As a first-order approximation E_z may be considered as a perturbation. Thus in the conventional crossed-field device the E_z component is larger in magnitude than in the Kino gun model where through proper electrode configuration the E_z field is reduced to zero. This is perhaps the reason why a noise figure lower[14] than that in conventional crossed-field devices has been obtained by using a Kino gun.

2. A great deal of experimental work to reduce the noise output has been carried out at the CSF Laboratories[28]. By introducing several appropriately biased grids in the neighborhood of the cathode a considerable reduction in the noise output has been obtained. A large noise reduction has also been obtained by introducing a screen-grid between

the cathode and the gun anode. These results can be explained qualitatively from the information obtained after solving Eq. 4.92.

From a simple mathematical model (without considering space-charge effects) the cutoff cyclotron frequencies for the two diodes (one corresponding to the cathode-anode spacing and the other corresponding to the cathode-screen grid spacing) are given by

$$\omega_{cc} = \frac{\sqrt{2\,\eta\,V_o}}{d} \tag{5.41}$$

and

$$\omega_{ccs} = \frac{\sqrt{2\,\eta\,V}}{d'_1} \quad , \tag{5.42}$$

where the suffix s refers to the screen grid which is held at potential V. The parameters d and d'_1 refer to the cathode-anode spacing and cathode-screen grid spacing respectively. This is shown in Fig. 5.22.

Let

$$V = a\,V_o\,\frac{d'_1}{d} \quad , \tag{5.43}$$

where a is a constant and for a linear relationship a = 1.0. From Eqs. 5.41 and 5.42 it can be shown that

$$\frac{\omega_{ccs}}{\omega_{cc}} = \sqrt{\frac{d}{d'_1}} > 1 \quad \text{for} \quad a = 1.0 \tag{5.44}$$

and

$$\frac{\omega_c}{\omega_{cc}} > \frac{\omega_c}{\omega_{ccs}} \quad , \tag{5.45}$$

where ω_c is the cyclotron frequency corresponding to the applied magnetic field. Thus by introducing the screen grid, the effective value of the

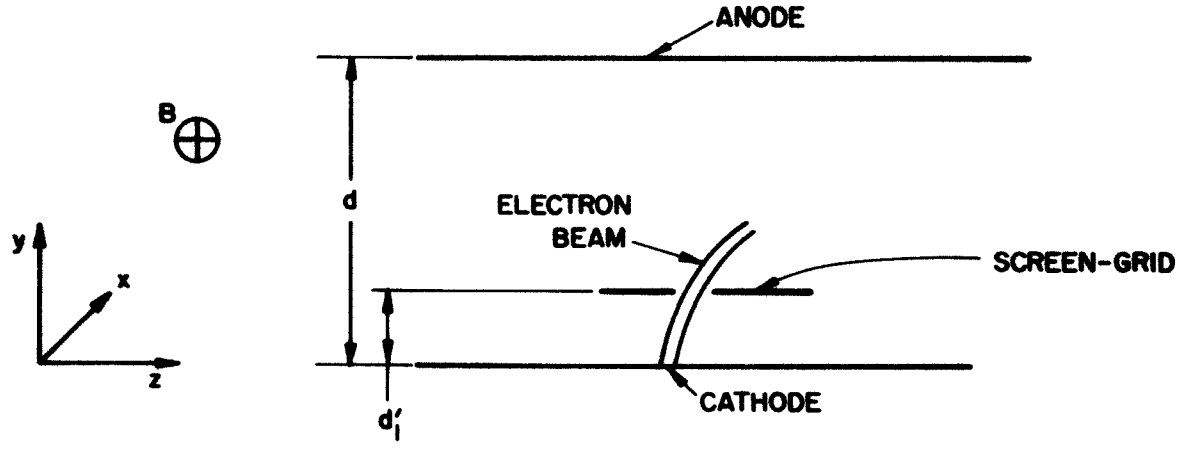

FIG. 5.22 A CROSSED-FIELD DIODE WITH A SCREEN-GRID.

cutoff magnetic field is increased in the cathode-screen grid diode. This is equivalent to saying that the effective value of the magnetic field is reduced in the diode. In this manner the range for which $(d\dot{y}_o/dy)/\dot{y}_o < 0$ is reduced. Since large positive values of the growth factor α occur in the region for which $(d\dot{y}_o/dy)/\dot{y}_o < 0$ a considerable reduction in noise is obtained by introduction of the screen grid which reduces the range of $(d\dot{y}_o/dy)/\dot{y}_o$ for which $\alpha > 0$ is obtained. This also tends to reduce the average number of cycloids per unit electron in the potential minimum region.

The noise reduction techniques mentioned above were developed at the CSF Laboratories but no physical explanation was furnished for these schemes. The physical model outlined above in conjunction with the results obtained after solving Eq. 4.82 does explain qualitatively the following experimental observations made at the CSF Laboratories.

a. As V_s, the potential at the screen grid, is increased the noise output is decreased. By increasing the value of V_s, the value of ω_{ccs} is increased and thus the value of ω_c/ω_{ccs} is decreased. This effectively reduces the region for which $(d\dot{y}_o/dy)/\dot{y}_o < 0$ and gives a reduction in noise.

b. As the cathode-screen grid spacing d_1' is decreased, the noise output is decreased. The reduction in the value of d_1' causes an increase in the value of ω_{ccs} and the reduction in noise can be explained as outlined in the above paragraph.

This noise reduction scheme has further advantages in that, as the value of ω_c/ω_{ccs} is reduced, it is possible to draw larger cathode currents and thereby the perveance of the tube is increased. However for high power tubes, the screen grid beam interception may cause some

heat dissipation problems at the screen grid. By adjusting the screen-grid potential appropriately some compromise between the noise reduction and the gun perveance can be obtained.

3. Pollack[29] has carried out a one-dimensional Monte Carlo analysis for noise transport in the gun region. A more detailed comparison between Pollack's results and those of the general Monte Carlo analysis is given in Chapter VII. Though these results are limited to values of $B/B_c \leq 1$, the results explain the large values of the growth factor α in the region for which $(d\dot{y}_o/dy)/\dot{y}_o < 0$ Pollack's results are given in Figs. 5.23 through 5.25 and the various parameters as defined by Pollack are given by

$$F_o \triangleq \frac{1}{T_o} \triangleq \frac{\sqrt{2\,\eta\,V_o}}{d} \tag{5.46}$$

and

$$R^2 = \frac{< i^2 >}{2\,e\,I_a\,\Delta f}\ , \tag{5.47}$$

where $< i^2 >$ corresponds to the mean square current fluctuations at the anode and I_a is the d-c anode current. Figure 5.23 shows plots of the anode current spectrum as a function of f/F_o for several values of B/B_c. Figure 5.24 shows the plots of the anode velocity spectrum as a function of f/F_o for two values of B/B_c and Fig. 5.23 shows the plots of R^2 as a function of B/B_c for the results obtained from the experimental and Monte Carlo analysis by Pollack. From all these curves it is evident that as the value of the parameter B/B_c is increased the noise fluctuations are also increased and larger growth in these fluctuations occurs in the region $\pi < \omega_c T < 2\pi$ for which $(d\dot{y}_o/dy)/\dot{y}_o < 0$.

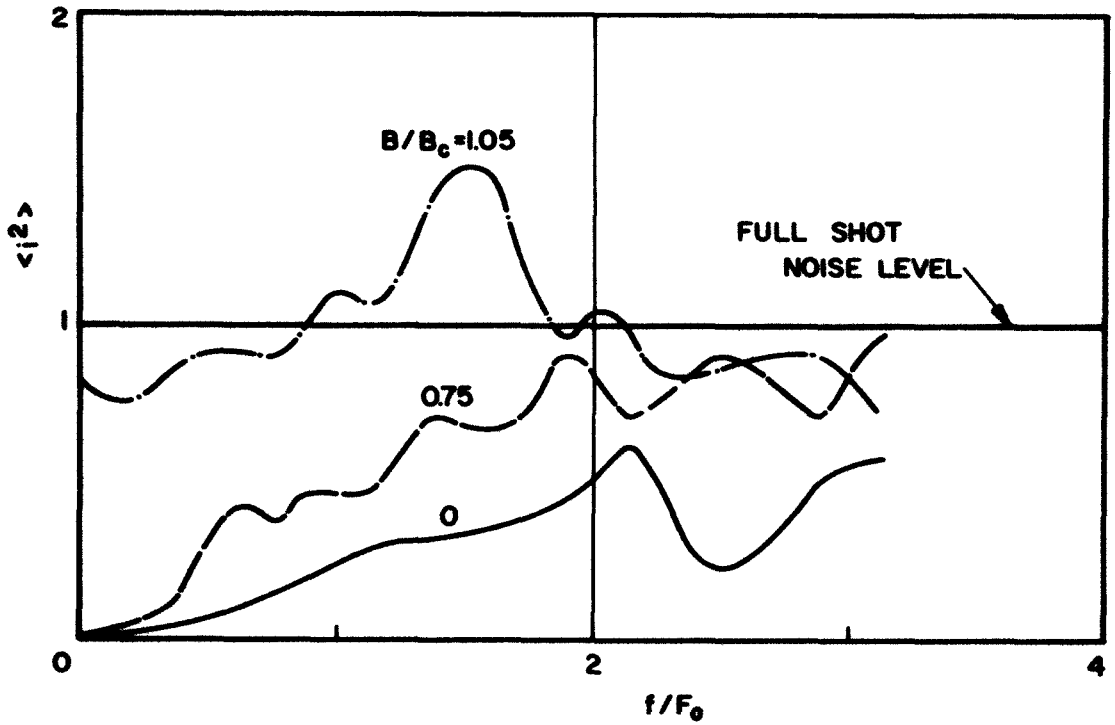

FIG. 5.23 ANODE CURRENT SPECTRUM VS. f/F_o. (POLLACK)

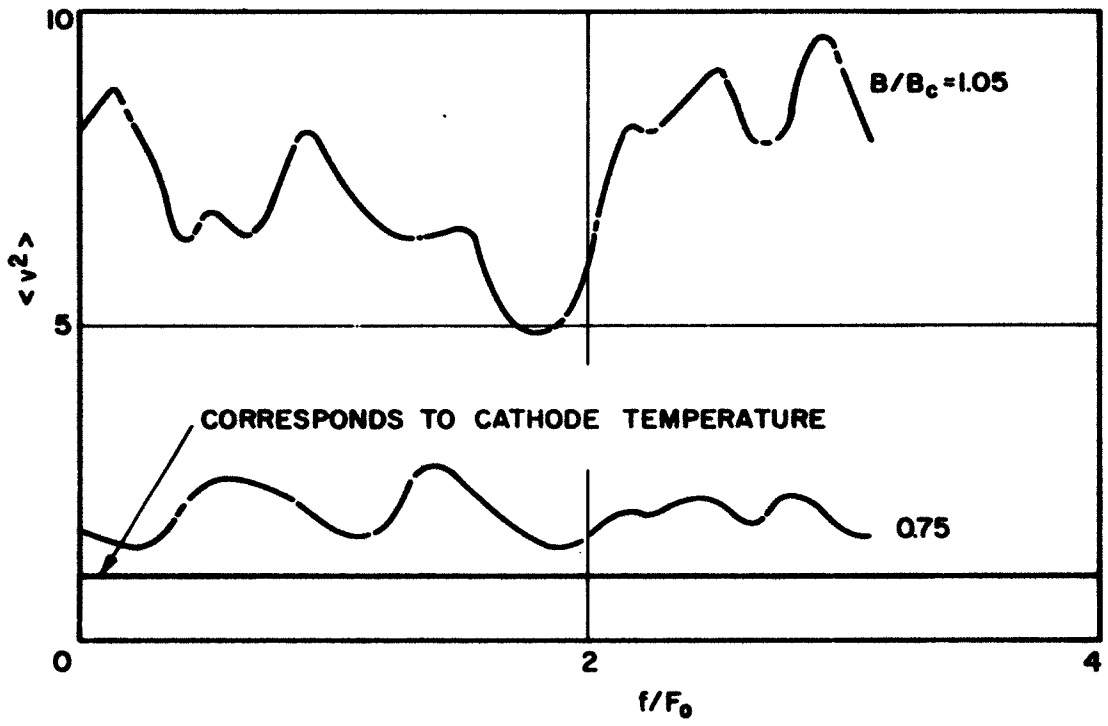

FIG. 5.24 ANODE VELOCITY SPECTRUM VS. f/F_o. (POLLACK)

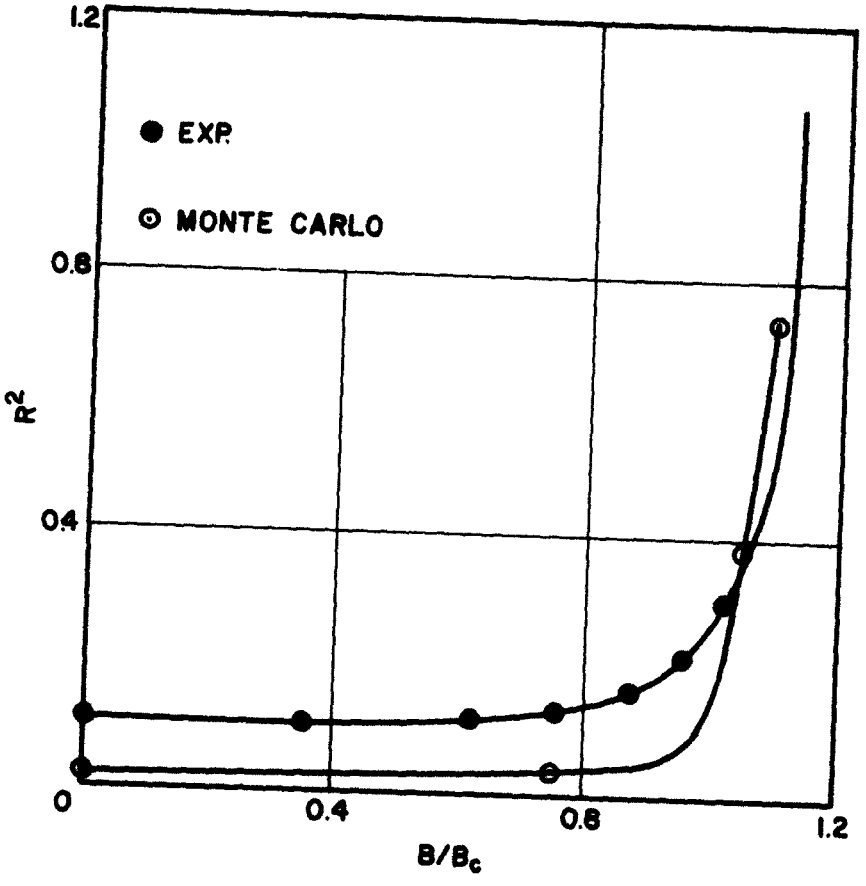

FIG. 5.25 R^2 VS. B/B_c. (POLLACK)

4. In connection with Eq. 5.40, it was mentioned that the growth factor α can be positive when $(d\dot{y}_o/dy)/\dot{y}_o < 0$. This can occur when $\dot{y}_o > 0$ and $d\dot{y}_o/dy < 0$ or vice versa. For an ideal case when the electrons enter the interaction region with an appropriate velocity the electrons traverse straight-line trajectories in the interaction region. For nonideal conditions the beam traverses a cycloidal motion in the interaction region. By assuming a regular periodicity in the cycloidal motion as equal to $4\pi/\omega_c$, $(d\dot{y}_o/dy)/\dot{y}_o < 0$ is obtained in the following regions of one single cycloid:

$$\pi < \omega_c T < 2\pi \tag{5.48}$$

and

$$2\pi < \omega_c T < 3\pi \quad . \tag{5.49}$$

For other cycloids the corresponding regions are defined by Eqs. 5.48 and 5.49 by transforming the time axis appropriately. For a different periodicity in the cycloidal motion, the corresponding values of $\omega_c T$ for which $(d\dot{y}_o/dy)/\dot{y}_o < 0$ would be changed. It can be seen from Fig. 5.26 that the larger the cycloidal motion in the interaction region, the larger the value of the range for y for which $(d\dot{y}_o/dy)/\dot{y}_o < 0$ and thereby large values of the total growth may be obtained. The range for which $2\pi < \omega_c T < 3\pi$ occurs when the beam is moving toward the sole. In this region (in addition to the region given by Eq. 5.48) the electrons observe very large values of the growth factors and hence the a-c perturbations grow up very rapidly. This explains qualitatively why a large fraction of the electron beam can be collected on the sole[10,11,12,13] even though it may be many volts negative with respect to the cathode from which the beam originated. This also explains that if the electrons

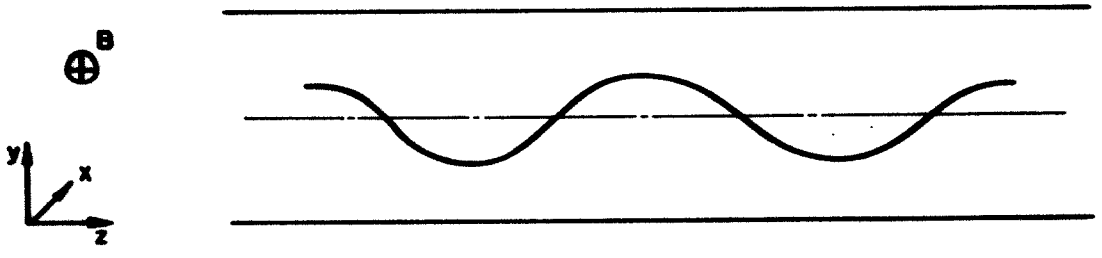

FIG. 5.26 CYCLOIDING BEAM IN THE INTERACTION REGION.

are traversing straight-line trajectories, there are no regions for which $(d\dot{y}_o/dy)/\dot{y}_o < 0$. Thus the large growth factors are not obtained and the sole current is negligible or much smaller[14] than that observed in conventional crossed-field devices. The amplification due to a velocity slipping stream is still possible and would lead to some finite amplification factor. It may be pointed out here that since the space-charge density in the interaction region is less than that in the gun region, the conventional, fast space-charge wave is always a forward wave.

These studies also explain some of the observations made by Miller[13] who found that the electron equivalent temperature is increased considerably when the electrons are allowed to enter a potential depressed region and thus traverse several cycloids before they come out from this depressed region. It is in the process of traversing these cycloids that the electron equivalent temperature is increased.

5.7 Conclusions

The results given in this chapter are in agreement with some of the results given in Chapter III, namely that the perturbation may grow faster when the beam is being decelerated along the y-axis.

The physical significance of these large values of the growth factor is not clear as yet, but it is noticed that large values of α are possible when the beam is being decelerated along the y-axis. A similar analogy has been shown by Tien and Field[30] for O-type devices where, by decelerating the beam along the axial direction, a large amplification may be obtained.

In the case of a crossed-field beam large values of α are obtained in the region given by Eq. 5.48 where the beam is decelerated along the

y-axis but at the same time the beam as a whole is being accelerated. In the region given by Eq. 5.49 the beam as a whole is being decelerated. In order to solve the propagation of a perturbation at an angular frequency ω in this region it will be necessary to solve for the steady-state variables first and then use Eq. 4.82 to solve for the propagation constants.

CHAPTER VI. DERIVATION OF MONTE CARLO EQUATIONS

6.1 Introduction

The study of noise transport from the cathode (or the potential minimum for a space-charge-limited operation) is most often based upon a small-signal perturbation analysis as discussed in the previous chapters. The small-signal analysis is justified when the variations in the different parameters are very small as compared to the average values of these parameters. This requirement makes a small-signal analysis inappropriate in the potential minimum region, which even includes electrons at zero velocities.

The Monte Carlo method or technique involves in general an interesting combination of sampling theory and numerical analysis. Briefly this method may be described as the device of studying an artificial stochastic model of a physical or mathematical process. The novelty of the method lies in the fact that when it is difficult to solve a problem by standard numerical methods there may exist a stochastic process with distributions or parameters which satisfy the original equations and it may actually be more efficient to construct such a process and compute the statistics than to attempt to use the standard methods. The Monte Carlo method involves the generation of an artificial realization of a stochastic process by a sampling procedure, the particular procedure being determined by the underlying probabilistic laws of the stochastic process.

In the application of the Monte Carlo method for studying noise phenomena in microwave tubes, the discrete nature of the electron is preserved and no assumption regarding the linearity of the working

equations is necessary which is a great advantage in this method as compared to methods based upon a small-signal analysis. This method is an exact simulation of the diode and the electrons are emitted from the cathode in a random manner. The initial velocities of the emitted electrons vary in a random manner also. The presence or absence of the potential minimum is determined by the number of electrons present in the diode, which in turn depends upon the selected value of the current density. The electrons are emitted at discrete intervals of time, after which the space-charge forces are computed to determine the exact flow of the electrons. The fluctuations in the velocity and the current are determined for each interval of time for some specified locations in the diode and the noise parameters can be determined from these fluctuations. This method was first applied to O-type devices for a short-circuited diode by Tien and Moshman[21]. This analysis has been extended to an O-type open-circuited diode by Dayem and Lambert[22] who also took into account a weighting factor due to the fact that the calculations were restricted to a noninfinite total time interval.

The various equations for evaluating parameters in the development of a noise figure expression are derived in this chapter. The configuration and the coordinate system are shown in Fig. 6.1. The analysis presented in this chapter is essentially three dimensional and the finite length of the beam in the direction of the magnetic field is also considered. However, because of the magnitude of the computations involved, the electron configuration is considered to be uniform along the x-axis and the y-z plane of observation is restricted to $x = a/2$, which corresponds to the mid-point of the cathode along the x-axis. This results in the final equations corresponding to a two-dimensional

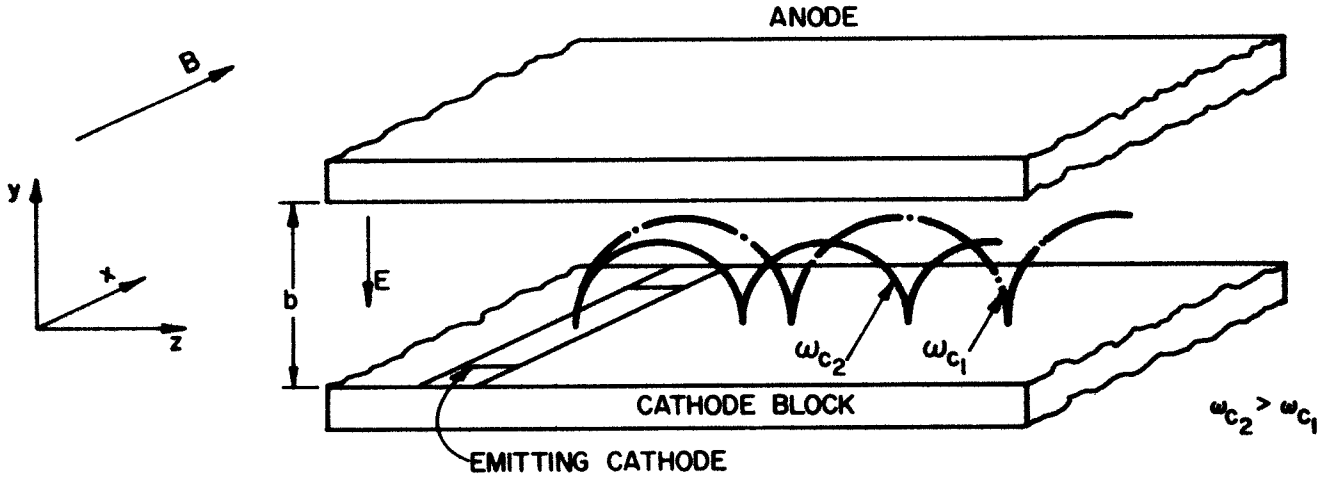

FIG. 6.1 A SCHEMATIC OF "RAJECTORY OF A SINGLE ELECTRON IN A CROSSED-FIELD DIODE.

problem in addition to a great saving in computer time. For this reason the effect of the higher order space-charge waves may be neglected. The electrons are assumed to be emitted in a random manner, both in number and the y-z components of velocities. The random electron emission time is also considered. The random numbers are generated in a pseudo manner for every unit interval of time. The modification of the equations because of the noninfinite data is also discussed. Provision is made to simulate the diode for noise transport analysis for the combination of the following two conditions leading to four possible cases:

1. Space-charge-limited or temperature-limited operation.
2. Open-circuited or short-circuited diode.

6.2 Assumptions Made in This Analysis

In this analysis, the following assumptions are made:

1. Nonrelativistic mechanics.
2. The force due to r-f magnetic field on an electron is neglected.
3. The finite length of the beam with a uniform electron configuration along the x-axis is assumed.
4. The effect of direct collisions between electrons is neglected.
5. The emission process is ergodic, i.e., the time average is equal to the ensemble average.
6. The velocity distribution and the electron emission number are completely uncorrelated.
7. The initial velocity components are of Maxwellian distribution.
8. Poisson distribution for electron emission number is assumed.
9. The electrons which cannot escape the potential minimum and thus return to the cathode do not influence the emission.

10. The electric fields are constant during every unit time interval Δt.

11. The magnetic field has only one component along the x-axis and it is uniform.

6.3 Random Electron Emission Number

As mentioned in Section 6.1, the number of electrons emitted in each unit time interval varies in a random manner. If it is assumed that there is no correlation between the velocity and the current variations for the electrons being emitted from the cathode in any unit time interval, the number of electrons emitted in each unit time interval will vary according to Poisson's distribution. If n_a represents the average number of electrons emitted from the cathode per unit time interval, then the probability f(s) that s electrons are emitted in any unit time interval Δt is given by Poisson's distribution as

$$f(s) = \frac{e^{-n_a} n_a^s}{s!} \tag{6.1}$$

In order that the range of random numbers being generated lies between 0 and 1, the cumulative distribution function F(s) or the probability that s or few electrons are emitted in this time interval is given by

$$F(s) = \sum_{s=0}^{s=s} f(s) \tag{6.2}$$

so that

$$0 < F_s < 1 \ . \tag{6.3}$$

Then the number of electrons emitted in this unit time interval is s if

$$F\left(s - \frac{1}{2}\right) \leq R_s \leq F\left(s + \frac{1}{2}\right) , \tag{6.4}$$

where R_s is the random number and the range of its values is between 0 and 1.

In any unit time interval Δt_i a random number R_{s_i} is generated and its value compared according to Eq. 6.4. This concludes the generation of s_i electrons in the time interval Δt_i. The evaluation of the function F(s) is discussed in Section 7.2.

6.4 Random Electron Emission Velocity

After the generation of s electrons as described in Section 6.3, it is necessary to associate some velocities with each of these electrons. As mentioned in Section 6.1, the velocity components (y and z components) associated with any one of the s_i electrons generated in the time interval Δt_i vary in a random manner also. In addition it is assumed that the z-component velocity distribution is full-Maxwellian, i.e., both positive and negative values of the z-component velocity are allowed, but the y-component velocity distribution is half-Maxwellian, i.e., only positive values of the y-component velocity are allowed. For a one-dimensional case the probability[21] that an electron emitted with an initial velocity between v and v+dv is

$$\frac{mv}{kT} e^{-\frac{mv^2}{2kT}} . \tag{6.5}$$

This corresponds to the number of electrons n(v) emitted per unit area and unit time[32] in the velocity range from v to v+dv. The cumulative distribution function of Eq. 6.5 is

$$1 - e^{-\frac{mv^2}{2kT}} \quad . \tag{6.6}$$

If R is a random number, 1-R is also a random number. By equating Eq. 6.6 to 1-R the relation between the random velocity and the random number is given by

$$1 - R = 1 - e^{-\frac{mv^2}{2kT}} \quad . \tag{6.7}$$

By assuming that the distribution functions for the two velocity components can be written as in Eq. 6.5 the two random numbers R_i and G_i associated with the two velocity components (y and z components respectively) are defined as

$$R_i \triangleq e^{-m\frac{\dot{y}_i^2}{2kT}} \tag{6.8a}$$

and

$$G_i \triangleq e^{-m\frac{\dot{z}_i^2}{2kT}} \quad , \tag{6.8b}$$

or the two velocity components can be written as

$$\dot{y}_i = \left(\frac{2kT}{m}\right)^{1/2} (-\ln R_i)^{1/2} \quad , \tag{6.9a}$$

$$\dot{z}_i = \pm\left(\frac{2kT}{m}\right)^{1/2} (-\ln G_i)^{1/2} \quad , \tag{6.9b}$$

where again the range of random numbers is given by

$$0 < R_i < 1$$

and

$$0 < G_i < 1 \quad .$$

For the sake of convenience the z-component velocity given by Eq. 6.9b is taken with a plus or a minus sign depending upon whether the random number V_s is greater or less than 0.5 respectively. Again the range of the value of the random number V_s lies between 0 and 1.

Equations 6.9a and 6.9b are modified to include the scaling factor $D_1(\ell,t)$ for space and time coordinates and the modified equations are written as

$$\dot{y}_i = D_1(\ell,t)\left(\frac{2kT}{m}\right)^{1/2}(-\ln R_i)^{1/2} \tag{6.11a}$$

and

$$\dot{z}_i = \pm D_1(\ell,t)\left(\frac{2kT}{m}\right)^{1/2}(-\ln G_i)^{1/2} \quad . \tag{6.11b}$$

The necessity of the scaling factor $D_1(\ell,t)$ arises because of the limited memory storage and the computation time involved in the solution of the equations derived in this chapter. The evaluation of this factor will be described in detail in Section 7.2.

The random numbers R_i, G_i and V_s are to be generated for each of the s electrons generated in a unit time interval Δt_i as discussed in Section 6.1.

6.5 Random Electron Emission Time

The emission process from a cathode is of a pseudo continuous nature and all the s electrons corresponding to the unit time interval Δt_i are not emitted simultaneously at one instant, whether it is the beginning or the end of the time interval being considered. In order that the simulation conditions correspond more exactly to the practical configuration, the emission times of the various s_i electrons should be

distributed in the interval Δt_i in a random manner. Thus if the time interval between times t_i and $t_i+\Delta t_i$ is being considered, then the ε_i electrons are emitted at times $t_i+R'_1\Delta t_i$, $t_i+R'_2\Delta t_i$, ... $t_i+R'_{\varepsilon_i}\Delta t_i$, where the numbers R'_1, R'_2, ... , R'_{ε_i} are random numbers and the range of the values of these numbers is between 0 and 1. The ε_i electrons emitted in this manner will move under the influence of the existing electrostatic and magnetic forces for times $(1-R'_1)\Delta t_i$, $(1-R'_2)\Delta t_i$ ... $(1-R'_{\varepsilon_i})\Delta t_i$ respectively. As described in Section 6.6, the argument of the trigonometric functions involved in the trajectory equations of the electrons depends upon the fraction of the time interval for which the electrostatic and the magnetic forces act on the electrons. This involves more work in computing the trigonometric functions and for this reason it is assumed that the ε_i electrons are emitted simultaneously but from different points of the cathode, i.e., the ε_i electrons are emitted at time t_i from the randomly distributed points $y_o + R''_{\varepsilon_i}\dot{y}_{\varepsilon_i}\Delta t$, $z_o + G''_{\varepsilon}|\dot{z}_{\varepsilon_i}|\Delta t$, where R''_{ε_i} and G''_{ε_i} are random numbers and the range of the values of these random numbers is given by

$$0 < R''_{\varepsilon_i} < 1$$

and

$$-1 < G''_{\varepsilon_i} < 1 \qquad (6.12)$$

and the point (y_o,z_o) corresponds to the central point of the cathode.

The error introduced in this manner will be very small if the selected value of Δt is small.

6.6 Trajectory Equations for Electrons

The equations of motion for an electron in a crossed-field geometry shown in Fig. 6.1 are written as

$$\ddot{x} = -\eta E_{x_T} , \tag{6.13a}$$

$$\ddot{y} = -\eta[E_{y_T} + B\dot{z}] \tag{6.13b}$$

and

$$\ddot{z} = -\eta[E_{z_T} - B\dot{y}] , \tag{6.13c}$$

where E_{x_T}, E_{y_T} and E_{z_T} represent the total field components and it is assumed that the magnetic field has a uniform x-component. By differentiating Eq. 6.13b with respect to t, substituting for $\ddot{z}$ from Eq. 6.13c, simplifying and then integrating with respect to t, the following may be obtained:

$$\ddot{y} + \omega_c^2 y = -\eta E_{y_T} - \int \eta\omega_c E_{z_T} dt + k_1 , \tag{6.14}$$

where k_1 is the constant of integration. In developing the trajectory equations from Eqs. 6.13, it is assumed that the total field components remain constant during the given unit time interval. Equation 6.14 is thus reduced to

$$\ddot{y} + \omega_c^2 y = -\eta E_{y_T}(t_i) + \eta \omega_c E_{z_T}(t_i)\Delta t + k_1 . \tag{6.15}$$

For evaluating the constant k_1, various quantities in Eq. 6.15 are referred to at time $t_i(\Delta t_i = 0)$ and Eq. 6.13b is used. k_1 is then given by

$$k_1 = \omega_c^2 y(t_i) - \omega_c \dot{z}(t_i) , \tag{6.16}$$

where $y(t_i)$ and $\dot{z}(t_i)$ represent the y-coordinate and the z-directed velocity respectively at the start of the time interval Δt_i. By substituting for k_1 from Eq. 6.16 into Eq. 6.15, the following is obtained:

$$\ddot{y} + \omega_c^2 y = -\eta E_{y_T}(t_i) + \eta \omega_c E_{z_T}(t_i)\Delta t - \omega_c \dot{z}(t_i) + \omega_c^2 y(t_i) \quad . \quad (6.17)$$

The solution to Eq. 6.17 is given by

$$y(t_i+\Delta t) = \frac{\eta E_{z_T}(t_i)}{\omega_c^2}[\omega_c\Delta t - \sin \omega_c\Delta t] - \left[\frac{\eta E_{y_T}(t_i)}{\omega_c^2} + \frac{\dot{z}(t_i)}{\omega_c}\right]$$

$$\cdot \left(1 - \cos \omega_c\Delta t\right) + \frac{\dot{y}(t_i)}{\omega_c} \sin \omega_c\Delta t + y(t_i) \quad . \quad (6.18)$$

From Eqs. 6.13b and 6.18, the z expression for $z(t_i+\Delta t)$ is written as

$$z(t_i+\Delta t_i) = -\frac{\eta E_{z_T}(t_i)}{\omega_c^2}[1 - \cos \omega_c\Delta t] - \left[\frac{\eta E_{y_T}(t_i)}{\omega_c^2} + \frac{\dot{z}(t_i)}{\omega_c}\right](\omega_c\Delta t$$

$$- \sin \omega_c\Delta t) + \frac{\dot{y}(t_i)}{\omega_c}[1 - \cos \omega_c\Delta t] + \dot{z}(t_i)\Delta t + z(t_i) \quad . \quad (6.19)$$

From Eq. 6.13a, the following is obtained:

$$x = -\eta \frac{(\Delta t)^2}{2} E_{x_T}(t_i) + \dot{x}(t_i)\Delta t + x(t_i) \quad (6.20)$$

and

$$\dot{x} = -\eta E_{x_T}(t_i)\Delta t + \dot{x}(t_i) \quad . \quad (6.21)$$

In Section 6.7, while deriving the expression for the space-charge potential, the three-dimensional analysis was reduced to two

dimensional by assuming uniform electron distribution along the x-axis throughout the diode. This restricts the values of $E_{x_T}(t_i)$ equal to zero except at the edges of the beam. The values of E_{x_T} at the edges may also be assumed to be zero by the use of the end hats which prevent the beam from spreading in the x-direction. The x-directed velocities are taken as zero by giving zero values to the initial x-directed velocities. Thus all the electrons remain in the same y-z plane.

The corresponding expressions for $\dot{z}(t_i+\Delta t)$ are given by

$$\dot{z}(t_i+\Delta t) = -\frac{\eta E_z(t_i)}{\omega_c}\sin\omega_c\Delta t - \left[\frac{\eta E_{y_T}(t_i)}{\omega_c} + \dot{z}(t_i)\right](1-\cos\omega_c\Delta t) + \dot{y}(t_i)\sin\omega_c\Delta t + \dot{z}(t_i) \quad (6.22)$$

and

$$\dot{y}(t_i+\Delta t) = \frac{\eta E_z(t_i)}{\omega_c}(1-\cos\omega_c\Delta t) - \left[\frac{\eta E_{y_T}(t_i)}{\omega_c} + \dot{z}(t_i)\right]\sin\omega_c\Delta t + \dot{y}(t_i)\cos\omega_c\Delta t \quad . \quad (6.23)$$

Equations 6.18, 6.19, 6.22 and 6.23 represent the position and the velocity coordinates of an electron at the end of the unit time interval Δt_i in terms of the initial parameters evaluated at time t_i. The various electrons located at different points at time t_i are accounted for individually for the purpose of computing the space-charge fields. The error involved in these results will be small if the value of Δt and the elementary areas $dy_j\ dz_j$ discussed in Section 7.2 are taken as small.

6.7 Derivation of the Three-Dimensional Space-Charge Potential and Fields

As mentioned in Section 6.1, the Monte Carlo technique for calculating the noise transport in a crossed-field diode takes into account the space-charge fields due to several electrons distributed in the diode. At time $t = 0$, when there are no electrons in the diode, the potential distribution is given by Laplace's equation. The electrons emitted at later intervals will experience different potential distributions depending upon the electron distribution in the diode at time t_i. In Section 7.3 it will be described how different initial conditions may be used in order to make full use of the available computer memory throughout the complete execution of the program. However, after several unit intervals of time (this number is determined more or less arbitrarily), it will be necessary that the trajectory and the velocity equations given by Eqs. 6.18, 6.19, 6.22 and 6.23 include the total field components which depend upon the actual distribution of the electrons in the crossed-field diode. In this section an expression for the three-dimensional space-charge potential due to a charge q of a point (x_j, y_j, z_j) is derived by Green's function. The space-charge potential using Green's function was first derived by Gandhi and Rowe[31] for the interaction region and this expression for the space-charge potential has been modified appropriately for the gun region. The details for this derivation are given in Appendix F and the final expression for the space-charge potential V_{sc-j} at a point $(a/2, y, z)$ due to electrons uniformly distributed along the x-axis is given by

$$V_{sc-j}\left(\frac{a}{2}, y, z\right) = -\frac{|e|}{h\pi^2\epsilon_o} \ln \frac{1 + e^{-\frac{2\pi}{d}|z-z_j|} - 2\, e^{-\frac{\pi}{d}|z-z_j|} \cos\frac{\pi}{d}(y+y_j)}{1 + e^{-\frac{2\pi}{d}|z-z_j|} - 2\, e^{-\frac{\pi}{d}|z-z_j|} \cos\frac{\pi}{d}(y-y_j)}$$

$$\cdot\, W_{sc}\, N_j \quad , \qquad (6.24)$$

where

$$W_{sc} = \frac{1}{2}\tan^{-1}\frac{e^{-\frac{\pi}{a}|z-z_j|}\sin\frac{\pi h}{2a}}{1 - e^{-\frac{\pi}{a}|z-z_j|}\cos\frac{\pi h}{2a}}$$

$$+ \frac{1}{4}\tan^{-1}\frac{2\, e^{-\frac{\pi}{a}|z-z_j|}\sin\frac{\pi h}{2a} + e^{-\frac{2\pi}{a}|z-z_j|}\sin\frac{\pi h}{a}}{1 + e^{-\frac{2\pi}{a}|z-z_j|}\cos\frac{\pi h}{a} + 2\, e^{-\frac{\pi}{a}|z-z_j|}\cos\frac{\pi h}{2a}} \quad , \qquad (6.25)$$

N_j refers to the total number of electrons uniformly distributed in the jth mesh of volume $h\, dy_j\, dz_j$ and the center of gravity of these electrons is at the point $(a/2, y_j, z_j)$.

It may be pointed out here that by assuming uniform electron distribution bounded between $a-h/2$ and $a+h/2$ along the x-axis, the three-dimensional problem has been reduced to two dimensional and for convenience sake the N_j electrons may be considered as distributed in the elementary box of area $dy_j\, dz_j$, the y-z plane being located at $x = a/2$. This point is further discussed in Section 7.2.

The expression for the space-charge potential is advantageous as compared to that derived by the image method where the expression for the space-charge potential is determined by the effect of an infinite

number of images of a charge q at a point (x_j, y_j, z_j) and of course it is difficult to sum these infinite terms to obtain an analytic approximation within reasonable accuracy. Moreover, the image method fails to show an explicit dependence of V_{sc} on the parameters h and a. The reciprocity in Eq. 6.24 is evident; it can be shown that for $|z-z_j| = 0$, W_{sc} is independent of the values of h and a (except h = 0) and its value is equal to $\pi/4$.

The method for deriving the field components $E_{y_{sc-j}}(a/2,y,z)$ and $E_{z_{sc-j}}(a/2,y,z)$ due to N_j electrons uniformly distributed in the jth mesh of volume $h\, dy_j\, dz_j$ is given in Appendix F and the field components are given by the following equations:

$$E_{y_{sc-j}}\left(\frac{a}{2},y,z\right) = \frac{4|e|}{h\pi d\epsilon_o} \frac{e^{-\frac{\pi}{d}|z-z_j|}}{W'_{sc}} \left[\left(1 + e^{-\frac{2\pi}{d}|z-z_j|}\right)\cos\frac{\pi}{d}y - 2\, e^{-\frac{\pi}{d}|z-z_j|}\cos\frac{\pi}{d}y_j\right] N_j\, W_{sc} \sin\frac{\pi}{d}y_j \qquad (6.26)$$

and

$$E_{z_{sc-j}}\left(\frac{a}{2},y,z\right) = \mp \frac{4|e|}{h\pi\epsilon_o d} \frac{e^{-\frac{\pi}{d}|z-z_j|}}{W'_{sc}} \left\{\left[1 + e^{-\frac{2\pi}{d}|z-z_j|}\right]\left[1 - 2\, e^{-\frac{\pi}{d}|z-z_j|}\cos\frac{\pi}{d}y\cos\frac{\pi}{d}y_j\right] + 2\, e^{-\frac{2\pi}{d}|z-z_j|}\left[1 + \cos\frac{2\pi y}{d} + \cos\frac{2\pi y_j}{d}\right]\right\} N_j\, W'_{sc} \sin\frac{\pi}{d}y\cdot\sin\frac{\pi}{d}y_j \,, \qquad (6.27)$$

where

$$W'_{sc} = \left[1 + e^{-\frac{2\pi}{d}|z-z_j|} - 2\,e^{-\frac{\pi}{d}|z-z_j|}\cos\frac{\pi}{d}(y+y_j)\right]\left[1 + e^{-\frac{2\pi}{d}|z-z_j|} - 2\,e^{-\frac{\pi}{d}|z-z_j|}\cos\frac{\pi}{d}(y-y_j)\right] \quad (6.28)$$

and the minus and plus signs in Eq. 6.27 correspond to the conditions of $z > z_j$ and $z < z_j$ respectively. For $y = y_j$, $E_{y_{sc-j}} = 0$ and for $z = z_j$, $E_{z_{sc-j}} = 0$. The space-charge potential $V_{sc}(a/2,y_i,z_i)$ due to all the electrons distributed in the crossed-field diode is then given by

$$V_{sc}\left(\frac{a}{2},y_i,z_i\right) = \sum_j A_{ij}\,N_j \quad , \qquad (6.29)$$

where $A_{ij}N_j$ is given by the right-hand side of Eq. 6.24 for $y = y_i$ and $z = z_i$.

It should be pointed out here that the points $(a/2,y_i,z_i)$ for various values of i correspond to the centroids of various rectangles in the diode and the electrons are assumed to be uniformly distributed in every rectangle. This assumption is necessary in order to reduce the computation time. The division of the diode into various rectangles is described in Section 7.2. After such a division is made, it is possible to calculate numerically the values of A_{ij} given in Eq. 6.29 for various combinations of all the rectangles. This is referred to as the evaluation of the space-charge potential constants in this chapter.

The total potential and the two field components are given by

$$V_T\left(\frac{a}{2},y,z\right) = \frac{y}{d}V_o + V_{sc}\left(\frac{a}{2},y,z\right) , \tag{6.30a}$$

$$E_{y_o}\left(\frac{a}{2},y,z\right) = -\frac{V_o}{d} + E_{y_{sc}}\left(\frac{a}{2},y,z\right) \tag{6.30b}$$

and

$$E_{z_o}\left(\frac{a}{2},y,z\right) = E_{z_{sc}}\left(\frac{a}{2},y,z\right) , \tag{6.30c}$$

where V_o is the d-c potential applied at the anode at $y = d$ with respect to the cathode at $y = 0$ which is held at the zero potential. The two space-charge field components are evaluated by summing over the terms given by Eqs. 6.26 and 6.27 respectively for all the rectangles. This summation is similar to that given by Eq. 6.29. The suffix o has been used on the two field components since these expressions do not include the a-c field components. These components are derived in Section 6.9 and should be added to the d-c field components for an open-circuited diode. This point is discussed in detail in Section 6.9. In Eqs. 6.18, 6.19, 6.22 and 6.23 for trajectories and velocity components, the two field components are used and it is not necessary to evaluate the total potential. However, it can be seen that the computation of the two field components involves twice the computation time as compared to that for the space-charge potential and this time is proportional to the square of the total number of rectangles in the diode. Thus in order to save computation time, the two field components may be computed from the total voltage by the following equations:

$$(E_{y_o})_i = -\frac{V_T\left(\frac{a}{2}, y_{i+1}, z_i\right) - V_T\left(\frac{a}{2}, y_i, z_i\right)}{y_{i+1} - y_i} \tag{6.31a}$$

and

$$(E_{z_o})_i = -\frac{V_T\left(\frac{a}{2}, y_i, z_{i+1}\right) - V_T\left(\frac{a}{2}, y_i, z_i\right)}{z_{i+1} - z_i}, \tag{6.31b}$$

where the suffix i refers to the designation of the rectangle in the diode. The error involved in using Eqs. 6.31 will be less if the size of the rectangles is small. In any case a compromise between the computation time and the desired accuracy will be necessary.

6.8 Space-Charge Weighting Constants

In the evaluation of the space-charge constants as described in Section 6.6 from Eq. 6.24, it can be seen that a substitution of $y = y_j$ and $z = z_j$ in Eq. 6.2 gives rise to a singularity. This is similar to the singularity obtained after substituting $r = 0$ in an expression for the potential due to an electron at a point distant r from the test point. In this problem the space-charge constant A_{ii} may be substituted as equal to zero if the rectangles are very closely spaced and the number of electrons in the ith rectangle is negligible or if the space-charge potential is evaluated for every electron. For the present division of the crossed-field diode into a rather smaller number of rectangles (discussed in Section 7.2) it would be quite erroneous to substitute $A_{ii} = 0$ since one rectangle may have many electrons. For evaluating the space-charge constant A_{ii}, an arbitrary but uniform distribution of the electrons in the ith rectangle is assumed and this is shown in Fig. 6.2; the space-charge constants at the center

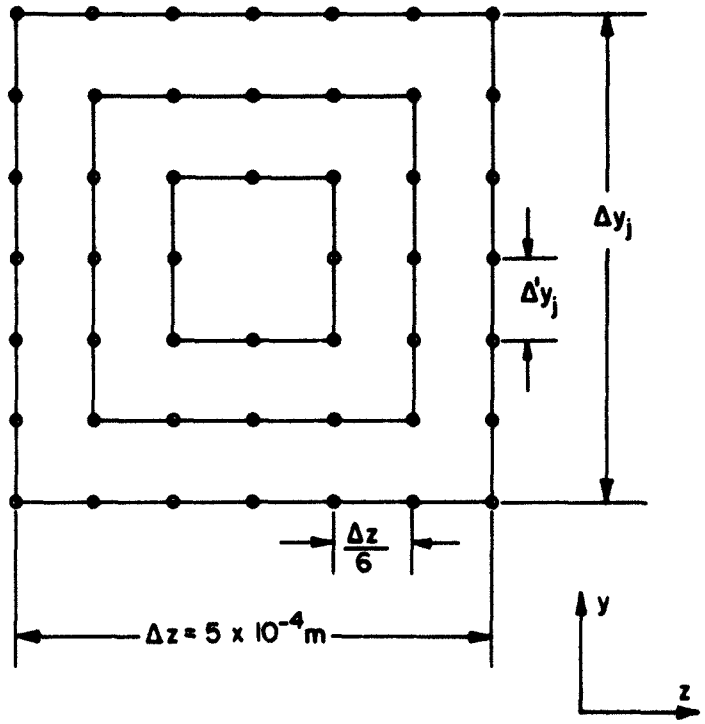

FIG. 6.2 A UNIFORM ELECTRON DISTRIBUTION ASSUMED TO EVALUATE THE SPACE-CHARGE WEIGHTING CONSTANT.

of the rectangle due to all the electrons in the same rectangle are evaluated. The mean values of the constants for the various rectangles, known as the space-charge weighting constants, are to be evaluated for rectangles distributed along the y-axis; in other words, $\mathring{A}_{ii}$'s are functions of y only. Also, since the space-charge potential is an even function of $z-z_j$, it is not necessary to compute these constants for all the electrons located as shown in Fig. 6.2; instead these constants may be computed for those electrons for which $z-z_j \geq 0$. However, in the process of evaluating the weighting constant A_{ii}, all the electrons in a rectangle are to be considered and the mean value of the space-charge constants for all the electrons in the ith rectangle is to be evaluated. Because of relatively larger values of Δy for rectangles numbered 11 - 17 (see Section 7.2), the value of $\Delta y'$, referred to as the distance between two neighboring electrons along the y-axis in Fig. 6.2, is reduced to $\Delta y_j/12$.

6.9 A-c Electric Fields, Velocities and Current Densities

As mentioned in Section 6.1, the noise transport in a crossed-field diode may be analyzed for any one of the four combinations from the following conditions:

1. Space-charge-limited or temperature-limited diode.
2. Short-circuited or open-circuited diode.

Condition 1 requires an additional restriction on the total number of electrons emitted and this in turn is related to the value of the operating temperature of the cathode which determines the saturation current density.

For condition 2, the case of an open-circuited diode requires an addition of a-c electric field components to the total d-c field

components given by Eqs. 6.31. For a short-circuited diode there are no a-c electric fields and the practical case of a finite impedance across the diode is rather difficult to analyze. For an open-circuited diode both the y-z components of the total a-c current density are equal to zero. This is expressed in terms of the corresponding Maxwell's equations as

$$-\frac{\partial H_x}{\partial y} = \epsilon_o \frac{\partial E_z}{\partial t} + (\rho \dot{z})_{a-c} = 0 \tag{6.32a}$$

and

$$\frac{\partial H_x}{\partial z} = \epsilon_o \frac{\partial E_y}{\partial t} + (\rho \dot{y})_{a-c} = 0 \ . \tag{6.32b}$$

From Eqs. 6.32, the two a-c field components are written as

$$\Delta E_{z_i}(t_i) = -\left[(\rho \dot{z})_{t_{i,i}}\right]_{a-c} \frac{\Delta t}{2\epsilon_o} \tag{6.33a}$$

and

$$\Delta E_{y_i}(t_i) = -\left[(\rho \dot{y})_{t_{i,i}}\right]_{a-c} \frac{\Delta t}{2\epsilon_o} \ , \tag{6.33b}$$

where $\Delta E_{z_i}(t_i)$ and $\Delta E_{y_i}(t_i)$ represent the two a-c field components acting on all the electrons in the ith rectangle at time t_i for a unit time interval Δt. Similarly $[(\rho \dot{z})_{t_{i,i}}]_{a-c}$ $[(\rho \dot{y})_{t_{i,i}}]_{a-c}$ represent the two a-c current densities evaluated at time t_i for the ith rectangle. A division by two is made so as to take the average effect.

Thus the a-c field components are evaluated from the two total current densities at time t_i and the two average current densities for the corresponding rectangle. In a one-dimensional case the total current density may be evaluated by knowing the total number

of electrons crossing the plane of interest per unit time per unit area and the a-c value of the current density at time t_i may be evaluated by taking the difference of the total current density at time t_i and the average value of the current density. This technique is quite simple for a one-dimensional model but is not easily applicable to the present two-dimensional problem. The current densities and the velocity components for the two-dimensional problem may be determined as described in the following paragraphs.

In fact, there are four parameters to be used in determining the noise spectrum in this problem. The equations for the noise spectrum are derived in Section 6.9 and the parameters to be used are:

1. The two a-c current density components.
2. The two a-c velocity components.

These parameters are to be evaluated for those rectangles which are of interest and for many unit time intervals. The two current density components are also used in evaluating the a-c field components given by Eqs. 6.33 when an open-circuited diode is being considered. For evaluating the a-c components, it is necessary to determine first the d-c components corresponding to the various rectangles. As mentioned in Section 6.1, the Monte Carlo technique for evaluating the noise transport is a more exact simulation of the diode and the d-c values of the four parameters may be obtained by averaging over the values of these parameters over a very large number of unit time intervals. For reducing the computation time, a very close approximation may be made so that once the diode has been filled with electrons the average values may be obtained from the data for several (noninfinite) number of time intervals and if necessary these average values may be used in

evaluating the a-c parameters in the subsequent set of time intervals. The average values obtained as a result of the first set of time intervals may be used in evaluating the a-c parameters in the next set of intervals and so on. This approximation is considerably time saving and the error involved in this approximation is small if the number of unit time intervals in each set is relatively large.

In Appendix G, some methods for averaging which are suitable for the present analysis are discussed and the selection of one method or the other is a matter of convenience. It is also shown in this appendix that it is not necessary to compute all four of the parameters as a function of time since the current densities are related to the velocities by the space-charge density. This saves computation time considerably. The two average velocity components for the ith rectangle are written as

$$(\dot{y}_o)_i = \frac{1}{(N_o)_i L} \sum_{t_i} \sum_{n_k} \dot{y}_i(t_i,n_k) \tag{6.34a}$$

and

$$(\dot{z}_o)_i = \frac{1}{(N_o)_i L} \sum_{t_i} \sum_{n_k} \dot{z}_i(t_i,n_k) \quad , \tag{6.34b}$$

where $\dot{y}_i(t_i,n_k)$ and $\dot{z}_i(t_i,n_k)$ refer to the two velocity components of the n_kth electron at time t_i for the ith rectangle. Summation over n_k includes all the electrons in the ith rectangle, while summation over t_i is carried out to include L unit time intervals. The average number of electrons $(N_o)_i$ for the ith rectangle is given by

$$(N_o)_i = \frac{1}{L} \sum_{t_i} N_i(t_i) \quad , \tag{6.35}$$

where $N_i(t_i)$ corresponds to the total number of electrons in the ith rectangle at time t_i. Equation 6.35 determines the value for $(\rho_o)_i$, the charge density for the ith rectangle, and this is given by

$$(\rho_o)_i = -|e| \frac{(N_o)_i}{h\, dy_i\, dz_i} \quad . \tag{6.36}$$

From Eqs. 6.34 and 6.36, the two average current density components for the ith rectangle are given by

$$(J_{y_o})_i = -\frac{|e|}{h\, dy_i\, dz_i\, L} \sum_{t_i} \sum_{n_k} \dot{y}_i(t_i,n_k) \tag{6.37a}$$

and

$$(J_{z_o})_i = -\frac{|e|}{h\, dy_i\, dz_i\, L} \sum_{t_i} \sum_{n_k} \dot{z}_i(t_i,n_k) \quad . \tag{6.37b}$$

The instantaneous values of the velocity components at time t_i for the ith rectangle are given by

$$\dot{y}_i(t_i) = \frac{1}{N_i(t_i)} \sum_{n_k} \dot{y}_i(t_i,n_k) \tag{6.38a}$$

and

$$\dot{z}_i(t_i) = \frac{1}{N_i(t_i)} \sum_{n_k} \dot{z}_i(t_i,n_k) \quad . \tag{6.38b}$$

The corresponding current density components are then given by

$$J_y(t_i) = \frac{-|e|}{h\, dy_i\, dz_i} \sum_{n_k} \dot{y}_i(t_i,n_k) \tag{6.39a}$$

and

$$J_z(t_i) = \frac{-|e|}{h\, dy_i\, dz_i} \sum_{n_k} \dot{z}_i(t_i,n_k) \quad . \tag{6.39b}$$

The two a-c current density components at time t_i for the ith rectangle can be obtained from Eqs. 6.37 and 6.39 and are given by

$$\tilde{J}_{y_i}(t_i) = \left[(\rho\dot{y})_{t_{i,i}}\right]_{a\text{-}c} = \frac{-|e|}{h\, dy_i\, dz_i} \left[\sum_{n_k} \dot{y}_i(t_i,n_k) - \frac{1}{L} \sum_{t_i} \sum_{n_k} \dot{y}_i(t_i,n_k) \right. \tag{6.40a}$$

and

$$\tilde{J}_{z_i}(t_i) = \left[(\rho\dot{y})_{t_{i,i}}\right]_{a\text{-}c} = \frac{-|e|}{h\, dy_i\, dz_i} \left[\sum_{n_k} \dot{z}_i(t_i,n_k) - \frac{1}{L} \sum_{t_i} \sum_{n_k} \dot{z}_i(t_i,n_k) \right] , \tag{6.40b}$$

where the sign ~ is used to indicate the a-c parameters. Similarly the corresponding a-c velocity components are given by

$$\tilde{\dot{y}}_i(t_i) = \frac{N_i(t_i)}{(N_o)_i} \left[\frac{1}{N_i(t_i)} \sum_{n_k} \dot{y}_i(t_i,n_k) - \frac{1}{(N_o)_i L} \sum_{t_i} \sum_{n_k} \dot{y}_i(t_i,n_k) \right] \tag{6.41a}$$

and

$$\tilde{\dot{z}}_i(t_i) = \frac{N_i(t_i)}{(N_o)_i}\left[\frac{1}{N_i(t_i)}\sum_{n_k}\dot{z}_i(t_i,n_k) - \frac{1}{(N_o)_i L}\sum_{t_i}\sum_{n_k}\dot{z}_i(t_i,n_k)\right] , \tag{6.41b}$$

where a weighting factor $N_i(t_i)/(N_o)_i$ is introduced in Eqs. 6.41a and 6.41b so that the average values of $\tilde{\dot{y}}_i(t_i)$ and $\tilde{\dot{z}}_i(t_i)$, averaged over L number of unit time intervals, tend to be zero. Then the a-c field components are given by using Eqs. 6.33 and 6.40.

$$\Delta E_{y_i}(t_i) = \frac{\Delta t|e|}{2\epsilon_o h\, dy_i\, dz_i}\left[\sum_{n_k}\dot{y}_i(t_i,n_k) - \frac{1}{L}\sum_{t_i}\sum_{n_k}\dot{y}_i(t_i,n_k)\right] \tag{6.42a}$$

and

$$\Delta E_{z_i}(t_i) = \frac{\Delta t|e|}{2\epsilon_o h\, dy_i\, dz_i}\left[\sum_{n_k}\dot{z}_i(t_i,n_k) - \frac{1}{L}\sum_{t_i}\sum_{n_k}\dot{z}_i(t_i,n_k)\right] . \tag{6.42b}$$

These values of the a-c field components are added to those obtained from Eqs. 6.31 when an open-circuited diode is being considered and the total field components are to be used in evaluating the trajectories and the velocity components of electrons given by Eqs. 6.18, 6.19, 6.22 and 6.23.

6.10 Correlation Functions and Spectra of Diode Noise

As mentioned in Section 6.9, the noise spectra of the crossed-field diode is evaluated from the two a-c current density components and the two a-c velocity components. These a-c parameters are given by Eqs. 6.40 and 6.41 and are characterized by the following properties:

1. They are not instantaneous values, but represent the average values averaged over the time interval Δt between t_i and $t_i+\Delta t$.
2. Each of these a-c parameters represents a discrete value equally spaced Δt apart.
3. These parameters are computed over a noninfinite total time interval.

In determining the correlation functions and the diode noise from the four a-c parameters given by Eqs. 6.40 and 6.41, the two a-c parameters defined as the variations in the total velocity and the total current density corresponding to the ith rectangle are written as

$$\vec{\tilde{J}}_i(t_i) \triangleq \vec{i}\,\lambda_1\,\tilde{J}_{z_i}(t_i) + \vec{j}\,\mu_1\,\tilde{J}_{y_i}(t_i) \tag{6.43a}$$

and

$$\vec{\tilde{u}}_i(t_i) \triangleq \vec{i}\,\lambda_2\,\tilde{z}_i(t_i) + \vec{j}\,\mu_2\,\tilde{y}_i(t_i) \quad , \tag{6.43b}$$

where $\vec{i}$ and $\vec{j}$ are the two unit vectors along the z- and y-axes respectively and λ_1, μ_1, λ_2 and μ_2 are the coupling factors. The values of these factors are determined by the type of coupling of the corresponding a-c parameters to the output and the absolute values of these factors may vary between 0 and 1.

For the a-c velocity $\vec{\tilde{u}}_i(t_i)$, the two-dimensional kinetic voltage $\vec{\tilde{V}}_i(t_i)$ may be defined as

$$\vec{\tilde{V}}_i(t_i) = -\frac{m}{|e|}\left[\vec{i}\,\lambda_2\,\tilde{z}_i(t_i) + \vec{j}\,\mu_2\,\tilde{y}_i(t_i)\right]|\mu_{o_i}| \quad , \tag{6.44}$$

where $|u_{o_i}|$ is the absolute value of the average velocity, defined as

$$|u_{o_i}| = (\dot{y}^2_{o_i} + \dot{z}^2_{o_i})^{1/2} \quad . \tag{6.45}$$

The definition of the kinetic voltage given by Eq. 6.44 follows directly from the energy gain equations similar to that of the one-dimensional kinetic voltage.

The auto-correlation function $C(\tau)$ for a complex variable $x(t)$ is defined by

$$C(\tau) = \lim_{T\to\infty} \frac{1}{2T} \int_{-T}^{T} x(t+\tau)\, x^*(t)\, dt \quad , \tag{6.46}$$

where $x^*(t)$ represents the complex conjugate of $x(t)$ where $x(t)$ can be considered as a generalized variable. By making use of Eqs. 6.43, 6.44, and 6.46, the auto-correlation functions $C_{\tilde{J}}(\tau,i)$ and $C_{\tilde{V}}(\tau,i)$ for $\vec{\tilde{J}}(t,i)$ and $\vec{\tilde{V}}(t,i)$ respectively are given by the following equations:

$$C_{\tilde{J}}(\tau,t) = \lim_{T\to\infty} \frac{1}{2T} \int_{-T}^{T} \Big\{\lambda_1^2\, \tilde{J}_z(t+\tau,i)\, \tilde{J}_z^*(t,i) + \mu_1^2\, \tilde{J}_y(t+\tau,t)\, \tilde{J}_y^*(t,i)\Big\}\, dt \tag{6.47a}$$

and

$$C_{\tilde{V}}(\tau,i) = \lim_{T\to\infty} \frac{1}{2T} \int_{-T}^{T} \Big\{\lambda_2^2\, \tilde{z}(t+\tau,i)\, \tilde{z}^*(t,i) + \mu_2^2\, \tilde{y}(t+\tau,i)\, \tilde{y}^*(t,i)\Big\} \cdot \left(\frac{u_{o_i}}{\eta}\right)^2 dt \quad , \tag{6.47b}$$

where the suffix i corresponding to the ith rectangle is shifted within the parenthesis. The variations in the y-component of an a-c parameter are independent of the variations in the z-component of the same a-c parameter for the ith rectangle; of course, the two variations for the i+1th rectangle are related to the two variations for the ith rectangle in a rather complex manner. This is also clear from the fact that the dot product between orthogonal vectors in developing Eqs. 6.47 gives zero values. It may also be shown that the auto-correlation functions are even functions of the argument τ. In the present problem, all the variables are real functions of t and i, thus

$$\tilde{J}_z^*(t,i) = \tilde{J}_z(t,i) \quad ,$$

$$\tilde{J}_y^*(t,i) = \tilde{J}_y(t,i) \quad , \tag{6.48}$$

Because of the noninfinite and discrete nature of the expected data, Eqs. 6.47 reduce to (after using Eq. 6.48):

$$C'_{\tilde{J}}(\mu\Delta t,i) = \frac{1}{2N+1} \sum_{\nu=-N}^{N} \Big\{ \lambda_1^2 \, \tilde{J}_z[(\nu+\mu)\Delta t,i] \cdot \tilde{J}_z(\nu\Delta t,i)$$

$$+ \mu_1^2 \, \tilde{J}_y \, [(\nu+\mu)\Delta t,i] \cdot \tilde{J}_y(\nu\Delta t,i) \Big\} \tag{6.49a}$$

and

$$C'_{\tilde{V}}(\mu\Delta t,i) = \frac{1}{2N+1} \sum_{\nu=-N}^{N} \Big[\lambda_2^2 \, \tilde{z}[(\nu+\mu)\Delta t,i] \cdot \tilde{z}(\nu\Delta t,i)$$

$$+ \mu_2^2 \, \tilde{y} \, [(\nu+\mu)\Delta t,i] \cdot \tilde{y}(\nu\Delta t,i) \Big] \left[\frac{u_{o_i}}{\eta} \right]^2 \quad , \tag{6.49b}$$

where the symbols N, ν, and μ are defined as

$$T_n = N\Delta t$$

$$t = \nu\Delta t \qquad \nu = 1, 2, \ldots N$$

$$\tau = \mu\Delta t \qquad |\mu| = 0, 1, 2 \ldots, M \ , \tag{6.50}$$

where T_n is the length of the record and the prime sign is added to the two auto-correlation functions indicating that these functions are based upon noninfinite and discrete data. The variable ν refers to the discrete position along the time axis. The variable μ is used to determine the auto-correlation or cross-correlation functions at any discrete position corresponding to the value of μ along the time axis. It is shown later in this section that by properly selecting the maximum value of μ, a fairly good estimate of the power spectrum densities can be made in the neighborhood of the selected frequency f. The maximum limit of μ is referred to as M in Eq. 6.61. Since the practical case is limited for positive time intervals only, the a-c parameters reduce to

$$\mathfrak{J}_y[(\nu+\mu)\Delta t,i] = \mathfrak{J}_z[(\nu+\mu)\Delta t,i] = \tilde{z}[(\nu+\mu)\Delta t,i] = \tilde{y}[(\nu+\mu)\Delta t,i] = 0 \tag{6.51}$$

for all i's under the condition $\nu > N-\mu$. With the following designation,

$$C'_J(\mu\Delta t,i) = C'_J(\mu,i) \ ,$$

$$J'_z[(\nu+\mu)\Delta t,i] = J'_z(\nu+\mu,i) \ , \tag{6.52}$$

etc., and with the condition given by Eq. 6.51, Eqs. 6.49 are reduced to

$$C'_{\tilde{I}}(\mu,i) = \frac{1}{N-\mu}\sum_{\nu=1}^{N-\mu}\left[\lambda_1^2\,\tilde{J}_z(\nu+\mu,i)\cdot\tilde{J}_z(\nu,i) + \mu_1^2\,\tilde{J}_y(\nu+\mu,i)\cdot\tilde{J}_y(\nu,i)\right]A_i^2 \tag{6.53a}$$

and

$$C'_{\tilde{V}} = \left[\frac{u_{o_i}}{\eta}\right]^2\frac{1}{N-\mu}\sum_{\nu=1}^{N-\mu}\left[\lambda_2^2\,\tilde{z}(\nu+\mu,i)\cdot\tilde{z}(\nu,i) + \mu_2^2\,\tilde{y}(\nu+\mu,i)\,\tilde{y}(\nu,i)\right] , \tag{6.53b}$$

where $C'_{\tilde{I}}(\mu,i)$ corresponds to the current fluctuations instead of current density fluctuations and A_i is the effective cross-sectional area of the beam corresponding to the ith rectangle. The cross-correlation functions of any two variables $x(t)$ and $y(t)$ are defined as

$$A_{xy}(\tau) = \lim_{T\to\infty}\frac{1}{2T}\int_{-T}^{T} x(t+\tau)\,y^*(t)\,dt \tag{6.54a}$$

and

$$A_{yx}(\tau) = \lim_{T\to\infty}\int_{-T}^{T} y(t+\tau)\,x^*(t)\,dt \quad . \tag{6.54b}$$

Proceeding in the same manner as in the development of Eqs. 6.53, the cross-correlation functions of the two variables, namely, the fluctuations in the current and the kinetic potential for the noninfinite discrete data, are given by

$$B_{\tilde{V},\tilde{I}}(\mu,i) = -\left[\frac{u_{o_i}A_i}{\eta}\right]\frac{1}{N-\mu}\sum_{\nu=1}^{N-\mu}\lambda_1\lambda_2\,\tilde{z}(\nu,i)\cdot\tilde{J}_z(\nu+\mu,i)$$

$$+\,\mu_1\mu_2\,\tilde{y}(\nu,i)\,\tilde{J}_y(\nu+\mu,i)\Big] \tag{6.55a}$$

and

$$A_{\tilde{I},\tilde{V}}(\mu,i) = -\left[\frac{u_{o_i}A_i}{\eta}\right]\frac{1}{N-\mu}\sum_{\nu=1}^{N-\mu}\left[\lambda_1\lambda_2\,\tilde{\mathcal{I}}(\nu+\mu,i)\cdot\tilde{J}_z(\nu,i)\right.$$

$$\left.+\,\mu_1\mu_2\,\tilde{\mathcal{J}}(\nu+\mu,i)\cdot\tilde{J}_y(\nu,i)\right] , \quad (6.55b)$$

The noise power spectrum corresponding to some fluctuations given by x(t) is obtained by the Fourier transform of the autocorrelation function $C_x(\tau)$ defined by Eq. 6.46, and is given by

$$W_x(f) = \int_{-\infty}^{\infty} C_x(\tau)e^{-j2\pi f\tau}\,d\tau \quad . \qquad (6.56)$$

In a practical case the length of the record is discrete and noninfinite and hence this record will not lead to the true estimate of the power spectrum. Blackman and Tukey[23] have shown that a more reliable estimate of smoothed values of the true spectral density may be obtained by taking the Fourier transform of the modified apparent correlation function. This function is obtained by multiplying the actual correlation functions obtained in a practical situation (given by Eqs. 6.53 and 6.55) by suitable even functions of τ. This function modifies the apparent correlation function for different lags and thus is often referred to as a lag window. The modified apparent correlation functions are often far from being respectable estimates of the true correlation functions but their transforms are very respectable estimates of smoothed values of the true spectral density. This method of obtaining the spectral density helps also in reducing the computation

time by defining $|\tau| \leq T_m < T_n$, where T_n is the length of the record and T_m is the maximum lag which one desires to use.

Blackman and Tukey have discussed various functions of τ, defined by $D(\tau)$ for this purpose, and the selection of one or the other depends upon how $Q(f)$ defined as the Fourier transform of $D(\tau)$ is distributed in the frequency domain. The various equations describing the Fourier transform of the apparent modified correlation function $C(\tau)$ have been derived by Blackman and Tukey, but a few equations are given here for the sake of continuity. The modified correlation function $C_i(\tau)$ is defined as

$$C_i(\tau) = D_i(\tau)\, C'_i(\tau) \quad , \tag{6.57}$$

then

$$\text{avg. } \{C_i(\tau)\} = D_i(\tau)\, C(\tau) \quad , \tag{6.58}$$

where $C(\tau)$ is the true auto-correlation function and Eq. 6.58 follows from Eq. 6.57 because of ergodicity assumed in this analysis. The relationship between $P_i(f)$, the Fourier transform of $C_i(\tau)$ and $P(f)$, the true power spectrum, is given by a convolution integral

$$\text{avg. } \{2\, P_i(f_i)\} = \int_0^\infty H_i(f;f_i)\; 2\, P(f)\, df \quad , \tag{6.59}$$

where

$$H_i(f;f_i) = Q_i(f+f_i) + Q_i(f-f_i) \quad . \tag{6.60}$$

Thus the expected estimates will have their average values obtained by smoothing of the true power spectral density $P(f)$ over frequencies "near" f_i and these estimates will not be the same as the

estimates of $P(f_1)$ itself. Thus in selecting the function $D_1(\tau)$, it is necessary that the Fourier transform $Q_1(f)$ is concentrated near $f = 0$ and is vanishingly small at frequencies far from $f = 0$. For this purpose, the function $D_1(\tau)$ should be flat and rather blocky with smooth and gentle variations. Since $D_1(\tau)$ is defined as equal to zero for $|\tau| > T_m$, the following function has been selected for this problem as a result of compromise:

$$D(\mu) = \frac{1}{2}\left(1 + \cos\frac{\pi\mu}{M}\right) \qquad \mu = 0, 1 \ldots M-1$$

$$= 0 \qquad \text{for} \quad \mu \geq M \ , \tag{6.61}$$

where μ is defined in Eq. 6.50 and M is defined as

$$T_m = M\Delta t \ . \tag{6.62}$$

Then $Q(f)$, the Fourier transform of $D(\mu)$, is given by

$$Q(f) = \frac{1}{2}Q_o(f) + \frac{1}{4}\left[Q_o\left(f + \frac{1}{2T_m}\right) + Q_o\left(f - \frac{1}{2T_m}\right)\right] \ , \tag{6.63}$$

where

$$Q_o(f) = 2T_m \frac{\sin 2\pi f T_m}{2\pi f T_m} \tag{6.64}$$

and is the Fourier transform of the function

$$D_1(\mu) = 1 \quad \text{for} \quad \mu \leq M$$

$$= 0 \qquad \mu > M \ . \tag{6.65}$$

The variation of $Q(f)$ and $Q_o(f)$ as a function of T_m is given in Fig. 6.3 and the justification made in modifying the apparent correlation function by multiplying $C'(\tau)$ by $D(\tau)$ is apparent. This is based upon the restriction that the function $Q_1(f)$ should be concentrated near $f = 0$ and vanishingly small at frequencies far from $f = 0$; this restriction follows from Eqs. 6.59 and 6.60.

The self-power spectral densities $\psi(f,i)$ and $\Phi(f,i)$ corresponding to the current and velocity fluctuations respectively for the ith rectangle are given by

$$\psi(f,i)\Delta f = \sum_{\mu=0}^{M-1} \left(1 + \cos \frac{\pi\mu}{M}\right) \frac{1}{N-\mu} \sum_{\nu=1}^{N-\mu} \left[\lambda_1^2 \tilde{J}_z(\nu+\mu,i)\, \tilde{J}_z(\nu,i) + \mu_1^2 \tilde{J}_y(\nu+\mu,i)\, \tilde{J}_y(\nu,i)\right] A_i^2 \cos 2\pi f\mu\Delta t \quad (6.66a)$$

and

$$\Phi(f,i)\Delta f = \sum_{\mu=0}^{M-1} \left(1 + \cos \frac{\pi\mu}{M}\right) \left[\frac{u_{o_i}}{\eta}\right]^2 \frac{1}{N-\mu} \sum_{\nu=1}^{N-\mu} \left[\lambda_2^2 \tilde{z}(\nu+\mu,i)\, \tilde{z}(\nu,i) + \mu_1^2 \tilde{y}(\nu+\mu,i)\, \tilde{y}(\nu,i)\right] \cos 2\pi f\mu\Delta t \quad , \quad (6.66b)$$

where use is made of Eqs. 6.53, 6.56 and 6.57 and the fact that the auto-correlation functions are even functions of τ. Similarly the cross power spectral densities corresponding to the cross-correlation functions defined by Eqs. 6.55 are given by

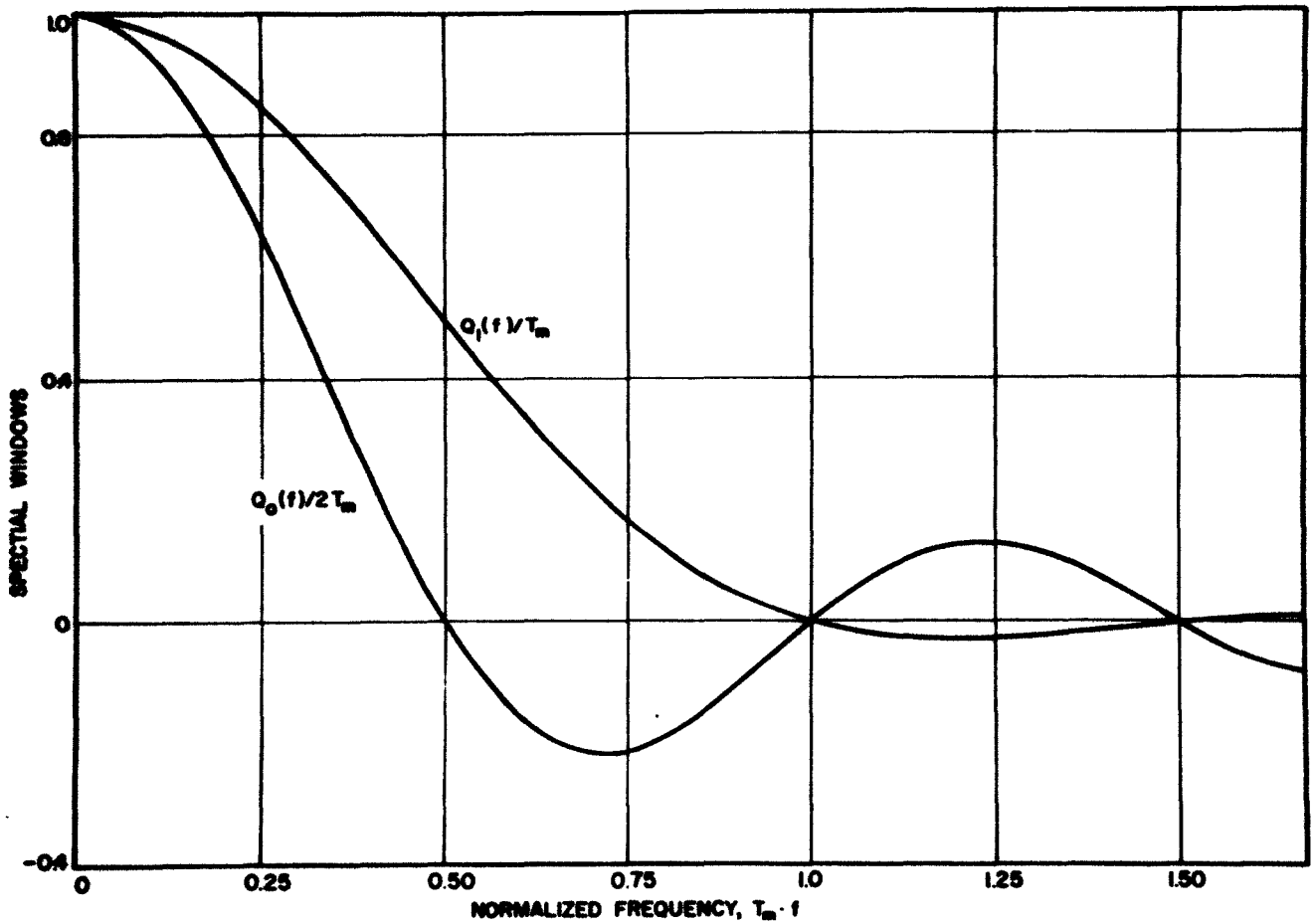

FIG. 6.3 SPECTRAL WINDOW VS. NORMALIZED FREQUENCY.

$$\Pi(f,i)\Delta f = \sum_{\mu=0}^{M-1} \frac{1}{2}\left(1 + \cos\frac{\pi\mu}{M}\right)\left[B(\mu,i) + A(\mu,i)\right] \cos 2\pi f\mu\Delta t \quad (6.67a)$$

and

$$\Lambda(f,i)\Delta f = \sum_{\mu=0}^{M-1} \frac{1}{2}\left(1 + \cos\frac{\pi\mu}{M}\right)\left[B(\mu,i) - A(\mu,i)\right] \sin 2\pi f\Delta t \quad , \quad (6.67b)$$

where the property of cross-correlation functions, namely

$$C_{xy}(-\tau) = C_{yx}(\tau) \quad , \quad (6.68)$$

is also assumed in developing Eqs. 6.67. The significance of the parameters ψ, Φ, Π and Λ has been discussed in detail by Haus[33] and this approach has been used by Dayem to determine the noise transport in traveling-wave tubes for a one-dimensional case using the Monte Carlo technique.

In Eqs. 6.66 and 6.67 these parameters have been defined for the ith rectangle in a general form and this will be of use to determine the noisiness of the various sections of the beam. By assuming Haus's formulas for minimum noise figure, $F(f,i)$ can be used for the ith rectangle; then

$$F(f,i) = 1 + \left[S(f,i) - \Pi(f,i)\right]\frac{2\pi}{kT} \quad , \quad (6.69)$$

where

$$S(f,i) = \left[\psi(f,i)\,\Phi(f,i) - \Lambda^2(f,i)\right]^{1/2} \quad . \quad (6.70)$$

By using a lag window defined by Eq. 6.61 a more reliable estimate of the noise spectrum may be expected from a discrete data of finite length but the exact identification of the frequencies should not be

expected. This is because of the limitations imposed on the selection of the function $D(\tau)$. However, a smoothed estimate of noise spectrum in the neighborhood of the desired frequency can be estimated. Thus it is not necessary to compute the noise figure at all the frequencies; instead these computations should be made at frequencies spaced over intervals of at least $1/T_m$ which follows directly from the definition of $Q(f)$ given by Eq. 6.63 and the discussion following Eqs. 6.59 and 6.60.

CHAPTER VII. RESULTS OF MONTE CARLO ANALYSIS

7.1 Introduction

The equations derived in the last chapter for the noise transport in a three-dimensional problem are quite general. In order to apply these equations to a practical situation, it is necessary to choose some specific numerical values for the various independent parameters. It is then necessary to consider a practical diode and divide it into many rectangles. As mentioned in Section 6.7, the electron distribution is assumed to be uniform along the x-axis and, by integrating the space-charge potential with respect to x between the limits $(a-h)/2$ and $(a+h)/2$, the three-dimensional problem is reduced to a two-dimensional problem. This corresponds to the evaluation of the fluctuations in the current and the velocity in the y-z plane located at $x = a/2$ which is the center of the beam along the x-axis. Thus the beam width does not appear explicitly in some of the equations in this chapter. Numerical values for the various parameters defined in the last chapter are substituted on the basis of a compromise between the accuracy and the computation time. In the latter section of this chapter the results of the analysis are given.

7.2 Choice of Parameters

7.2.1 Spatial Division of the Diode. In Section 6.7 the method of determination of the space-charge potential is outlined. For this purpose, the complete diode is divided into a few rectangles and the electrons in each rectangle are assumed to be uniformly distributed. The choice of the number of rectangles is based on a compromise between

the desired accuracy and the amount of computation time involved. Because of the small values of the velocities of the electrons near the cathode, it is considered essential that the rectangles in this region be closely spaced. In the presence of a magnetic field B ($B \geq B_c$), the y-component of the electron velocity near the anode is also small and thus the rectangles near the anode should also be closely spaced. This division of the diode along the y-axis is sufficiently general so that any value of $B \geq B_c$ may be used for evaluating noise transport in the gun region. In a specific case when $B > B_c$ and the electrons do not come close to the anode, it is advantageous to have less spacing between the two consecutive rectangles in the middle of the diode and not worry about the spacing of the rectangles near the anode. Considering various factors such as computer time, available computer memory and the variation of the velocities, the value of Δy, the distance between the two neighboring rectangles along the y-axis, has been selected as

$$\begin{aligned}
\Delta y &= 5.0 \times 10^{-6}\ \text{m} & 0 \leq y \leq 2.5 \times 10^{-5} \\
\Delta y &= 3.5 \times 10^{-5}\ \text{m} & 2.5 \times 10^{-5} \leq y \leq 2.0 \times 10^{-4} \\
\Delta y &= 3.0 \times 10^{-4}\ \text{m} & 2.0 \times 10^{-4} \leq y \leq 1.4 \times 10^{-3} \\
\Delta y &= 6.0 \times 10^{-4}\ \text{m} & 1.4 \times 10^{-3} \leq y \leq 5.0 \times 10^{-3} \quad . \qquad (7.1)
\end{aligned}$$

Unless specified, mks units are used throughout.

The value of the parameter d, the cathode-anode spacing, is taken as 0.5 cm which is the same as that used by Van Duzer[11] and in the density function method discussed in Chapters IV and V of this report. For greater accuracy, it is desirable to have as many rectangles as possible, however the computation time required for the evaluation of the space-charge potential varies as the square of the total number of the

rectangles in the diode. It is expected that the division of the diode given by Eq. 7.1 will yield a good compromise between accuracy and the computation time. For the division of the diode along the z-axis it is noticed that for nonuniform spacing Δz, the total number of the space-charge constants discussed in Section 6.7 varies as square of the total number of the rectangles and this would require a larger memory and computation time for the solution of this problem. For a uniform spacing Δz, the total number of space-charge constants varies proportionately to the total number of divisions along the z-axis. Considering this problem and the other problems in relation to the total number of rectangles and noting that our main interest lies with phenomena in the gun region, a total number of thirteen divisions along the z-axis with an equal spacing of

$$\Delta z = 5 \times 10^{-4} \text{ m} \tag{7.2}$$

are taken. This makes the total number of rectangles in the diode 260.

It is convenient to specify the plots of the results obtained from this analysis in terms of the numbers of different rectangles. For the convenience of the reader Table 7.1 is included to indicate the division of the diode in 260 rectangles. The data for $\dot{y}_i(t_i)$, $\dot{z}_i(t_i)$ and $N_i(t_i)$ were taken for the rectangles with underlined numbers. The correlation functions and the various noise parameters are computed for fifteen rectangles and this correspondence is given by

$$\begin{array}{llll} 71 \rightarrow 1 \ , & 73 \rightarrow 2 \ , & 97 \rightarrow 3 \ , & 120 \rightarrow 4 \ , \\ 125 \rightarrow 5 \ , & 157 \rightarrow 6 \ , & 158 \rightarrow 7 \ , & 165 \rightarrow 8 \ , \\ 166 \rightarrow 9 \ , & 167 \rightarrow 10 \ , & 248 \rightarrow 11 \ , & 249 \rightarrow 12 \ , \\ 256 \rightarrow 13 \ , & 257 \rightarrow 14 \ , & \text{and} & 258 \rightarrow 15 \ . \end{array} \tag{7.3}$$

Table 7.1

Division of the Diode and Beam Configuration

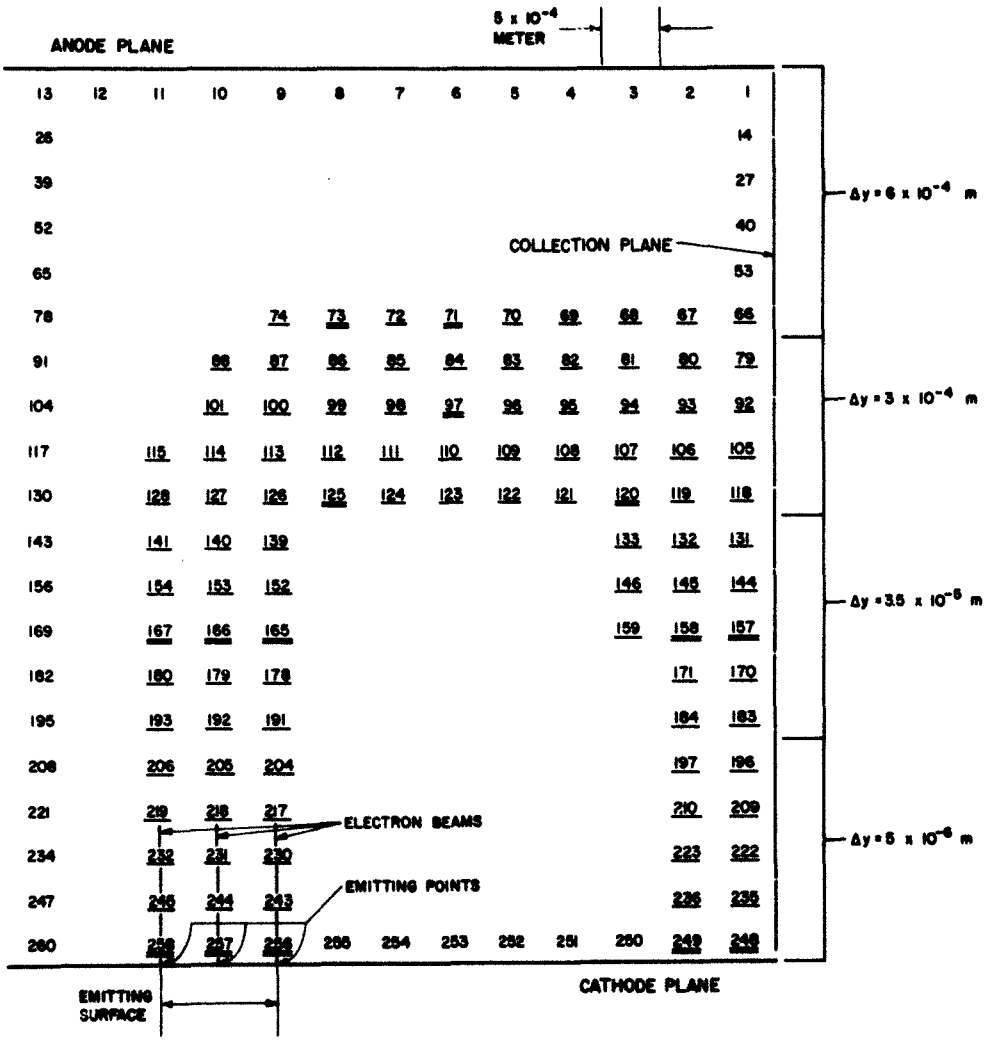

These fifteen rectangles are denoted by double underscores and the results are designated by numbers 1 through 15 of the rectangles.

The evaluation of the space-charge potential from Eq. 6.29 involves the evaluation of the space-charge constants for various combinations of the coordinates of the centers of these rectangles. This space-charge potential is to be evaluated at the end of every Δt time interval. For this reason, it has been considered necessary to compute these constants $A_{ij}(A_{ij} = A_{ji})$ and store them in the available computer memory. At the end of every unit time interval, the electrons are counted in each rectangle and Eq. 6.29 is used for the evaluation of the space-charge potential.

7.2.2 Choice of Unit Time Interval. It was noted in Section 6.10 that the fluctuations in the current and the velocity, recorded every Δt interval, represent the average values averaged over the time interval Δt. Thus if $x(t)$ is a continuous function of time and $y(t)$ represents the average of $x(t)$ averaged over the time Δt and given by

$$y(t) = \frac{1}{\Delta t} \int_{\zeta=t-\Delta t}^{t} x(\zeta)\, d\zeta \quad , \tag{7.4}$$

then the power spectrums $P_y(f)$ and $P_x(f)$ for the functions $y(t)$ and $x(t)$ respectively are related as

$$P_y(f) = \left(\frac{\sin \pi f \Delta t}{\pi f \Delta t}\right)^2 P_x(f) \quad . \tag{7.5}$$

This illustrates that averaging over Δt attenuates the spectrum at high frequencies.

A derivation for the final power spectrum for the discrete data is given in Appendix H. This derivation has been given by Dayem[22] and is included here for the sake of continuity. The final relation is given by

$$P(f) = Q(f)^* \left[\left(\frac{\sin \pi f/f_o}{\pi f/f_o} \right)^2 \sum_{n=-\infty}^{\infty} \frac{P_x(f-nf_o)}{\left(\frac{nf_o}{f} - 1 \right)^2} \right] , \qquad (7.6)$$

where $f_o = 1/\Delta t$ and the asterisk indicates the convolution. The term $Q(f)$ has been defined in Eq. 6.63. If f/f_o is very small then

$$P_y(f) \approx P_x(f) \qquad (7.7)$$

from Eq. 7.5 and then only the $n = 0$ term need be considered in the series expansion on the right-hand side of Eq. 7.6. This is known as protection against "aliasing". Thus with the proper choice of Δt, it is possible to reduce aliasing to a negligible amount in the frequency range of interest. For this purpose Δt is taken as

$$0 < \Delta t < \frac{0.1}{|f|} . \qquad (7.8)$$

Assuming the upper limit for $|f|$ to be 10 Gc for this analysis, the limiting value of Δt is given by

$$\Delta t = 10^{-11} \text{ seconds.} \qquad (7.9)$$

<u>7.2.3 Number of Electrons Emitted Per Unit Time Interval</u>. It is noted in Section 6.3 that the number of electrons emitted per unit time interval is given by Poisson's distribution expressed by Eq. 6.1. In order to determine the number of electrons emitted in different unit time

intervals from Eqs. 6.1 through 6.4 in association with the random numbers generated in each unit time interval, it is necessary to determine first the value of n_a, the average number of electrons emitted per unit time interval. The value of the parameter n_a depends upon the values of the following parameters:

1. The dimensions h and w which are the length and the width of the cathode along the x- and z-axes respectively.
2. The saturation current density I_s; this parameter is determined by the nature of the cathode and the operating temperature T_c.
3. The unit time interval Δt.

With the choice of the cathode parameters as

$$h = 2 \times 10^{-2} \text{ m}$$

$$w = 1 \times 10^{-3} \text{ m}$$

$$I_s = 5 \times 10^{3} \text{ amps/m}^2 \tag{7.10}$$

which are practical values for a typical injected-beam crossed-field tube, the total number of electrons emitted per unit time interval is given by

$$n_a = \frac{hw\, I_s \Delta t}{|e|} \simeq 6.25 \times 10^{6} \quad . \tag{7.11}$$

The value of I_s given by Eq. 7.10 is selected to give space-charge-limited operation of the diode; for a temperature-limited diode the value of I_s will be greatly reduced. Now if it is assumed that one-third of the emitted electrons are reflected back to the cathode as a result of the presence of the potential minimum (this number depends very much upon the degree of the space-charge limiting and is taken here

arbitrarily as one third) and that an electron takes, on the average, approximately 200 unit time intervals to reach the exit plane at $z = 6.5 \times 10^{-3}$ m, the total number of electrons in the diode would be of the order of 10^8. It would be almost impossible to account for the positions and the velocities for these individual electrons. This difficulty may certainly be alleviated by considering a diode with reduced dimensions according to the following scaling equations*.

$$\frac{x_2}{x_1} = \frac{y_2}{y_1} = \frac{z_2}{z_1} = D_1 \quad , \qquad t_2 = t_1 \quad ,$$

$$E_2 = D_1 E_1 \qquad \mu_{o2} = \mu_{o1}/D_1$$

$$B_2 = B_1 \qquad \rho_2 = \rho_1/D_1$$

$$J_2 = J_1 \qquad V_2 = D_1^2 V_1$$

$$\epsilon_{o2} = \epsilon_{o1}/D_1 \qquad q_2 = D_1^2 q_1 \quad , \tag{7.12}$$

where suffixes 1 and 2 refer to the two systems in consideration and D_1 is the geometrical scaling parameter.

Essentially this is equivalent to considering the original diode, generating an average number of n_a/D_1^2 electrons per unit interval, multiplying the number of electrons in each rectangle (after the counting is over) by a factor D_1^2, and then computing the various parameters.

---

* The equations of motion and Maxwell equations are preserved in the two systems. This scaling is different from that given by Spangenberg, K. R., Vacuum Tubes, McGraw Hill Book Company; 1958.

Statistically speaking, this alternative is equivalent to considering groups of electrons, each group consisting of identical D_1^2 electrons located at the center of gravity of the respective group (this is assumed for convenience in numerical computations). The electrons in each group are also assumed to be uniformly distributed so that the electrostatic forces among these D_1^2 electrons balance out. In a statistical sense the larger the sample, the more reliable the results, but considering the problems of the required memory and the computation time, the second alternative is considered, i.e., each unit of charge is equivalent to a charge of D_1^2 number of electrons, and this alternative is rather straightforward. The value of the parameter D_1^2 is given in a later part of this section.

In order to simulate the electron emission and the electron flow in the crossed-field diode under consideration closer to the actual electron flow in a practical tube, it will be necessary to consider electron emission from various points distributed along the z-axis on the cathode of width w. In such a case it will be necessary to have the diode divided into divisions along the z-axis, each division being smaller or at least equal to the spacing between the two adjacent points on the cathode from where the electrons are being emitted. This will again increase the total number of rectangles which will then increase the required memory and the computation time. For this purpose, only three emitting points on the cathode are considered, with the total emission from these three points being equal to the total emission from the complete cathode. It is also pointed out here that as mentioned in Section 7.1 the three-dimensional problem has been reduced to a two-dimensional problem and thus the parameter h, the length of the

cathode along the x-axis does not appear explicitly. The parameter N_j, the total number of electrons in the jth rectangle of volume $h\ dy_j\ dz_j$, given in Eq. 6.29 for the evaluation of the space-charge potential may be taken as the number of electrons in the jth rectangle of area $dy_j\ dz_j$ in the y-z plane without any loss in generality provided all the electrons are also emitted and their motion observed in the same y-z plane which happens to be located at $x = a/2$. This is justified since electron emission is considered to be uniform along the x-axis and in this manner the difficulty of keeping track of electrons emitted from the cathode from various points distributed along the x-axis is avoided. Also this does not affect the evaluation of the space-charge potential.

As stated above the total emission from the cathode is simulated from three points on the cathode and these three points are taken as $(a/2, 0, z_{o1})$, $(a/2, 0, z_{o2})$ and $(a/2, 0, z_{o3})$. The values of z_{o1}, z_{o2} and z_{o3} are given by 0.125 cm, 0.175 cm and 0.225 cm respectively. These three points correspond to the two edge points and one central point of the cathode of width $w = 0.1$ cm. Furthermore these points are also taken as centers of the three divisions each of width $\Delta z = 5 \times 10^{-4}$ m along the z-axis. In order to take into account the electrons with negative z-directed velocities the value of z_{o1} is not taken as zero. Considering the size of the computer memory, which can be used to keep account of the positions and velocities of the electrons, the parameter n_a, representing the average number of electrons emitted from each of the three points of the cathode per unit time interval, is taken as 7. This corresponds to N_a, the average value of the number of electrons emitted from the cathode per unit time interval, equal to 21. The value of D_1^2, the square of the scaling parameter, is then $= 2.97 \times 10^5$.

Figure 7.1 shows the variation of F(s) given by Eq. 6.2, versus s. For every unit time interval a random number is compared with the value of F(s) and the number of electrons generated is determined by Eq. 6.4. The number of electrons generated from each of the three points is determined independently.

7.3 Initial Conditions and Execution of the Program

It was mentioned in the last chapter that by using appropriate initial conditions, i.e., values of the minimum potential and its position close to the actual values, the computer memory could be used most effectively. For this purpose the results for the potential distribution obtained in Chapter V were used. This potential distribution is given in Figs. 5.6 and 5.7. Figure 7.2 shows the flow chart for the execution of the program. Phase A refers to those time intervals when the diode is being filled with electrons and use is made of the initial conditions, while Phase B refers to those unit time intervals during which the self-consistent space-charge potential is determined. The space-charge fields are evaluated to determine the trajectories and velocities of the various electrons in the diode. This part of the program is necessary in order to obtain steady-state conditions in the diode. Phase C which is not shown in Fig. 7.2 refers to the execution of the program as in Phase B but the data, i.e., the number of electrons in the various rectangles and their average velocity components, are recorded for several unit time intervals. The rectangles chosen for this purpose were determined on the basis of the beam profile which is shown in Fig. 7.3. During Phase B of the program the number of electrons in the various rectangles, their associated average velocity components and the total potential corresponding to the centroids of these rectangles were determined for several

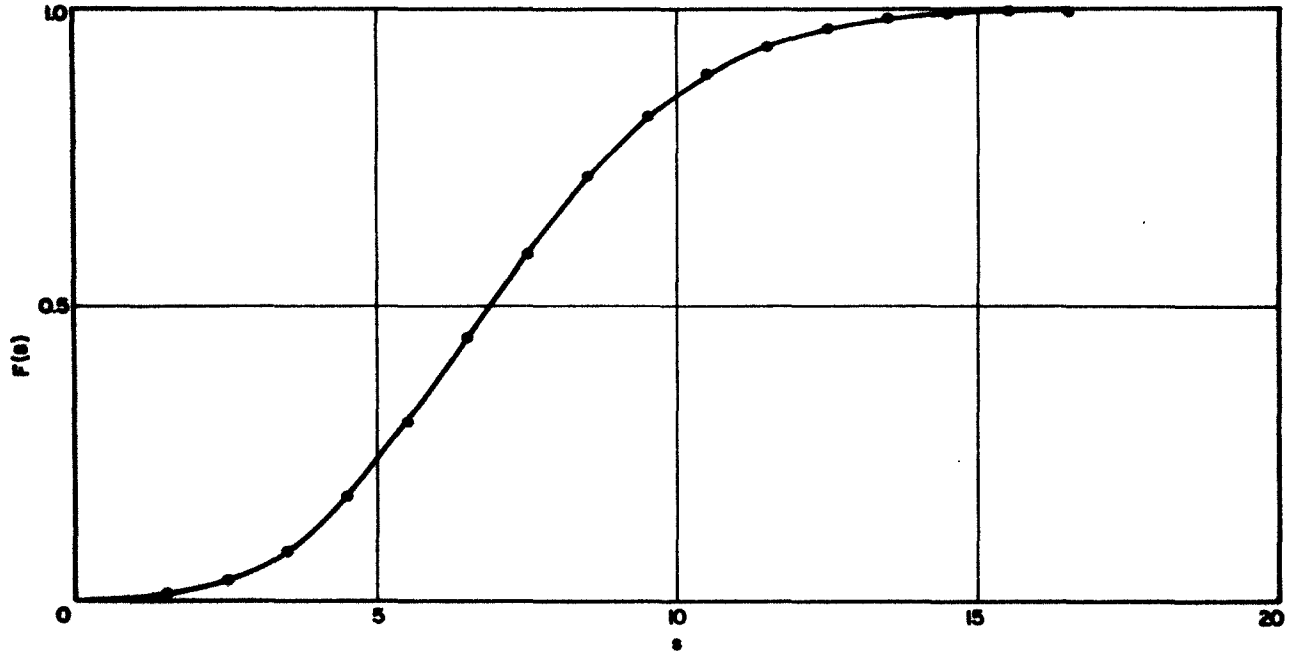

FIG. 7.1 F(s) VS. s. (n_a = 7.0)

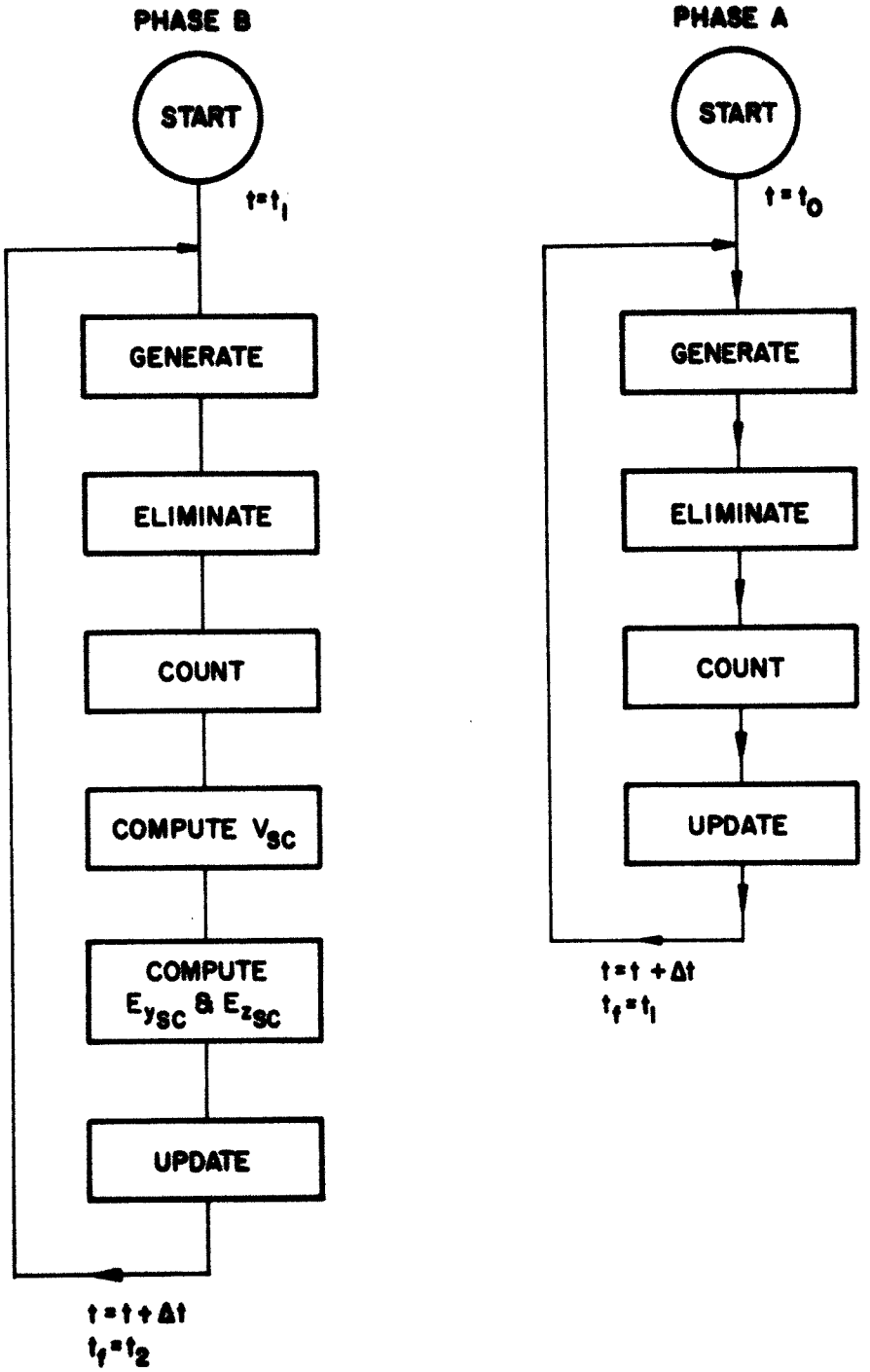

FIG. 7.2 FLOW DIAGRAM FOR MONTE CARLO ANALYSIS.

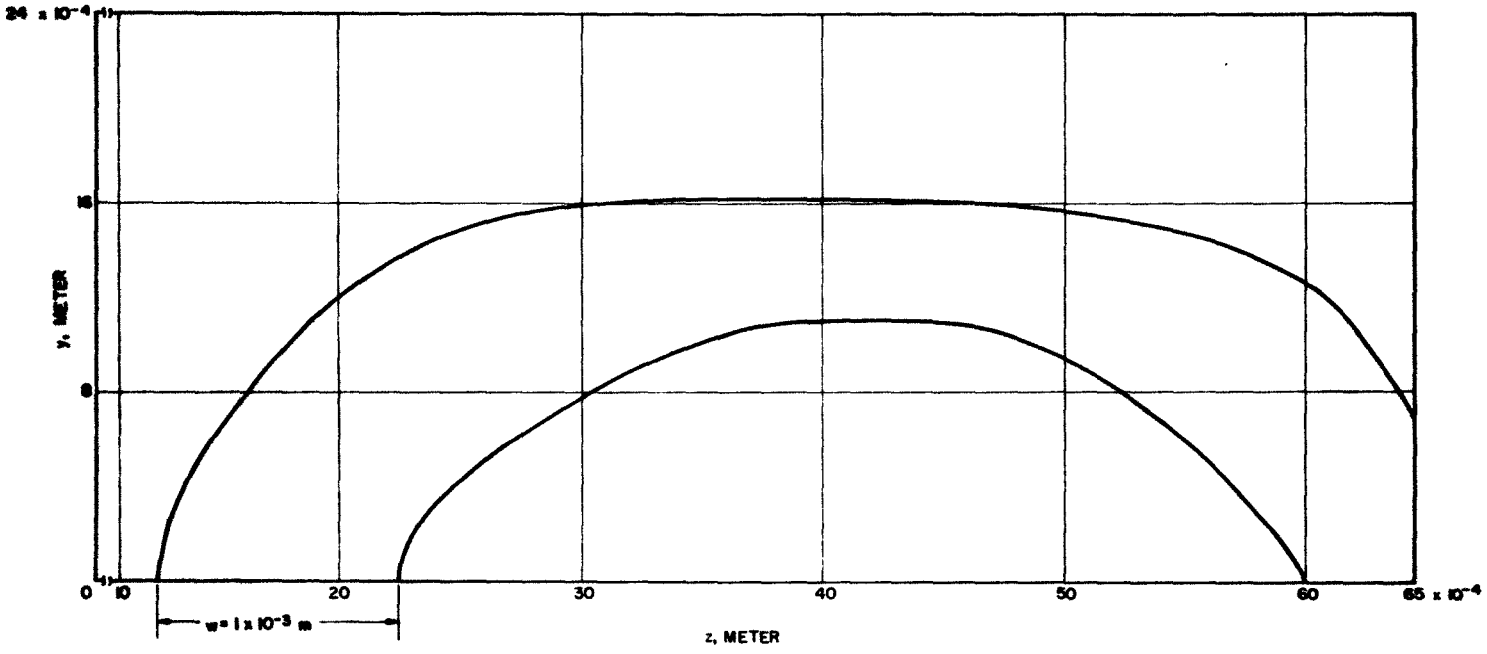

FIG. 7.3 BEAM PROFILE IN y-z PLANE UNDER STEADY-STATE CONDITIONS. (V_o = 500 VOLTS, $\omega_c = 4.75 \times 10^9$ RAD/SEC, $d = 5 \times 10^{-3}$ m)

uniformly spaced unit time intervals. At the same time the average values of the number of electrons, the average velocity components and the total potential corresponding to the centroids of the various rectangles were determined for every 50 unit time intervals. The average values of the position coordinates of the various electrons in these rectangles were also determined for every 50 unit time intervals. All this data was required in order to determine whether the steady-state conditions were reached or not. This would also determine the fluctuations of the various parameters from time to time.

The section "generate" in Fig. 7.2 refers to the generation of random number of electrons from the three points and association with these electrons random velocity components and positions of emission as described in Sections 6.3 through 6.5. The section "eliminate" in Fig. 7.2 refers to the elimination of electrons which strike the planes $z = 0$, $z = 6.5 \times 10^{-3}$ m, $y = 0$ and $y = 5.0 \times 10^{-3}$ m.

The section "count" refers to determining the number of electrons in the various rectangles and the average velocity components associated with these electrons. In Phase B this section also includes the averaging of the velocity components, number of electrons and the position coordinates for these rectangles for every 50 unit time intervals.

The section "update" refers to the computation of the velocity and position coordinates of the various electrons in the diode at the end of each unit time interval. Space-charge potential and fields are computed for each rectangle for which N_j (the number of electrons in the jth rectangle) is not equal to zero. The details for these computations have been given in Sections 6.7 and 6.8.

It should also be noted here that in the initial stages of the execution of the program the beam bent over a little more than was anticipated and no electrons were collected at the plane $z = 6.5 \times 10^{-3}$m. For this reason the value of ω_c, the cyclotron frequency, was changed from 5×10^9 rad/sec to 4.75×10^9 rad/sec.

7.4 Results

Figure 7.4 shows the total number of electrons in the diode as a function of time. Curve "a" refers to the case when the initial conditions for y_m and V_m from Chapter V were used for the first 202 time intervals and then the program was executed according to Phase B in Fig. 7.2. Curve "b" refers to the case in which the data was obtained solely from Phase B in Fig. 7.2. From the two curves in Fig. 7.4 it is clear that if the initial conditions are quite different from the actual conditions it is necessary to terminate Phase A and start with Phase B after an appropriate number of unit time intervals if an overall computer time saving is desired.

Figures 7.5 and 7.6 show the average trajectories and velocity components respectively versus $\omega_c T$ corresponding to the two phases, A and B. It is interesting to note from these figures that when there are no initial conditions imposed the variation of the trajectories and velocity components of the initially emitted electrons is very nearly the same as that for a temperature-limited case. The velocity $\dot{y}$ is maximum when $\omega_c T = \pi/2$ and then $(z/y) = 0.57$, $(\dot{z}/\dot{y}) = 1.0$. Since $\dot{y} = 0$ for $\omega_c T = \pi$, $(\dot{z})_{\omega_c T=\pi}/(\dot{y})_{\omega_c T=\pi/2} = 2$. y is maximum for $\omega_c T = \pi$ for zero initial velocities and $E_z = 0$. The corresponding values obtained from Figs. 7.5 and 7.6 indicate that $\dot{y}$ is maximum when $\omega_c T = 1.45$, $(z/y)_{\omega_c T=\pi/2} = 0.64$, $(\dot{z}/\dot{y})_{\omega_c T=\pi/2} = 1.2$, $(\dot{z})_{\omega_c T=\pi}/(\dot{y})_{\omega_c T=\pi/2} = 2.16$ and y is maximum for

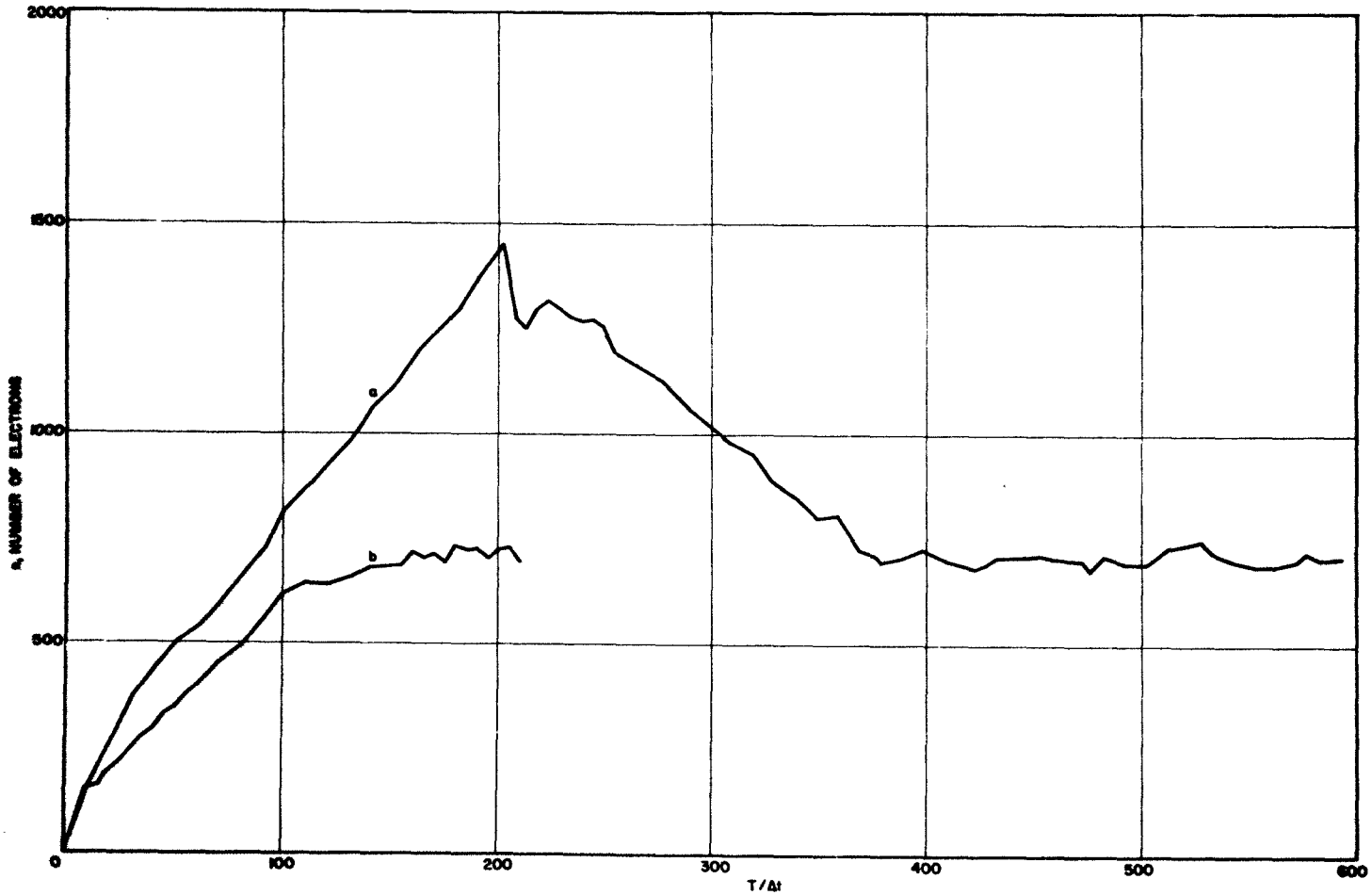

a. Phase A of Fig. 7.2 $0 < T/\Delta t \leq 202$ b. Phase B of Fig. 7.2 $T/\Delta t > 0$
Phase B of Fig. 7.2 $T/\Delta t > 202$

FIG. 7.4 TOTAL NUMBER OF ELECTRONS VS. $T/\Delta t$.

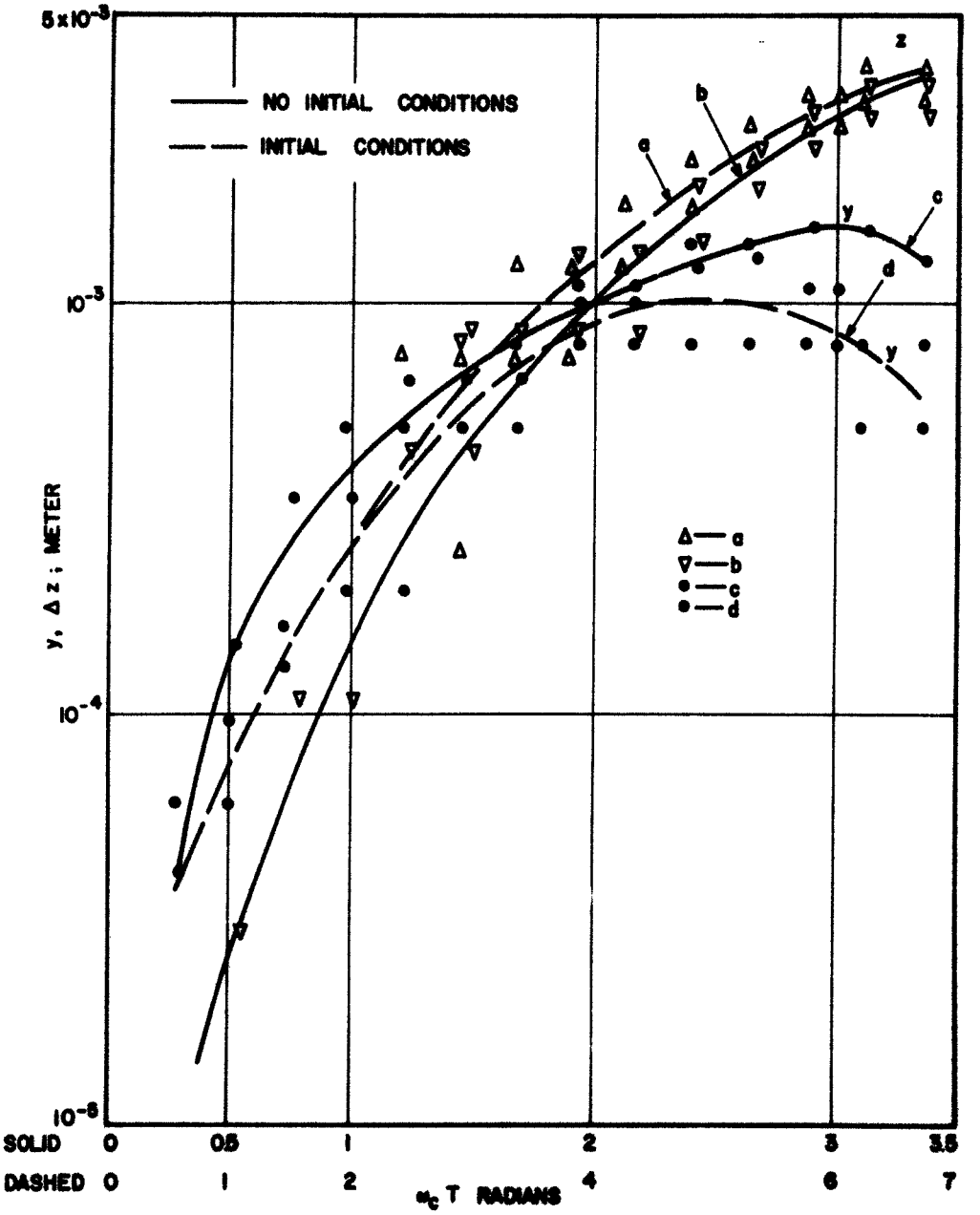

FIG. 7.5 TRAJECTORIES VS. $\omega_c T$.

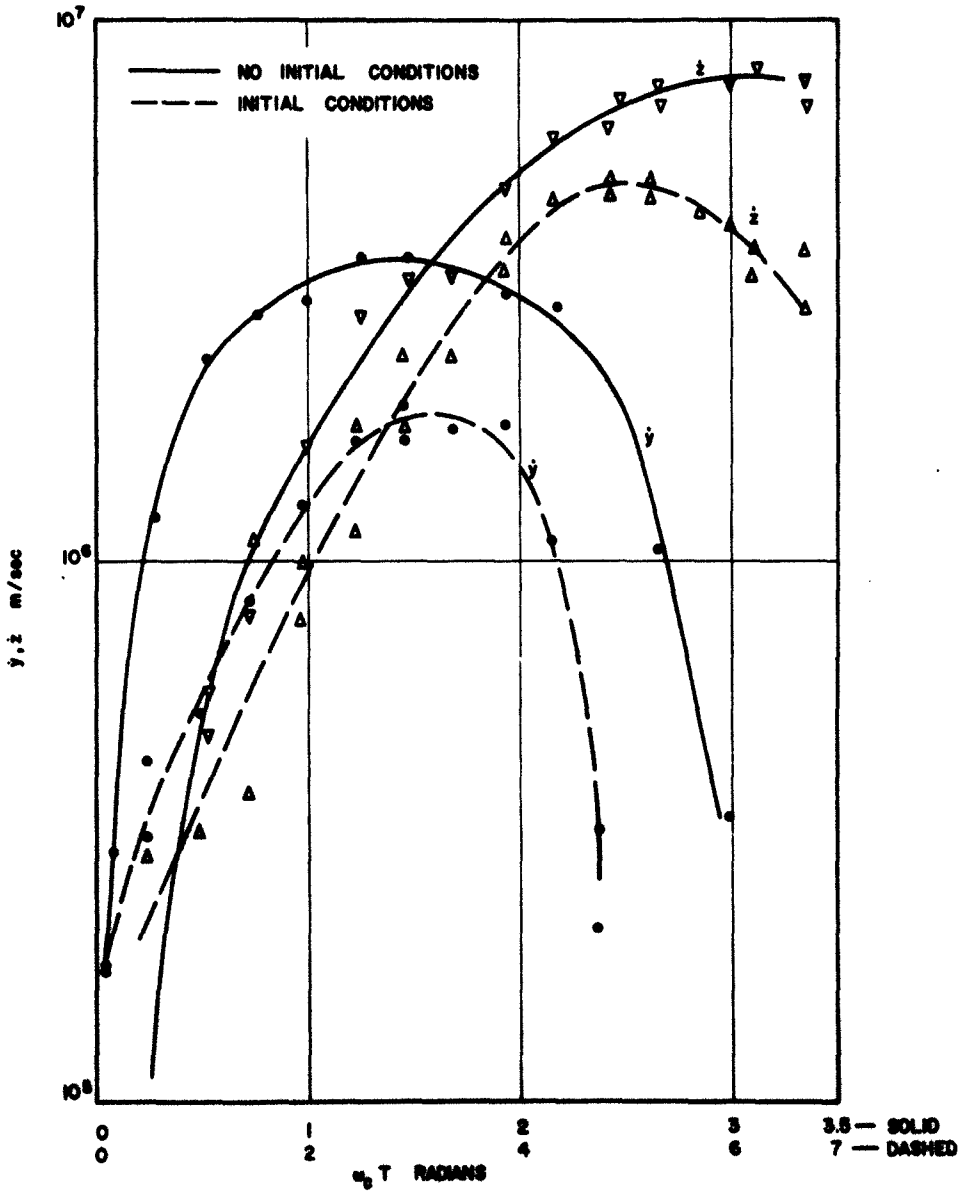

FIG. 7.6 VELOCITY COMPONENTS VS. $\omega_c T$.

$\omega_c T \simeq 3.0$. These deviations may be ascribed to the effects of initial velocities and the fact that $E_z \neq 0$ during the later time intervals when V_{sc} is sufficient to change the trajectories considerably. Since the electrons were not tracked individually it is not convenient to plot the trajectories and velocity components for the steady-state conditions.

When the initial conditions are imposed the trajectories and velocity components are analogous to the results obtained from the Kino gun model. For a Kino gun $\dot{y}$ is maximum when $\omega_c T = \pi$, $(z/y)_{\omega_c T=\pi} = 0.94$, $(\dot{z}/\dot{y})_{\omega_c T=\pi} = \pi/2$, $(\dot{y})_{\omega_c T=2\pi} = 0$, $(\dot{z})_{\omega_c T=2\pi}/(\dot{y})_{\omega_c T=\pi} = \pi$ and y is maximum for $\omega_c T = 2\pi$ for zero initial velocities and $E_z = 0$. The corresponding values obtained from Figs. 7.5 and 7.6 indicate that $\dot{y}$ is maximum when $\omega_c T = \pi$, $(z/y)_{\omega_c T=\pi} = 0.69$, $(\dot{z}/\dot{y})_{\omega_c T=\pi} = 1.14$, $(\dot{z})_{\omega_c T=5}/(\dot{y})_{\omega_c T=\pi} = 2.63$ and y is maximum for $\omega_c T = 5.1$. These deviations may be ascribed to initial velocity effects and the presence of the potential minimum assumed in computing the results given in Figs. 7.5 and 7.6. It should be noted that the computed results correspond to the centroids of the various rectangles and would lead to some error. This error can be made small if the spacing between the neighboring rectangles is small.

The results shown in Figs. 7.5 and 7.6 correspond to the initially emitted electrons and these results do indicate that the presence of the potential minimum causes a large increase in the transit time of an electron from the cathode to the gun exit. Needless to say only those electrons for which the initial velocities are sufficient enough to overcome the potential minimum barrier are considered.

Figure 7.7 shows the potential variation, averaged over 1000 unit intervals during Phase B of Fig. 7.2. The average values of y are used in plotting Fig. 7.7 where averaging of y for a rectangle refers to the

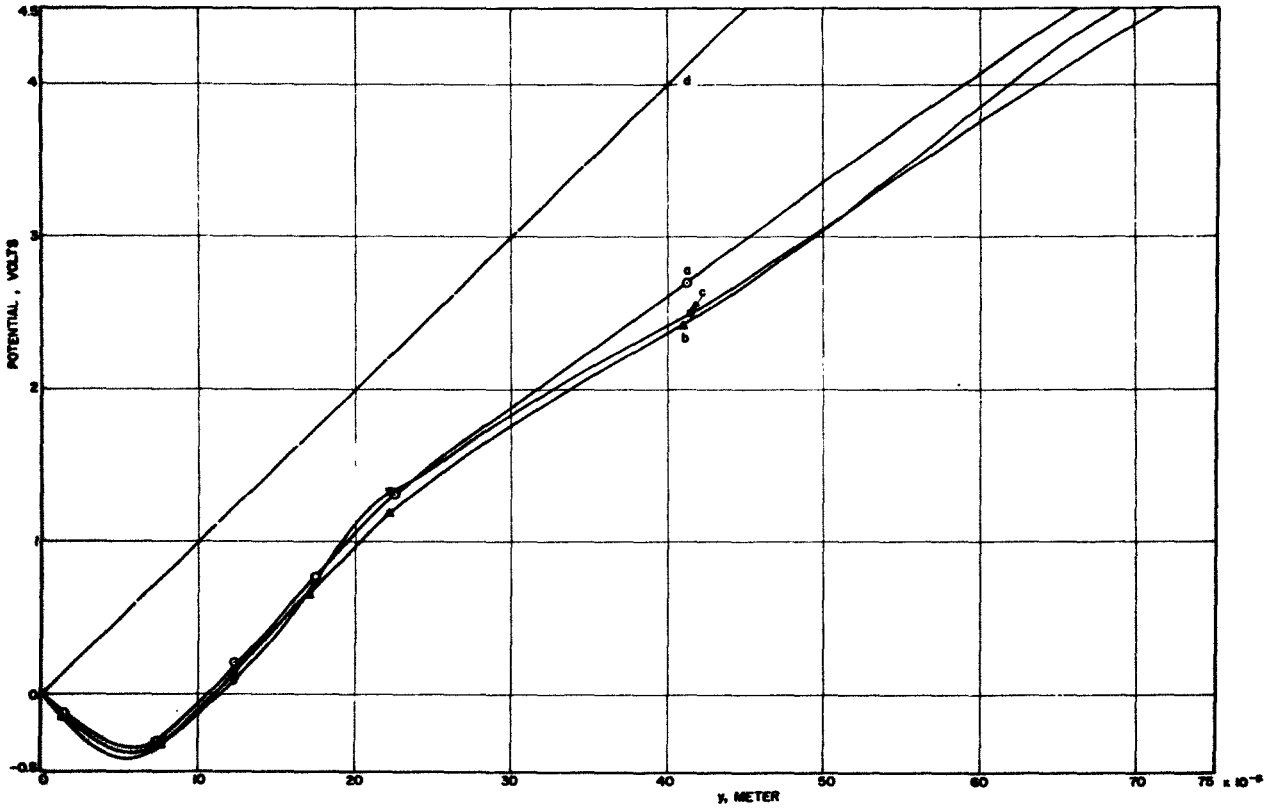

a. Outer Edge c. Inner Edge
b. Central Region d. Zero Space Charge

FIG. 7.7 POTENTIAL VARIATION ALONG THE BEAM. (V_o = 500 VOLTS, $\omega_c = 4.75 \times 10^9$ RAD/SEC, $d = 5 \times 10^{-3}$ m)

average value of the y-coordinate of all the electrons in the same rectangle. This averaging process was executed so as to eliminate any gross errors in computing the space-charge constants A_{ij} defined in Section 6.7. Curves "a", "b" and "c" refer to $z = 12.5 \times 10^{-4}$, 17.5×10^{-4} and 22.5×10^{-4} m respectively. The value of $|V_m|$ is largest for curve "b" as expected because of greater space-charge depression in the central region of the beam. The average values of V_m and y_m are - 0.375 volt and 5.5×10^{-6} m respectively. For $y > y_m$ the space-charge depression for the inner edge fluctuates around that of the central region of the beam. This is due to the fact that as the velocity of an electron increases the effect of the magnetic field becomes more and more pronounced and the electrons from the outer part of the beam move inward. The fluctuations of curve "c" with respect to curve "b" depend upon an increase in the number of electrons in the two portions of the beam. This effect of the transverse magnetic field is clearly shown in Fig. 7.8 which indicates the potential distribution for larger values of y. The larger value of $|V_m| = 0.375$ volt is due to a larger value of saturation current density, I_s. The influence of the electrons returning to the cathode on the value of I_s and whether this large value of $|V_m|$ exists or not in a practical device is not yet clearly understood.

In Section 7.3 it was noticed that during the computations of the values of $(n_o)_i$, the average number of electrons in the ith rectangle and the average values of the velocity components were computed to insure against gross errors in the calculation. This averaging process was executed for all the rectangles and some of these results are given in Tables 7.2a through 7.2c for rectangles 1, 11 and 14 respectively. Table 7.3 gives the average values of N_o, $\dot{z}_o$, $\dot{y}_o$, J_{zo} and J_{yo} for the fifteen

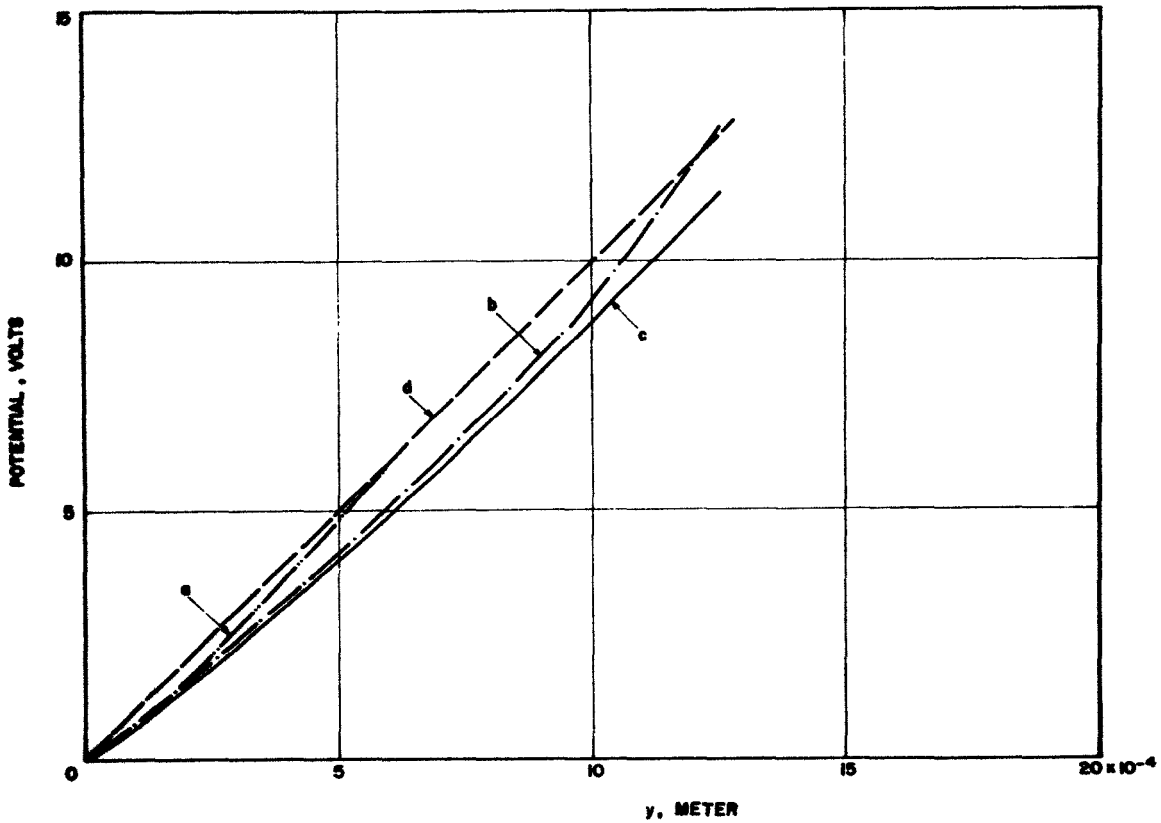

a. Outer Edge
b. Central Region
c. Inner Edge
d. Zero Space Charge

FIG. 7.8 POTENTIAL VARIATION ALONG THE BEAM. (V_o = 500 VOLTS, $\omega_c = 4.75 \times 10^9$ RAD/SEC, $d = 5 \times 10^{-3}$ m)

Table 7.2a

Average Values of the Number and Velocity Components of Electrons in Rectangle 1

N (No. of Time Intervals)	n_o	$\dot{z}_o$ (m/sec) $\times 10^6$	$\dot{y}_o$ (m/sec) $\times 10^5$
1-50	19.6	7.21	7.02
51-100	22.2	7.18	6.94
101-150	20.3	7.20	7.74
151-200	19.7	7.12	7.38
201-250	22.6	7.21	7.75
251-300	20.9	7.14	7.88
301-350	20.8	7.14	7.06
351-400	19.0	7.19	8.13
401-450	22.7	7.18	7.39
451-500	19.4	7.17	7.89
501-550	20.6	7.22	7.36
591-640	18.2	7.16	7.33
641-690	20.3	7.21	7.24
691-740	19.9	7.14	8.11
741-790	21.8	7.20	7.39
791-840	18.8	7.11	7.16
841-890	17.9	7.20	7.77
891-940	19.1	7.16	7.18
941-990	21.4	7.19	7.16
991-1040	22.2	7.15	8.49

Table 7.2b

Average Values of the Number and Velocity Components of Electrons in Rectangle 11

N (No. of Time Intervals)	n_o	$\dot{z}_o$ (m/sec) x 10^4	$\dot{y}_o$ (m/sec) x 10^5
1-50	0.16	-4.18	-5.15
51-100	0.34	15.8	-8.26
101-150	0.76	-7.95	-3.54
151-200	0.44	3.06	-4.3
201-250	0.14	17.1	-7.71
251-300	0.62	10.6	-7.77
301-350	0.66	9.37	-5.82
351-400	0.42	-2.68	-1.27
401-450	0.52	-7.02	-3.94
451-500	0.70	6.36	-8.74
501-550	0.52	1.6	-6.45
591-640	0.74	0.61	-6.03
641-690	0.12	-16.4	-2.89
691-740	0.66	0.762	-7.0
741-790	0.40	24.5	-7.62
791-840	0.26	15.4	-10.1
841-890	0.36	-12.5	-4.53
891-940	0.68	-10.1	-3.09
941-990	0.62	- 8.47	-4.34
991-1040	0.76	9.77	-4.83

Table 7.2c

Average Values of the Number and Velocity Components of Electrons in Rectangle 14

N (No. of Time Intervals)	n_o	$\dot{z}_o$ (m/sec) $\times 10^3$	$\dot{y}_o$ (m/sec) $\times 10^4$
1-50	19.9	7.53	6.98
51-100	18.9	3.49	8.72
101-150	20.4	-11.9	6.81
151-200	19.9	3.58	6.73
201-250	17.3	-14.6	9.50
251-300	21.3	2.64	6.12
301-350	20.3	10.7	6.4
351-400	18.2	-6.32	9.45
401-450	21.2	-6.92	6.75
451-500	18.9	13.0	8.60
501-550	20.7	21.9	6.85
591-640	20.5	8.76	6.71
641-690	19.6	5.74	6.67
691-740	19.9	-9.36	7.42
741-790	22.9	-0.233	5.29
791-840	20.8	5.87	6.87
841-890	20.7	8.81	6.17
891-940	19.6	9.43	8.42
941-990	18.9	2.27	9.50
991-1040	22.1	0.716	5.79

Table 7.3

Average Values of the Number of Electrons, Velocity and Current Density Components (Averaged Over 1000 Unit Time Intervals)

Rectangle No.	n_o	$\dot{z}_o$ (m/sec) x 10^6	$\dot{y}_o$ (m/sec) x 10^6	$-J_{zo}$ (amps/m^2) x 10^2	$-J_{yo}$ (amps/m^2) x 10^2
1	20.41	7.18	0.75	11.74	1.22
2	9.45	6.58	2.49	4.98	1.88
3	2.85	5.60	1.12	2.56	0.51
4	0.005	2.94	-2.66	0.0023	-0.002
5	2.22	2.44	2.69	0.87	0.96
6	5.78	0.36	-0.37	2.86	-2.97
7	0.432	0.71	-0.79	0.42	-0.468
8	3.40	0.56	1.63	2.61	7.6
9	3.85	0.51	1.63	2.68	8.6
10	3.59	0.47	1.70	2.33	8.4
11	0.49	0.018	-0.57	0.085	-2.71
12	0.032	0.336	-0.8	0.103	0.245
13	20.74	0.0017	0.065	0.341	12.92
14	20.00	0.0033	0.073	0.64	14
15	20.81	-0.0022	0.068	-0.44	13.5

rectangles and are averaged over 1000 unit time intervals. This data is quite helpful in interpreting the results.

It is noticed that the cross-sectional area of the beam does not remain constant and it is necessary to evaluate this area to compute the correlation functions and the noise parameters. The effective cross-sectional area corresponding to the ith rectangle was computed by using the following equations:

$$\pi/4 + 0.1 < \theta_i < \pi/2 \ , \qquad A_i = h\, dz_i \operatorname{cosec} \theta_i$$

$$\pi/4 - 0.1 < \theta_i < \pi/4 + 0.1 \ , \qquad A_i = h\sqrt{(dy_i)^2 + (dz_i)^2}$$

$$0 < \theta_i < \pi/4 - 0.1 \ , \qquad A_i = h\, dy_i \sec \theta_i \ , \tag{7.13}$$

where

$$\theta_i = \tan^{-1} \frac{|(\dot{y}_o)_i|}{|(\dot{z}_o)_i|} \ . \tag{7.14}$$

7.5 Correlation Functions

Recall that the upper limit for frequency is taken as 10 Gc. The limiting values of N and M as defined in Eq. 6.50 depend upon the total number of time intervals for which the data is obtained and the maximum value of lag used in evaluating the correlation functions and various noise parameters. Furthermore the ratio N/M corresponds to the number of degrees of freedom as defined by Blackman and Tukey[23]. The number of degrees of freedom determine the "confidence interval" within which the true value of the spectrum would be relative to the estimated value with a given probability. Under the Gaussian assumption for a random variable x(t) the stability of the spectral estimates can be described by an equivalent Chi-square distribution having k degrees of freedom[23],

where

$$k = 2\left(\frac{N}{M} - \frac{1}{3}\right) , \tag{7.15}$$

and it is assumed that the spectrum of x(t) is reasonably flat, i.e., does not contain peaks whose width is comparable with 1/2 Tm.

When using a lag window it is not necessary to compute the various noise parameters at all the frequencies; instead these parameters may be computed at intervals of 1/2 Tm. Selecting this frequency interval as 500 mc gives M = 100. The value of N is taken as 1000 and thus $k \simeq 20$. This indicates[23] that if the true value is x, then among estimates 80 percent would fall between 0.62 x and 1.42 x, while 10 percent would fall below 0.62 x and 10 percent would fall above 1.42 x. Increasing the value of N to 2000 which means increasing the computer time by approximately a factor of two gives the corresponding limiting values of the estimates as 0.72 x and 1.3 x. Decreasing the value of M the number of degrees of freedom increases although this would increase the value of Δf. For these reasons the values of N and M as given above are considered reasonably good.

Figures 7.9 and 7.10 are plots of the auto-correlation functions for the a-c kinetic voltage and current fluctuations respectively for the data corresponding to rectangles 1 and 2. The correlation for large values of μ is small and the effect of the lag window would give the values of the two normalized correlation functions identically zero for $\mu = 100$.

7.6 Noise Parameters

Figures 7.11 and 7.12 are plots of Π/S versus f for several rectangles. The parameter Π/S represents the correlation between the a-c

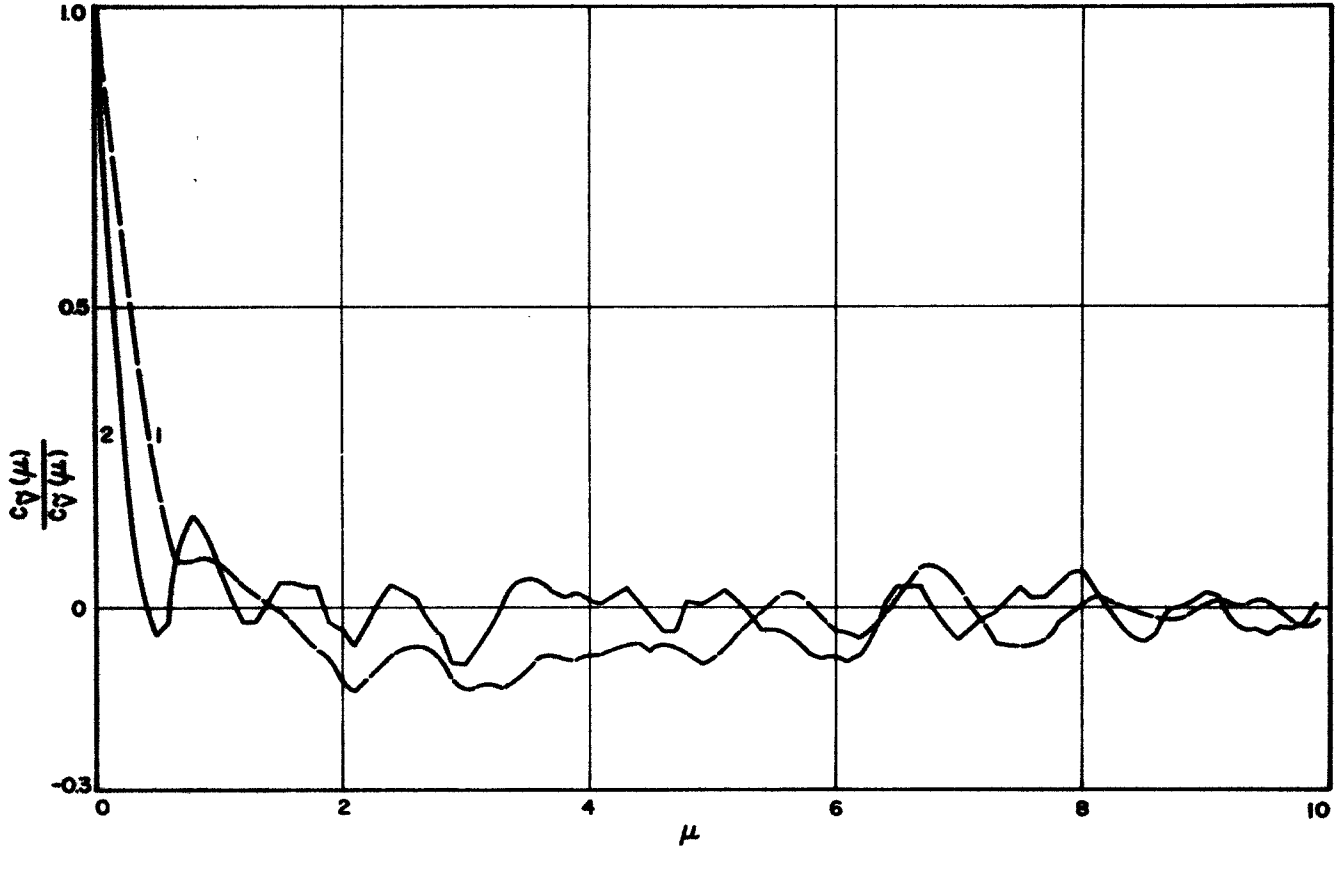

FIG. 7.9 NORMALIZED AUTO-CORRELATION FUNCTION FOR THE A-C KINETIC VOLTAGE VS. μ.

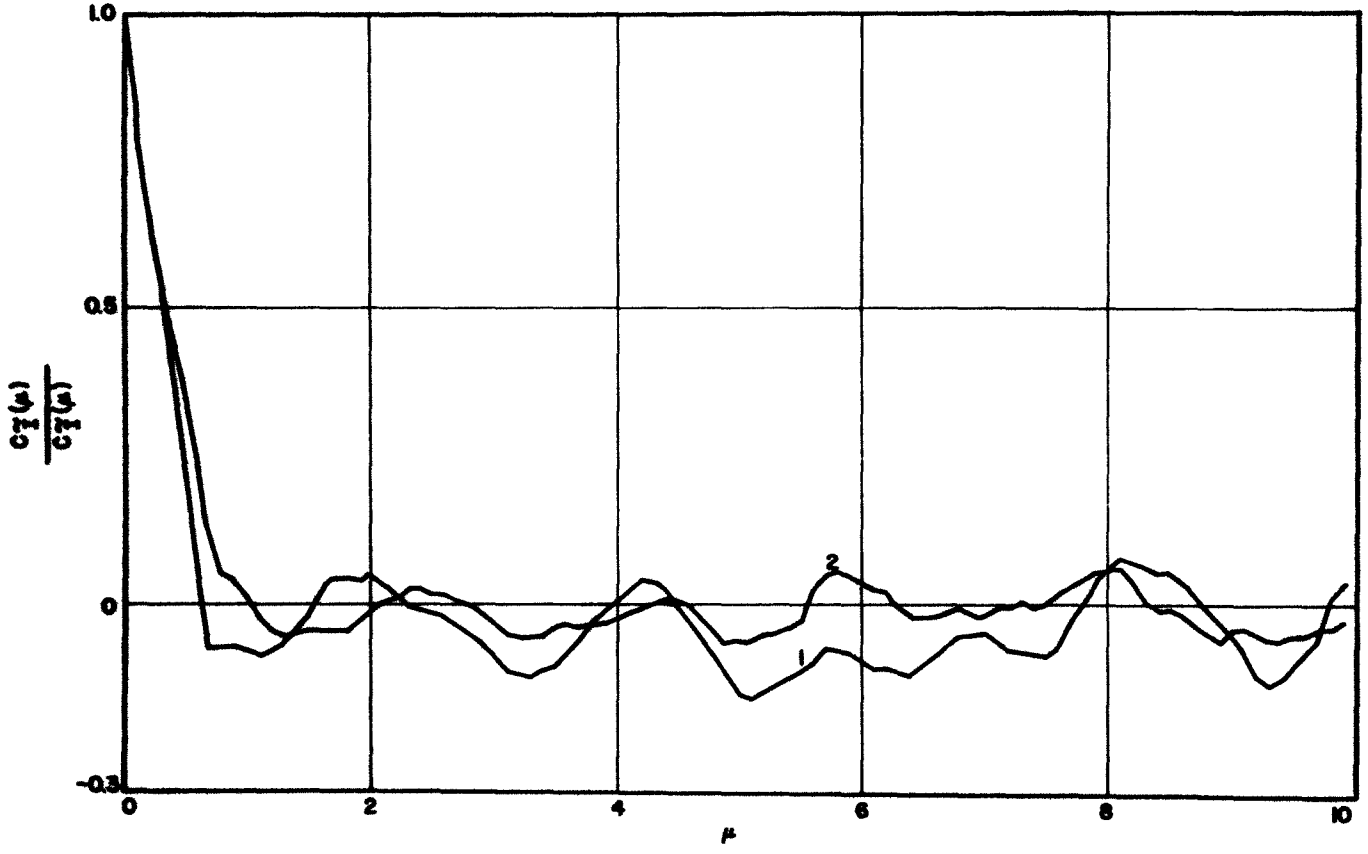

FIG. 7.10 NORMALIZED AUTO-CORRELATION FUNCTION FOR THE CURRENT FLUCTUATIONS VS. μ.

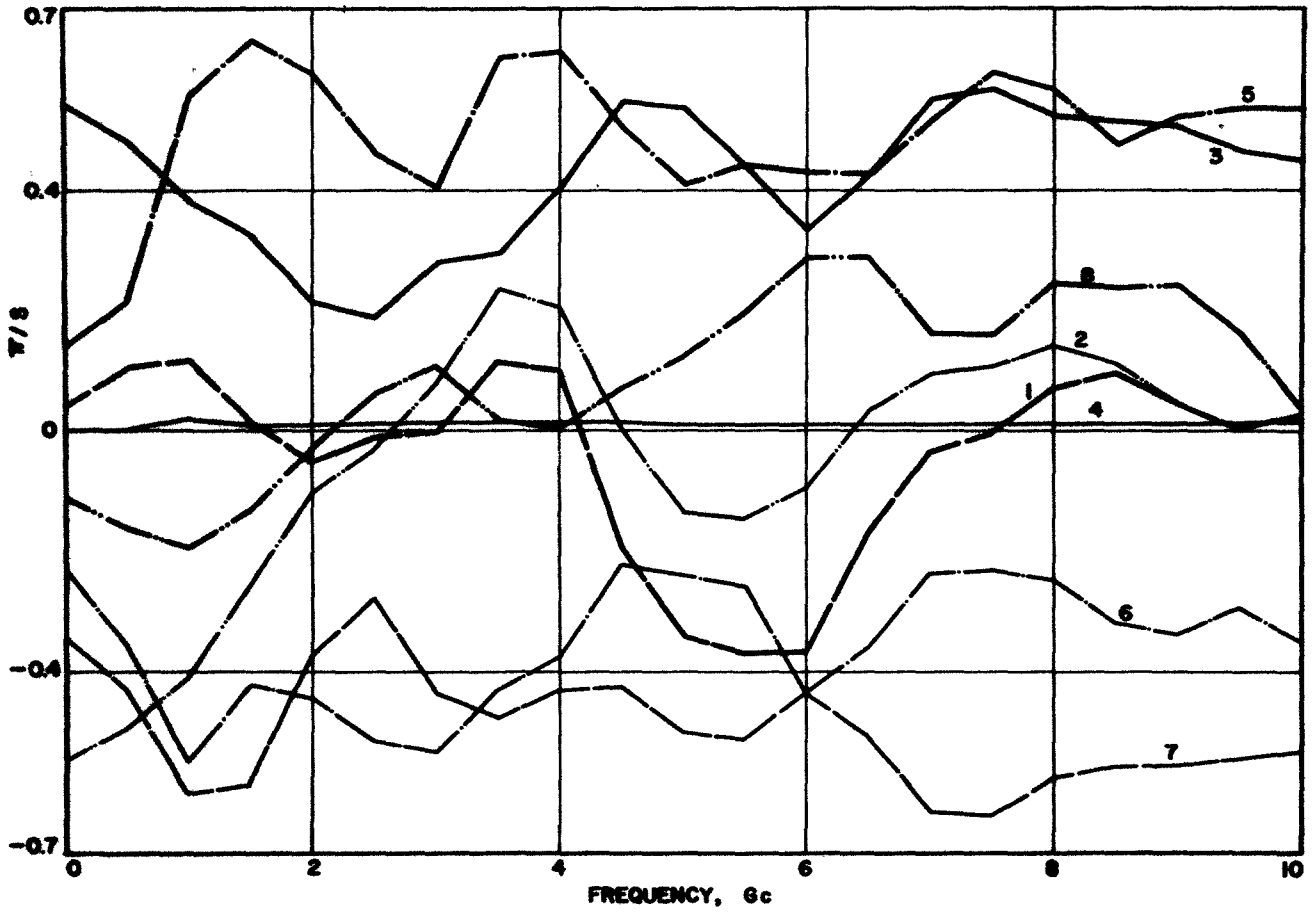

FIG. 7.11 Π/S VS. f.

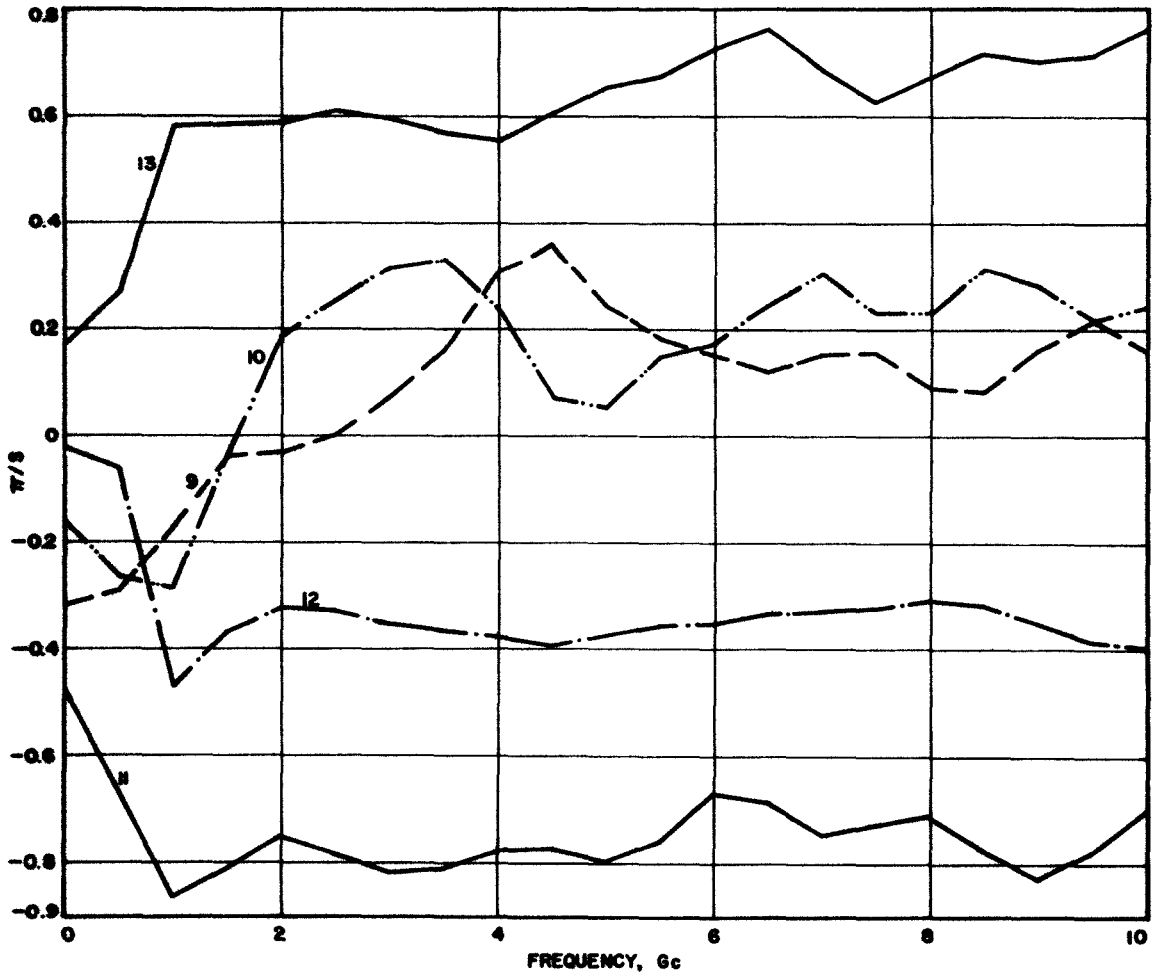

FIG. 7.12 Π/S VS. f.

kinetic voltage and current fluctuations. It can be seen from the plots in Figs. 7.11 and 7.12 that Π/S is quite large and for some plots it fluctuates between positive and negative values. The interpretation[33] of these parameters has been given for O-type devices. Haus's theory[33] for evaluating the noise figure for O-type devices has been used to evaluate the various noise parameters for different sections of the crossed-field beam. The interpretation of the parameter Π can be made in terms of the slow and fast space-charge waves. The propagation constants of these waves are modified due to the transverse magnetic field. A negative value of Π usually corresponds to an increase in the negative energy of the slow wave and a decay in the fast wave provided the total energy is considered constant. According to this interpretation it can be seen from the plots in Figs. 7.11 and 7.12 that the fast wave is amplified in the potential minimum region. As the beam is accelerated the slow wave is amplified for small values of ω and the fast wave is amplified for large values of ω. It is quite likely that for small values of ω the conventional fast wave is a backward wave (as found from the results of the density method given in Chapter V) and these results cannot be appropriately interpreted for the fast wave for small values of ω. In the region where the beam bends over and nonlaminarity of the beam could be considerable, whether the fast wave or slow wave is amplified depends upon the position of the beam. It is interesting to note the slow-wave amplification from the plots corresponding to rectangles 6, 7, 11 and 12. This indicates that in the process of traversing a cycloid the fast wave energy has been transferred to the slow wave or both the waves have been amplified although the overall growth of the slow wave is larger than that of the fast wave.

Figures 7.13 and 7.14 show the variation of S/S_o versus f for several rectangles. S_o refers to the value of S for rectangle No. 14 for f = 0. It can be seen from these plots that as the beam is accelerated the value of S is also increased and in some of the rectangles in the region which would normally be the gun exit the value of S is extremely large. This indicates that the beam energy has increased. The parameter S usually refers to the sum of the negative energy in the slow wave and positive energy in the fast wave. As the beam is decelerated in completing the cycloid the value of S is reduced, however when the beam reaches the point of the same potential from which it originated it appears that there is an overall increase in the value of S. This increase in the value of S after the completion of a cycloid may be due partly to the absence of the potential minimum in this region. These results indicate an increase in the beam energy and are in agreement with the experimental results of large sole currents which are usually noticed even if the sole voltage is negative with respect to the cathode.

Figures 7.15 through 7.18 are plots of normalized $S-\Pi$ and $S+\Pi$ versus f. It can be seen from the plots in Figs. 7.16 and 7.18 that the value of $S+\Pi > S-\Pi$ near the cathode. Usually $S-\Pi$ and $S+\Pi$ are interpreted in terms of the negative and positive energies of the slow and fast waves respectively. It can be seen from these plots that for rectangles away from the cathode the value of $S-\Pi \gtrsim S+\Pi$. This indicates that the negative energy of the slow wave increases at a faster rate. The results given in Chapter V indicate that this growth is possible when $(d\dot{y}_o/dy)/\dot{y}_o < 0$. This conclusion was obtained on the basis of a filamentary beam model and the results obtained from the Monte Carlo analysis show a growth in the two waves even if this condition is not satisfied as

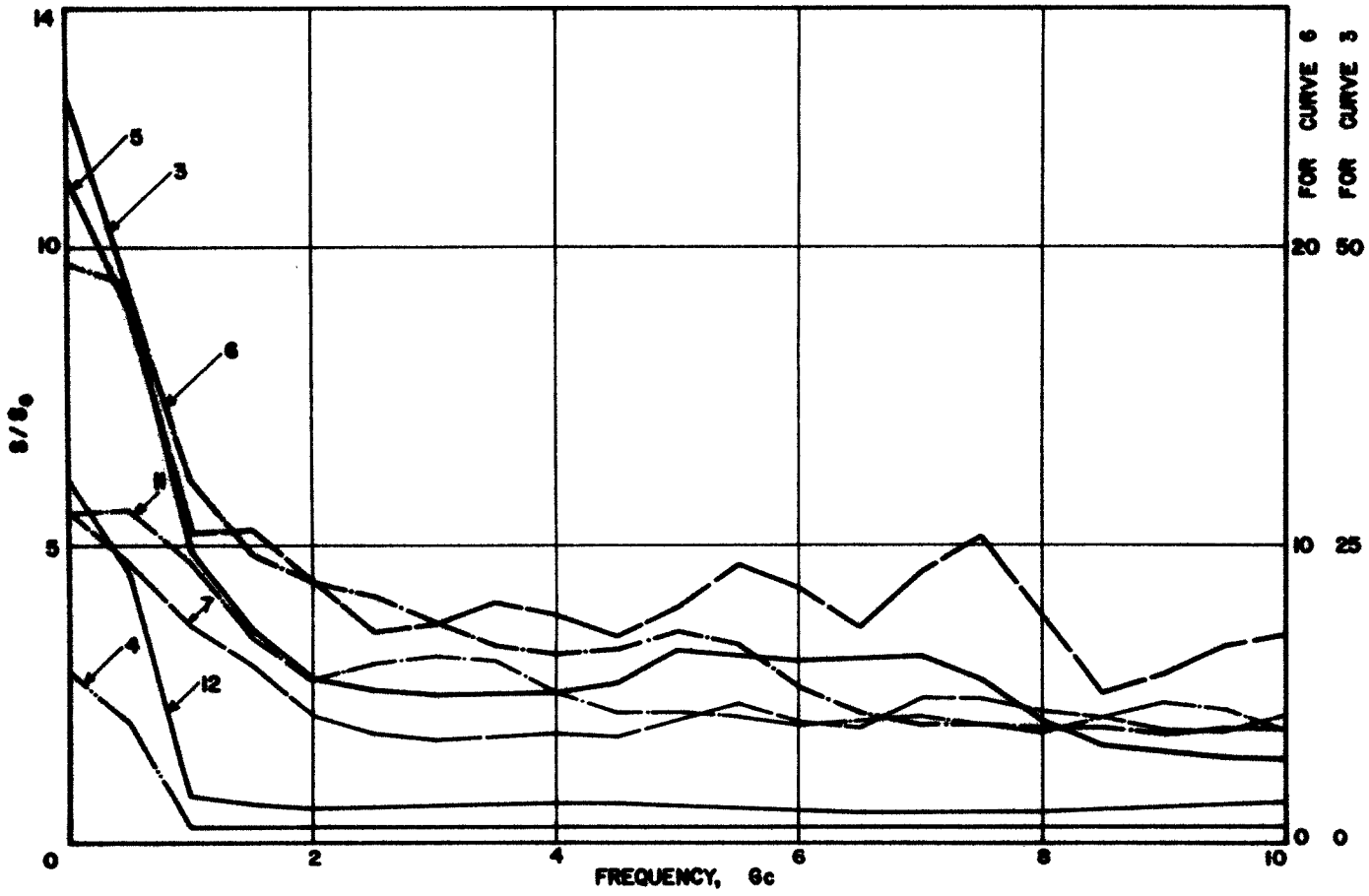

FIG. 7.13 S/S_o VS. f.

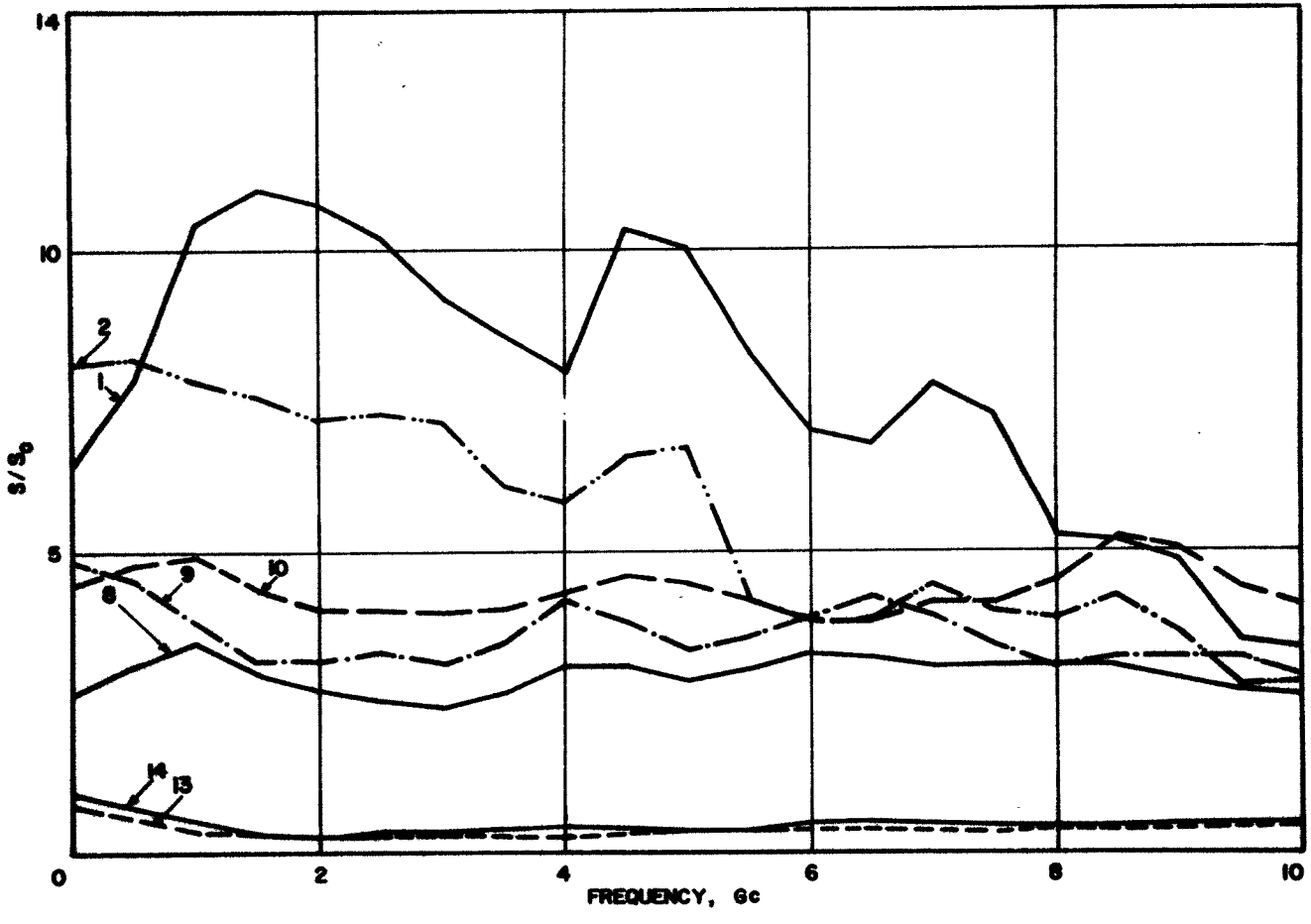

FIG. 7.14 S/S_o VS. f.

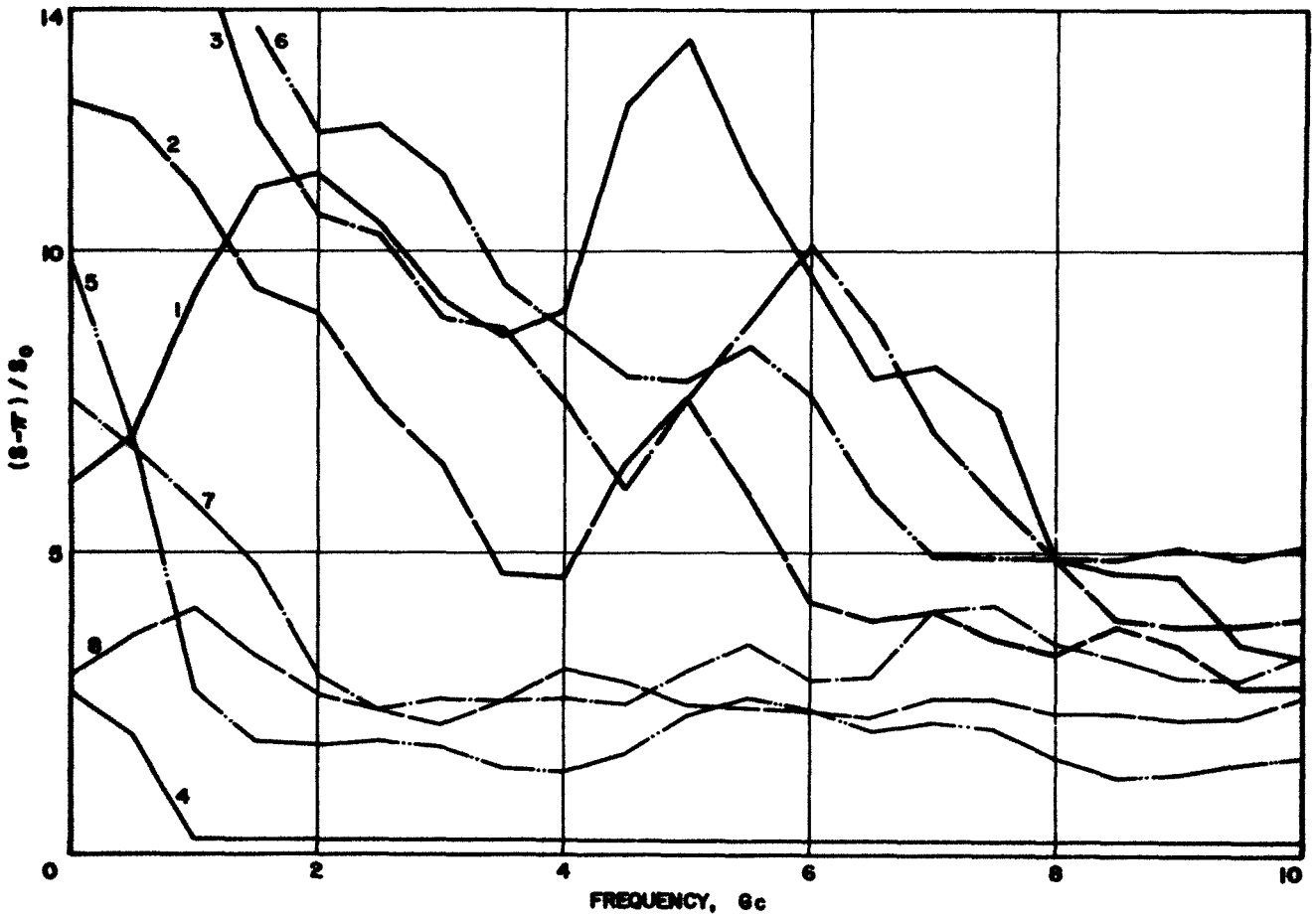

FIG. 7.15 $(S-\Pi)/S_o$ VS. f.

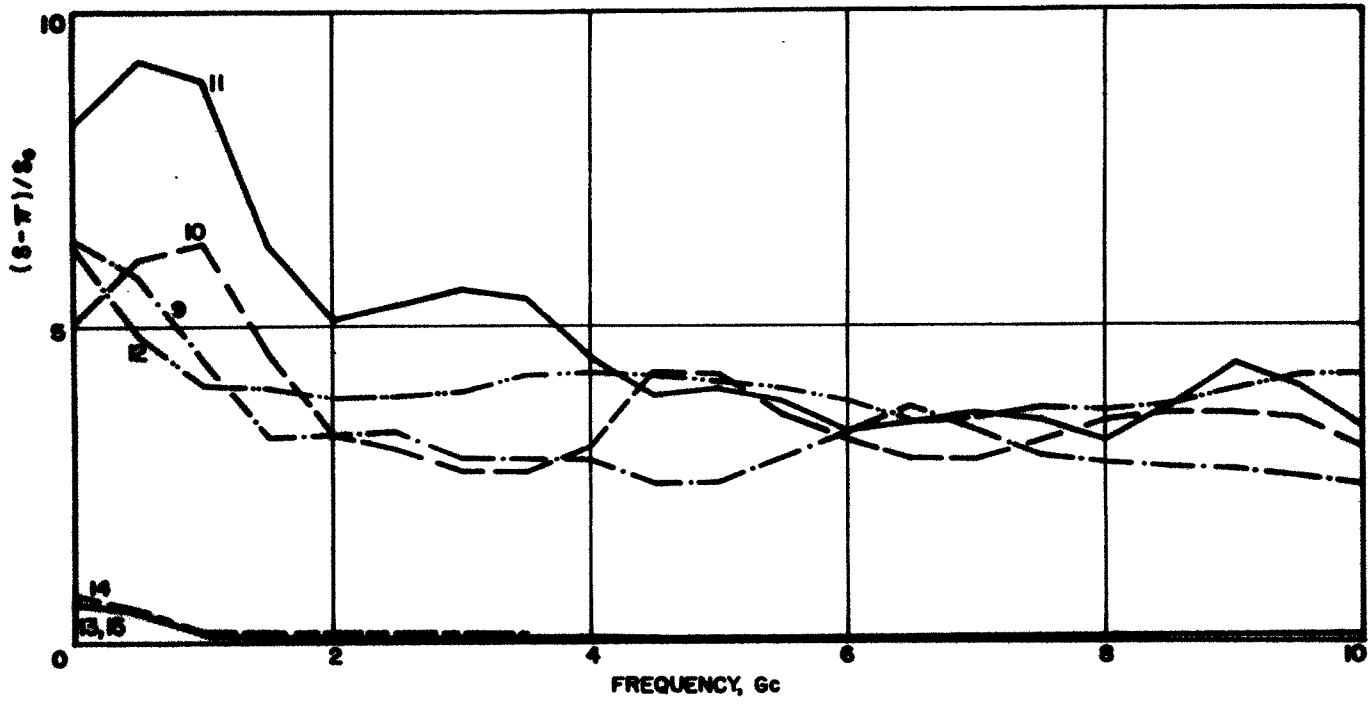

FIG. 7.16 $(S-\Pi)/S_o$ VS. f.

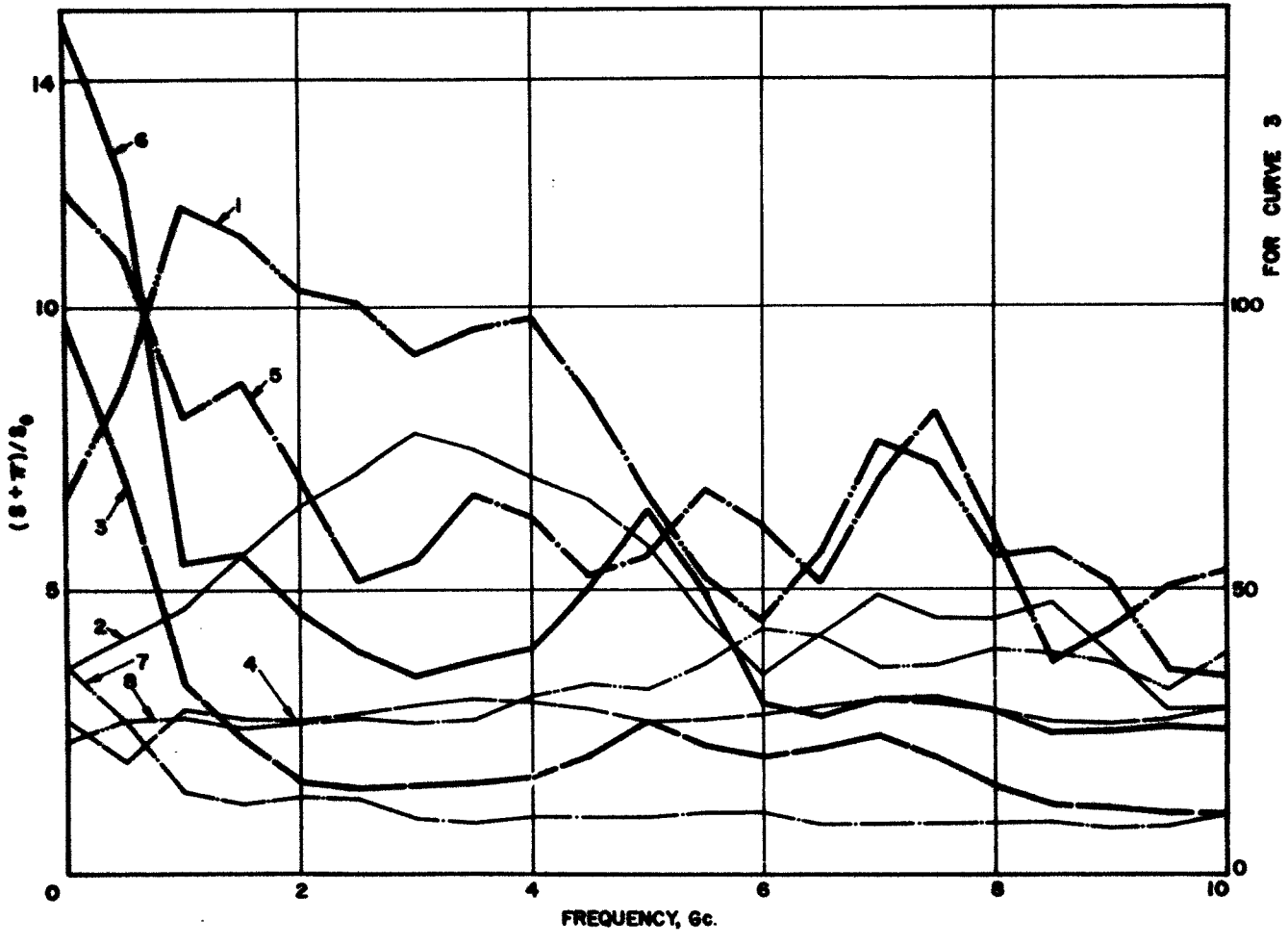

FIG. 7.17 $(S+\Pi)/S_o$ VS. f.

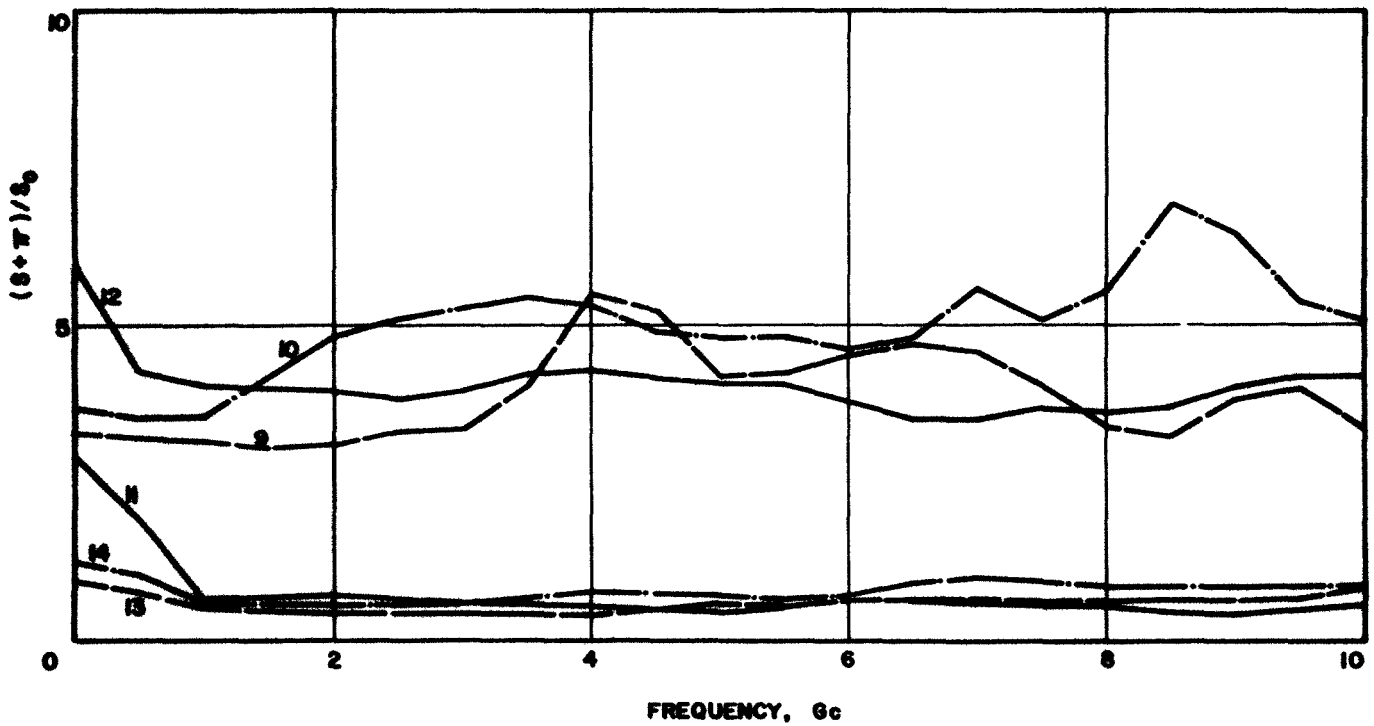

FIG. 7.18 $(S+N)/S_o$ VS. f.

noticed from the plots for rectangles 8, 9 and 10. However the larger growth rates for rectangles for which this condition is satisfied show a qualitative agreement between the two results. It is interesting to note that at the end of the cycloid the energies of both waves have increased but the overall growth for the slow wave has been larger than that for the fast wave. This is also in qualitative agreement with the results given in Chapter V that for $(d\dot{y}_o/dy)/\dot{y}_o < 0$ the value of $\alpha_4 > \alpha_5$ if y is increased further. It may appear within some frequency ranges that S-Π is decreasing and S+Π is increasing or vice versa as f is increasing; this indicates a loss in the negative energy of the slow wave and an increase in the positive energy of the fast wave respectively or vice versa. However it will be difficult to make a general statement regarding the variation of S-Π and S+Π as a function of f.

Figures 7.19 and 7.20 show the variation of ψ/ψ_o versus f. It is interesting to note from these plots that the spectral density due to current fluctuations is reduced as the beam traverses the complete cycloid. Thus the presence of the potential minimum reduces the current fluctuations considerably. In general it may be concluded that ψ/ψ_o is either constant or it decreases as f is increased for all the rectangles except those near the cathode. Some of the peaks in the curves for rectangles 6 and 8 may be explained on the basis of the upper and lower limits of the confidence interval, 1.42 x and 0.62 x, as explained in Section 7.4. For rectangles near the cathode the spectral density due to current fluctuations increases as f is increased. From the results given in Chapter III it is also found that the current fluctuations increase as $R \triangleq \omega/\omega_c$ is increased. Since the value of ψ/ψ_o for all the rectangles is very small as compared to that of the rectangles near the

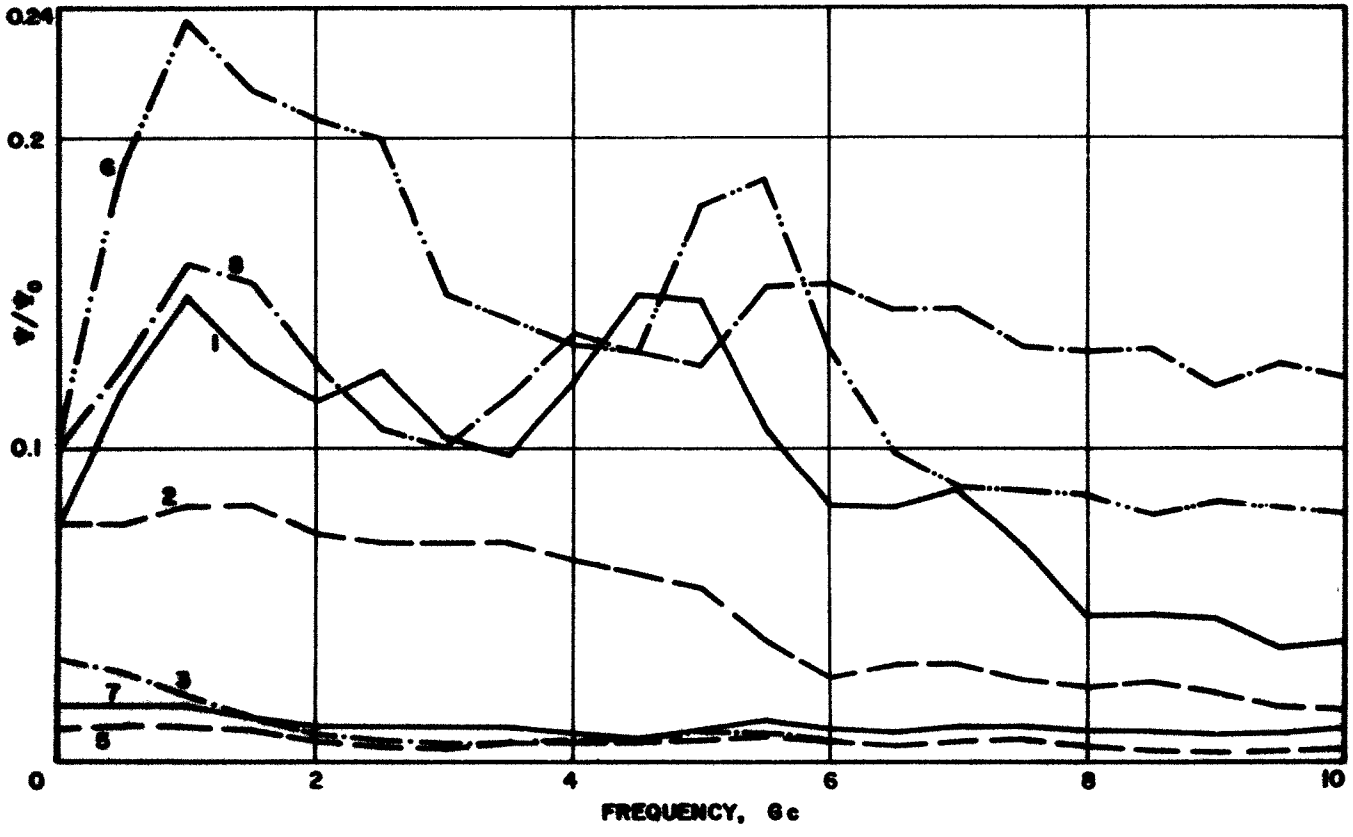

FIG. 7.19 ψ/ψ_o VS. f.

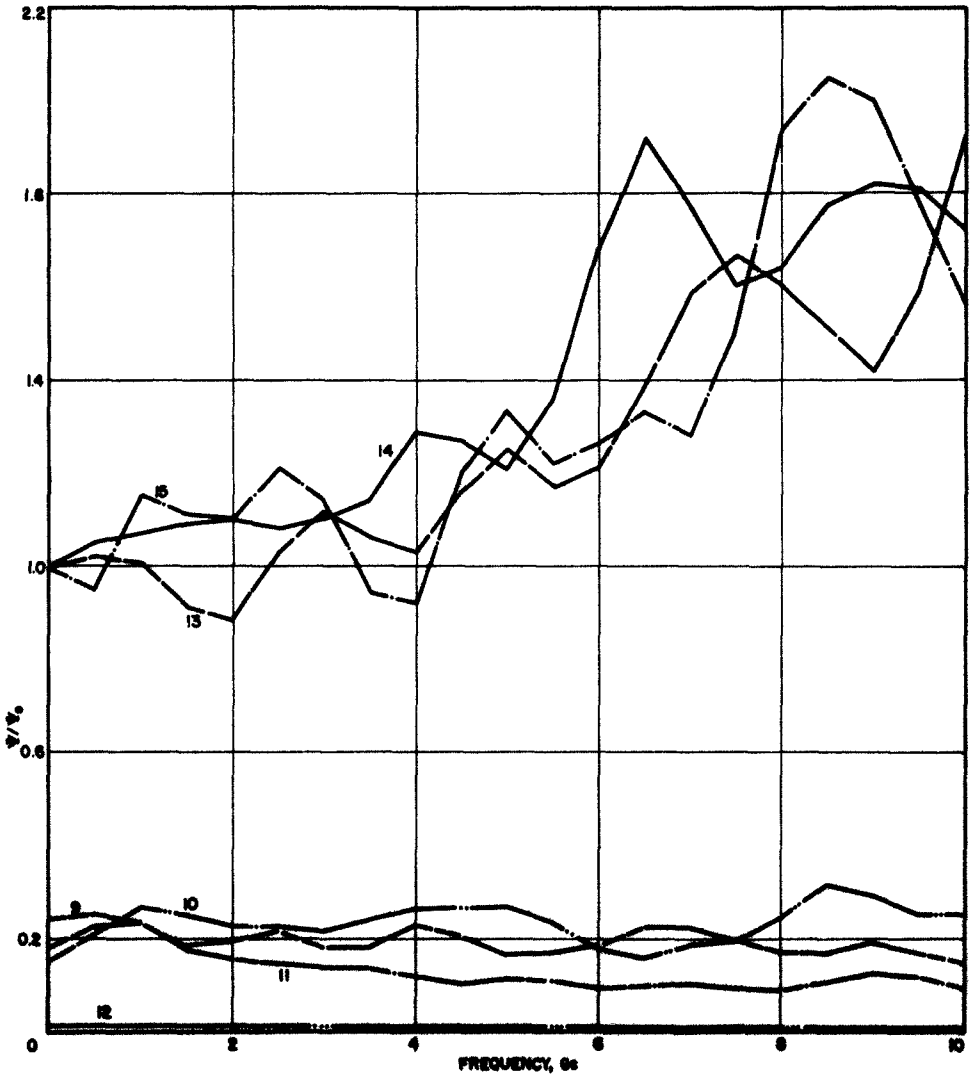

FIG. 7.20 ψ/ψ_0 VS. f.

cathode it may be concluded that some minimum excitation of current fluctuations is necessary in order to notice an appreciable change in the value of ψ/ψ_o as a function of f.

Figures 7.21 and 7.22 show the variation of the spectral density due to the a-c kinetic voltage. It can be seen from these plots that the velocity fluctuations do not decrease as the beam traverses the cycloid; instead the velocity fluctuations are increased. As the beam is accelerated the velocity fluctuations increase and reach very large values at the height of the cycloid. As the beam is then decelerated the velocity fluctuations are decreased, however there is a net growth in velocity fluctuations as the cycloid is completed. This behavior of velocity fluctuations is different from that of the current fluctuations, namely, that the current fluctuations are considerably reduced due to the presence of the potential minimum although the velocity fluctuations are not reduced and instead they increase considerably. This is also in contrast to the results for O-type devices, namely, that both ψ and Φ are decreased as the beam is accelerated. Because of the large values of the axial magnetic field in O-type devices there is no mixing of electrons from one layer to another. Moreover the electrons in various layers along any cross section perpendicular to the beam are traveling at approximately the same velocity. However in crossed-field devices there is no provision for avoiding mixing of electrons from one layer to another layer unless laminar flow is assured, and this causes a wide velocity distribution in a crossed-field beam. This illustrates also the advantages of a Kino gun[15] where more laminar electron flow could be expected.

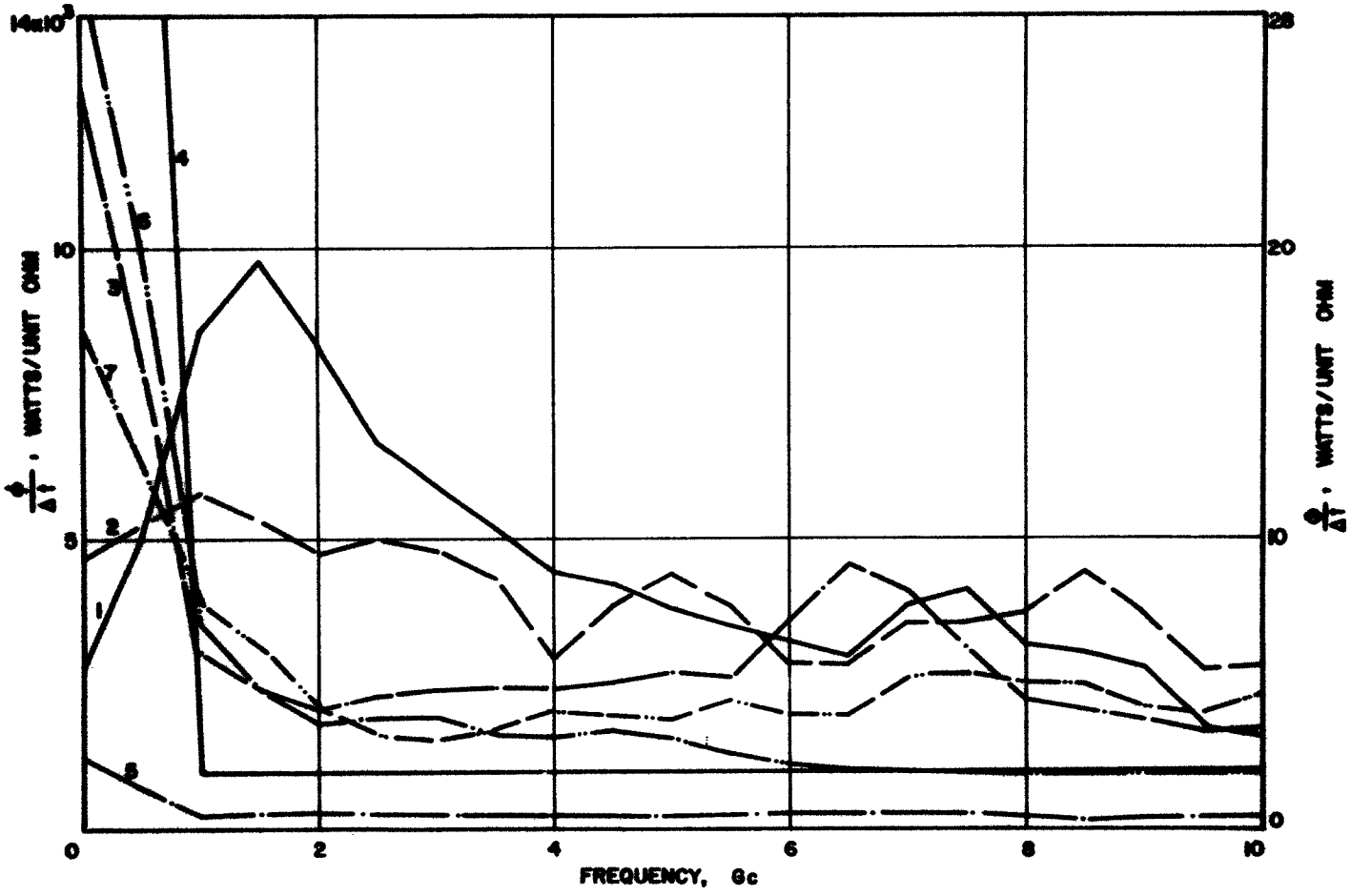
14x10^3
10
5
0
2
4
6
8
10
28
20
10
0
FREQUENCY, Gc
Φ/ΔT, WATTS/UNIT OHM
Φ/ΔT, WATTS/UNIT OHM
1
2
3
4
5
6
7

FIG. 7.21 Φ VS. f.

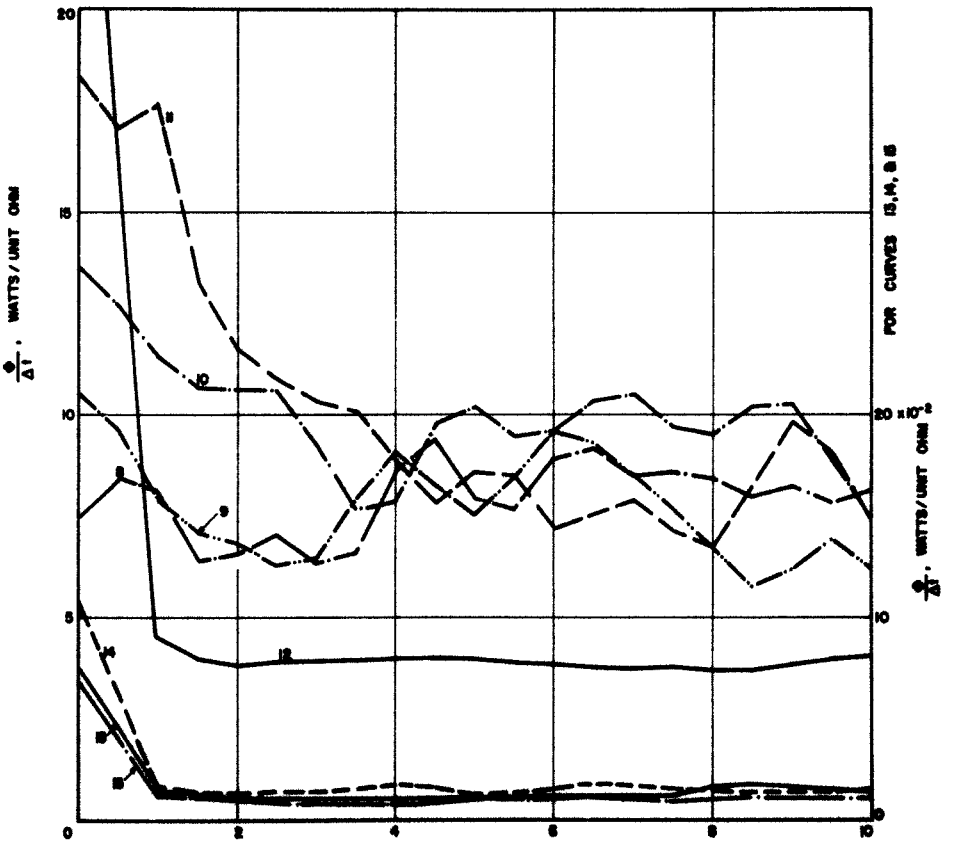

FIG. 7.22 Φ VS. f.

It is also interesting to note from Figs. 7.21 and 7.22 that the velocity fluctuations decrease as f is increased. This result is in qualitative agreement with the results given in Chapter III. The fact that the velocity fluctuations are maximum around f = 0 seems to illustrate why Miller[13] and Van Duzer[11] have found larger values of the electron equivalent temperature. The results given in Chapter IX, for the experimental study of noise, also indicate large values of the electron equivalent temperature.

Figures 7.23 and 7.24 show the variation of noise figure F versus f. Since the values of S and Π were normalized with respect to the value of S for rectangle 14 at f = 0, the noise figure, F is computed from the following formula:

$$F = 10 \log_{10} \left[1 + \frac{S-\Pi}{S_o} \frac{T_c}{T} \right] , \qquad (7.16)$$

where T_c is the cathode temperature and T is the room temperature; T_c = 1000° k and T = 300° k. The variation of F for rectangles 13 and 15 is nearly the same as that for rectangle 14 and hence the curve for rectangle 14 only is drawn. It can be seen from these plots that as the beam is accelerated the value of F is increased and reaches a maximum value at the height of the cycloid. As the beam is decelerated the value of F is decreased. The value of F for rectangle 6 is larger than that for rectangle 7. This may be due to larger values of the average number of electrons in rectangle 6 as illustrated in Table 7.3. It is further noticed that at the end of the cycloid the value of F is at least 10 db larger than that at the start of the cycloid. The value of F for rectangle 12 is lower than that for rectangle 11 and is due to the larger

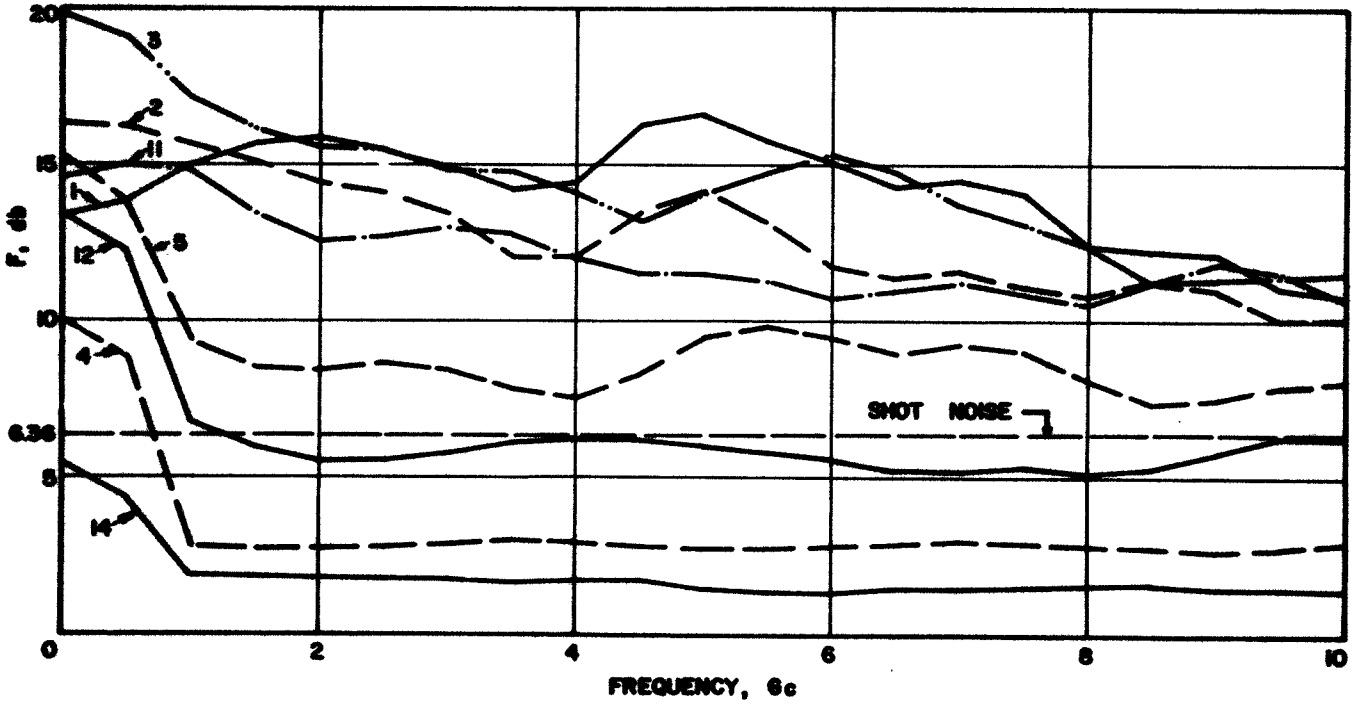
20
15
10
6.36
5
0
2
4
6
8
10
F, db
FREQUENCY, Gc
SHOT NOISE
3
2
11
1
12
5
4
14

FIG. 7.23 F VS. f.

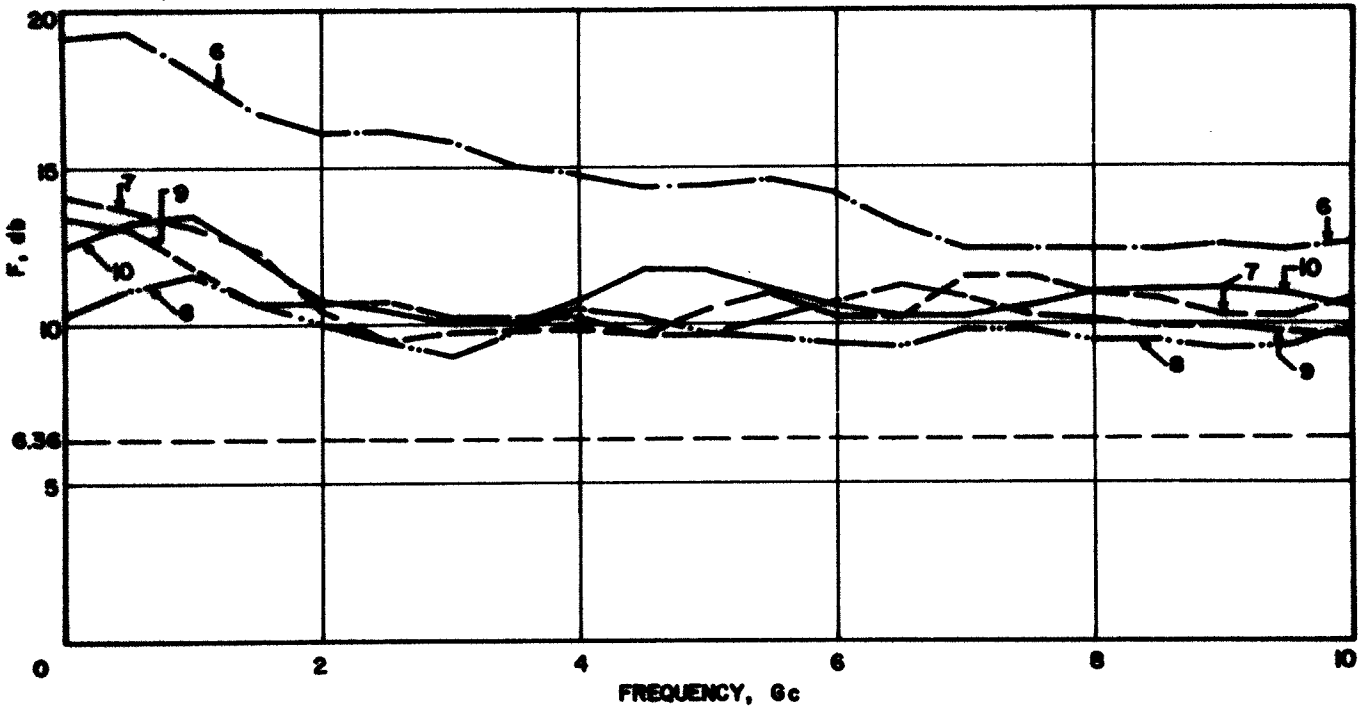

FIG. 7.24 F VS. f.

value of the average number of electrons in rectangle 11 as illustrated in Table 7.3.

The increase in the value of F is primarily due to an increase in the velocity fluctuations as found from the plots in Figs. 7.21 and 7.22. In general the value of F reaches the value of F for shot noise (6.36 db for $S/S_o = 1.0$ and $\Pi = 0$) for large values of f and this behavior is very similar to that of O-type devices except that for O-type devices the value of F at low frequencies is smaller than that of shot noise.

7.7 Conclusions

In this chapter results for the auto-correlation functions and the various noise parameters for different portions of the beam are given. This information has been very helpful in interpreting the noise behavior of crossed-field tubes and correlating the results with experimental results. It is found that V_m and y_m do not have the same values for all values of z. This would mean a, y and z variation of the several d-c and a-c parameters. The correlation between the a-c kinetic voltage and current fluctuations is quite large. This may be partly due to the fact that the velocity and current density components were related through the space-charge density. This relationship was used for the instantaneous and average values of these parameters. It is not clear how much effect this would have on the a-c fluctuations as defined in the last chapter. It is interesting to note that in the Monte Carlo analysis of a two-dimensional O-type diode, Wen* has noticed values of Π as high as 0.85 which is somewhat higher than the values calculated here.

---

* Electron Physics Laboratory, The University of Michigan, forthcoming report.

These results indicate that both the fast and slow waves grow although the overall growth rate of the slow wave is larger than that for the fast wave. The larger values of growth are noticed in the latter part of the first half of the cycloid and these results are in agreement with those given in Chapter V. Some finite growth of the two waves is also found in the earlier part of the cycloid. This is different from the results given in Chapter V where no such growth is noticed. This may be due to the fact that the higher order modes and the d-c z-component field are not considered in the density method. It is interesting to note that most of the plots given in Chapter III indicate a finite growth in the earlier part of the cycloid.

The larger noise figure in crossed-field devices is possibly due to larger values of the velocity fluctuations. It is noticed that the current fluctuations are very much smoothed out due to the presence of the potential minimum but there is no reduction in the velocity fluctuations and instead the velocity fluctuations are increased as the beam is accelerated. It is noticed that the values of Φ for rectangles 4 and 5 are much larger than those for rectangles 1 and 2. This shows that the inner edge of the beam has larger velocity fluctuations and would give larger values of the electron equivalent temperature. This result is in agreement with the results given by Rao and Whinnery[26] and are also in agreement with those of Pollack[29], namely that for the values of B/B_c for which Pollack obtained results for the anode current and velocity fluctuations, the velocity fluctuations are larger than that corresponding to the cathode temperature while the current fluctuations are less than or equal to those for the shot noise. The values of F for rectangles 4 and 5 are smaller than those for rectangles 1 and 2. This illustrates

an important point that the noise in a beam should be specified in terms of both F and electron equivalent temperature. It is anticipated that large values of the velocity fluctuations are due to mixing of electrons from one layer to another layer and could be reduced considerably if a laminar flow is assured.

In a statistical analysis the mean square error is inversely proportional to the square root of the number of samples under examination. In this analysis all the electrons have not been considered individually and a scaling parameter D_1 is used; this means that D_1^2 electrons are identical in terms of their position coordinates and velocity components. It is expected that the total number of electrons considered individually is still quite large and the mean square error will not be large.

CHAPTER VIII. EXPERIMENTAL INVESTIGATION OF NOISE IN INJECTED-BEAM CROSSED-FIELD DEVICES

8.1 Introduction

In order to achieve the maximum potential of crossed-field devices in terms of their high efficiency, with a maximum possible signal-to-noise ratio, it is important to analyze the noise origin and its propagation in these devices. These studies will hopefully lead to some practical methods of reducing the amount of noise output usually experienced. As this noise appears principally under space-charge-limited conditions, it is believed that the source of noise is due to the presence of the potential minimum, meaning thereby that there is relatively large growth of perturbation in the gun region. These perturbations may arise near the potential minimum.

Experimental investigation of the noise phenomenon cannot be ignored because of the approximations used in the analytic methods such as the density function method and the Llewellyn method. This nonlinearity of the potential minimum region is considered in the Monte Carlo method for analyzing the transport of noise. Since the physical configuration of the diode considered in these analytical approaches is somewhat different from that of the usual type of experimental tubes the results must be correlated with experimental results accordingly.

The experimental device designed for the purpose of noise studies is shown in Fig. 8.1. This experimental device is of a versatile nature and consists of the following major parts:

1.)PUSH PULL SEAL DRIVE-MECHANISM 2.) PUMP OUTLET 3.) PUSH PULL SEAL CASING
4.) GLASS ENVELOPE 5.) SOLE 6.) BASE PLATE 7.) ANODE 8.) COLLECTOR
9.) PROBE GUIDE RODS 10.) PROBE GUIDE 11.) TUBING 12.) CATHODE BLOCK MOUNT
13.) PLATE FOR D-C PINS

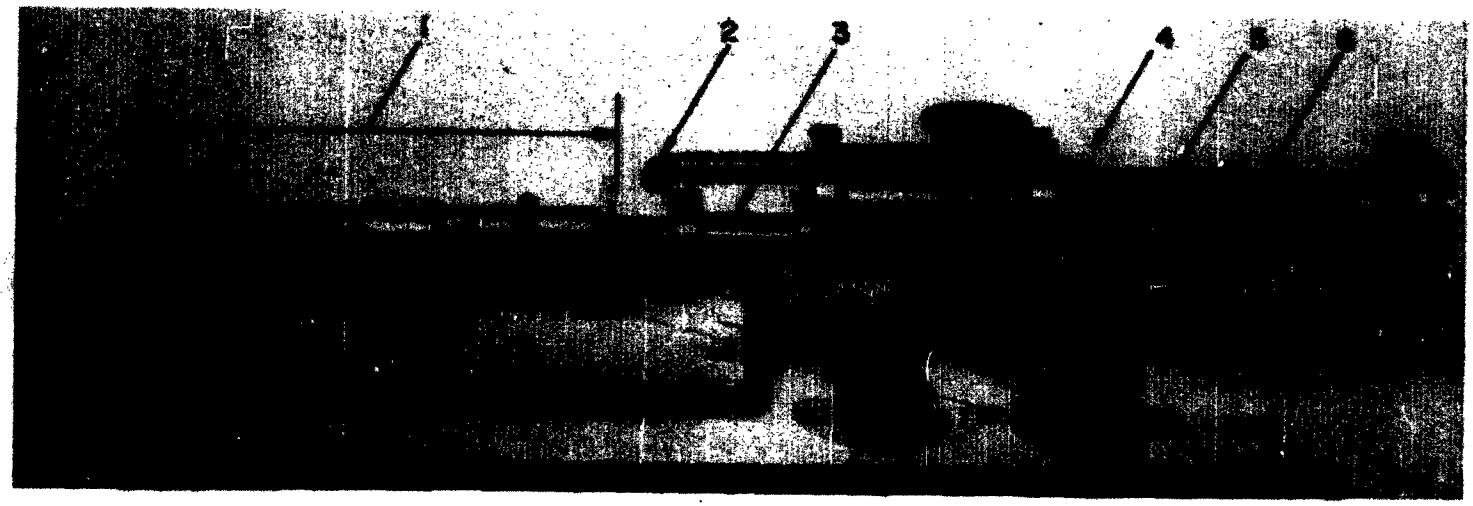

FIG. 8.1 AN OVERALL ASSEMBLY OF THE CROSSED-FIELD DEVICE.

1.)PUSH PULL SEAL DRIVE-MECHANISM 2.) PUMP OUTLET 3.) PUSH PULL SEAL CASING
4.) GLASS ENVELOPE 5.) SOLE 6.) BASE PLATE 7.) ANODE 8.) COLLECTOR
9.) PROBE GUIDE RODS 10.) PROBE GUIDE 11.) TUBING 12.) CATHODE BLOCK MOUNT
13.) PLATE FOR D-C PINS

FIG. 8.1 AN OVERALL ASSEMBLY OF THE CROSSED-FIELD DEVICE.

1. The electron gun.
2. The sole and the sole segments.
3. The slotted anode.
4. The collector.
5. R-f injection and detection probes.
6. Push-pull seal and driving mechanism.

8.2 The Electron Gun

The electron gun for crossed-field devices may be either of the following two types:

1. The electrons are accelerated to the required d-c velocity and are then allowed to enter the uniform magnetic field region through a transition region. Because of the restrictions in the variation of the magnetic field in the transition region, this technique is not used very often.
2. In practical tubes, the electrons are accelerated by a d-c potential in the presence of an orthogonal magnetic field. The electrons under the influence of both the electric and magnetic fields describe cycloidal trajectories. In an ideal device the electrons are allowed to enter the interaction region when the y-directed velocity is zero and the z-directed velocity is of an appropriate magnitude so as to give straight-line motion of the electrons in the interaction region.

The electron gun used in this experimental device is of the latter type. The cathode assembly consists of three separate (isolated) cathodes placed side by side. The main reason for splitting them into three separate cathodes is to enable the study of multistream phenomenon similar to that in O-type devices described by Haeff[34]. These three cathodes

may be operated independently under the same gun anode voltage and magnetic field and provisions have been made to use any type of cathode.

Gould[16] has developed a formula for the diocotron gain in the interaction region of the crossed-field device which can be used to estimate the rate of growth of any perturbation. Its reliability has been verified experimentally by Harris[35] and Sato[36]. From similar measurements it seems possible to estimate the overall growth in the gun region provided a modulating device is used very close to the cathode. The structure used for modulating and demodulating the beam in these two cases was restricted to a relatively narrow bandwidth. After considering the range of frequencies of signals detected as noise in these devices, it was deemed necessary to use probes for r-f injection and detection purposes. The efficiency of such a probe as an antenna varies with frequency, but this makes it possible to cover a much larger bandwidth than if cavities were used. Because of the use of the probes and the three segmented cathodes, the minimum distance between the anode and the sole in the interaction region is limited.

Table 8.1 presents the results of a few calculations concerning the various parameters d, y_o, z_o, V_o, I_o, B and G, for the three cathodes. The parameters d, y_o, z_o, and d_1 are indicated in Fig. 8.2. These parameters are defined as

d = distance between the gun anode and the cathode;

y_o, z_o = the coordinates of a point in the y-z plane where the electron under consideration has zero y-directed velocity, and the z-directed velocity is of an appropriate magnitude to give straight-line path in the interaction region;

V_o = the gun anode voltage (also equal to the anode voltage);

Table 8.1

G as a Function of d for Idealized Flow

d	V_o	y_o	z_o	I_o	B	G/f_{mc}
Inch	Volts	Inch	Inches	ma	Gauss	db/m
	V_{o2} 500	0.3	0.471	6.8		1.52
0.4	V_{o3} 362	0.217	0.341	4.2	85.6	2.3
	V_{o1} 638	0.383	0.601	9.8		1.06
	V_{o2} 500	0.45	0.707	3.0		1.01
0.6	V_{o3} 408	0.367	0.577	2.52	57.1	1.55
	V_{o1} 592	0.533	0.837	3.86		0.79
	V_{o2} 500	0.6	0.942	1.7		0.76
0.8	V_{o3} 431	0.517	0.812	1.36	42.8	0.96
	V_{o1} 569	0.682	1.072	2.06		0.63
	V_{o2} 500	0.75	1.178	1.1		0.60
1.0	V_{o3} 445	0.667	1.048	0.93	34.4	0.72
	V_{o1} 555	0.833	1.308	1.28		0.52
	V_{o2} 500	1.2	1.885	0.425		0.38
1.6	V_{o3} 465	1.117	1.755	0.382	21.4	0.42
	V_{o1} 535	1.283	2.015	0.470		0.32

(It has been assumed that the beam from the central cathode lies in the center of the interaction region and the length of the beam in the direction of the magnetic field is taken as 0.8 inch.)

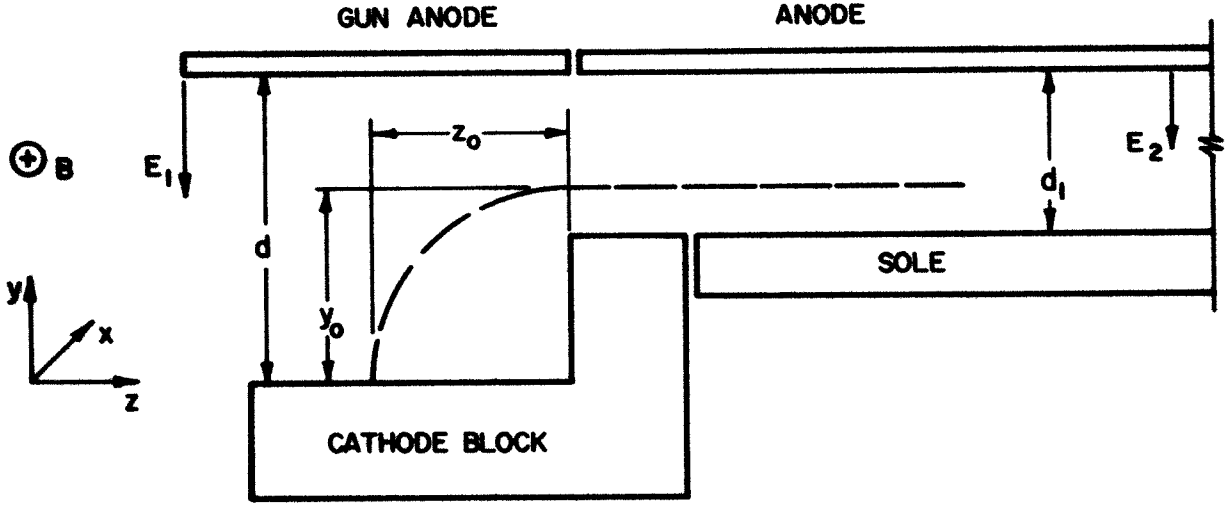

FIG. 8.2 AN IDEAL TRAJECTORY OF AN ELECTRON EMITTED FROM THE CENTER OF THE CATHODE.

I_o = the current emitted from the cathode under space-charge-limited conditions, computed from the Child-Langmuir law;

B = the magnetic flux density; and

G = the diocotron gain as computed from Gould's formula;

$$G = \frac{2.4\ I_o f}{B_o\ w\ u_o^3} \times 10^{12}\ \text{db/m} \quad , \tag{8.1}$$

in which

f = the signal frequency in c/s,

w = the width of the beam in meters,

u_o = the average z-directed velocity in the interaction region,

B_o = the magnetic flux density in Wb/m^2,

I_o = the beam current in amps.

In all these cases d_1, the distance between the sole and the anode, is taken as d/2.

In Table 8.1, y_o and z_o are computed for the electrons emitted from the center of the respective cathodes. Subsuffixes 1, 2 and 3 refer to the three cathodes respectively, cathode No. 2 being the central cathode and cathode No. 3 being the one closer to the interaction region.

Figures 8.3 and 8.4 indicate the space-charge-free trajectories of nine electrons emitted from the three cathodes. Two of the three electrons from each cathode are from the extreme edges. These trajectories were plotted with the use of an analog computer according to the technique developed by Rowe and Martin[37] and these plots of trajectories may be interpreted for different values of the spacing d by varying the values of the space scaling parameter and by changing the scaling constant involving the value of the magnetic field.

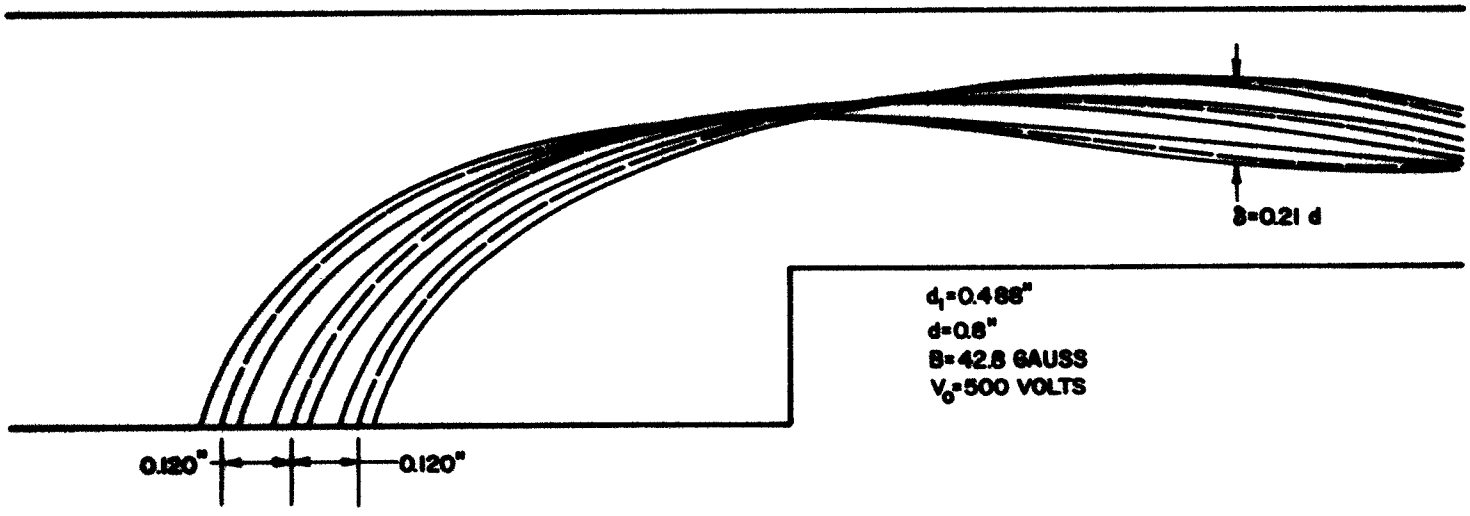

FIG. 8.3 ELECTRON TRAJECTORIES FROM THE THREE CATHODES. (ZERO SPACE CHARGE)

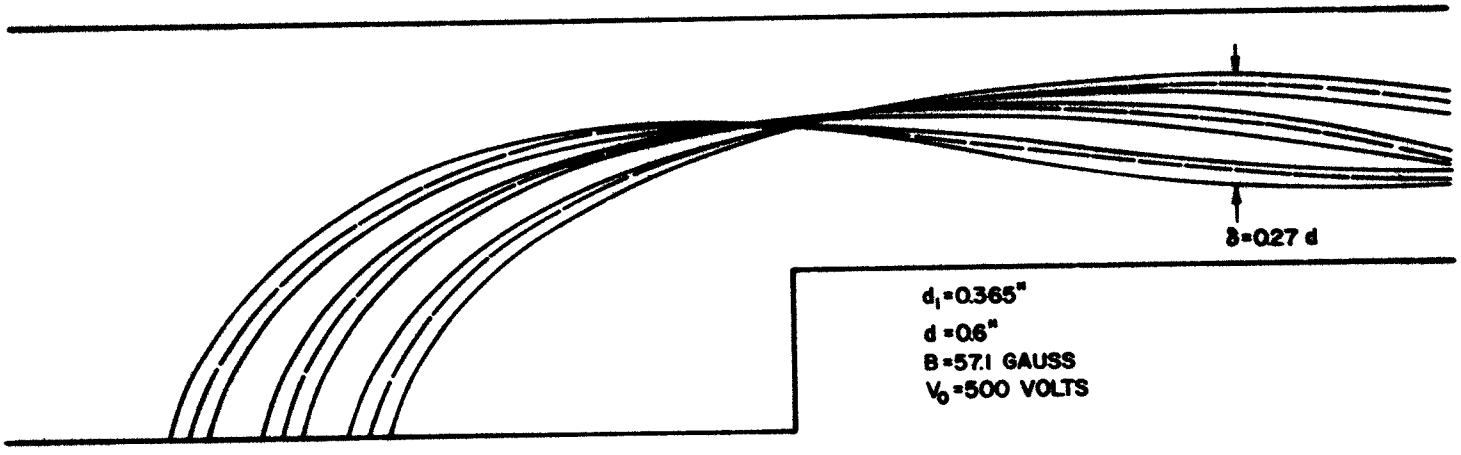

FIG. 8.4 ELECTRON TRAJECTORIES FROM THE THREE CATHODES. (ZERO SPACE CHARGE)

Figures 8.3 and 8.4 correspond to d = 0.8 inch and 0.6 inch respectively. Figures 8.5 and 8.6 are for different gun anode and anode voltages; these voltages are indicated as V_{o1}, V_{o2} and V_{o3}. When the electrons are emitted from the center of the respective cathodes, the value of the parameter y_o is the same for the three cathodes. The trajectory plots in Figs. 8.5 and 8.6 ensure at least straight-line motion of the electrons to a maximum possible degree when these cathodes are operated separately.

A value of d_1 = 0.365 inch which corresponds to d = 0.6 inch in Fig. 8.4. It appears from Fig. 8.6 that if the gun anode were given a downwards slope, it might be possible to operate the three cathodes simultaneously with a smaller value of δ. The analytic treatment for such a case is rather difficult. Three values of θ (θ indicated in Fig. 8.7, θ = 5, 10 and 20 degrees) were tried. For higher values of θ, there is a tendency to give electron collection. The positions of the cathodes were varied so as to obtain near optimum trajectories. According to this design the effective distance d for computing the total current emitted from the three respective cathodes from the Child-Langmuir law is different for the three cathodes and this varies with the angle θ also.

In Table 8.2, δ/d_1, I_{o1}/I_{op}, I_{o2}/I_{op} and I_{o3}/I_{op} are tabulated for various values of θ, where I_{o1}, I_{o2} and I_{o3} represent the total currents from the three cathodes respectively for different values of θ. I_{op} refers to the total current emitted from any one of the three cathodes (the three currents being equal) for a planar gun anode θ = 0).

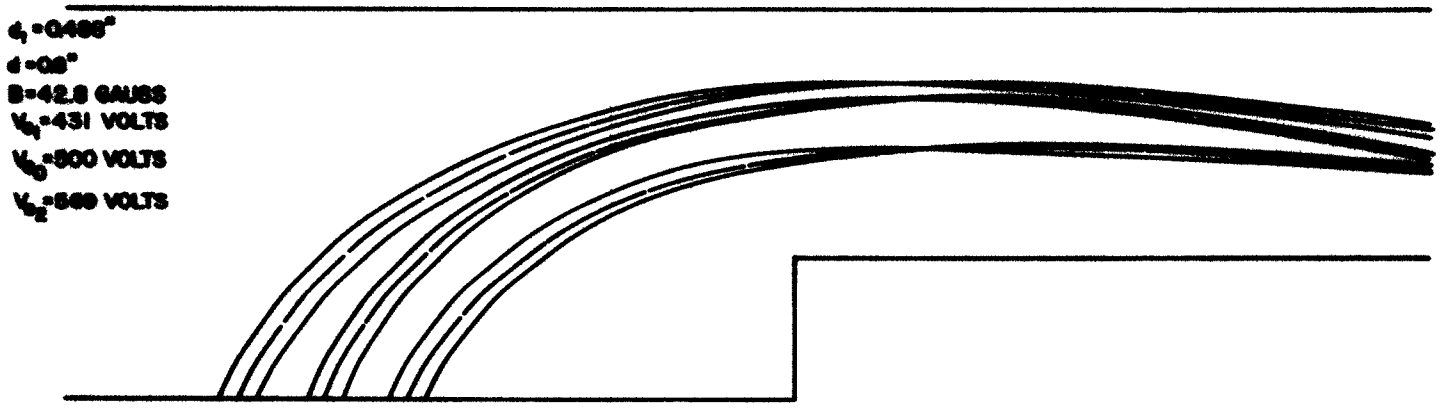

FIG. 8.5 ELECTRON TRAJECTORIES FROM THE THREE CATHODES. (ZERO SPACE CHARGE)

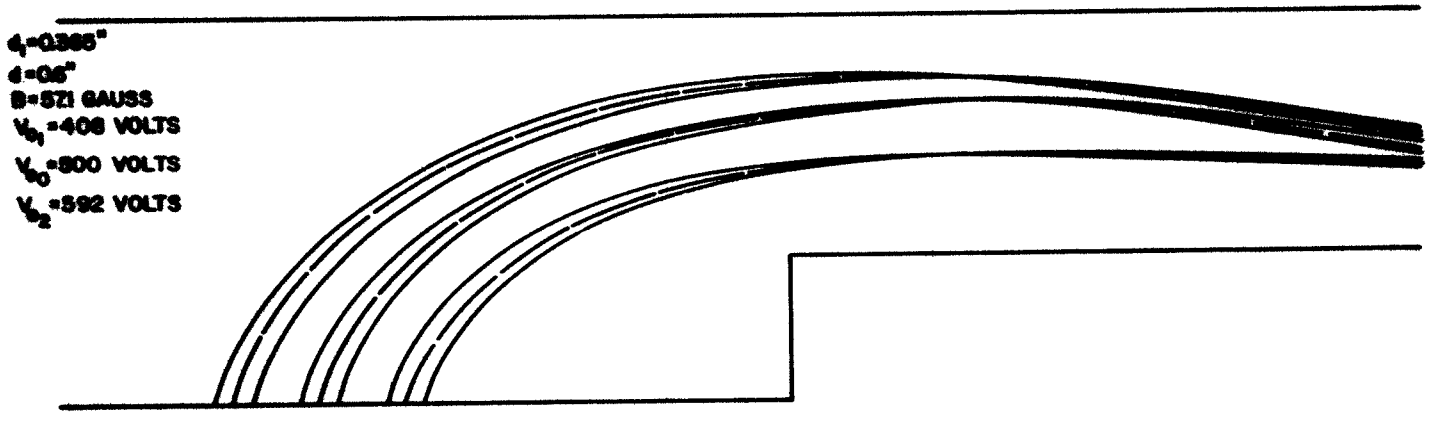

FIG. 8.6 ELECTRON TRAJECTORIES FROM THE THREE CATHODES. (ZERO SPACE CHARGE)

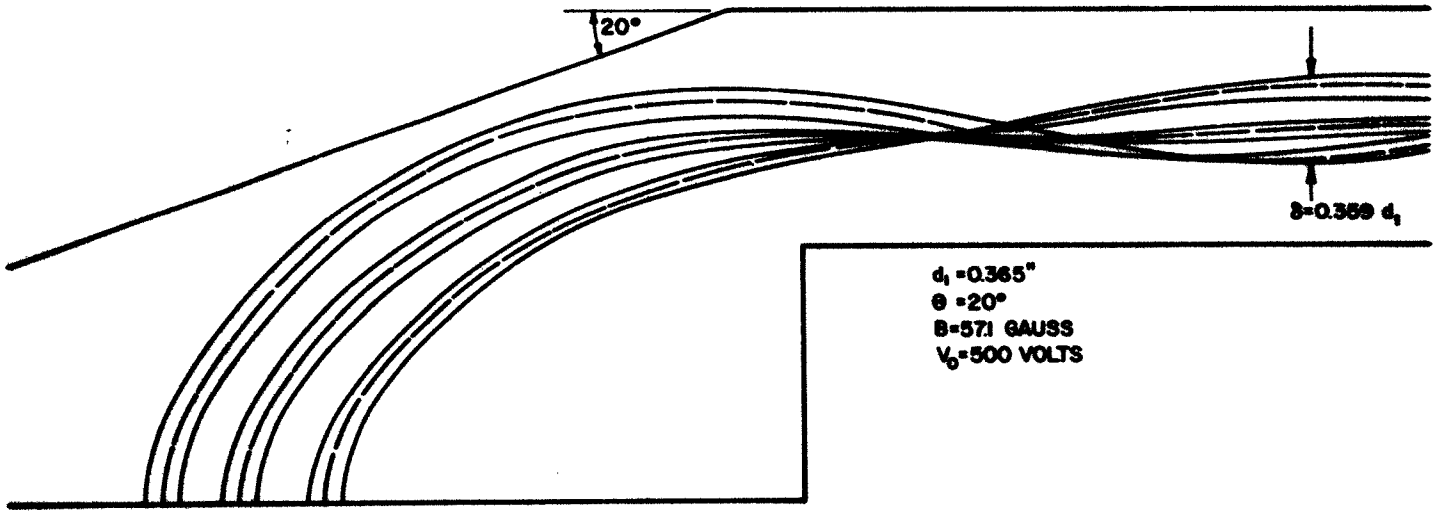

FIG. 8.7 ELECTRON TRAJECTORIES FROM THE THREE CATHODES. (ZERO SPACE CHARGE)

Table 8.2

Maximum Deviation in Trajectories as a Function of Angle θ

$\theta_{DEG.}$	δ/d_1	I_{o1}/I_{op}	I_{o2}/I_{op}	I_{o3}/I_{op}
5	0.42	1.14	1.1	1.07
10	0.39	1.36	1.26	1.14
20	0.36	1.77	1.46	1.22

Considering the values tabulated in Table 8.2, θ = 20 degrees was selected and the trajectories for the nine electrons corresponding to this case are shown in Fig. 8.7. Provisions have been made to operate the gun anode and the anode at two different voltages. End hats have been included to avoid the dispersion of the beam in the direction of the magnetic field. The cathode block assembly showing the slots for the three cathodes, small holes for r-f injection probes and the block mount is shown in Fig. 8.8.

8.3 The Sole and the Sole Segments

The sole electrode is essentially a smooth conducting sheet and forms one of the two parallel plates of the crossed-field tube drift region. The presence of noise in crossed-field tubes has been correlated with the presence of the sole current which probably arises due to poor beam focusing techniques.

A great deal of experimental investigation regarding the existence and distribution of the sole current has been carried out by Miller[13]. The sole segments used in this structure are in the form of glazed molybdenum blocks insulated from one another and the sole. These segments rest freely in the slots cut in the sole structure which is also provided with end hats and molybdenum blocks (see Fig. 8.9).

1) HOLES FOR R-F PROBES 2.) SLOTS FOR CATHODES 3.) CATHODE BLOCK
4.) CATHODE BLOCK MOUNT 5.) HOLES FOR COAXIAL CABLES
6.) HOLES FOR D-C LEADS

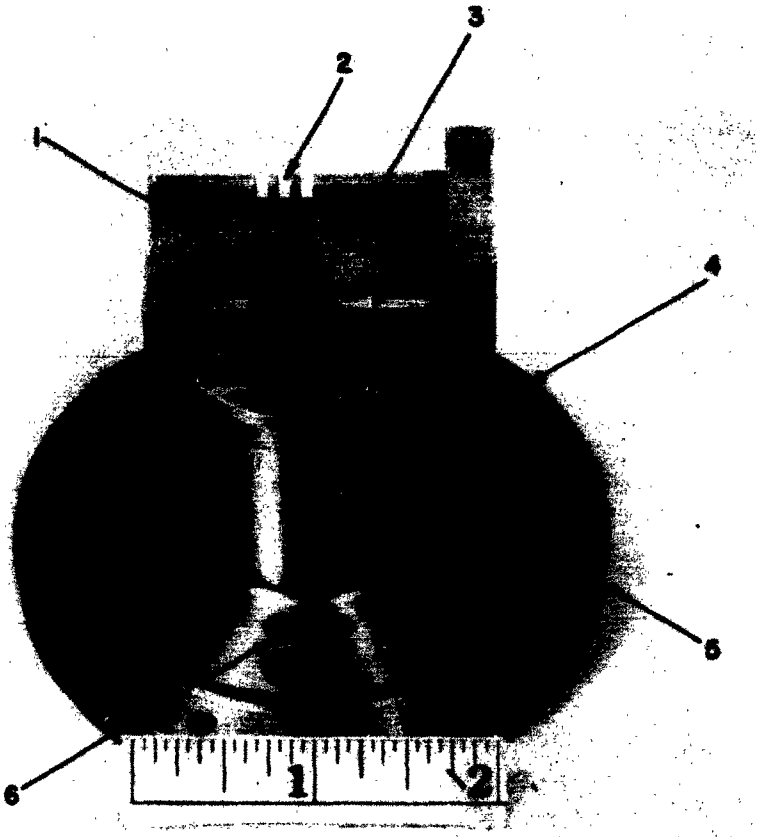

FIG. 8.8 CATHODE BLOCK WITH SLOTS FOR THREE CATHODES AND HOLES FOR R-F PROBES MOUNTED ON THE CATHODE BLOCK MOUNT.

1.) GLAZED MOLYBDENUM BLOCKS 2.) CERAMIC SUPPORTS

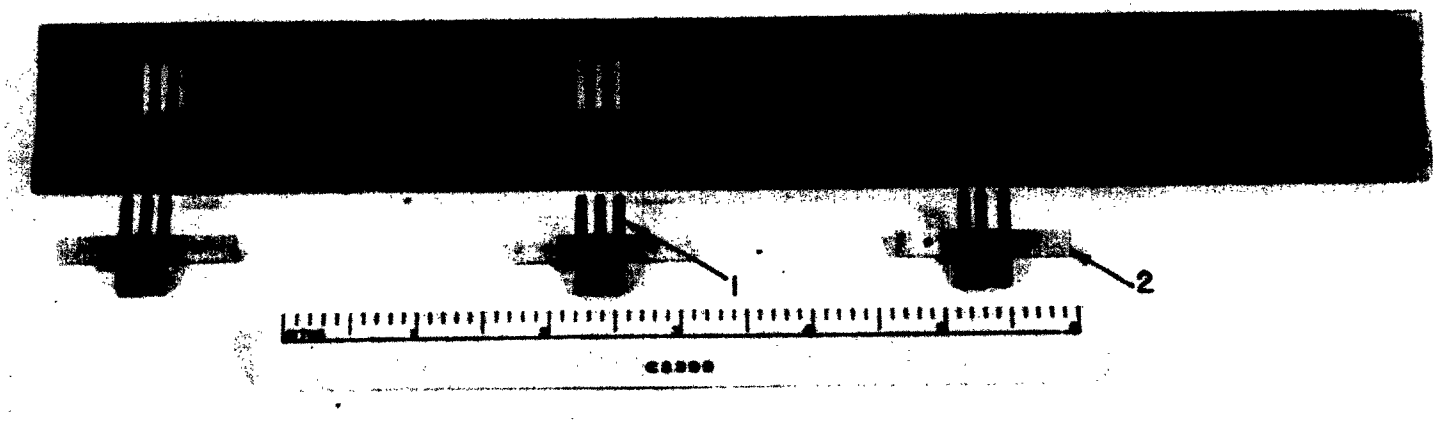

FIG. 8.9 SOLE STRUCTURE WITH GLAZED MOLYBDENUM BLOCKS.

8.4 The Slotted Anode

The slotted anode is the second parallel plate of the crossed-field tube drift region. This plate has three slots equally spaced and the central slot corresponds to the center of the beam. The r-f probes for detection purposes pass through these slots to permit probing in the magnetic field direction. The presence of the end hats restricts the beam spreading in the direction of the magnetic field, but it is very likely that oscillations of the electrons along the x-axis may be one of the major causes of noise in crossed-field devices.

The complete assembly of the gun anode, anode, sole structure and base plate is shown in Fig. 8.10. The gun anode and the anode are insulated from each other and the spacing between the three parallel plates is precisely adjusted by the ceramic spacer, also shown in Fig. 8.10.

8.5 The Collector

The collector electrode consists of three parts -- two metal plates and a BeO plate. The BeO plate has a reasonably high heat conductivity and a high d-c insulating resistance. The metal plate closest to the anode structure forms the high-voltage plate and the stainless steel tubes are attached to the other metal plate (termed the ground plate) to carry cooling water.

8.6 R-f Injection and Detection

As mentioned in Sections 8.2 and 8.4, one of the purposes of this investigation is to inject an r-f signal very close to the potential minimum and study its propagation in the drift region. Needless to say these probes may be used for studying the d-c characteristics of the beam

1.) GUN ANODE 2.) ANODE 3.) SLOTS FOR R-F PROBES 4.) CERAMIC SPACERS
5.) BASE PLATE 6.) SOLE

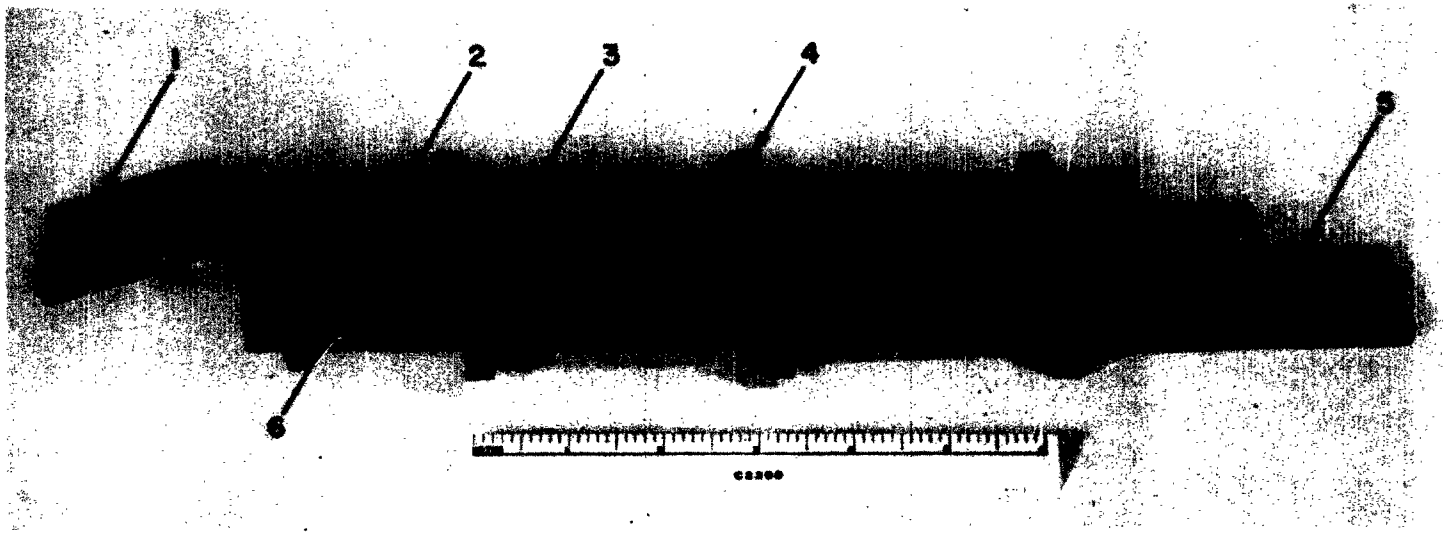

FIG. 8.10 ASSEMBLY OF GUN ANODE, ANODE, SOLE AND BASE PLATE.

also. In the present design of the gun anode it will be difficult to detect the propagation in the gun region, but an overall estimate of the propagation can be estimated from the measurements in the drift region. The r-f injection and r-f detection probes are also arranged in the direction of the magnetic field.

The inner conductor of the r-f injection coaxial cables is molybdenum with an outer conductor of inconnel tubing and these cables were constructed according to the technique developed by Nunn and Paul[38]. In all there are nine r-f probes in the gun region and an additional three r-f probes are introduced in the region between the sole and the cathode block.

The r-f detector probes are the extensions of the inner conductors of rigid copper coaxial cables with teflon as the dielectric material. These cables pass through a hollow stainless steel tubing which forms a part of the push-pull seal and the driving mechanism (to be described in Section 8.7). A schematic of these twelve probes is shown in Fig. 8.11.

8.7 Push-Pull Seal and Driving Mechanism

In order to make some measurements on the propagation of any perturbation, it is necessary that the detecting devices be distributed uniformly along the beam and, if it is not possible to have a number of detecting devices, it should be possible to move them back and forth. For the present study a push-pull seal was developed. This makes it possible to move a stainless steel tubing back and forth by a gear-screw arrangement shown in Fig. 8.14. Three coaxial cables pass through the slots in the anode structure. To avoid vibrations and lateral movement of the tubing, and hence that of the inner conductors of the coaxial

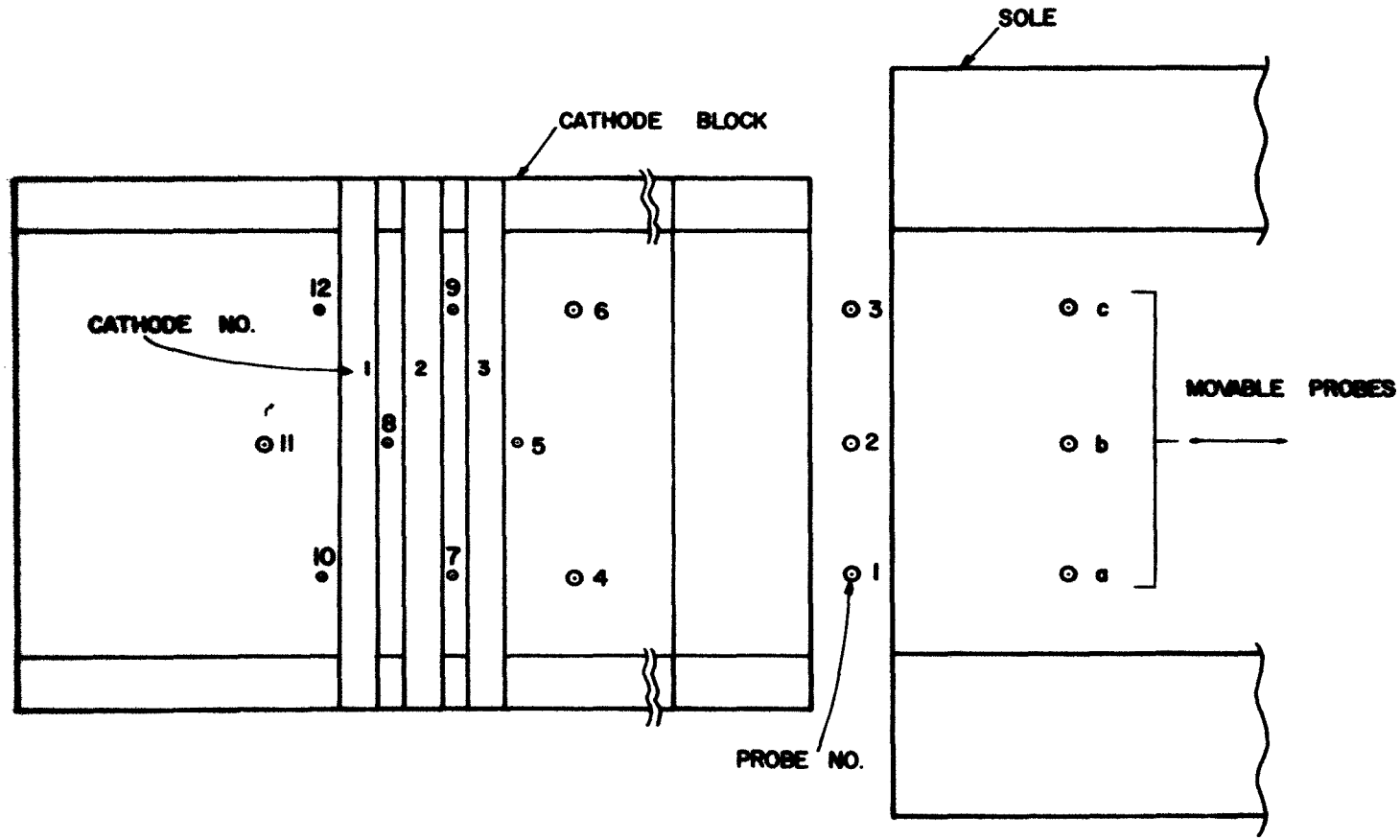

FIG. 8.11 PROBES AND CATHODES CONFIGURATION.

cables, it is guided by a trolley which is further guided by two polished rods spanning the tube and supported at the two end manifolds.

The design of the push-pull seal is similar to that used by Slocum[39] and consists of alternately spaced teflon and stainless steel washers which are compressed by a heavy spring, thereby making a vacuum seal. The complete assembly drawing of this seal is shown in Fig. 8.12. The movements of the detecting probes can be directly transformed to an x-y plotter by a geared helipot arrangement. The assembly drawing of the complete device is shown in Figs. 8.13 and 8.14. Figure 8.13 illustrates the tube and the push-pull seal while Fig. 8.14 relates to the wheel and gear-screw mechanism used to move the probes. The plate shown on the right-hand side of Fig. 8.14 is fastened to the casing shown on the left side of Fig. 8.13 by means of screws.

The overall assembly of the tube mounted on the vacuum station is shown in Fig. 8.15. The wheel and the gear-screw drive mechanism to drive the push-pull seal can be seen on the left side of Fig. 8.15. After the connections have been made to the appropriate points on the tube, the magnet shown on the right side of Fig. 8.16 may be moved to an appropriate position. The collector is inclined at an angle of 10 degrees and one set of sole segments can easily be seen in Fig. 8.16. The connectors for the r-f input probes are staggered and their layout may be seen in Fig. 8.17. The movable tubing which carries three coaxial cables and the attached trolley which is guided by two rods stretched across the tube may also be seen clearly in Fig. 8.17. The positions of the blocks which support the main folds are adjusted and the rods which support the blocks extend across the magnet. This makes it convenient to move the magnet without disturbing the support.

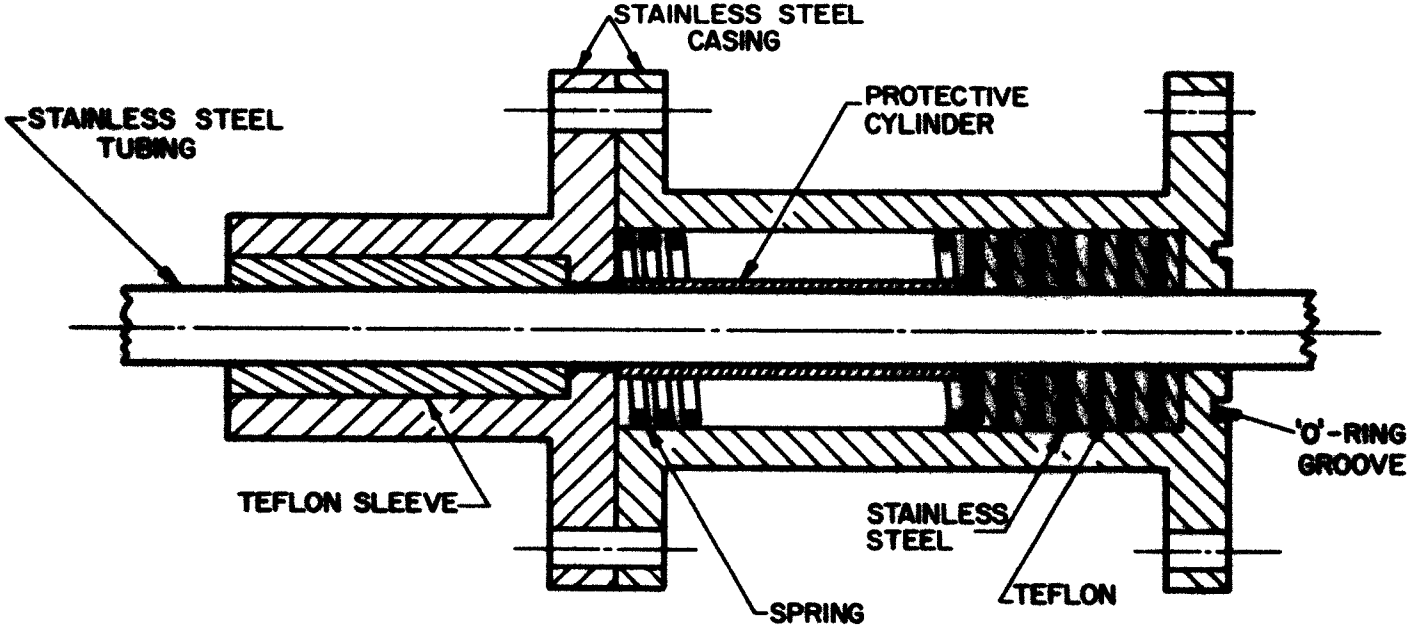

FIG. 8.12 ASSEMBLY DRAWING OF PUSH-PULL SEAL.

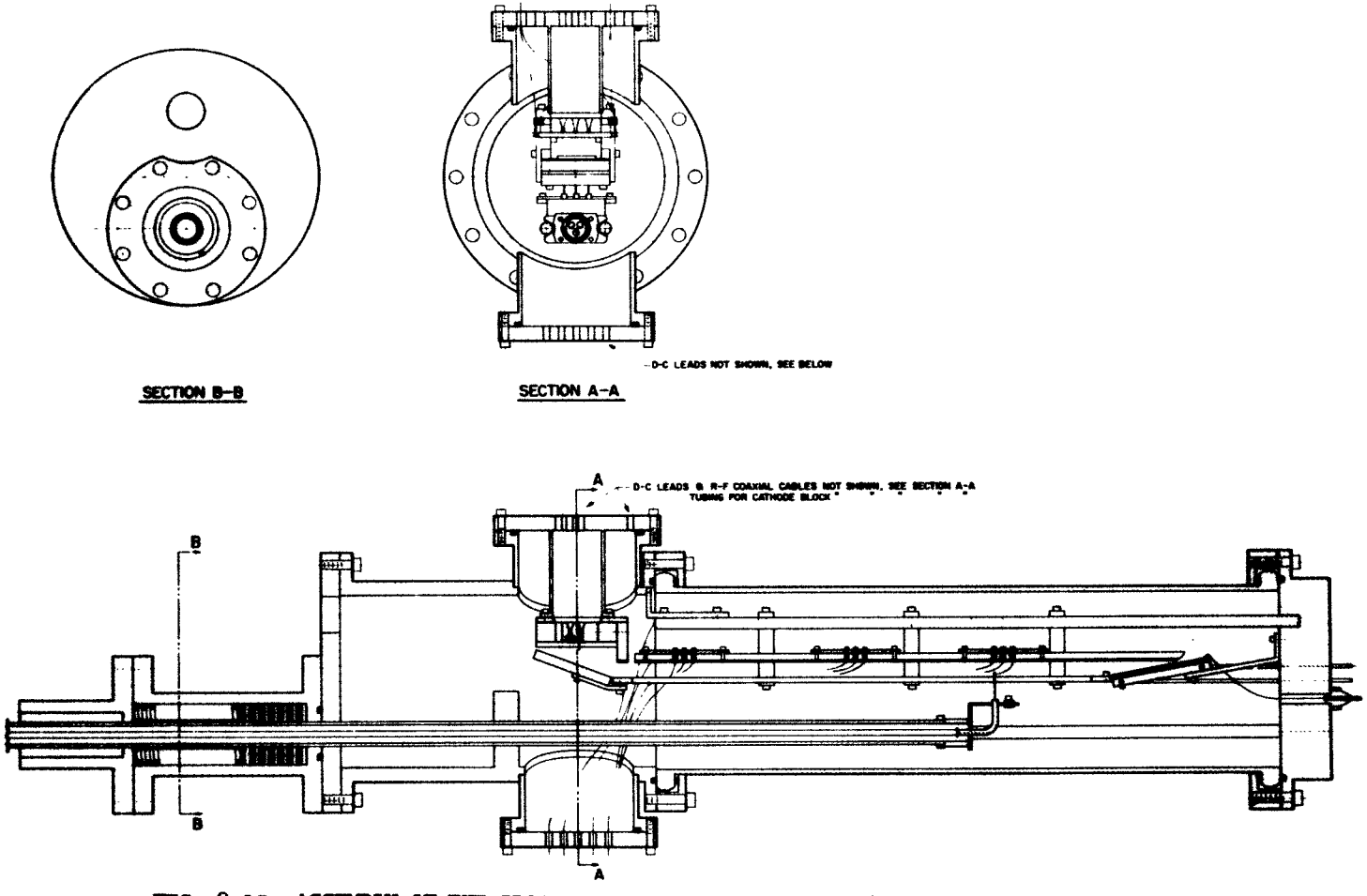

FIG. 8.13 ASSEMBLY OF THE CROSSED-FIELD NOISE ANALYZER (TUBE AND PUSH-PULL SEAL).

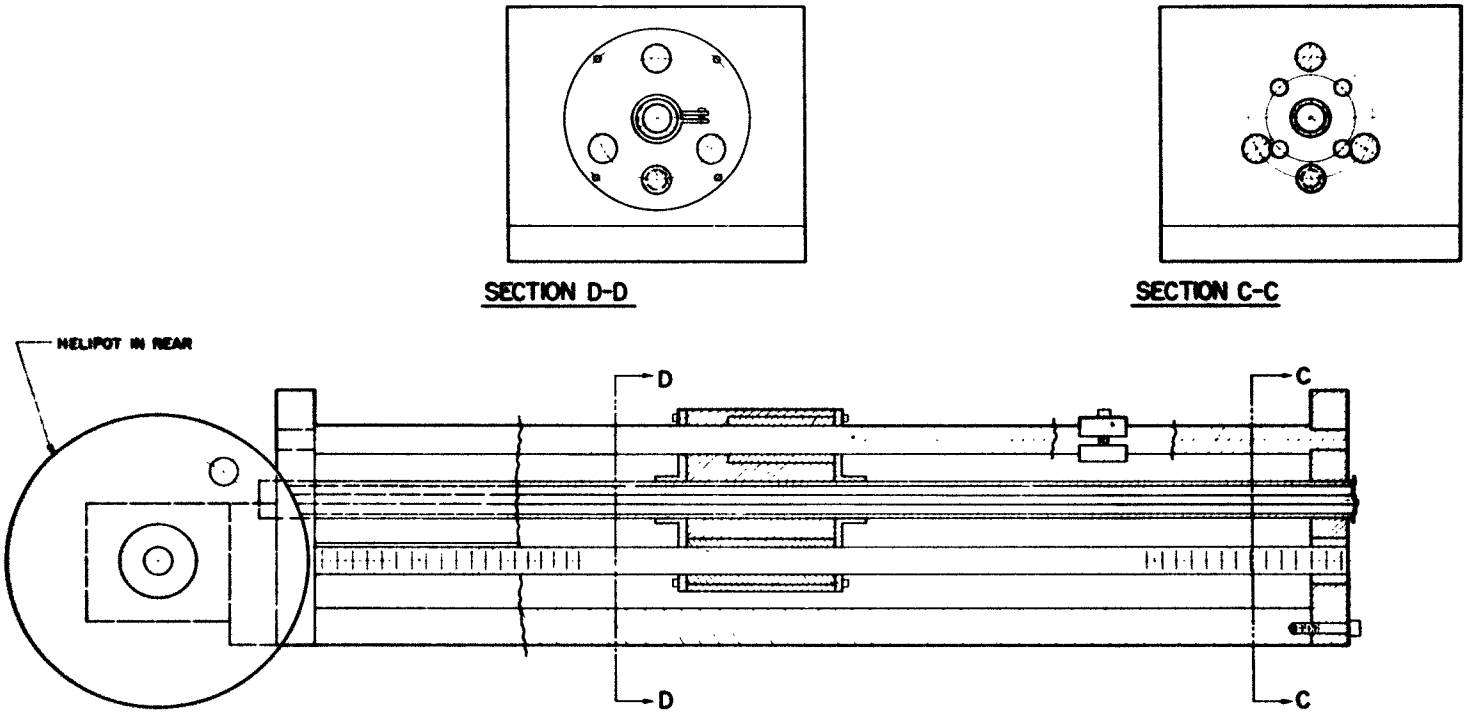

ELECTRON PHYSICS LABORATORY UNIVERSITY OF MICHIGAN	CROSSED-FIELD NOISE ANALYZER (DRIVE MECHANISM)
PROJECT 02854	DESIGNED BY: R. P. WADHWA DRAWN BY: G. BEAUCHAMP APPROVED BY: 11-20-61
D-10,041A	

FIG. 8.14 ASSEMBLY OF THE CROSSED-FIELD NOISE ANALYZER (WHEEL AND GEAR-SCREW MECHANISM).

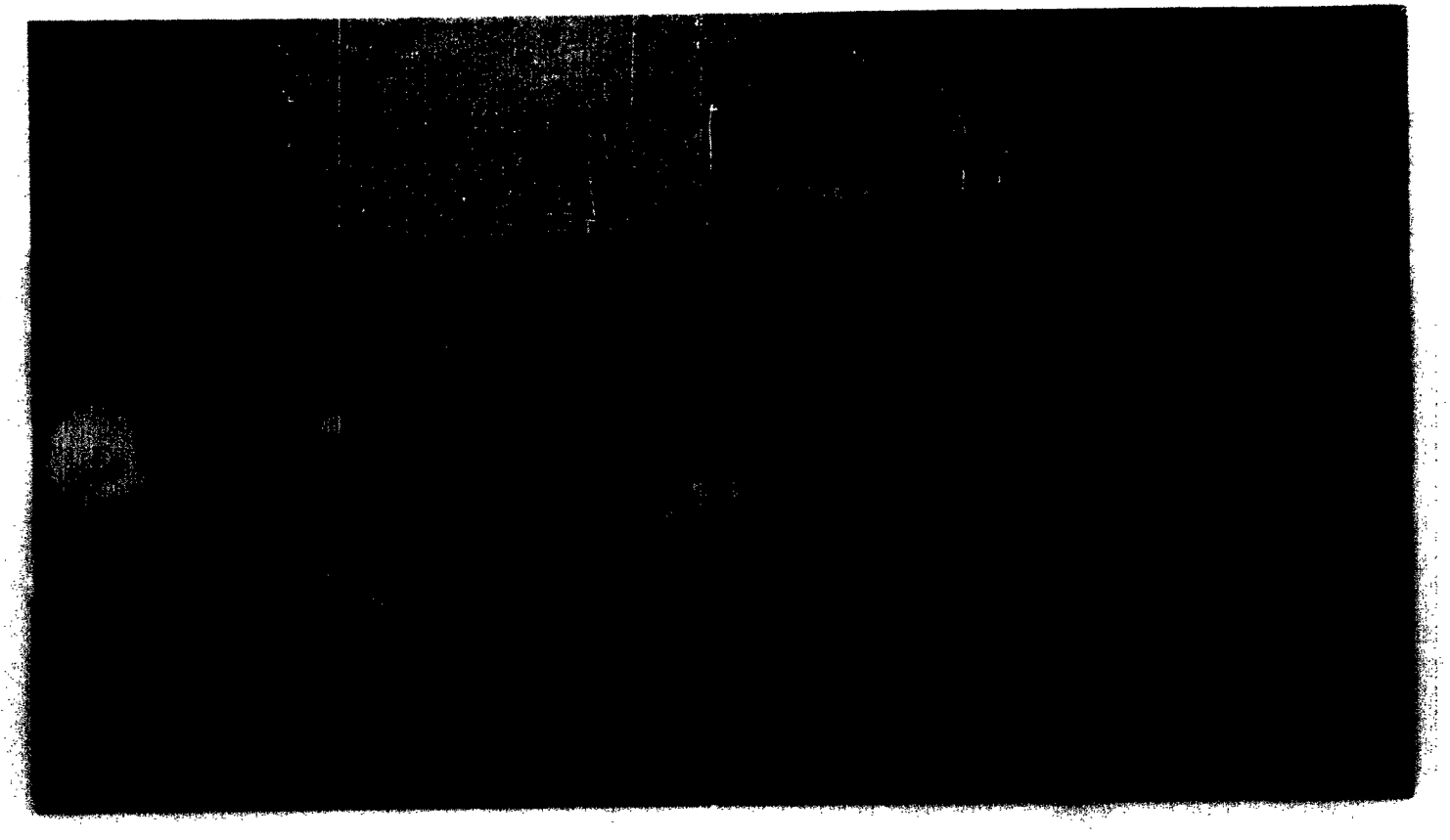

FIG. 8.15 THE OVERALL ASSEMBLY OF THE NOISE ANALYZER MOUNTED ON THE VACUUM STATION.

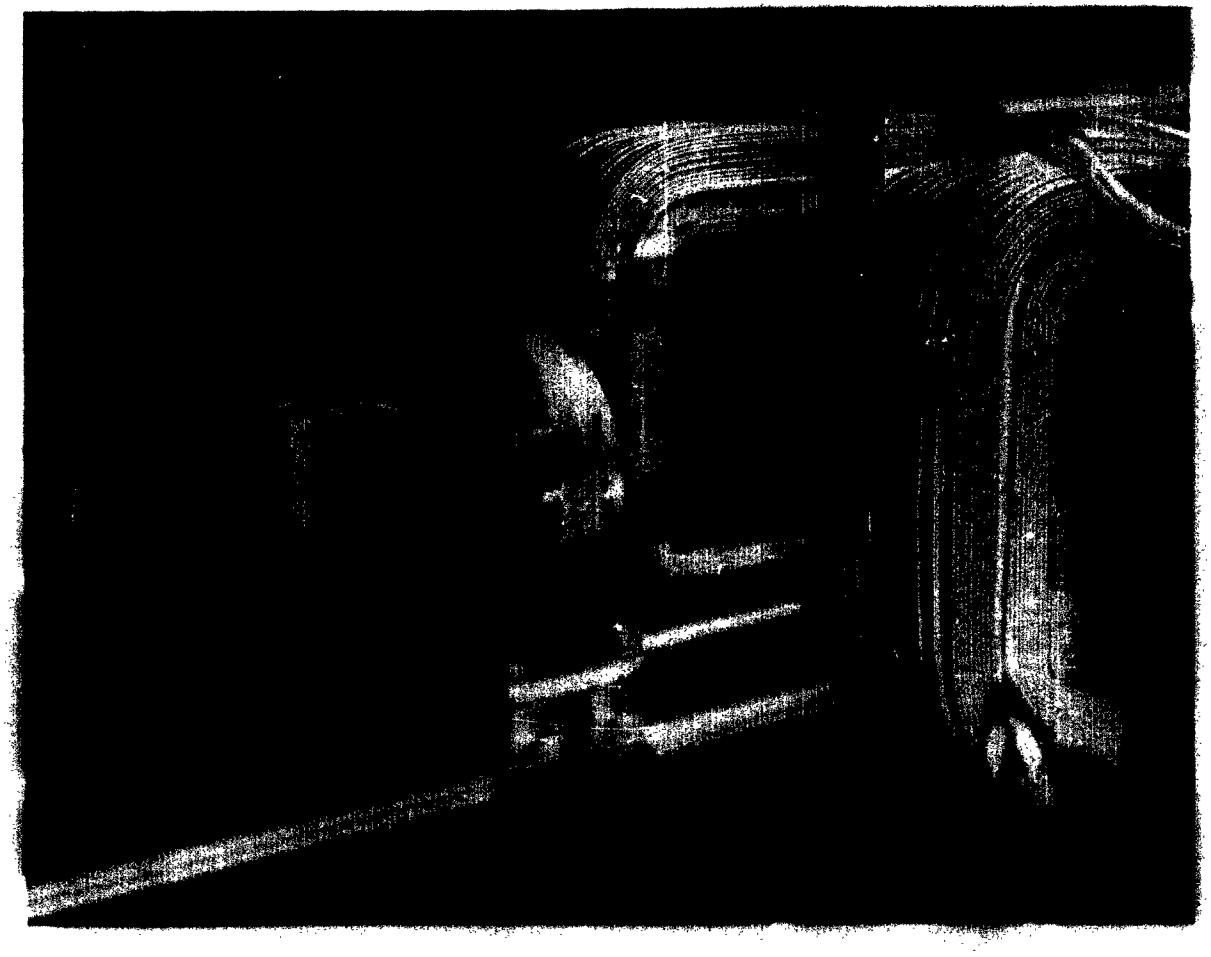

FIG. 8.16 THE RIGHT-HAND SIDE OF THE NOISE ANALYZER SHOWING THE COLLECTOR, SOLE, ANODE, BASE-PLATE AND SUPPORTING RODS.

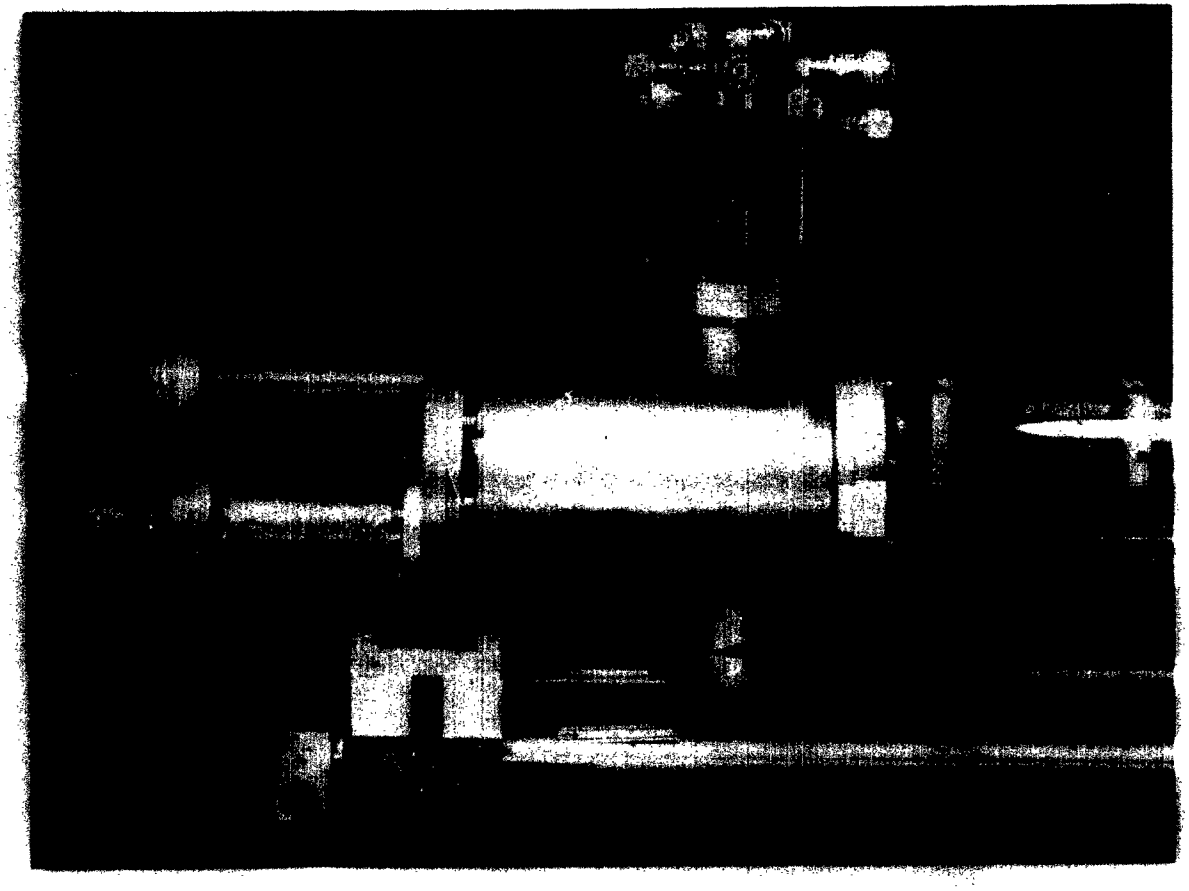

FIG. 8.17 R-F INPUT PROBES AND THE MOVABLE PROBES.

For vacuum purposes there is a provision for an auxiliary pump so that the preliminary checks for leakage etc. may be made before the tube is coupled to the main vacuum station. This also helps in reducing the time spent in evacuating the tube if some degree of vacuum is achieved in the tube with the help of the auxiliary pump and there is also a provision for an ion pump.

CHAPTER IX. EXPERIMENTAL RESULTS

9.1 Introductory Remarks

From the previous studies[10,11,13,28] of noise in crossed-field devices, it has been found that the noise output is considerably increased when the operation of the device is changed from temperature-limited to space-charge-limited.

It was originally suggested by Professor J. E. Rowe a few years ago that this increase in noise in a space-charge-limited crossed-field device is due to the fact that an electron may traverse several cycloids in the potential minimum region before it overcomes the potential barrier and moves into the gun region or returns to the cathode. Thus for an electron moving into the gun region the transit time from the cathode to any arbitrary plane in the gun region is extremely large. In this respect space-charge-limited operation in crossed-field devices is quite different than space-charge-limited operation in O-type devices. The results of the density function analysis, given in Chapter V, indicate that the a-c fluctuations experience extremely large growth rates when an electron traverses a cycloiding movement and this explains qualitatively the hypothesis originally given by Professor J. E. Rowe.

It has also been noticed[28] that for a given geometry the total noise output is quite dependent on the ratio B/B_c where B is the actual magnetic field intensity and B_c is the cutoff magnetic field intensity. From the experimental work[28] done at the CSF Laboratories, it appears that there is a definite value of B/B_c which may be defined as $(B/B_c)_{cr}$ for a given configuration, such that if $B/B_c > (B/B_c)_{cr}$, the noise

content is significant. For a certain value of B/B_c, the noise content is maximum and for larger values of the magnetic field, the noise is reduced as the value of the magnetic field is increased. From a study[28] of different geometrical configurations it has been found that $(B/B_c)_{cr} > 1$ in general. It is apparent that for $B/B_c \leq 1$ there is a negligible beam transmission in the interaction region and for $B/B_c > 1$, there is a finite beam transmission in the interaction region and the growth phenomenon, if it exists, occurs over a longer length of the beam. The reduction of noise at larger values of the magnetic field is primarily due to the reduction in the beam current since the number of electrons crossing the potential minimum barrier is reduced as the magnetic field is increased.

It has also been noticed from the previous experimental data[10,11,13,28] that for $B/B_c < 1$ the cathode current is constant and for $B/B_c > 1$ the cathode current decreases as B/B_c is increased. Because of the inclined gun anode in the noise analyzer described in the previous chapter, it is difficult to calculate the values of B_c for different combinations of the three cathodes. For this reason the cathode current is measured as a function of the magnetic field in order to determine the value of B_c.

Figure 9.1 shows the plots for the normalized cathode current versus magnetic field for several values of the heater power for cathode No. 1 (No. 3 cathode being closer to the interaction region). The space-charge-limited operation of the cathode was confirmed at zero magnetic field. Since the cathode current is decreased as the magnetic field is increased, the space-charge-limited operation of the device is justified for all values of B if it is space-charge-limited for B = 0. The plots

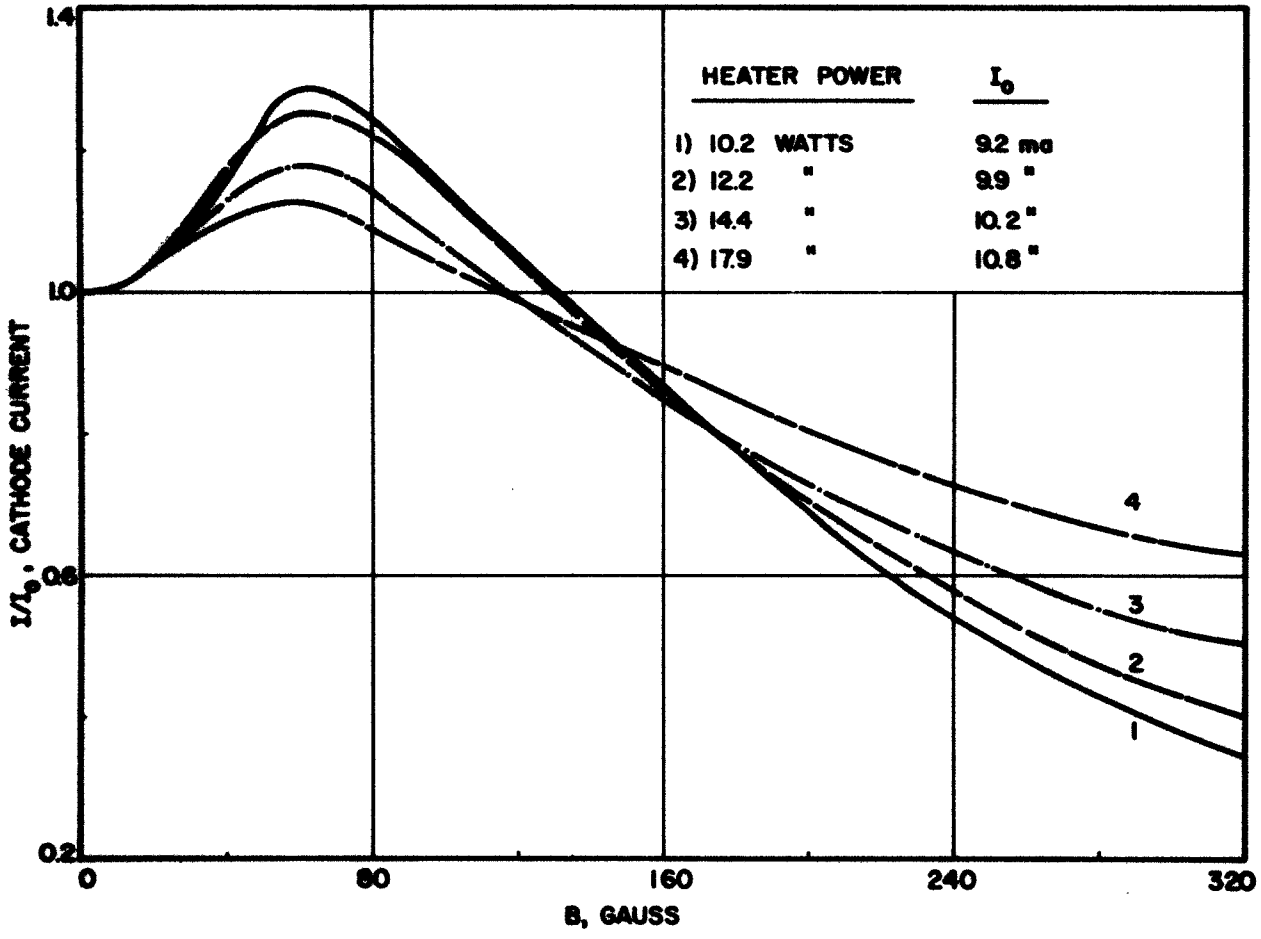

FIG. 9.1 NORMALIZED CATHODE CURRENT VS. MAGNETIC FIELD.

in Fig. 9.1 are normalized with respect to the cathode current I_o for $B = 0$ and the various values of the heater power and the corresponding cathode current I_o are also shown in Fig. 9.1. Insofar as is known no such data for a crossed-field diode has appeared. The increase in the current from cathode No. 2 as B is increased is less than that for cathode No. 1, and this increase in the current from cathode No. 3 is less than for cathode No. 2. It is likely that this variation of the cathode current may be due to the fact that the gun anode is inclined. The maximum values of the cathode currents for different values of the heater power occur for the same value of the magnetic field designated as B_m and it might be that this value of the magnetic field is related to B_c.

In an effort to determine the value of B_c for various combinations of the cathodes, it was noticed that the current from cathode No. 3 is greatly affected by the currents from cathode Nos. 1 and 2, while the current from cathode No. 2 is greatly affected by current from cathode No. 1. This is due to the presence of the magnetic field which changes the direction of the beam and this causes a space-charge depression of voltage in front of the neighboring cathode to the right, thereby reducing the current from the neighboring cathode. Figures 9.2 through 9.4 show the plots of the normalized currents for various values of the magnetic field. The cathode currents for $B = 0$ are shown in Table 9.1. These currents are referred to as I_{o1}, I_{o2}, and I_{o3}.

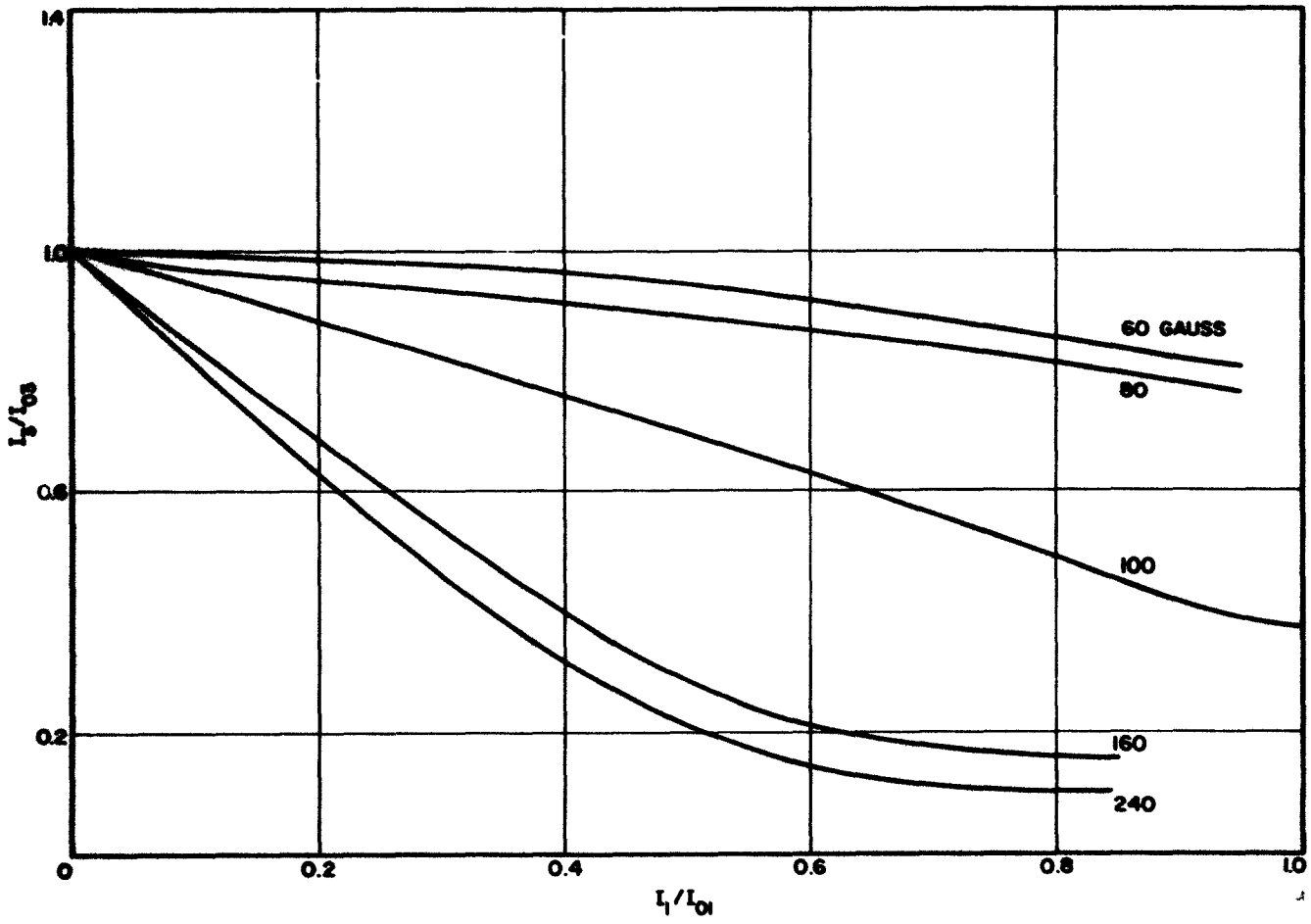

FIG. 9.2 I_3/I_{03} VS. I_1/I_{01}.

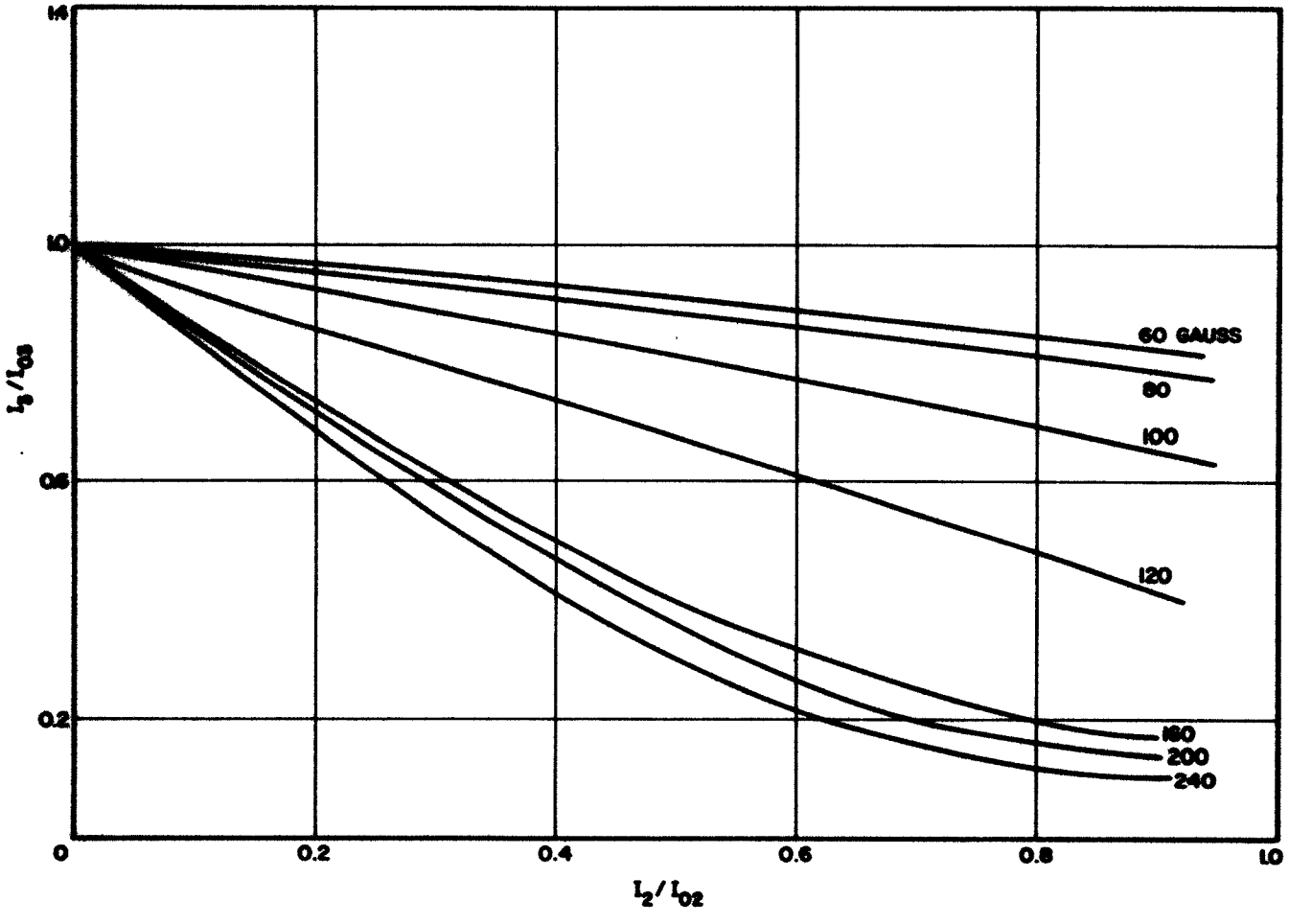

FIG. 9.3 I_3/I_{03} VS. I_2/I_{02}.

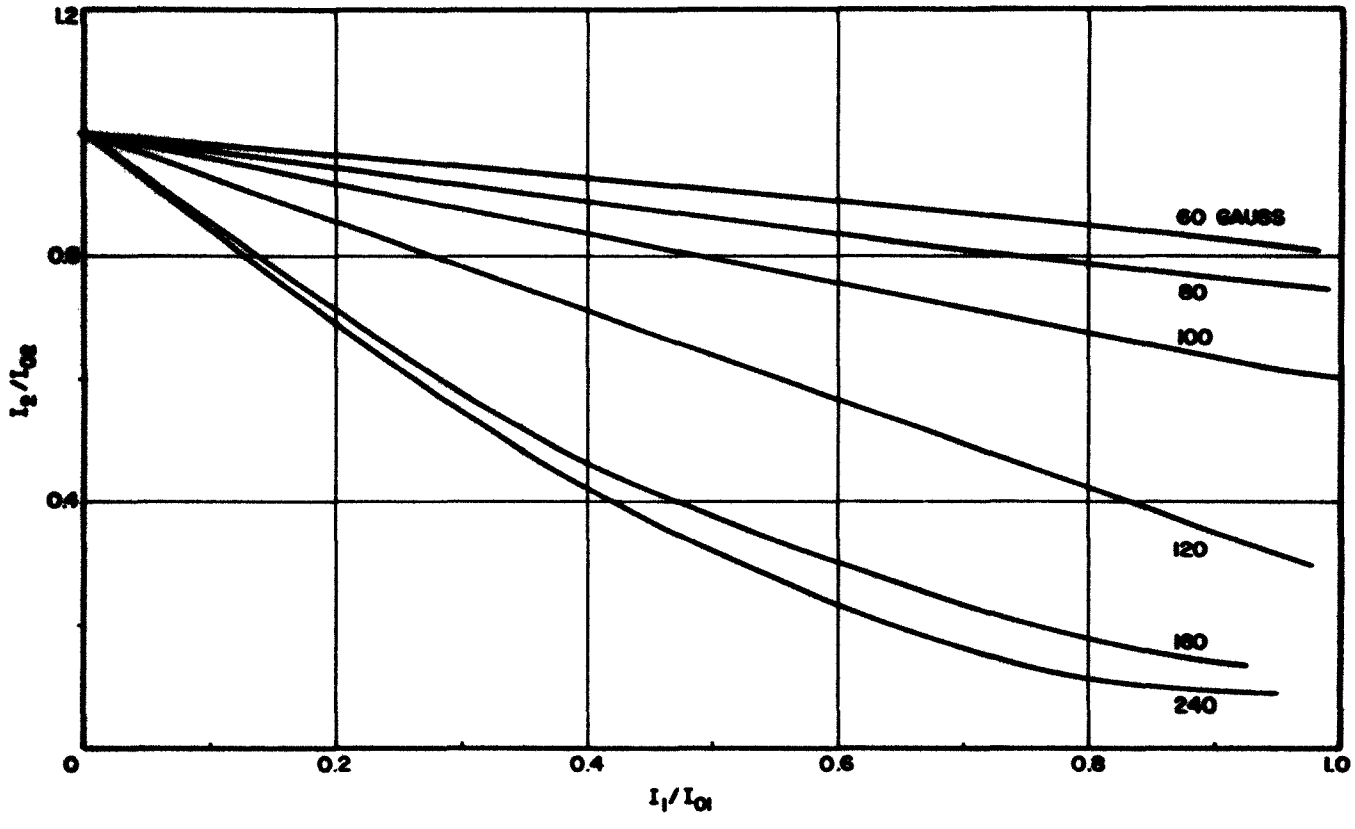

FIG. 9.4 I_2/I_{02} VS. I_1/I_{01}.

Table 9.1

Individual Cathode Currents as a Function of the Magnetic Field

Magnetic Field Gauss	I_{o1} ma	I_{o2} ma	I_{o3} ma
60	5.6	4.5	3.9
80	5.4	4.1	3.4
100	5.2	3.9	3.1
120	4.9	3.6	2.8
160	4.2	2.8	2.1
240	2.6	1.9	1.3

Figure 9.5 shows the plots of I_{o1}/I_{o3} and I_{o2}/I_{o3} versus B and these results are compared with the theoretical results obtained from Table 8.2 developed for filamentary beams originating from the centers of the respective cathodes. The plots in Fig. 9.5 seem to indicate that because of the inclined gun anode, the emission from cathode No. 1 is more affected than that from cathode No. 2 and this effect is enhanced as the magnetic field is increased. This is in agreement with the conclusion made from the plots shown in Fig. 9.1.

Because of this observed effect of one cathode current over the other, the three cathodes were operated independently. It is possible that by properly biasing the cathodes, some predetermined values of currents from the cathodes when operated simultaneously could be obtained but this requires a great deal of trial and error experimentation. Since the exact value of B_c is not known, the magnetic field is referred to in terms of its absolute value in the following data.

Figure 9.6 outlines the design details of the coupling probes and their VSWR characteristics are shown in Fig. 9.7. The dotted curve refers

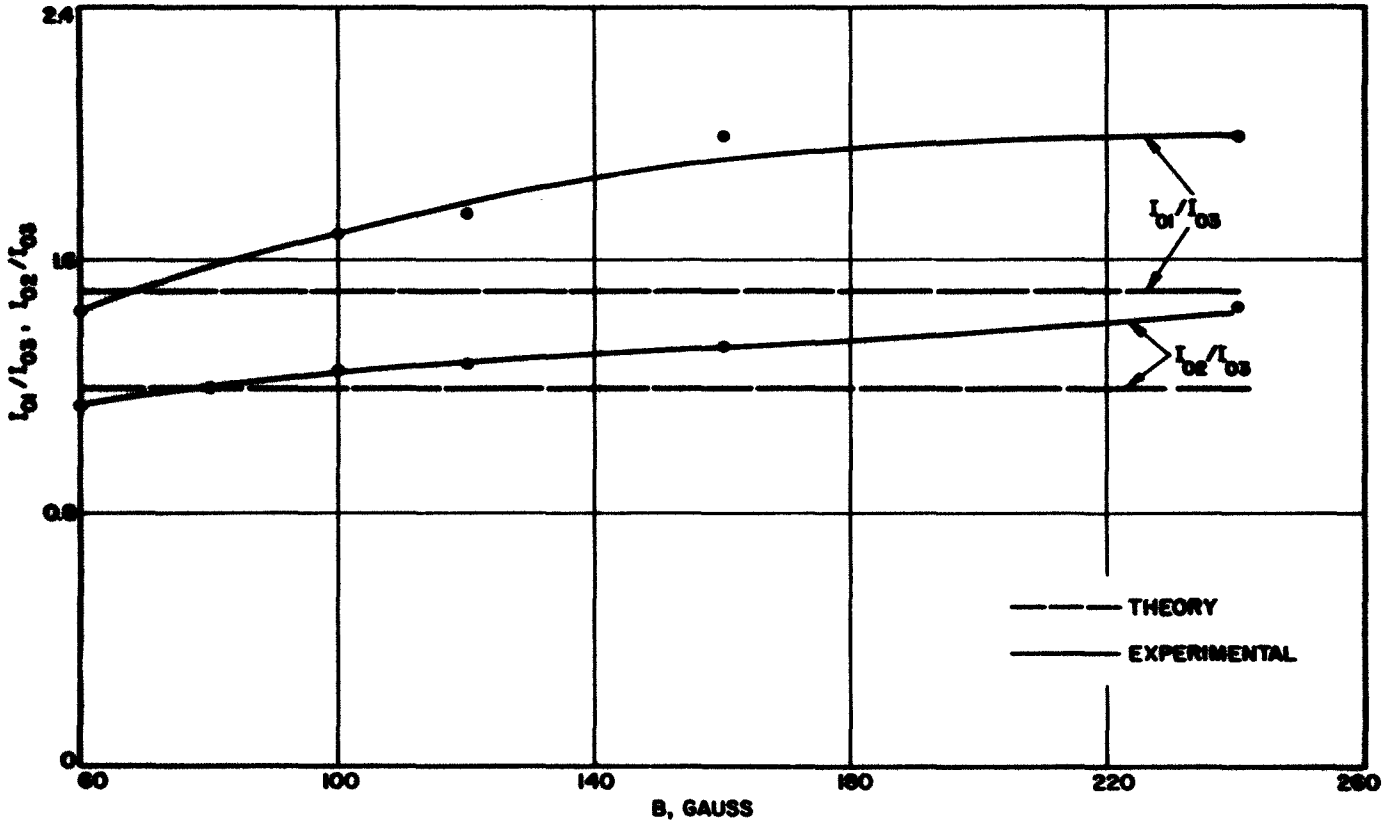

FIG. 9.5 I_{01}/I_{03} AND I_{02}/I_{03} VS. B.

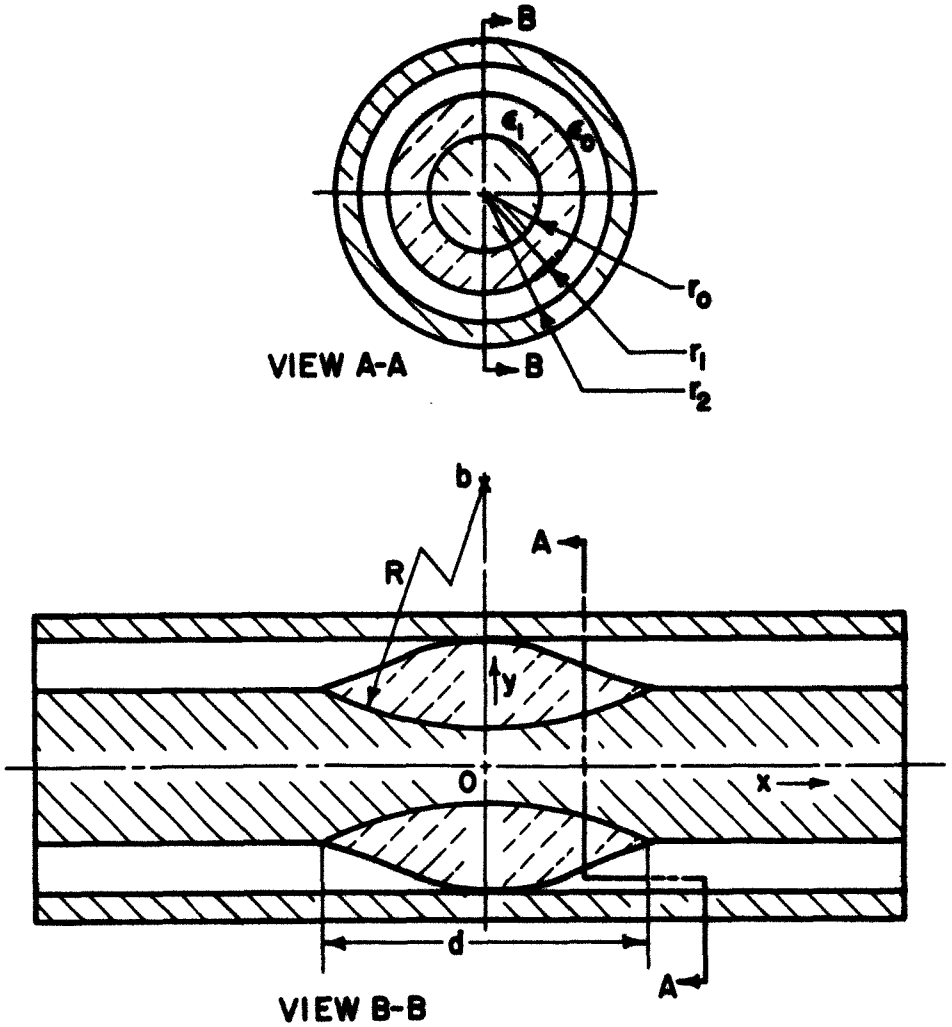

b = CENTER OF UNDERCUT CIRCLE = 2.208 INCHES

R = RADIUS OF UNDERCUT CIRCLE = 2.2 INCHES

d = LENGTH OF CENTER-CONDUCTOR UNDERCUT SECTION = 0.5 INCH

r_0 = OUTSIDE RADIUS OF INNER CONDUCTOR = 0.022 INCH

r_1 = RADIUS OF GLASS SEAL

r_2 = INSIDE RADIUS OF OUTER CONDUCTOR = 0.51 INCH

ϵ_0 = FREE-SPACE PERMITTIVITY

ϵ_1 = PERMITTIVITY OF GLASS = $5\epsilon_0$

FIG. 9.6 DIMENSIONS OF THE INNER AND OUTER CONDUCTORS FOR THE GLASS-VACUUM SEAL.

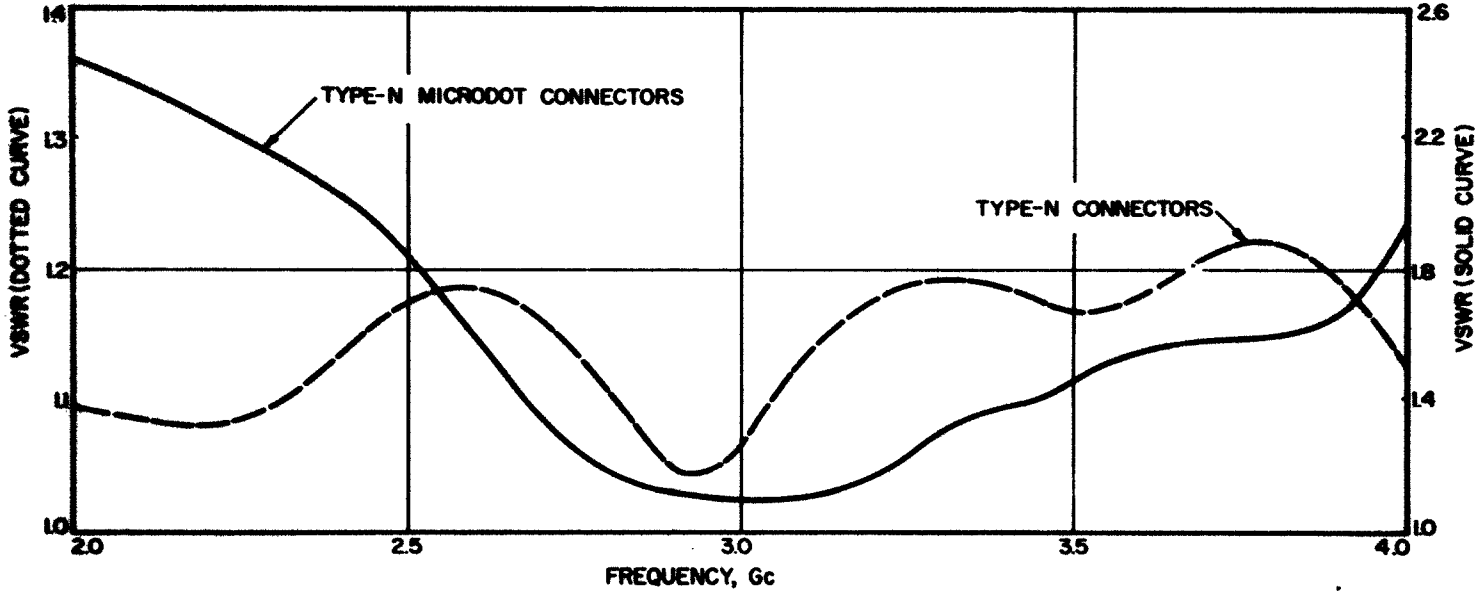

FIG. 9.7 VSWR CHARACTERISTICS OF GLASS VACUUM SEAL WITH TWO TYPES OF CONNECTORS.

to the seal with two type-N connectors attached to the coaxial line (with the seal on one end) approximately 2.5 inches long. The solid curve refers to the seal, one type-N connector, one microdot right angle plug with a TNC adapter and another adapter for transition from TNC-type to N-type connector. Thus the quality of the seal is limited primarily by the nature of the connectors attached to the coaxial line. The type-N connectors cannot be used in this case because of the relatively small distance between the centers of any two adjacent r-f coaxial cables.

Table 9.2 indicates the beam transmission for cathode No. 2 for different values of cathode current. The beam current was varied by the cathode bias voltage while the anode and sole voltages were varied in order to obtain maximum beam transmission. This data corresponds to B = 136 gauss and V_{acc} = 500 volts.

Table 9.2

Variation of Beam Transmission with Beam Current

Beam Current ma	V Anode Volts	V Sole Volts	Beam Transmissions Percent
5.1	413	-65	46.5
4.5	560	-48	48.5
3.75	545	-26	50.0
3.0	554	-19	50.0
2.0	601	-10	52.2
1.0	611	-8	69.0
0.7	609	-18	66.0
0.6	611	-16	66.0

In other words the beam transmission improved as the beam current was reduced. This is probably due to the fact that the gun was designed on the basis of space-charge-free trajectories. The data for the beam transmission given in Table 9.2 corresponds somewhat closer to that of a typical conventional crossed-field device. The noise properties of this gun are given in the following sections.

9.2 Evaluation of Electron Equivalent Temperature

The electron equivalent temperature[40] has been determined by studying the volt-ampere characteristics at the various probes and the sole segments. It was noticed that the cathode current changed when the voltage at the cathode probes was varied. However, volt-ampere characteristics have been studied at the input probes at the exit of the gun region and the movable probes. The typical volt-ampere characteristics of the three input probes (namely probe Nos. 1, 2 and 3 as shown in Fig. 8.11) are shown in Figs. 9.8 and 9.9. Probes 1, 2 and 3 are equally spaced in the positive direction of the magnetic field.

From similar data for the three cathodes, the electron equivalent temperature for these probes is calculated and is shown in Figs. 9.10 through 9.12 as a function of the magnetic field. It is seen from these figures that the electron equivalent temperature is reduced as ω_c is increased. This is in qualitative agreement with the data obtained by r-f measurements at the CSF Laboratories[28].

In evaluating the electron equivalent temperature it is assumed that the electrons have a Maxwellian velocity distribution. The discrepancy in the experimental points from the smooth curves drawn in these figures may be due to lack of a Maxwellian velocity distribution. For such cases the average electron equivalent temperature is evaluated. It

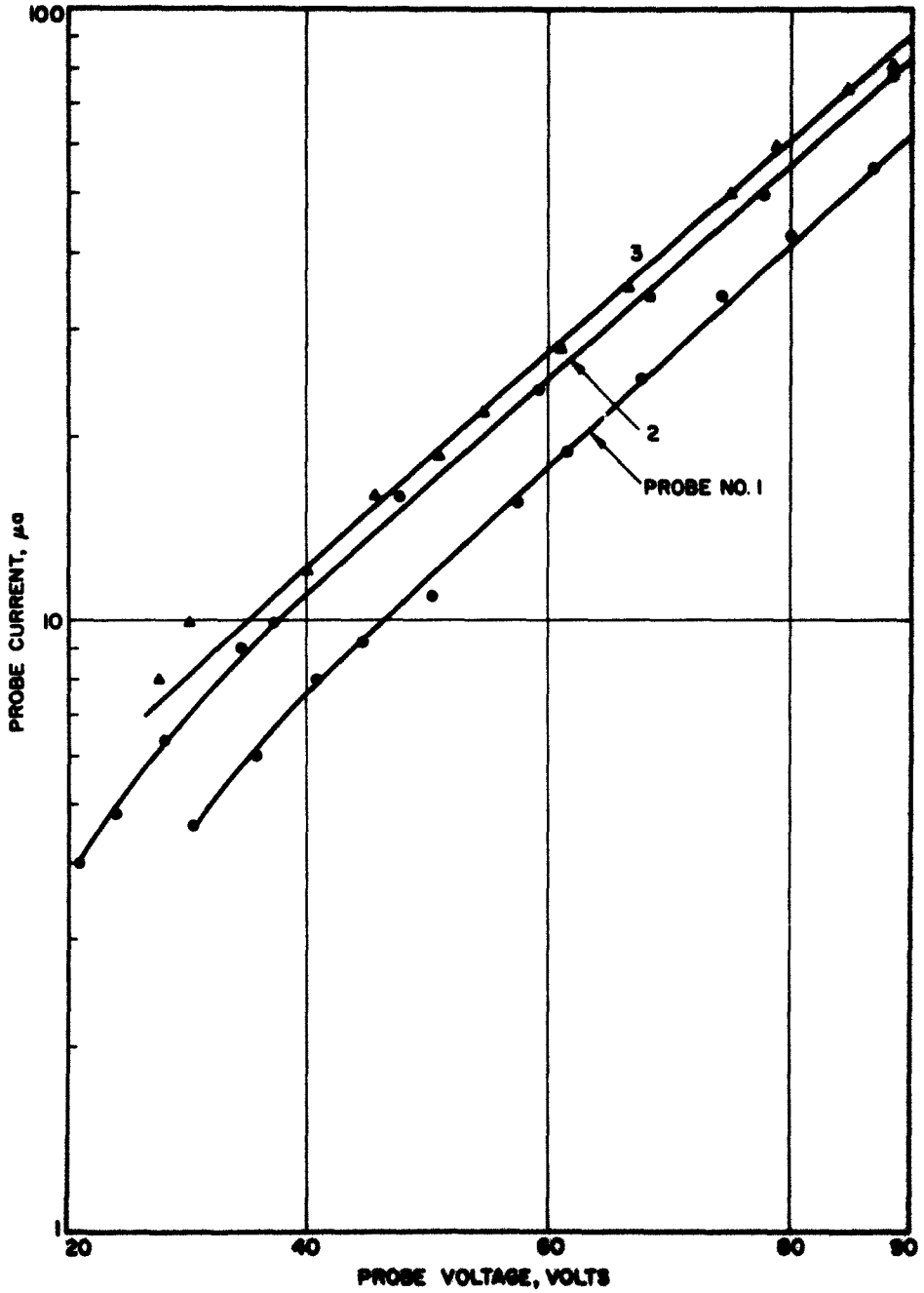

FIG. 9.8 PROBE CURRENT VS. PROBE VOLTAGE. B = 120 GAUSS, I_{cg} = 3.4 ma, V_{acc} = 420 VOLTS, V_{an} = 360 VOLTS.

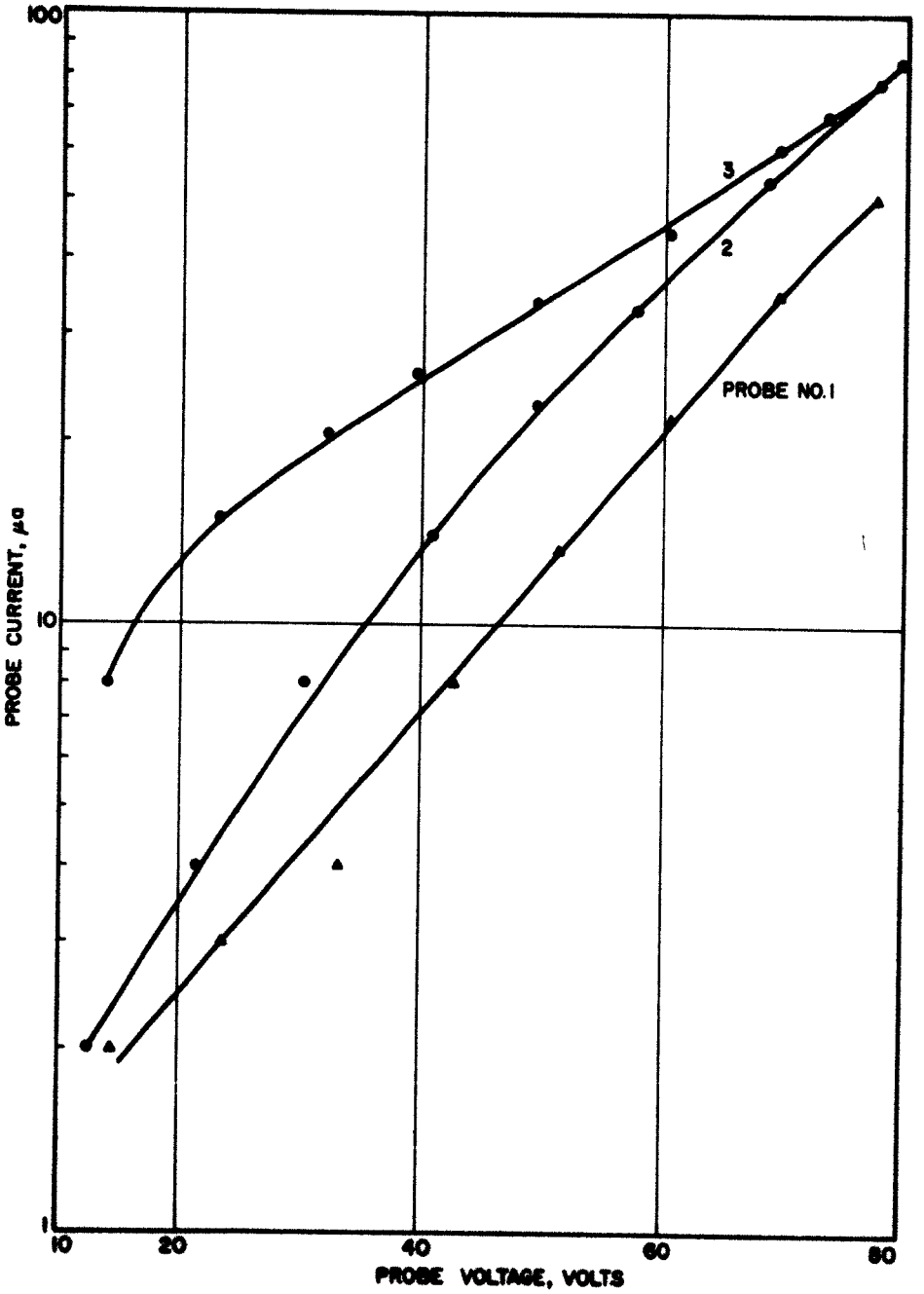

FIG. 9.9 PROBE CURRENT VS. PROBE VOLTAGE. B = 140 GAUSS, I_{os} = 2.8 ma, V_{acc} = 420 VOLTS, V_{an} = 360 VOLTS.

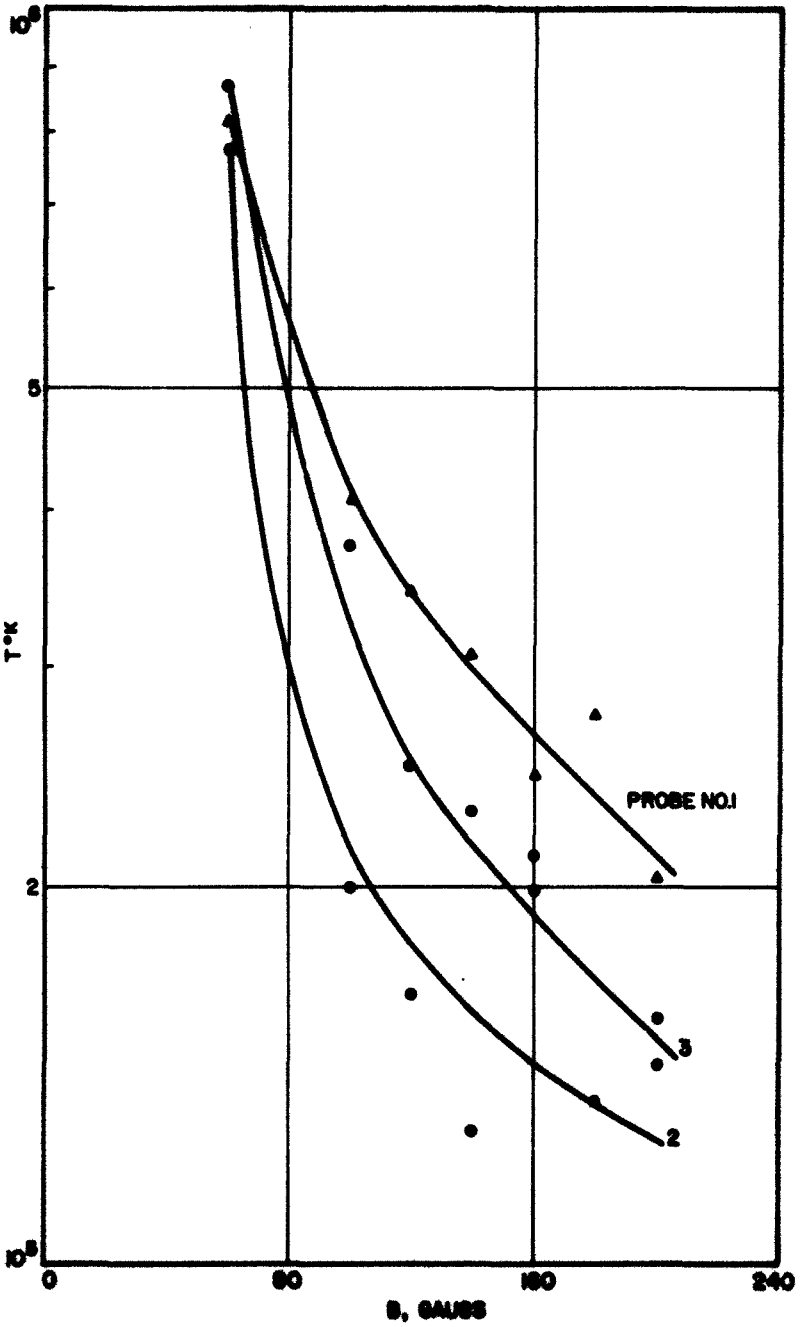

FIG. 9.10 VARIATION OF ELECTRON EQUIVALENT TEMPERATURE VS. B. CATHODE NO. 1. V_{acc} = 420 VOLTS, V_{an} = 360 VOLTS, V_{SOLE} = 0 VOLT.

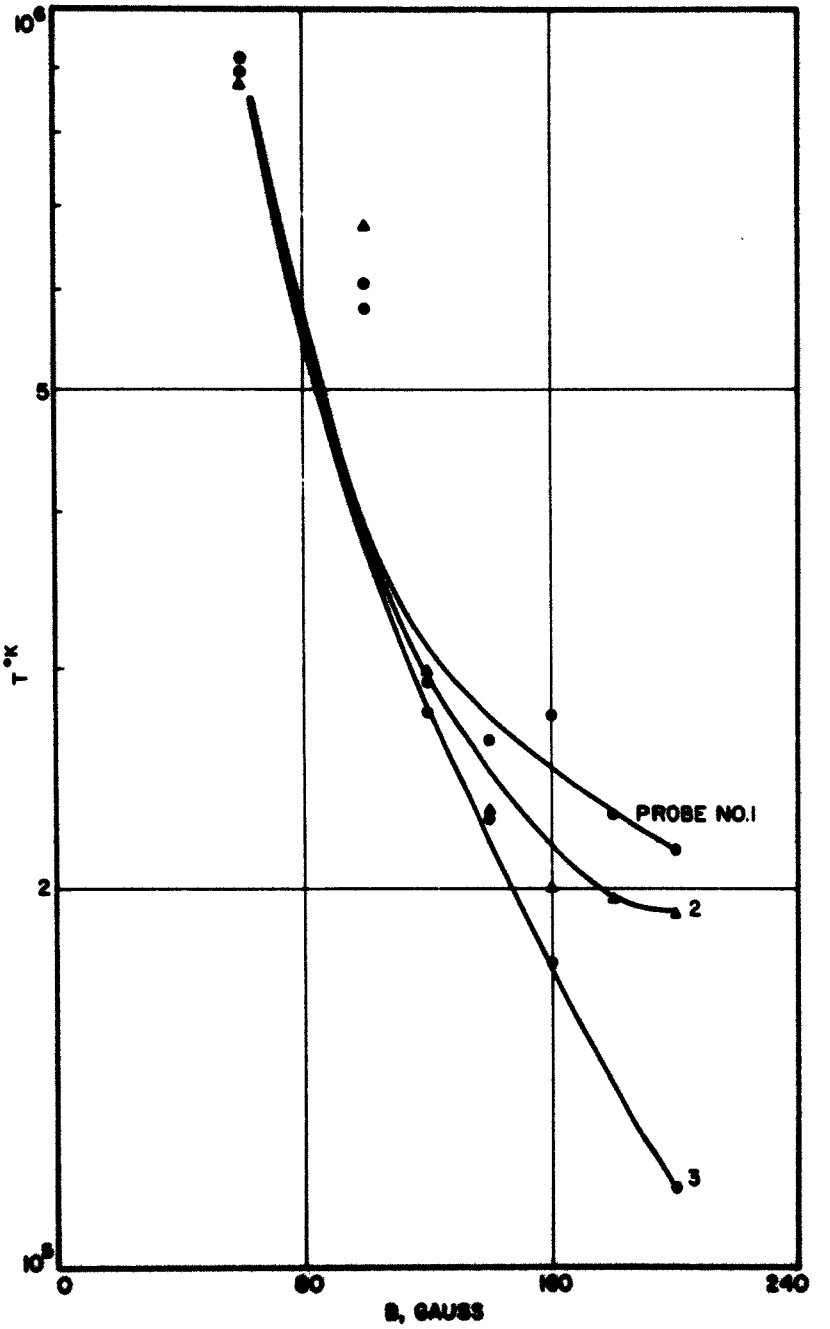

FIG. 9.11 VARIATION OF ELECTRON EQUIVALENT TEMPERATURE VS. B. CATHODE NO. 2. V_{acc} = 420 VOLTS, V_{an} = 360 VOLTS, V_{SOLE} = 0 VOLT.

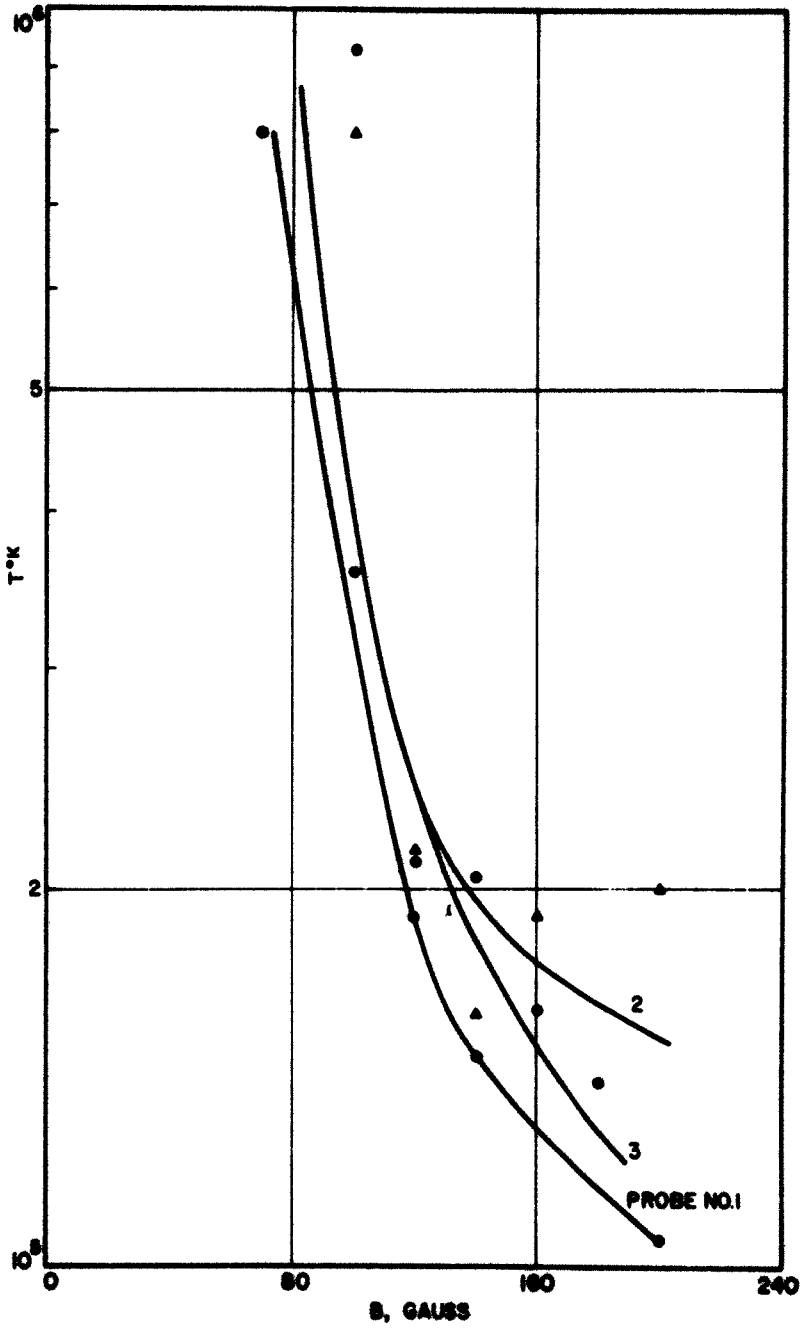

FIG. 9.12 VARIATION OF ELECTRON EQUIVALENT TEMPERATURE VS. B. CATHODE NO. 3. V_{acc} = 420 VOLTS, V_{an} = 360 VOLTS, V_{SOLE} = 0 VOLT.

may be possible to obtain a slightly different value of the electron equivalent temperature by varying the anode voltage to a region where a Maxwellian velocity distribution may be a better approximation. This might also require a correction due to a change in the cathode current as the magnetic field is changed.

The large numerical values of the equivalent temperature seem to indicate a large noise content of the beam. It is interesting to note from these figures that the difference in the noise equivalent temperature for the three probes is increased as the value of B is increased, indicating that the velocity distribution in the direction of the magnetic field is not uniform. It seems to indicate also that for large values of B either the cathode emission is nonuniform in the direction of the magnetic field or there is a random electron movement along the x-axis, and the degree of this movement seems to depend upon the value of the magnetic field.

The greater noise in magnetrons when operated as cold cathode devices than when operated as hot cathode devices seems also due to nonuniform emission along the cathode.

In order to study the variation of the electron equivalent temperature along the beam, volt-ampere characteristics for the movable probes and sole segments were studied. Figure 9.13 shows the volt-ampere characteristics for probe No. a for four values of z. It can be seen from these plots that there is no significant change in the slope of the plots and hence the electron equivalent temperature is not appreciably altered along the beam. For similar data for the sole segments it was also inferred that there is no significant change in the electron equivalent temperature except for some small fluctuations along the beam.

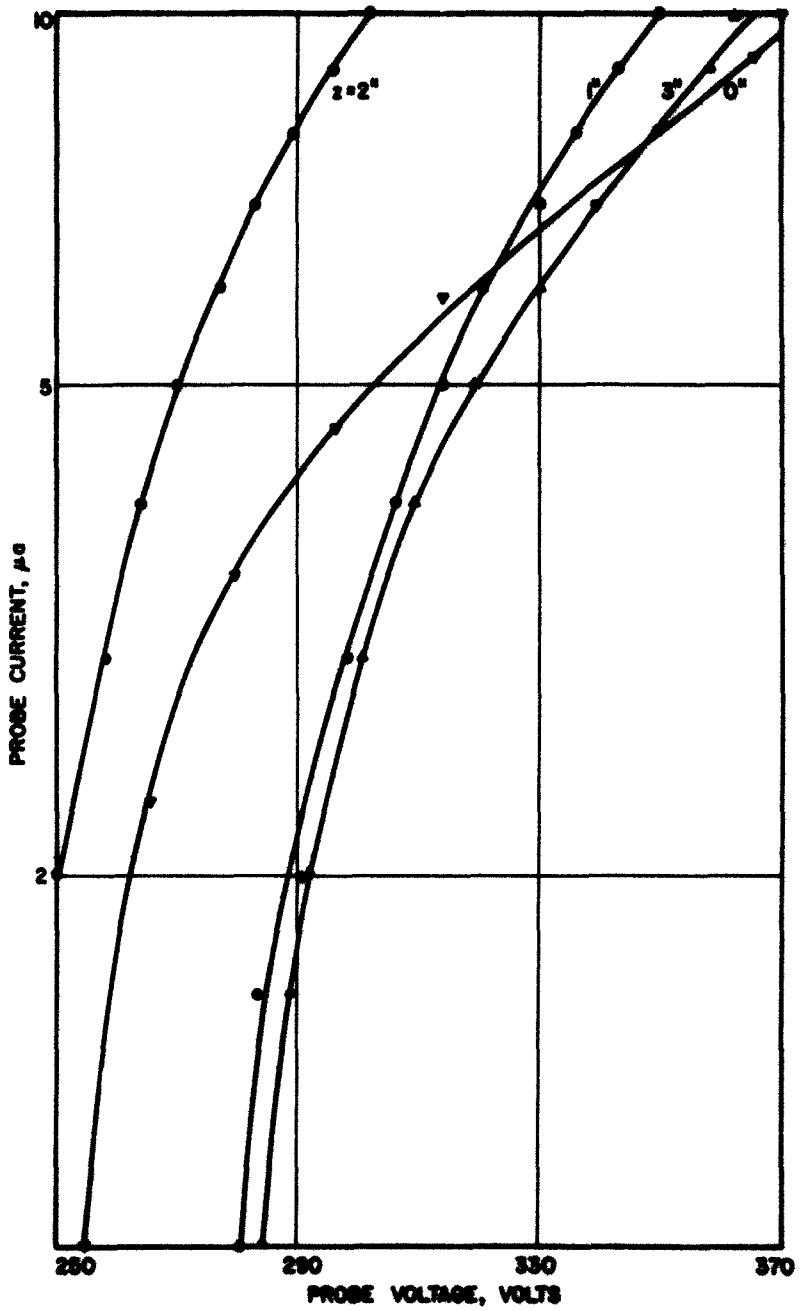

FIG. 9.13 VOLT-AMPERE CHARACTERISTICS FOR PROBE NO. a FOR DIFFERENT VALUES OF z. B = 120 GAUSS, $I_{CATHODE}$ = 3 ma, V_{acc} = 420 VOLTS, V_{an} = 360 VOLTS, V_{SOLE} = 0 VOLT.

9.3 R-f Studies of the Beam

By introducing an r-f signal at high frequencies at the input probes it was noticed that the direct signal pickup at the movable probes was too strong to indicate any change in the signal due to the presence of the beam. It is probably due to a lack of beam modulation. The injection at low frequencies (less than 250 mc/s at the input probes) is discussed in Section 9.5.

Some intrinsic oscillations within the beam were detected and the frequency of the r-f signal detected at the input probes at the exit of the gun region and the movable probes was in the neighborhood of 75 mc/s. This frequency could be changed by changing the d-c parameters such as the anode voltage, cathode bias, gun-anode voltage or the magnetic field but within a narrow limit. It is felt that this change in frequency is very similar to the frequency pushing effects in the conventional magnetrons. The harmonics of the 75 mc/s signal were also present but the signal level of the harmonics reduced as the order of the harmonic increased. For example the second harmonic signal level was about one half of the fundamental signal level and the amplitudes of the higher harmonics were too small to be detected on the spectrum analyzer.

It may be pointed out here that the level of the detected signal does not remain constant as any of the d-c parameters are changed. Figure 9.14 indicates the plots of the r-f signal level, cathode current and the change in the signal frequency as a function of the cathode bias. Figure 9.15 shows the plots of the r-f signal level and the change in signal frequency as a function of the magnetic field. The change in magnetic field also causes a change in the cathode current and thus the dependence of the r-f signal level on the magnetic field will be quite

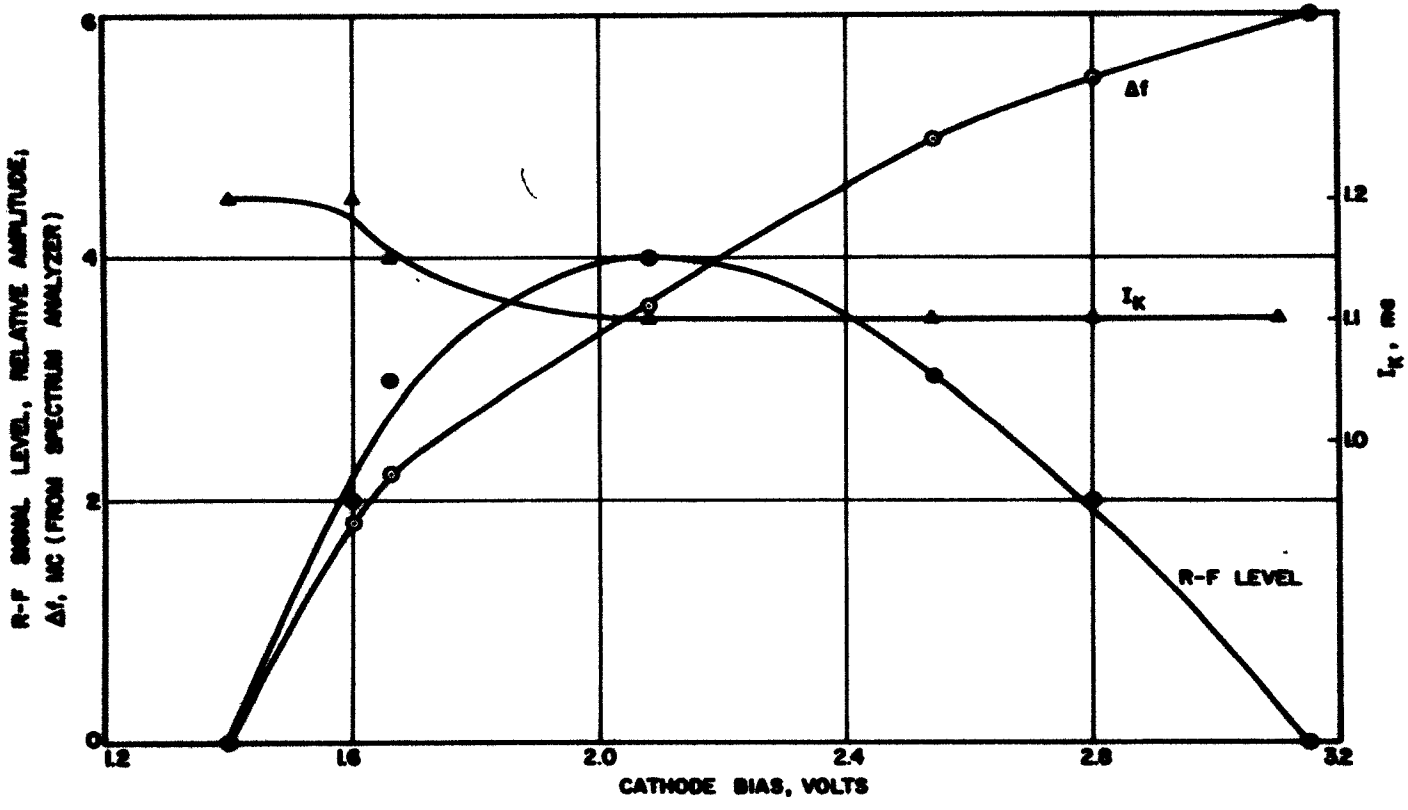

FIG. 9.14 R-F SIGNAL LEVEL, CATHODE CURRENT AND CHANGE IN SIGNAL FREQUENCY AS A FUNCTION OF CATHODE BIAS. B = 150 GAUSS, V_{acc} = 356 VOLTS, V_{an} = 260 VOLTS.

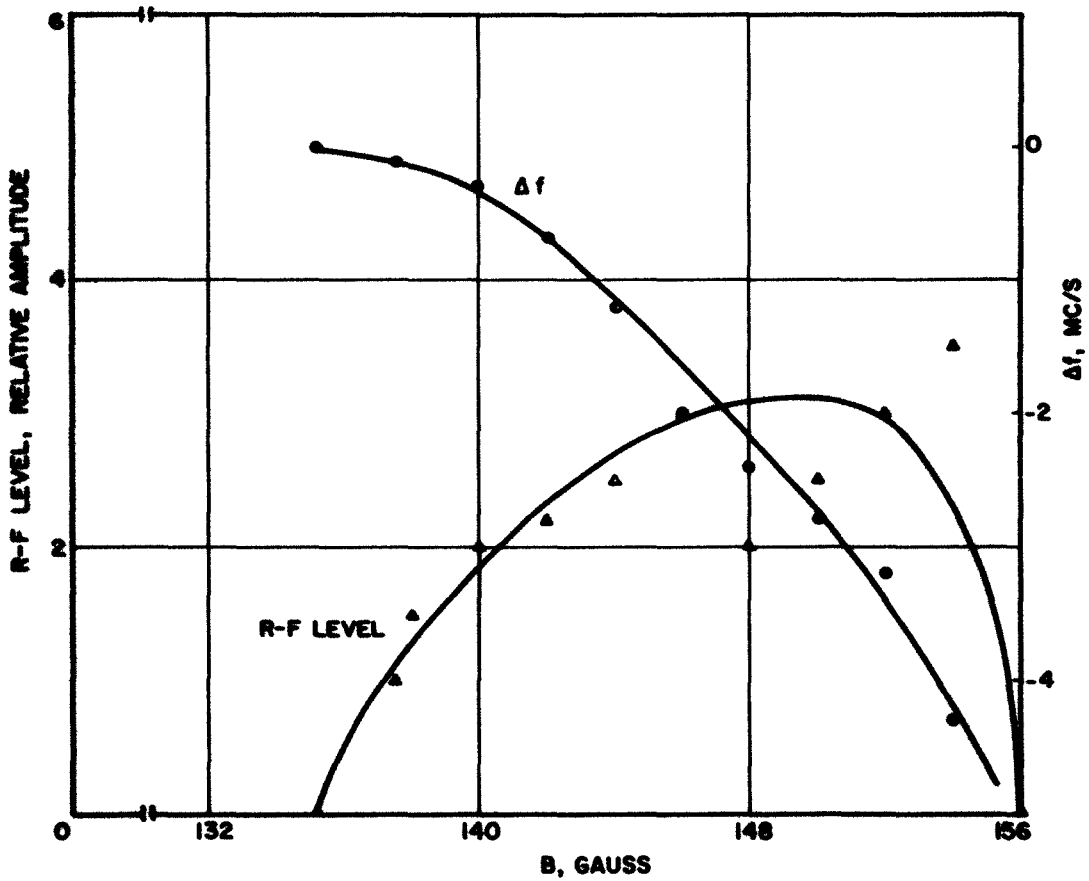

FIG. 9.15 R-F SIGNAL LEVEL AND CHANGE IN SIGNAL FREQUENCY AS A FUNCTION OF MAGNETIC FIELD. (PROBE NO. a) I_k = 1.75 ma, V_{acc} = 356 VOLTS, V_{an} = 246.5 VOLTS.

complicated. Figure 9.16 shows the plots of the r-f signal level as a function of the anode voltage.

Figures 9.14 through 9.16 indicate that the level of the noise signal frequencies can be reduced significantly by adjusting the d-c parameters appropriately. It will be quite difficult to explain this noise reduction phenomenon analytically but the results of a simplified model[41] of a double beam with a certain velocity slip in the two beams drifting in the interaction region indicate that an r-f signal will grow provided the conditions on the various d-c parameters are satisfied. This growth phenomenon is limited within a certain range of the values of the d-c parameters.

9.4 Variation of R-f Signal Along the Beam

By sliding the movable probes along the beam it was noticed that the r-f signal level and the d-c current detected by the probe varied along the beam. It was found necessary to keep the probe voltage at a level so that the secondary emission was negligible. This was determined on the basis of the volt-ampere characteristics for the probes.

It was noticed that the probe d-c current varied periodically indicating that the beam was cycloiding in the interaction region and the r-f signal also varied along the beam. It may be pointed out here that by varying the probe voltage the probe current could be varied over a wide limit without varying the r-f signal level and its frequency. Figures 9.17 and 9.18 show the plots of the r-f signal level for probe Nos. a and c respectively as a function of distance along the beam. The average value of the wavelength as determined from these two plots is 0.92 inch for probe No. a and 0.94 inch for probe No. c, while the calculated value

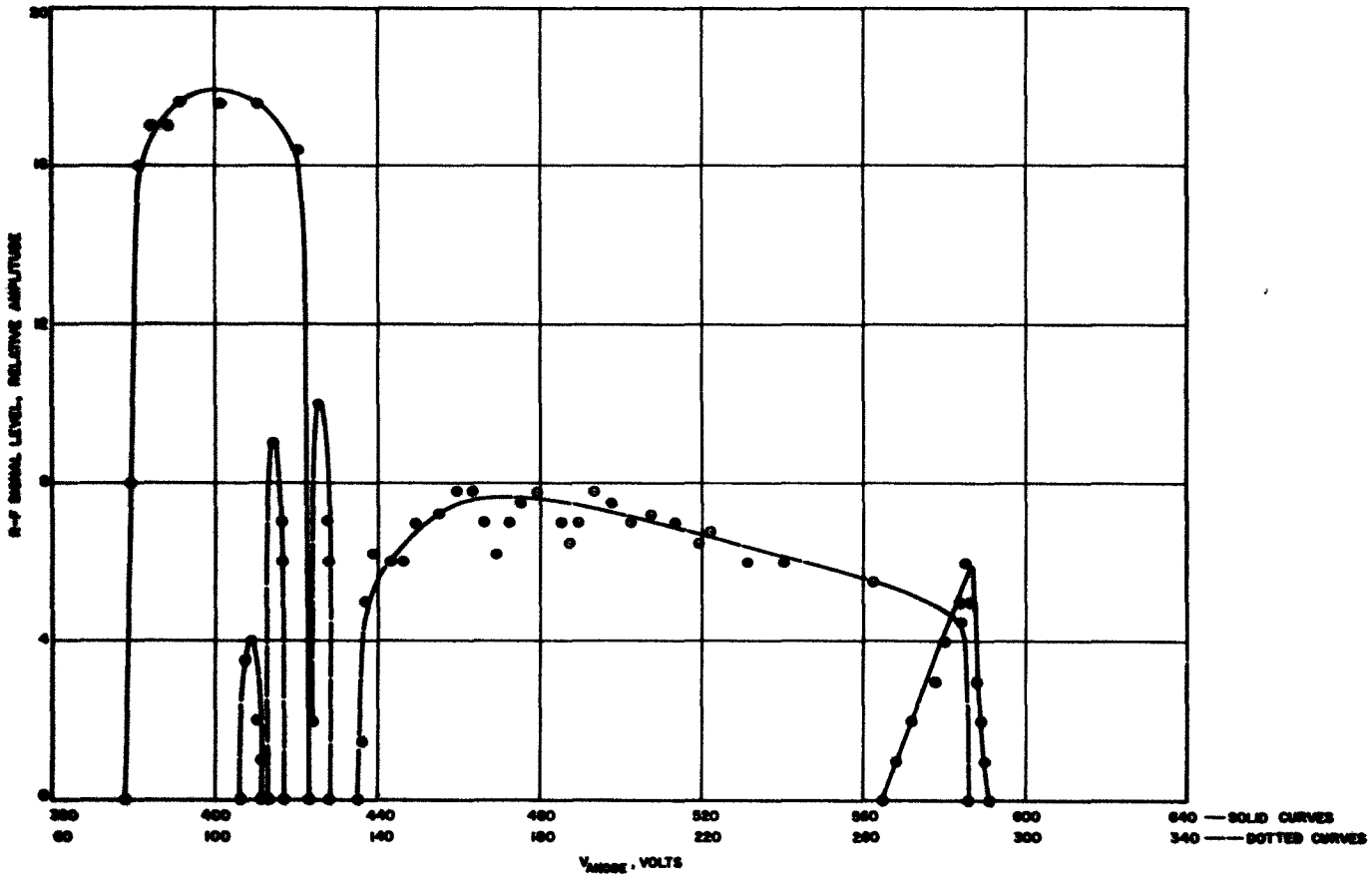

FIG. 9.16 R-F SIGNAL LEVEL AS A FUNCTION OF ANODE VOLTAGE. (PROBE NO. a)

B = 150 GAUSS, I_k = 1.75 ma, V_{acc} = 260 VOLTS.

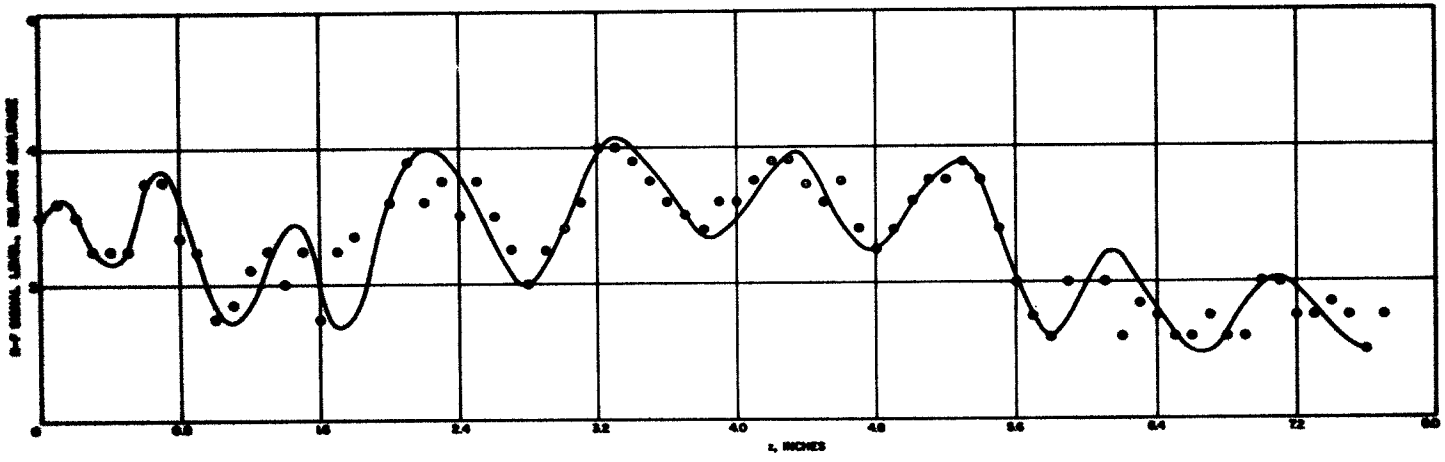

FIG. 9.17 VARIATION OF R-F SIGNAL LEVEL ON PROBE NO. a VS. DISTANCE. B = 150 GAUSS, I_k = 0.9 ma, V_{acc} = 356 VOLTS, V_{an} = 260 VOLTS, $V_{PROBE\ NO.\ c}$ = 190 VOLTS, $V_{PROBE\ NO.\ a}$ = 220 VOLTS.

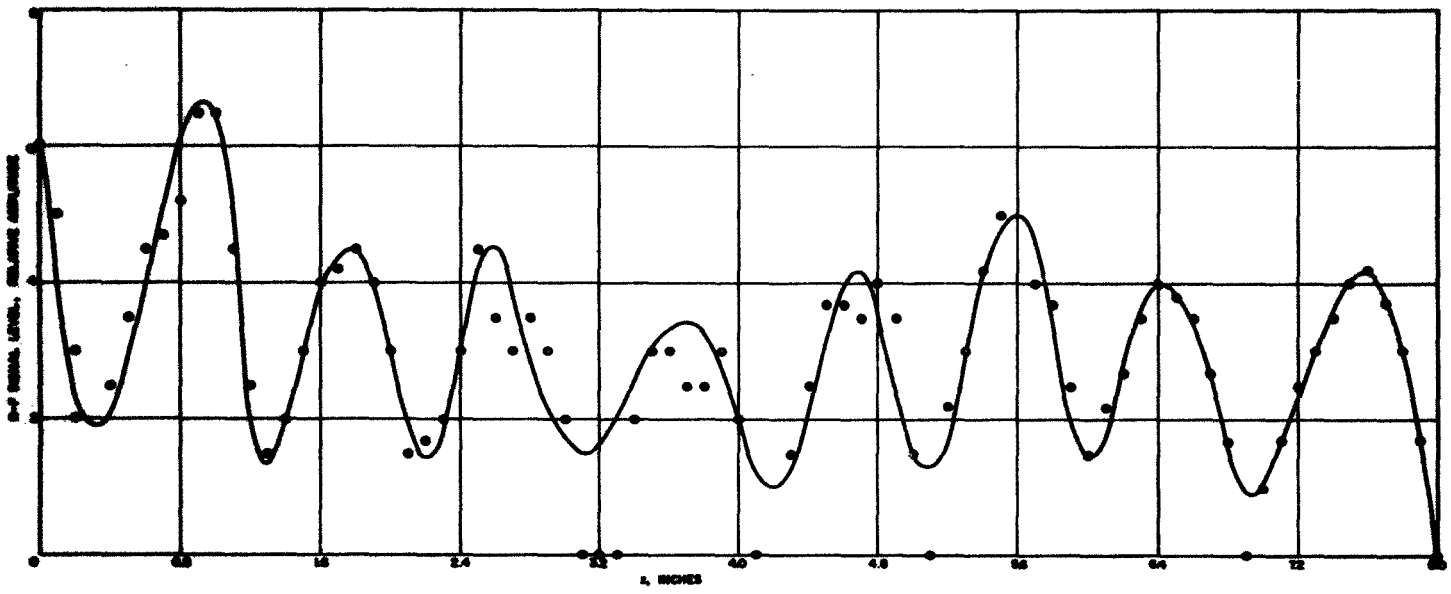

FIG. 9.18 VARIATION OF R-F SIGNAL LEVEL ON PROBE NO. c VS. DISTANCE. B = 150 GAUSS, I_k = 0.9 ma, V_{acc} = 356 VOLTS, V_{an} = 260 VOLTS, $V_{PROBE\ NO.\ a}$ = 190 VOLTS, $V_{PROBE\ NO.\ c}$ = 220 VOLTS.

of the wavelength from the formula $\lambda = (|E|/fB)$, is equal to 1.05 inch, where

$|E| = V_o/d$,

V_o = anode voltage,

d = anode-sole spacing,

B = magnetic field intensity,

f = frequency of the signal.

In evaluating the value of $|E|$, the space-charge effects are neglected because they would tend to reduce the actual value of $|E|$ and hence the d-c velocity of the beam would be less than the calculated value. Thus the actual value of the wavelength would be less than 1.05 inch. This study also indicates that the actual noise signal originated in the gun region. It may be noticed from these two figures that there is a small phase difference between the signals detected by probe Nos. a and c. This is due to a very small difference in the lengths of the two r-f coaxial lines.

Figure 9.19 shows the plot of the d-c probe current versus z (distance along the beam) and the data corresponds to the measurements made on probe No. a with similar data being obtained for other probes. This plot indicates the cycloiding nature of the beam and the measured value of the average cycloidal wavelength $\lambda_c = 0.295$ inch. For a temperature-limited model the calculated value of $\lambda_c = 0.179$ inch. In a practical case because of the finite space charge, the value of $\lambda_c > 0.179$ inch. It is interesting to note that the various pronounced peaks occur at an interval of approximately 1.0 inch which is very nearly equal to the wavelength calculated from the r-f measurements. This indicates a pronounced effect of r-f wave propagating along the beam on the beam trajectory. The decrease in probe current with the distance

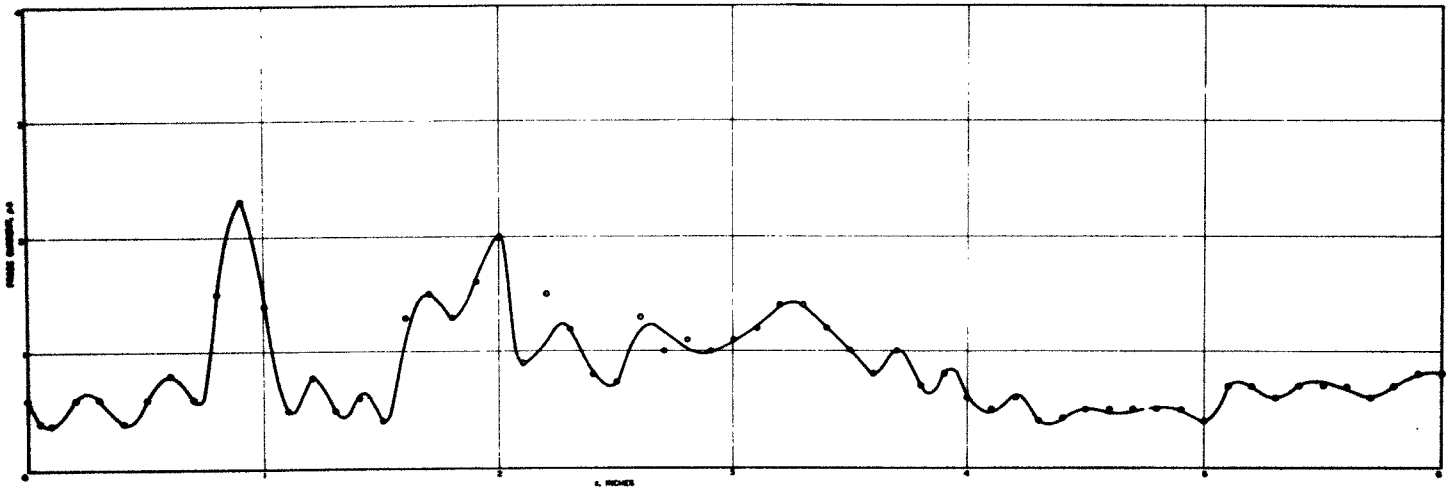

FIG. 9.19 PROBE CURRENT VS. z. (PROBE NO. a) B = 150 GAUSS, I_k = 0.9 ma, V_{acc} = 356 VOLTS, V_{an} = 260 VOLTS, V_{p_a} = 220 VOLTS.

seems to indicate that either the beam current has been reduced after a finite collection of the current at the anode and/or sole or there is an inherent tendency in such devices to reduce the amplitude of the cycloid with distance.

9.5 R-f Injection

It is mentioned in Section 9.3 that when an r-f signal was introduced at the input probes the direct signal pickup at the movable probes was too strong to indicate any change in the signal level due to the presence of the beam. This occurred when the frequency of the applied r-f signal was quite high. The detection of the noise signal due to intrinsic oscillations within the beam led to an injection of an r-f signal in the same frequency range as the frequency of the oscillations. When an r-f signal in this frequency range was introduced at the probes in the gun region, the direct pickup in the absence of the beam at the movable probes or at the input probes at the exit of the gun region was too small to be detected by the spectrum analyzer. However, when this r-f signal was injected at the input probes at the exit of the gun region, the direct pickup on the movable probes was too large to indicate any change due to the presence of the beam. For this reason the input probes in the gun region were used as an injection system. The following data refers to when Cathode No. 2 was in operation and the r-f signal was introduced at probe No. 8 which is the nearest to this cathode for the purpose of a greater degree of modulation. Under these conditions the intrinsic oscillations were suppressed.

The variation of the r-f signal level with various d-c parameters is similar to that of the oscillation signal level mentioned in the last two sections. However, the signal frequency could be changed from about

60 mc/s to about 250 mc/s. For higher frequencies the direct pickup was again too strong. Figure 9.20 shows the variation of the r-f signal level and the cathode current versus cathode bias. Figure 9.21 shows the variation of the r-f signal level versus the magnetic field and it can be seen that these variations are very sensitive to the magnetic field. Figure 9.22 shows the variation of the r-f signal level and the cathode current versus gun anode (accelerator) voltage. Figure 9.23 shows the variation of the r-f signal level versus anode voltage. The variations of the r-f signal level with the anode voltage are due to the fact that a finite portion of the anode extends in the gun region and variations in the anode voltage changes the potential profile in the gun region considerably.

In order to determine the variation of the r-f signal level as a function of the degree of space charge, the heater power was varied and the r-f signal level determined. Figure 9.24 shows the variation of the r-f signal level and the cathode current versus the heater power. It may be seen that the r-f signal level varies proportionately to the heater power.

Figure 9.25 shows the variation of the r-f signal level as a function of distance. The plot is shown up to $z = 2$ inches but for larger values of z the r-f signal level was smaller than the threshold signal and could not be detected on the spectrum analyzer. The measured value of the wavelength obtained from the plot shown in Fig. 9.25 is equal to 0.68 inch while the calculated value of λ from the formula $\lambda = |E|/fB$ is equal to 0.7 inch. It is noticed that the r-f signal level decreased with distance. This may be due to a reduction in the beam current because of collection of the beam current at the anode and sole.

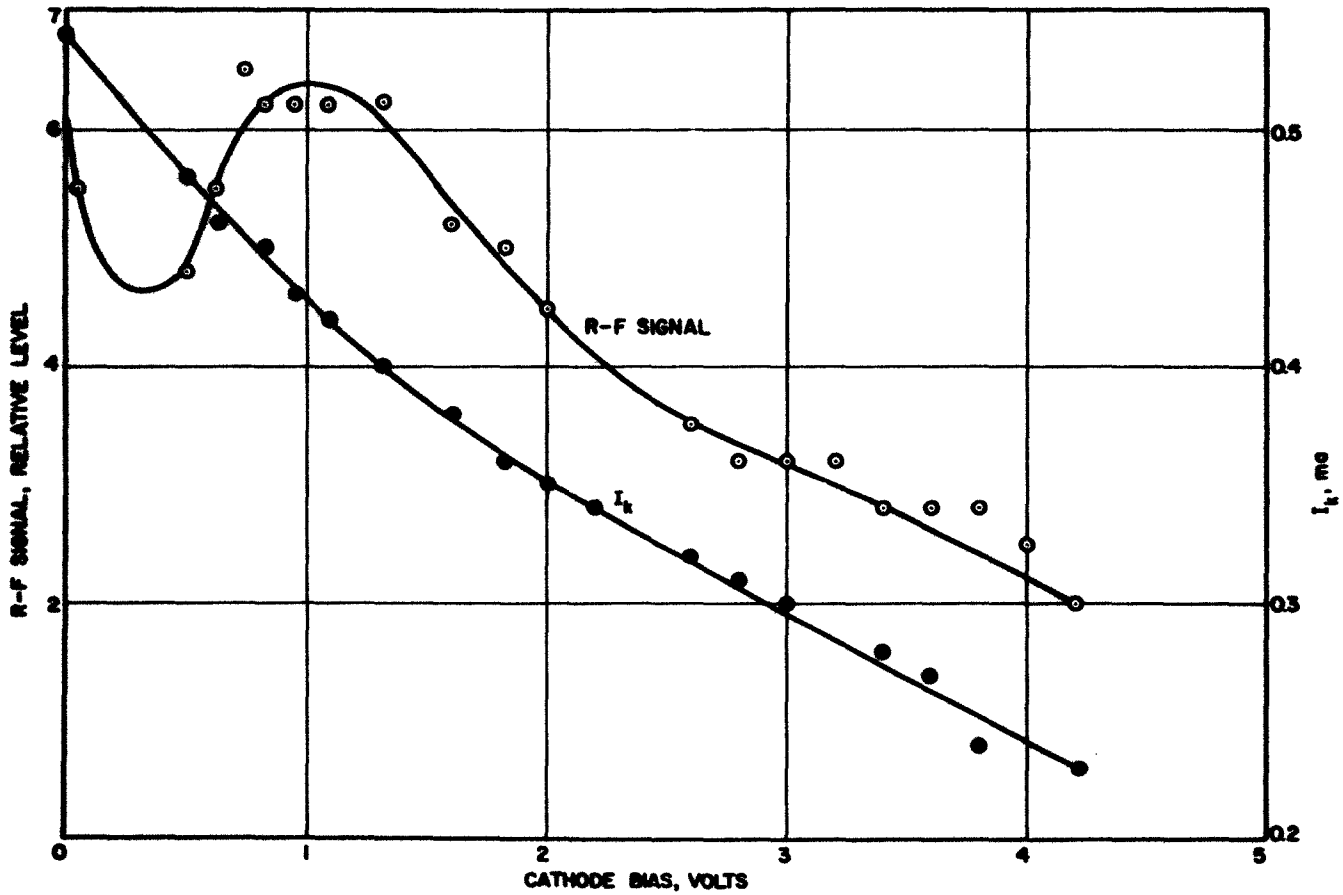

FIG. 9.20 R-F SIGNAL LEVEL AND CATHODE CURRENT VS. CATHODE BIAS. (PROBE NO. a)

B = 164 GAUSS, V_{acc} = 292 VOLTS, V_{an} = 425 VOLTS, f = 95 mc, P_h = 22.3 WATTS.

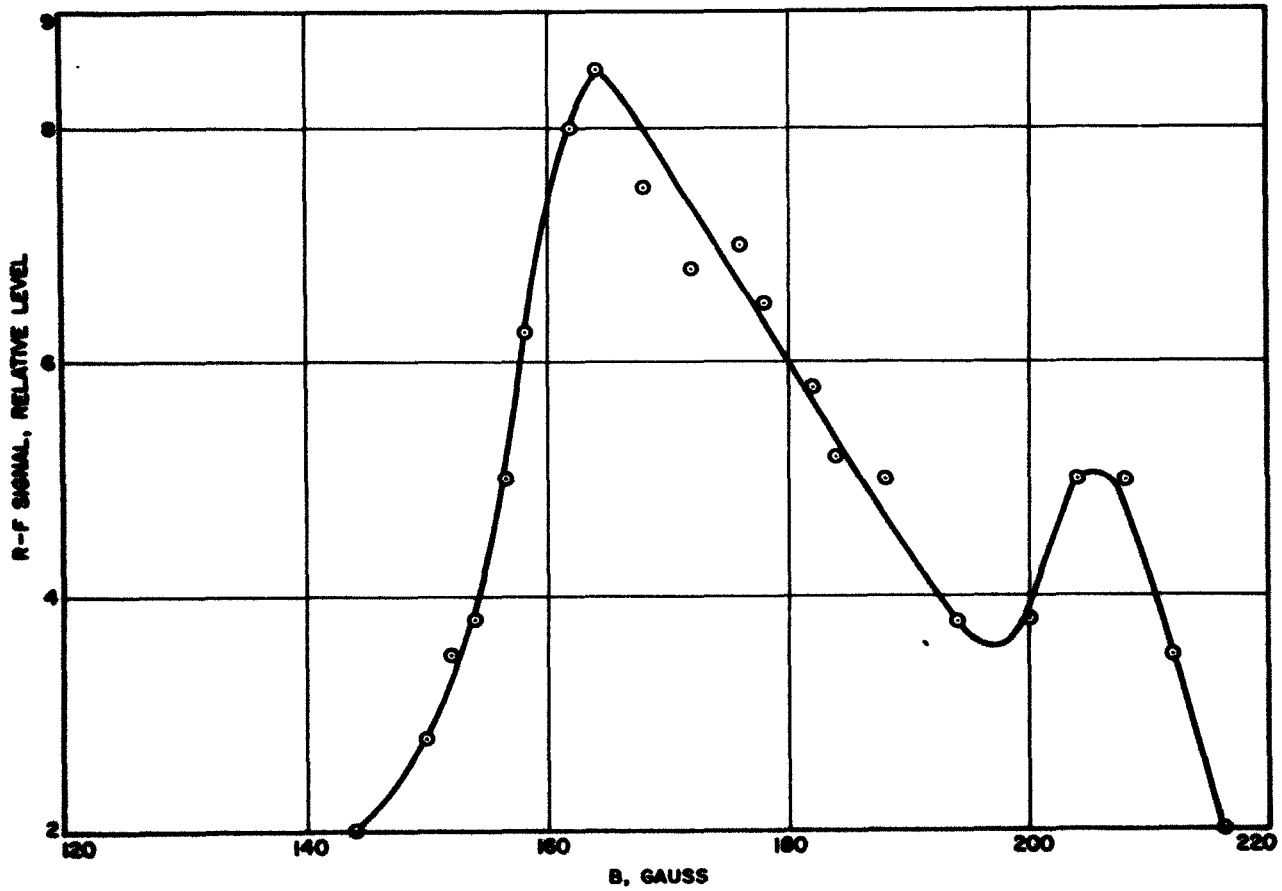

FIG. 9.21 R-F SIGNAL LEVEL VS. MAGNETIC FIELD. (PROBE NO. a)

V_{acc} = 290 VOLTS, V_{an} = 411 VOLTS, f = 95 mc, P_h = 22.3 WATTS.

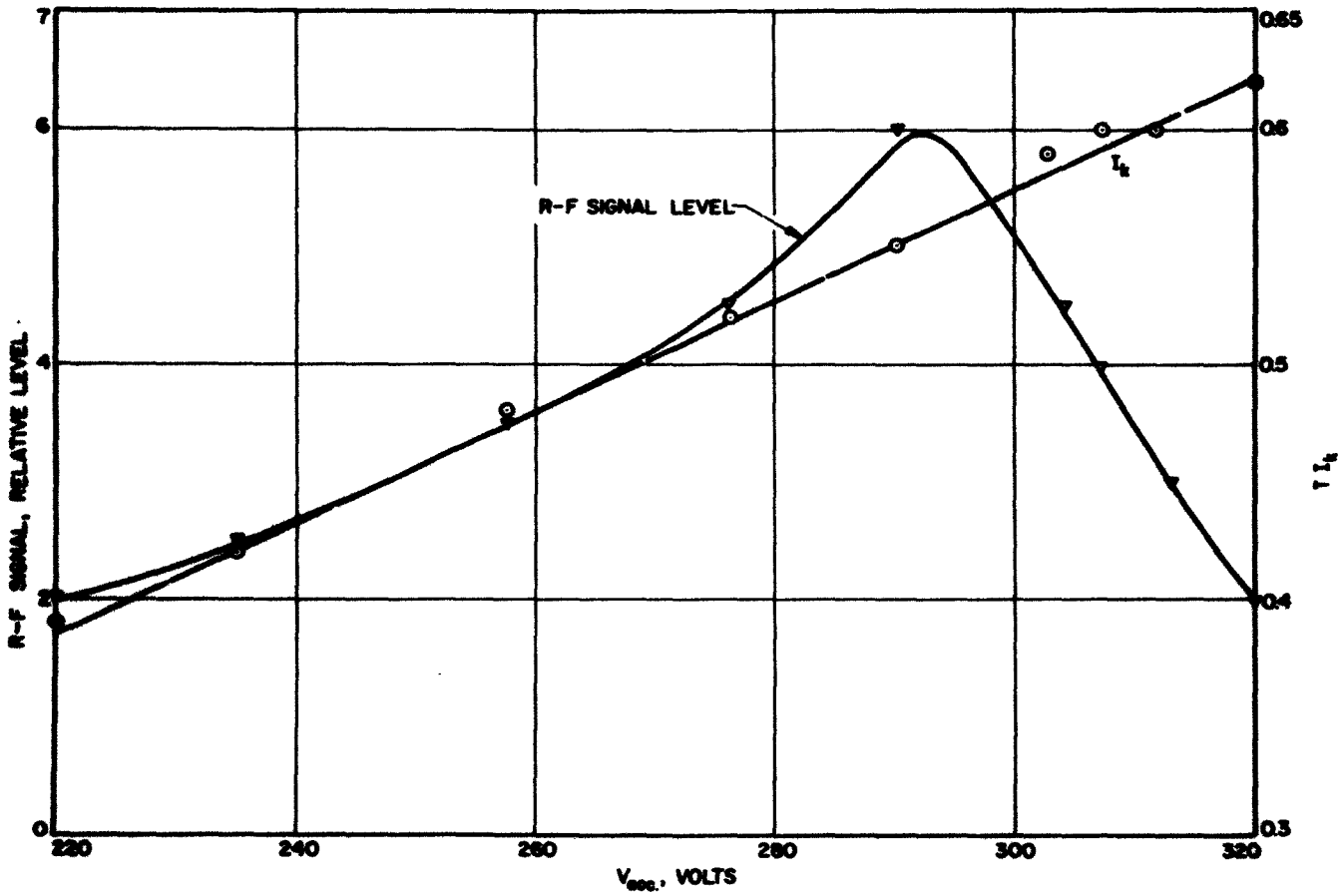

FIG. 9.22 R-F SIGNAL LEVEL AND CATHODE CURRENT VS. GUN ANODE VOLTAGE. (PROBE NO. a)

B = 160 GAUSS, V_{an} = 425 VOLTS, f = 95 mc, P_h = 22.3 WATTS.

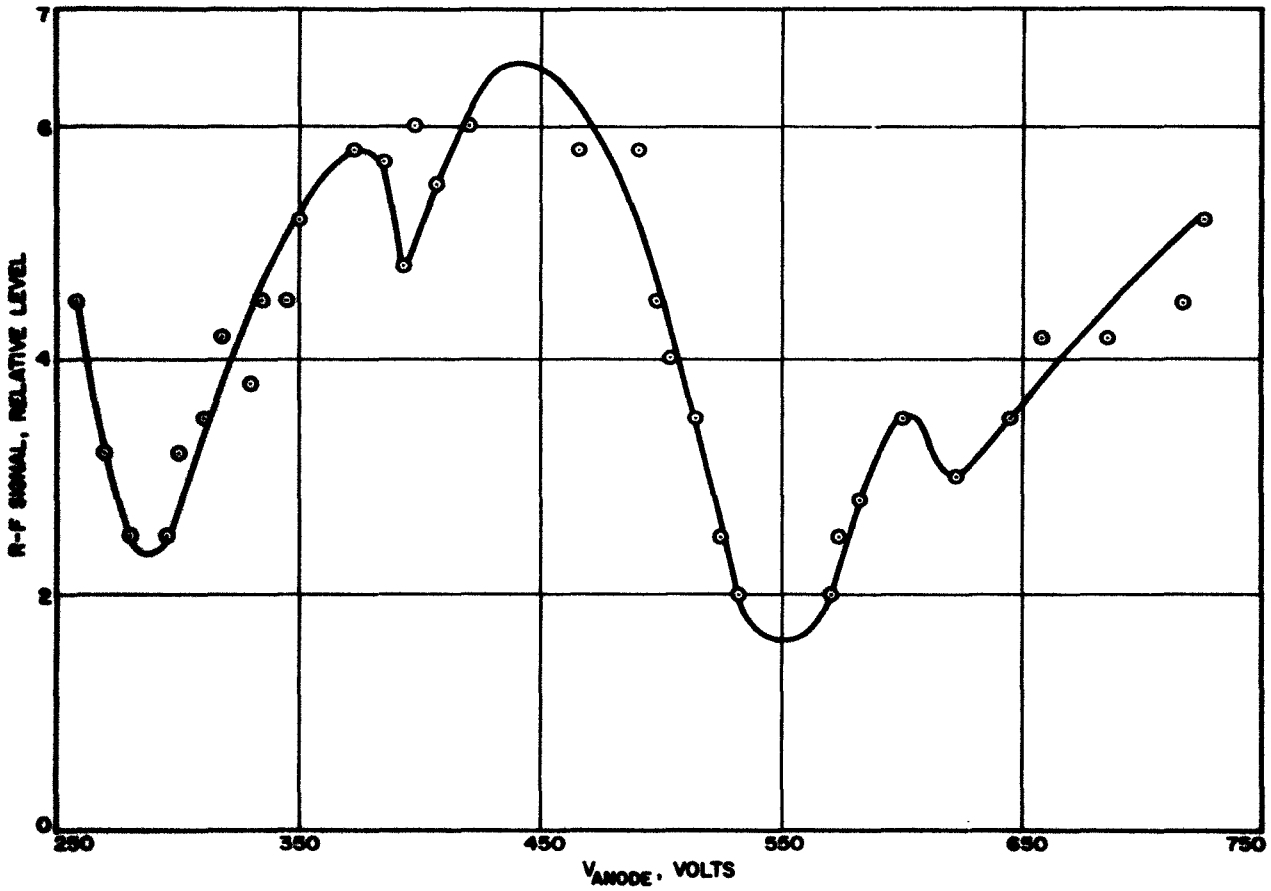

FIG. 9.23 R-F SIGNAL LEVEL VS. ANODE VOLTAGE. (PROBE NO. a) B = 160 GAUSS, I_k = 0.54 ma, V_{acc} = 290 VOLTS, f = 95 mc, P_h = 22.3 WATTS.

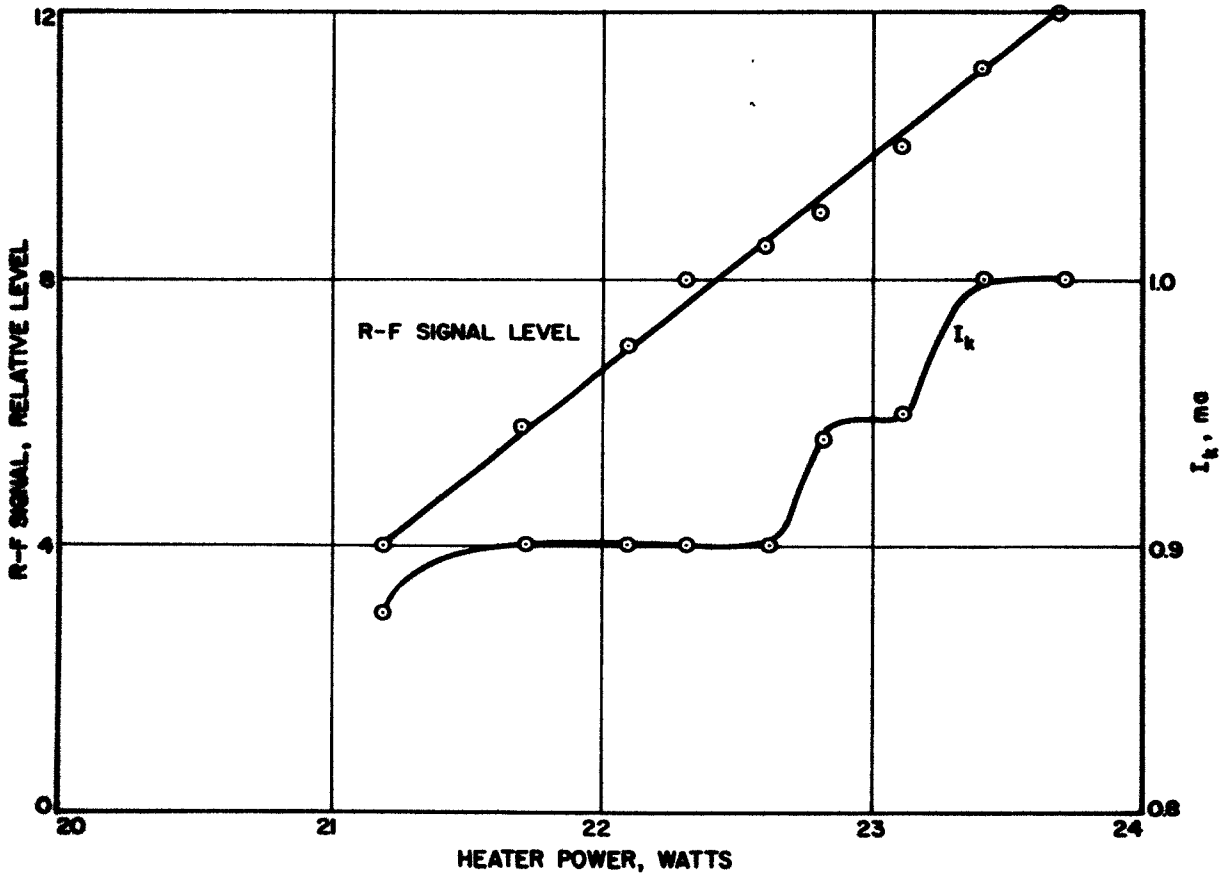

FIG. 9.24 R-F SIGNAL LEVEL AND CATHODE CURRENT VS. HEATER POWER. (PROBE NO. a) B = 160 GAUSS, V_{acc} = 412 VOLTS, V_{an} = 403 VOLTS, f = 140 mc, CATHODE BIAS = 0 VOLT.

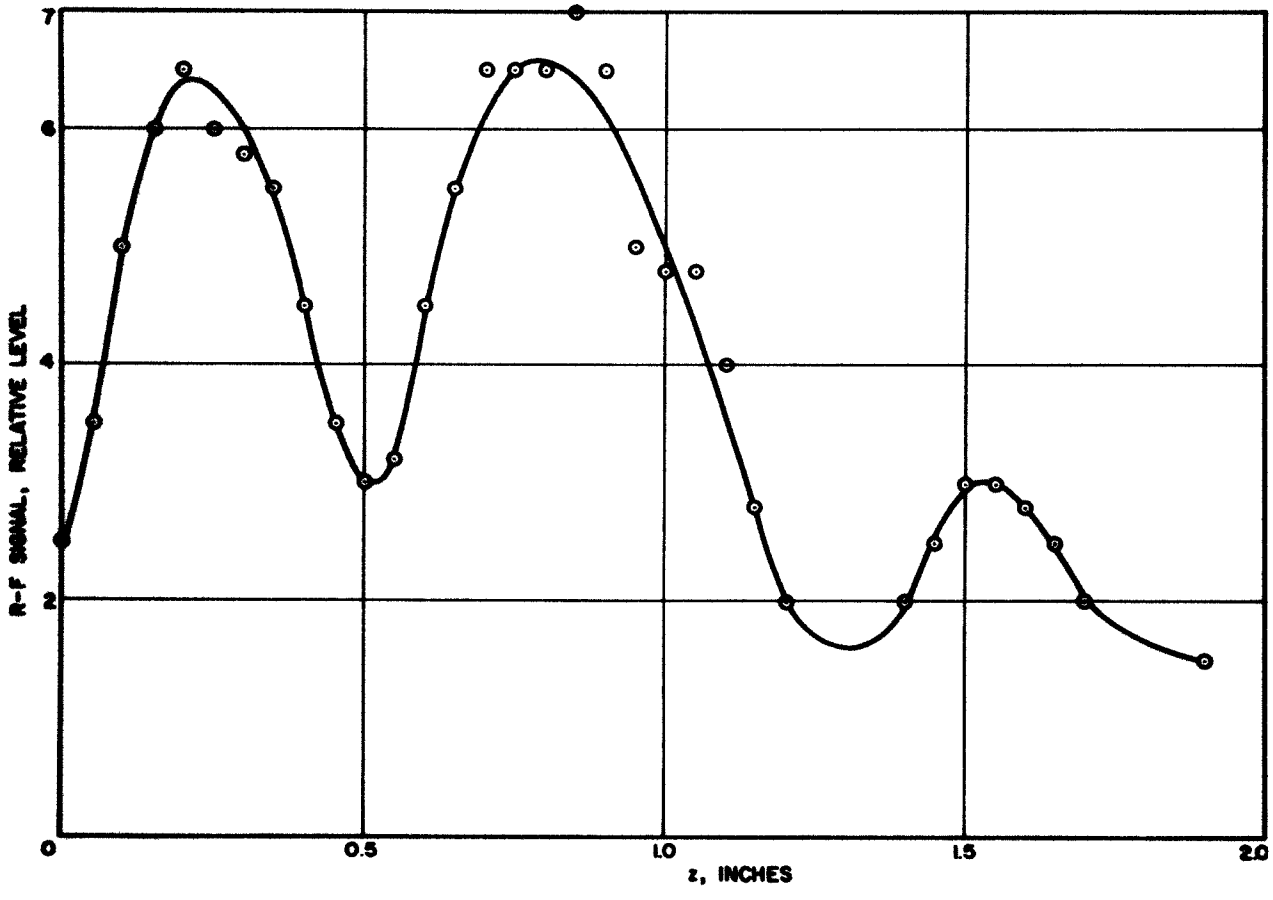

FIG. 9.25 R-F SIGNAL LEVEL VS. z. (PROBE NO. a) B = 164 GAUSS,

V_{acc} = 292 VOLTS, V_{an} = 425 VOLTS, f = 170 mc, P_h = 22.3 WATTS.

The signal level at the middle probe was about 1.5 - 2.0 times larger than at the two side probes. This indicates that the r-f field is maximum at the center of the beam and is reduced in the direction of the magnetic field.

CHAPTER X. SUMMARY, CONCLUSIONS AND SUGGESTIONS FOR FURTHER STUDY

10.1 Summary and Conclusions

The general purpose of this study has been to investigate noise transport in crossed-field devices. Most of the work reported in the preceding chapters refers to noise transport in the gun region, although some results based upon the Llewellyn-Peterson equations are given for the noise transport in the interaction region. Some experimental data for the interaction region is also given.

In deriving the Llewellyn-Peterson equations both current density components are considered. The resulting electron trajectories are compared with those obtained from the Kino gun model. The noise transport coefficients are written in a general form so that any physical model may be used in evaluating the noise transport. Furthermore these coefficients are written in terms of the two velocity components separately and a few checks are made to show the correlation. It is also shown that these coefficients reduce to the usual Llewellyn coefficients for the case of $\omega_c = 0$ and to Van Duzer's coefficients in the Kino gun model for $\omega \to 0$. One set of coefficients can be used for evaluating the noise transport in the gun region as well as in the interaction region. Only a few specific cases are evaluated.

For the gun region the noise transport coefficients are evaluated for the Kino gun model, the temperature-limited case and the quasi space-charge-limited case for several values of the perturbation frequency. It is noticed that the perturbations grow significantly in the gun region. For the interaction region these coefficients are evaluated for an

idealized flow when $\dot{z}$ = constant. It is noticed that the perturbations grow faster if the beam current is increased and/or the magnetic field is decreased which agrees qualitatively with experimental results.

From the results of the density method given in Chapter V it is found that the value of $|V_m|$ increases as ω_c is increased. The contribution from the initial tangential velocity in evaluating the various d-c parameters is considerable. A good agreement between the theoretical and experimental results for the cathode current is found. The variation of the several d-c parameters as a function of $\omega_c T$ and ω_c is found in good agreement with the Kino gun[15] results except that the normal y-component of the current density is not constant along the beam as assumed in the Kino gun model.

The fifth degree determinantal equation derived to study the propagation of a perturbation along the beam indicates the presence of the five waves. These waves correspond to the synchronous wave, the two modified space-charge waves and two backward waves. For large values of ω_p (i.e., near the cathode) the two backward waves refer to one growing wave and the other a declining wave. The value of the growth rate for the growing wave (or the attenuation rate for the declining wave) decreases with y. The two space-charge waves and the synchronous wave are attenuated if $(d\dot{y}_o/dy)/\dot{y}_o > 0$. If $(d\dot{y}_o/dy)/\dot{y}_o < 0$, the two space-charge waves experience very large values of growth while the synchronous wave is increasingly attenuated for larger values of ω_p and the conventional fast space-charge wave is found to be a backward wave for small values of ω. It is noted that because of continuously changing d-c parameters the propagation constants for the five waves do

not remain constant. Based upon the results obtained after solving the determinantal equation, several experimental observations are explained.

In deriving the equations for noise transport based upon the Monte Carlo analysis, numerical techniques are used to derive the equations for position and velocity coordinates of an electron. The derivation of correlation functions and power spectral densities is also based upon numerical techniques. These equations are of a general nature and can be used without any restriction except for a compromise between accuracy and computer time. The space-charge potential used in the force equations is derived using the Green's function.

The results of the Monte Carlo analysis given in Chapter VII indicate a growth of the slow wave which is larger than that of the fast wave. The two waves grow as the beam is accelerated and then decay as the beam is decelerated, but there is an overall growth of the two waves over a complete cycloid. Most of the growth occurs in the latter part of the first half of the cycloid. These results are in agreement with those given in Chapter V. It is anticipated that the finite growth in the earlier part of the first half of the cycloid is due to higher order modes and d-c z-component electric field which are neglected in the density method.

The potential minimum aids in reducing the current fluctuations although the velocity fluctuations are increased as the beam is accelerated. The velocity fluctuations are decreased as the beam is decelerated, however there is an overall increase in the velocity fluctuations in traversing a complete cycloid. It is also found that the inner edge of the beam has larger velocity fluctuations and this will give larger values of the electron equivalent temperature for the inner

edge. This result is in good agreement with the results given by Rao and Whinnery[26]. These explain why large values of electron equivalent temperature are obtained in crossed-field tubes. It is anticipated that large values of the velocity fluctuations are due to electron mixing from one layer to another and this illustrates the importance of a laminar and noncycloiding flow. The velocity fluctuations are found to decrease as f is increased and the current fluctuations for rectangles near the cathode increase as f is increased. These results are in agreement with the results given in Chapter III from the Llewellyn-Peterson equations.

It is noticed that the noise figure F decreases as f is increased and it is anticipated that F would approach asymptotically the value for shot noise at large values of f.

In operating a set of cathodes placed side by side in the experimental noise analyzer (or even otherwise in a crossed-field geometry) there is a space-charge reduction in voltage due to the bending of a beam because of magnetic field and this affects the beam current from the neighboring cathodes. This is of prime importance in designing a multi-cathode or even a wide cathode for large values of beam power. It is noticed that the electron equivalent temperature as evaluated in the interaction region is extremely high and is decreased as the value of the magnetic field is increased. It is also noticed that by adjusting the d-c parameters appropriately some coherent oscillations may be produced and the frequency of these oscillations may be varied by changing the d-c parameters. The r-f signal does not show any increase in the interaction region but instead its magnitude is decreased along the beam. Injection of an r-f signal in the gun region also indicates

the same behavior, i.e., the magnitude of the r-f signal as picked up at the movable probes can be varied by changing the d-c parameters. The r-f signal detected at the movable probes in the absence of the beam is too small to be detected by the spectrum analyzer. However this data is limited to low frequencies ($f < 250$ mc) because for higher frequencies the direct pickup becomes significant. The r-f signal in this case also is reduced along the beam. This may be partially due to some electron collection at the anode and sole.

10.2 Suggestions for Further Study

The study of noise in crossed-field devices is in a stage of infancy and a great deal of theoretical as well as experimental work is needed in order to realize low noise figures.

The calculations for the noise transport coefficients in the interaction region have revealed some minima. As in O-type devices the position of the minima with regard to the r-f input can change the noise figure; it would be very interesting to orient some study in developing a generalized expression for noise figure and determine the distance of the minima from the r-f input which would lead to a reduced noise figure. It would also be necessary to evaluate the noise transport coefficients for some additional cases depending upon the phase and the magnitude of the various perturbations at the a-plane. It is not yet clear how these results will be modified by considering several trajectories simultaneously. If it is later deemed feasible on the basis of time and cost, some additional physical models may be considered for evaluating noise transport in the gun region.

The results given in Chapter V have indicated that the E_z field component plays a major role and if E_z is made equal to zero, the

perturbations will remain constant in magnitude. Because a filamentary beam model is discussed here, it is not clear as yet how these results will be modified when several trajectories are considered simultaneously. It would be interesting to extend this analysis to wider cathodes and this corresponds to consideration of several trajectories simultaneously. The larger values of the growth factor violate the small-signal assumption used in deriving the determinantal equation. This would require extension of the small-signal analysis to a large-signal analysis of beams with wider cathodes. A wider cathode may be simulated by a finite number of electron trajectories. A density method analysis considering several velocity classes would be quite useful in the study of noise.

For a low-noise device it is necessary that the beam should not be of a cycloiding nature and from this point of view the gun design is quite important. The results given in Chapter V have indicated the regions of a beam which are most susceptible to perturbations and this would require a new type of gun which eliminates those regions for which $(d\dot{y}_o/dy)/\dot{y}_o < 0$.

It has been found from the results of the Monte Carlo analysis that the larger noise figures are due to a wide range of velocity fluctuations and it is anticipated that this is due to the mixing of electrons from one layer to another in the beam. This illustrates the importance of a laminar flow. For this reason a Monte Carlo analysis for a Kino gun would be very helpful. The effect of the a-c z-component field due to the current fluctuations as a result of an open-circuited diode for a Kino gun model may be considerable. This analysis of the Kino gun model may be extended to small lengths in the interaction region.

The computations of the various noise parameters for the remaining rectangles would give some additional information about the noise transport.

The experimental investigation has indicated that r-f signal does not grow in the interaction region. This may be partially due to some beam collection at the earlier regions of the anode and sole. For this purpose it will be worthwhile to extend this investigation with a number of anode and sole segments; of course, if a laminar noncycloiding beam is obtained, this may not be as important.

The measurement of electron equivalent temperature was limited in the interaction region only. This is due to the fact that the r-f probes in the gun region are almost parallel to the beam and this requires relatively higher d-c voltages on these probes. This would modify the beam characteristics and is not desirable. It is felt that by making these probes L-shaped, this study could be made in the gun region also.

Whether the r-f signal is due to coherent oscillations or due to some injected r-f signal, it is noticed that the r-f output may be considerably controlled by appropriately adjusting the d-c parameters. This knowledge is very helpful in designing practical devices. Whether this would also reduce the electron equivalent temperature or not would require such measurements at various points along the beam in the gun region. An r-f study based upon this orientation would be extremely helpful in further understanding noise transport phenomena. A reasonably large size crossed-field diode scaled appropriately for this study would be very useful. In such a case it might be convenient to determine the radiation characteristics of the probe and thus the effective modulation

of the beam. This will help in obtaining some quantitative agreements. The modification of the probes to extend this study to higher frequencies is also deemed necessary.

Some studies not reported here have led to a transmission-line analogy[25] of crossed-field beams. By using analogous techniques as used in O-type devices a perturbation at an angular frequency may be increased or reduced effectively as desired. This study may be extended to some special types of transformers for noise reduction purposes.

The study of r-f injection and propagation in the gun region with a multi-cathode structure and with different types of guns would be of considerable help in the study of noise in crossed-field devices. This may also suggest some new techniques for microwave amplification.

APPENDIX A. DERIVATION OF THE TIME PERTURBATION δ_z

In deriving coefficients given by Eqs. 2.25, a perturbation δ_z in transit time T is assumed. The equation for δ_z is given by Eq. 2.21 and is derived in the following manner.

Integrate Eq. 2.12 step by step three times with respect to t and introduce initial conditions on the velocity and acceleration parameters corresponding to the a-plane and designated by the suffix "a" to evaluate the constants of integration in the three steps of integration. This gives an expression for z. On the right-hand side of this equation a perturbation δ_z given by Eq. 2.20 is introduced and the various terms are simplified. The second-order terms involving the product of two a-c functions are neglected. Then z on the left-hand side of the equation is cancelled with the d-c part of z on the right-hand side of the equation. On the right-hand side the terms involving δ_z are grouped together and the coefficient of δ_z is found to be the d-c part of $\dot{z}$. Use is made of Eqs. B.12 and B.14 to convert the two a-c components of the acceleration at the a-plane to the other known a-c fluctuations at the a-plane. After the various terms are grouped in an appropriate manner, the following relation is obtained:

$$- \dot{z}_{d-c}\, \delta_z\, e^{-j\omega t} = \tilde{I}\, \delta_{z_1} + \tilde{q}_{z_{a1}}\, \delta_{z_2} + \tilde{q}_{y_{a1}}\, \delta_{z_3} + \dot{z}_{a1}\, \delta_{z_4} + \dot{y}_{a1}\, \delta_{z_5} \quad . \tag{A.1}$$

The general procedure used in deriving Eq. A.1 is very similar to that of Llewellyn and hence the minor details are omitted. The various functions in Eq. A.1 are given by

$$\delta_{z_1} = -\frac{H_1 - H_3}{\omega_c^3} + \frac{T^2 e^{-jR\omega_c T}}{2jR\omega_c} \sin \bar{\alpha} \quad , \tag{A.2}$$

$$\delta_{z_2} = -\frac{F_1}{2R\omega_c^3} - \frac{T^2 e^{-jR\omega_c T}}{2jR\omega_c} \quad , \tag{A.3}$$

$$\delta_{z_3} = -\frac{F_2}{2jR\omega_c^3} \quad , \tag{A.4}$$

$$\delta_{z_4} = -\frac{F_2}{2\omega_c} + T e^{-jR\omega_c T} \tag{A.5}$$

and

$$\delta_{z_5} = -\frac{F_1}{2j\omega_c} + \frac{\omega_c T^2}{2} e^{-jR\omega_c T} \quad , \tag{A.6}$$

where

$$F_{1,2} = \frac{H_e e^{j\omega_c T}}{[j(R+1)]^3} \mp \frac{H_f e^{-j\omega_c T}}{[j(R-1)]^3} \quad , \tag{A.7}$$

$$F_{3,4} = \frac{e^{j\omega_c T} - e^{-jR\omega_c T}}{j(R+1)} \mp \frac{e^{-j\omega_c T} - e^{-jR\omega_c T}}{j(R-1)} \tag{A.8}$$

$$F_{5,6} = \frac{G_e e^{j\omega_c T}}{[j(R+1)]^2} \mp \frac{G_f e^{-j\omega_c T}}{[j(R-1)]^2} \quad , \tag{A.9}$$

$$G_{s,d} = 1 - e^{-j(2R \pm 1)\frac{\omega_c T}{2}} - j(2R \pm 1)\frac{\omega_c T}{2} e^{-j(2R \pm 1)\frac{\omega_c T}{2}} \quad , \tag{A.10}$$

$$H_{s,d} = G_{s,d} - \frac{1}{2}\left[j(2R \pm 1)\frac{\omega_c T}{2}\right]^2 e^{-j(2R \pm 1)\frac{\omega_c T}{2}} \quad , \tag{A.11}$$

$$G_{e,f} = 1 - e^{-j(R \pm 1)\omega_c T} - j(R \pm 1)\omega_c T\, e^{-j(R \pm 1)\omega_c T} \tag{A.12}$$

and

$$H_{e,f} = G_{e,f} - \frac{1}{2}\left[j(R \pm 1)\omega_c T\right]^2 e^{-j(R \pm 1)\omega_c T} \quad . \tag{A.13}$$

The first and the second suffixes correspond respectively to the upper and lower signs on the right-hand side of the above equations. It should also be pointed out that in the expression for z there are terms of the type exp $j\omega t_a$ and in these terms t_a is substituted from Eq. 2.20. The functions $\bar{\alpha}$ and R are given by Eqs. 2.15 and 2.23 respectively, while the functions H_1 and H_3 are given by Eqs. C.11 and C.12.

APPENDIX B. DERIVATION OF INITIAL CONDITIONS

In the derivation of Eq. 2.21, the initial conditions given by Eqs. 2.22 are used. These initial conditions are derived in the following manner.

From the equations of motion given by Eqs. 2.1

$$E_y = -(\ddot{y} + \omega_c \dot{z}) \frac{1}{\eta} \tag{B.1}$$

and

$$E_z = -(\ddot{z} - \omega_c \dot{y}) \frac{1}{\eta} \quad . \tag{B.2}$$

The total y-component of current density including the convection current density and the displacement current density is given by

$$I_{T_y} = q_{T_y} + \epsilon_o \frac{\partial}{\partial t} E_y \tag{B.3}$$

or

$$\tilde{I}_{T_y} = \tilde{q}_{T_y} + \frac{\partial}{\partial t} (\ddot{y} + \omega_c \dot{z}) \quad , \tag{B.4}$$

where the following definition has been utilized:

$$\tilde{I}_{T_y} \triangleq \frac{e}{m\epsilon_o} I_{T_y} \quad . \tag{B.5}$$

Similarly

$$\tilde{I}_{T_z} = \tilde{q}_{T_z} + \frac{\partial}{\partial t} (\ddot{z} - \omega_c \dot{y}) \quad . \tag{B.6}$$

At $t = t_a$

$$\tilde{I}_{T_y} = \left(\tilde{I}_D + \tilde{I}_1 e^{j\omega t_a}\right) \cos \bar{\alpha} \tag{B.7}$$

and

$$\tilde{I}_{T_z} = \left(\tilde{I}_D + \tilde{I}_1 e^{j\omega t_a}\right) \sin \bar{\alpha} \quad , \tag{B.8}$$

where $\bar{\alpha}$ is given by Eq. 2.15. By assuming sinusoidal variations, Eqs. B.4 and B.7 may be used to give, for $t = t_a$,

$$\tilde{I}_1 \cos \bar{\alpha} = \tilde{q}_{y_{a1}} + j\omega \left(\dot{y}_{a1} + \omega_c \dot{z}_{a1}\right) \quad , \tag{B.9}$$

where

$$\tilde{q}_{T_y} = \tilde{q}_{y_a} + q_{y_{a1}} e^{j\omega t_a} \tag{B.10}$$

is assumed at

$$t = t_a \quad . \tag{B.11}$$

Equation B.9 is solved for $\dot{y}_{a1}$ which is given by

$$\dot{y}_{a1} = \frac{1}{j\omega}\left(\tilde{I}_1 \cos \bar{\alpha} - \tilde{q}_{y_{a1}} - j\omega\, \omega_c\, \dot{z}_{a1}\right) \quad . \tag{B.12}$$

Similarly, by assuming

$$\tilde{q}_{T_z} = \tilde{q}_{z_a} + q_{z_{a1}} e^{j\omega t_a} \tag{B.13}$$

for $t = t_a$ and making use of Eqs. B.6 and B.13, the following is obtained:

$$\dot{z}_{a1} = \frac{1}{j\omega}\left(I_1 \sin \bar{\alpha} - q_{z_{a1}} + j\omega\, \omega_c\, \dot{y}_{a1}\right) \quad . \tag{B.14}$$

APPENDIX C. DERIVATION OF THE MATRIX COEFFICIENTS FOR NOISE TRANSPORT EVALUATIONS

The various coefficients for evaluating the noise transport from the a-plane to the b-plane (see Fig. 2.1) are given by Eqs. 2.25. These coefficients involve $\dot{z}$ in the denominator. In this appendix a brief summary of the procedure for deriving these coefficients is given. The procedure for deriving the coefficients given by Eqs. 2.35 is very similar and will not be discussed. In both cases the general procedure for deriving these coefficients is similar to that developed by Llewellyn for the case $\omega_c = 0$.

From Eq. B.4, the a-c part of the equation may be written as

$$\tilde{q}_{y_1} e^{j\omega t} = \tilde{I}_1 e^{j\omega t} \cos\left(\frac{\omega_c}{2} T + \bar{\alpha}\right) - \frac{\partial}{\partial t}(\ddot{y} + \omega_c \dot{z}) \quad . \qquad (C.1)$$

Similarly from Eq. B.6

$$\tilde{q}_{z_1} e^{j\omega t} = \tilde{I}_1 e^{j\omega t} \sin\left(\frac{\omega_c}{2} T + \bar{\alpha}\right) - \frac{\partial}{\partial t}(\ddot{z} - \omega_c \dot{y}) \quad , \qquad (C.2)$$

where use is made of Eqs. 2.7. The expression for $\ddot{y}$ is obtained by integrating Eq. 2.13 and introducing the initial conditions corresponding to $t = t_a$ at the a-plane, and then introducing the time perturbation given by Eq. 2.20; $\dot{y}$ is obtained by integrating $\ddot{y}$ and introducing the initial conditions as before, and then introducing the time perturbation δ_z; $\ddot{z}$ is obtained by integrating Eq. 2.12 and introducing the initial conditions, and then the time perturbation δ_z. Similarly $\dot{z}$ is obtained by integrating $\ddot{z}$, the initial conditions are introduced followed by the perturbation. When deriving expressions for q_{y_b} and q_{z_b}, it is

convenient to consider expression $\ddot{y} + \omega_c \dot{z}$ and $\ddot{z} - \omega_c \dot{y}$, rather than considering $\ddot{y}$, $\ddot{z}$, $\dot{y}$ and $\dot{z}$ separately. The terms are then differentiated with respect to t and the terms grouped together after using Eqs. B.12, B.14 and A.1 to obtain the coefficients in the final form.

Similarly expressions for $\dot{y}_b$ and $\dot{z}_b$ are derived by introducing perturbation δ_z in expressions for $\dot{y}$ and $\dot{z}$ respectively. Use is made of Eqs. B.12, B.14 and A.1 to give the coefficients in the final form. The coefficients a_{21}, a_{31}, a_{41} and a_{51}, which are rather restricted to the physical model discussed in Section 2.1, are given by

$$a_{21} = \left[1 - jR\frac{\tilde{I}_D}{\omega_c^2 \ell}\left(H_1 - H_3 - \frac{\omega_c^2 T^2 \sin\bar{\alpha}}{2jR} e^{-jR\omega_c T}\right)\right] \sin\left(\frac{\omega_c T}{2} + \bar{\alpha}\right)$$

$$- jR\left[\frac{H_5}{2} + \left(\frac{F_3 + F_4 - jF_5 - jF_6}{2j}\right)\left(1 + \frac{1}{2R}\right) e^{j\bar{\alpha}} + \frac{F_3 - F_4 + jF_5 - jF_6}{2j}\left(1 - \frac{1}{2R}\right) e^{-j\bar{\alpha}}\right.$$

$$\left. + \frac{H_8}{2} + \frac{\sin\bar{\alpha} - \omega_c T\cos\bar{\alpha}}{jR} e^{-jR\omega_c T}\right], \qquad (C.3)$$

$$a_{31} = \left[1 - jR\frac{\tilde{I}_D}{\omega_c^2 \ell}\left(H_1 - H_3 - \frac{\omega_c^2 T^2 \sin\bar{\alpha}}{2jR} e^{-jR\omega_c T}\right)\right] \cos\left(\frac{\omega_c T}{2} + \bar{\alpha}\right)$$

$$- jR\left[- j\frac{H_6}{2} - \frac{H_7}{2j} + \frac{F_3 + F_4 - jF_5 - jF_6}{2}\left(1 + \frac{1}{2R}\right) e^{j\bar{\alpha}}\right.$$

$$\left. - \frac{F_3 - F_4 + jF_5 - jF_6}{2}\left(1 - \frac{1}{2R}\right) e^{-j\bar{\alpha}} + \frac{\cos\bar{\alpha} + \omega_c T\sin\bar{\alpha}}{jR} e^{-jR\omega_c T}\right], \qquad (C.4)$$

$$a_{41} = \frac{1}{\omega_c^2}\,\frac{e}{m\epsilon_o}\left[\frac{\dot{z}}{\omega_c \dot{z}}\left(H_1 - H_3 - \frac{\omega_c^2 T^2 \sin\bar{\alpha}}{2jR}\,e^{-jR\omega_c T}\right)\right.$$

$$- \frac{H_7}{2j} + \frac{F_5+F_6}{2j}\left(1 + \frac{1}{2R}\right)e^{j\bar{\alpha}} + \frac{F_5-F_6}{2j}\left(1 - \frac{1}{2R}\right)e^{-j\bar{\alpha}}$$

$$\left. + \frac{\omega_c T \sin\bar{\alpha}}{jR}\,e^{-jR\omega_c T}\right] \quad (C.5)$$

and

$$a_{51} = \frac{1}{\omega_c^2}\,\frac{e}{m\epsilon_o}\left[\frac{\dot{y}}{\omega_c \dot{z}}\left(H_1 - H_3 - \frac{\omega_c^2 T^2 \sin\bar{\alpha}}{2jR}\,e^{-jR\omega_c T}\right)\right.$$

$$- \frac{H_8}{2} + \frac{F_5+F_6}{2}\left(1 + \frac{1}{2R}\right)e^{j\bar{\alpha}} - \frac{F_5-F_6}{2}\left(1 - \frac{1}{2R}\right)e^{-j\bar{\alpha}}$$

$$\left. + \frac{\omega_c T \cos\bar{\alpha}}{jR}\,e^{-jR\omega_c T}\right] . \quad (C.6)$$

Similarly the coefficients a'_{21}, a'_{31}, a'_{41} and a'_{51} derived in terms of $\dot{y}$ are given by

$$a'_{21} = \left[1 + R\,\frac{\tilde{I}_D}{\omega_c^2 \dot{y}}\left(H_2 - H_4 + \frac{\omega_c^2 T^2 \cos\bar{\alpha}}{2R}\,e^{-jR\omega_c T}\right)\right]\sin\left(\frac{\omega_c T}{2} + \bar{\alpha}\right)$$

$$- jR\left[\frac{H_5}{2} + \frac{F_3+F_4-jF_5-jF_6}{2j}\left(1 + \frac{1}{2R}\right)e^{j\bar{\alpha}} + \frac{F_3-F_4+jF_5-jF_6}{2j}\left(1 - \frac{1}{2R}\right)e^{-j\bar{\alpha}}\right.$$

$$\left. + \frac{H_8}{2} + \frac{\sin\bar{\alpha} - \omega_c T \cos\bar{\alpha}}{jR}\,e^{-jR\omega_c T}\right] , \quad (C.7)$$

$$a'_{31} = \left[1 + R\frac{\tilde{I}_D}{\omega_c^2 \dot{y}}\left(H_2 - H_4 + \frac{\omega_c^2 T^2 \cos\bar{\alpha}}{2R} e^{-jR\omega_c T}\right)\right]\cos\left(\frac{\omega_c T}{2} + \bar{\alpha}\right)$$

$$- jR\left[- j\frac{H_8}{2} - \frac{H_7}{2j} + \frac{F_3 + F_4 - jF_5 - jF_6}{2}\left(1 + \frac{1}{2R}\right)e^{j\bar{\alpha}} - \frac{F_3 - F_4 + jF_5 - jF_6}{2}\right.$$

$$\left.\cdot\left(1 - \frac{1}{2R}\right)e^{-j\bar{\alpha}} + \frac{\cos\bar{\alpha} + \omega_c T\sin\bar{\alpha}}{jR} e^{-jR\omega_c T}\right], \quad (C.8)$$

$$a'_{41} = \frac{1}{\omega_c^2}\frac{e}{m\epsilon_o}\left[\frac{j\ddot{z}}{\omega_c \dot{y}}\left(H_2 - H_4 + \frac{\omega_c^2 T^2 \cos\bar{\alpha}}{2R} e^{-jR\omega_c T}\right) - \frac{H_7}{2j}\right.$$

$$+ \frac{F_5 + F_6}{2j}\left(1 + \frac{1}{2R}\right)e^{j\bar{\alpha}} + \frac{F_5 - F_6}{2j}\left(1 - \frac{1}{2R}\right)e^{-j\bar{\alpha}}$$

$$+ \frac{\omega_c T\sin\bar{\alpha}}{jR} e^{-jR\omega_c T} \quad (C.9)$$

and

$$a'_{51} = \frac{1}{\omega_c^2}\frac{e}{m\epsilon_o}\left[\frac{j\ddot{y}}{\omega_c \dot{y}}\left(H_2 - H_4 + \frac{\omega_c^2 T^2 \cos\bar{\alpha}}{2R} e^{-jR\omega_c T}\right) - \frac{H_8}{2}\right.$$

$$\left.+ \frac{F_5 + F_6}{2}\left(1 + \frac{1}{2R}\right)e^{j\bar{\alpha}} - \frac{F_5 - F_6}{2}\left(1 - \frac{1}{2R}\right)e^{-j\bar{\alpha}} + \frac{\omega_c T\cos\bar{\alpha}}{jR} e^{-jR\omega_c T}\right],$$

(C.10)

where

$$H_{1,2} = \frac{H_s\, e^{j\frac{\omega_c}{2}T + j\bar{\alpha}}}{2j\left[j\left(R + \frac{1}{2}\right)\right]^3} \mp \frac{H_d\, e^{-j\frac{\omega_c}{2}T - j\bar{\alpha}}}{2j\left[j\left(R - \frac{1}{2}\right)\right]^3}\ , \tag{C.11}$$

$$H_{3,4} = \frac{H_e\left(1 + \frac{1}{2R}\right) e^{j\omega_c T + j\bar{\alpha}}}{j\ [j(R+1)]^3} \mp \frac{H_f\left(1 - \frac{1}{2R}\right) e^{-j\omega_c T - j\bar{\alpha}}}{j\ [j(R-1)]^3}\ , \tag{C.12}$$

$$H_{5,6} = \frac{\left[1 - e^{-j[R+(1/2)]\omega_c T}\right] e^{j(\omega_c T/2) + j\bar{\alpha}}}{[R+1/2]}$$

$$\mp \frac{\left[1 - e^{-j[R-(1/2)]\omega_c T}\right] e^{-j(\omega_c T/2) - j\bar{\alpha}}}{[R-1/2]} \tag{C.13}$$

and

$$H_{7,8} = \frac{G_s\, e^{j\frac{\omega_c}{2}T + j\bar{\alpha}}}{\left[j\left(R + \frac{1}{2}\right)\right]^2} \mp \frac{G_d\, e^{-j\frac{\omega_c}{2}T - j\bar{\alpha}}}{\left[j\left(R - \frac{1}{2}\right)\right]^2}\ . \tag{C.14}$$

The first and second suffixes correspond to the upper and lower signs respectively. The functions denoted by F, G and H are defined in Appendix A and R is given by Eq. 2.23.

APPENDIX D. REDUCTION OF NOISE TRANSPORT COEFFICIENTS TO VAN DUZER'S COEFFICIENTS

Equations 2.25 and 2.34 represent the matrix coefficients given by Eq. 2.24. These coefficients are useful in evaluating the noise transport in crossed-field devices and the choice of one form or the other depends upon the selection of one of the two velocity components provided the small-signal assumption is not violated. It was noted in Section 2.1 that Van Duzer[11] has also derived similar coefficients in terms of $\dot{y}$ for the Kino gun model and the use of these coefficients is restricted to the gun region only. Furthermore, Van Duzer does not consider the contributions from the z-component of the a-c current density. For an open-circuited diode some of Van Duzer's coefficients do not show any dependence upon the signal frequency, while the other coefficients vary either proportionally or inversely proportionally to the signal frequency. Van Duzer's coefficients do include one phase term given by $\exp\text{-}j(\omega/\omega_c)\theta$ and this is why only the magnitudes of these coefficients will be considered.

In this appendix it is shown that the set of Van Duzer's coefficients for an open-circuited diode is a special case of the corresponding set given by Eqs. 2.34 when the Kino gun[15] model is considered and ω is assumed negligible. Since Van Duzer's coefficients involve $\dot{y}$ in the denominator, the coefficients given by Eqs. 2.34 are considered only for this illustration. For this purpose Van Duzer's matrix relation for the open-circuited diode is rewritten as

$$\begin{bmatrix} \dot{y}_b \\ q_{y_b} \\ \dot{z}_b \end{bmatrix} = \begin{bmatrix} \bar{A}_{22} & \bar{A}_{23} & \bar{A}_{24} \\ \bar{A}_{32} & \bar{A}_{33} & \bar{A}_{34} \\ \bar{A}_{42} & \bar{A}_{43} & \bar{A}_{44} \end{bmatrix} \begin{bmatrix} \dot{y}_a \\ q_{y_a} \\ \bar{z}_a \end{bmatrix} . \tag{D.1}$$

Van Duzer's coordinate configuration is altered to correspond to that shown in Fig. 2.1 and the coefficients in Eq. D.1 are written in capital letters to distinguish them from the coefficients given by Eqs. 2.25 and 2.34. By considering only three variables given in Eq. D.1, Eq. 2.24 is written in a reduced form as

$$\begin{bmatrix} \dot{y}_b \\ q_{y_b} \\ \dot{z}_b \end{bmatrix} = \begin{bmatrix} a'_{55} & a'_{53} & a'_{54} \\ a'_{35} & a'_{33} & a'_{34} \\ a'_{45} & a'_{43} & a'_{44} \end{bmatrix} \begin{bmatrix} \dot{y}_a \\ q_{y_a} \\ \dot{z}_a \end{bmatrix} . \tag{D.2}$$

In order to show the reduction of the coefficients given by Eq. D.2 to those given by Eq. D.1 for $\omega \to 0$ and the Kino gun model, the functions W_1, W_2, W_3 and W_4 given by Eqs. 2.26 are considered. These functions reduce to the following for the case of $\omega = 0$:

$$W_1\Big|_{\omega=0} = -\frac{1 - \cos\theta}{j} , \tag{D.3a}$$

$$W_2\Big|_{\omega=0} = 0 , \tag{D.3b}$$

$$W_3\Big|_{\omega=0} = \frac{\sin\theta}{j} \tag{D.3c}$$

and

$$W_4\Big|_{\omega=0} = -\sin\theta . \tag{D.3d}$$

The following equations are also obtained for $\omega = 0$:

$$-\left.\frac{F_2}{2}\right|_{\omega=0} = \cos\theta - 1 \tag{D.4a}$$

and

$$\left(j\frac{F_4}{2} + \frac{F_5}{2}\right)_{\omega=0} = j\theta \quad , \tag{D.4b}$$

where

$$\theta = \omega_c T \tag{D.5}$$

and F functions are defined in Appendix A.

By using Eqs. D.3 through D.5, the coefficients given by Eq. D.2 reduce to the case of $\omega = 0$ as

$$a'_{55} = -\frac{y}{\omega_c \dot{y}}\sin\theta + \cos\theta \quad , \tag{D.6a}$$

$$a'_{53} = \frac{e}{jm\epsilon_o R\omega_c^2}\left[(1 - \cos\theta)\frac{y}{\omega_c \dot{y}} - \sin\theta\right] \quad , \tag{D.6b}$$

$$a'_{54} = (1 - \cos\theta)\frac{y}{\omega_c \dot{y}} - \sin\theta \quad , \tag{D.6c}$$

$$a'_{35} = j\frac{m\epsilon_o}{e}R\omega_c^2\left(1 + \frac{y}{\omega_c^2 \dot{y}}\right)\sin\theta \quad , \tag{D.6d}$$

$$a'_{33} = \frac{y}{\omega_c^2 \dot{y}}(\cos\theta - 1) + \cos\theta \quad , \tag{D.6e}$$

$$a'_{34} = j \frac{m\epsilon_o}{e} R\omega_c^2 \left(1 + \frac{\ddot{y}}{\omega_c^2 \dot{y}}\right) (\cos\theta - 1) \quad , \tag{D.6f}$$

$$a'_{45} = 0 \quad , \tag{D.6g}$$

$$a'_{43} = 0 \tag{D.6h}$$

and

$$a'_{44} = 1 \quad , \tag{D.6i}$$

where the equation

$$\ddot{z} = \omega_c \dot{y} \quad , \tag{D.7}$$

which is used in the Kino gun model, has been used in obtaining Eqs. D.6. It has been mentioned above that Van Duzer's coefficients include one phase term given by $\exp[-j(\omega/\omega_c)\theta]$. This phase term reduces to unity for $\omega \to 0$ and under these conditions the magnitudes of the coefficients given by Eqs. D.6 are the same as those of Van Duzer's corresponding coefficients defined by the matrix relation D.1. It was noted in Section 2.1 that for the case of an open-circuited diode, the coefficients given by Eqs. 2.25 and 2.35 correspond to those for a general case and this is why the reduction of the primed coefficients to the corresponding Van Duzer's coefficients is discussed only for the case of an open-circuited diode.

APPENDIX E. DERIVATION OF EXPRESSIONS FOR E_{z_1} AND E_{y_1}

In order to derive the a-c voltage induced at the b-plane as a result of the a-c fluctuations it is necessary to know the a-c expressions for E_{z_1} and E_{y_1} and then the a-c voltage is determined by the relation

$$\int_0^T dV = -\int_0^T \left[E_{z_1} \dot{z}\, dT + E_{y_1} \dot{y}\, dT \right] , \tag{E.1}$$

where T refers to the transit time between the a and b planes. From the a-c parts of the equations of motion E_{z_1} and E_{y_1} are given by

$$- \eta E_{y_1} = \ddot{y}_1 + \omega_c \dot{z}_1 \tag{E.2}$$

and

$$- \eta E_{z_1} = \ddot{z}_1 - \omega_c \dot{y}_1 \quad . \tag{E.3}$$

For determining $\ddot{y}_1$, $\ddot{z}_1$, $\dot{z}_1$ and $\dot{y}_1$ a perturbation δ_z given by Eq. 2.20 (or δ_y given by Eq. 2.31) is introduced in the expressions for $\ddot{y}$, $\ddot{z}$, $\dot{y}$ and $\dot{z}$ and the a-c terms are grouped together to give

$$- \eta E_{y_b} = E_1 \tilde{I} + E_2 \tilde{q}_{z_a} + E_3 \tilde{q}_{y_a} + E_4 \dot{z}_a + E_5 \dot{y}_a \tag{E.4}$$

and

$$- \eta E_{z_b} = E_6 \tilde{I} + E_7 \tilde{q}_{z_a} + E_8 \tilde{q}_{y_a} + E_9 \dot{z}_a + E_{10} \dot{y}_a \quad . \tag{E.5}$$

Suffix 1 has been omitted in Eqs. E.4 and E.5 for the sake of convenience and the various E coefficients are given by

$$E_1 = \frac{\bar{y}+\omega_c\bar{z}}{\omega_c^3\bar{z}}\left(H_1 - H_3 - \frac{\omega_c^2T^2}{2jR}e^{-jR\omega_cT}\sin\bar{\alpha}\right) - \frac{H_6+H_7}{2j\omega_c}$$

$$+\frac{F_3+F_4-jF_5-jF_6}{2\omega_c}\left(1+\frac{1}{2R}\right)e^{j\bar{\alpha}} - \frac{F_3-F_4+jF_5-jF_6}{2\omega_c}\left(1-\frac{1}{2R}\right)e^{-j\bar{\alpha}}$$

$$+\frac{\cos\bar{\alpha}+\omega_cT\sin\bar{\alpha}}{jR\omega_c}e^{-jR\omega_cT}, \quad (E.6)$$

$$E_2 = \left[-\frac{\bar{y}+\omega_c\bar{z}}{\omega_c^2\bar{z}}F_1 + \frac{F_4}{2j} - W_3\right]\frac{1}{R\omega_c}, \quad (E.7)$$

$$E_3 = \left[\frac{\bar{y}+\omega_c\bar{z}}{\omega_c^2\bar{z}}\frac{F_2}{2j} - W_2 - \frac{e^{-jR\omega_cT}}{j}\right]\frac{1}{R\omega_c}, \quad (E.8)$$

$$E_4 = \left[\frac{\bar{y}+\omega_c\bar{z}}{\omega_c^2\bar{z}}W_4 + \frac{W_2}{j}\right]\omega_c, \quad (E.9)$$

$$E_5 = \left[-\frac{\bar{y}+\omega_c\bar{z}}{\omega_c^2\bar{z}}\frac{W_1}{j} - \frac{F_4}{2} - \frac{W_3}{j}\right]\omega_c, \quad (E.10)$$

$$E_6 = \frac{\ddot{z}-\omega_c\dot{y}}{\omega_c^3\dot{z}}\left(H_1 - H_3 - \frac{\omega_c^2T^2}{2jR}e^{-jR\omega_cT}\sin\bar{\alpha}\right) + \frac{H_5+H_8}{2\omega_c}$$

$$+ \frac{F_3+F_4-jF_5-jF_6}{2j\omega_c}\left(1+\frac{1}{2R}\right)e^{j\bar{\alpha}} + \frac{F_3-F_4+jF_5-jF_6}{2j\omega_c}\left(1-\frac{1}{2R}\right)e^{-j\bar{\alpha}}$$

$$- \frac{\omega_cT\cos\bar{\alpha} - \sin\bar{\alpha}}{jR\omega_c}e^{-jR\omega_cT} , \qquad (E.11)$$

$$E_7 = -\left[\frac{\ddot{z}-\omega_c\dot{y}}{\omega_c^2\dot{z}}W_1 + W_2 + \frac{e^{-jR\omega_cT}}{j}\right]\frac{1}{R\omega_c} , \qquad (E.12)$$

$$E_8 = \left[\frac{\ddot{z}-\omega_c\ddot{y}}{\omega_c^2\dot{z}}\frac{F_2}{2j} - \frac{F_4}{2j} + W_3\right]\frac{1}{R\omega_c} , \qquad (E.13)$$

$$E_9 = \left[\frac{\ddot{z}-\omega_c\dot{y}}{\omega_c^2\dot{z}}W_4 - \frac{F_4}{2} - \frac{W_3}{j}\right]\omega_c \qquad (E.14)$$

and

$$E_{10} = j\left[\frac{\ddot{z}-\omega_c\ddot{y}}{\omega_c^2\dot{z}}W_1 + W_2\right]\omega_c . \qquad (E.15)$$

The sinusoidal variations as exp $j\omega t$ are understood. The expressions for E_{y_b} and E_{z_b} in terms of $\dot{y}$ are given by

$$-\eta E_{y_b} = E_1'\tilde{I} + E_2'\tilde{q}_{z_a} + E_3'\tilde{q}_{y_a} + E_4'\dot{z}_a + E_5'\dot{y}_a \qquad (E.16)$$

and

$$- \eta E_{z_b} = E'_6 \tilde{I} + E'_7 q_{z_a} + E'_8 \tilde{q}_{y_a} + E'_9 \dot{z}_a + E'_{10} \dot{y}_a \quad , \tag{E.17}$$

where

$$E'_1 = \frac{\ddot{y}+\omega_c \ddot{z}}{\omega_c^3 \dot{y}} \left[j(H_2 - H_4) - \frac{\omega_c^2 T^2}{2jR} e^{-jR\omega_c T} \cos \bar{\alpha} \right] - \frac{H_6 + H_7}{2j\omega_c}$$

$$+ \frac{F_3 + F_4 - jF_5 - jF_6}{2\omega_c} \left(1 + \frac{1}{2R}\right) e^{j\bar{\alpha}} - \frac{F_3 - F_4 + jF_5 - jF_6}{2\omega_c} \left(1 - \frac{1}{2R}\right) e^{-j\bar{\alpha}}$$

$$+ \frac{\cos \bar{\alpha} + \omega_c T \sin \bar{\alpha}}{jR\omega_c} e^{-jR\omega_c T} \quad , \tag{E.18}$$

$$E'_2 = \left[- \frac{\ddot{y}+\omega_c \ddot{z}}{\omega_c^2 \dot{y}} \frac{F_2}{2} + \frac{F_4}{2j} - W_3 \right] \frac{1}{R\omega_c} \quad , \tag{E.19}$$

$$E'_3 = \left[- \frac{\ddot{y}+\omega_c \ddot{z}}{\omega_c^2 \dot{y}} W_1 - W_2 - \frac{e^{-jR\omega_c T}}{j} \right] \frac{1}{R\omega_c} \quad , \tag{E.20}$$

$$E'_4 = - j \left[\frac{\ddot{y}+\omega_c \ddot{z}}{\omega_c^2 \dot{y}} W_1 + W_2 \right] \omega_c \quad , \tag{E.21}$$

$$E'_5 = \left[\frac{\ddot{y}+\omega_c \ddot{z}}{\omega_c^2 \dot{y}} W_4 - \frac{F_4}{2} - \frac{W_3}{j} \right] \omega_c \quad , \tag{E.22}$$

$$E'_6 = \frac{\dddot{z}-\omega_c\ddot{y}}{\omega_c^3\dot{y}}\left[j(H_2-H_4) - \frac{\omega_c^2T^2}{2jR}\cos\bar{\alpha}\right] + \frac{H_5+H_8}{2\omega_c}$$

$$+ \frac{F_3-F_4-jF_5-jF_6}{2j\omega_c}\left(1+\frac{1}{2R}\right)e^{j\bar{\alpha}} + \frac{F_3-F_4+jF_5-jF_6}{2j\omega_c}\left(1-\frac{1}{2R}\right)e^{-j\bar{\alpha}}$$

$$- \frac{\omega_c T\cos\bar{\alpha} - \sin\bar{\alpha}}{jR\omega_c}e^{-jR\omega_c T} \quad , \qquad (E.23)$$

$$E'_7 = -\left[\frac{\dddot{z}-\omega_c\ddot{y}}{\omega_c^2\dot{y}}\,\frac{F_2}{2j} + W_2 + \frac{e^{-jR\omega_c T}}{j}\right]\frac{1}{R\omega_c} \quad , \qquad (E.24)$$

$$E'_8 = \left[-\frac{\dddot{z}-\omega_c\ddot{y}}{\omega_c^2\dot{y}}\,W_1 - \frac{F_4}{2j} + W_3\right]\frac{1}{R\omega_c} \quad , \qquad (E.25)$$

$$E'_9 = \left[\frac{\dddot{z}-\omega_c\ddot{y}}{\omega_c^2\dot{y}}\,\frac{W_1}{j} - \frac{F_4}{2} - \frac{W_3}{j}\right]\omega_c \qquad (E.26)$$

and

$$E'_{10} = \left[\frac{\dddot{z}-\omega_c\ddot{y}}{\omega_c^2\dot{y}}\,W_4 - \frac{W_2}{j}\right]\omega_c \quad . \qquad (E.27)$$

The F functions have been defined in Appendix A; H functions have been defined in Appendix C; W functions have been defined by Eqs. 2.26; and R is defined by Eq. 2.23. The functions $\dddot{y}$, $\dddot{z}$, $\ddot{y}$, $\ddot{z}$, $\dot{y}$ and $\dot{z}$ refer to

the d-c quantities and their selection depends upon the physical model under consideration.

The equivalence between the primed and the unprimed E coefficients is evident when $\dot{z}' = \dot{y}' = \ddot{z}' = \ddot{y}' = 0$ for the ideal conditions in the interaction region. This is similar to the equivalence between the primed and the unprimed noise transport coefficients. Again, as in the case of the noise transport coefficients for the case of an open-circuited diode when $I = 0$, these E coefficients can be used for any physical model and the expressions for $\dot{z}'$, $\dot{y}'$, $\ddot{z}'$, $\ddot{y}'$, $\dot{z}$ and $\dot{y}$ are used accordingly. In general, as in the case of the noise transport coefficients, the unprimed E coefficients are more useful than the primed coefficients.

APPENDIX F. DERIVATION OF THE THREE-DIMENSIONAL SPACE-CHARGE POTENTIAL

In Section 6.7 it was pointed out that the Monte Carlo technique for evaluating the noise transport takes into account the actual electron distribution in the diode. For calculating the trajectories and velocities of the several electrons distributed in the diode, it is necessary to develop expressions for the space-charge voltage and fields in terms of the number of electrons, which depend upon the y-z coordinates of the various electrons and the test point under consideration.

In Section 7.2 the division of the diode into a finite number of rectangles is described and the various electrons in each rectangle are assumed to be concentrated at the center point of the rectangle. First the space-charge potential due to a charge q at a point (x_j, y_j, z_j) is determined and then superposition is used to determine the potential at a point (x,y,z) due to all the electrons distributed in the diode. It was noted in Section 6.7 that the expression for space-charge potential using the Green's function was also derived by Gandhi and Rowe[31] and has been modified to suit the requirements for this problem. The Poisson's equation for a single charge q at a point (x_j, y_j, z_j) is given by

$$\nabla^2 V = -\frac{q}{\epsilon_o}\,\delta(x-x_j)\,\delta(y-y_j)\,\delta(z-z_j) \quad . \tag{F.1}$$

This charge is located in the elementary block of volume $h\,dy_j dz_j$ shown in Fig. F.1. With the boundary conditions

$$V = 0 \quad \text{for} \quad x = 0 \;,\; x = a \tag{F.2}$$

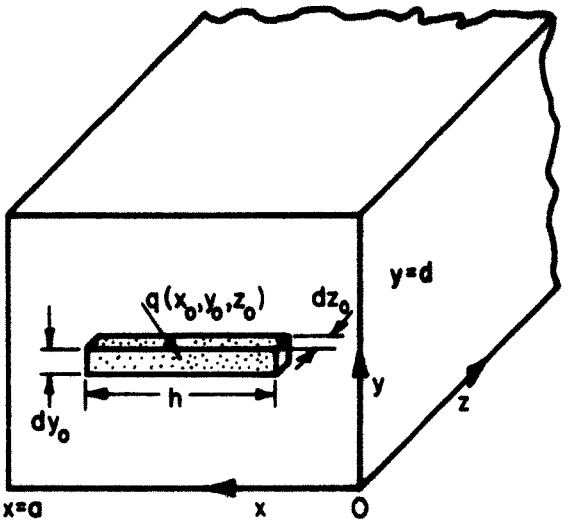

FIG. F.1 SPACE-CHARGE DISTRIBUTION IN AN ELEMENTARY BOX OF VOLUME h dy_o dz_o.

and

$$V = 0 \quad \text{for} \quad y = 0 \ , y = d \ , \tag{F.3}$$

and by using the method of separation of variables for the homogeneous part of Eq. F.1, V is given by

$$V = \sum_{m,n} \sin \frac{m\pi y}{d} \sin \frac{n\pi x}{a} Z(z) \ , \tag{F.4}$$

where Z(z) is a function of z coordinate only and includes the arbitrary constant. By substituting for V from Eq. F.4 in Eq. F.1, multiplying the resulting equation by $\sin(m\pi y/d) \cdot \sin(n\pi x/a)$ on both sides and integrating with respect to x and y within the limits

$$0 \leq x \leq a$$

and

$$0 \leq y \leq d \ , \tag{F.5}$$

the following is obtained:

$$\left[\frac{d^2}{dz^2} - \left(\frac{m\pi}{d}\right)^2 - \left(\frac{n\pi}{a}\right)^2 \right] \frac{ad}{4} Z(z) = - \frac{q}{\epsilon_o} \sin \frac{m\pi y_j}{d} \sin \frac{n\pi x_j}{a} \delta(z-z_j) \ . \tag{F.6}$$

Equation F.6 can be solved by a one-dimensional Green's function to give

$$V = \frac{2q}{\pi\epsilon_o} \sum_m \sum_n (m^2a^2+n^2d^2)^{-1/2} \sin \frac{m\pi y_j}{d} \sin \frac{n\pi x_j}{a} \sin \frac{m\pi y}{d} \sin \frac{n\pi x}{a} \cdot e^{-\frac{\pi}{ad}(m^2a^2+n^2d^2)^{1/2} |z-z_j|} \ . \tag{F.7}$$

By substituting for q, as

$$q = \rho_o \, dx_j \, dy_j \, dz_j \quad , \tag{F.8}$$

and assuming that ρ_o is not a function of x_j, Eq. F.7 can be integrated with respect to x_j within the limits a-h/2, a+h/2. Then substituting for ρ_o as

$$\rho_o = - \frac{|e| \, N_j}{h \, dy_j \, dz_j} \tag{F.9}$$

the expression for space-charge potential is given by

$$V_{sc}\left(\frac{a}{2},y,z\right) = - \frac{4|e|}{h\pi\epsilon_o} \sum_j \sum_m \sum_n (m^2a^2+n^2d^2)^{-1/2} \frac{a}{n\pi} \sin \frac{m\pi y_j}{d} \sin \frac{m\pi y}{d}$$

$$\cdot \sin^2 \frac{n\pi}{2} \sin \frac{n\pi h}{2a} \, e^{-\frac{\pi}{ad}(m^2a^2+n^2d^2)^{-1/2} |z-z_j|} \, N_j \quad , \tag{F.10}$$

where x = a/2 is substituted and summation over j is made to include all the rectangles, N_j referring to the number of electrons in the jth rectangle. For crossed-field devices $(d/a) \ll 1$ and the approximations

$$(m^2a^2+n^2)^{-1/2} \frac{1}{n} \simeq \frac{1}{mna} \tag{F.11}$$

and

$$(m^2a^2+n^2d^2)^{1/2} \simeq m_a + n_d \tag{F.12}$$

may be made with reasonable accuracy. The errors involved in these approximations have been discussed by Gandhi and Rowe and a reasonable compromise between the computer time and the accuracy can be achieved. The summation over m and n can be made by using different forms of the following equation:

$$\sum_{n=1}^{\infty} \lambda^n e^{j\alpha n} = \frac{\lambda e^{j\alpha}}{1-\lambda e^{j\alpha}} \tag{F.13}$$

for $\lambda < 1$ and α real to give

$$V_{sc}\left(\frac{a}{2},y,z\right) = -\frac{|e|}{h\pi^2\epsilon_o}\sum_j \ln\frac{1+e^{-\frac{2\pi}{d}|z-z_j|}-2\,e^{-\frac{\pi}{d}|z-z_j|}\cos\frac{\pi}{d}(y+y_j)}{1+e^{-\frac{2\pi}{d}|z-z_j|}-2\,e^{-\frac{\pi}{d}|z-z_j|}\cos\frac{\pi}{d}(y-y_j)}$$

$$\cdot W_{sc}\,N_j \quad , \quad (F.14)$$

where W_{sc} is defined by Eq. 6.25.

For derivation of the space-charge fields, the expressions for $E_{y_{sc}}$ and $E_{z_{sc}}$ are written directly from Eq. F.10 to give

$$E_{z_{sc}} = \mp\frac{4|e|}{hd\epsilon_o}\sum_j\sum_m\sum_n \frac{1}{n\pi}\sin\frac{m\pi y_j}{d}\sin\frac{m\pi y}{d}\sin^2\frac{n\pi}{2}\sin\frac{n\pi h}{2a}$$

$$\cdot e^{-\frac{\pi}{ad}(m^2a^2+n^2d^2)^{1/2}|z-z_j|}\,N_j \qquad (F.15)$$

and

$$E_{y_{sc}} = \frac{4|e|}{h\pi\epsilon_o}\sum_j\sum_m\sum_n (m^2a^2+n^2d^2)^{-1/2}\frac{ma}{nd}\sin\frac{m\pi y_j}{d}\cos\frac{m\pi y}{d}\sin^2\frac{n\pi}{2}$$

$$\cdot\sin\frac{n\pi h}{2a}\,e^{-\frac{\pi}{ad}(m^2a^2+n^2d^2)^{1/2}|z-z_j|}\,N_j \quad , \quad (F.16)$$

where the minus and plus signs in Eq. F.15 correspond to the conditions of $z > z_j$ and $z < z_j$ respectively.

Summation over m and n is made as above to give

$$E_{z_{sc}} = \sum_j E_{z_{sc-j}} N_j$$

and

$$E_{y_{sc}} = \sum_j E_{y_{sc-j}} N_j \quad ,$$

where the expressions for $E_{y_{sc-j}}$ and $E_{z_{sc-j}}$ are given by Eqs. 6.26 and 6.27 respectively.

APPENDIX G. AVERAGING METHODS FOR VELOCITY AND CURRENT-DENSITY COMPONENTS

In Section 6.9, expressions for the a-c fields are developed in terms of the instantaneous and average velocity components corresponding to the ith rectangle. The expressions for the a-c current density components are also derived in terms of the instantaneous and average current-density components corresponding to the ith rectangle. It was shown in this section that for a one-dimensional case for O-type devices the current density can easily be computed in terms of the number of electrons crossing a plane per unit time and per unit area. This technique cannot easily be applied for a two-dimensional case when the electrons move along the y- and z-axes. For this purpose the current density and velocity components are taken as

$$J_y = \rho_o \dot{y}$$

and

$$J_z = \rho_o \dot{z} \quad . \tag{G.1}$$

This involves computation of only three variables, namely J_y, J_z and ρ_o or $\dot{y}$, $\dot{z}$ and ρ_o. Thus the computation time and the size of the memory required for the Monte Carlo analysis can be reduced considerably. Even though this numerical evaluation does involve some correlation between the velocity and the current-density components, it is far better than using any other rather complicated process which may also involve a considerable amount of computer time and the size of the memory required. The instantaneous values of $\dot{y}$, $\dot{z}$ and ρ_o are defined as

$$\dot{y}_i(t_i) = \frac{1}{N_i(t_i)} \sum_{n_k} \dot{y}_i(t_i,n_k) \quad , \tag{G.2}$$

$$\dot{z}_i(t_i) = \frac{1}{N_i(t_i)} \sum_{n_k} \dot{z}_i(t_i,n_k) \tag{G.3}$$

and

$$\rho_i(t_i) = -\frac{|e|}{h\ dy_i\ dz_i} N_i(t_i) \quad , \tag{G.4}$$

where the various terms have been defined in Section 6.9. It is also mentioned in Section 6.10 that these instantaneous values represent the average values averaged over a time interval Δt between time t_i and $t_i + \Delta t$. By using Eqs. G.1 through G.4, the instantaneous current-density components are given by

$$J_{y_i}(t_i) = -\frac{|e|}{h\ dy_i\ dz_i} \sum_{n_k} \dot{y}_i(t_i,n_k) \tag{G.5}$$

and

$$J_{z_i}(t_i) = -\frac{|e|}{h\ dy_i\ dz_i} \sum_{n_k} \dot{z}_i(t_i,n_k) \quad . \tag{G.6}$$

The following two cases are based upon different definitions of the averaging processes for evaluating the d-c and a-c velocity and current-density components.

<u>Case A</u>. For this case define

$$\left(\dot{y}_o\right)_i = \frac{1}{L} \sum_{t_i} \frac{1}{N_i(t_i)} \sum_{n_k} \dot{y}_i(t_i,n_k) \quad , \tag{G.7}$$

$$\left(\dot{z}_o\right)_i = \frac{1}{L} \sum_{t_i} \frac{1}{N_i(t_i)} \sum_{n_k} \dot{z}_i(t_i,n_k) \tag{G.8}$$

and

$$(\rho_o)_i = - \frac{|e|}{L\ h\ dy_i\ dz_i} \sum_{t_i} N_i(t_i)$$

$$= - \frac{|e|(N_o)_i}{h\ dy_i\ dz_i} \quad . \tag{G.9}$$

From Eqs. G.1 and G.7 through G.9, the following equations are obtained:

$$\left(J_{y_o}\right)_i = (\rho_o)_i\ (\dot{y}_o)_i$$

$$= - \frac{|e|(N_o)_i}{L\ h\ dy_i\ dz_i} \left[\sum_{t_i} \frac{1}{N_i(t_i)} \sum_{n_k} \dot{y}_i(t_i,n_k) \right] \tag{G.10}$$

and

$$\left(J_{z_o}\right)_i = (\rho_o)_i\ (\dot{z}_o)_i$$

$$= - \frac{|e|(N_o)_i}{L\ h\ dy_i\ dz_i} \left[\sum_{t_i} \frac{1}{N_i(t_i)} \sum_{n_k} \dot{z}_i(t_i,n_k) \right] . \tag{G.11}$$

The a-c variables are then defined by the following equations (using Eqs. G.2 through G.11):

$$\tilde{\dot{y}}_i(t_i) = \frac{1}{N_i(t_i)} \sum_{n_k} \dot{y}_i(t_i,n_k) - \frac{1}{L} \sum_{t_i} \frac{1}{N_i(t_i)} \sum_{n_k} \dot{y}_i(t_i,n_k) \quad , \quad (G.12)$$

$$\tilde{\dot{z}}_i(t_i) = \frac{1}{N_i(t_i)} \sum_{n_k} \dot{z}_i(t_i,n_k) - \frac{1}{L} \sum_{t_i} \frac{1}{N_i(t_i)} \sum_{n_k} \dot{z}_i(t_i,n_k) \quad , \quad (G.13)$$

$$\tilde{J}_{y_i}(t_i) = - \frac{|e|}{h\ dy_i\ dz_i} \left[\frac{(N_o)_i}{N_i(t_i)} \sum_{n_k} \dot{y}_i(t_i,n_k) - \frac{(N_o)_i}{L} \sum_{t_i} \frac{1}{N_i(t_i)} \sum_{n_k} \dot{y}_i(t_i,n_k) \right] \quad (G.14)$$

and

$$\tilde{J}_{z_i}(t_i) = - \frac{|e|}{h\ dy_i\ dz_i} \left[\frac{(N_o)_i}{N_i(t_i)} \sum_{n_k} \dot{z}_i(t_i,n_k) - \frac{(N_o)_i}{L} \sum_{t_i} \frac{1}{N_i(t_i)} \sum_{n_k} \dot{z}_i(t_i,n_k) \right] \quad , \quad (G.15)$$

where the weighting functions $(N_o)_i/N_i(t_i)$ in the expressions for $J_{y_i}(t_i)$ and $J_{z_i}(t_i)$ are introduced so that the average values of $\tilde{J}_{y_i}(t_i)$ and $\tilde{J}_{z_i}(t_i)$ averaged over L unit intervals of time tend to be of zero value.

Case B. For this case define

$$(\dot{y}_o)_i = \frac{1}{(N_o)_i L} \sum_{t_i} \sum_{n_i} \dot{y}_i(t_i,n_k) \quad , \tag{G.16}$$

$$(\dot{z}_o)_i = \frac{1}{(N_o)_i L} \sum_{t_i} \sum_{n_k} \dot{z}_i(t_i,n_k) \tag{G.17}$$

and

$$(\rho_o)_i = - \frac{|e|}{L\ h\ dy_i\ dz_i} \sum_{t_i} N_i(t_i) \quad . \tag{G.18}$$

From Eqs. G.1 and G.16 through G.18 the following equations are obtained:

$$\left(J_{z_o}\right)_i = (\rho_o)_i\ (\dot{y}_o)_i = - \frac{|e|}{L\ h\ dy_i\ dz_i} \sum_{t_i} \sum_{n_k} \dot{y}_i(t_i,n_k) \tag{G.19}$$

and

$$\left(J_{z_o}\right)_i = (\rho_o)_i\ (\dot{y}_o)_i = - \frac{|e|}{L\ h\ dy_i\ dz_i} \sum_{t_i} \sum_{n_k} \dot{z}_i(t_i,n_k) \quad . \tag{G.20}$$

The a-c variables are then defined by the following equations:

$$\tilde{\dot{y}}_i(t_i) = \frac{N_i(t_i)}{(N_o)_i} \left[\frac{1}{N_i(t_i)} \sum_{n_k} \dot{y}_i(t_i,n_k) - \frac{1}{(N_o)_i L} \sum_{t_i} \sum_{n_k} \dot{y}_i(t_i,n_k) \right] , \tag{G.21}$$

$$\tilde{\dot{z}}_i(t_i) = \frac{N_i(t_i)}{(N_o)_i} \left[\frac{1}{N_i(t_i)} \sum_{n_k} \dot{z}_i(t_i,n_k) - \frac{1}{(N_o)_i L} \sum_{t_i} \sum_{n_k} \dot{z}_i(t_i,n_k) \right] , \tag{G.22}$$

$$\tilde{J}_{y_i}(t_i) = -\frac{|e|}{h\, dy_i\, dz_i}\left[\sum_{n_k} \dot{y}_i(t_i,n_k) - \frac{1}{L}\sum_{t_i}\sum_{n_k} \dot{y}_i(t_i,n_k)\right] \quad (G.23)$$

and

$$\tilde{J}_{z_i}(t_i) = -\frac{|e|}{h\, dy_i\, dz_i}\left[\sum_{n_k} \dot{z}_i(t_i,n_k) - \frac{1}{L}\sum_{t_i}\sum_{n_k} \dot{z}_i(t_i,n_k)\right] , \quad (G.24)$$

where the weighting functions $N_i(t_i)/(N_o)_i$ in the expressions for $\tilde{\dot{y}}_i(t_i)$ and $\tilde{\dot{z}}_i(t_i)$ are introduced so that the average values of $\tilde{\dot{y}}_i(t_i)$ and $\tilde{\dot{z}}_i(t_i)$ averaged over L unit intervals of time tend to be of zero value.

Thus the basic difference between the two cases is the manner in which the velocity components are defined. In both cases it becomes necessary to introduce weighting functions either with the instantaneous current-density components or velocity components for the reasons given above. The use of the weighting function in the two cases discussed above can be avoided by using a method for averaging based upon a combination of the two cases. This involves more computing time and the size of the memory required is also increased. The selection of Case A or Case B depends upon how the various parameters are computed and the consideration for computer time and the memory size required. For Case A, it can be seen from Eqs. G.7 and G.8 that two extra divisions are necessary for each unit interval of time, while for Case B only two additional divisions are required. Since $(N_o)_i$ has to be computed for evaluating $(\rho_o)_i$, selection for Case B has been made for the present analysis.

The above two cases are discussed when the number of electrons and the velocity components for the ith rectangle are to be determined. Similarly the two cases can be discussed when the number of electrons and current-density components are to be determined; the velocity components being determined from the current-density components. Essentially, the two techniques are identical and the selection of one or the other is arbitrary.

APPENDIX H. DERIVATION FOR THE FINAL POWER SPECTRUM FOR FINITE DISCRETE DATA

An expression for final power spectrum is given by Eq. 7.6 in Section 7.2.2. This expression is useful in considering the numerical value of the unit time interval. A detailed derivation of this expression is given by Dayem and Lambert[22] and a brief summary is given here for the sake of continuity.

The power spectrum $P_y(f)$ for the auto-correlation function $C(\tau)$ for a discrete data is given by

$$\tilde{P}_y(f) = \int_{-\infty}^{\infty} \Delta t \sum_{n=-\infty}^{\infty} \delta\,(\tau - n\Delta t)\; C(\tau)\; e^{-j\omega\tau}\, d\tau \quad , \qquad \text{(H.1)}$$

where $\delta\,(\tau - n\Delta t)$ is the Dirac delta function. The right-hand side of Eq. H.1 can be written in the form of a convolution integral of the Fourier transforms P_y and $\sum_{-\infty}^{\infty} \delta(f - n/\Delta t)$ of $C(\tau)$ and $\Delta t \sum_{n=-\infty}^{\infty} \delta(\tau - n\Delta t)$ respectively, by

$$\tilde{P}_y(f) = \int_{-\infty}^{\infty} \sum_{n=-\infty}^{\infty} \delta(f - \nu - nf_o)\; P_y(\nu)\; d\nu$$

$$= P_y(f) + \sum_{n=1}^{\infty} \left[P_y(f - nf_o) + P_y(f + nf_o) \right] \quad . \qquad \text{(H.2)}$$

The part of $\tilde{P}_y(f)$ in the range $0 \leq f_o/2$ is known as the principal part and $\tilde{P}_y(f)$ is usually called the "aliased" spectrum[22] of the process because the power density at frequency $(f' \pm nf_o)$ in the true spectrum $P_y(f)$, where $n = 1, 2, \ldots \infty$ is aliased at f' in the principal part of

$\tilde{P}_y(f)$. It is obvious that the true spectrum $P_y(f)$ cannot be recovered from the aliased spectrum $\tilde{P}_y(f)$ unless the former vanished for $|f| > f_o/2$. It can be seen from Eq. 7.5 that, by considering the various variables such as the velocity and current density as average values averaged over the time interval Δt, the spectrum $P_y(f)$ attenuates for large values of f. Thus the effect of aliasing can be neglected if $f/f_o \ll 1$.

For the finite data, the notion of a lag window has been introduced in Section 6.10. The power spectrum P(f) of the modified auto-correlation function is given by

$$P(f) = \int_{-\infty}^{\infty} Q(f-\mu)\, \tilde{P}_y(\mu)\, d\mu \quad , \tag{H.3}$$

where $\tilde{P}_y(f)$ is the Fourier transform of $C(\tau)$ and is defined by Eq. H.1. By substituting for Q(f) from Eq. 6.63 the following is obtained:

$$P(f) = \frac{1}{2}\bar{P}_y(f) + \frac{1}{4}\bar{P}_y\left(f + \frac{1}{2T_m}\right) + \frac{1}{4}\bar{P}_y\left(f - \frac{1}{2T_m}\right) \quad , \tag{H.4}$$

where $\bar{P}_y(f)$ is given by Eq. H.3 when $Q_1(f)$ defined by Eq. 6.64 is substituted for Q(f). This corresponds to considering a lag window[22] defined Eq. 6.65. From Eq. H.4 it can be seen that the modification of the auto-correlation function $C(\tau)$ by the time function $D(\tau)$ is equivalent to a smoothing of the spectrum in accordance with the rule shown in Eq. H.4. It is also mentioned in Section 6.10 that because of the smoothing in the neighborhood of frequency f there are considerably overlapping frequency regions if $|f_2 - f_1| < 1/2T_m$. However if $|f_2 - f_1| = 1/T_m$, the overlap is small. Thus the parameter $1/T_m$ can be

considered to give resolution in cycles per second. Now by using Eqs. 7.5, H.2 and H.3, the following is obtained:

$$P(f) = Q(f)* \sum_{n=-\infty}^{\infty} \left(\frac{\sin \pi(f-nf_o)\,\Delta t}{\pi(f-nf_o)\,\Delta t} \right)^2 P_x(f-nf_o)$$

$$= Q(f)* \left[\left(\frac{\sin \pi f/f_o}{\pi f/f_o} \right)^2 \sum_{n=-\infty}^{\infty} \frac{P_x(f-nf_o)}{\left(\frac{nf_o}{f} - 1 \right)^2} \right] , \qquad (H.5)$$

where the sign * means convolution and $f_o = 1/\Delta t$. For $|f| = 0.1\ f_o$, Eq. H.5 is reduced to

$$P(f) = Q(f)* \left[P_x(0.1f_o) + \frac{P_x(0.9f_o)}{81} + \frac{P_x(1.1f_o)}{121} + \frac{P_x(1.9f_o)}{361} + \cdots \right] , \qquad (H.6)$$

where

$$\frac{\sin \frac{\pi f}{f_o}}{\pi f/f_o} \simeq 1 \quad \text{for} \quad f \leq 0.1\ f_o \qquad (H.7)$$

is assumed in Eq. H.6. For frequencies $f < 0.1\ f_o$ the denominators in Eq. H.6 would become even larger. Thus for our purposes when $f < 0.1\ f_o$

$$P(f) = Q(f)*\ P_x(f) \qquad (H.8)$$

is a very good approximation.

BIBLIOGRAPHY

1. Siegman, A. E., "Microwave Noise Fluctuations in the Potential Minimum Region of an Electron Beam", Tech. Report No. 401-1, Stanford Electronics Laboratory, Stanford University; April 22, 1957.

2. Watkins, D. A., "Noise at the Potential Minimum in the High Frequency Diode", Jour. Appl. Phys., vol. 26, pp. 622-624; May, 1955.

3. Siegman, A. E., and Bloom, S., "An Equivalent Circuit for Microwave Noise at the Potential Minimum", Trans. PGED-IRE, vol ED-4, pp. 295-299; October, 1957.

4. Whinnery, J. R., "Noise Phenomenon in the Region of the Potential Minimum", Trans. PGED-IRE, vol. ED-1, pp. 221-236; December, 1954.

5. Bloom, S., and Peter, R. W., "Transmission-Line Analogy of a Modulated Electron Beam", RCA Review, vol. 15, pp. 95-112; March, 1954.

6. Pierce, J. R., Traveling Wave Tubes, D. Van Nostrand, New York; 1950.

7. Sproul, R. L., "Excess Noise in Cavity Magnetrons", Jour. Appl. Phys., vol. 18, pp. 314-320; March, 1947.

8. Mayper, V., "Noise Generation in Pre-Oscillating Magnetrons", Quarterly Progress Report, M.I.T. Research Laboratory of Electronics; April 15, 1948.

9. Linder, E. G., "Effect of High Energy Electron Random Motion upon the Shape of the Magnetron Cutoff Curve", Jour. Appl. Phys., vol. 9, pp. 331-334; May, 1938.

10. Epsztein, B., "QK 603 Final Engineering Report on Research and Development of Crossed E-H Field Microwave Tubes", Raytheon Manufacturing Co., CSF Raytheon Contract No. 12; July, 1958.

11. Van Duzer, T., "Noise in Crossed-Field Beams", Series No. 60, Issue No. 280, Electronics Research Laboratory, The University of California, Berkeley; May 23, 1960.

12. Little, R. P., Rupel, H. M., and Smith, S. T., "Beam Noise in Crossed Electric and Magnetic Fields", Jour. Appl. Phys., vol. 29, p. 1376; September, 1958.

13. Miller, M. H., "Study of High Temperature Electrons Originating in Streams Flowing in Crossed D-c Electric and Magnetic Fields", Tech. Report No. 26, Electron Tube Laboratory, The University of Michigan; July, 1958.

14. Anderson, J. R., "Noise Measurements on an M-Type Backward-Wave Amplifier", Proc. IRE, vol. 48, No. 5, pp. 946-947; May, 1960.

15. Kino, G. S., "A New Type of Crossed-Field Gun", Trans. PGED-IRE vol. ED-7, pp. 179-185; July, 1960.

16. Gould, R. W., "Space-Charge Effects in Beam Type Magnetrons", Jour. Appl. Phys. vol. 28, pp. 594-604; May, 1957.

17. Llewellyn, F. B., Electron Inertia Effects, Cambridge University Press, New York; 1939.

18. Llewellyn, F. B., and Peterson, L. C., "Vacuum-Tube Networks", Proc. IRE, vol. 32, pp. 144-146; March, 1944.

19. Rando, J. F., and Whinnery, J. R., "Noise-Figure Measurements and Calculations", Fourth Quarterly Progress Report, Study of Crossed-Field Amplifiers, Electronics Research Laboratory, The University of California, Berkeley; February 28, 1961.

20. Twiss, R. Q., "On the Steady State and Noise Properties of Linear and Cylindrical Magnetrons", Sc.D Dissertation, Department of Electrical Engineering, Massachusetts Institute of Technology; January, 1949.

21. Tien, P. K., and Moshman, J., "Monte-Carlo Calculation of Noise Near the Potential Minimum of a High Frequency Diode", Jour. Appl. Phys., vol. 27, pp. 1067-1078; September, 1956.

22. Dayem, A. H., and Lambert, C. A., (Mrs.), "Noise Near the Potential Minimum of an Open Circuit Diode", Private Communication.

23. Blackman, R. B., and Tukey, J. W., "The Measurement of Power Spectra", Dover Publications Inc., New York; 1958.

24. Leblond, A. F., "Study of the Electron Trajectories in Guns for M-Type Tubes", Brit. Proc. Inst. Elec. Engrs., vol. 105, part B, Supplement No. 12, pp. 1021-1023; 1958.

25. Wadhwa, R. P., and Rowe, J. E., "Transmission-Line Analogy of Crossed-Field Beams", Tech. Rept. No. 57, Electron Physics Laboratory, The University of Michigan; December, 1962.

26. Rao, R. A., and Winnery, J. R., "Noise Identification and Reduction", Third Quarterly Progress Report, Study of Crossed-Field Amplifiers, Electronics Research Laboratory, The University of California, Berkeley; 1960.

27. Miller, M. H., and Dow, W. G., "Experimental Study of Anomalous Electron Stream Behavior", Jour. Appl. Phys., vol. 32, No. 2, pp. 274-281; February, 1961.

28. Arnaud, J., "Study of Noise in M-Type Carcinotrons Beam Instability Problem", CSF Rept. W. R. 734, CSF-Raytheon Contract No. 20, Quarterly Report; April-June, 1961.

29. Pollack, M., Private Communication.

30. Tien, P. K., and Field, L. M., "Space-Charge Waves in an Accelerated Electron Stream for Amplification of Microwave Signals", Proc. IRE, vol. 40, No. 6; June, 1952.

31. Gandhi, O. P., and Rowe, J. E., "Nonlinear Analysis of Crossed-Field Amplifiers", Nachrichtentechnische Fachberichte, vol. 22, pp. 135-144, Germany; 1961.

32. Smullin, L. D., and Haus, H. A., Noise in Electron Devices, John Wiley and Sons, Inc., New York, Chapter I, pp. 1-44; 1959.

33. _____, ibid, Chapter III, pp. 77-153.

34. Haeff, A. V. "The Electron Wave Tube, A Novel Method of Generation and Amplification of Microwave Energy", Proc. IRE, vol. 37, pp. 4-10; 1949.

35. Harris, D. J., "Microwave Amplification Using an Unstable Electron Beam in Crossed Electric and Magnetic Fields", Proc. Inst. Elec. Engrs., vol. 105, part B, Supplement No. 11, pp. 645-647; 1958.

36. Sato, T., "An Experimental Investigation of Crossed-Field Interaction", Tech. Report No. 385-5, Stanford Electronics Laboratories, Stanford University; February 8, 1960.

37. Rowe, J. E., and Martin, R. J., "An Electron-Trajectory Calculator and Its Component Poisson Cell", Proc. Inst. Elec. Engrs., vol. 105, part B, Supplement No. 12, pp. 1024-1032; 1958.

38. Nunn, Jr., W. M., and Paul, L. E., "A Broadband Glass-to-Metal Coaxial Vacuum Seal", Trans. PGMTT-IRE, vol. MTT-9, No. 3, pp. 248-251; May, 1961.

39. Slocum, K. W., Private Communication.

40. Dow, W. G., Fundamentals of Engineering Electronics, John Wiley and Sons, Inc., New York, pp. 503-506; 1952.

41. Wadhwa, R. P., "Multiple-Beam Crossed-Field Interaction", Tech. Rept. No. 56, Electron Physics Laboratory, The University of Michigan; December, 1962.

LIST OF SYMBOLS

A_1	Correction factor used in evaluating $\dot{y}_{i_c}$, value taken as $A_1 = 1.01$.
A_i	Effective beam cross-sectional area of the ith rectangle, m^2.
A_{ij}	Space-charge constant, volts. $(i = 0, 1..., i,..., j = 0, 1,... j,...)$
$A_{yx}(\tau)$	Cross-correlation function, watts.
a	Effective width in the direction of the magnetic field, m.
a_{ij}	Noise transport coefficients. $(i = 1,..., 5, j = 1,..., 5)$
B	Magnetic field intensity, webers/m^2.
B_o	D-c magnetic field intensity, webers/m^2.
B_c	Cutoff magnetic field intensity, webers/m^2.
B_m	Value of magnetic field for which the cathode current is maximum, webers/m^2.
$C(\tau)$	Auto-correlation function, watts/unit ohm.
c	Velocity of light, m/sec.
D	Normalized distance variable defined by $D = 2\pi e\ I_D/(m\epsilon_o)\ \omega_c^3$, m.
$D(\tau)$	Lag window defined by $D(\tau) = (1+\cos\pi\tau/Tm)/2$.
D_o	Value of D for ideal injection conditions, m.
D_1	Spatial scaling parameter.
d	Anode-cathode spacing, m.
d_1	Anode-sole spacing, m.
d_1'	Cathode-screen grid spacing, m.
dy_i	Incremental value in y at $y = y_i$, m.
dz_i	Incremental value of z at $z = z_i$, m.
E_o	Constant y-directed d-c field, volts/m.
E_x	x-component of the total field volts/m.

$E_{x_T}(t_i)$	x-component of the total field at time t_i, volts/m.
E_y	y-component of the total field, volts/m.
E_{y_o}	y-component of the d-c field, volts/m.
$(E_{y_o})_i$	y-component of the d-c field for the ith rectangle, volts/m.
E_{y_1}	y-component of the a-c field, volts/m.
$E_{y_{sc}}$	y-component of the space-charge field, volts/m.
$E_{y_T}(t_i)$	y-component of the total field at time t_i, volts/m.
E_z	z-component of the total field, volts/m.
E_{z_o}	z-component of the d-c field, volts/m.
$(E_{z_o})_i$	z-component of the d-c field for the ith rectangle, volts/m.
E_{z_1}	z-component of the a-c field, volts/m.
$E_{z_{sc}}$	z-component of the space-charge field, volts/m.
$E_{z_T}(t_i)$	z-component of the total field at time t_i, volts/m.
e	Electron charge, coulombs.
F(f,i)	Noise figure at frequency f for the ith rectangle.
F(s)	Cumulative distribution function for emitting s number of electrons.
f	Frequency, cycles/sec.
f(s)	Probability of emitting s electrons in time Δt.
G	Diocotron gain, db/m.
G_i	Random number associated with the initial z-component velocity.
h	Width of the cathode in the direction of the magnetic field, m.
I_o	Beam current, amp.
I_{o1}	Beam current from the first cathode, amp.
I_{o2}	Beam current from the second cathode, amp.

I_{o3}	Beam current from the third cathode, amp.
I_{op}	Beam current from one of the three cathodes, for a gun-anode parallel to the cathode,(in this case $I_{o1} = I_{o2} = I_{o3} = I_{op}$), amp.
I_1	A-c beam current density amps/m^2.
$\tilde{I}_1$	Defined by $\tilde{I}_1 = I_1\ e/m\epsilon_o$.
I_D	D-c beam current density, amps/m^2.
$\tilde{I}_D$	Normalized distance variable defined by $\tilde{I}_D = I_D\ e/m\epsilon_o$.
I_s	Saturation beam current density amps/m^2.
I_T	Total beam current density amps/m^2.
$\tilde{I}_T$	Defined by $\tilde{I}_T = I_T\ e/m\epsilon_o$.
I_y	y-component beam current density, amps/m^2.
$\tilde{I}_y$	Defined by $\tilde{I}_y = I_y\ e/m\epsilon_o$.
I_{y_o}	y-component d-c current density, amps/m^2.
I_z	z-component beam current density, amps/m^2.
$\tilde{I}_z$	Defined by $\tilde{I}_z = I_z\ e/m\epsilon_o$.
I_{z_o}	z-component d-c current density, amps/m^2.
j	$j = \sqrt{-1}$.
$\vec{\tilde{J}}_i(t_i)$	A-c current density vector at time t_i for the ith rectangle, amp/m^2.
$(J_{y_o})_i$	y-component d-c averaged current density for the ith rectangle, amps/m^2.
$J_{y_i}(t_i)$	Total y-component current density at time t_i for the ith rectangle.
$\tilde{J}_{y_i}(t_i)$	y-component a-c current density at time t_i for the ith rectangle.
$(J_{z_o})_i$	z-component averaged d-c current density for the ith rectangle, amps/m^2.
$J_{z_i}(t_i)$	z-component total current density at time t_i for the ith rectangle, amps/m^2.

$\tilde{J}_{z_i}(t_i)$	z-component a-c current density at time t_i for the ith rectangle, amps/m^2.
k	Boltzmann constant, joules/degree Kelvin.
L	Total number of unit time intervals used for averaging.
M	Maximum value of μ used in evaluating spectral power densities.
m	Mass of an electron, kgm.
$(N_o)_i$	Averaged number of electrons for the ith rectangle.
N_a	Average number of electrons emitted per unit time interval from the cathode.
$N_i(t_i)$	Total number of electrons in ith rectangle at time t_i.
N_j	Total number of electrons in the jth rectangle.
n(v)	Number of electrons per unit volume, $1/m^3$.
n_a	Average number of electrons emitted per unit time interval from each of the three different points on the cathode.
n_k	kth electron.
q_y	y-component total convection current density, amps/m^2.
q_{y_a}	y-component total convection current density at the a-plane, amps/m^2.
$q_{y_{a1}}$	y-component a-c convection current density at the a-plane, amps/m^2.
$\tilde{q}_{y_{a1}}$	Defined by $\tilde{q}_{y_{a1}} = q_{y_{a1}} e/m\epsilon_o$.
$q_{y_{b1}}$	y-component a-c convection current density at the b-plane.
q_z	z-component total convection current density, amps/m^2.
q_{za}	z-component total convection current density at the a-plane, amps/m^2.
$q_{z_{a1}}$	z-component a-c convection current density at the a-plane, amps/m^2.
$\tilde{q}_{z_{a1}}$	Defined by $\tilde{q}_{z_{a1}} = q_{z_{a1}} e/m\epsilon_o$.

$q_{z_{b1}}$	z-component a-c convection current density at the b-plane, amps/m^2.
R	Ratio of perturbation angular frequency to the cyclotron frequency, defined by $R = \omega/\omega_c$.
R_i	Random number associated with the initial y-component velocity.
R_{s_i}	Random number associated with emission of s_i electrons in ith unit time interval.
S(f,i)	Haus's noise parameter.
s_i	Defined by $s_i = (-2\eta V_m + \omega_c^2 y_m^2)\ mA_i^2/kT$.
s_i'	Value of s_i for $\omega_c = \omega_{cc}$.
s_i	Number of electrons emitted in ith unit time interval.
T_m	Total time used for evaluating spectral power densities, defined by $T_m = M\Delta t$, sec.
T_n	Total length of the record, sec.
T	Transit time, sec.
T-L	Temperature limited.
t	Thickness of the beam along the y-axis, m.
t_o	Emission time of the electron, sec.
t_a	Electron entrance time at the a-plane, sec.
u	Normalized y-component initial velocity.
u_{o_i}	Averaged velocity for the ith rectangle, m/sec.
u_c	Normalized value of $\dot{y}_{i_c}$.
$\vec{u}_i(t_i)$	A-c velocity vector for the ith rectangle at time t_i, m/sec.
V(y)	Potential as a function of y, volts.
V_o	D-c anode potential, volts.
V_{o1}	Potential distribution in the potential minimum region, volts.
V_{o2}	Potential distribution in the gun region, volts.
V_1	Potential at $y = y_1$.

$\vec{V}_i(t_i)$	A-c kinetic vector potential for the ith rectangle at time t_i, volts.
V_m	Potential at the potential minimum, volts.
V'_m	Value of V_m at $\omega_c = \omega_{cc}$, volts.
V_T	Total potential, volts.
V_{sc}	Space-charge potential, volts.
V_{y_c}	Normalized value of $\dot{y}_{i_c}^2$.
V_{y_i}	Normalized value of $\dot{y}_i^2$.
v	Normalized z-component initial velocity.
W(f)	Noise power spectrum in the neighborhood of the frequency f, watts sec.
W_{sc}	Space-charge weighting function.
w	Length of the cathode along the z-axis, m.
$\dot{x}$	x-component velocity, m/sec.
$\ddot{x}$	x-component acceleration, m/sec^2.
$\dot{x}(t_i)$	x-component velocity of an electron at time t_i, m/sec.
$\dot{y}$	y-component velocity, m/sec.
$\ddot{y}$	y-component acceleration, m/sec^2.
$\dddot{y}$	Total derivative of $\ddot{y}$ with respect to time, m/sec^3.
$\dot{y}(t_i)$	y-component velocity of an electron at time t_i, m/sec.
y_o	y-coordinate for ideal conditions in the interaction region, m.
$\dot{y}_o$	y-component d-c velocity, m/sec.
$(\dot{y}_o)_i$	y-component averaged velocity for the ith rectangle, m/sec.
$\dot{y}_1$	y-component a-c velocity, m/sec.
$\ddot{y}_1$	y-component a-c acceleration, m/sec^2.
$\dot{y}_a$	y-component velocity at the a-plane, m/sec.
$\ddot{y}_a$	y-component acceleration at the a-plane, m/sec^2.

$\dot{y}_{a1}$	y-component a-c velocity at the a-plane, m/sec.
$\ddot{y}_{a1}$	y-component a-c acceleration at the a-plane, m/sec^2.
$\dot{y}_{b1}$	y-component a-c velocity at the b-plane, m/sec.
y_{cr}	Value of y for which $d\dot{y}_o/dy = 0$, m.
$\dot{y}_i$	y-component initial velocity of an electron, m/sec.
$\bar{\dot{y}}_i$	y-component ensemble average initial velocity, m/sec.
$\dot{y}_i(t_i)$	y-component velocity for the ith rectangle at time t_i, m/sec.
$\tilde{\dot{y}}_i(t_i)$	y-component a-c velocity for the ith rectangle at time t_i, m/sec.
$\dot{y}_i(t_i,n_k)$	y-component velocity of the n_kth electron in the ith rectangle at time t_i, m/sec.
$\dot{y}_{i_c}$	Initial normal critical velocity, m/sec.
y_j	y-coordinate of the centroid of the jth rectangle in the Monte Carlo analysis, m. (In the density method analysis y_j refers to the y-coordinate of the jth plane.)
y_m	Position of the potential minimum, m.
y_m'	Value of y_m for $\omega_c = \omega_{cc}$, m.
$\dot{z}$	z-component velocity, m/sec.
$\ddot{z}$	z-component acceleration, m/sec^2.
$\dddot{z}$	Total derivative of $\ddot{z}$ with respect to time, m/sec^3.
$\dot{z}(t_i)$	z-component velocity of an electron at time t_i, m/sec.
z_o	z-coordinate at which beam enters the interaction region for ideal conditions, m.
$\dot{z}_o$	z-component d-c velocity, m/sec.
$(\dot{z}_o)_i$	z-component averaged velocity for the ith rectangle, m/sec.
$\dot{z}_1$	z-component a-c velocity, m/sec.
$\ddot{z}_1$	z-component a-c acceleration, m/sec^2.
$\dot{z}_a$	z-component velocity at the a-plane, m/sec.
$\ddot{z}_a$	z-component acceleration at the a-plane, m/sec^2.

$\dot{z}_{a1}$	z-component a-c velocity at the a-plane, m/sec.
$\ddot{z}_{a1}$	z-component a-c acceleration at the a-plane, m/sec^2.
$\dot{z}_{b1}$	z-component a-c velocity at the b-plane, m/sec.
$\dot{z}_i$	z-component initial velocity of an electron, m/sec.
$\overline{\dot{z}}_i$	z-component ensemble average initial velocity, m/sec.
$\dot{z}_i(t_i)$	z-component velocity for the ith rectangle at time t_i, m/sec.
$\tilde{\dot{z}}_i(t_i)$	z-component a-c velocity for the ith rectangle at time t_i, m/sec.
$\dot{z}_i(t_i,n_k)$	z-component velocity of the n_kth electron in the ith rectangle at time t_i, m/sec.
z_j	z-coordinate of the centroid of the jth rectangle (in the Monte Carlo analysis), m. (In the density method analysis z_j refers to the z-coordinate of the jth plane.)
α_i	Growth rate of the ith wave, nepers/m.
$\overline{\alpha}$	Phase constant defined by $\overline{\alpha} = \omega_c(t_a-t_o)/2 - \Phi/2$, radians.
β_i	Propagation constant of the ith wave, 1/m.
γ_i	Complex propagation constant, $(\gamma_i = \alpha_i+j\beta_i)$.
$\Delta E_{z_i}(t_i)$	y-component a-c field for the ith rectangle at time t_i, volts/m.
$\Delta E_{z_i}(t_i)$	z-component a-c field for the ith rectangle at time t_i, volts/m.
Δf	Spectral bandwidth, cycles/sec.
Δt	Unit of time, sec.
δ	Maximum thickness of the beam along the y-axis, m.
δ_y	Perturbation in transit time as evaluated from y-trajectory, sec.
δ_z	Perturbation in transit time as evaluated from z-trajectory, sec.
ϵ_o	Free-space dielectric constant, farads/m.
η	Defined by $\eta = \lvert e/m \rvert$, coulombs/kgm.

θ	Transit angle defined as $\theta = \omega_c T$, radians.
θ_o	Value of θ for which the effect of the initial velocities is negligible in evaluating the electron trajectories, radians.
$\Lambda(f,i)$	Haus's noise parameter for the ith rectangle.
λ_1	Coupling coefficient which relates z-component a-c current density fluctuations to the total a-c current density fluctuations.
λ_2	Coupling coefficient which relates z-component a-c velocity fluctuations to the total a-c velocity fluctuations.
μ	Defined by $\tau = \mu\Delta t$, $\mu = 0,1,\ldots, M$.
μ_o	Free-space permeability, henrys/m.
μ_1	Coupling coefficient which relates y-component a-c current density fluctuations to the total a-c current density fluctuations.
μ_2	Coupling coefficient which relates y-component a-c velocity fluctuations to the total a-c velocity fluctuations.
$\Pi(f,i)$	Haus's noise parameter for the ith rectangle.
ρ	Total space-charge density, coulombs/m^3.
ρ_o	D-c space-charge density, coulombs/m^3.
$(\rho_o)_i$	Average space-charge density for the ith rectangle, coulombs/m^3.
ρ_{o1}	D-c space-charge density in the potential minimum region, coulombs/m^3.
ρ_{o2}	D-c space-charge density in the gun region, coulombs/m^3.
ρ_1	A-c space-charge density, coulombs/m^3.
τ	This indicates the time for which the correlation functions are evaluated, sec.
$\Phi(f,i)$	Self-power spectral density for the velocity fluctuations for the ith rectangle, watts/unit ohm.
Φ	Phase constant defined by Eq. 2.8, radians.
$\Psi(f,i)$	Self-power spectral density for the current fluctuations for the ith rectangle, watts/unit ohm.

$\psi(y)$	Normalized normal velocity neglecting the initial velocities.
ω	Perturbation frequency, rad/sec.
ω_p	Plasma frequency, rad/sec.
ω_c	Cyclotron frequency defined by $\omega_c = \eta B$, rad/sec.
ω_{cc}	Cutoff cyclotron frequency for the cathode-anode diode, rad/sec.
ω_{ccs}	Cutoff cyclotron frequency for the cathode-screen grid diode, rad/sec.

DISTRIBUTION LIST

No. Copies	Agency
1	Commanding General, U. S. Army Electronics Research & Development Laboratory, Fort Monmouth, New Jersey, ATTN: Adjutant Branch; Mail, File & Records
1	Commanding General, U. S. Army Electronics Research & Development Laboratory, Fort Monmouth, New Jersey, ATTN: Chief, Technical Documents Center
3	Commanding General, U. S. Army Electronics Research & Development Laboratory, Fort Monmouth, New Jersey, ATTN: Chief, Technical Information Division (FOR RETRANSMITTAL TO ACCREDITED BRITISH AND CANADIAN GOVERNMENT REPRESENTATIVES)
1	Commanding General, U. S. Army Electronics Research & Development Laboratory, Fort Monmouth, New Jersey, ATTN: Director of Research/or Engineering
1	Commanding Officer, U. S. Army Electronics Research & Development Laboratory, Fort Monmouth, New Jersey, ATTN: Technical Information Division, FOR RETRANSMITTAL TO: FRENCH MILITARY ATTACHE
1	Commanding Officer, U. S. Army Electronics Research & Development Laboratory, Fort Monmouth, New Jersey, ATTN: Radar Division, Surveillance Department
1	Commanding Officer, U. S. Army Electronics Research & Development Laboratory, Fort Monmouth, New Jersey, ATTN: SELRA/SL-PR, Mr. Garoff
1	Commanding Officer, U. S. Army Electronics Research & Development Laboratory, Fort Monmouth, New Jersey, ATTN: SELRA/SL-PR, Technical Staff
1	Commanding Officer, U. S. Army Electronics Research & Development Laboratory, Fort Monmouth, New Jersey, ATTN: SELRA/SL-PRG, Mr. Zinn
1	Commanding Officer, U. S. Army Electronics Research & Development Laboratory, Fort Monmouth, New Jersey, ATTN: SELRA/SL-PRT, Mr. Kaplan
3	Continental Army Command Liaison Office, U. S. Army Electronics Research & Development Laboratory, Fort Monmouth, New Jersey
1	Mail & Records, Electronic Components Research Department, U. S. Army Electronics Research & Development Laboratory, Fort Monmouth, New Jersey

No. Copies	Agency
5	Project Engineer, Electronic Components Research Department, U. S. Army Electronics Research & Development Laboratory, Fort Monmouth, New Jersey, ATTN: SELFM/EL-PR
1	Commander, Army Rocket & Guided Missile Agency, ATTN: Technical Library, Redstone Arsenal, Alabama
1	Commanding Officer, U. S. Army Signal Equipment Support Agency, Fort Monmouth, New Jersey, ATTN: SELFM/ES-ASA
1	U. S. Army Signal Corps, The University of Michigan, P. O. Box 618, Ann Arbor, Michigan, ATTN: John P. Dennis, Resident Contract Administrator
1	Commanding General, Aberdeen Proving Ground, Aberdeen, Maryland, ATTN: Development & Proof Service, Fire Control Division, Capt. Alter
1	Commander, Air Force Cambridge Research Laboratories, ATTN: Research Library, CRXL-R, L. G. Hanscom Field, Bedford, Massachusetts
1	Commander, Air Force Cambridge Research Center, Air Research & Development Command, 224 Albany Street, Cambridge 39, Massachusetts, ATTN: Tube Group
1	Commanding Officer, Air Force Office of Scientific Research, Washington 25, D. C., ATTN: SRYA
10	Commander, Armed Services Technical Information Agency, Arlington Hall Station, Arlington 12, Virginia
1	Commanding General, U. S. Army Electronic Proving Ground, Fort Huachuca, Arizona
1	The European Office, U. S. Army Research & Development Liaison Group, APO 757, New York, New York, FOR RETRANSMITTAL TO: Contractor, DA 91-508-EUC-986
1	Commanding General, U. S. Army Electronics Command, ATTN: AMSEL-RD, Fort Monmouth, New Jersey
1	Commanding General, White Sands Missile Range, New Mexico, ATTN: ORDBS-OM-Technical Library-169
1	Mr. W. J. Reigger, Code 691 A4, Microwave Tube Branch, Bureau of Ships, Department of the Navy, Washington 25, D. C.
1	Mr. J. J. Sullivan, Code 691 A4, Microwave Tube Branch, Bureau of Ships, Department of the Navy, Washington 25, D. C.
1	Dr. Robert T. Young, Chief, Electron Tube Branch, Diamond Ordnance Fuze Laboratories, Washington 25, D. C.

No. Copies	Agency
1	Director, U. S. Naval Research Laboratory, Code 2027, Washington 25, D. C.
1	Commanding Officer and Director, U. S. Navy Electronics Laboratory, San Diego 52, California
1	Commander, Rome Air Development Center, Griffiss Air Force Base, Rome, New York, ATTN: RAYLD
1	Commanding Officer, 9560th TSU, Signal Corps Electronics Research Unit, P. O. Box 205, Mountain View, California
2	Commander, Aeronautical Systems Division, Wright-Patterson Air Force Base, Ohio, ATTN: ASRNET
1	Applied Radiation Corporation, Walnut Creek, California, ATTN: Mr. N. J. Norris
1	Bell Telephone Laboratories, Inc., Murray Hill Laboratory, Murray Hill, New Jersey, ATTN: H. M. Olson
1	Bell Telephone Laboratories, Inc., Murray Hill Laboratory, Murray Hill, New Jersey, ATTN: Dr. J. R. Pierce
1	Mr. A. G. Peifer, Bendix Corporation, Research Laboratories, Northwestern Highway and 10 1/2 Mile Road, Detroit 35, Michigan
1	Dr. J. G. Meeker, Bendix Corporation, Research Laboratories, Northwestern Highway and 10 1/2 Mile Road, Detroit 35, Michigan
1	Bendix Corporation, Systems Planning Division, Ann Arbor, Michigan, ATTN: Technical Library
1	Professor R. M. Saunders, Chairman, Department of Electrical Engineering, University of California, Berkeley 4, California
1	The Electronics Research Laboratory, 427 Cory Hall, University of California, Berkeley 4, California, ATTN: Mr. A. Simmons
1	Professor W. G. Worcester, University of Colorado, Department of Electrical Engineering, Boulder, Colorado
1	Columbia University, Columbia Radiation Laboratory, 538 W. 130th Street, New York 27, New York
1	Dr. George E. Dombrowski, Associate Professor of Electrical Engineering, The University of Connecticut, Storrs, Connecticut
1	Mr. C. Dalman, Cornell University, Department of Electrical Engineering, Ithaca, New York

No. Copies	Agency
1	Dr. Bernard Arfin, Eitel-McCullough, Inc., San Bruno, California
1	Mr. Donald Priest, Eitel-McCullough, Inc., San Bruno, California
1	Mr. T. Marchese, Federal Telecommunication Laboratory, Inc., 500 Washington Avenue, Nutley, New Jersey
1	University of Florida, Department of Electrical Engineering, Gainesville, Florida
1	General Electric Company, Electron Tube Division of the Research Laboratory, The Knolls, Schenectady, New York, ATTN: Dr. E. D. McArthur
1	Mr. S. Webber, General Electric Microwave Laboratory, 601 California Avenue, Palo Alto, California
1	Harvard University, Technical Reports Collection, Room 303A, Pierce Hall, Cambridge 38, Massachusetts, ATTN: Librarian
1	Dr. John Mendel, Hughes Aircraft Company, Electron Tube Laboratory, Culver City, California
1	Hughes Aircraft Company, Florence and Teale, Culver City, California, ATTN: Mr. Nicholas E. Devereux, Technical Document Center
1	Mr. James B. Maher, Librarian, R & D Technical Library, Hughes Aircraft Company, Culver City, California
1	University of Illinois, Electrical Engineering Research Laboratory, Urbana, Illinois, ATTN: Technical Editor
1	Carlyle Barton Laboratory, The Johns Hopkins University, Charles and 35th Streets, Baltimore 18, Maryland, ATTN: Librarian
1	Litton Industries, 1025 Brittan Avenue, San Carlos, California, ATTN: Dr. N. Moore
1	Mr. R. Butman, Massachusetts Institute of Technology, Lincoln Laboratory, P. O. Box 73, Lexington 73, Massachusetts
1	Document Library, Massachusetts Institute of Technology, Research Laboratory of Electronics, Cambridge 39, Massachusetts
1	Signal Corps Liaison Office, Massachusetts Institute of Technology, 77 Massachusetts Avenue, Bldg. 20C-116, Cambridge, Massachusetts, ATTN: Dr. A. D. Bedrosian

No. Copies	Agency
1	Dr. S. F. Kaisel, Microwave Electronic Corporation, 4061 Transport Street, Palo Alto, California
1	University of Minnesota, Department of Electrical Engineering, Minneapolis, Minnesota, ATTN: Dr. W. G. Shepherd
1	Ohio State University, Department of Electrical Engineering, Columbus 10, Ohio, ATTN: Professor E. M. Boone
1	Polytechnic Institute of Brooklyn, Library, Microwave Research Institute, Brooklyn 1, New York
1	Mr. W. C. Brown, Spencer Laboratory, Wayside Road, Raytheon Company, Burlington, Massachusetts
1	Raytheon Company, Spencer Laboratories, Burlington, Massachusetts, ATTN: John M. Osepchuk
1	Spencer Laboratory Library, Raytheon Company, Wayside Road, Burlington, Massachusetts, ATTN: W. W. Teich
1	Dr. Bernard Hershenov, RCA Laboratories, Princeton, New Jersey
1	Accessions Department (International Exchange Section) National Lending Library for Science and Technology, Boston SPA, Yorkshire, England
1	Dr. W. M. Webster, Director, Electronic Research Laboratory, RCA Laboratory, Princeton, New Jersey
1	Technical Library, Radio Corporation of America, RCA Laboratories, Princeton, New Jersey
1	Mr. Hans Jenny, RCA Electron Tube Division, 415 S. 5th Street, Harrison, New Jersey
1	Mr. P. Bergman, Sperry Corporation, Electronic Tube Division, Gainesville, Florida
1	Sperry Gyroscope Company, Great Neck, Long Island, New York, ATTN: English Library
1	Electronics Research Laboratory, Stanford University, Stanford, California, ATTN: Mr. David C. Bacon, Assistant Director
1	Microwave Laboratory, Librarian, W. W. Hansen Laboratories of Physics, Stanford University, Stanford, California
1	Stanford Research Institute, Stanford, California, ATTN: Mr. M. Pease

No. Copies	Agency
1	Dr. Louis R. Bloom, Sylvania Electric Products, Inc., Physics Laboratory, 208-20 Willetts Point Blvd., Bayside, L. I., New York
1	Mr. Ernest E. Hollis, Sylvania Electronic Systems, 100 First Avenue, Waltham 54, Massachusetts
1	Dr. J. Needle, Sylvania Microwave Tube Laboratory, 500 Evelyn Avenue, Mountain View, California
1	Varian Associates, 611 Hansen Way, Palo Alto, California, ATTN: Technical Library
1	Mr. A. E. Harrison, University of Washington, Department of Electrical Engineering, Seattle 5, Washington
1	Dr. D. A. Roberts, Watkins-Johnson Company, 3333 Hillview Avenue, Palo Alto, California
1	Dr. D. A. Watkins, Watkins-Johnson Company, 3333 Hillview Avenue, Palo Alto, California
1	Mr. Sheldon S. King, English Librarian, Westinghouse Electric Corporation, P. O. Box 284, Elmira, New York
1	Mr. Gerald Klein, Manager, Microwave Tubes Section, Applied Research Department, Westinghouse Electric Corporation, Box 746, Baltimore 3, Maryland
1	Dr. Om P. Gandhi, Central Electronics, Engineering Research Institute, Pilani, Rajasthan, India

AD _____

The University of Michigan, Electron Physics Laboratory, Ann Arbor, Michigan. NOISE TRANSPORT IN CROSSED-FIELD DEVICES, by R. P. Wadhwa. December, 1962, 401 pp. incl. illus. (Contract No. DA-36-039 AMC-00027(E), Project No. 3A99-13-001)

This study of generation and propagation of noise in injected-beam crossed-field devices could easily be applied to the investigation of analogous phenomena in magnetrons and other types of crossed-field devices. Llewellyn-Peterson equations are derived. The final noise transport coefficients are expressed in both the normal and tangential velocity components and are evaluated for different physical models and for several values of the perturbation and plasma frequencies.

By considering Maxwellian velocity distribution and potential minimum several d-c parameters are evaluated for two values of magnetic field and are used to solve for the propagation constants. A large growth is found when the beam is decelerated along the normal axis. The growth for the slow wave is larger than that for the fast wave. Numerical techniques are used to generate noise and investigate its propagation along the beam by using the Monte Carlo technique. Various parts of the beam are analyzed. The current fluctuations are greatly reduced by the potential minimum while the velocity fluctuations are increased or decreased as the beam is accelerated or decelerated respectively, although there is an overall growth in traversing a complete cycloid. The overall growth of the slow wave is larger than that of the fast wave. The measured value of the electron equivalent temperature is very large and remains nearly constant in the interaction region. The intrinsic oscillations and the propagation of an r-f signal injected near the cathode can be controlled by varying the d-c parameters.

UNCLASSIFIED

1. Development of Llewellyn-Peterson Equations
2. Results of Llewellyn-Peterson Analysis
3. Development and Results of Density Function Analysis
4. Derivation and Results of Monte Carlo Analysis
5. Experimental Investigation of Noise in Injected-Beam Crossed-Field Devices
6. Experimental Results
I. Wadhwa, R. P.

UNCLASSIFIED

AD _____

The University of Michigan, Electron Physics Laboratory, Ann Arbor, Michigan. NOISE TRANSPORT IN CROSSED-FIELD DEVICES, by R. P. Wadhwa. December, 1962, 401 pp. incl. illus. (Contract No. DA-36-039 AMC-00027(E), Project No. 3A99-13-001)

This study of generation and propagation of noise in injected-beam crossed-field devices could easily be applied to the investigation of analogous phenomena in magnetrons and other types of crossed-field devices. Llewellyn-Peterson equations are derived. The final noise transport coefficients are expressed in both the normal and tangential velocity components and are evaluated for different physical models and for several values of the perturbation and plasma frequencies.

By considering Maxwellian velocity distribution and potential minimum several d-c parameters are evaluated for two values of magnetic field and are used to solve for the propagation constants. A large growth is found when the beam is decelerated along the normal axis. The growth for the slow wave is larger than that for the fast wave. Numerical techniques are used to generate noise and investigate its propagation along the beam by using the Monte Carlo technique. Various parts of the beam are analyzed. The current fluctuations are greatly reduced by the potential minimum while the velocity fluctuations are increased or decreased as the beam is accelerated or decelerated respectively, although there is an overall growth in traversing a complete cycloid. The overall growth of the slow wave is larger than that of the fast wave. The measured value of the electron equivalent temperature is very large and remains nearly constant in the interaction region. The intrinsic oscillations and the propagation of an r-f signal injected near the cathode can be controlled by varying the d-c parameters.

UNCLASSIFIED

1. Development of Llewellyn-Peterson Equations
2. Results of Llewellyn-Peterson Analysis
3. Development and Results of Density Function Analysis
4. Derivation and Results of Monte Carlo Analysis
5. Experimental Investigation of Noise in Injected-Beam Crossed-Field Devices
6. Experimental Results
I. Wadhwa, R. P.

UNCLASSIFIED

AD _____

The University of Michigan, Electron Physics Laboratory, Ann Arbor, Michigan. NOISE TRANSPORT IN CROSSED-FIELD DEVICES, by R. P. Wadhwa. December, 1962, 401 pp. incl. illus. (Contract No. DA-36-039 AMC-00027(E), Project No. 3A99-13-001)

This study of generation and propagation of noise in injected-beam crossed-field devices could easily be applied to the investigation of analogous phenomena in magnetrons and other types of crossed-field devices. Llewellyn-Peterson equations are derived. The final noise transport coefficients are expressed in both the normal and tangential velocity components and are evaluated for different physical models and for several values of the perturbation and plasma frequencies.

By considering Maxwellian velocity distribution and potential minimum several d-c parameters are evaluated for two values of magnetic field and are used to solve for the propagation constants. A large growth is found when the beam is decelerated along the normal axis. The growth for the slow wave is larger than that for the fast wave. Numerical techniques are used to generate noise and investigate its propagation along the beam by using the Monte Carlo technique. Various parts of the beam are analyzed. The current fluctuations are greatly reduced by the potential minimum while the velocity fluctuations are increased or decreased as the beam is accelerated or decelerated respectively, although there is an overall growth in traversing a complete cycloid. The overall growth of the slow wave is larger than that of the fast wave. The measured value of the electron equivalent temperature is very large and remains nearly constant in the interaction region. The intrinsic oscillations and the propagation of an r-f signal injected near the cathode can be controlled by varying the d-c parameters.

UNCLASSIFIED

1. Development of Llewellyn-Peterson Equations
2. Results of Llewellyn-Peterson Analysis
3. Development and Results of Density Function Analysis
4. Derivation and Results of Monte Carlo Analysis
5. Experimental Investigation of Noise in Injected-Beam Crossed-Field Devices
6. Experimental Results
I. Wadhwa, R. P.

UNCLASSIFIED

AD _____

The University of Michigan, Electron Physics Laboratory, Ann Arbor, Michigan. NOISE TRANSPORT IN CROSSED-FIELD DEVICES, by R. P. Wadhwa. December, 1962, 401 pp. incl. illus. (Contract No. DA-36-039 AMC-00027(E), Project No. 3A99-13-001)

This study of generation and propagation of noise in injected-beam crossed-field devices could easily be applied to the investigation of analogous phenomena in magnetrons and other types of crossed-field devices. Llewellyn-Peterson equations are derived. The final noise transport coefficients are expressed in both the normal and tangential velocity components and are evaluated for different physical models and for several values of the perturbation and plasma frequencies.

By considering Maxwellian velocity distribution and potential minimum several d-c parameters are evaluated for two values of magnetic field and are used to solve for the propagation constants. A large growth is found when the beam is decelerated along the normal axis. The growth for the slow wave is larger than that for the fast wave. Numerical techniques are used to generate noise and investigate its propagation along the beam by using the Monte Carlo technique. Various parts of the beam are analyzed. The current fluctuations are greatly reduced by the potential minimum while the velocity fluctuations are increased or decreased as the beam is accelerated or decelerated respectively, although there is an overall growth in traversing a complete cycloid. The overall growth of the slow wave is larger than that of the fast wave. The measured value of the electron equivalent temperature is very large and remains nearly constant in the interaction region. The intrinsic oscillations and the propagation of an r-f signal injected near the cathode can be controlled by varying the d-c parameters.

UNCLASSIFIED

1. Development of Llewellyn-Peterson Equations
2. Results of Llewellyn-Peterson Analysis
3. Development and Results of Density Function Analysis
4. Derivation and Results of Monte Carlo Analysis
5. Experimental Investigation of Noise in Injected-Beam Crossed-Field Devices
6. Experimental Results
I. Wadhwa, R. P.

UNCLASSIFIED

AD _____

The University of Michigan, Electron Physics Laboratory, Ann Arbor, Michigan. NOISE TRANSPORT IN CROSSED-FIELD DEVICES, by R. P. Wadhwa. December, 1962, 401 pp. incl. illus. (Contract No. DA-36-039 AMC-00027(E), Project No. 5A99-13-001)

This study of generation and propagation of noise in injected-beam crossed-field devices could easily be applied to the investigation of analogous phenomena in magnetrons and other types of crossed-field devices. Llewellyn-Peterson equations are derived. The final noise transport coefficients are expressed in both the normal and tangential velocity components and are evaluated for different physical models and for several values of the perturbation and plasma frequencies.

By considering Maxwellian velocity distribution and potential minimum several d-c parameters are evaluated for two values of magnetic field and are used to solve for the propagation constants. A large growth is found when the beam is decelerated along the normal axis. The growth for the slow wave is larger than that for the fast wave. Numerical techniques are used to generate noise and investigate its propagation along the beam by using the Monte Carlo technique. Various parts of the beam are analyzed. The current fluctuations are greatly reduced by the potential minimum while the velocity fluctuations are increased or decreased as the beam is accelerated or decelerated respectively, although there is an overall growth in traversing a complete cycloid. The overall growth of the slow wave is larger than that of the fast wave. The measured value of the electron equivalent temperature is very large and remains nearly constant in the interaction region. The intrinsic oscillations and the propagation of an r-f signal injected near the cathode can be controlled by varying the d-c parameters.

UNCLASSIFIED

1. Development of Llewellyn-Peterson Equations
2. Results of Llewellyn-Peterson Analysis
3. Development and Results of Density Function Analysis
4. Derivation and Results of Monte Carlo Analysis
5. Experimental Investigation of Noise in Injected-Beam Crossed-Field Devices
6. Experimental Results

I. Wadhwa, R. P.

UNCLASSIFIED

AD _____

The University of Michigan, Electron Physics Laboratory, Ann Arbor, Michigan. NOISE TRANSPORT IN CROSSED-FIELD DEVICES, by R. P. Wadhwa. December, 1962, 401 pp. incl. illus. (Contract No. DA-36-039 AMC-00027(E), Project No. 5A99-13-001)

This study of generation and propagation of noise in injected-beam crossed-field devices could easily be applied to the investigation of analogous phenomena in magnetrons and other types of crossed-field devices. Llewellyn-Peterson equations are derived. The final noise transport coefficients are expressed in both the normal and tangential velocity components and are evaluated for different physical models and for several values of the perturbation and plasma frequencies.

By considering Maxwellian velocity distribution and potential minimum several d-c parameters are evaluated for two values of magnetic field and are used to solve for the propagation constants. A large growth is found when the beam is decelerated along the normal axis. The growth for the slow wave is larger than that for the fast wave. Numerical techniques are used to generate noise and investigate its propagation along the beam by using the Monte Carlo technique. Various parts of the beam are analyzed. The current fluctuations are greatly reduced by the potential minimum while the velocity fluctuations are increased or decreased as the beam is accelerated or decelerated respectively, although there is an overall growth in traversing a complete cycloid. The overall growth of the slow wave is larger than that of the fast wave. The measured value of the electron equivalent temperature is very large and remains nearly constant in the interaction region. The intrinsic oscillations and the propagation of an r-f signal injected near the cathode can be controlled by varying the d-c parameters.

UNCLASSIFIED

1. Development of Llewellyn-Peterson Equations
2. Results of Llewellyn-Peterson Analysis
3. Development and Results of Density Function Analysis
4. Derivation and Results of Monte Carlo Analysis
5. Experimental Investigation of Noise in Injected-Beam Crossed-Field Devices
6. Experimental Results

I. Wadhwa, R. P.

UNCLASSIFIED

AD _____

The University of Michigan, Electron Physics Laboratory, Ann Arbor, Michigan. NOISE TRANSPORT IN CROSSED-FIELD DEVICES, by R. P. Wadhwa. December, 1962, 401 pp. incl. illus. (Contract No. DA-36-039 AMC-00027(E), Project No. 5A99-13-001)

This study of generation and propagation of noise in injected-beam crossed-field devices could easily be applied to the investigation of analogous phenomena in magnetrons and other types of crossed-field devices. Llewellyn-Peterson equations are derived. The final noise transport coefficients are expressed in both the normal and tangential velocity components and are evaluated for different physical models and for several values of the perturbation and plasma frequencies.

By considering Maxwellian velocity distribution and potential minimum several d-c parameters are evaluated for two values of magnetic field and are used to solve for the propagation constants. A large growth is found when the beam is decelerated along the normal axis. The growth for the slow wave is larger than that for the fast wave. Numerical techniques are used to generate noise and investigate its propagation along the beam by using the Monte Carlo technique. Various parts of the beam are analyzed. The current fluctuations are greatly reduced by the potential minimum while the velocity fluctuations are increased or decreased as the beam is accelerated or decelerated respectively, although there is an overall growth in traversing a complete cycloid. The overall growth of the slow wave is larger than that of the fast wave. The measured value of the electron equivalent temperature is very large and remains nearly constant in the interaction region. The intrinsic oscillations and the propagation of an r-f signal injected near the cathode can be controlled by varying the d-c parameters.

UNCLASSIFIED

1. Development of Llewellyn-Peterson Equations
2. Results of Llewellyn-Peterson Analysis
3. Development and Results of Density Function Analysis
4. Derivation and Results of Monte Carlo Analysis
5. Experimental Investigation of Noise in Injected-Beam Crossed-Field Devices
6. Experimental Results

I. Wadhwa, R. P.

UNCLASSIFIED

AD _____

The University of Michigan, Electron Physics Laboratory, Ann Arbor, Michigan. NOISE TRANSPORT IN CROSSED-FIELD DEVICES, by R. P. Wadhwa. December, 1962, 401 pp. incl. illus. (Contract No. DA-36-039 AMC-00027(E), Project No. 5A99-13-001)

This study of generation and propagation of noise in injected-beam crossed-field devices could easily be applied to the investigation of analogous phenomena in magnetrons and other types of crossed-field devices. Llewellyn-Peterson equations are derived. The final noise transport coefficients are expressed in both the normal and tangential velocity components and are evaluated for different physical models and for several values of the perturbation and plasma frequencies.

By considering Maxwellian velocity distribution and potential minimum several d-c parameters are evaluated for two values of magnetic field and are used to solve for the propagation constants. A large growth is found when the beam is decelerated along the normal axis. The growth for the slow wave is larger than that for the fast wave. Numerical techniques are used to generate noise and investigate its propagation along the beam by using the Monte Carlo technique. Various parts of the beam are analyzed. The current fluctuations are greatly reduced by the potential minimum while the velocity fluctuations are increased or decreased as the beam is accelerated or decelerated respectively, although there is an overall growth in traversing a complete cycloid. The overall growth of the slow wave is larger than that of the fast wave. The measured value of the electron equivalent temperature is very large and remains nearly constant in the interaction region. The intrinsic oscillations and the propagation of an r-f signal injected near the cathode can be controlled by varying the d-c parameters.

UNCLASSIFIED

1. Development of Llewellyn-Peterson Equations
2. Results of Llewellyn-Peterson Analysis
3. Development and Results of Density Function Analysis
4. Derivation and Results of Monte Carlo Analysis
5. Experimental Investigation of Noise in Injected-Beam Crossed-Field Devices
6. Experimental Results

I. Wadhwa, R. P.

UNCLASSIFIED